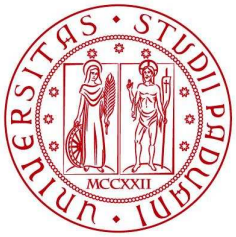

UNIVERSITÀ
DEGLI STUDI
DI PADOVA

Sede Amministrativa: Università degli Studi di Padova
Dipartimento di Fisica e Astronomia

SCUOLA DI DOTTORATO DI RICERCA IN ASTRONOMIA
Ciclo XXIV

THE ROLE OF DUST IN MODELS OF POPULATION SYNTHESIS

Direttore della scuola: Ch.mo Prof. Giampaolo Piotto
Supervisore: Ch.mo Prof. Cesare Chiosi
Correlatore: Dott. Lorenzo Piovan
Correlatore: Dott.ssa Rosaria Tantalo

Dottoranda
Letizia Pasqua Cassarà

"A l'alta fantasia qui mancò possa;
ma già volgeva il mio disio e 'l velle,
sì come rota ch'igualmente è mossa,
***l'amor che move il sole e l'altre stelle**."*

Dante Alighieri
Divina Commedia
Paradiso
Canto XXIII

Dedicated to my mum

Riassunto

In questi ultimi anni, lo studio delle galassie ad alto redshift è un argomento in piena evoluzione dal punto di vista osservativo; le survey fotometriche hanno consentito osservazioni di galassie sempre più distanti e deboli con una crescente efficienza, permettendo uno studio via via più approfondito dell'evoluzione galattica al variare del redshift. Le osservazioni mostrano un Universo ad alto-z fortemente oscurato dalle polveri: l'effetto della polvere é di assorbire la radiazione stellare nel range UV/ottico dello spettro elettromagnetico e di riemettere tale radiazione nell'infrarosso, modificando quindi profondamente la forma delle distribuzioni spettrali di energia (SEDs) delle galassie oscurate (Silva et al. 1998; Piovan et al. 2006b; Popescu et al. 2011), e di ostacolare l'interpretazione dei loro parametri fisici fondamentali, quali l'età, la metallicità, la funzione iniziale di massa (IMF), le popolazioni stellari (SSP), la storia di formazione stellare. Solo tenendo conto dell'emissione proveniente da tutte le lunghezze d'onda è possibile studiare le proprietà delle galassie per mezzo della sintesi evolutiva di popolazione (EPS).

Ha quindi notevole importanza calcolare sequenze evolutive di modelli spettrali di galassie di diverso tipo morfologico, includendo gli effetti della polvere, sia nell'universo locale che ad alto redshift (Narayanan et al. 2010; Jonsson et al. 2010; Grassi et al. 2010; Pipino et al. 2011; Popescu et al. 2011): questo approccio ovviamente aumenta la complessità del lavoro e porta in genere ad avere un numero molto più elevato di parametri che influenzano i risultati delle simulazioni, da confrontare con le osservazioni.

In questa tesi, gli effetti della polvere sulle galassie sono stati profondamente studiati e analizzati sia dal punto di vista chimico che spettrofotometrico, per galassie di diversi tipo morfologici, a vari livelli, cercando di migliorare il trattamento dell' estinzione, emissione, formazione ed evoluzione della polvere nelle nostre simulazioni. In questo lavoro: (a) abbiamo introdotto e studiato gli effetti della polvere nelle isocrone e nelle popolazioni stellari, introducendo un trattamento allo stato dell'arte della fase di ramo asintotico delle giganti (AGB), per stelle di massa piccola e intermedia, considerando le *shells* di polveri circondanti tali oggetti; (b) abbiamo sviluppato e testato modelli *state-of-art* di galassie di diversi tipi morfologici, (E, S0, Sa, Sb, Sc,

Sd e dischi), includendo tutti gli effetti locali e globali legati all'estinzione e emissione delle polveri. Abbiamo presentato e testato i modelli in diversi sistemi fotometrici, sia per l'Universo locale che ad alto redshif; (c) allo scopo di migliorare le informazioni fornite dal codice chimico al codice di sintesi di popolazione, abbiamo sviluppato e presentato una descrizione attuale dell'evoluzione e della formazione della polvere nelle galassie a spirale, trattando in modo completo gli *yields* di polvere e i processi di accrescimento/distruzione. Questo modello raffinato sarà poi in futuro utilizzato come base per i modelli spettro-fotometrici, che includano un'interfaccia chimica più avanzata. In particolare, la Via Lattea stato scelta come il laboratorio ideale per studiare il ciclo della polvere (Zhukovska et al. 2008) e il susseguente impatto dello stesso sulla formazione delle galassie, con l'obiettivo di (1) estendere il modello chimico polveroso alle galassie ellittiche, di tipo intermedio e *starburst* e (2) interfacciarlo al nostro codice spettro-fotometrico.

Abstract

During these last years, with the advent of modern telescopes and satellites, studies about *high redshift galaxies* are topics in great development from an observational point of view; photometric surveys permit observations of very far and faint galaxies with bigger efficiency, thus allowing to study the galactic evolution with redshift. Observations show a strongly obscured high-z universe featuring huge quantities of dust (Omont et al. 2001; Shapley et al. 2001; Bertoldi et al. 2003; Robson et al. 2004; Wang et al. 2008; Wang et al. 2008; Gallerani et al. 2010; Michałowski et al. 2010; Michałowski et al. 2010). Dust absorbs the stellar radiation in the UV/optical range of the electromagnetic spectrum and re-emits it in the IR, so it deeply changes the shape of the observed spectral energy distributions (SEDs) of obscured galaxies (Silva et al. 1998; Piovan et al. 2006b; Popescu et al. 2011), hampering their interpretation in terms of the fundamental physical parameters, such as age, metallicity, initial mass function (IMF), mix of stellar populations, star formation history (SFH). Only taking into account all the spectral range of emission it is possible to study the properties of galaxies by means of the evolutionary population synthesis (EPS) models.

It is therefore mandatory to calculate evolutionary sequences of spectral models for galaxies of various morphological types, including the effects of dust, both for the local universe and high redshift objects (Narayanan et al. 2010; Jonsson et al. 2010; Grassi et al. 2010; Pipino et al. 2011; Popescu et al. 2011): this approach leads to a growing complexity and typically to a much larger set of parameters influencing the results of the simulations to be then compared with the observations.

In this thesis, the effects of dust on galaxies have been deeply studied and considered in both chemical and spectro-photometric simulations of galaxies of different morphological types at many different levels, trying to improve the treatment of dust extinction, emission, formation and evolution in our models.
In this work: (a) we introduced and studied the effects of dust in isochrones and SEDs of SSPs with an improved state-of-art treatment of the AGB phase in intermediate and low mass stars, taking into account circumstellar dust shells around them; (b) we developed and tested state-of-art models of galaxies of different morphological

types, E, S0, Sa, Sb, Sc, Sd and disks, with the inclusion of all the local and global effects of dust extinction and emission. We presented and tested the models in many different photometric systems, both for the local and high redshift universe; (c) in order to improve upon the information supplied by the chemical code to the EPS, we developed and presented a state-of-art description of the evolution and formation of dust in spiral galaxies, with a complete treatment of dust yields and dust accretion/destruction processes. This refined model should be in future used to support the spectro-photometric models with a more advanced chemical interface. In particular, the Milky Way has been chosen as the ideal laboratory to study the dust cycle (Zhukovska et al. 2008) and its impact on the wider subject of galaxy formation, with the target to later (1) extend the dusty chemical model to ellipticals, intermediate type and starburst galaxies and (2) interface it to our spectro-photometric code.

Contents

List of Figures

List of Tables

Introduction

In the fascinating subject of the origin and evolution of galaxies, the interstellar dust is acquiring a primary role because of its growing importance in the observations of the high-z Universe (Omont et al. 2001; Shapley et al. 2001; Bertoldi et al. 2003; Robson et al. 2004; Wang et al. 2008; Wang et al. 2008; Gallerani et al. 2010; Michałowski et al. 2010; Michałowski et al. 2010) and the theoretical spectrophotometric, dynamical, and chemical modelling of galaxies (Narayanan et al. 2010; Jonsson et al. 2010; Grassi et al. 2010; Pipino et al. 2011; Popescu et al. 2011).

Indeed, the evidence of highly obscured QSOs and galaxies already in place at high-z leads necessarily to a new generation of theoretical models where dust is a key ingredient that cannot be neglected, if we want to obtain precious clues on the fundamental question about when and how galaxies formed and evolved.

First of all, dust absorbs the stellar radiation in the UV/optical range of the electromagnetic spectrum and re-emits it in the IR, so deeply changing the shape of the observed spectral energy distributions (SEDs) of obscured galaxies (Silva et al. 1998; Piovan et al. 2006b; Popescu et al. 2011); second, it strongly affects the production of molecular hydrogen and the local amount of UV radiation in galaxies thus playing a strong role in the star formation process via the cooling mechanisms (Yamasawa et al. 2011). The inclusion of dust in the models leads to a growing complexity and typically to a much larger set of parameters influencing the results of the simulations to be then compared with the observations.

Dust takes part to the long debated question about the origin and formation of galaxies, e.g.: when galaxies became obscured to the stellar light? What is the stellar formation rate of primordial galaxies? For what concerns the observations of galaxies of the local Universe, there are two main circumstances in which dust interacts with the stellar light, meaning that it locally influences the stellar spectra.

For a certain fraction of their life (at the beginning and in the first evolutionary phases of star life), very young stars are embedded in their parental MCs. Even if this period is short, its effect on the light emitted by these stars cannot be neglected as a significant fraction of light is shifted, by interstellar dust located between the

observer and stars, from the UV-optical to the IR region of the spectrum. One can observe directly light from young stars when the first-born, massive stars evolve and their strong stellar winds and mass loss, intense ionizing radiation fields and final explosions as type II SNe will eventually destroy the MCs in which they are embedded. The time scale for this process to occur is supposedly similar to the lifetime of the most massive stars in the population.
Moreover, low and intermediate mass stars, during the AGB phase may form an outer dust-rich shell of material obscuring and reprocessing the radiation emitted by the underneath stars. The final effect, in all these cases, is the absorption of the stellar light in the UV-optical and the re-emission of a great amount of this light in the NIR-MIR-FIR.
Stars and dust are so tightly interwoven not only *locally* (stars-MCs, stars-circumstellar dust shell), but also *globally* (stars, gas and dust mixed in the galactic environment) because they are the main components of galaxies.
The old stars, AGB stars and young stars are all mixed in the interstellar medium which pervades every galaxy in different way depending on its morphological type and its evolutionary history. In disc galaxies, with active mild star formation, dust is partly associate to the diffuse ISM, party to the molecular regions with stars formation and partly to the circumstellar envelopes of AGB stars with evenly balanced contribution from all the three kinds of source; the presence of dust is more spectacular in galaxies with strong star formation. In starburst galaxies, the situation is the same but now the key role is played by the region of intense star formation. In elliptical galaxies, which show weak emission in FIR (*IRAS*), dust is essentially associated to AGB stars of small mass that continuously lose mass refueling the ISM of gas and dust.

From these considerations, it appears clear that dust plays an important role in relation to the formation and evolution of galaxies; it affects the observed SED of a galaxy, hampering its interpretation in terms of the fundamental physical parameters, such as age, metallicity, initial mass function (IMF), mix of stellar populations, star formation history (SFH).

In this thesis, the effects of dust on galaxies have been deeply studied and considered in both chemical and spectro-photometric simulations of galaxies of different morphological types at many different levels, trying to improve in the treatment of dust extinction, emission, formation and evolution in our models.

- We introduced and studied the effects of dust in isochrones and SEDs of SSPs

with an improved state-of-art treatment of the AGB phase in intermediate and low mass stars, taking into account circumstellar dust shells around them. AGB stars must be included very carefully in population synthesis models, since the contribution of stars on the upper AGB can be very important;

- we developed and tested state-of-art models of galaxies of different morphological types, E, S0, Sa, Sb, Sc, Sd and disks, with the inclusion of all the local and global effects of dust extinction and emission.

- We presented and tested the models in many different photometric systems, both for the local and high redshift universe;

- in order to improve upon the information supplied by the chemical code to the EPS, we developed and presented a state-of-art description of the evolution and formation of dust in spiral galaxies, with a complete treatment of dust yields and dust accretion/destruction processes. Indeed, three main basic ingredients enter the problem influencing the total dust budget and the kind of mixture of the dust grains: the types and amounts of dust injected by AGB stars and SNe and the accretion and destruction processes of dust in the interstellar medium (ISM). They govern the relative abundances of the gas and dust components of the ISM of a galaxy. This refined model should be in future used to support the spectro-photometric models with a more advanced chemical interface. In particular, the Milky Way has been chosen as the ideal laboratory to study the dust cycle (Zhukovska et al. 2008) and its impact on the wider subject of galaxy formation with the target to later (1) extend the dusty chemical model to ellipticals, intermediate type and starburst galaxies and (2) interface it to our spectro-photometric code.

The outline of this thesis is as follows.

In **Chapter 1** the building blocks of the evolutionary population synthesis models, namely *isochrones* and *SSPs*, are presented, and the main improvements we introduced - the possibility of choosing between different kind of IMFs and the new physically consistent treatment of the AGB phase for low and intermediate mass stars, starting from the work of Weiss & Ferguson (2009) - are discussed. The effects of the circumstellar dust shells around AGB stars on stellar radiation are considered using a suitable library of dusty SEDs of AGB stars, whose features are described in this chapter.
In **Chapter 2**, it is reviewed the method adopted to perform synthetic photometry fin order to derive magnitudes and colors of four different kinds of theoretical models, starting from their SEDs: stars, isochrones, single stellar populations and galaxies

of different morphological type. This process can be done both in the local and high redshift universe: the evolution of SEDs with the redshift can be made applying the K-correction and the E-correction to the rest-frame models, as shown in the chapter presenting galaxy models. A global overview of the different telescopes and satellites, instruments and surveys, whose broad-band photometric systems are included in our database, is presented.

In **Chapter 3**, we apply our isochrones and SSPs to the study of star clusters in order to validate them and trying to put in evidence the effect of the dust shells around AGB stars, in order to examine the effect of (1) the improved TP-AGB and (2) the new library of dusty AGB stars. At this purpose, in particular we take into account data from the Small and Large Magellanic Cloud (SMC and LMC), that allow to compare SSP models for the metallicities where the effect of dust shells should be stronger.

In **Chapter 4**, we discuss our theoretical model of galaxies of different morphological types, considering their physical components, the spatial distribution of stars and ISM and the evaporation of the MCs. Moreover, a general description of the structure of the Fortran code which perform the model SEDs is given, together with the discussion about the role accomplished by every subroutine.

In **Chapter 5** we present our models of galaxies of different morphological type, taking into account the effects of dust emission and extinction, both for the local and high redshift universe. A quick summary about the dust properties and the mixture adopted into these models is also provided. The main characteristics of the SEDs and their evolution with the redshift are described. The models are tested with observational data of the local universe and with photometric data from recent surveys.

In **Chapter 6**, we simulated the formation, evolution and composition of dust in the MW, both locally in the Solar Ring and radially along the Galactic Disk. We build up a detailed dusty chemical model starting from the pioneering study by Dwek (1998) and taking into account the more recent ones like Zhukovska et al. (2008). The theoretical model we are building up stems from the basic one with infall by Chiosi (1980), however updated to the more recent version with radial flows of matter and presence of a central bar developed by Portinari & Chiosi (2000). The model follows the evolution of the abundances in dust and gas of a number of elements involved in dust, includes star-dust injection and the formation/destruction of dust. The model stands upon the best prescriptions available in literature concerning star-dust yields, dust accretion, destruction and condensation in the AGB winds and SNe explosions.

The main observational test is made by the data on element depletion provided by the Solar Ring of the MW, to which we will compare our results. At the same time, obviously, classical constraints about abundances in stars, SNa rate, surface

densities, radial gradients and so on are checked to be satisfied to get a fully consistent picture.

Finally, in **Discussion**, we discuss the main results, and some future plans are drawn.

Chapter 1

Isochrones and SSPs

The definition of *evolutionary track*, for a star of fixed mass M and chemical composition μ, is the path that the star follows across the theoretical H-R diagram during its evolution.
The evolutionary track is therefore a curve that instantaneously identifies the temperature and luminosity of a star.

Using these tracks, one can compute *isochrones*, which are the loci of the same age for stars of different masses. It is worth recalling that the precise shape of an isochrone depends on the properties of the underlying evolutionary tracks, while the relative number of stars in different portion of the isochrone is governed by the assumed $\Phi(M)$ (IMF) and the lifetimes of the stars present in the isochrone in different evolutionary stages.

By integrating the contribution of each isochrone element along the whole isochrone, and coupling the isochrones with libraries of stellar spectra and an IMF, one can derive the spectral energy distribution, *SED*, of an SSP of any age and metallicity.
The SSP, *single* or *simple* stellar populations, depending on the authors, assumes that all stars are coeval and share the same chemical composition.
The SSP SEDs have great astronomical interests: first, they are used to test properties of globular clusters, since these are the simplest stellar populations in nature, while complex systems like galaxies, which are made up by various stellar generations, are modelled by convolving the SEDs of the SSPs with a suitable star formation history.
SSPs are the building blocks ingredients either for EPS classical models (Arimoto & Yoshii 1987; Bressan et al. 1994; Silva et al. 1998; Buzzoni 2002; Bruzual & Charlot 2003; Buzzoni 2005; Piovan et al. 2006b), or for galaxy models from *cosmo-chemo-dynamical* simulations, like the ones presented in Tantalo et al. (2010). The different and sequential steps that have to be followed in order to obtain the spectral energy distribution for a galaxy (of different morphological types, like *elliptical* and

disk ones) by means of the EPS are well visualized in the Fig. 1.1, that we show in order to present the global glance at the problem:

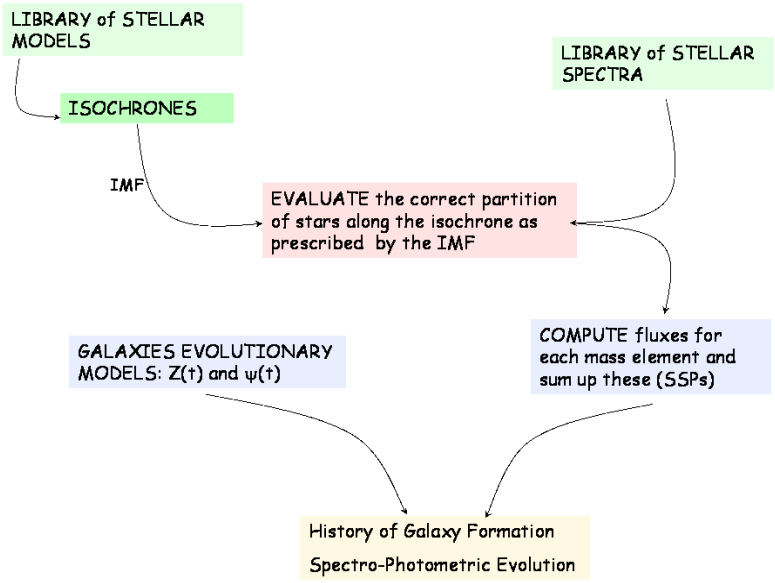

Figure 1.1: From the libraries of stellar models and spectra to galaxies' models.

It is clear how several ingredients are required in order to simulate the SEDs of galaxies of different morphological types: libraries of stellar tracks, libraries of stellar spectra and a chemical code able to simulate in some way the history of star formation and chemical enrichment of the galaxy. Also, it is worth noticing that this scheme, already not so simple, does not include dust. The introduction of the dust with its effect on stellar spectra and the emission in the infrared, adds further complications to the problem, like the introduction of a geometry where sources and dust are distributed, the physical description of the interaction of the dust with stellar radiation and the problem of the origin and formation of the dust itself.

1.1 Isochrones: details

Stellar evolutionary tracks and isochrones are key inputs for a wide range of astrophysical studies; they are essential to the interpretation of photometric and spectroscopic observations of resolved and unresolved stellar populations, like the simple age-dating of star clusters, up to the derivation of star formation histories of resolved galaxies and the modelling of their spectrophotometric evolution (as proved in the Chap. 5).

Many groups have published large grids of stellar isochrones, covering a wide range of stellar parameters (age, mass, metal content and so on) to became useful in stellar population synthesis of galaxies. For instance the Geneva database of stellar evolution tracks and isochrones (Lejeune & Schaerer 2001), the various release of stellar tracks and isochrones from Padua (Bertelli et al. 1994; Girardi et al. 2002; Marigo et al. 2008; Bertelli et al. 2008), the BaSTI database from Teramo (Pietrinferni et al. 2004; Pietrinferni et al. 2006; Cordier et al. 2007) and the Dartmouth database (Dotter et al. 2008), just to mention a few widely used in literature.

For this work, large grid of isochrones of different metallicities (Z=0.1, 0.05, 0.02, 0.004, 0.008, 0.0004, 0.0001) with initial helium content going from 0.23 up to 0.480 according to the enrichment law $\Delta Y/\Delta Z$=2.5 and with fine age spacing have been calculated. The underlying stellar models are those of the classical Padova Library calculated with convective overshooting and widely applied to galaxies, described in Alongi et al. (1993), Bressan et al. (1993), Fagotto et al. (1994a), Fagotto et al. (1994b), Fagotto et al. (1994c), Girardi et al. (1996). All evolutionary phases, from ZAMS up to the stage of PN formation or central C-ignition are included, as appropriate to the mass of the last living star of age t. The isochrones span the age range from 3×10^6 yr to 15 Gyr for all the metallicities, with the exception of the Z=0.05; we decided to extend the range of ages up to 20 Gyr in order to show the onset of the *AGB manqué* stars for this metallicity.

AGB manqué stars

The evolution of high metallicities stars of low mass is a subject of interest because of their potential ability to provide correct explanation of the UV-excess observed in elliptical galaxies (Bressan et al. 1994). The high metallicity ($Z_\odot$) low-mass stars, after a normal He-burning phase (red-HB), skip the standard TP-AGB and soon after the early AGB phase is completed, proceed toward the WD regime: these stars are called P-EAGB. At even ($3Z_\odot$) high metallicities, the old HB stars of normal mass (0.55-0.6 $M_\odot$) can spend a significant fraction of the core He-burning phase at high T_{eff} and skip the entire AGB phase to directly evolve toward the WD regime. These stars are named Hot-HB and AGB-manqué and they play a crucial role in the UV-upturn of massive elliptical galaxies (Greggio & Renzini 1990; Castellani & Tornambe 1991; Bressan et al. 1994). For a given M_{HB}, both the lower hydrogen content in the envelope, and the enhanced CNO processing in the H-burning shell, because of the high metallicity, concur to burn out the envelope much faster than in stars of the same mass but lower metallicity and hence helium content. The Fig. 1.2 shows isochrones corresponding to models of these types, for two values of metallic-

ity, Z=0.05 (**left panel**) and Z=0.1 (**right panel**). The isochrones are plotted with ages log(t/yr)= 10.26, 10.28, 10.30 (Z=0.05) and log(t/yr)= 9.95, 9.98, 10.00, 10.02, 10.04, 10.08, 10.11, 10.15, 10.18 (for Z=0.1).

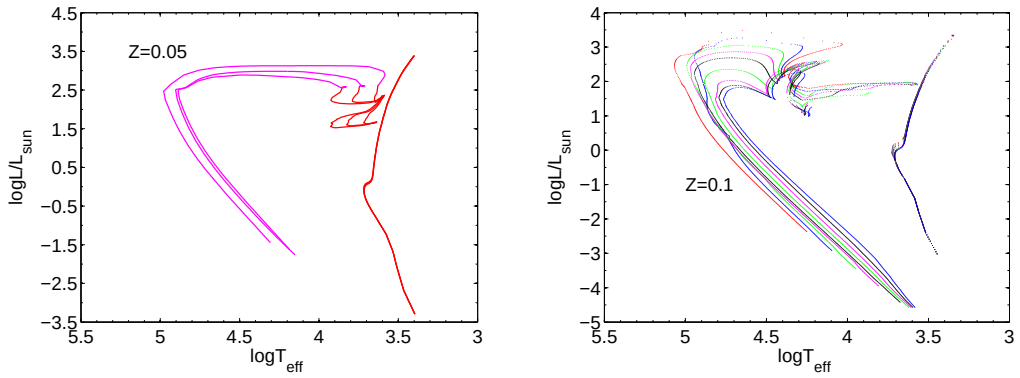

Figure 1.2: AGB-manqué stars for two metallicities: Z=0.05 (**left panel**) and Z=0.1 (**right panel**). The isochrones are plotted with ages log(t/yr)= 10.26, 10.28, 10.30 (Z=0.05) and log(t/yr)= 9.95, 9.98, 10.00, 10.02, 10.04, 10.08, 10.11, 10.15, 10.18 (for Z=0.1). In the **left panel**, the red lines represent the pre-AGB manqué phase. In the **right panel**, every isochrone is drawn in a different color, from the ZAMS up to the stage of PN formation.

The isochrones used in this study present some significant improvement compared to the classical ones of *Padova stellar evolutionary tracks and isochrones* [1], that up to now have been used to calculate dusty SSP SEDs and then SEDs for galaxies of different morphological types - see for instance Piovan et al. (2006a), Piovan et al. (2006b) -. The main improvements introduced in the calculation of these isochrones are:

- the possibility of choosing between different kind of IMFs. The considered IMFs are: Salpeter (Salpeter 1955), Larson (Larson 1998), - with different parameters for the Milky Way disk or for Solar Neighbourhood (Portinari et al. 2004a) - Kennicutt (Kennicutt 1998), the original Kroupa IMF (Kroupa 1998), a revised and more recent version of this IMF (Kroupa 2007), Chabrier (Chabrier 2003), Scalo (Scalo 1986), Arimoto (Arimoto & Yoshii 1987). In Sect. 1.1.4, there is a summary of this topic.

- the treatment of the AGB phase for stars of different masses is now more physically consistent, allowing to distinguish between C-rich and O-rich AGB stars and with improved opacities. It starts from the work of Weiss & Ferguson

[1] http://pleiadi.pd.astro.it/

(2009). These AGB stars are obtained with full evolutionary calculations with GARSTEC (see Sect. 1.1.3) and allow to greatly improve upon the previous dusty models by Piovan et al. (2003), where it was not possible to follow the evolution of the C and O surface abundances and the C/O transition was artificially adapted from Marigo & Girardi (2001) models.

Isochrones of metallicity Z=0.1 and Z=0.0001

For the highest metallicity included in our list, that is Z=0.1, we can not introduce the new description for the AGB stars, since the highest metallicity included in the Weiss' database is Z=0.04. Therefore, for stars in this evolutionary phase, we cannot distinguish the *O-rich* surface composition from the *C-rich* one. It follows that we can not introduce for the subsequent SSPs calculation (or eventually for the calculation of the colors of these isochrones in color-magnitude diagrams) the new dusty AGB libraries, presented in Sect. 1.5. We plan to improve upon this point when evolutionary models of AGB stars for this metallicity will be available. Even if, for this metallicity, the effect of AGB manquè or Hot-HB stars is strong and appears earlier than in the Z=0.05 case, that is about at 8.5 Gyr, still many stars follow the AGB path. We expect that these stars develop a thick envelope due to the high abundance of metals available to be included into dust in the shell around the cool star that will be very obscured. In consequence of this missing information on the metal richest stars, we must pay attention that in the case of objects reaching very high metallicities, our description of the MIR-FIR emission by SSP could lack the contribution of these deeply attenuated AGB stars. It would be interesting therefore to produce a database of isochrones at varying the initial mass function and with a complete AGB description, able to span th whole metallicity range from Z=0.0001 up to the high value Z=0.1, in order to examine in a more consistent way the properties of objects very enriched in metals, like for example giant ellipticals (Bressan et al. 1994). In the same way as for the highest metallicity, we miss the required information for the lowest metallicity tracks (Girardi et al. 1996) with Z=0.0001: in this latter case we simply adopt the nearest AGB models with Z=0.0001 by Weiss & Ferguson (2009), being confident that there is a small difference in Z and we do not expect huge differences between the models. Indeed, the behaviour of the tracks is more regular that in the opposite case at very high metallicity.

In this section we focus on the new isochrones calculated considering the new treatment of the asymptotic giant branch phase. Extended sets of isochrones are presented in the theoretical HR diagrams (Fig. 1.3): we show three values of metallicity, namely Z=0.02 (solar value), Z=0.004 (metallicity normally adopted for the Small Magel-

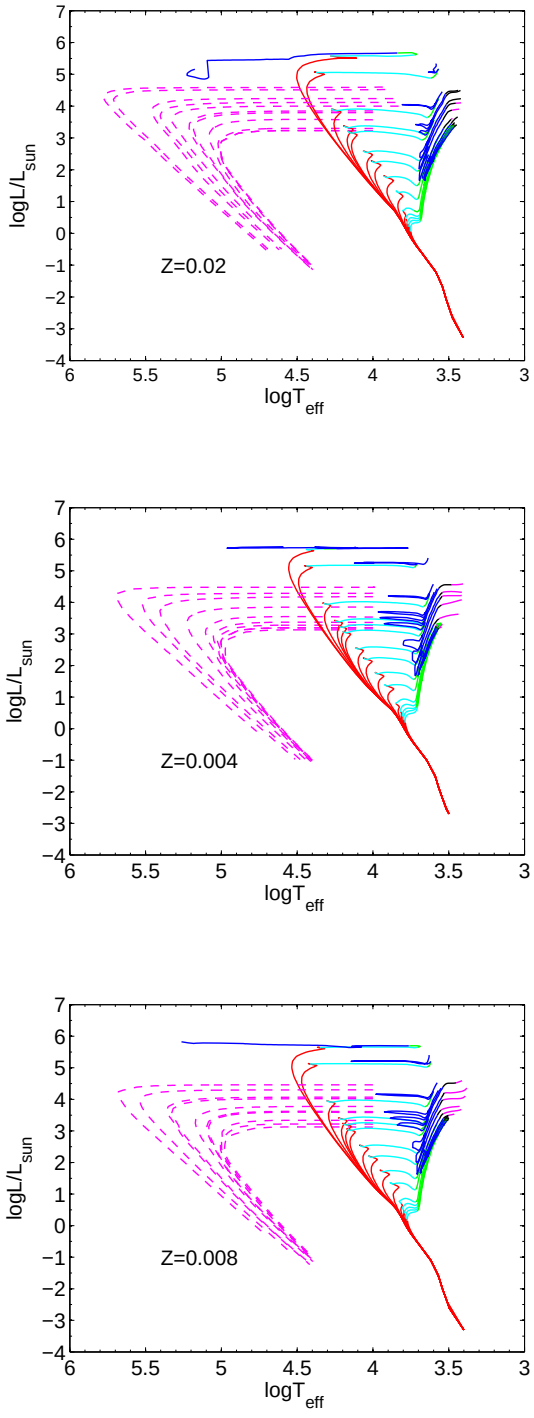

Figure 1.3: Isochrones in the theoretical HR diagram, considering all the evolutionary phases, starting from the zero-age-main sequence up to the stage of PN formation or central carbon ignition, depending on the initial stellar mass. Three metallicities are considered: Z=$Z_{\odot}$, Z=Z_{SMC}, Z=Z_{LMC}. The isochrone are plotted with ages covering the interval from log(t/yr)=6.70 up to 10.18.

lanic Cloud) and Z=0.008 (metallicity normally adopted for the Large Magellanic Cloud). The isochrones are drawn in different colors according to their evolutionary phase; the evolution of the single star of a certain mass is followed starting from the ZAMS (continuous red lines), going through the RGB base (continuous cyan lines), the RGB phase (continuous green lines), the RGB tip and/or the beginning of the HB (continuous blue lines), up to the TP-AGB phase (the path through the AGB with stars having O-rich surface abundances is in black while the C-rich case with C/O>1 is in magenta) and, finally, the stage of PN formation, drawn in dotted magenta lines. As it is well known, not all the stars follow the whole sequence; this depend on their initial mass. Independently of the chemical composition, stars can be classified into three categories according to their initial mass, evolutionary history, and final fate: low-mass stars, intermediate-mass stars, and massive stars. Since the isochrones are plotted with ages from log(t/yr)=6.70 to 10.18, both the three mass intervals are represented. It is in particular interesting to notice the intermediate mass range, which develops the most prominent AGB path. By means of the new opacities (Weiss & Ferguson 2009), the path of the isochrone extends toward low temperatures.

In the Figs. 1.4, 1.5, 1.6 are shown the isochrones for all the analyzed values of the metallicity (in addiction to the above Z, also Z=0.05, Z=0.0004 and Z=0.0001) but zooming in the region of the early AGB (E-AGB) and thermally pulsing AGB (TP-AGB), since the main improvement that we introduce in our calculation is the detailed description of the AGB phase, together with the possibility to investigate the surface composition for the AGB stars, and to distinguish between the O-rich surface and C-rich surface. This is a fundamental improvement that allows us to couple to the models the new library of dusty AGB stars presented in this thesis. Even if there are many models of synthetic and real-time AGB calculations, few models in literature are able to include really updated description of the AGB. For instance Bertelli et al. (1994) did not include Third Dredge-Up (TDU) effect and Hot Bottom Burning (HBB). Also the opacities were not calculated for variable (O-rich or C-rich) chemical mixtures, but only for solar scaled composition. Only more recent work (Marigo 2002; Marigo et al. 2008; Ventura & Marigo 2009) have been able to take into account all of these point in detail, but or they are synthetic sets or AGB stars or the set of models have been limited in the mass and metallicity coverage. In particular, Weiss & Ferguson (2009) has been the first to take into account all the crucial points about TDU, HBB and modified opacities according to the continuous effect of the TDU. In our plot, the beginning and the end of each evolutionary phase is indicated with a little star; for the sake of illustration, we show only few ages in order to avoid a too crowded figure. The age range is adapted for every Z, depending when the TP-AGB phase starts. Thus:

- Z=0.05: from log(t/yr)=7.78 to 10.30;
- Z=0.02: from log(t/yr)=7.90 to 10.18;
- Z=0.004, Z=0.008 and Z=0.0004: from log(t/yr)=8.10 to 10.18;
- Z=0.0001: from log(t/yr)=8.00 to 10.18.

The above trend is expected and it is due to the way the increase in metallicity for the isochrones is treated. When Z increase, passing from Z=0.0001 up to Z=0.05, the helium content also increases and it goes from 0.23 up to 0.480, ($\frac{\Delta Y}{\Delta Z}$=2.5), while the hydrogen content decrease. According to the fuel consumption theorem (Renzini & Buzzoni 1986): "*the contribution by any Post Main Sequence evolutionary phase to the total luminosity of a simple stellar population is proportional to the amount of nuclear fuel burned in that phase*". Also the duration of the single phase is proportional to the amount of nuclear fuel burned in that phase: so, higher metallicity stars, with lower hydrogen content, have a shorter main-sequence phase and they reach the AGB phase earlier than stars of lower metallicity.

All these isochrones are calculated considering the Salpeter law as IMF: even if we can choose between different laws, varying the IMF in the calculation of isochrones reflects only in the way the different bin of masses are populated; the change in the IMF is much more evident when calculating SEDs of SSPs, as it will be shown later. The following considerations can be made:

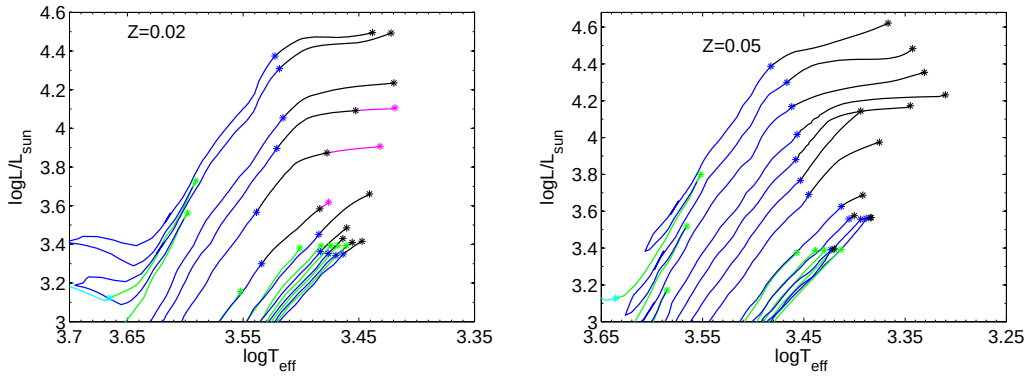

Figure 1.4: Isochrones in the HR diagram, zooming in the region of the E-AGB and TP-EAGB for two metallicity values of the original tracks. The isochrones are plotted with ages log(t/yr)=7.90 to 10.18 for Z=0.02 (solar value) and log(t/yr)=7.78 to 10.30 for Z=0.05 (see Sect. 1.1 for explanations): the youngest are *top/left*). Pre-TP-AGB phases end when the blue stars appear, while on the TP-AGB the surface O-rich and C-rich configurations are drawn in black and magenta lines, respectively.

-Solar and super-solar metallicities, i.e. for $Z \geq 0.02$: These stars usually have C/O<1, even if a late transition to the C-rich phase may take place due to the final dredge-up events, in agreement with the observations. The transition occurs only for some isochrones of intermediate age and solar metallicity (while there is no transition in the super-solar case) and it happens at very low T_{eff} in the final stages of the TP-AGB phase, while the isochrones of super-solar metallicity show only the O-rich surface. The youngest isochrones, as expected, present the longest AGB path in the diagram. In the oldest isochrones of both metallicities (lower part of the paths in the diagram), the dredge-up is not operating and the TP-AGB phase simply align above the previous early-AGB phase. These isochrones increase in luminosity and bend to the left at their upper end, due to the progressive thinning of the stellar envelope.

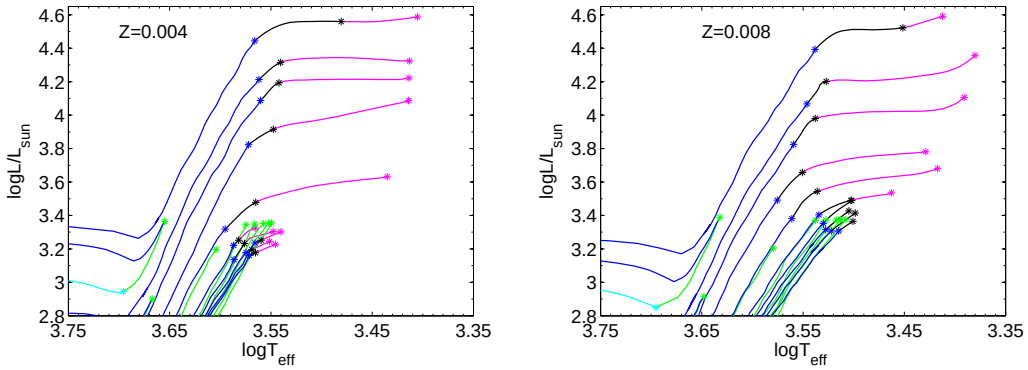

Figure 1.5: As in the Fig. 1.4, but for Z=0.004 and Z=0.008. The isochrone are plotted with ages log(t/yr)=8.10 to 10.18 for both values of Z.

-Sub-solar metallicities, i.e. for $0.004 \leq Z < 0.02$: These stars show an extended C-rich phase which starts even at younger ages. This is due to the activation of the ON cycle,which converts O into N, in such a way that the C/O ratio is predicted to increase above unity (Ventura et al. 2002; Marigo et al. 2008). The development of the C-rich surface, moreover, starts at higher effective temperatures (compared to isochrones of solar metallicity), because the lower molecular concentrations in stars' atmospheres (Marigo et al. 2008).

-Low metallicities, i.e. for $Z < 0.004$: the features described for isochrones of moderate metallicities are here more evident: the transition to C-rich surface starts at even higher effective temperatures and the majority of the ages show exclusively the C-star phase: only few isochrones of intermediate ages show a previous O-rich surface. Our results can be compared with the ones by Marigo et al. (2008): with

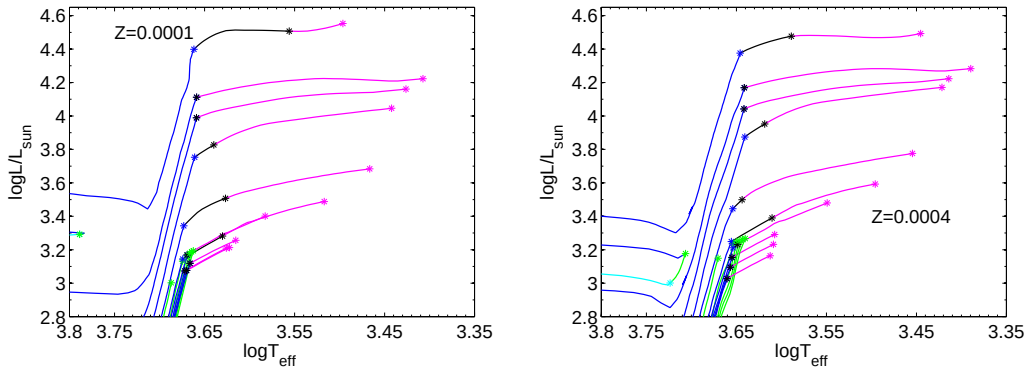

Figure 1.6: As in the Fig. 1.4, but for Z=0.0001 and Z=0.0004. The isochrone are plotted with ages log(t/yr)=8.00 to 10.18 for Z=0.0001 and log(t/yr)=8.10 to 10.18 for Z=0.0004.

some differences there is a general good agreement between the most refined synthetic models available in literature and the results obtained with Weiss & Ferguson (2009) full evolutionary models: in particular, the agreement is ultimately due to the fact that both of them include modern recipes to scale the opacities in agreement with the C/O mixture of the atmosphere. For example the lowest temperatures reached by the AGB stars are similar and the trend of the partition between C and O stars with the metallicity is more or less the same. In any case it is worth noticing that, at the level of galaxies, the ultimate target of this thesis, what matters is the consistency of the general scheme in terms of different metallicities and O-rich/C-rich paths and not the specific detail. In particular, since we want to introduce dust around AGB stars, it is crucial a proper evolution and splitting between the O-rich and C-rich phase and a realistic description of the mass-loss, in order to correctly connect dust grains to the underlying star and obtain a realistic optical depth of the envelope.

1.1.1 Asymptotic Giant Branch stars: an introduction

As already explained, we introduce in our isochrones and hence SEDs of SSPs a new treatment of the Asymptotic Giant Branch stars, starting from the work of Weiss & Ferguson (2009).

For populations with an age of a few hundred million to about 2 billion years, the contribution of intermediate mass stars cannot be ignored. Because of their high luminosity they contribute significantly to the integrated light, and due to their low surface temperatures, they dominate the spectra and colors in the near infrared.

All stars in the mass range from about 0.8 $M_\odot$ to $\sim$ 6-8$M_\odot$ (the upper limit changes depending on the authors: both long tradition Padua or Garching models set this

limit to the conservative value of 6 solar masses) will become AGB stars.
The AGB is the last nuclear burning phase of stellar evolution for stars of this mass range: this phase is very short compared with other evolutionary phases, lasting less than 1% of the main sequence lifetime.
AGB stars are evolved objects: they are found in the high luminosity and low-temperature region of the HR-diagram. Indeed, these objects have evolved through core H and helium burning and they are sustained against gravitational collapse by alternate H-shell and He-shell burning.
AGB stars undergo thermal pulsations (the explosive ignition of the He-rich shell), that cause the convective mixing of C-rich gas with the outer stellar envelope. After repeated thermal pulses a star can evolve from an O-rich giant to a C-rich star: this process occurs when C/O ratios ≥ 1.

During the TP-AGB phase, the He-burning shell becomes thermally unstable every 10^5 years or so, depending on the core mass. The energy provided by the TP drives the convective zone in the He-rich inter-shell region, that mixes the products of the He nucleo-synthesis. The stars is expanding and the He-shell is pushed out to cooler regions where it is almost extinguished: the convective envelope can move inwards (in mass) to region previously mixed by the the flash-driven convective zone. This phenomena is known as the third dredge-up (TDU) and it is the responsible for enriching the surface in ^{12}C and other products of He-burning, as well as heavy elements. Following the TDU, the star contracts and the He-shell is re-ignited, providing most of the surface luminosity for the next inter-pulse period.

This cycle of *inter-pulse-thermal pulse-dredge-up* can occur many times during the AGB phase, depending on the initial stellar mass and its composition, as well as on the mass-loss rate.

In intermediate-mass AGB stars ($M \gtrsim 4M_{\odot}$) the convective envelope can dip into the top of the H-shell, and the nuclear burning can occur at the base of the convective envelope: this event is called *hot bottom burning* (HBB) and can dramatically change the surface composition. Indeed, the convective turn-over time of the envelope is ≈ 1 year, hence the whole envelope will be processed a few thousand times for inter-pulse period.

1.1.2 Synthetic models and full evolutionary models

The Padova and BaSTI stellar model libraries have included the TP-AGB with updated recipes - see for instance Marigo et al. (2008) and Cordier et al. (2007) - by making use of *synthetic AGB-models*.
Up to now, synthetic AGB-models try to predict basic stellar parameters, $L(t)$, $T_{eff}(t)$ and stellar yields, without resorting to calculations of full models, but using

relationships obtained from full calculations. However, they are by no means merely reproducing the full models: they are using basic properties, (the mass of the helium core or the luminosity of the helium shell) as function of time as input for calculations of mass loss, effective temperature, envelope composition and even nucleo-synthesis at the bottom of the convective envelope. All synthetic models depends on results from full stellar modelling, because they can treat effects like the third-dredge up or mass loss as an additional property, which is then usually calibrated by comparison with observed AGB-star samples.

The new asymptotic giant branch model calculated by Weiss & Ferguson (2009) include the latest physical ingredients, and they are obtained for a large variety of stellar compositions. Apart from the aspect of updated constitutional physics and more extensive chemical composition, these models take into account a consistent treatment of C enrichment of the envelope due to the third dredge-up (TDU) and related opacities. This includes influence on the opacities, which has been shown by Marigo (2002) to be crucial for stars' temperature.
This, in turn, is the most important parameter for dust-driven mass loss, which dominates the late AGB evolution and the transition to the post AGB.

Mass Loss

The evolution along the AGB is characterized by the internal nuclear processes, leading to increasing luminosities and larger stellar radii, and by strong mass loss due to stellar winds, which depends on mass, radius, luminosity and chemical composition of the envelope. Mass loss in one of the turning aspect of AGB evolution: it determines how and when the TP-AGB phase ends, what yields can be expected from these kind of stars, and it influences possible nuclear reactions at the bottom of the convective envelope. The most widely used formulas used for the AGB evolution calculations are those by Vassiliadis & Wood (1993) and Bloecker (1995). For instance in the old dusty models of the Padova group by Piovan et al. (2003), the Vassiliadis & Wood (1993) mass-loss formula was adopted to describe wind and super-wind phase.
For his investigation, Weiss & Ferguson (2009) used the following mass loss prescriptions: as the basic formula, for the RGB evolution and pre-AGB evolution, the Reimers (1975) relation is used:

$$\dot{M} = -4 \times 10^{-13} \frac{(L/L_{\odot})(R/R_{\odot})}{(M/M_{\odot})} \eta_R \tag{1.1.1}$$

This is consistent with the adopted mass-loss by Bertelli et al. (1994) and companion papers and it is important to secure some consistency between the GARSTEC and Padua models, together with similar compositions of the stellar initial models entering the calculations based upon Grevesse & Noels (1993). Once on the AGB,

observed mass loss rates are higher than the Eq. 1.1.1 would indicate: in this case, for carbon-rich chemical compositions, (in which nearly all oxygen is bound in CO, and the excessive carbon gives rise to carbon-based molecules and dust) the mass loss rate by Wachter et al. (2002):

$$\log \dot{M}_{AGB} = -4.52 + 2.47 \log \left(10^{-4} \frac{L}{L_\odot}\right) \\ -6.81 \log \left(\frac{T_{eff}}{2600K}\right) - 1.95 \log \left(\frac{M}{M_\odot}\right) \tag{1.1.2}$$

For the case of oxygen-rich stars, (C/0 < 1), the empirical fitting formula by van Loon et al. (2005), obtained from dust-enshrouded oxygen-rich AGB stars, is considered:

$$\log \dot{M}_{AGB} = -5.65 + 1.05 \log \left(10^{-4} \frac{L}{L_\odot}\right) - 6.3 \log \left(\frac{T_{eff}}{3500K}\right) \tag{1.1.3}$$

As a star leaves the AGB, T_{eff} increases: using hydro-simulations of dust envelopes around evolving post-AGB stars, Schönberner & Steffen (2007) show that the strong mass loss should deal with effective temperatures of 5000 or 6000 K: this behavior is reproduced keeping the AGB-wind mass loss rates until the pulsation period P has decreased to 150 day. From there to $P = 100$ days, taken to be the beginning of the post AGB phase, a linear transition to the post AGB wind is done. From there on, Weiss used the Eq. 1.1.1 or, if the rate is larger, the radiation-driven wind formula:

$$\dot{M}_{CSPN} = -1.29 \times 10^{-15} L^{1.86} \tag{1.1.4}$$

Opacities

The carbon-enhancement of the stellar envelopes (due to the TDU) is consistently treated by using opacity tables at varying the C/O-ratio and by employing theoretical mass loss rates for carbon stars.
The outer envelope structure of AGB stars depends considerably on the opacities; carbon-enriched molecular opacities reduce effective temperatures significantly, and they lead to much better agreement of the colors of the synthetic populations with the observations. The possibility to compute the opacities for any chemical composition is a huge advantage: the effects detected in the models help to account for a number of observational properties of carbon stars.

Therefore, new opacity tables have been prepared for C-enhanced mixtures. For high temperatures, OPAL-tables for atomic opacities (Iglesias & Rogers 1996) were obtained from the OPAL-website [2], and for low temperatures new tables for molecular opacities were generated following Ferguson et al. (2005). In all cases, the

[2] http://physci.llnl.gov/Research/OPAL

chemical compositions of low- and high-T tables agree and tables from the different sources are combined (Weiss & Schlattl 2008).

For the absorption properties, one has to know which molecules are present in cool stellar matter. The spectra of cool giant stars of spectral types M, S and C, are dominated by totally different molecular absorption bands in the visual and infrared, depending on which, carbon or oxygen, is the most abundant element.

The key point is the *C/O ratio*, because of the high binding energy of the molecules: oxygen rich stars (C/O ratio less than ≈ 1) show strong bands of TiO, VO, H_20, while for carbon rich stars basically all O is bound in CO, and they show large absorption features of C_2, CN, SiC and some HCN and C_2H_2 (formed from the remaining carbon).
So, the C/O-ratio is more important than the absolute carbon abundance in the stellar mixture: the additional opacity tables were produced as a function of a variable C/O-ratio for different (X, Y, Z)-mixtures. As said, the increase in carbon leads to *lower effective temperature* (Marigo 2002), mainly by the increase in total metallicity and this effect is crucial to reproduce observational data. The opposite happens if the metallicity is fixed: an increase in C/O can initially lead to lower opacities and higher effective temperatures as compared to a solar-scaled mixture.

1.1.3 Linking Padua and GARSTEC models

The metallicities of the models available in Weiss & Ferguson (2009) are five, that is Z=0.05, 0.02, 0.004, 0.008, 0.0004. The ideal case would be to have a perfect match between the metallicities of the Padova evolutionary tracks and the GARSTEC tracks, however this is not possible for all the cases. In particular the extreme (lowest and highest) metallicities of the Padua set, that is Z=0.0001 and Z=0.1 are not available. For the highest value we need to wait for new models matching that metallicity: the presence of the AGB-manquè and Hot-HB stars makes things too cumbersome to allow us to extend in some way the models for Z=0.05 to the highest value. For Z=0.0001 we adopt the AGB models of Z=0.0004 suitably adapted to the case: the more regular evolutionary behaviour allows this match as a first approximation (keeping in mind our ultimate purpose of galaxy models and therefore the need for a complete database) until AGB tracks of similar metallicity will be available. Up to now we do not consider the case for an *α-enhanced* metal mixture but only the solar-scaled one and for each metallicity 11 initial masses between 1 and 6 $M_\odot$. The masses are: 1.0, 1.2, 1.5, 1.6, 1.8, 2.0, 2.6, 3.0, 4.0, 5.0, 6.0 $M_\odot$.
For all of them, Weiss & Ferguson (2009) have been able to follow the evolution of stars starting from the ZAMS and continued as far as possible with the aim of reaching the white dwarfs cooling tracks.

These calculations have been made using the GARSTEC code, that is able to follow low-mass stars through the core helium flash and many thermal pulses on the AGB without human intervention, because of the numerical improvements introduced in it. Nevertheless, towards the end of TP-AGB phase, convergence problems can occur. For more details about the properties of the code, see Weiss & Schlattl (2008).
For every star mass, lifetimes on the main sequence, the RGB (considered as the time between the end of the central hydrogen and the beginning of the central He-burning), the core helium burning, until the onset of the first thermal pulse are provided. These lifetimes agree with those of the Padova library (Bertelli et al. 1994; Girardi et al. 2000).
The standard procedure to include the AGB evolution is the smoothing procedure: thermal pulses are smoothed in order to guarantee a safe calculation of the isochrones (Bertelli et al. 1994; Girardi et al. 2002; Bertelli et al. 2008). This procedure has always been adopted in the different versions of the Padova libraries of isochrones, carefully smoothing the AGB paths, with good results obtained along the years.

As an example of this, in the Figs. 1.8 and 1.7 is shown the evolutionary track for a star of M=4$M_{\odot}$. The thermally-pulsing phase is evident: over-imposed, we show the *smooth* function used in both cases.
Some comments are worth to be made about the reasons for which it is common use to "clean" the pulses:

- in theory it would be possible, but in practice it is numerically very cumbersome, to interpolate between the oscillating L-T_{eff} paths of stars of different mass. The AGB is extended over a very short time-scale (Weiss & Ferguson 2009) and the interpolation between L-T_{eff} pulses would require a too much thinly spaced time-step, corresponding to infinitesimal mass changes.

- Star clusters have a small number of AGB stars, as expected according to the short duration of the double shell H-He nuclear burning phase: observing clusters we do not expect therefore in any way to be able to reconstruct, in some observational color-color or color-magnitude diagram, the path covered by the pulses. Let us suppose now that we are observing a galaxy with a population much bigger than a cluster: it may happen in this case that we have a lot of AGB stars in our empirical HR diagram so that in principle we could hope to see the path described by the AGB stars. What in practice would happen is that stars of different masses would overlap each other with their own pulses and the result would be a stream containing all the AGB stars of different mass just taken in a different part of their AGB path, vanishing any effort to see the outline of the pulses.

- The libraries of stellar spectra commonly used, with or without dust, that are required to connect the simulations to the observations, have not, in general, a very refined grid in T_{eff} and g, in order to obviously keep the dimension of the library acceptable. Therefore, even preserving the pulses in the interpolations (or for example adding the pulses a posteriori to the isochrone by getting the pulse profile from the properties of the stars, like core-mass and so on) and assuming to have enough observed AGB stars, it would not be possible to cover the very thin spacing in T_{eff} with the library of stellar spectra. All the effort would be simply lost dealing with a library that has not enough coverage in temperature and gravity.

Maybe, the only way by which it could be interesting to keep the pulses is to produce HR "empirical" diagrams (HRD) directly from the stellar evolutionary tracks. Only in this precise case, we could eventually expect some differences using tracks with pulses as input of the HRD simulator instead of artificially "cleaned" tracks. For example, the highest AGB masses could be sampled out of the AGB stream with a luminosity higher than the tracks "smoothed", if you put a high mass AGB star in the synthetic HRD when it is in the L-peak. In some way the region of the HRD where AGB stars could be sampled, would be larger. For most of the mass range, in any case, pulses of different masses would overlap even in the Montecarlo simulations vanishing any difference between the "cleaned/not cleaned" cases.

What we really need is in any case the *general* trend for the AGB phase to be included in a realistic way in the population synthesis models for galaxies and not to reproduce some specific object.

According to the previous arguments, for every mass, before interpolating between the evolutionary tracks in order to calculate the isochrones, the TP-AGB tracks have been "cleaned" of their variations due to the TP phase.

The smoothing procedure is computed using the MATLAB smooth function that suitably allowed us to perform the whole procedure, while an extrapolation to masses lower than $1M_{\odot}$ has been adopted. Indeed, the lower mass considered when calculating evolutionary tracks is 0.6 $M_{\odot}$: we extend the results obtained by Weiss & Ferguson (2009) until 0.8 $M_{\odot}$ trying to scale consistently all the physical variables (luminosity, T_{eff}, time-scales) obtained for the 1 $M_{\odot}$. For even lower masses, than never reach the C-rich phase, a simple description is adopted in agreement with Bertelli et al. (1994) and Piovan et al. (2003).
To summarize, the following steps have been taken in order to include a more physically consistent treatment of the TP-AGB phase in our isochrones :

- For every stellar mass involved in the AGB evolution and for all the available metallicities, we calculated the beginning, the duration and the end of all the

evolutionary phases of interest (starting from the MS, up to the end of the TP phase), in order to carefully select the TP-AGB phase;

- As discussed in Weiss & Schlattl (2008) and summarized here, the major part of the models, but not all, evolved to the very end of the AGB, defined as the point when the model leaves the AGB towards hotter T_{eff} and the pulsation period has dropped below 100 days. In most cases, for the lower masses, the models evolved to virtually the end of the phase, but for the highest masses (typically 5 and 6 $M_{\odot}$) this is not true: in such cases, due to the amount of mass loss and the size of the remaining envelope, Weiss & Ferguson (2009) gives an estimate of the TPs and time still needed to complete the TP-AGB phase. We used this estimate of the number of missing TPs in order to evaluate correctly the TP-AGB lifetime for all the masses of our interest not completely evolved.

- Using the MATLAB computing language, we plotted for every mass, the different model properties ($M/M_{\odot}$), age (yr), $\dot{M}$, $\log(L/L_{\odot})$, $\log T_{eff}$, log g, X_c, Y_c, M_{c1}, M_{c2}, C_s and O_s. In order: current mass of the star, age of the model in yr, mass-loss, luminosity, effective temperature, gravity, central abundances of hydrogen and helium, mass of the core under the hydrogen or the helium shells, surface abundances of carbon and oxygen). Finally we used the smoothing procedure in order to reproduce every property. At this purpose we used the MATLAB *cftool* (Curve Fitting Toolbox) and in particular the Smooth Options Loess, that is a locally weighted scatter plot smooth. These method use linear least squares fitting, and a a second-degree polynomial. The span parameter, that is the number of data points used to compute each smoothed value is suitably varied. For all locally weighted smoothing methods like loess, if the span is less than 1, it is interpreted as the percentage of the total number of data points. For the physical variable not oscillating there is no need to smooth the data and the span can be adapted to low values in such a way to keep the shape and the form of the original data for that track. See the MATLAB Help or the online *http://www.mathworks.it/help/techdoc/index.html* documentation for more detailed information and examples about this point.

- Once selected and smoothed the AGB part of the tracks, we carefully selected the start and end of the E-AGB, the end of the TP-AGB and the eventual O-rich/C-rich transition. This is required if we want that the interpolations between different masses when calculating the isochrones keep the correct C-rich and O-rich partition. We connected for every stellar mass the TP-AGB part by Weiss & Ferguson (2009) to the end of the E-AGB phase of the evolutionary tracks in Bertelli et al. (1994) and, finally,

- we calculated the whole set of isochrones for a wide number of ages and for the available metallicities, considering different laws for the IMF.

The following point should be underlined. Two different sets of evolutionary tracks are connected. In principle the best solution would clearly be to use a completely coherent set of tracks from the highest to the lowest mass and able to cover all the evolutionary phases. This is not possible in our case because Bertelli et al. (1994) miss the post E-AGB evolution, while Weiss & Ferguson (2009) calculated the evolution only in the AGB range of intermediate mass stars, lacking therefore the lowest masses and high-mass stars evolving in type II SNe. Another good solution would be to use the end of the E-AGB of the Bertelli-Fagotto models as input in the GARSTEC model to calcolate the TP-AGB evolution. But this required to organize a priori the work with this specific idea to complete the classical set of Bertelli tracks with full evolutionary AGB path and it has not be done. We had to adapt to the best possibility, trying to minimize the errors. Indeed, we carefully checked that, with some exceptions, the shift we had to apply to connect the Weiss & Ferguson (2009) TP-AGB to the end of the Bertelli et al. (1994) E-AGB were not too high but of the order of 5-10 % in the masses and of few percent in the logarithmic scales of temperature and luminosities that is acceptable, once considered our final target of galaxy models. The timescales for the AGB evolutionary paths in GARSTEC models has been correctly joined to the end of Bertelli E-AGB. Finally, it is worth noticing that the GARSTEC code is son of the Padova code (and this latter one is an improved version of the original R. Kippenhanh code; Cesare Chiosi - private communication about the history of this stellar evolution codes), that the two codes use similar initial compositions (Grevesse & Noels 1993) for the stars and the same mass-loss recipe up to the AGB (Reimers 1975) and so no, allowing for some confidence that the results are not so dramatically different and in first approximation can be connected. We scaled luminosity, T_{eff}, core mass, envelope mass of the GARSTEC tracks in order to match the end E-AGB values.

In Figs. 1.7 and 1.8 we can see two example of the adopted smoothing procedure for a star of 4 $M_{\odot}$ and solar metallicity. In particular on the **left panels** we can see the details of the smooth for the TP-AGB part of the track.

1.1.4 The Initial Mass Function

The initial mass function specifies the distribution in mass of a newly formed stellar population and it is frequently assumed to be a simple power law (for example, the well known Salpeter law). Together with the time-modulation of the star-formation rate, the IMF dictates the evolution and fate of galaxies and star clusters - for a review of the subject, see Kroupa (2002a) -.

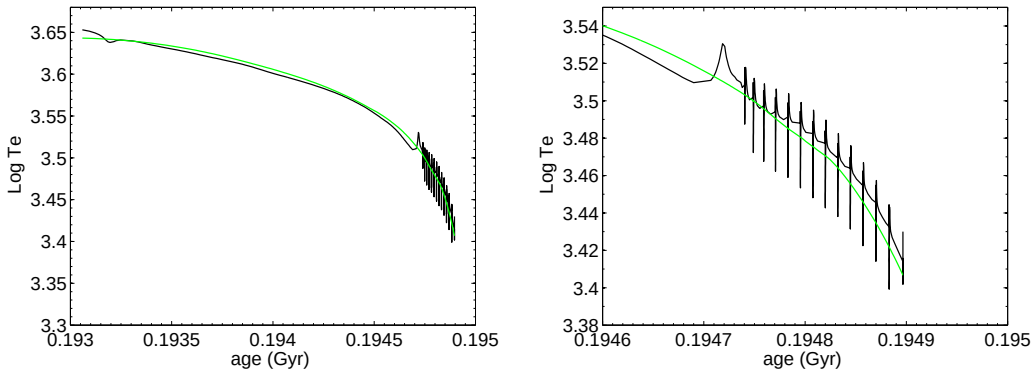

Figure 1.7: The evolutionary track for a star of M=4 $M_{\odot}$ and Z=0.02, with a zoom on the AGB phase. Superimposed to the track, the smooth function used in this case.

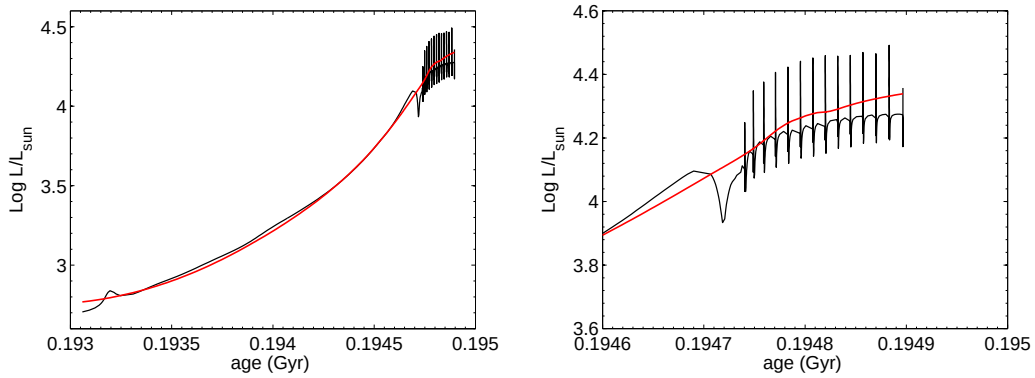

Figure 1.8: As in Fig. 1.7, but here the evolution of the luminosity along the track for the same star of solar metallicity is considered.

Brown dwarfs and very low mass stars whose lifetimes are longer than the age of the Universe, in practice lock up forever the chemical elements present in the ISM at the age of their birth, whereas intermediate and high mass stars of short life continuously enrich the environment with the products of thermonuclear reactions, thus driving the chemical evolution of the host system. The same stars in this mass ranges are also the factories of star-dust to be injected into the ISM by SNe explosions and strong stellar winds.

The adoption of an IMF has many effects worth being mentioned here, at the level of (1) isochrones; (2) SEDs of SSPs and (3) star-dust injection in the ISM. All of them are interesting for the purposes of this thesis. Let us start from the last point.

A different slope of the IMF in the intermediate-high mass range would imply a different relative population of the stars contributing to the dust yields. Second, the net yield of metals and dust per stellar generation varies. According to its definition - see for instance Tinsley (1980a), Pagel (1997) and Portinari et al. (2004b) - the net yield is the the amount of metals globally produced by a stellar generation over the the fraction of mass locked up in living stars and remnants. Therefore, efficiency of metal and dust enrichment depends not just on the amount of metals produced per unit mass involved in star formation but on the ratio between this and the mass that remains locked in remnants or ever-lived low mass stars. The locked-up fraction, is therefore as crucial to the metal and dust enrichment as is the absolute number of the high-mass stars directly responsible for the production of star-dust itself. In a given model of fixed total mass, it is clear that an IMF bending down steeply at low masses will lead to a different locked up fraction with respect to a power-law, low-mass oriented IMF. The metal and dust production is accordingly affected.
Since IMFs are proportional laws, they are normalized assuming that the total mass encompassed by the IMF from the lower, M_L, to the upper, M_U, mass limit of stars is equal to 1 $M_\odot$.

What are these limits? Normally the upper limit can be equally choose as 100 or 120 $M_\odot$, because there are few high mass stars, compared to the whole population of stars. The lower limit, instead, is a delicate issue, because if one decreases this limit, the amount of low mass stars increases, with respect to the number of high mass stars. This effect reflects on the study of the integrate light of the single stellar populations, since SSPs less luminous (for mass unity) can be created. One solar mass of SSPs with more very low mass stars will be less luminous.

To take into account this question, following Talbot (1975) and Bressan et al. (1994), we use the parameter ζ, which describes the fraction of total mass in form of stars stored in the IMF above a given mass M_*. M_* is the minimum mass contributing to the nucleo-synthetic enrichment of the ISM over a timescale of the order of the galaxy life:

$$\zeta = \frac{\int_{M_*}^{M_U} \phi\,(M)\,dM}{\int_{M_L}^{M_U} \phi\,(M)\,dM}. \tag{1.1.5}$$

This equation, at varying ζ and for fixed M_U and M_*, can be reversed numerically to determine the lower limit M_L of the distribution. To an IMF with a *bigger low mass limit*, more massive stellar populations correspond; when the SSPs fluxes are normalized to 1 $M_\odot$, less luminous SSPs are obtained. The tail of the sequence correspond to stars that contribute in an efficient way to the whole population mass *but* they do not contribute, in practice, to the luminosity of the whole stellar population. These are objects with lifetimes extremely long, eventually longer then the Hubble

time; they will not leave the main sequence.
The effect of different IMFs on SEDs and isochrones will be also discussed later with the results of the calculations. We shortly present now the IMFs we have included in our calculations of isochrones and hence SSPs. For the purposes of our study the IMF is assumed to be constant in time and space.
The IMFs included in our model are:

- The Salpeter IMF. Salpeter-like IMFs are very popular. These are an extension over the desired mass range of the original Salpeter IMF Salpeter (1955). This IMF is $\phi(M) = C_S M^{-1.35}$ with C_S depending on the value of ζ. For a mass range $[0.1 - 100]\, M_\odot$ (Portinari et al. 2004b) we have $C_s = 0.1716$ and a $\zeta = 0.3925$.

- The Kroupa IMF. In a series of papers Kroupa revised and updated the power-law IMF with a set of continuous multi-slope power-laws (Kroupa et al. 1993; Kroupa 2001; Kroupa 2002a; Kroupa 2002b; Kroupa 2007).
  In the following we consider two cases.
  First, the IMF derived by Kroupa (1998) for field stars in the Solar Neighbourhood. This IMF is typical of models of chemical evolution of disk galaxies (Boissier & Prantzos 1999; Boissier & Prantzos 2000; Prantzos & Boissier 2000; Hou et al. 2008).

$$\phi(M) = \begin{cases} C_{Kr1} M^{-0.5} & M_L \leq M < 0.5 M_\odot; \\ C_{Kr2} M^{-1.2} & 0.5 M_\odot \leq M < 1 M_\odot; \\ C_{Kr3} M^{-1.7} & 1 M_\odot \leq M < M_U. \end{cases} \tag{1.1.6}$$

  For $M_L = 0.1 M_\odot$ and $M_U = 100 M_\odot$, we obtain $\zeta = 0.405$.
  Second, the Kroupa (2007) IMF, where taking as lower and upper limits $M_L = 0.01 M_\odot$ and $M_U = 100 M_\odot$ we get $\zeta = 0.38$, slightly lower than in the above Kroupa (1998), because of the lower limit extended to brown dwarf regime.

$$\phi(M) = \begin{cases} C_{K1} M^{0.7} & M_L \leq M < 0.08 M_\odot; \\ C_{K2} M^{-0.3} & 0.08 M_\odot \leq M < 0.5 M_\odot; \\ C_{K3} M^{-1.3} & 0.5 M_\odot \leq M < 1 M_\odot; \\ C_{K4} M^{-1.7} & 1 M_\odot \leq M < M_U. \end{cases} \tag{1.1.7}$$

- The Larson IMF. Larson (1998) proposed an IMF in which the relative percentage of very low mass stars and sub-stellar objects is decreased due to the presence of an exponential cut-off. As a consequence of this there is a negligible contribution to the locked-up mass, and in contrast a very high net yield

per stellar generation, and a high production of metals and dust. The Larson (1986) IMF is

$$\phi\left(M\right) = C_L M^{-1.35} \exp\left(-\frac{M_L}{M}\right). \tag{1.1.8}$$

This IMF recovers the Salpeter IMF at high masses, whereas at low masses the exponential cut-off determines the steep downfall after the peak mass $M_P = M_L/1.35 = 0.25 M_\odot$. For a typical mass range $[0.01 - 100] M_\odot$ we have $\zeta = 0.653$ thus allowing for a high number of intermediate-high mass stars. For the present aims, we will simply keep M_L constant with time or metallicity.
We also consider the possibility for a modified Larson IMF adapted to the Solar Neighbourhood, in which the slope in the power-law factor for the high mass range has the value $M^{-1.7}$, according to Scalo (1986) and in agreement with recent IMFs proposed by Kroupa (see above). In this last case with the same mass range $[0.01 - 100]$, we have $\zeta = 0.5$, lower than the other case.

- The Chabrier IMF. Along the line of thought of Larson (1998), Chabrier (2001) proposes:

$$\phi\left(M\right) = C_C M^{-2.3} \exp\left[\left(-\frac{M_C}{M}\right)^{1/4}\right]. \tag{1.1.9}$$

The two parameters in Eq. 1.1.9 are tuned on local field low mass stars and the functional form is proved to be valid down to the brown dwarfs regime Chabrier (2002). With a mass range $[0.01 - 100] M_\odot$ and $M_C = 716.4$ we get $C_C = 40.33$ and $\zeta = 0.545$, not as high as in the Larson IMF, but still leading to high net yield and low locked up mass fraction.

- The Kennicutt IMF. The Kennicutt (1983) IMF is used in literature to describe the global properties of spiral galaxies and it is inspired by the observations of $H\alpha$ luminosities and equivalent width in external galaxies (Kennicutt et al. 1994; Portinari et al. 2004; Sommer-Larsen 1996). With a mass range $[0.1 - 100] M_\odot$, we get $\zeta = 0.59$.

$$\phi\left(M\right) = \begin{cases} C_{Ke1} M^{-0.4} & M_L \leq M < 1 M_\odot; \\ C_{Ke2} M^{-1.5} & 1 M_\odot \leq M < M_U. \end{cases} \tag{1.1.10}$$

- The Arimoto IMF. This top-heavy IMF has been suggested by Arimoto & Yoshii (1987) to simulate elliptical galaxies and is introduced just for the sake of comparison as an extreme case: $\phi\left(M\right) = C_A M^{-1.0}$. With a mass range $[0.1 - 100] M_\odot$, we get $\zeta = 0.5$.

- The Scalo IMF. This IMF is a double power-law function Scalo (1986): with a mass range $[0.1 - 100]M_{\odot}$, we get $\zeta = 0.32$.

$$\phi(M) = \begin{cases} C_{Sca} M^{-1.35} & M_L \leq M < 2M_{\odot}; \\ C_{Sca} M^{-1.7} & 2M_{\odot} \leq M < M_U. \end{cases} \quad (1.1.11)$$

  It is worth recalling that IMF with slope $(1.6 \sim 1.7)$ in the high mass range, i.e. steeper than the Salpeter value like this one, are widely used in literature in chemical models of the Milky Way even with dust (Matteucci & François 1989; Chiappini et al. 1997; Chiappini et al. 1997; Dwek 1998; Romano et al. 2000; François et al. 2004; Calura et al. 2008).

In the Tab. 1.1, we summarize the mass ranges and the ζ for the different types of IMFs.

Table 1.1: Mass ranges and the ζ for the different types of IMFs.

IMF	M_{inf}	M_{sup}	ζ
Salpeter	0.1	100	0.3925
Larson	0.1	100	0.653
Kennicutt	0.1	100	0.59
Kroupa (original)	0.1	100	0.405
Chabrier	0.1	100	0.545
Arimoto	0.1	100	0.5
Kroupa 2002-2007	0.01	100	0.38
Scalo	0.1	100	0.32
Larson Solar Neighbourhood	0.01	100	0.5

1.2 Single (or Simple) Stellar Populations

The most elementary population of stars is the so-called *Single* (or *Simple*, depending on the authors) *Stellar Population*, consisting of stars born at the same time in a burst of star formation activity of negligible duration, with the same chemical composition.

SSPs are the basic tool to understand the spectro-photometric properties of more complex system like galaxies: galaxies are not SSPs because stars of different metallicity and age are present.
However, a complex population can always be expanded in a series of SSPs: the stellar content of a galaxy can be modelled as the convolution of many SSPs of different

composition and age, each of which is weighted by the rate of star formation at the age at which it was born.

As said before, by integrating the contribution of each isochrone element along the whole isochrone, the integrated spectral energy distribution, SED, $ssp_\lambda(\tau^{'}, Z)$ of a SSP of any age and metallicity has been derived. This is given by:

$$ssp_\lambda(\tau^{'}, Z) = \int_{M_l}^{M_u} \Phi(M) f_\lambda(M, \tau^{'}, Z) dM \tag{1.2.1}$$

where f_λ is the monochromatic flux of a star of mass M, metallicity $Z(t)$ and age given by $\tau^{'}$. $\Phi(M)$ is the IMF. The integrated $ssp_\lambda(\tau^{'}, Z)$ refers to an ideal SSP of total mass 1 $M_\odot$ whose component stars distribute in mass according to the IMF over the range $[M_l - M_u]$.
The total luminosity of a SSP is obtained by integrating $ssp_\lambda(\tau^{'}, Z)$ over the whole range of wavelengths:

$$L_{SSP}(\tau^{'}, Z) = \int_0^\infty ssp_\lambda(\tau^{'}, Z) \tag{1.2.2}$$

In more detail, the various steps by which the theoretical SED of an SSP is derived are the following:

(a) given an age, the corresponding isochrone in the HRD is divided in elemental intervals small enough to assure that the luminosity, gravity, and T_{eff} in them are nearly constant (the isochrone is approximated to series of virtual stars, for each of which we know the spectrum);

(b) in each elemental interval the star mass spans a suitable range ΔM fixed by the evolutionary rate, therefore the number of stars per elemental interval is proportional to the integral of the initial mass function (IMF) over the range ΔM (the differential luminosity function);

(c) finally, the contribution to the flux at each wavelength of the spectrum by each elemental interval is weighed on the number of stars in it and their luminosity.

To summarize, the basic ingredients of the SSP SEDs are the isochrones and their path in the theoretical HRD, in turn functions of the initial chemical composition. For the details about the set of isochrones used for this work and its characteristic see Sect. 1.1), the IMF (in our case, we included many IMF to choose from, presented in Sect. 1.1.4), and a library of stellar spectra for different values of T_{eff}, gravity, and chemical composition. We used two libraries of stellar spectra. The first one is for objects which are not embedded into dust and it is from Lejeune et al. (1998), which stands on the Kurucz (1995) release of theoretical spectra, however with several important implementations. For $T_{eff} < 3500\ ^\circ K$ the spectra of dwarf stars by Allard & Hauschildt (1995) are included and for giant stars the spectra by Fluks

et al. (1994) and Bessell et al. (1989), Bessell et al. (1991) are considered. Following Bressan et al. (1994), for $T_{eff} > 50000\ ^{\circ}K$, the library has been extended using black body spectra. The library of stellar spectra for dusty stars, in practice AGB stars, will be discussed in detail in the next sections.

1.3 SEDs of SSPs

An extended grid of SEDs of SSPs has been calculated, according to the set of isochrones whose features have been presented in the Sect. 1.1.
Here we underline again the crucial points:

- the SSPs are based, up to the pre-TP-AGB phase, on the isochrones by Bertelli et al. (1994) up to the E-AGB and for the PN phase;
- the treatment of the TP-AGB phase is done following the work of Weiss & Ferguson (2009) (see Sect. 1.1.3);
- the stellar models extend from the ZAMS to either the stage of PN formation or central carbon ignition, depending upon the mass of the most evolved star in the isochrone;
- in low mass stars, passing from the tip of red giant branch (T-RGB) to the HB or clump, mass-loss by stellar winds is included according to the Reimers (1975) rate with η=0.45;
- the mass loss law adopted during the AGB phase is presented in Sect. 1.1.2;
- SSPs are presented (see Sect. 1.1.4) for nine different prescription for the IMF: four power-laws (Salpeter, Arimoto & Yoshii, Kennicutt, and Kroupa 1998), three exponential-laws (Larson - for Milky Way disk or for solar neighbourhood- and Chabrier) and a multi-slope power laws (Kroupa 2007 and Scalo).
- The effect of the circumstellar dusty shells around AGB stars on stellar radiation are now considered using a suitable library of dusty SEDs of AGB stars (see 1.4).

1.3.1 A comparison with the old SSPs

Before considering the effect of circumstellar dusty shells around AGB stars, in this section we compare the old SSPs as computed starting from the work of Bertelli et al. (1994) and the new database of SSPs, elaborated for our purposes, now considering as *only improvement* the inclusion of the TP-AGB phase from Weiss & Ferguson (2009).

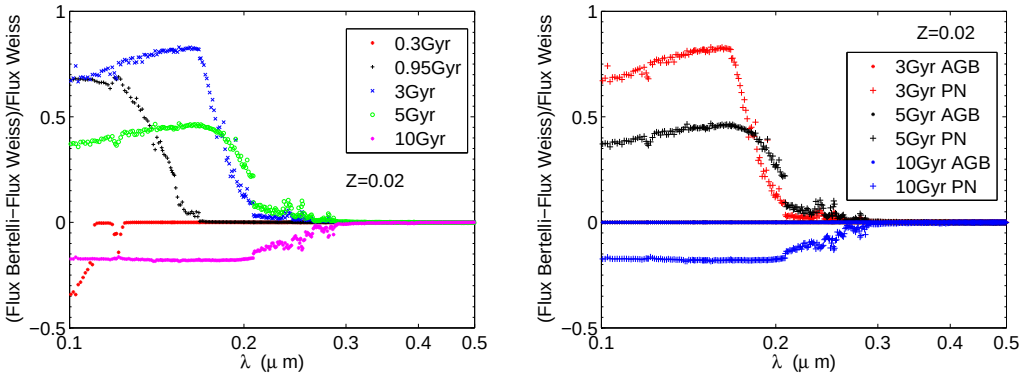

Figure 1.9: **Left panel**: comparison of the flux of our new SSPs and the flux of the *old* SSPs, vs. λ, at varying the age of the stellar population. The considered ages and metallicity are indicated. **Right panel**: the same but now the comparison of the *cumulated* fluxes, up to the end of the AGB phase and of the PN phase, for few selected ages.

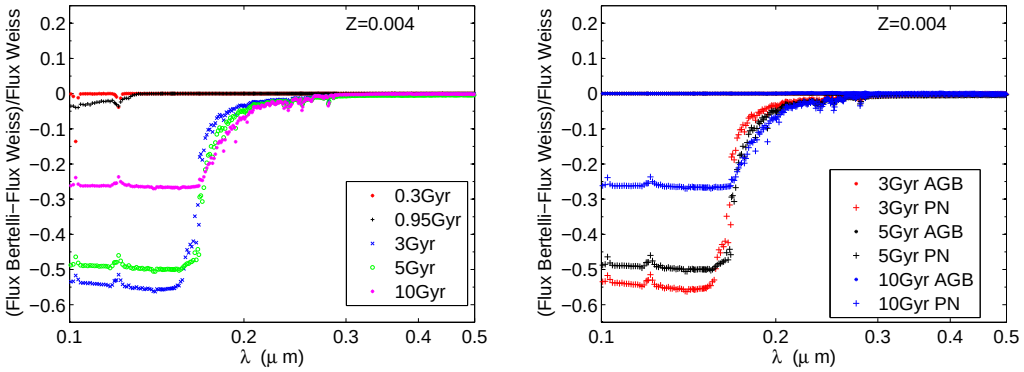

Figure 1.10: The same as in Fig. 1.9, but for Z=0.004

On the **left panel** of the Figs. 1.9, 1.10, 1.11, we present the residual values in the UV-optical range, while in Fig. 1.13 we show the residual values for the optical-near IR range where AGB emit most of their light. We take into account the differences between the flux of the old (indicated in the Figs. as *Flux Bertelli*) and the new (*Flux Weiss*) SSPs as a function of the wavelength (at varying the age of the stellar population), for different values of Z.

On the **right panel** of the same Figs. 1.9, 1.10, 1.11, we show the residual values now analyzing the *cumulated* fluxes, up to the end of the AGB phase or of the PN phase, for few selected ages. In contrast to what one would expect, the main differences between SSPs stand on the UV region, up to 0.3 μm, while from 0.5 μm up to the

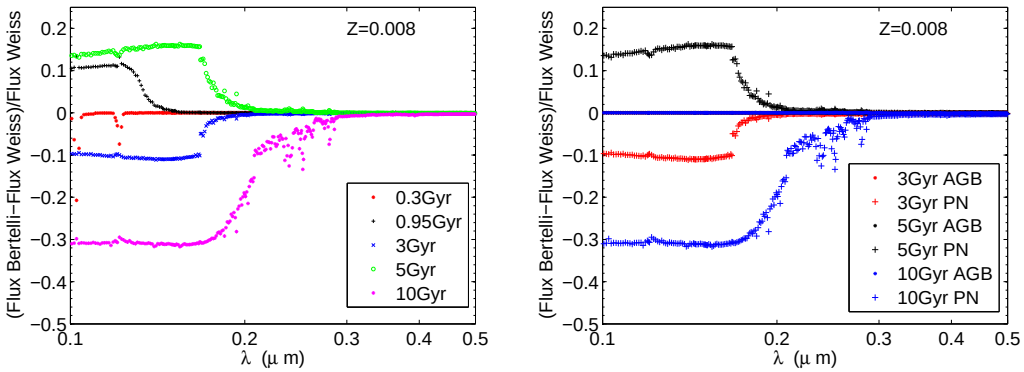

Figure 1.11: As in figure 1.9, but for Z=0.008.

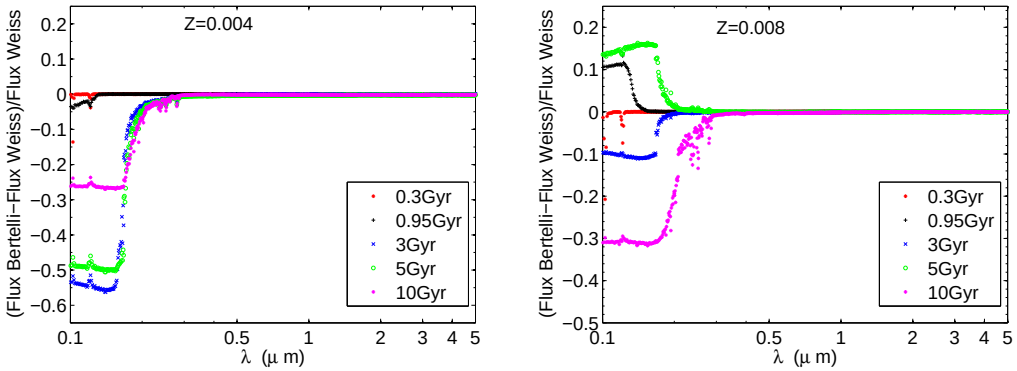

Figure 1.12: **Left panel**: comparison of the flux of our new SSPs and the flux of the *old* SSPs, vs. λ, at varying the age of the stellar population for two metallicities, namely Z=0.004 and Z=0.008. The range of wavelengths most suitable to observe eventual differences due to the AGB-phase only is considered.

IR range (where AGB stars emit most of their light) the residual values are virtually zero at all ages as it can be easily seen from Fig. 1.13.

This is a good proof that there is consistency between the two set of SSPs, as differences are quite small, above all for young ages and in the near IR part of the spectra, where databases are distinct, due to the different treatments of the AGB phase. The differences in the UV range, instead, are due by the distinct mass loss rate adopted during the AGB phase by Bertelli and by Weiss (and hence, in our work). The old set of SSPs consider the Vassiliadis & Wood (1993) formula; in our code, as discussed in Sect. 1.1.2, the mass loss rate is by Wachter et al. (2002), Eq. 1.1.3 or the empirical fitting formula by van Loon et al. (2005), Eq. 1.1.3, depending on

the chemical compositions of the stars. For the same star of a fixed initial mass, the adoption of distinct mass loss rates produce, when the thermally pulsing phase is completed, stars with different final core masses; hence, the corresponding associated PN is different leading to the observed differences. This is evident when observing the **right panel** of the Figs. 1.9, 1.10, 1.11: the cumulate fluxes up to the end of the AGB phase do not contribute at the residual values, while the inclusion of the contribution from the PN phase change the residual values up to the 30%. Moreover, this effect increases at decreasing ages, as expected: higher mass stars experience a larger mass loss rate and the final core mass may result different.

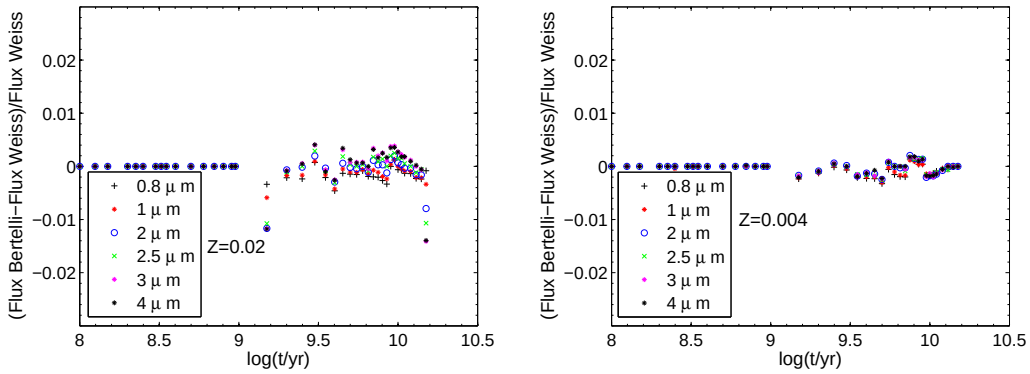

Figure 1.13: The same as in the **left panel** of the Fig. 1.9, but in this case we considered the residual values as a function of age, at varying the λ, for Z=0.02 (**left panel**) and Z=0.004 (**right panel**).

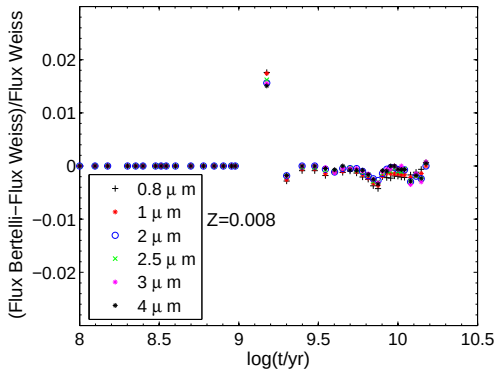

Figure 1.14: As in Fig. 1.13, but for Z=0.008.

The Figs. 1.13 and 1.14 present the residual values (normalized differences between the flux of our SSPs and the flux of the old ones), vs. age, at varying the reference

wavelength, for different values of Z (as usual, we focus on Z=0.02, Z=0.004 and Z=0.008). For all these cases, we do not consider the effect of circumstellar dusty shell around AGB stars; so, we expect that these cool M and C stars emit the majority of their flux in the range $\sim$ 1-4 μm (the inclusion of dust shift the emission toward longer wavelengths). The agreement is very good, and the two set show a few percents of differences, that start at about log(t/yr)=9. This suggest us that the when comparing SSPs for what matters the total amount of flux emitted *without dust*, there is in practice not much difference between the two sets. In particular for the youngest ages with the most massive AGB stars (log(t/yr)>9) and the strongest emissione the agreement is even better. This is ultimately due to a similar duration of the AGB for the Padua and GARSTEC models. Indeed, we expect that most of the differences will appear in the path in the HRD (new opacities allow for AGB tracks extended toward low temperatures), in particular once dust is included. To conclude this section, we show in the Fig.1.15 the theoretical $[V-K]$ color as a function of age for our SSPs and for the old SSPs in the range 0.1 to 15 Gyr, for all the considered values of the metallicity.

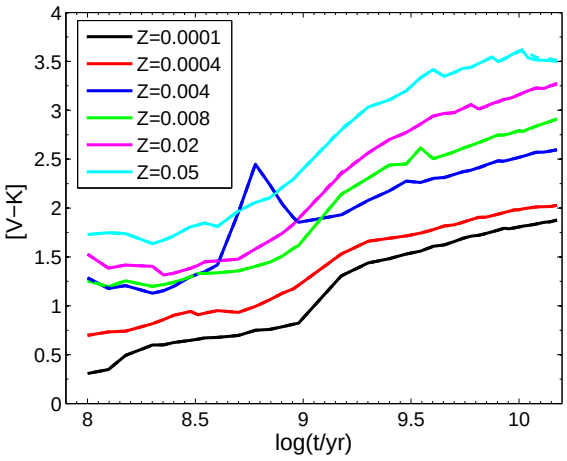

Figure 1.15: Theoretical $[V-K]$ color as a function of the age (from 0.1 to 15 Gyr), for the indicated values of metallicity. Two different sets of SSPs are shown, the *old* SSPs (as Bertelli et al. (1994)) and the *new* ones presented here (*without considering the contribution of circumstellar dusty shell* around AGB stars), even if no remarkable differences can be appreciated and in practise they are superimposed.

As it is evident, when looking at the integrated color, there is no difference between the two kind of SSPs. There is only a little shift for Z=0.05 at t$\geq$ 10 Gyr: new SSPs show a redder color with respect to the old ones, but in practice this shift is so small that it can be neglected. We show only one color, but the same considerations hold when looking at other colors, for instance $[B-V]$ or $[J-8\mu m]$. As already

discussed, it proves that the inclusion of the AGB phase from Weiss & Ferguson (2009) on the evolutionary stellar tracks of Bertelli has been done in a consistent way: the evolutionary times ultimately agree, even if different mass loss rates have been adopted in the two cases.

1.4 Circumstellar dust around AGB stars

AGB stars are one of the main sources of dust: it is safely known that low and intermediate mass stars going through the AGB evolutionary phase are between the main injectors of dust in the ISM. It is worth underlying that other evolutionary phases of low and intermediate mass stars are not so crucial as dust factories: dust formation in RGB and Early AGB stars is poorly efficient because of the not favourable wind properties and the low mass loss rate (Gail et al. 2009). Indeed, as far as it concerns the light travelling to the observer, in practice no effect of local obscuration of the underlying radiation, due to the an eventual dust shell around, is usually considered in HR diagram simulations or calculations of SSP SEDs. Only Thermally pulsing AGB stars are expected to form dust in significant amount and be locally obscured in such a way that we need to introduce the obscuration due to the circumstellar dust shell around (Piovan et al. 2003).

TP-AGB stars have been the subject of an impressive number of studies based on the theory of stellar evolution and going from synthetic models (see for example Groenewegen & de Jong (1993), Marigo et al. (1996), Wagenhuber & Groenewegen (1998), Marigo (2002), Izzard & Poelarends (2006), Marigo & Girardi (2007)) to full calculations of evolutionary, even hydrodynamical, models (see for instance Herwig et al. (1997), Karakas et al. (2002), Ventura et al. (2002), Herwig (2004), Weiss & Ferguson (2009)). Also, dust formation on AGB stars has been the subject of more and more refined and detailed models (Gail et al. 1984; Gail & Sedlmayr 1985; Gail & Sedlmayr 1987; Dominik et al. 1993; Gail & Sedlmayr 1999; Ferrarotti & Gail 2002; Ferrarotti & Gail 2006; Gail et al. 2009), able to calculate the amount of newly formed dust in M-stars, S-stars and C-stars, along a sequence of growing C/O ratio. This ratio determines the dust mixtures formed in the outflows (Piovan et al. 2003; Ferrarotti & Gail 2006; Gail et al. 2009). AGB stars with $C/O < 1$ are oxygen rich stars, that produce dust grains mainly formed by refractory elements, generically defined as silicates, like pyroxenes and olivines, oxides like alumina and maybe iron dust. When the C/O ratio is higher than one, we have carbon rich stars on whose outflow carbon dust, SiC and maybe iron dust can condensate. SiC is detected by means of the typical MIR feature. When $C/O \approx 1$ then we get S-stars where quartz and iron dust should form (Ferrarotti & Gail 2002). However the C-rich or O-rich phases dominate, so that for example the contribution of eventual SiC

produced during the S phase can be neglected compared to the SiC produced during the carbon-star phase.

Depending on the initial mass, the metallicity and the complex interplay between the third dredge-up and the mass-loss, the star will become or not carbon-rich. Typically, low mass stars are not able to become C-rich, because they loose the envelope before that carbon overcomes the oxygen abundance, while intermediate mass stars are able to reach $C/O > 1$, even if in some cases only for a short part of the TP-AGB as it happens for the most massive AGB stars.

1.4.1 Modelling a dusty envelope

The problem of the radiative transfer in the dusty shells that form around AGB stars has been addressed by many authors in literature (see the classical review by Habing (1996) and references therein). The best approach would clearly be to couple the equations describing the radiative transfer through the dusty envelope with the hydro-dynamical equations for the motion of the two components, dust and gas, taking into account the interplay between gas, dust and radiation pressure. For the purposes of this work, it is however enough to limit ourselves to solve the problem of the radiative transfer through the envelope. Indeed our purpose is to build a library of dusty SEDs to be used to quickly determine the effects of dust around AGB stars on the emitted light, and not to study the dynamical behaviour of the outflows.
According to Ivezic & Elitzur (1997), the radiative transfer equation satisfies the property of scale invariance: the physical dimension of any system can be increased and decreased in an arbitrary way without affecting the radiative properties, as long as optical depths and spatial variation of the opacity remain the same. Two systems with different dimensions and absorption coefficients, but with the same total optical depths and auto-similar distributions of opacities and "*source functions*" will produce the same intensity of the radiation field. Rowan-Robinson (1980) first applied the radiative transfer scale invariance to the IR emission of a central source surrounded by a dust shell. Subsequently, Ivezic & Elitzur (1997) presented a general formulation of the problem in arbitrary geometry and distribution of dust, and studied in detail the case of a spherical shell of dust heated up by a central source. They also pointed out that the concept of scale invariance is particularly useful when the absorption coefficient does not depend on the radiation intensity. Unfortunately, as a consequence of this, the analysis by Ivezic & Elitzur (1997) cannot be applied to emission or photo-ionization lines (where the absorption coefficient can depend on the intensity of the radiation field via its effects on the level populations) but only to the continuum of the radiation coming from dust heated by a central source.

1.4.2 The optical depth

At the purpose to get the outgoing flux filtered through the circumstellar dust shell, we apply the classical numerical code DUSTY by Ivezic & Elitzur (1997). Since the original DUSTY code could not handle too a detailed wavelengths grid without becoming computationally very demanding, the latest freely available DUSTY version - 2.06 - has been suitably modified in such a way to be able to handle a wide number of wavelengths. In this way we have been allowed to cover with an acceptable computational effort: (1) the stellar part of the spectrum with the classical Kurucz-Lejeune grid (Lejeune et al. 1998) and (2) the dusty part of the spectrum in the IR including all the wavelengths for which the optical properties and features of the dust in the envelope are available. The spherical symmetry approximation on which DUSTY is based is adopted for the sake of simplicity. The key parameter that we need to specify to solve the radiative transfer problem and to calculate the flux emerging from the dust is the optical depth τ_λ of the shell which is defined as follows:

$$\tau_\lambda = \int_{r_{in}}^{r_{out}} d\tau_\lambda (r) = \int_{r_{in}}^{r_{out}} k_\lambda (r)\, \rho_d (r)\, dr \tag{1.4.1}$$

where $k_{\lambda,d}$ is the overall dust extinction coefficient per mass unit and ρ_d is the dust mass density. In principle, they both depend on the radial distance r from the central source. The integral is evaluated over the thickness of the shell from the innermost to the outermost radius. If we now apply the continuity equation for the gas and dust (Schutte & Tielens 1989; Piovan et al. 2003) we can recast the optical depth of Eq. 1.4.1 as

$$\tau_\lambda = \int_{r_{in}}^{r_{out}} k_\lambda (r)\, \frac{\dot{M}(r)\, \delta (r)}{4\pi r^2 v_d (r)} dr \tag{1.4.2}$$

where δ is the dust-to-gas ratio in the shell. To proceed further, the mass-loss rate $\dot{M(r)}$, the expansion velocity of the dust $v_d(r)$, the extinction coefficient $k_\lambda(r)$ and the dust-to-gas ratio δ together with their radial dependence must be specified. Common assumptions are the following ones (Groenewegen 1993; Bressan et al. 1998; Piovan et al. 2003; Groenewegen 2006; Marigo et al. 2008): at any given time the rate of mass-loss and the velocity are constant with r. The same holds for the optical properties of the dust and the dust-to-gas ratio. The radial dependence is neglected. With these simplifications and assuming that $r_{out} \gg r_{in}$ and $r_{in} \sim r_c$ we have

$$\tau_\lambda = \frac{\delta \dot{M} k_\lambda}{4\pi v_\infty r_c} \tag{1.4.3}$$

where v_∞ is the terminal velocity of the wind and the condensation radius r_c is used as innermost distance from which dust starts to absorb the stellar radiation. We can

assume with good approximation that $v_d(r) \sim v_\infty$ because of the small drift between gas and dust (Groenewegen 1993). The extinction coefficient for unit mass k_λ is in general given by:

$$k_\lambda = \frac{\sum_i n_i \sigma_i(a,\lambda)}{\rho_d} = \frac{\sum_i n_i \pi a^2 Q_i(a,\lambda)}{\rho_d} \tag{1.4.4}$$

where the summation is extended over all the types of grain which populate the envelope, σ_i and n_i are the cross section and the number of grains for unit volume of the i-th dust type, respectively. For the sake of simplicity only one typical dimension a of the grain is assumed. If we make explicit ρ_d, the total mass density of the grains for unit volume, as

$$\rho_d = \frac{4}{3}\pi a^3 \sum_i n_i \rho_i. \tag{1.4.5}$$

where ρ_i is the mass density of one grain of dust type i assumed spherical, we can finally get:

$$\tau_\lambda = \frac{3\delta \dot{M}}{16\pi v_\infty r_c} \frac{\sum_i n_i Q_i(a,\lambda)/a}{\sum_i n_i \rho_i} \tag{1.4.6}$$

Starting from Eq. 1.4.6, introducing a single type of grains and properly normalizing the various quantities, it is possible to easily recover the expression adopted by Groenewegen (2006) for the optical depth. The inner radius of the shell can be derived from the total luminosity conservation $L = 4\pi R_*^2 \sigma T_{eff}^4 = 4\pi r_c^2 \sigma T_d^4$, thus obtaining that (Marigo et al. 2008):

$$\tau_\lambda = A_d \delta \dot{M} v_\infty^{-1} L^{-1/2} \tag{1.4.7}$$

where A_d depends on the adopted mixture of dust:

$$A_d = \frac{3}{8} T_d^2 \left(\frac{\sigma}{\pi}\right) \frac{\sum_i n_i Q_i(a,\lambda)/a}{\sum_i n_i \rho_i} \tag{1.4.8}$$

Different kind of dust would imply different condensation temperature T_d, thus leading to different radii r_c. For the sake of simplicity and also adapting the model to the DUSTY requirements, only a single condensation temperature will be adopted even in the case of a multi-component dust shell. What we need is now to connect the typical quantities defining the optical depth of the shell with the typical parameters of a full stellar model calculated on the AGB according to the extensive database by Weiss & Ferguson (2009). From the AGB models we can get the luminosity and effective temperature of the star, L and T_{eff}, the mass loss rate $\dot{M}$, the metallicity Z, the C/O ratio and the elemental composition of the star at the surface. These physical inputs have to be connected to the ingredients entering the optical depth.

To simulate the terminal velocity of the wind Bressan et al. (1998) and Piovan et al. (2003) adopted, eventually slightly corrected, the simple recipes by Vassiliadis & Wood (1993) and Habing et al. (1994). In this thesis we include the recent formulation of the problem by Elitzur & Ivezić (2001), also adopted in Marigo et al. (2008). They propose a general formula able to summarize their results for dusty winds:

$$v_\infty = \left(A\dot{M}_{-6}\right)^{1/3} \cdot \left(1 + B\frac{\dot{M}_{-6}^{4/3}}{L_4}\right)^{-1/2} \tag{1.4.9}$$

where the velocity is in Km s^{-1}, $\dot{M}_{-6}$ is the mass-loss rate in units of 10^{-6} $M_\odot yr^{-1}$ and finally L_4 is the luminosity of the AGB star in $10^4 L_\odot$. The two parameters A and B are defined as (Elitzur & Ivezić 2001):

$$A = 3.08 \times 10^5 T_{c3}^4 Q_* \sigma_{22}^2 \Psi_0^{-1} \tag{1.4.10}$$

$$B = \left(2.28\frac{Q_*^{1/2}\Psi_0^{1/4}}{Q_V^{3/4}\sigma_{22}^{1/2}T_{c3}}\right)^{-4/3} \tag{1.4.11}$$

The meaning of the various parameters contained in A and B is the following one. T_{c3} is the dust condensation temperature in units of 10^3. Literature values range from 800 K to 1500 K (Rowan-Robinson & Harris 1982; David & Papoular 1990; Suh 1999; Suh 2000; Lorenz-Martins & Pompeia 2000; Lorenz-Martins et al. 2001; Suh 2002). Our choice for the temperature is in the range from 1000 K to 1500 K depending on the dust mixture adopted and the C/O ratio (see below for more details), thus in agreement with most of the literature and with similar works on dusty AGBs by Groenewegen (2006) and Marigo et al. (2008). Q_* is defined as an average over the Planck function $B(\lambda, T_{\rm eff})$:

$$Q_* = \frac{\pi}{\sigma T_{\rm eff}^4}\int Q\left(a,\lambda\right) B\left(\lambda, T_{\rm eff}\right) d\lambda \tag{1.4.12}$$

where $Q\left(a,\lambda\right)$ is the sum of the absorption and scattering radiation pressure efficiencies, assuming isotropic scattering. The cross section σ_{22} is defined by the following relation with the gas cross section:

$$\sigma_g = \sigma_{22} \cdot 10^{-22} {\rm cm}^2 \tag{1.4.13}$$

where

$$\sigma_g = \pi a^2 \frac{\sum_i n_i}{\sum_i n_{i,g}} = \frac{3}{4}\frac{A_g m_H}{a\overline{\rho}}\delta \tag{1.4.14}$$

where $n_{i,g}$ is the gas numerical density, $A_g \simeq 4/(4X_H + X_{He})$ is the mean molecular weight of the gas (Marigo et al. 2008), m_H is the atomic mass unit and $\overline{\rho}$ is the

average mass density of the grains calculated on the eventual mixture of dust, given by $\overline{\rho} = \sum_i n_i \rho_i / \sum_i n_i$. The parameter Ψ_0 is defined in Elitzur & Ivezić (2001) as:

$$\Psi_0 = \frac{Q_P\left(T_{eff}\right)}{Q_P\left(T_d\right)} \tag{1.4.15}$$

where the subscript P means an average over the Planck function of the absorption efficiency, similar to the average that defines Q_* in Eq. 1.4.12. It must be underlined that in Elitzur & Ivezić (2001) the temperature of the star is assumed to be fixed at 2500 K: in our case we will take into account the variation of T_{eff} introducing every time the temperature of the current stellar model. Finally, the last parameter in Eqs. 1.4.10 and 1.4.11 is Q_V, the absorption efficiency in the visual.

1.4.3 Mass loss

Another critical parameter entering Eq. 1.4.6 for the optical depth is the mass-loss along the AGB, that crucially influences the length of the AGB evolution and the gas and dust yields. It is currently widely accepted and supported by hydro-dynamical calculations that large amplitude pulsations are required for accelerating the mass outflow from the stellar surface of AGB stars until the gas cools enough that refractory elements can condense into dust. Once dust grains are formed, they transfer by collisions energy and momentum from the stellar radiation field to the gas so that the flow velocity may grow enough to exceed the escape velocity (Gilman 1972). Mass-loss grows with time until the so-called super-wind regime: the star quickly evolves into a planetary nebula by stripping away all the envelope and leaving a bare core that evolves in the HR diagram to high temperatures. A typical formulation adopted in literature (Bressan et al. 1998; Piovan et al. 2003) is the Vassiliadis & Wood (1993) one. Weiss & Ferguson (2009) adopts a different and more refined formulation for the mass-loss rate depending on the C/O ratio. Indeed, for the oxygen rich stars the van Loon et al. (2005) formula based upon dust-enshrouded oxygen-rich AGB stars, while for carbon stars, the rate proposed by Wachter et al. (2002) is adopted. The current mass-loss rate is available for each stellar model along the evolutionary tracks and can be introduced into Eq. 1.4.6. The estimate of the mass-loss is crucial, because according to Elitzur & Ivezić (2001) a minimum mass-loss is required to form enough dust to be able to accelerate the gas beyond the escape velocity. The minimum mass-loss is:

$$\dot{M}_{min} = 3 \times 10^{-9} \frac{M^2}{Q_* \sigma_{22}^2 L_4 T_{k3}^{1/2}} \tag{1.4.16}$$

where T_{k3} is the kinetic temperature at the inner boundary of the shell that we

simply put $T_{k3} \approx T_{c3}$. It may easily happen to have optically thin envelopes such that $\dot{M} \lesssim \dot{M}_{min}$, where dust is formed but according to Elitzur & Ivezić (2001) not able to support the wind. We apply therefore the recipe proposed by Marigo et al. (2008) and evaluate the expansion velocity by means of $\dot{M}_{min}$ in such a way to still have a v_∞ to insert in the expression for τ_λ.

1.4.4 Dust-to-gas ratio

Another crucial parameter to be inserted into Eq. 1.4.6 is the dust-to-gas ratio. In Piovan et al. (2003) the dust-to-gas ratio was obtained by simply inverting a relation between velocity, luminosity and dust-to-gas ratio based upon the results by Habing et al. (1994). However, along the years, more and more refined models of AGB stars simulating the process of dust formation in the envelope have been presented in literature (Gail et al. 1984; Gail & Sedlmayr 1985; Gail & Sedlmayr 1987; Dominik et al. 1993; Gail & Sedlmayr 1999; Ferrarotti & Gail 2001; Ferrarotti & Gail 2002; Ferrarotti 2003) until the recent paper by Ferrarotti & Gail (2006) presenting detailed dust yields for O-rich and C-rich stars. Dust formation is usually described through the concept of key species, where the key element is defined as the one least abundant between the ones required to form the dust compounds which formation we want to describe. This key species determines and controls the process of formation and for AGB stars. The dust grains included in the detailed Ferrarotti & Gail (2006) models are pyroxenes, olivines, quartz and iron dust for O-rich M-stars, quartz and iron dust for S-stars with C/O$\sim$1 and, finally, silicon carbide and carbonaceous grains for carbon rich C-stars. For each one of them, according to the abundances adopted by Weiss & Ferguson (2009) the key element will be silicon, iron or carbon, depending on the grain type. Indeed, only the abundances of C and O may change during the AGB evolution due to the third dredge-up and the HBB, while the abundances of Mg, Si, S and Fe do not change. Introducing the key elements and the equations of continuity for the two fluids gas and dust, the dust-to-gas ratio can be expressed as (Ferrarotti 2003):

$$\delta = \frac{\dot{M}_d}{\dot{M} - \dot{M}_d} = \frac{\sum_i \dot{M} X_i \frac{A_{d,i}}{n_{d,i} A_i} f_{d,i}}{\dot{M} - \sum_i \dot{M} X_i \frac{A_{d,i}}{n_{d,i} A_i} f_{d,i}} \tag{1.4.17}$$

where the summation is over all the dusty compounds. Simply, $\dot{M}X_i$ is the abundance of the i-th key-element in the wind, $\dot{M}X_i f_{d,i}$ is the fraction of the key element condensed into dust. Dividing by $n_{d,i} A_i m_H$, with $n_{d,i}$ number of atoms of the key elements that we need to form one dust unit and A_i atomic weight of the i-th element,

we get the number of dust units. Finally multiplying for the mass of one dust unit $A_{d,i}m_H$ we get the total mass of the i-th dusty compounds.

We need now to subdivide the AGB evolution in three region corresponding to different C/O ratio: we follow Ferrarotti & Gail (2006) and define two critical carbon abundances. We have $\epsilon_{C,1} = \epsilon_O - 2\epsilon_{Si}$ and $\epsilon_{C,2} = \epsilon_O - \epsilon_{Si} + \epsilon_S$ where $\epsilon = X/A$ is the abundance in mol g^{-1}. We can therefore define two critical C/O ratios, that is $(C/O)_1 = 0.9$ and $(C/O)_2 = 0.97$ that allow to subdivide the evolution along the AGB in the three classes M-stars, S-stars and C-stars.

O-rich M-stars. O-rich AGB stars of M spectral type, characterized in our adopted scheme by a C/O ratio minor than 0.9, show two typical features at $10\mu m$ and $18\mu m$ either in absorption or in emission depending on the optical depth of the surrounding envelope. These features are usually attributed to stretching and bending modes of Si-O bonds and O-Si-O groups and clearly probe the existence of silicate grains in the shell of matter around the star. Because of the strong bond between O and C in the carbon monoxide, it is believed that all C will be blocked into CO molecules and no C is available to the formation of dust grain with other elemental species of low abundance. In contrast, the fraction of O not engaged in CO reacts with other elements such as Mg and Si and forms various types of compounds, like pyroxenes and olivines. Iron dust can accrete in the envelope as well. Applying Eq. 1.4.17 to the specific case we get:

$$\dot{M}_d = \dot{M}\left(X_{\rm Si}\frac{A_{\rm sil}}{A_{\rm Si}}f_{\rm sil} + X_{\rm Fe}\frac{A_{\rm iro}}{A_{\rm Fe}}f_{\rm iro}\right) \tag{1.4.18}$$

where X_{Si} and X_{Fe} are the mass fractions of the key elements involved (iron for iron dust grains and silicon for silicates), A_{Si} and A_{Fe} are the atomic weight and A_{sil} and A_{iro} are the mass numbers of one typical unit of dust for silicates and iron respectively (Zhukovska et al. 2008). According to the dust types included in Ferrarotti & Gail (2006) we have that silicates includes olivines/pyroxenes/quartz: $f_{\rm sil} = f_{\rm ol} + f_{\rm pyr} + f_{\rm qu}$ and the mean molecular weight of the mixture of silicates is $A_{\rm sil} = \left(A_{\rm ol}f_{\rm ol} + A_{\rm pyr}f_{\rm pyr} + A_{\rm qu}f_{\rm qu}\right)/f_{\rm sil}$. The total fraction of silicates is calculated according to Ferrarotti (2003):

$$f_{\rm sil} = 0.8\frac{\dot{M}}{\dot{M} + 5\times10^{-6}}\sqrt{\frac{\epsilon_{\rm C,1} - \epsilon_{\rm C}}{\epsilon_{\rm C,1}}} \tag{1.4.19}$$

we still need to specify f_{ol}, f_{pyr} and f_{qu}. According to Ferrarotti & Gail (2001) the mixtures crucially depends on the ratio between the abundances of Mg and Si that is about 1.06 for the solar abundances (Zhukovska et al. 2008). For a typical M-star: f_{ol}/f_{pyr}=4 and f_{ol}/f_{qu}=22. Finally for the iron dust:

$$f_{\rm iro} = 0.5 \frac{\dot{M}}{\dot{M} + 5 \times 10^{-6}} \tag{1.4.20}$$

S-stars. In our scheme we include S-stars for the range $0.90 \leq \mathrm{C/O} \leq 0.97$, that is when $\mathrm{C/O} \lesssim 1$. In this range the poorly available O allows for a dust mixture that will be iron-dust dominated. The situation can be described again by Eqs. 1.4.18 and 1.4.20. The silicates are again subdivided with the same ratios as for M-stars (Ferrarotti & Gail 2002), while the condensation fraction is lower than Eq. 1.4.19:

$$f_{\rm sil} = 0.1 \frac{\dot{M}}{\dot{M} + 5 \times 10^{-6}} \tag{1.4.21}$$

C-rich C-stars. Through continuous dredge-up of carbon into the envelope during the thermally pulsing AGB phase, M-stars eventually reach a carbon abundance in the outer layers larger than that of oxygen. According to the adopted scheme we start to describe a C-rich environment of dust formation in the envelope when $\mathrm{C/O} \geq 0.97$. When this occurs the formation of O-rich dust ceases and it is replaced by that with C-rich compounds: the C-star phase begins. Therein after, the continuous formation of C-rich dust makes the envelopes of these stars more and more optically thick. By loosing mass at very high rates, they get enshrouded by thick envelopes that absorb and scatter the UV-optical radiation into the IR and radio range. According to Ferrarotti & Gail (2006) two kind of dust are included, that is: carbonaceous grains, that are the natural product of such a C-rich environment and silicon carbide (SiC). Indeed, almost all these stars show an emission feature at $11.3 \mu m$, due to SiC, whose presence was predicted by Gilman (1969) and confirmed by Hackwell (1972) through observations. Applying Eq. 1.4.17 to the C-stars case we get:

$$\dot{M}_d = \dot{M} \left(X_{\rm C} \frac{\mathrm{A_{SiC}}}{\mathrm{A_C}} \mathrm{f_{SiC}} + \mathrm{X_C f_{car}} \right) \tag{1.4.22}$$

with obvious meaning of the symbols. In particular $\mathrm{f_{car}}$ and $\mathrm{f_{SiC}}$ are evaluated following Ferrarotti (2003). That is for $f_{\rm SiC}$ Eq. 1.4.20 is used while:

$$f_{\rm car} = 0.5 \frac{\dot{\mathrm{M}}}{\dot{\mathrm{M}} + 5 \times 10^{-6}} \left(\frac{\epsilon_{\rm C} - \epsilon_{\rm O}}{\epsilon_{\rm O}} \right) \tag{1.4.23}$$

Once the dust-to-gas ratio is specified we know all the parameters that enters the Eq. 1.4.6 of the optical depth. Therefore we can proceed in the following way: once a point of given $(\mathrm{L}, \mathrm{T}_{eff})$ belonging to a stellar evolutionary track or to an isochrone is determined together with its properties we can connect the point to the corresponding model of dusty AGB determining the final SEDs with dust effects included. In particular, for every AGB theoretical point (from isochrone or evolutionary tracks) we need: L, T_{eff}, $\dot{\mathrm{M}}$, C/O ratio and the elemental abundances at the surface X_i.

What we get at the end is the optical depth τ, the key-parameter of the problem and hints about the mixture of dust formed in the envelope thus determining the extinction coefficients Q to be used in the radiative transfer problem.

1.5 The library of dusty spectra

Since the end target is to get stellar spectra eventually modified by the effects of the dust shell around the AGB star, the more correct way to face this problem would be to real-time calculate for every model the corresponding SEDs to be used in the model of interest (such as HR diagrams, or SEDs of SSPs), connecting the theoretical inputs to the radiative transfer ones step by step. However, this way to face the problem adopted in the SEDs of SSPs by Piovan et al. (2003) is very slow. Indeed it depends on the computational time required to solve the radiative transfer problem and the precision required: it can be acceptable only if the number of models to be calculated is small, thus obviously in this latter case poorly describing the isochrone/track. We choose in this work to sacrifice a bit the precision due to the tight correlation between the physical quantities of the stellar model and the on the spot solution of the radiative transfer problem, in order to obtain a much more handy descriptions. This implies to a priori calculate a library of dust enshrouded AGB stars trying to cover with an acceptable number of models the space of the parameters.
We calculated two libraries of obscured SEDs, one for O-rich M-stars and one for C-rich carbon stars, each of them made by 600 spectra. The space of the parameters has been subdivided in the following way, eventually taking into account what could be varied in the DUSTY input:

1. the optical depth τ obtained from Eq. 1.4.6 by means of the physical quantities describing the stellar model underlying the dust shell. For each group (C-stars and M-stars) we calculated a total amount of 25 optical depths, going from 0.000045 to 40 at the MIR reference wavelength that is chosen depending on the dust mixture as it will be discussed below.

2. the profile of the input SEDs from the star embedded in the dusty shell and heating the dust. Since the total luminosity is not a key parameter of the radiative transfer problem we just need the normalized flux $\lambda \cdot F_\lambda$ in some arbitrary units. The following libraries of stellar spectra have been adopted: for the O-rich stars we use the Lejeune et al. (1997) library that for cool M-stars includes the semi-empirical Fluks et al. (1994) spectra; for the C-rich stars we select a suitable number of spectra from the recent Aringer et al. (2009)

models of dust-free carbon stars. For the library of M-stars 6 temperatures are selected, that is 2500 K, 2800 K, 3000 K, 3200 K, 3500 K and 4000 K. The gravity g of the star does not enter the problems because it is not specified by the Fluks et al. (1994) library that uses a sequence of semi-empirical spectra. In the same way we selected 6 temperatures from the library by Aringer et al. (2009), that is 2400 K, 2700 K, 3000 K, 3200 K, 3400 K and 3900 K. Since we also have the possibility to choose the C/O ratio, we selected two values for our library, that is C/O = 1.05 and C/O = 2. The mass and gravity used as input are M = 2 $M_{\odot}$ and $g = 0.0$. The metallicity is the solar one.

3. the dust composition to be adopted to describe the envelope.
   C-stars. Several types of dust grains are confirmed by the observations in C-rich AGB stars: in particular amorphous carbon (AMC), silicon carbide (SiC), and magnesium sulphide (MgS), to mention the three main types. We rely on the results by Suh (1999) and Suh (2000) that derived new opacities for the AMC, that are consistent with the Kramers-Kronig dispersion relations and reproduce the observational data. The models improve upon previous studies (Blanco et al. 1998; Groenewegen et al. 1998) and are characterized by two components, SiC and AMC. Since the optical constants of MgS are not measured for a sufficiently wide range of wavelengths (Suh 2000; Hony et al. 2002) the presence of MgS is neglected. AMC and SiC influence the outgoing spectrum in a different way: while the effects of AMC propagate over the whole spectrum, those of SiC are limited to the 11μm feature as observationally indicated. Lorenz-Martins & Lefevre (1994) and Groenewegen (1995) suggest that the ratio SiC to AMC decreases at increasing optical depth of the dusty envelope. According to Suh (1999), for optically thin dust shells ($\tau_{10} \leq 0.15$) where τ_{10} is the optical depth at 10 μm, the strong 11μ m feature requires about 20% of SiC dust grains to fit the observational data; for dust shells with intermediate ($0.15 \leq \tau_{10} \leq 0.8$) about 10% SiC dust grains are needed, whereas for shells with larger optical depths, in which the 11μm feature is either much weaker or missing at all, no SiC is required. The optical constants of αSiC by Pégourié (1988) are adopted to calculate the opacity for SiC and according to the considerations above we consider two extreme compositions: the first one with 100% AMC only, while the second one with 80 % AMC and 20% SiC. The reference optical depth has been chosen as 11.33 μ m for the 100% AMC mixture, while we adopt 11.75 μ m for the 80 % AMC and 20% SiC mixture.
   M-stars. In the circumstellar environment of M-stars a wide number of dust grains is formed: we limit the number of dust mixtures for the envelope trying to describe what the so-called dust condensation sequence proposed by Tielens

(1990). According to this scenario, at increasing the mass-loss the dust composition changes going from dust rich in oxides of aluminium and magnesium (like Al_2O_3, $MgAl_2O_4$ and (Mg,Fe)O) at low $\dot{M}$, to a mixture with both oxides and olivines, until a composition dominated by the silicates with amorphous silicates and crystalline silicates at high $\dot{M}$. This kind of sequence seems to be able to reproduce the changes and the evolution observed in the shape of the 10 μm feature. Even if this scheme is clearly matter of debate in literature (van Loon et al. 2006), it is coherent with samples of stars of different metallicity, thus allowing to use it as a plausible scenario for the dust condensation sequence in O-rich stars. Indeed, this simple scheme agree with observations of M-type stars in the LMC with Z$\simeq$ 0.008 (Dijkstra et al. 2005), of evolved stars in 47-Tuc at [Fe/H]$\simeq$ -0.7 (Lebzelter et al. 2006) (that is Z$\simeq$ 0.004 according to the transformations by Bertelli et al. (1994)), of bulge stars (Blommaert et al. 2006) with metallicity more or less sub-solar ($<$ [Fe/H] $>\simeq -0.19$) and, finally, of Galactic AGB stars (Heras & Hony 2005). Three possible compositions are included: (1) a pure 100% Al_2O_3 with optical properties from Begemann et al. (1997); (2) a mixed composition with 60% Al_2O_3 and 40% silicates with the optical properties of these latter ones taken from David & Pegourie (1995); (3) a full silicates model for high mass-loss rates, with two possibile choices for the silicates. A full composition with optical properties from David & Pegourie (1995) just for the sake of eventual comparison with other models (Groenewegen 2006) and a more elaborate description based upon the models and calculations by Suh (1999, Suh (2002). Indeed, Suh (1999) presented optical constants that satisfy both the Kramers-Kronig relation and the observed properties of O-rich AGB stars. He adopted different silicates opacities at varying the 10 μm feature, namely cold and warm silicates. The model has been then refined in Suh (2002) taking into account crystalline silicates through a so called crystallinity parameter α, since in many AGB stars with high mass-loss rates, ISO hi-res observations revealed the presence of prominent bands of crystalline silicates, like enstatite ($MgSiO_3$) and forsterite (Mg_2SiO_4) (Waters et al. 1996; Waters & Molster 1999). The adopted opacity functions for these latter ones are taken from Jaeger et al. (1998). Following Piovan et al. (2003), we adopt here $\alpha = 0.1$ for stars with low mass-loss rates and moderately optically thick shells of matter ($\tau_{10} < 15$), whereas for O-rich stars with high mass-loss rates and very thick shells ($\tau_{10} > 15$) we prefer the value $\alpha = 0.2$. Finally, in all the models the relative contents of enstatite ($MgSiO_3$) and forsterite (Mg_2SiO_4) are the same as in Suh (2002), i.e. we adopt the same relative contribution for the two components. Finally, we took into account the recent results by McDonald et al. (2011), who explored dust production in very metal poor stars

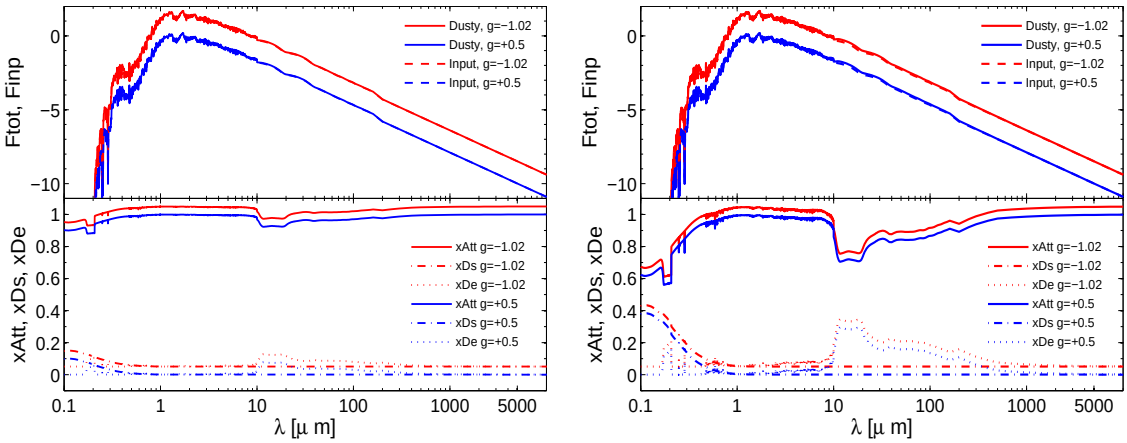

Figure 1.16: Dusty AGB spectra as obtained with the radiative transfer code DUSTY. The input parameters are: M-type underlying stars with T_{eff}=2500 and L=3000$L_{\odot}$, optical depth τ=0.004513 (**left panel**) and τ=0.022382 (**right panel**) and dust composition number 2 for O-rich stars with 60% Al_2O_3 and 40% silicates.

in ω Cen, going from about Z$\simeq$0.0002 to Z$\simeq$0.002. They found that metallic iron seems to dominate dust production in metal-poor O-rich stars. According to this we adopt a 100% iron mixture to simulate the envelope in metal-poor stars with a thin shell of dust around. The optical properties for iron are taken from Ordal et al. (1988). The following reference wavelengths are adopted for the τ grid: 11.75 μm for both pure alumina oxides and oxides plus silicates, while 10.20 μm is selected for both the pure silicates cases.

4. the temperature T on the inner boundary of the dust shell, that we select to be 1000 K or 1500 K depending on the kind of dust mixture (Piovan et al. 2003).

Finally, it is worth noticing the following detail about the luminosity of the stars underlying the shell. For C-stars we kept the luminosity specified by Aringer et al. (2009), while for M-stars, since the Fluks et al. (1994) empirical spectra do not include any information about the luminosity but only the specific intensity, we fixed the luminosity to L=3000$L_{\odot}$. The library of dusty stellar spectra is therefore calculated for a fixed luminosity of the underlying objects. This is not a problem, since the luminosity does not affect the solution of the radiative transfer (Ivezic & Elitzur 1997) and the shape of the outgoing SEDs. The flux will be therefore, when required, scaled to the real luminosity of the AGB star we are going to model.
In Figs. 1.16, 1.16 and 1.16 we show six examples of results obtained with the radiative transfer code DUSTY. In particular, we selected the following combination of the input parameters: M-type underlying stars with T_{eff}=2500 and L=3000$L_{\odot}$, optical depth going from the low value τ=0.004513 up to a thick envelope with

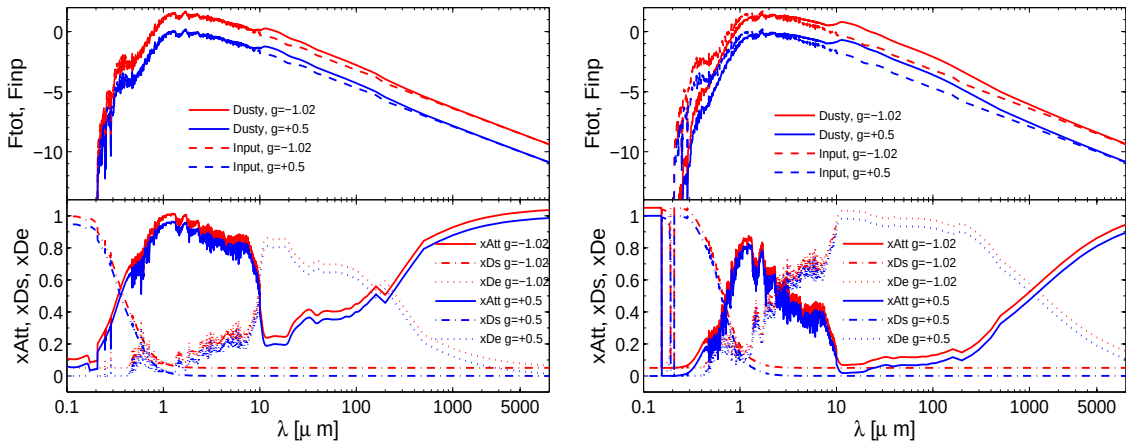

Figure 1.17: The same as in Fig. 1.16, only for two different optical depths, that is τ=0.208266 (**left panel**) and τ=1.306290 (**right panel**)

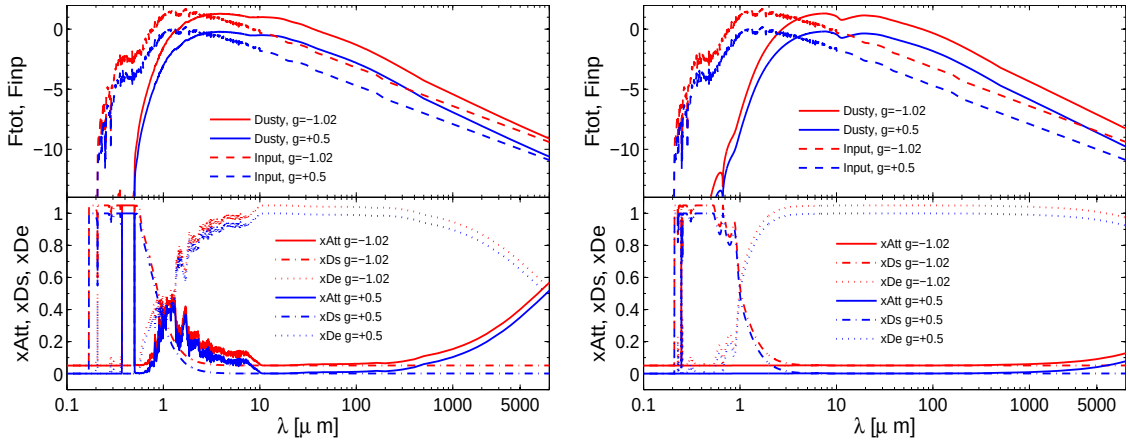

Figure 1.18: The same as in Fig. 1.16, only for two different optical depths, that is τ=6.000000 (**left panel**) and τ=30.000000 (**right panel**)

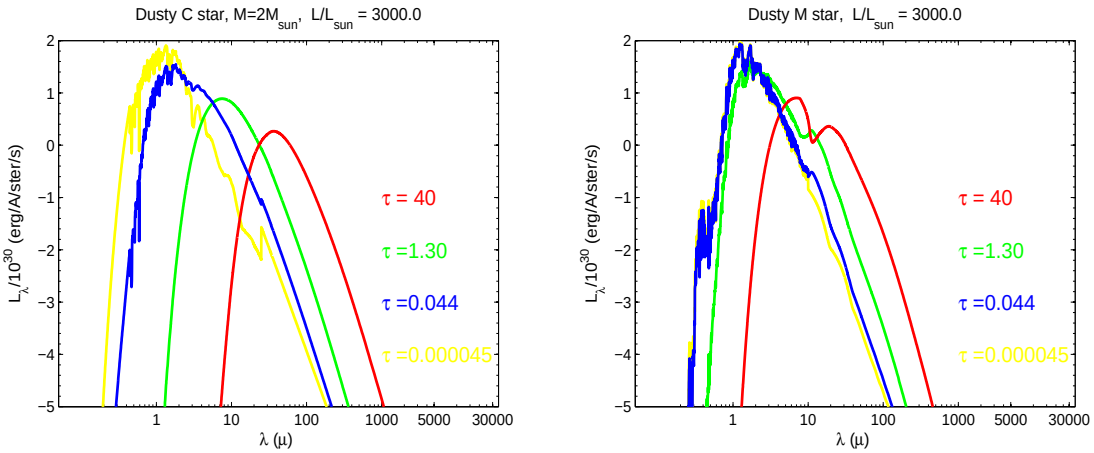

Figure 1.19: Dusty AGB spectra at varying the optical depth for Carbon stars (**left panel**) and M-stars Oxygen rich (**right panel**).

τ=30.000000 (**right panel**) and dust composition number 2 for O-rich stars with 60% Al_2O_3 and 40% silicates. In each figure, the **upper panel** shows the results for two different gravities (g=-1.02 and g=0.5) of the input spectrum from the Fluks et al. (1994) models. We apply an artificial shift for the sake of representation, otherwise, the two spectra would be coincident. Indeed, as expected and verified, there is no dependence from the gravity in the Fluks et al. (1994) spectra so that it is not required to consider the gravity of the underlying star between the input parameter. At growing the optical depth, the stellar features in the UV-optical-near IR region disappear and a more and more featureless SED appears: this is ultimately due to the smooth optical properties of the selected composition. The stellar light is shifted more and more toward longer wavelengths at growing the optical depth: for the lowest optical depths the input and output spectra are almost coincident, while the effect of dust is clear for the highest τ values. In the **lower panels** we show: xAtt (continuous line), the fractional contribution of the attenuated input radiation to the total flux; xDs (dot-dashed line) the fractional contribution of the scattered radiation to the total flux and, finally, xDe (dotted line) the fractional contribution of the dust emission to the total flux. We can see from the sequence of figures that, as expected, at growing the optical depth τ: (1) the fraction of not attenuated or scattered light escaping the dusty shell decreases and (2) the dust contribution becomes overwhelming already at $\tau \sim 1$.

Finally, in Fig. 1.19 we show a sequence of obscured AGB spectra, both for carbon and oxygen rich stars. It is evident how the SEDs becomes more and more shifted toward long wavelengths at growing the optical depth. In this particular case the spectra with 100% AMC dust composition are shown as limit case with no feature

of the SiC at 11.3μm. For the O-rich stars it is worth noticing that when the optical depth is very high the silicate feature at 9.7μm becomes an absorption feature as observed (Suh 1999; Suh 2002).

1.6 SEDs of SSPs with dusty AGB Stars

In the Figs. 1.20, 1.21, 1.22 we plot the SEDs of SSPs with or without dust around AGB stars for different ages and for all the metallicities included in the database.

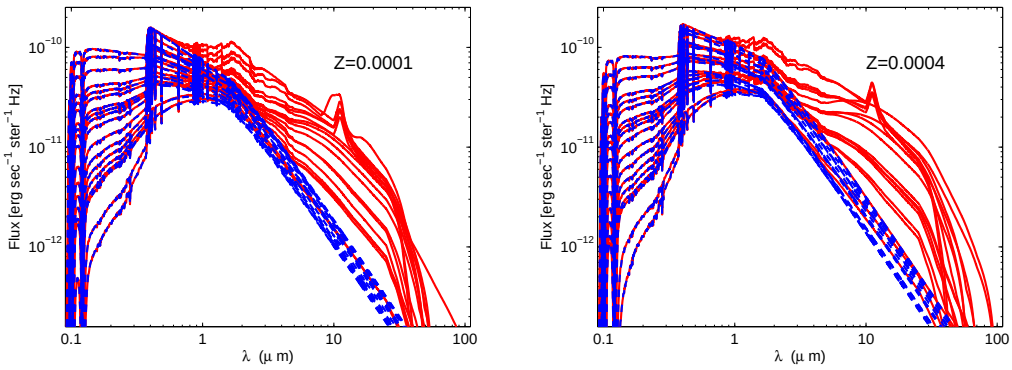

Figure 1.20: SEDs F_ν vs. λ for the SSPs with Z=0.0001 (**left panel**) and Z=0.0004 (**right panel**), ages from 0.1 to 2 Gyr. The dusty circumstellar envelopes in AGB stars have been considered (red continuous lines); the classical SSPs without dust are also shown (blue dotted lines). From the bottom to the top the displayed ages are (from the oldest to the youngest): 2.0, 1.5, 0.95, 0.9, 0.8, 0.7, 0.6, 0.5, 0.4, 0.35, 0.325, 0.3, 0.25, 0.2, 0.15, 0.125, 0.1 Gyr.

The range of ages for the displayed SEDs is from 0.1 to 2 Gyr and it is meant to represent the range of ages for young-intermediate ages of the stellar populations. In Fig. 1.23 we show an old range of ages from 6 to 10 Gyr, that is meant to represent what happens for old stellar populations. It is evident that for the old ages the effect of dust around AGB stars is small, due to the effect of AGB stars of small mass with small mass-loss and few pulses, not able to build a significant dust shell around the embedded objects, whereas, as expected the effect is much more significant for the youngest ages when AGB stars start to shine. Only for the highest metallicity of Z=0.05 we have some significant effect of the dust around AGB stars. A better view of the difference brought by dust is shown in Figs. 1.24, 1.25, 1.26, in which the new and old SEDs are compared for a few selected ages in order to make the figures less crowded. The differences are remarkable and hold for all metallicities.
In the old SSPs models without dust, the spectra do not extend into the medium and far IR, but sharply decline for wavelengths longer than about 3-4 μm. The spectra

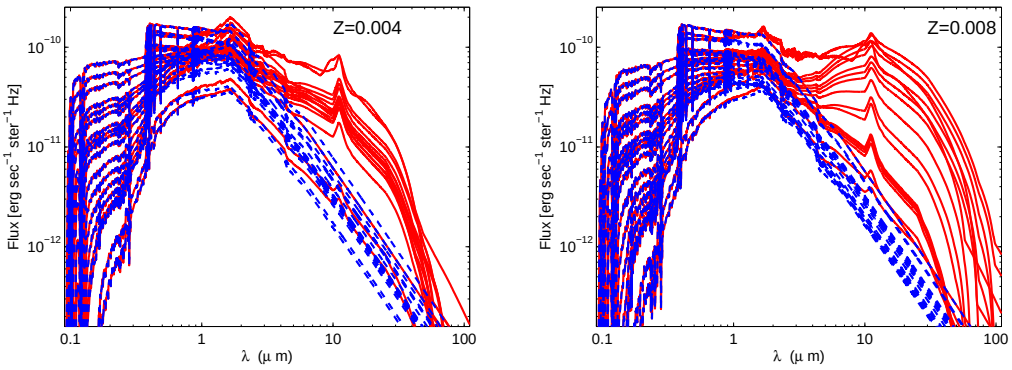

Figure 1.21: As in the figure 1.20, but for Z=0.004 (**left panel**) and Z=0.008 (**right panel**).

of the new SSPs, instead, extend toward long wavelengths and there is a not at all negligible amount of flux also in the MIR and FIR.

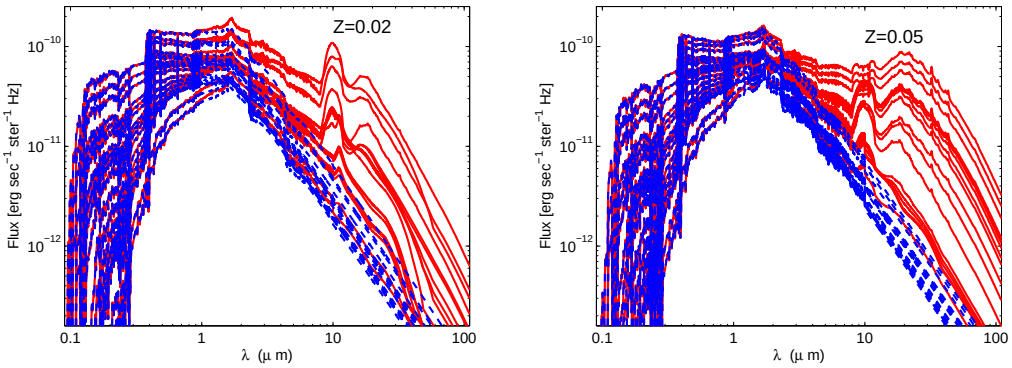

Figure 1.22: As in the Fig. 1.20, but for Z=0.02 (**left panel**) and Z=0.05 (**right panel**).

The differences start at about 1 μm: in the IR range up to 3-4 μm the flux of dusty SSPs is lower than the old one: this is due to the fact that dusty envelopes shift the emission of M and C stars toward longer wavelengths. The amount of energy shifted to longer wavelengths is larger for the young ages; indeed more massive and luminous AGB stars are present. It is worth noticing the different IR spectrum of the new SSPs, the evolution of the features of silicon carbide at 11.3 μm and amorphous silicate at 9.7 μm in particular. Considering the different metallicities, we can observe the following peculiarities:

- Z=0.0004 and Z=0.0001. For stars of very low metallicity, as already discussed

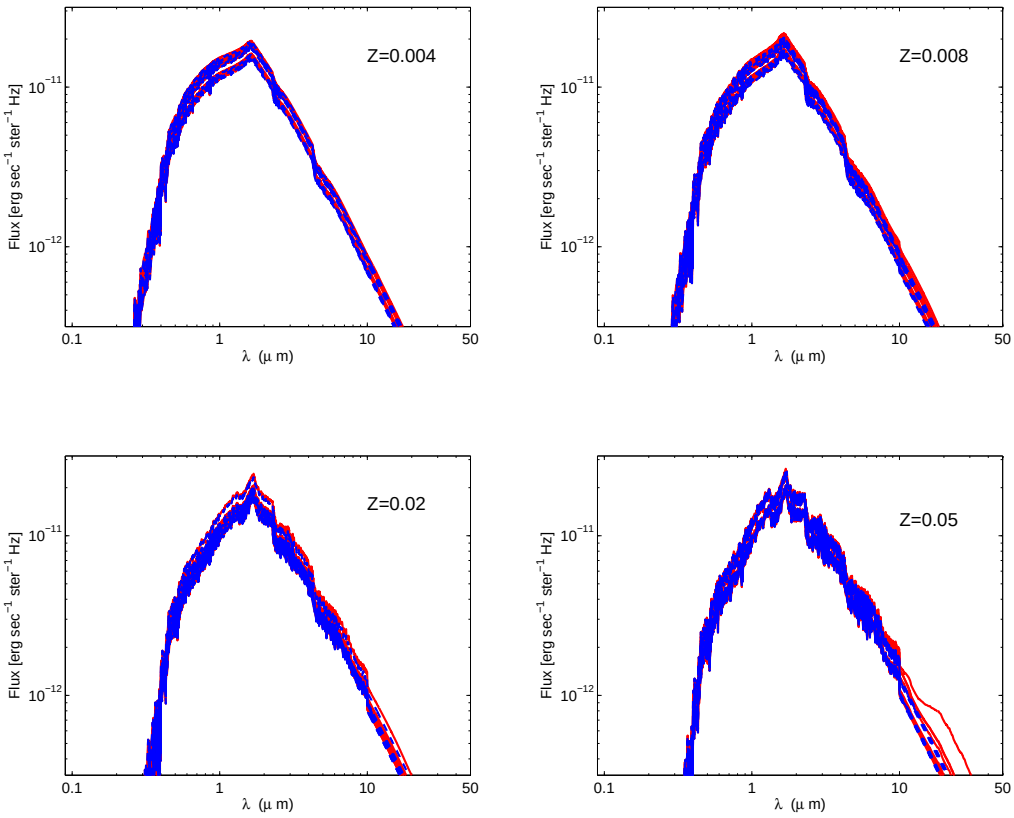

Figure 1.23: SEDs F_ν vs. λ for the SSPs with Z=0.004 (**upper-left panel**) , Z=0.008 (upper-right panel), Z=0.02 (lower-left panel) and Z=0.05 (**lower-right panel**) and ages from 6 to 10 Gyr. The dusty circumstellar envelopes in AGB stars have been considered (red continuous lines); the classical SSPs without dust are also shown (blue dotted lines). From the bottom to the top the displayed ages are (from the oldest to the youngest): 6, 6.5, 7, 7.5, 8, 8.5, 9, 9.5, 10 Gyr.

in Sect. 1.1.1, the TDU is particulary efficient during the AGB phase in enriching the surface in ^{12}C and other products of He-burning; hence, these stars present a C-rich surface for most of their evolution. This dominion of dusty C-rich stars leads to SEDs where for many ages, in particular for the youngest ones, the silicon carbide feature is clearly visible. For the oldest ages however amorphous carbon dominates and we obtain a featureless spectrum without the 11.3 μ m feature. The poor amount of metals in the envelope does not allow for high optical depths, in such a way that the amount of radiation that is re-emitted in the MIR/FIR region is not so high as for higher metallicities.

- Z=0.004 and Z=0.008 : for most of the ages, the spectrum does not show the features due to amorphous and crystalline silicates, because the C-stars domi-

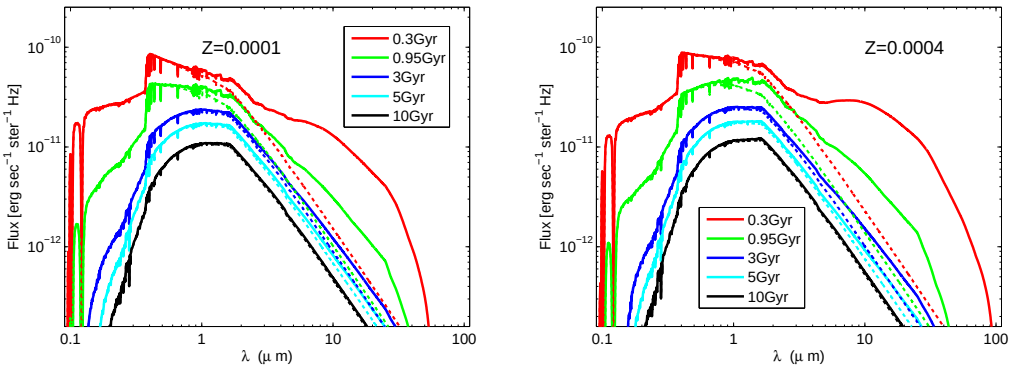

Figure 1.24: Detailed comparison of SEDs for old SSPs (dotted lines) and new SSPs (continuous lines) for Z=0.0001 (**left panel**) and Z=0.0004 (**right panel**). The considered ages are indicated in the legend.

nate (the 11.3 μm feature of SiC is indeed prominent). This is quite different from what was obtained in Piovan et al. (2003) where the O-rich phase at these metallicities played a role determining an evolution of the MIR features from O-rich to C-rich environment. In that case for intermediate ages, such as 3 Gyr, the O-stars of low optical depth influenced the spectrum and the 9.7 μm feature could be seen in emission, while for the older ages, from 5 Gyr onward, the O-stars dominated, so the spectrum became more articulated and the features due to crystalline silicates started to appear at long wavelengths in the IR. This switch of the feature does not happen anymore at these metallicities, simply because of the evolution of the C/O ratio predicted by Weiss & Ferguson (2009) that leads to a different path. It must be observed that, compared to Piovan et al. (2003) in general the amount of energy shifted is minor: this is due to the lower optical depths, now more realistically connected to the composition and mass-loss of the underlying star. The optical depths obtained now are, however, in good agreement with those calculated in Groenewegen (2006) for similar rates of mass loss.

- Z=0.02. For the youngest ages, the luminosity interval in which C-stars appear becomes in this case very small, and the stars at the AGB tip, with the highest mass-loss rate and the highest optical depth, are O-stars. So, the SSP spectrum becomes dominated by the 9.7 μm feature. it appears in emission and not in absorption, as expected in envelopes with not high optical depth. No crystalline silicates features appear, since, according to the models by Suh (2002) already described, we need higher optical depths.

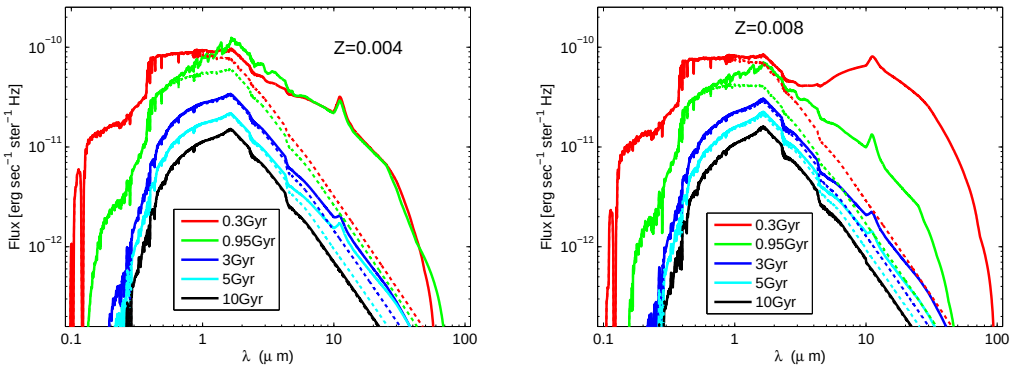

Figure 1.25: As in the Fig. 1.24, but for Z=0.004 (**left panel**) and Z=0.008 (**right panel**).

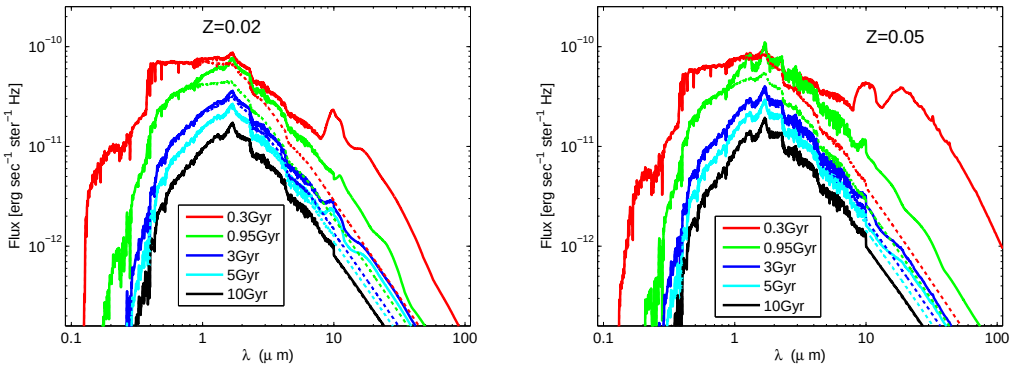

Figure 1.26: As in the Fig. 1.24, but for Z=0.02 (**left panel**) and Z=0.05 (**right panel**).

- Z=0.05. AGB stars of super-solar metallicities show only the O-rich surface (1.4, **left panel**) and do not reach the C-rich phase. At 0.3 Gyr, the SSPs spectra show the presence of both amorphous silicates (at $\sim$ 10 μm) and features due to cristalline silicate ($\sim$ 30 μm) At increasing ages, we also see the 9.7 μm feature starting to appear in absorption. All of these is due to the high optical depth, due to the increased dust-to-gas ratio.

1.6.1 Temporal evolution

To test how the presence of dusty shell around AGB stars would affect the theoretical colors of our SSPs at varying the age of the stellar population, in this section we look at the temporal evolution of some significant colors.

This is shown in the Figs. 1.27, 1.28 and 1.29 for the colors [B − V], [V − K]

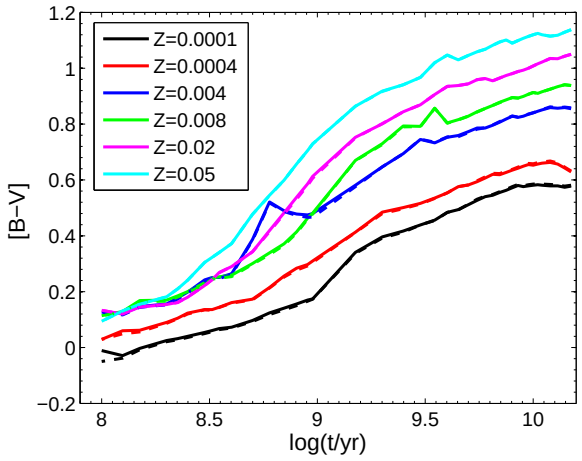

Figure 1.27: The integrated $[B-V]$ color of SSPs as a function of the age, in the range of ages from 0.1 until 15 Gyr, for all the considered values of metallicity Z. The continuous lines represent the color for the *no dusty AGB* SSPs, while the dotted lines are the *dusty AGB* SSPs.

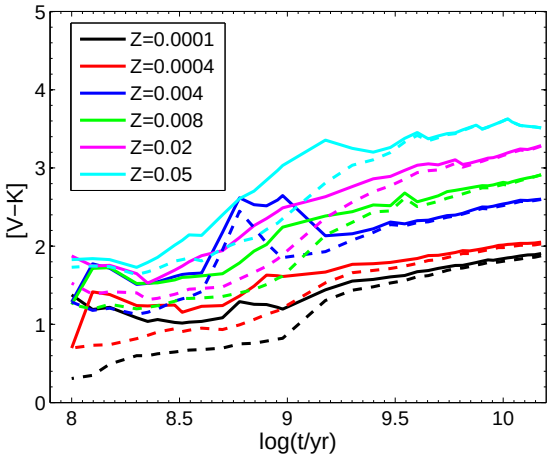

Figure 1.28: The same as in Fig. 1.27, but for the integrated $[V-K]$ color.

and $[J-8\mu m]$, both taking (continuous lines) or not into account (dotted lines) the effect of the circumstellar dusty shells around AGB stars. The age range goes from the time at which the first AGB stars appears after the central He-burning until the very old ages when the contribution of AGB stars to the integrate fluxes of the SSP is very low. As already pointed out, the effect of circumstellar dusty shells around AGB stars is that they absorb the radiation of these cool stars around 1-2μm and re-emit it at longer wavelengths. Dust shifts the flux from J and K bands to longer wavelength: this effect is stronger at shorter wavelength (J band) than at the longer

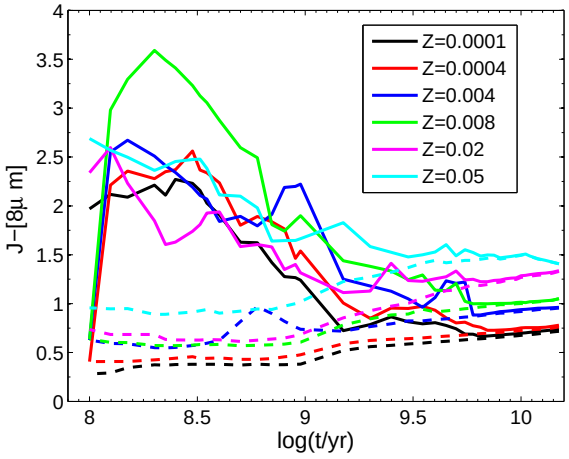

Figure 1.29: The same as in Fig. 1.27, but for the $[J-8\mu m]$ color.

ones (like K band), and this is the reason why the J magnitude tends to increase more than the K magnitude. In the Spitzer $8\mu m$ pass-band, we mostly see flux shifted from AGB stars, since even the coolest AGB emit in a negligible way in that band without dust around. For [V − K] color the effect is simpler because dust increases only the K magnitude without changing the V magnitude (too at short wavelength to be significantly affected by AGB stars) and thus producing bluer colors. As expected, the effect of dust is quite undetectable in the UV/optical pass-bands. Indeed, the [B − V] colors are in practice not sensible to the presence of dust.

1.7 SSPs colors at varying the IMF

As discussed before, the monochromatic flux of a single stellar population of age t and metallicity Z at the wavelength λ is defined as:

$$SSP_\lambda(t,Z) = \int_{M_L}^{M_U(t)} f_\lambda(M,t,Z)\Phi(M)dM \tag{1.7.1}$$

where $f_\lambda(M,t,Z)$ is the monochromatic flux emitted by a star of mass M, age t and metallicity Z; $\Phi(M)dM$ is the IMF; M_L is the lower mass between all the stellar masses of the population, while M_U is the bigger stellar mass between all the stars still alive at the age t. In the case of SSPs, the possibility of choosing between different laws for the IMF have the following consequences:

1. when the upper and lower limit are decided, the mass range is determined and also the *whole mass of the stellar population*, that is the integral of the IMF between these two limits;

2. as indicated from the Eq. 1.7.1, the IMF determines the number of stars with masses in the range M to $M + \delta M$ along the different bins of the isochrone.

So, changing the lower limit of the IMF, from one side increases the integrated mass of the stellar population, from the other side rearrange the way stars populate the different bins of mass along the isochrone. To a smaller value of the *lower limit* of the IMF, more massive populations correspond; when the SSPs fluxes are normalized to 1 $M_{\odot}$, less luminous SSPs are obtained. The tail of the sequence corresponds to stars that contribute in an efficient way to the whole population mass *but* they do not contribute, in practice, to the luminosity of the whole stellar population.

Table 1.2: All the IMFs are normalized to the unit mass over the mass range of validity. The following nine IMFs are considered: Salpeter, Larson, Kennicutt, original/old Kroupa, Chabrier, Arimoto, new Kroupa multi-slope power law 2002-2007, Scalo and, finally, Larson adapted to the Solar Neighbourhood. The upper mass limit is always 100 $M_{\odot}$, whereas the lower limit is chosen according to the discussion made in Sect. 1.1.4. In the table we show (1) the number of stars with M¿1$M_{\odot}$ which do not contribute to the chemical enrichment. We also sub-divided the two main star-dust factories SNe and AGB stars, in such a way to have clear the way by which stars contribute to the integrated light and to the chemical enrichment. All the masses are in solar units.

IMF	M<1 [1]	$1 \leq$ M $<$ 6 [2]	M $\geq$ 6 [3]
Salpeter	0.6075	0.2285	0.1640
Larson (Milky Way Disk)	0.3470	0.3568	0.2962
Kennicutt	0.4094	0.3883	0.2023
Kroupa (original)	0.5948	0.3016	0.1036
Chabrier	0.4550	0.3517	0.1933
Arimoto	0.5000	0.1945	0.3055
Kroupa 2002-2007	0.6198	0.2830	0.0972
Scalo	0.6802	0.2339	0.0859
Larson (Solar Neighbourhood)	0.5614	0.3130	0.1256

[1]Fractional mass of stars that do not contribute to the dust budget of stellar origin. [2]Fractional mass of stars that contribute to the star-dust budget via the AGB channel. [3]Fractional mass of stars that contribute to the star-dust budget via the type II SNæ channel.

As discussed in Sect. 1.1.4, the Kroupa multi-slope power law, the original Larson, the Larson adapted for the Solar Neighbourhood and the Chabrier IMFs have as lower limit 0.01 $M_{\odot}$, while the remaining laws starts from $0.1M_{\odot}$. This feature is graphically show in the Fig. 1.30, that illustrates the fraction in mass predicted by different IMFs; moreover, it also reflects on the fractional mass of stars that contribute (via the AGB channel or the type II SNe) or not to the star-dust budget,

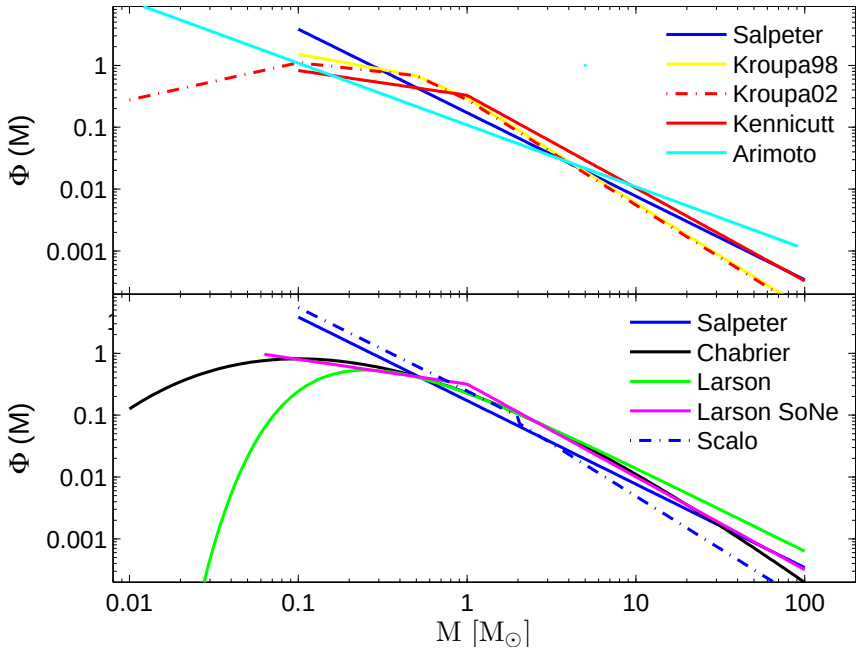

Figure 1.30: Fraction in mass predicted by different IMFs as indicated in the legend. The Salpeter IMF is shown in both the panels for the sake of comparison and since it is widely used. All the masses are in solar units and all the IMFs are normalized to the unity over the mass range of validity.

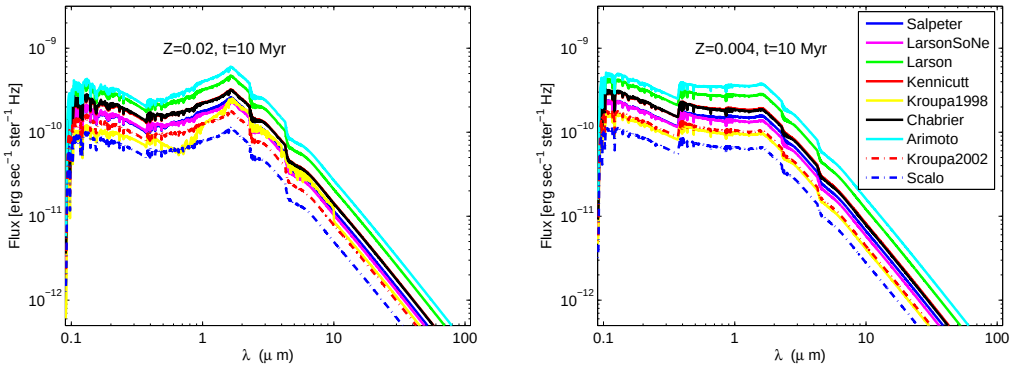

Figure 1.31: Comparison between the new dusty SSPs, for a fixed age (in this case, t=10 Myr) and metallicity (**left panel**: Z=0.02, **right panel**: Z=0.004) at varying the initial mass function (as the legend indicates).

as we are going to analyze in the last chapter of this thesis.

Indeed, different IMFs influence in a crucial way the injection of dust into the ISM. For every generation of stars, the relative amount of newly born massive objects able to produce dust via the SNa channel and the amount of low and intermediate mass

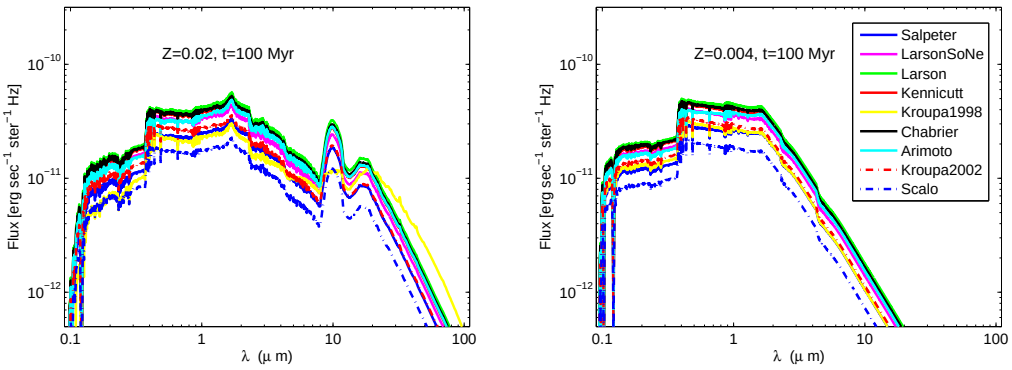

Figure 1.32: As in Fig. 1.31, but now the age is fixed at t=100 Myr.

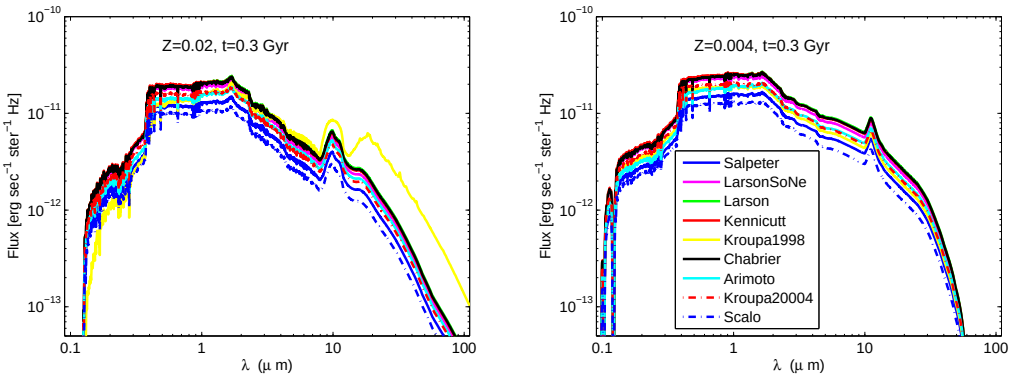

Figure 1.33: The same as in Fig. 1.31, but now the age is fixed at t=0.3 Gyr.

stars refueling the ISM with the dust produced through the TP-AGB phase both depend on the IMF. This last one also determines the timescales of stardust injection and the relative contribution by SNe and AGB stars. The Tab. 1.2 shows the mass fraction in different mass intervals predicted by different IMFs. Some IMFs (like those by Kroupa, Larson Solar Neighbourhood and Scalo) predict a small number of SNe compared to others (like those by Larson, Kennicutt or Chabrier) that are more generous in the number of massive stars and hence Type II SNe. Therefore the Kroupa, Larson Solar Neighbourhood and Scalo IMFs predict a small number of massive stars thus negatively influencing the amount of dust of stellar origin injected into the ISM. Hence, the effects induced by variations in the IMF can be very large, above all during the earlier stages of the evolution. In this sense, we can expect that in high-redshift obscured galaxies with high SFR some IMFs may be not able

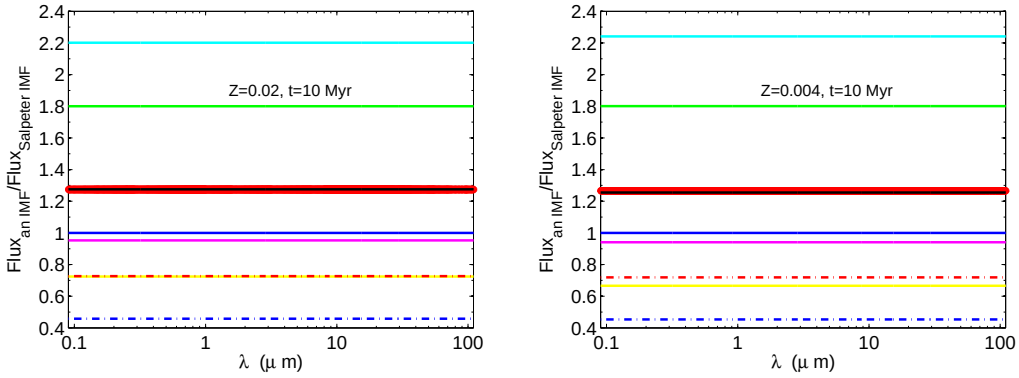

Figure 1.34: The evolution with the wavelength λ of the ratio between SSPs fluxes predicted by different IMFs. All the comparison are made using the Salpeter IMF as reference and the association between the lines color and style and the IMF is the same that in the Fig. 1.31, as the legend indicates. The considered age is t=10 Myr, while two values of the metallicity are taken into account: on the **left panel**, Z=0.02, while on the **right panel**, Z=0.004. All the IMFs are normalized to the unit over the mass range of validity.

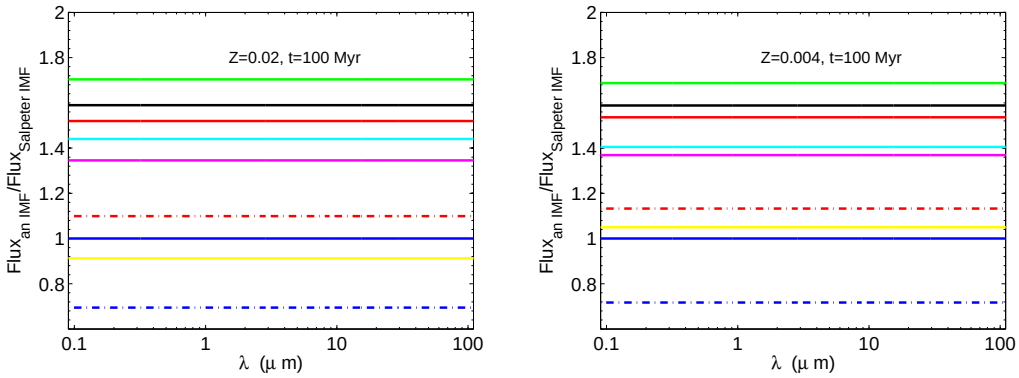

Figure 1.35: The same as in Fig. 1.34, but now the considered age is t=100 Myr.

to produce the amounts of observed dust if it is due mainly to stellar origin Draine (2009). So, before dust by accretion in the ISM and dust injected by stars become comparable, the effect of the IMF is very important, above all if the SFR is low: it determines the amount of dust present in the galaxy. For a more detailed analysis of this phenomenon, see the paper of Piovan et al. (2011b) or the related chapter in this work. For what concerns the role played by AGB stars, IMFs richer in intermediate mass stars (looking at the Tab. 1.2 we see that the Chabrier, Larson and Kennicutt IMFs predict a greater fractional mass of stars that contribute to the star-dust bud-

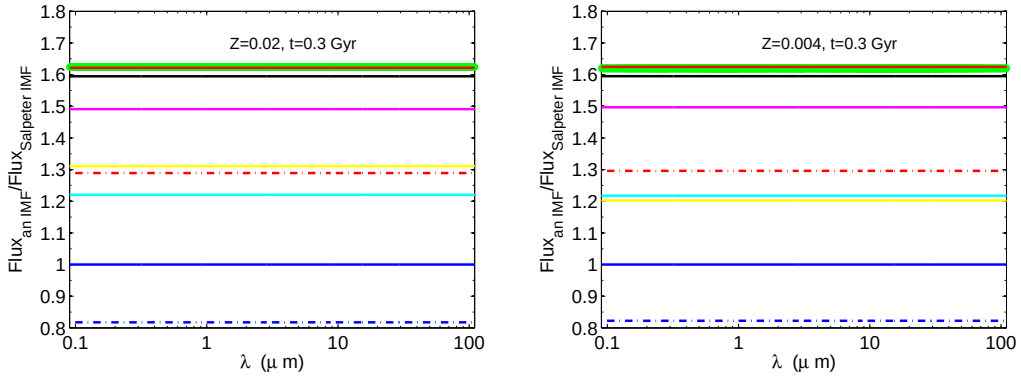

Figure 1.36: The same as in Fig. 1.34, but now the considered age is t=0.3 Gyr.

get via the AGB channel and therefore will be influenced by the dust shells around) will produce bigger amounts of dust by AGB stars.

It is worth noticing that small differences in the Fig. 1.30, above all for $M > 10M_{\odot}$, are very important and have a strong influence when the stellar population is young and vice versa: indeed, if we look at the Fig. 1.34, we can see that the IMF that forecast the greatest flux for the SSPs is the Arimoto one, followed by the classical Larson and the Kennicutt ones (the Chabrier IMF is practically superimposed to the Kennicutt IMF), in agreement to what the Fig. 1.30 suggests. When the age of the stellar population is t=0.3 Gyr (Fig. 1.36), the contribution of the intermediate mass stars that enrich the total budget of stardust via the AGB channel is predominant: the governing IMF is the Kennicutt one, as expected also from the Tab. 1.2: between $1 \leq M < 6$, this IMF predict the greatest amount of mass fraction. Almost superimposed, we found the Larson and the Chabrier IMFs, whose contribution to the fractional mass of AGB stars is trivial respect to the Kennicutt one. The same trend is evident in Fig. 1.33 for Z=0.004, while for Z=0.02 we can notice the effect of the Kroupa 1998, that we discuss later. These three IMFs are clearly separated in Fig. 1.35: moreover, for these two values of age, the lower IMF are the Salpeter and the Scalo: the Arimoto IMF, due to its $1/M$ trend, remains high, even if the greater value of predicted mass fractions for this IMF is for low star masses ($M < 1M_{\odot}$). The Figs. 1.31 underline this issue: for both considered values of metallicity, the greater flux is provided by the Arimoto IMF, followed by the usual Larson and Kennicutt/Chabrier. The Scalo IMF predicts a very small fraction of massive stars, favouring the greatest amount of low mass stars when compared to the other IMFs: as the Tab. 1.30 show, there is the 68% of stars with $M < 1M_{\odot}$. This effect obviously reflects in a lower amount of flux for the stellar population when

this IMF is used to calculate theoretical SSPs (see for example both panels of the Figs. 1.31, 1.32 and 1.33): as already discussed, this large quantity of low mass stars in practice do not contribute to the luminosity of the stellar population *but* to the whole mass.

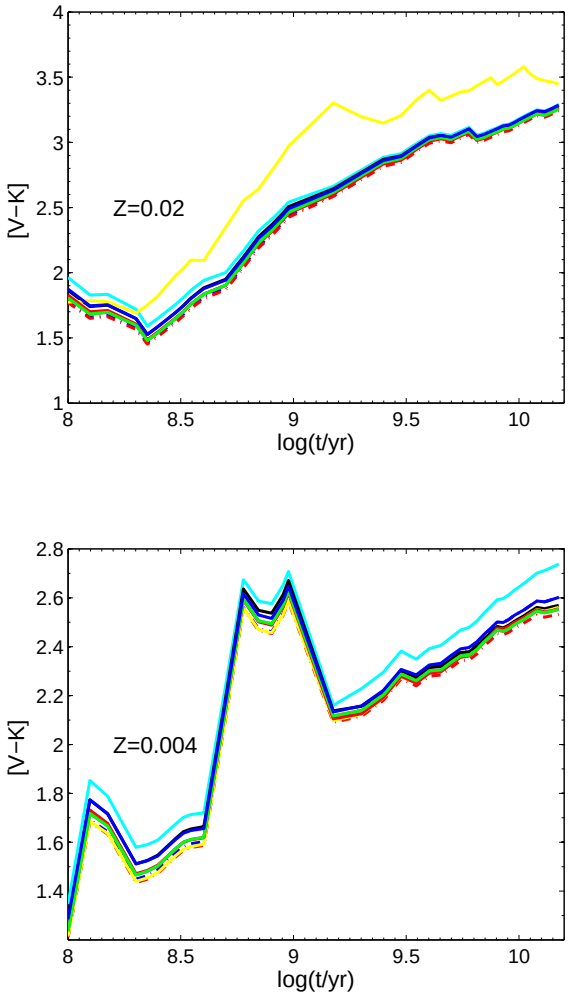

Figure 1.37: Theoretical [V − K] color as a function of age (from 0.1 to 15 Gyr) for SSPs, for the indicated values of the metallicity. Nine different prescriptions for the IMF are shown: the association between the lines color and style and the IMF is the same as in the Figs. 1.31, as the legend indicates.

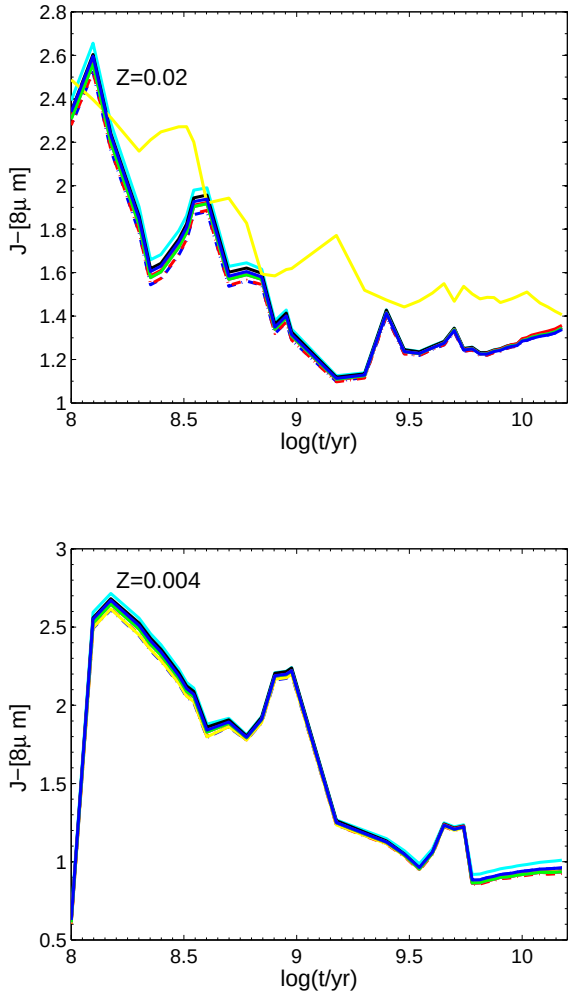

Figure 1.38: As in Fig. 1.37, but for the J-[8μ m] color.

1.8 SSPs colors at varying the metallicity

Changing the metallicity do not influence the way the IMFs work; indeed, as the Figs. 1.34, 1.35 and 1.36 illustrate, the ratio between the fluxes predicted for the single stellar population at varying the IMFs (considering different ages) is quite the same for both Z=0.02 and Z=0.004. There are some differences, but they are really small. However, we point out that:

- for $t = 0.3$ Gyr, the ratio between the Kroupa 1998 and the Salpeter IMF passes from 1.2 (Z=0.004) to 1.3 (Z=0.02); this is also evident in the Fig. 1.33. While for the other IMF the trend remain the same at varying the metallicity, the Kroupa (1998) IMF shifts a certain amount of flux from the UV part of the

spectrum to the IR wavelengths. The use of this IMF in some way mimics the effect of varying the metallicity of the stellar populations, in the sense we can observe quite the same spectral features in the **right panel** of the Fig. 1.22, where the integrated SEDs F_ν vs. λ for Z=0.05 and for the equivalent values of age are shown;

- the same effect is observable in the Fig. 1.35 and 1.32, even if in a smaller way;
- the effect is even smaller when looking at $t = 10$ Myr (Figs. 1.34 and 1.31).

Therefore, the influence of the metallicity is more evident at t=0.3 Gyr since the contribution of AGB stars is dominant: the differences due to Z can be explained by the fact that, as already discussed, the greater the metallicity adopted for the stellar population is, earlier the AGB phase starts (see Sect. 1.1.1).

1.9 Time Evolution of the colors at varying the IMF

Let us analyze now the Figs. 1.37 and 1.38, where the theoretical evolution of two color as a function of the age (from 0.1 to 15 Gyr) is considered. As usual, we show all the IMFs. The following considerations can be applied:

- as already pointed out, the evolution of the same color changes a lot when varying the metallicity (see for instance Figs. 1.27, 1.28 and 1.29) and taking into account or not the effect of circumstellar dust around AGB stars. All the SSPs we are dealing with in this section are the already mentioned *dusty AGB SSPs*. Therefore, the variation of the color due to the presence of dust is particulary evident, if comparing two different values of metallicity. Indeed, if we look at the **right panel** of the Fig. 1.37, we can clearly appreciate the *bump* between $8.6 \lesssim \log(\mathrm{t/yr}) \lesssim 9.2$, due to the development of the AGB phase, particulary evident at Z=0.004 and Z=0.008 (see Sect. 1.1.1), and not present for Z=0.02. For what concerns the effect of the IMF: the use of different laws for the IMF does not influence that much the examined integrated colors of the SSPs, with some exceptions: (a) for Z=0.02, when the AGB stars appear (approximately for log(t/yr)=8), the Kroupa 1998 IMF differs from the others; (b) for Z=0.004, the Arimoto IMF stands out of the other laws, forecasting a redder [V − K].
- When the J-[8μ m] color is taken into account, one has to remember that dust shifts the flux from J, K and 8μm bands to longer wavelengths and this effect is stronger at the shorter wavelength (J band) than at the longer ones (8 μm band): the J magnitude tends to increase more than the K and 8 μm

magnitudes. Now, the effect of different Z it is not so strong as in the previous case, even if Z=0.004 again has redder colors than the solar case as discussed before. Again, different IMFs do not change the evolution of the theoretical color J-[8μ m] (obviously magnitudes depend much more on the IMF as it can be seen from the plots with the fluxes of the SSPs), with the exception of the Kroupa (1998) IMF.

Chapter 2

Synthetic Photometry and photometric systems

2.1 Synthetic photometry

By synthetic photometry is intended the derivation of photometric quantities based on stellar intrinsic (and mostly theoretical) spectra. One of the fundamental goals of evolutionary population synthesis models is that of explaining the photometric data, e.g. color-magnitude diagrams (CMDs), luminosity functions, color histograms of stellar populations and/or integrated properties of unresolved stellar populations, as we will show in Chap. 3.
In order to compare our theoretical work with observational data, however, the basic output of stellar models – the surface luminosity L and effective temperature T_{eff} – must be first converted into the observable quantities, i.e. magnitudes, colors, indices, so that more quantitative and qualitative interpretations can be made by the observations.

In this chapter the method used to derive magnitudes and hence colors in different photometric systems is presented. To derive the theoretical magnitudes and colors we need to convolve the SEDs of the object of interest with the transmission curves desired.
In Sect. 2.1.1 the objects for which magnitudes and colors are computed will be presented while in Sect. 2.5 the different telescopes and surveys, for whom photometric systems are collected, are described.

2.1.1 Astrophysical objects of interest

We can calculate colors and magnitudes in different photometric systems (for a global glance about the photometric systems included in our database, see Tab. 2.1) for four

different kinds of objects, starting from their spectral energy distributions (*SEDs*): stars, isochrones, single stellar populations (SSPs) and galaxies of different morphological type. *This process can be done both in the local and in high redshift universe*: the evolution of SEDs with the redshift can be made applying the *K-correction* and the *E-correction* to the rest-frame models, as shown in Chap. 5.
The astrophysical objects we are dealing with are:

- **Isochrones**, which are the loci of the same age for stars of different masses. See Chap. 1, where details about the construction of the isochrones, their metallicities and the improvements we introduced are described in detail.

- **SSPs**, single stellar populations, which are one of the building blocks of the theoretical galaxy models. We deal with *classical* SSPs, which are already free of their parental clouds: for these SSPs we do not take into account the local effects of absorption/emission due to dust, but we consider the effect of circumstellar dusty shells around the AGB stars, that, as explained in Sect. 1.4, absorb the NIR radiation emitted by cool stars and re-emit at longer wavelengths. For a certain fraction of their life (at the beginning and in the first evolutionary phases of the life of a star), very young stars are embedded in the parental MCs. Even if this period is short, comparable to the lifetime of the most massive stars, its effect on the light emitted by these stars cannot be neglected as a significant fraction of the light is shifted by the interstellar dust located between the observer and stars, from the UV-optical to the IR region of the spectrum. Indeed, before the evaporation of the molecular clouds, *dusty* SSPs are needed, in order to model in a correct way the final SEDs of the galaxy. See Sect. 4.3 for a more complete explanation of this question and for the discussion about the time scale for the evaporation of the MC;

- **Dusty AGB stars**. The stars in the AGB evolutionary phase are, together with SNe, one of the main dust factories injecting dust into the ISM. The library of dusty spectra of M and C stars is presented in Sect. 1.4 and it has been used in the photometric code to calculate both SEDs of SSPs and isochrones in Optical/IR CMD.

- **Theoretical models of galaxies** (including the effect of dust) of different morphological types – elliptical galaxies, disc galaxies and *intermediate-type* galaxies subdivided in different relative mass fractions between disk and bulge –: see Chap. 4 for a detailed discussion of the topic (physical and chemical frameworks, components of galaxy models and the treatment of the dust);

2.2 Integrated magnitudes

In this section we describe the generic formalism to be applied in order to derive apparent and absolute magnitudes in a lot of photometric systems. This formalism has been presented in Girardi et al. (2002), in order to present generic equations that, by just changing in a minimum way the input quantities, can be used in a wide range of cases.

For a star, the spectral flux as it arrives at the Earth, f_λ, is related to the flux at the stellar surface, f^s_λ, by:

$$f_\lambda = \left(\frac{R}{d}\right)^2 f^s_\lambda \tag{2.2.1}$$

where R is the stellar radius, d is its distance. Once f_λ is known, the apparent magnitude m_{S_λ}, in a given pass-band with transmission curve S_λ comprised in the interval $[\lambda_1, \lambda_2]$, is given by:

$$m_{S_\lambda} = -2.5log\left(\frac{\int_{\lambda_1}^{\lambda_2} \lambda f_\lambda S_\lambda d\lambda}{\int_{\lambda_1}^{\lambda_2} \lambda f^0_\lambda S_\lambda d\lambda}\right) + m^0_{S_\lambda} \tag{2.2.2}$$

where f^0_λ represents a reference spectrum that produces a known apparent magnitude $m^0_{S_\lambda}$.
In this way f^0_λ and $m^0_{S_\lambda}$ completely define the zero-points of a synthetic photometric system. In Eq. 2.2.2, the integrands $\lambda f_\lambda S_\lambda$ are proportional to the photon flux (i.e. number of photons by unit time, surface, and wavelength interval) at the telescope detector.
This kind of integration applies well to the case of modern photometric systems that have been defined and calibrated using photon-counting devices such as CCDs.

However, more traditional systems, like the Bessell-Brett one, have been defined using energy-amplifier devices. In this case, energy integration, i.e.

$$m_{S_\lambda} = -2.5log\left(\frac{\int_{\lambda_1}^{\lambda_2} f_\lambda S_\lambda d\lambda}{\int_{\lambda_1}^{\lambda_2} f^0_\lambda S_\lambda d\lambda}\right) + m^0_{S_\lambda} \tag{2.2.3}$$

would be more appropriate to recover the original system.
The difference between energy and photon integration is usually very small, unless the pass-bands are extremely wide. Unless otherwise stated, in this thesis we will adopt the integration of photon counts.

2.2.1 Bolometric corrections

The starting point, when calculating absolute magnitudes, are libraries of stellar intrinsic spectra f^s_λ, as derived from atmosphere calculations for a grid of effective

temperature T_{eff}, surface gravities g, and metallicities Z. In this thesis we use the same library described in Piovan et al. (2006b).
Using the Eq. (2.2.1) and the Eq. (2.2.2), it is possible to calculate the absolute magnitude M_{S_λ} for a star of given T_{eff}, g, Z, F_λ (the flux at the distance $d = 10pc$):

$$M_{S_\lambda} = -2.5 \log \left[\left(\frac{R}{10pc} \right)^2 \frac{\int_{\lambda_1}^{\lambda_2} \lambda F_\lambda S_\lambda d\lambda}{\int_{\lambda_1}^{\lambda_2} \lambda F_\lambda^0 S_\lambda d\lambda} \right] + m_{S_\lambda}^0. \tag{2.2.4}$$

Since the quantities (T_{eff}, g, $[M/H]$) are not enough to specify R, we have to eliminate R from the equations. So, we use the bolometric corrections:

$$BC_{S_\lambda} = M_{bol} - M_{S_\lambda} \tag{2.2.5}$$

where the integrated absolute bolometric magnitude is derived from:

$$\begin{aligned} M_{bol} &= M_{bol,\odot} - 2.5 \log \left(\frac{L_{SSP_{object}}}{L_\odot} \right) \\ &= M_{bol,\odot} - 2.5 \log(4\pi R^2 F_{bol}/L\odot) \end{aligned} \tag{2.2.6}$$

with $F_{bol} = \int_0^\infty F_\lambda d\lambda = \sigma T_{eff}^4$ total emerging flux at the stellar surface, and constants adopted are: $M_{bol,\odot} = 4.72$, $L_\odot = 3.844 \times 10^{33}\ erg\ s^{-1}$.
The final equation for the bolometric corrections for any set of filter transmission curves S_λ is:

$$\begin{aligned} BC_{S_\lambda} = M_{bol,\odot} &- 2.5 \log \left[4\pi (10pc)^2 F_{bol}/L_\odot \right] \\ &+ 2.5 \log \left(\frac{\int_{\lambda_1}^{\lambda_2} \lambda F_\lambda S_\lambda d\lambda}{\int_{\lambda_1}^{\lambda_2} \lambda F_\lambda^0 S_\lambda d\lambda} \right) - m_{S_\lambda^0} \end{aligned} \tag{2.2.7}$$

Once BC_{S_λ} are computed, stellar absolute magnitudes follow from:

$$M_{S_\lambda} = M_{bol} - BC_{S_\lambda} \tag{2.2.8}$$

In this formalism, an extinction curve A_λ can be applied to all spectra of the stellar library, so as to allow the derivation of bolometric corrections (and synthetic absolute magnitudes) that already include extinction in a self-consistent way (see Eqs. 2.2.7 and 2.2.8). Hence, the extinction on each pass-band depends not only on the total amount of extinction, but also on the spectral energy distribution of each star (Grebel & Roberts 1995). Anyway, for the sake of simplicity, in the present work we will deal with the case $A_\lambda = 0$.

2.3 Reference spectra and zero-points

Photometric zero-points are meant to be the constant quantities that one should add to instrumental magnitudes in order to transform them to standard magnitudes, for each filter S_λ. In this work we do not make use of the instrumental magnitude, and hence such constants do need to be defined. By "zero-points" we refer to the quantities in Eq. (2.2.2) and Eq. (2.2.3) that depend only on the choice of f^0_λ and $m^0_{S_\lambda}$. They are constant for each filter, and are responsible for the conversion of the synthetic magnitude scale into a standard system.
As for these quantities, there are three different cases of interest:

2.3.1 VEGA magnitude systems

As first magnitude system, we have based the calibration on the reference spectrum of Vega, and we will refer to this photometric system as the *VEGA mag system*.

The *VEGA mag* offers a good approximation to many of the conventional photometric systems that use the spectrum of Vega to define the zero magnitude in any pass-band. In broadband photometry, the relevant pass-band integral is calculated first for the source spectrum of Vega, and the ratio of the two results is converted into a magnitude.
As the name suggests, this system makes use of Vega (α Lyr) as the primary calibrating star: the most famous among these systems is the Johnson, Bessell-Brett ($UBVRIJHKLMN$ filters) one, that can be accurately recovered by simply assuming that Vega has $V = 0.03\ mag$, and all the colors equal to 0. Other systems, like the Washington and the HST/WFPC2 one, follow a similar definition (some colors, however, are defined to have values slightly different from 0).

Calibrated empirical spectra of Vega are available (see for instance Hayes & Latham (1975) and Hayes (1985)), covering the wavelength range from 3300 to 10500 Å, an interval that can be extended down to 1150 Åwhen complemented with IUE spectra (Bohlin et al. 1990): they can be used to define VEGAmag systems in the optical and ultraviolet regions.

Nowadays the wavelength range accessible to present instrumentation is much wider, and a Vega spectrum covering the complete spectral range has become necessary. Synthetic spectra as those computed by Kurucz (1993) and Castelli & Kurucz (1994), fulfill this aim: in this case, the predicted fluxes at Vega's surface, F_λ, are scaled by the geometric dilution factor:

$$(R/d)^2 = (0.5\,\theta_{\rm d}/206264.81)^2 \tag{2.3.1}$$

where $\theta_{\rm d}$ is the observed Vega's angular diameter (in arcsec) corrected by limb dark-

ening. Recently, composite spectra of Vega have been constructed by assembling empirical and synthetic spectra together, in order to overcome and correct some small deficiencies characteristic of synthetic spectra. This has the precise scope of providing a reference spectrum for conversions between apparent magnitudes of real (observed) stars, and physical fluxes.

In this work, we have introduced a new synthetic model for Vega, with $T_{eff} = 9550$ K, $\log g = 3.95$, [M/H] $= -0.5$, and micro-turbulent velocity $\xi = 2\,\mathrm{km\,s^{-1}}$, the spectrum being provided by Kurucz *webpage*. [1]
The initial wavelengths range was 90.00 $nm < \lambda < 300009.49$ nm: we have extended this range up to $\lambda = 1100000$ nm, using a black-body spectrum. The resolution of the adopted Vega spectrum is now $R = 50000$ nm.
These are fundamental aspects when calculating colors and magnitudes using more recent photometric systems, which pass-bands (i.e. Herschel-SPIRE, PACS) can include the emission of very cool dust grains. The physical information on Vega are taken from by Aufdenberg et al. (2006).

Once the synthetic model F_λ^{Vega} is chosen, we need to re-scale it in order to obtain f_λ^{Vega} at the Earth's surface. This is done using the dilution factor (see Eq. (2.2.1)):

$$\left(\frac{R}{d}\right)^2 = 6.25 \times 10^{17}. \tag{2.3.2}$$

If we assume that the apparent Vega colors are equal to 0 in all pass-bands $\Delta\lambda$, we would obtain $Z_{\Delta\lambda} = 2.5 \log f_{\Delta\lambda,Vega}$, and Eq. (2.2.2) would become:

$$\begin{aligned} m_{VEGA,\Delta\lambda} &= Z_{\Delta\lambda} - 2.5 \log f_{\Delta\lambda} \\ &= -2.5 \log \frac{f_{\Delta\lambda}}{f_{\Delta\lambda,Vega}}. \end{aligned} \tag{2.3.3}$$

2.3.2 AB magnitude systems

Monochromatic AB magnitudes in the *AB* system were initially defined, in the original work by Oke (1964), as:

$$m_{\mathrm{AB},\nu} = -2.5\ \log f_\nu - 48.60. \tag{2.3.4}$$

This means that a reference spectrum of constant flux density per unit frequency

$$f^0_{\mathrm{AB},\nu} = 3.631 \times 10^{-20}\ \ [\mathrm{erg\,s^{-1}\,cm^{-2}\,Hz^{-1}}] \tag{2.3.5}$$

will have AB magnitudes $m^0_{\mathrm{AB},\nu} = 0$ at all frequencies ν. The zero-point value is chosen for convenience so that Vega AB_ν magnitudes are about 0 in the Johnson

[1] http://kurucz.harvard.edu/stars/VEGA/

V pass-band. This definition can be extended to any filter system, provided that we replace the monochromatic flux f_ν with the photon counts over each pass-band S_λ obtained from the star, compared to the photon counts that one would get by observing $f^0_{\mathrm{AB},\nu}$:

$$m_{AB,\nu} = -2.5 \log \left(\frac{\int d(\log \nu) f_\nu S_\nu}{\int d(\log \nu) f^0_{AB,\nu} S_\nu} \right) \tag{2.3.6}$$

otherwise expressed as:

$$m_{AB,\nu} = -2.5 \log \left(\frac{\int d(\log \nu) f_\nu S_\nu}{\int d(\log \nu) S_\nu} \right) - 48.60 \tag{2.3.7}$$

with f_ν expressed in $erg\ s^{-1}\ cm^{-2}\ Hz^{-1}$. Passing to wavelengths we derive the AB magnitudes:

$$m_{AB,\lambda} = -2.5 \log \left[\frac{\int_{\lambda_1}^{\lambda_2} (\lambda/hc) f_\lambda S_\lambda d\lambda}{\int_{\lambda_1}^{\lambda_2} (\lambda/hc) f^0_{AB,\lambda} S_\lambda d\lambda} \right] \tag{2.3.8}$$

where $f^0_{AB,\lambda} = f^0_{AB,\nu} c/\lambda^2$, and

$$\lambda_{pivot} = \sqrt{\frac{f_{AB,\nu}}{f_{AB,\lambda}} c} \tag{2.3.9}$$

is the pivotal wavelength that permits the transformation between frequencies and wavelengths.

2.3.3 ST magnitude systems

ST monochromatic magnitudes have been introduced by the HST team, and are defined by:

$$m_{\mathrm{ST},\lambda} = -2.5\ \log f_\lambda - 21.10\ . \tag{2.3.10}$$

In this way, a reference spectrum of constant flux density per unit wavelength

$$f^0_{ST,\lambda} = 3.631 \times 10^{-9}\ \ [\mathrm{erg\,s^{-1}\,cm^{-2}\,\AA^{-1}}] \tag{2.3.11}$$

will have ST magnitudes $m^0_{\mathrm{ST},\lambda} = 0$ at all wavelengths. Similarly to the case of AB magnitudes, this can be generalized to any pass-band system with:

$$m_{ST,\lambda} = -2.5 \log \left[\frac{\int_{\lambda_1}^{\lambda_2} (\lambda/hc) f_\lambda S_\lambda d\lambda}{\int_{\lambda_1}^{\lambda_2} (\lambda/hc) f^0_\lambda S_\lambda d\lambda} \right]. \tag{2.3.12}$$

This situation can be reproduced in this formalism with the adoption of $f^0_\lambda = f^0_{ST,\lambda}$ and $m^0_{ST,S_\lambda} = 0$.

2.4 An important consideration about the definition of *magnitude*

It is worth mentioning that some photometric systems make use of an unusual definition of magnitudes, or at least different from the definitions presented here and normally used (Girardi et al. 2002; Marigo et al. 2008). This problem arises only when using the Vega mag system. For every photometric system included in this thesis we analyze the reference article (see Tab. 2.1) in order to calculate magnitudes and then colors in a consistent way. Here we summarize the method used for every photometric system:

- **AKARI/ASTRO-F**, **SPITZER**, **ISO**, **DENIS**: we use the formula presented in Groenewegen (2006). The flux of the source is folded with the filter curves and flux-densities and magnitudes are calculated from, following the definition used by IRAS, ISOCAM and IRAC, see Blommaert et al. (2003):

$$m_\lambda = -2.5 \log \left(\frac{\int (\lambda/\lambda_0) F_\lambda R_\lambda d\lambda)}{\int R_\lambda d\lambda} \right) + m_0 \tag{2.4.1}$$

  with the usual definition of the terms. The zero-points, m_0, are calculated from a reference spectrum for Vega. We refer to Groenewegen (2006) for the information about the adopted flux densities for a zero-magnitude star, both for SPITZER and AKARI filters.

- **TYCHO-2**: we follow the formula presented in Maíz Apellániz (2006).
  Briefly, for a photon-counting detector, given the total system dimensionless sensitivity function $P(\lambda)$, the SED of the object $f_\lambda(\lambda)$, the SED of the reference spectrum $f_{\lambda,ref}(\lambda)$ and the zero-point ZP_p for the filter P, the magnitude is:

$$m_P = -2.5 \log \left[\frac{\int (P(\lambda) f_\lambda(\lambda) \lambda d\lambda)}{\int P(\lambda) f_{\lambda,ref}(\lambda) \lambda d\lambda} \right] + ZP_P. \tag{2.4.2}$$

- **UKDISS**: we follow the definition from Hewett et al. (2006). The mean flux density, $f_\lambda(P)$, in a broad pass-band defined by a dimensionless pass-band throughput function, $P(\lambda)$, is:

$$f_\lambda = \frac{\int P_\lambda f_\lambda(\lambda) \lambda d\lambda}{P_\lambda \lambda d\lambda} \tag{2.4.3}$$

  where $f_\lambda(\lambda)$ is the flux density of the target object.

- for the other systems, we use the Eq. (2.2.3).

Moreover, as one can see from Tab. 2.1, not all the photometric systems consider the three standard magnitude systems presented in 2.3. In order to avoid problems with the Vega magnitudes – (a) the flux density that corresponds to $m = 0$ differs at every wavelengths, and (b) the flux of Vega can become exceedingly small at wavelengths outside the UV-near-IR regime– the most recent systems prefer to use the AB magnitude system. This system is also called the *spectroscopic magnitude system*, because with its constant zero-point, it is useable at any wavelength in pass-bands of any width, and hence also for narrow band imaging and spectroscopy.

2.4.1 IRAS magnitudes

Same changes have been considered in our photometric code in order to deal with the photometric system of IRAS. IRAS was the satellite that opened a new era for the infrared astronomy: it increased the number of cataloged astronomical sources by about 70%, detecting about 350000 infrared sources. The IRAS filters are very broad ($\Delta\lambda/\lambda \leq 0.7$) and the response of the system changes a lot with the wavelength. To derive the theoretical IRAS monochromatic fluxes we convolved the SEDs of our objects with IRAS transmission curves.
Following Bedijn (1987), the monochromatic flux is defined as:

$$F_\lambda = \frac{\int F_\lambda \Phi_\lambda d\lambda}{\int \left(\frac{F^a_\lambda}{F^a_{0\lambda}}\right) \Phi_\lambda d\lambda} \tag{2.4.4}$$

where Φ_λ is the instrumental profile, F_λ is the theoretical flux distribution, F^a_λ is the assumed flux distribution, that for IRAS bands is $\propto \lambda^{-1}$, and $F^a_{0\lambda}$ is the assumed flux distribution referred to the central wavelength of the band as defined in Neugebauer et al. (1984).
If the source has a profile with a shape different from the dependence $\propto \lambda^{-1}$, one has to correct the flux using the so-called *K factor* given by:

$$K = \frac{\int \left(\frac{F_\nu}{F_{\nu 0}}\right) \Phi_\nu d\nu}{\int \left(\frac{F^a_\nu}{F^a_{\nu 0}}\right) \Phi_\nu d\nu} \tag{2.4.5}$$

and to divide the monochromatic flux resulting from Eq. (2.4.5) by this factor.

2.5 Photometric Systems included in our database: an overview

In this section we present a global overview of the different telescopes and satellites, instruments and surveys whose broad-band photometric systems are included in our

Table 2.1: Photometric systems:

Photometric system	Filter names	Wavelength range	Kind of zero-points	References for filters	Additional information
Bessell & Brett	$U_{\rm X}B_{\rm X}BV(RI)_{\rm C}$	3000 Å– 15.6 μm	Vega+AB	Bessell (1990)	
	$JHKLL'M$			Bessell & Brett (1988)	
Tycho-2	$V_{\rm T}B_{\rm T}$	3500 – 6650 Å	Vega+AB	Maíz Apellániz (2006)	
JOHNSON1966	$UBVRIJKLMN$	3000 Å– 13.8 μm	Vega+AB	Johnson (1966)	
SDSS	$ugriz$	2980 – 11230 Å	Vega+AB+ST	Fukugita et al. (1996)	details in Girardi et al. (2004)
UKIDSS	$ZYJHK_{\rm s}$	7995 Å– 2.50 μm	Vega	Hewett et al. (2006)	supersedes files distributed since 2006
2MASS	$JHK_{\rm s}$	1.05 – 2.39 μm	Vega+AB	Cohen et al. (2003)	supersedes Bonatto et al. (2004)
DENIS	$IJK_{\rm s}$	6990 Å– 2.46 μm	Vega+AB	Fouqué et al. (2000)	details in Cioni et al. (2006)
BATC	all 15 filters	307 – 9936 Å	AB	Yan et al. (2000)	supersedes files distributed since 2006
IRAS	4 filters	7 – 160 μm	Vega+AB	Neugebauer et al. (1984)	
HST/WFPC2	all wide filters	1130 – 11000 Å	Vega+ST+AB	Holtzman et al. (1995)	details in Girardi & Marigo (2007)
HST/ACS	all WFC+HRC	2645 – 9130 Å	Vega+ST+AB	Sirianni et al. (2005)	details in Girardi & Marigo (2007)
HST/NICMOS	JHK-equivalent	0.94 – 2.50 μm	Vega+ST+AB	D. Figer, priv. comm.	details in Girardi et al. (2002)
ISO	$SW1-SW10$, $LW1-LW11$	3.05 – 15 μm	Vega+AB	ISOCAM Observer's Manual	Moro & Munari (2000)
XMM/OM	$U\ V\ B\ UVW_1\ UVW_2\ UVM_2$	3.04 – 6.99 μm	Vega+AB	priv. comm.	XMM-Newton website
GALEX	$FUV\ NUV$	1340 – 3010 Å	AB	priv. comm.	
Spitzer	all MIPS+IRAC	2.96 – 200 μm	Vega+AB	Spitzer website	details in Groenewegen (2006)
AKARI	all filters	1.6 – 201 μm	Vega+AB	AKARI website	details in Groenewegen (2006)
WISE	4 filters	2.53 – 28.55 μm	Vega+AB	WISE website	
HERSCHEL	PACS and SPIRE filters	2.5 – 714.28 μm	Vega+AB	HERSCHEL website	
VLT/VIMOS	$UBVRI$	3310 – 9409 Å	Vega+AB	priv. comm.	ESO website
VLT/ISAAC	JHK_s	1 – 2.3 μm	Vega+AB	priv. comm.	ESO website
CFHT/MegaPrime	$u^*g'r'i'z'$	3000 Å– 11.1 μm	AB	Coupon et al. (2009)	
MSSSO/CASPIR	HJK_n	14.4 – 23.82 μm	Vega+AB	priv. comm.	McGregor et al. (1994)
ESO/WFI	wide filters	3469 – 8590 Å	Vega+AB	ESO/WFI website	supersedes Girardi et al. (2002)

database. Their photometric systems can be used in order to calculate colors and magnitudes, *both in local universe and at high redshift*. For the sake of clarity, they will be divided into three categories: (1) surveys, (2) space-based telescopes and (3) ground-based telescopes. Apart of the listed photometric systems, the most common standard systems are also included: Tycho-2 B_T and V_T (Maíz Apellániz 2006), the Bessel & Brett system (Bessell & Brett 1988; Bessell 1990), the first known standardized photoelectric photometric system and its reviewed version of 1966 (Johnson 1966). Since they are well known and widely used, we will not enter into more details for these photometric systems.

2.5.1 Astronomical surveys

An astronomical survey is a general map or image of a region of the sky, which lacks a specific observational target. Alternatively, this may comprise a set of many images of objects which share a common type or feature. Surveys are often restricted to one band of the electromagnetic spectrum due to instrumental limitations, although multi-wavelength surveys can be made by using multiple detectors, each sensitive to a different region of the electromagnetic spectrum.

SDSS

The Sloan Digital Sky Survey or SDSS is a major multi-filter imaging and spectroscopic redshift survey. SDSS uses a dedicated 2.5-m wide-angle optical telescope (located at Apache Point Observatory in New Mexico, United States), and takes images using a photometric system made by five filters (u, g, r, i and z). Over eight years of operations (SDSS-I, 2000-2005; SDSS-II, 2005-2008), it obtained deep, multi-color images covering more than a quarter of the sky and created 3D maps containing more than 930000 galaxies and more than 120000 quasars. Data collection began in 2000, and has mapped over 35% of the sky, with photometric observations of around 500 million objects and spectra for more than 1 million objects. The main galaxy sample has a median redshift of $z = 0.1$; there are redshifts for luminous red galaxies as far as $z = 0.6$, and for quasars as far as $z = 5$; the imaging survey has been involved in the detection of quasars beyond a redshift $z = 6$. The telescope's camera is made up of thirty CCD chips each with a resolution of 2048 $\times$ 2048 pixels, for a total of about 120 Mega-pixels. The chips are arranged in five rows of six chips. Each row has a different optical filter with average wavelengths of 355.1, 468.6, 616.5, 748.1 and 893.1 nm, with 95% completeness in typical seeing to magnitudes of 22.0, 22.2, 22.2, 21.3, and 20.5, for u, g, r, i, z, respectively.

COSMOS

The Cosmic Evolution Survey (COSMOS) is a Hubble Space Telescope (HST) Treasury Project to survey a two square degree equatorial field with the Advanced Camera for Surveys (ACS). It is the largest survey ever undertaken by HST, the project incorporates commitments from observatories around the world, such as the Very Large Array radio observatory, the European Space Agency's XMM-Newton satellite, and Japan's eight meter Subaru telescope. The primary goal of COSMOS is to study the relationship between large scale structure in the universe and the formation of galaxies, dark matter, and nuclear activity in galaxies. This includes a careful analysis of the dependence of galaxy evolution on environment. Details of the COSMOS catalogue are described in Capak et al. (2007) and Mobasher et al. (2007). It covers a 2 square degree area with deep panchromatic data and includes objects whose total i magnitudes (i' or i^*) are brighter that 25. The COSMOS multi-band catalogue embraces data from different telescopes, as listed in Tab. 2.2, and resents imaging data and photometry for this survey that cover various photometric bands between 0.3 μm and 2.4 μm.

Table 2.2: COSMOS Survey: Telescopes and optical/IR bands

Telescope	Filters	Instrument λ Sensitivity $\mathring{A}$
CFHT	u^*, i^*	3200-1000
CTIO	K_s	9000-25000
HST-ACS	F814W (i-band)	4000-11000
KPNO	K_s	9000-25000
SDSS	u, g, r, i, z	3200-11000
Subaru	B_J, V_J, g^+, r^+, i^+, z^+, NB816 (i-band)	4000-11000

GOODS

The Great Observatories Origins Deep Survey or GOODS is an astronomical survey based on observations of two separate fields centered on the Hubble Deep Field North (HDFN) and Chandra Deep Field South (CDFS) and includes ultra-deep images from ACS on HST, from the mid-IR space-telescope Spitzer, as well as from a number of ground-based facilities, as listed in Tab. 2.3. GOODS is intended to study the formation and evolution of galaxies in the distant universe.

Table 2.3: GOODS database: Telescopes and optical/IR bands

Telescope	Filters	Instrument λ Sensitivity $\mathring{A}$
ESO-WFI	U_{38}	3100-4000
VLT-VIMOS	U	3300-4000
ACS-HST	B(F435W), V(F606W), i(F775W), z(F850LP)	3400-11000
VLT-ISAAC	J, H, K_S	11000-24000
Spitzer - IRAC instrument	3.5, 4.5, 5.8, 8 μm	30000-100000

UKIDSS

The United Kingdom Infrared Telescope (UKIRT) Infrared Deep Sky Survey (UKIDSS) started on May 2005 and is a set of five surveys of complementary combinations of depth and area, employing the wavelength range 0.832.37 μm in up to five filters Z,Y, J, H, K, and extending over both high and low Galactic latitude regions of the sky. Four particular areas of investigation for UKIDSS are: "*the coolest and nearest brown dwarfs, high-redshift dusty starburst galaxies, elliptical galaxies and galaxy clusters at redshifts* $1 < z < 2$*, and the highest-redshift quasars, at* $z = 7$." [2], The survey instrument is the Wife Field Camera (WFCAM) on the UKIRT in Hawaii.

2MASS

Observations for the Two Micron All-Sky Survey (2MASS) began in 1997 and were completed in 2001. The Two Micron All Sky Survey (2MASS) project was designed to close the gap between current technical capability and knowledge of the near-infrared sky. In addition to this, 2MASS provided direct answers to immediate questions on the large-scale structure of the Milky Way and the Local Universe. The optimal use of the infrared space missions, such as HST/NICMOS, the Space Infrared Telescope Facility (SIRTF), and the Next Generation Space Telescope (NGST), as well as the powerful ground-based facilities, such as Keck I, Keck II, and Gemini, require a new census with vastly improved sensitivity and astrometric accuracy than that previously available. To achieve these goals, 2MASS has uniformly scanned the entire sky in three near-infrared bands to detect and characterize point sources brighter than about 1 mJy in each band. 2MASS used two highly-automated 1.3 m telescopes: each one was equipped with a three-channel camera, capable of observing the sky simultaneously at J (1.25 μm), H (1.65 μm), and K_s (2.17 μm).

[2] http://http://www.ukidss.org//

DENIS

DENIS is a deep survey of the Southern Sky in two near-infrared bands (J at 1.25 μm and K at 2.16 μm) and one optical band (I at 0.8 μm) simultaneously, using a one meter telescope (ESO, La Silla). The survey started in 1996 and operations at La Silla have been completed on 9 Sept. 2001. The main goal of the DENIS survey (see Epchtein et al. (1994) for a complete introduction to DENIS) was to bridge the gap between the optical surveys on Schmidt plates and the far-infrared IRAS survey. Many aspects of astrophysics benefited from such a survey, particulary studies of cool stars and heavily obscured regions.

BATC

The BATC (Beijing-Arizona-Taiwan-Connecticut) multi-color photometric survey aims mainly at obtaining the spectral energy distribution information of galaxies with redshift less than 0.5 (Xia et al. 2002), by using the 60/90 cm Schmidt Telescope of Beijing Astronomical Observatory (BAO) with 15 intermediate-band filters, which cover an optical wavelength range from 3200 to 9900 Å. These filters are specifically designed to exclude most of the bright and variable night-sky emission lines.

2.5.2 Space Telescopes

A space observatory is any instrument, such as a telescope, in outer space which is used for observations of distant planets, galaxies, and other outer space objects. This category is distinct from other observatories located in space that are pointed toward the earth for the purpose of reconnaissance and other types of information gathering.

IRAS

The Infrared Astronomical Satellite (IRAS) was the first-ever space-based observatory to perform an all-sky survey at wavelengths ranging from 8 to 120 μm in four broadband photometric channels centered at 12, 25, 60, and 100 μm. Launched on January 25, 1983, its mission lasted ten months. This satellite has opened a new era in modern astronomy: thousands of galaxies were detected to emit most of their light in the IR. After IRAS several space infrared telescopes have continued and greatly expanded the study of the infrared Universe, such as the Infrared Space Observatory launched in 1995, the Spitzer Space Telescope launched in 2003, and the AKARI Space Telescope launched in 2006.

Hubble Space Telescope

The Hubble Space Telescope (HST) is a space telescope that was carried into orbit by a Space Shuttle in 1990 and remains in operation. It is a 2.4 m reflecting telescope in low Earth orbit and Hubble's four main instruments observe in the near ultraviolet, visible, and near infrared. The only one of NASA's four *Great Observatories* (Hubble, Compton Gamma-Ray Observatory, Chandra X-Ray Observatory, and Spitzer Space Telescope) that is serviceable by Space Shuttle astronauts, Hubble has seen its capabilities grow immensely in its sixteen years of operation. This has been the direct result of the installation of new, cutting-edge scientific instruments and more powerful engineering components. Replacement of aging or failed parts has been an important part of servicing and has been responsible for the telescopes longevity. For more information about the mission, see `http://www.stsci.edu/hst/`. HST's current complement of science instruments includes three cameras, two spectrographs, and fine guidance sensors. Here we remember the main features of some of these.

- STIS (Space Telescope Imaging Spectrograph): it can study objects across a spectral range from the UV (115 nm) through the visible, red and the near-IR (1000 nm). The main advance in STIS is its capability for two-dimensional rather than one-dimensional spectroscopy: it can also record a broader span of wavelengths in the spectrum of a star at one time. As a result, STIS is much more efficient at obtaining scientific data than the earlier HST spectrographs.

- NICMOS (Near Infrared Camera and Multi-Object Spectrometer): it detects light with wavelengths between 0.8 and 2.5 μm.

- ACS (Advanced Camera for Surveys): a camera designed to provide HST with a deep, wide-field survey capability from the visible to near-IR, imaging from the near-UV to the near-IR. The primary design goal of the ACS Wide-Field Channel is to achieve a factor of 10 improvement in discovery efficiency, compared to WFPC2.

- COS (Cosmic Origins Spectrograph): it is designed to perform high sensitivity, moderate- and low-resolution spectroscopy of astronomical objects in the 115-320 nm wavelength range. It significantly enhances the spectroscopic capabilities of HST at ultraviolet wavelengths, and provides observers with unparalleled opportunities for observing faint sources of ultraviolet light.

- WFC3 (Wide Field Camera 3): it was installed during the 2009 servicing mission. The WFC3 has two camera channels: the UVIS channel that operates in the ultraviolet and visible bands, and the IR channel that operates in the

infrared. The performance of the two channels was designed to complement the performance of the ACS.

ISO

The Infrared Space Observatory (ISO) is an astronomical satellite that was operational between November 1995 and May 1998. It operated at wavelengths from 2.5 to 240 μm. With ISO deep MIR surveys for distant galaxies have been carried out for the first time. ISO carried an array of four scientific instruments:

- ISOCAM (Infrared Camera): a high-resolution camera covering 2.5 to 17 μm wavelength with two different detectors.

- ISOPHOT (Photo-polarimeter): an instrument designed to measure the amount of infrared radiation emitted from an astronomical object. The very broad wavelength range (from 2.4 to 240 μm) allowed to see the IR emissions of the coldest astronomical objects, such as interstellar dust clouds.

- SWS (Short Wave Spectrometer): a spectrometer covering the 2.4 to 45 μm. Observations with this instrument provided valuable information about the chemical composition, density and temperature of the universe.

- LWS (Long Wave Spectrometer): a spectrometer covering the 45 to 196.8 μm. This instrument did essentially the same as the SWS, but looked at much cooler objects than the SWS did. Particularly cold dust clouds between stars were studied with this instrument.

XMM

The XMM-Newton (X-ray Multi-Mirror Mission - Newton) is an orbiting X-ray observatory. It was launched by the ESA on 10 December 1999 and holds three X-ray telescopes. Other instruments onboard are two reflection grating spectrometers, and a 30 cm diameter Ritchey-Chretien optical/UV telescope. The original mission lifetime was two years, it has now been extended for further observations until 2012, and technically could operate until 2018. OM is the Optical Monitor, an instrument on XMM that allows simultaneous observations in both x-ray and optical / UV wavelengths. Examining objects in two different wavelengths at once gives a glimpse of the different mechanisms behind black holes, AGN, gamma ray bursts, blazars and quasars.

GALEX

The Galaxy Evolution Explorer (GALEX) is an orbiting UV space telescope launched on April 28, 2003. During its 29-month mission, which has recently been elongated, it will make observations in UV wavelengths to measure the history of star formation in the universe 80 % of the way back to the Big Bang. The spacecraft's mission is to observe hundreds of thousands of galaxies, with the goal of determining the distance of each galaxy from Earth and the rate of star formation in each galaxy. Near- and far-UV emissions as measured by GALEX can indicate the presence of young stars, but may also originate from old stellar populations.

SPITZER

The SPITZER mission (Werner et al. 2004), launched on 25 August 2003, carries a range of imaging filters that cover the near-, mid- and far-IR. This telescope first detected high redshift ($z > 1.5$) sources in the MIR, and allowed the astronomers to study the evolution of Star Formation across the Universe up to $z \sim 2$. The main results obtained by Spitzer are: (a) observations showed a strong luminosity evolution between $z = 0$ and $z = 1$, almost constant between $z = 1$ and $z = 2$; (b) the formation and evolution of galaxies has been a strong function of luminosity: IR luminosity density of galaxies dominated by LIRGs at $z < 2$, but ULIRGs contribution increases at high-z (Le Floc'h et al. 2005; Caputi et al. 2007); (c) 24-μm-selected samples are rich in AGN. Dusty-obscured (optically faint) AGNs at $z \sim 2$ are identified by means of a silicate absorption feature at 9.7 μm. Spitzer carries three instruments on-board:

- IRAC (Infrared Array Camera): an infrared camera operating simultaneously on four wavelengths (3.6 μm, 4.5 μm, 5.8 μm and 8 μm). The two shorter wavelength bands (3.6 μm and 4.5 μm) for this instrument remain productive after L-He depletion in the spring of 2009, at the telescope equilibrium temperature of around 30 K, so IRAC continues to operate as the *Spitzer Warm Mission*;

- IRS (Infrared Spectrograph): an infrared spectrometer with four sub-modules which operate at the wavelengths 5.3-14 μm (low resolution), 10-19.5 μm (high resolution), 14-40 μm (low resolution), and 19-37 μm (high resolution);

- MIPS (Multi-band Imaging Photometer for Spitzer): three detector arrays in the far infrared, with capabilities for imaging and photometry in broad spectral bands centered nominally at 24, 70, 160, and for low-resolution spectroscopy between 55 and 95 μm.

AKARI - ASTRO-F

AKARI (previously known as ASTRO-F or IRIS - Infra-Red Imaging Surveyor), was launched on 2006 February 21, and started observations in May of the same year. The primary purpose of the mission is to provide second-generation infrared catalogues so as to obtain a better spatial resolution and a wider spectral coverage than the first catalogues produced by the IRAS mission (Neugebauer et al. 1984). AKARI has a $68.5cm$ cooled telescope, together with two focal-plane instruments, which survey the sky in six wavelength bands from mid- to far-infrared: the Far-Infrared Surveyor (FIS) and Infrared Camera (IRC). FIS will perform the all-sky survey with 4 photometric bands at the wavelength range of 65, 90, 140, and 160 μm, and uses two kinds of array detectors. The IRC consists of three channels: the NIR channel operates from 1.8 to 5.3 μm; the MIR-S channel works in 5.413.1 μm; and the MIR-L channel covers 12.426.5 μm. All three channels are operated simultaneously.

WISE

Wide-field Infrared Survey Explorer (WISE) is a NASA infrared-wavelength astronomical space telescope launched on December 14, 2009. WISE served as a replacement for the Wide Field Infrared Explorer (WIRE), which failed within hours of reaching orbit in March 1999. WISE surveyed the sky in four wavelengths of the IR band, at a very high sensitivity. Its detector arrays have 5σ sensitivity limits of 120, 160, 650, and 2600 μJy at 3.3, 4.7, 12, and 23 μm. This is a factor of 1000 times better sensitivity than the survey completed in 1983 by the IRAS satellite in the 12 and 23 μm bands, and a factor of 500000 times better than the COBE satellite at 3.3 and 4.7 μm. On the other hand, IRAS could also observe 60 and 100 μm wavelengths, which WISE does not.

HERSCHEL

The European Space Agency's Herschel Space Observatory is a space observatory that cover a spectral range from the far infrared to sub-millimetre. It carries a single mirror of 3.5 m in diameter, that will collect long-wavelength radiation from some of the coldest and most distant objects in the Universe. The spacecraft was launched on 14 May 2009. Herschel carries three detectors:

- PACS (Photo-detecting Array Camera and Spectrometer): an imaging camera and low-resolution spectrometer covering wavelengths from 55 to 210 μm. The spectrometer has a spectral resolution between R=1000 and R=5000. It operates as an integral field spectrograph, combining spatial and spectral resolution. The imaging camera can image simultaneously in two bands (either

6085/85130 μm and 130210 μm) with a detection limit of a few mJy.

- SPIRE (Spectral and Photometric Imaging Receiver): an imaging camera and low-resolution spectrometer covering 194 to 672 μm wavelength. The spectrometer has a resolution between R=40 and R=1000 at a wavelength of 250 μm and is able to image point sources with brightness around 100 mJy and extended sources with brightness of around 500 mJy. The imaging camera has three bands, centered at 250, 350 and 500 μm. It should be able to detect point sources with brightness above 2 mJy and between 4 and 9 mJy for extended sources.

- HIFI (Heterodyne Instrument for the Far Infrared): a heterodyne detector which is able to electronically separate radiation of different wavelengths, giving a spectral resolution as high as R=107. The spectrometer can be operated within two wavelength bands, from 157 to 212 μm and from 240 to 625 μm.

GAIA

Gaia (or Global Astrometric Interferometer for Astrophysics) is a ESA astrometry space mission, and a successor to the ESA Hipparcos mission. Ariane space expects to launch Gaia for the ESA in March 2013. Gaia will compile a catalogue of approximately one billion stars to magnitude 20. Its objectives comprise:

- astrometric measurements, determining the positions, distances, and annual proper motions of stars with an accuracy of about 20 μas at 15 mag, and 200 μas at 20 mag;

- spectrophotometric measurements, providing multi-epoch observations of each detected object radial velocity measurements.

Hence Gaia will create an extremely precise three-dimensional map of stars throughout our Milky Way galaxy and beyond, and map their motions which encode the origin and subsequent evolution of the Milky Way. The spectrophotometric measurements will provide the detailed physical properties of each star observed, characterizing their luminosity, effective temperature, gravity and elemental composition. This massive stellar census will provide the basic observational data to tackle a wide range of important problems related to the origin, structure, and evolutionary history of our Galaxy. Large numbers of quasars, galaxies, extra-solar planets and solar system bodies will be measured at the same time. Gaia contains 3 separate instruments:

- the astrometry instrument (ASTRO), which is dedicated to measuring the angular position of the stars of magnitude 5.7 to 20;

- the photometric instrument, which allows the acquisition of spectra of stars over the 320-1000 nm spectral band, over the same magnitude 5.7-20;

- the high-resolution spectrometer to measure the radial velocity of the stars by acquiring high-resolution spectra in the spectral band 847-874 nm for objects up to magnitude 17.

2.5.3 Ground-based telescope and their instruments

Ground-based observatories, located on the surface of Earth, are used to make observations in the radio and visible light portions of the electromagnetic spectrum. The Earth's atmosphere is opaque to ultraviolet radiation, X-rays, and gamma rays and is partially opaque to infrared radiation: observations in these portions of the electromagnetic spectrum are best carried out from a location above the atmosphere of our planet (space-based telescopes). Most optical telescopes are housed within a dome or similar structure, to protect the delicate instruments from the elements.

Very Large Telescope

The Very Large Telescope array (VLT) is the flagship facility for European ground-based astronomy. It is made up of four separate optical telescopes organized in an array formation. The array is complemented by four movable Auxiliary Telescopes (ATs). They are built and operated at the Paranal Observatory. The VLT instrumentation programme includes large-field imagers, adaptive optics corrected cameras and spectrographs, as well as high-resolution and multi-object spectrographs and covers a broad spectral region, from 300 nm to 24 μm. Let us present only two of these instruments, whose filters are included in our list:

- VIMOS (VIsible Multi-Object Spectrograph): a four-channel multi-object spectrograph and imager, allows obtaining low-resolution spectra of up to 1000 galaxies at a time;

- ISAAC (Infrared Spectrometer And Array Camera): it is a cryogenic infrared imager and spectrometer, observing in the 1 to 5 μm range.

CFHT/MegaPrime

The CanadaFranceHawaii Telescope is located near the summit of Mauna Kea mountain on Hawaii's Big Island and is one of the observatories that comprise the Mauna Kea Observatory. Operational since 1979, the telescope is a Prime Focus/Cassegrain

configuration with a usable aperture diameter of 3.58 m [3]. CFHT hosts three *state-of-the-art* instruments:

- MegaPrime: it is an optical and near infrared instrument. The wide-field imager, MegaCam , consists of 36 2048 $\times$ 4612 pixel CCDs, covering a full 1 degree $\times$ 1 degree field-of-view with a resolution of 0.187 μas per pixel;
- WIRCam: it is an infrared mosaic of 4 detectors and 16 MegaPixels;
- ESPaDOnS: it is a new échelle spectrograph / spectropolarimeter.

MSSSO/CASPIR

CASPIR is a near-infrared spectrometer/imager being built for the Mount Stromlo and Siding Spring Observatories' 2.3 m telescope. This telescope is operated by the Australian National University (ANU) and it was constructed during the early 1980s. CASPIR provides direct imaging and spectroscopic capabilities in the 1-5 μm wavelength range. For more information about the telescope and its instrumentation, see McGregor et al. (1994).

MPG/ESO

The MPG/ESO telescope is a 2.2-m ground-based telescope at the ESO, in La Silla, Chile. It has been operating since 1984. The telescope hosts three instruments:

- WFI (Wide Field Imager): a focal reducer-type camera at the Cassegrain focus with a field of view as large as the full Moon;
- GROND(Gamma-Ray Burst Optical/Near-Infrared Detector): which chases the afterglows of gamma-ray bursts;
- FEROS (high-resolution spectrograph): it is used to make detailed studies of stars.

We conclude this section with the Fig. 2.2, where the sensitivity and the bands of some of the presented telescopes and missions are shown, and with the Fig.2.1 [5], that shows the 5 σ point source sensitivities of WISE and previous or planned all-sky surveys. The planned wavelength range for the JWST is indicated. The dot size shows the planned sky coverage.

[3] http://www.cfht.hawaii.edu/en/

[5] http://www.astro.ucla.edu/ wright/WISE/index.html

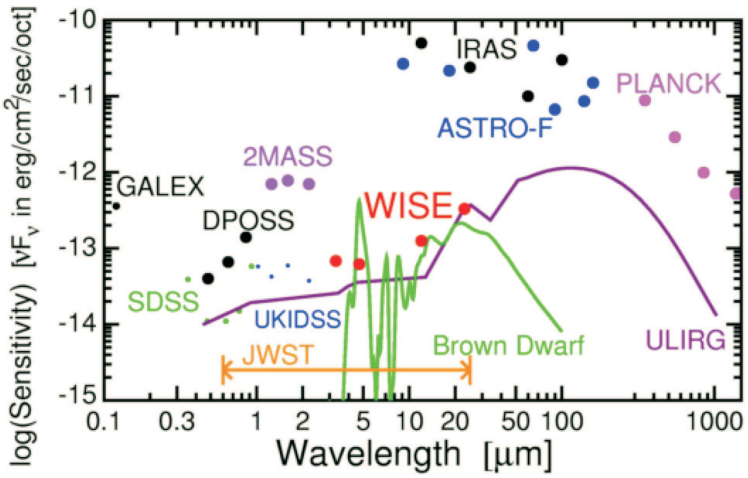

Figure 2.1: Sensitivities of WISE and previous or planned all-sky surveys.

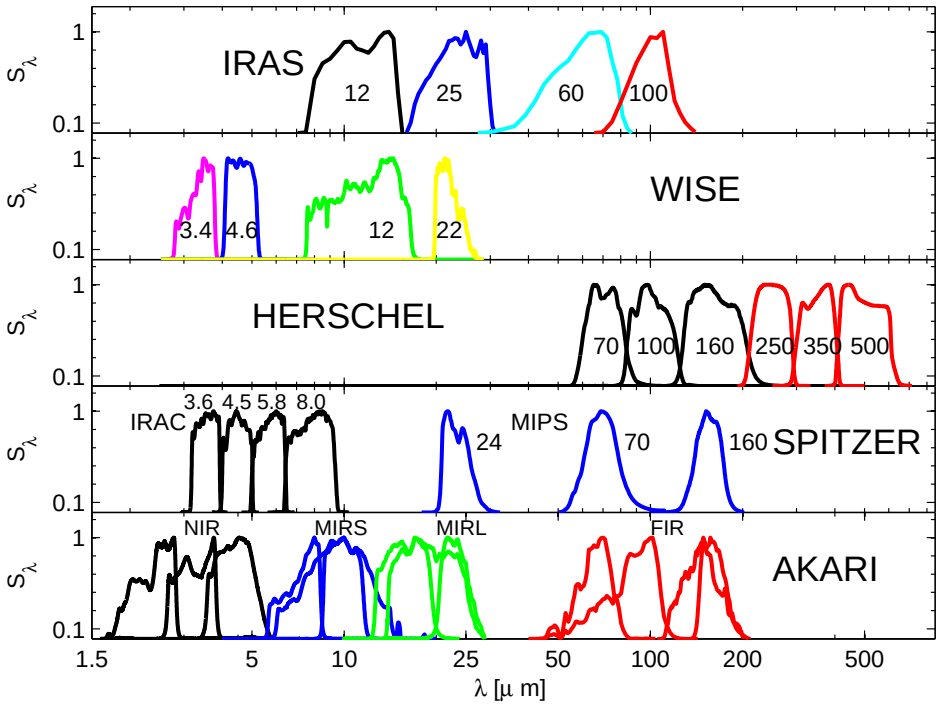

Figure 2.2: Sensitivity and bands of the some telescopes/missions, going from IRAS (1983) to WISE, Spitzer and Herschel.

Chapter 3

Star clusters: comparing results with observational data

Much of our understanding of galaxy formation and evolution comes from the analysis of stellar populations in galaxy of different morphological types, both in the present and early universe. The main parameters of these stellar systems widely used are ages and metallicities: the most efficient method to determine them for unresolved stellar systems in photometric surveys (especially at high redshift) is to compare their observed colors with the predictions of evolutionary population synthesis models - see Bressan et al. (1994), Bruzual A. & Charlot (1993), Silva et al. (1998), Tantalo et al. (1998), Buzzoni (2002), Bruzual & Charlot (2003), Buzzoni (2005), Piovan et al. (2006a), Piovan et al. (2006b), Galliano et al. (2008), Galliano et al. (2008), Popescu et al. (2011) -.

Evolutionary population synthesis models are based on SSPs. What usually is done is to empirically calibrate the SSP models to observations of real star clusters whose ages and metallicities have been determined independently, e.g., synthetic color-magnitudes diagrams (CMDs).

In this chapter we will apply our SSPs to the study of star clusters in order to validate them and in particular trying to put in evidence the effect of the dusty shells around AGB stars. Indeed the remaining part of the Bertelli et al. (1994) isochrones up to the TP-AGB has been tested and applied in an impressive number of papers, so what really matters for the purposes of this thesis is to examine the effect of (1) the improved TP-AGB and (2) the new library of dusty AGB stars. At this purpose, in particular we will take into account data from the Small and Large Magellanic Cloud (SMC and LMC), that allow to compare SSP models for the metallicities where the effect of dust shells around should be stronger.

3.1 The Magellanic Clouds

The globular cluster systems of the Magellanic Clouds provides a nice opportunity to investigate the integrated photometry and the spectral behavior of stellar populations as a function of the age and chemical composition. They are excellent templates for studies of stellar populations in external galaxies; moreover, they contain a significant population of intermediate-age massive star clusters which are not easily accessible in the Milky Way.

The Magellanic Clouds are close enough that star clusters within can be resolved into individual stars by high spatial resolution imaging from both ground and space based telescopes. Their empirical CMDs can be therefore used for detailed age calibration. The star clusters are also populated enough that their integrated colors are less sensitive to stochastic effects when compared to galactic open clusters.
One of the first study about integrated photometry for LMC clusters had been done by van den Bergh & Hagen (1968), while previous efforts in near-infrared involved Persson et al. (1983) and Ferraro et al. (1995). The NIR regime contains some very important diagnostics for deriving the basic properties of stellar system; moreover, it has been proved to be able to partially broke the age-metallicity degeneracy, particulary for stellar populations older than $\sim$ 300-400 Myr (Goudfrooij et al. 2001; Puzia et al. 2002; Hempel & Kissler-Patig 2004; Pessev et al. 2006).

The outline of this chapter is as follows. We compare:

- CMDs of LMC and SMC clusters and theoretical CMDs with the path of our isochrones, both taking into account or not the contribution of the circumstellar dusty shell around AGB stars;

- broad-band colors of LMC and SMC clusters as a function of the cluster age, and predicted theoretical colors os SSPs with *dusty AGB* or *no dusty AGB*.

3.2 Comparison with the observations: isochrones

In this section, we present the correlation between the colors of our isochrones (considering both the presence of *dusty AGB* and the *classical* AGB without the shell of dust around) and the observations. The best available data for the AGB population in galaxies is the data obtained from the extensive near and mid-infrared surveys of the Magellanic clouds. The data are taken from the SAGE (*Surveying the Agents of Galaxy Evolution*) catalogues (Blum et al. 2006; Bolatto et al. 2007), which match IRAC (or MIPS) data with 2MASS photometry. The SAGE project consists of Spitzer Space Telescope images of the Large Magellanic Cloud (SAGE-LMC) and the Small Magellanic Cloud and Magellanic Bridge (SAGE-SMC), in addition to

Spitzer spectroscopy of the dust composition in the Large Magellanic Cloud (SAGE-Spec, 30 Doradus) and Small Magellanic Cloud (SMC-Spec). The SAGE project *webpage* is `http://sage.stsci.edu/`. The survey is described in Meixner et al. (2006).

In the Figs. 3.1, 3.2, 3.3, 3.6, 3.7, 3.8, we plot the color-magnitude diagram for the Magellanic Clouds, considering the near- and mid-IR photometry and we superimpose our new and old isochrones, for different values of age, that are log(t/yr)=7.95, 8.10, 8.48, 8.60, 8.70, 8.90, 8.95, 9.18 and 9.30, corresponding to ages from t= 0.09 Gyr to 2 Gyr.

3.2.1 Large Magellanic Cloud

For the Large Magellanic Cloud, the old and new isochrones have been chosen with a metallicity Z=0.008; we adopted a distance modulus of 18.5, following the value most widely used in literature (Pessev et al. 2008).
The data are limited to a circular area of π square degrees centred on the LMC bar ($\alpha_{2000} = 5^h23^m.5$, $\delta = -6945'$), in order to include thousands of bright AGB stars and to exclude the presence of objects that do not belong to the cloud. Even with this trick, in all the CMDs for the LMC we can observe a narrow vertical finger on the left part of the CMDs, caused by foreground Milky Way stars and a contamination in the bottom right part, which consists of background galaxies. Moreover, in the Figs. 3.3, the objects with roughly [3.6]-[8] $\gtrsim$ 2 (the vertical finger in the bottom right part of the diagram) are not detected by 2MASS; they are likely background galaxies and young pre-main sequence stars.

3.2.2 Small Magellanic Cloud

For the SMC, we choose to superimpose to the data, a selection of isochrones of metallicity Z=0.004, in agreement with the average value estimated for the SMC; in this case, the adopted distance modulus is 19.05 (Pessev et al. 2008). The contamination of the objects which do not belong to the cloud is also visible in this case, and, as for the LMC, in the Figs. 3.3 the objects with roughly [3.6]-[8] $\gtrsim$ 2 are not detected by 2MASS.

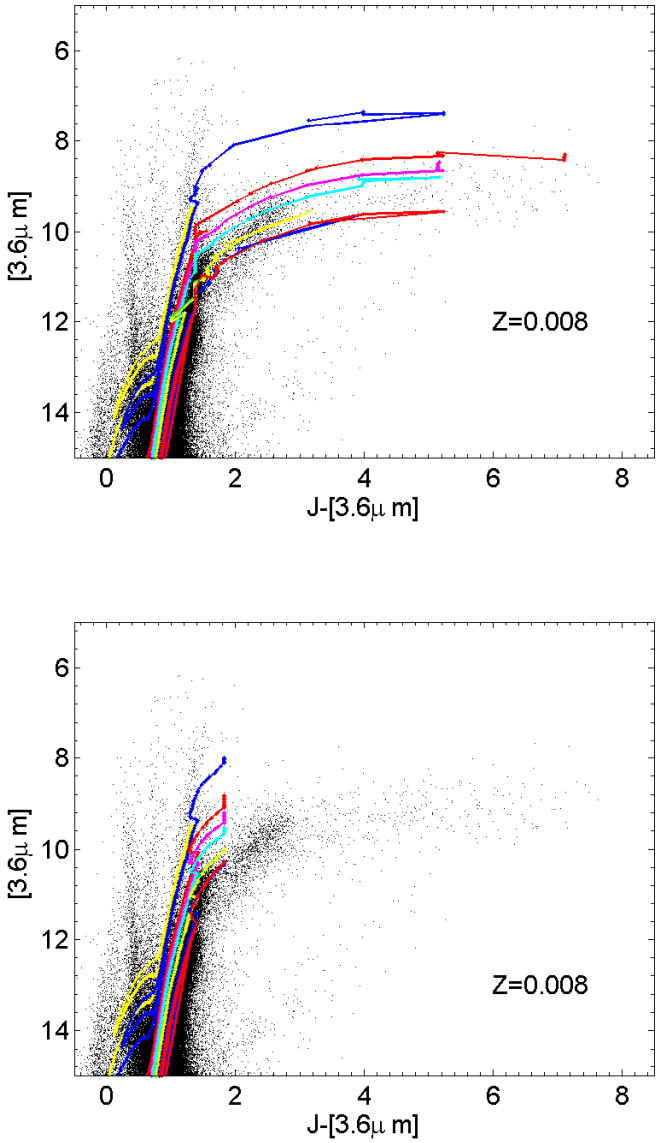

Figure 3.1: Comparison between the new (**upper panel**) and the old isochrones (**lower panel**) (with Z=0.008) and the near- to mid- infrared data for the LMC. In particular, we show the 2MASS+IRAC [3.6] vs. J-[3.6]. The isochrones are drawn in different colors according to their age: the ages are log(t/yr)= 7.95, 8.10, 8.48, 8.60, 8.70, 8.90, 8.95, 9.18 and 9.30 (the oldest are in the bottom right part of the CMDs).

3.2.3 Discussion of the results

In all of these plots, the contribution of the dusty circumstellar shell around AGB stars appears crucial. Without dust, the theoretical colors are *not able* to reproduce

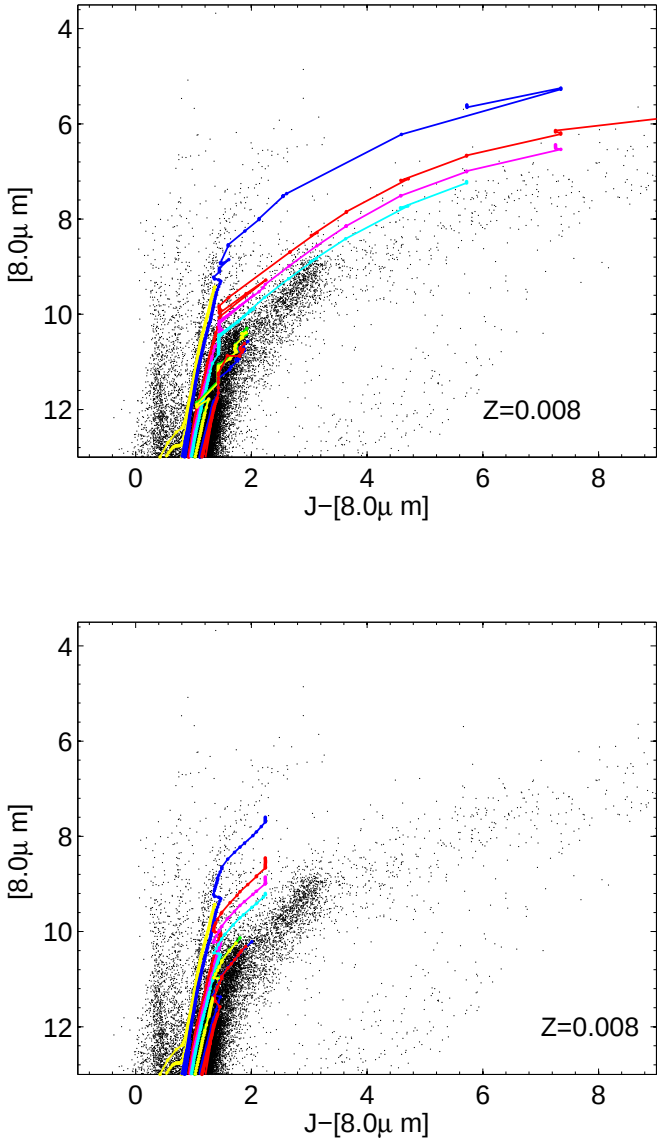

Figure 3.2: The same as in the Fig. 3.1, but for 2MASS+IRAC [8] vs. J-[8].

the region in the color-magnitude diagrams where the AGB stars lie. The AGB phase stops earlier and does not extend toward redder colors, as expected since there is no dust included able to make redder the spectrum. In general, the range of ages selected for the isochrones covers the region with the AGB stars, but in some cases we do not have an exact match of one of the isochrones of our set with the main AGB locus. The reason for this is that once the region populated by AGB stars has been embedded between two isochrones of different ages, it is just a matter to use a more

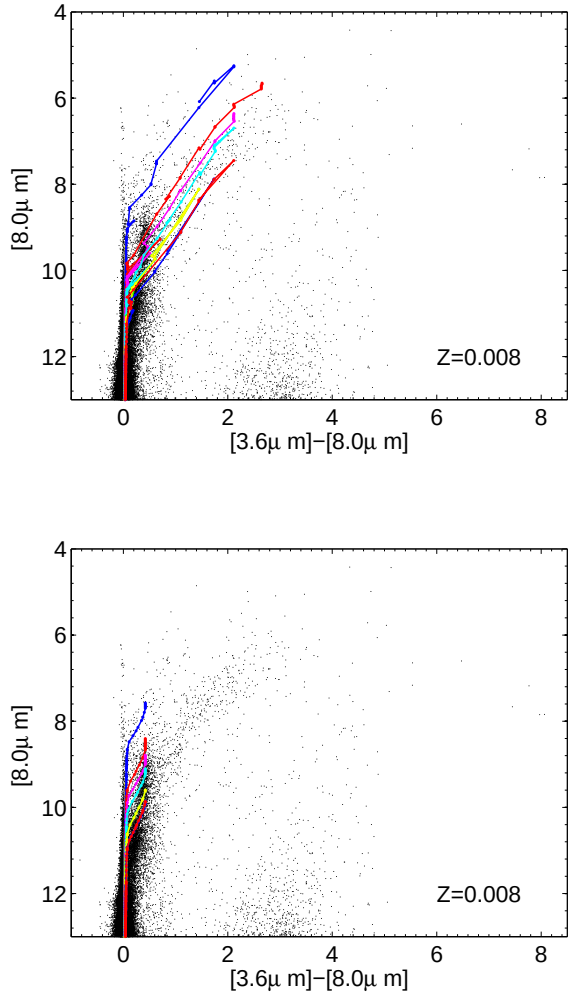

Figure 3.3: The same as in the Fig. 3.1, but for IRAC [8] vs. [3.6]-[8].

thinely spaced grid of ages to get the isochrone exactly matching the main AGB strip. For our purposes, in order to get a general validation of the models, it is enough to be sure that we can extend the path toward much redder colors and constrain the AGB locus between the represented ages. There is no need to keep refining or extending the grid of ages to get the best age reproducing the observational data. In particular the following considerations hold:

- at log(t/yr)=7.95 (the first value of range of ages considered, represented with a yellow line on the upper-left, well visible in all CMDs except in Figs. 3.3 and 3.8), AGB stars are not present, because the isochrone is still too young and the highest mass AGB star has still to reach the AGB evolutionary phase. The

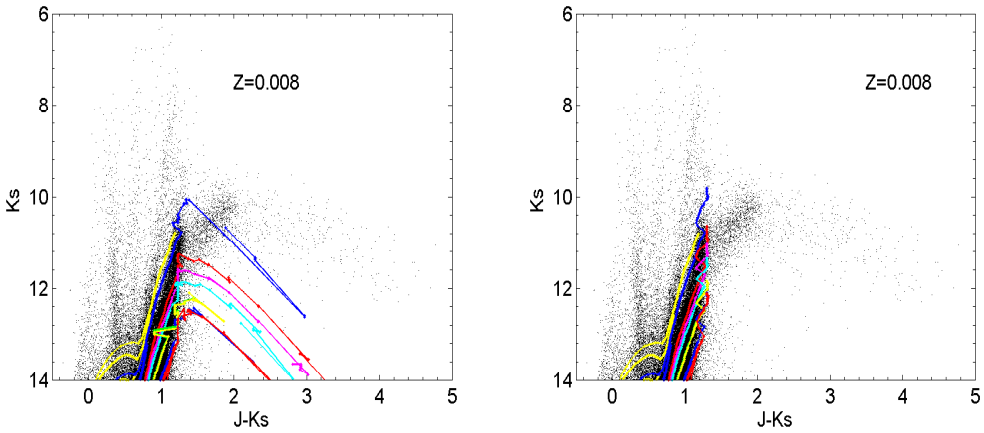

Figure 3.4: Comparison between the new (**upper panel**) and the old isochrones (**lower panel**) (with Z=0.008) and the near-infrared data for the SMC. In particular, we show the 2MASS K_S band vs. J-[K_S]. The isochrones are drawn in different colors according to their age: the ages are log(t/yr)= 7.95, 8.10, 8.48, 8.60, 8.70, 8.90, 8.95, 9.18 and 9.30 (the oldest are in the bottom right part of the CMDs).

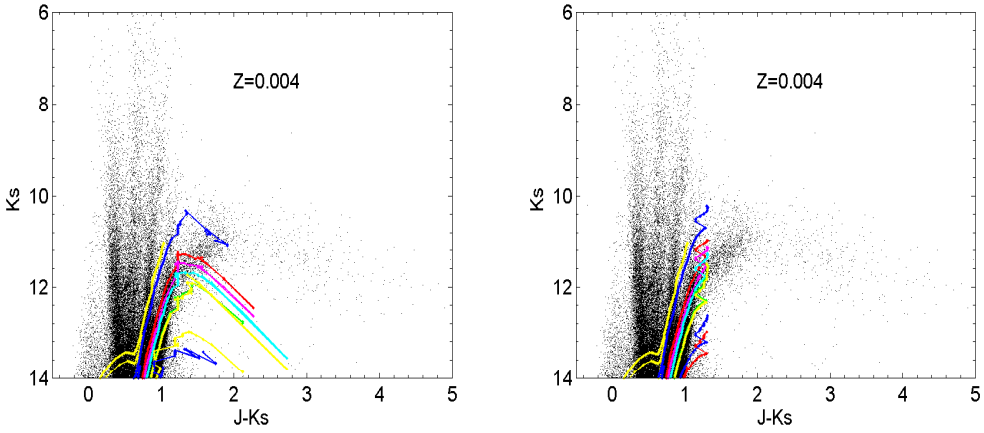

Figure 3.5: The same as in the Fig. 3.4, K_S band vs. J-[K_S], but for the SMC. The isochrones have been chosen with the metallicity Z=0.004.

most prominent near-IR stars are in this case red super-giants;

- in the range 8.10$\leq$ log(t/yr) $\leq$ 8.90 the TP-AGB phase is well developed: for the metallicities under examination, the intermediate mass stars in the AGB phase show an extended C-rich surface. The duration of the C-rich phase is due to the interaction between dredge-up, low-temperature opacities and mass

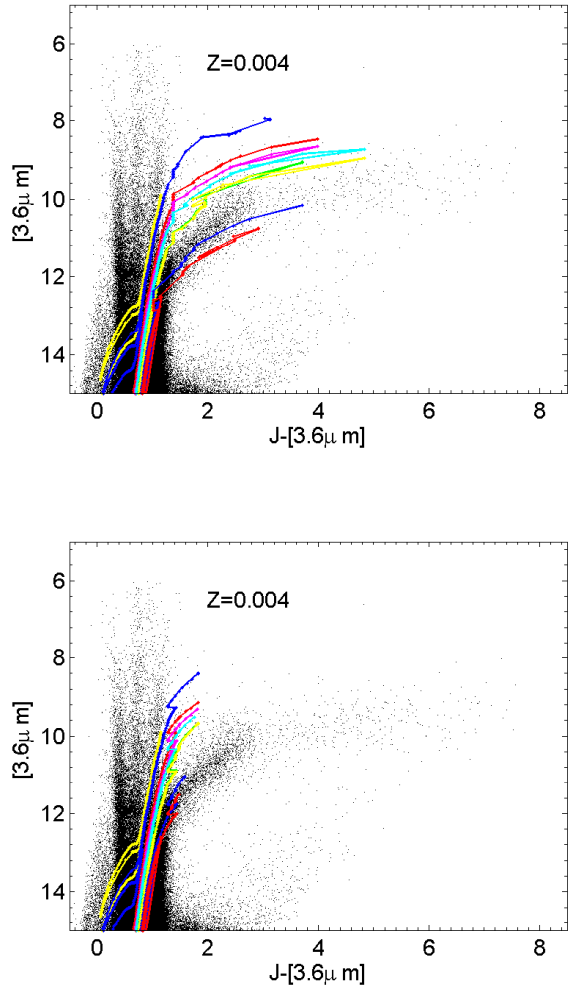

Figure 3.6: The same as in the Fig. 3.1, but 2MASS+IRAC [3.6] vs. J-[3.6] for the SMC. The isochrones are of Z=0.004.

loss. The efficiency of the TDU increases with lower metallicities: indeed it is pronounced for the values of Z we are considering (see also the Fig. 1.5). This is the range of ages that best reproduce the red tail of C-rich stars.

- in the range $9.18 \leq log(t/yr) \leq 9.30$ the TP-AGB phase starts to decline: the C-rich surface is less extended than before, even if its contribution to the red tail is still important.

This physical behaviour is quite the same for both the isochrones of Z=0.004 and Z=0.008; the main difference is the ∼0.5 mag shift of all the features, due to the different distance of the two Clouds. Anyway the agreement between models and

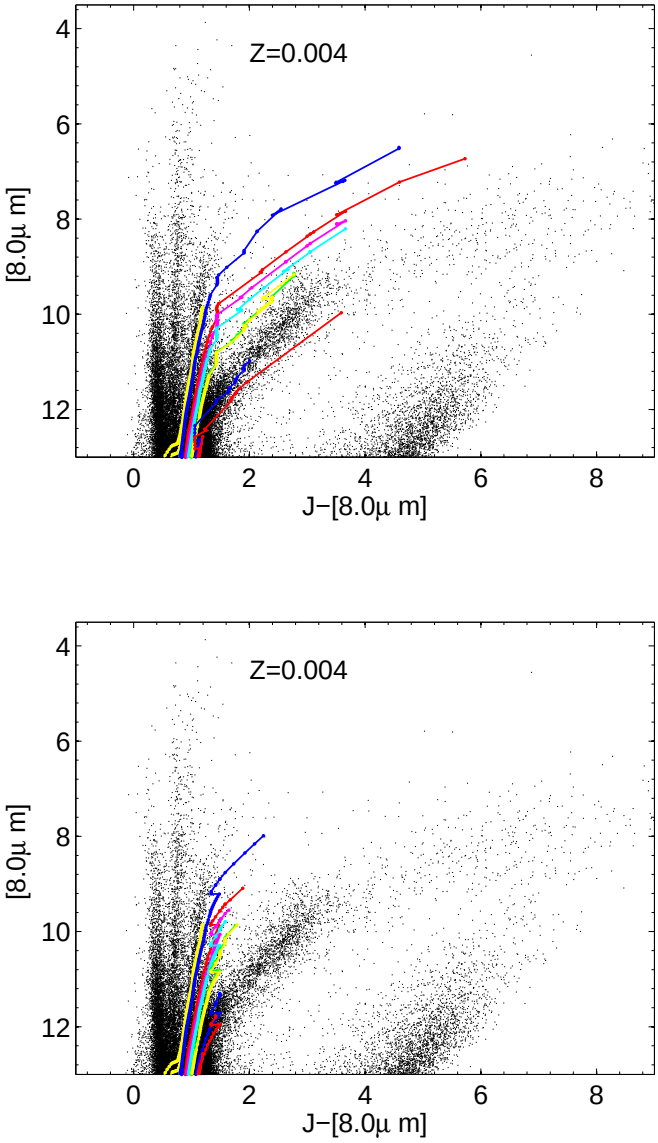

Figure 3.7: The same as in the Fig. 3.6, but 2MASS+IRAC [8] vs. J-[8].

observation is satisfactory for most of the CMDs and it is a significant step forward toward a realistic description of dust around AGB stars. Similar results have been obtained by Marigo et al. (2008) using synthetic models of TP-AGB and a library of dusty spectra of AGB stars. It can be noticed that our isochrones, once coupled with the library of dusty spectra, present a more regular behaviour in the CMDs compared to Marigo et al. (2008) which also tends to extend toward redder colors than us. This could be ultimately due to different optical depths adopted for the

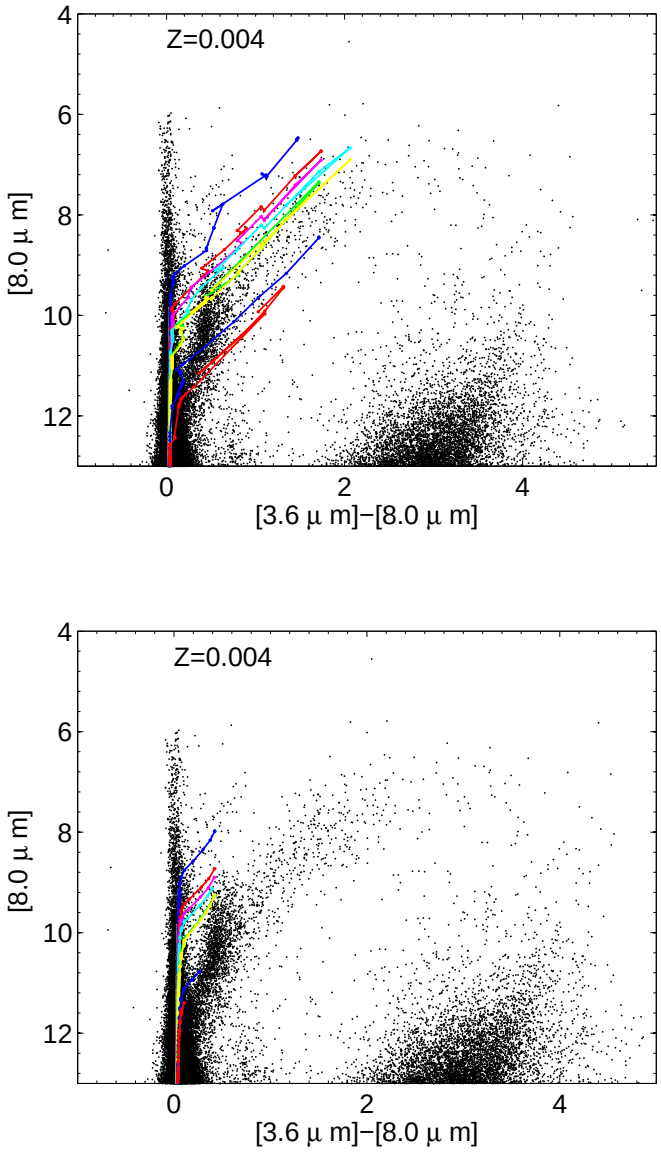

Figure 3.8: The same as in the Fig. 3.6, but for IRAC [8] vs. [3.6]-[8].

models, for instance due to different recipes for the mass loss rate, that crucially influences the τ.

The only CMD for which the results are not enough satisfactory is the fully near infrared CMD with 2-MASS results K_S band vs. J-[K_S]. Our isochrones, partially in agreement with the observations, tend to bend too early toward redder K_S magnitudes, while it would be required to keep the K_S magnitude more or less constant. It is hard to track what could be the reason for this systematic bending toward redder

K_S magnitudes, in particular since all the other NIR/MIR bands seems to behave well: it may be for instance due to some unrealistic absorption effect in the K_S band. We plan in the future to investigate in a deeper way this specific point.

3.2.4 Comparison with data: integrated colors of SSPs

The Figs. 3.10 and 3.9 show the temporal evolution of theoretical colors for SSPs with and without the contribution of dusty AGB stars. These colors are superimposed to optical and near-infrared colors of Large Magellanic star clusters, that are taken from the database of Pessev et al. (2006) and Pessev et al. (2008).

Pessev et al. (2006) present integrated NIR magnitudes (J, H, K_s) and colors for a large sample of star clusters in the LMC and SMC, using the data of the 2MASS. These clusters are of well-known ages and metallicities, available in the literature for the vast majority of the objects in the sample, and they can be safely used as a calibration data set for SSPs models. In the globular clusters of the Magellanic Clouds there are a lot of objects with ages in the range 0.3-3 Gyr; the integrated light properties of these systems are heavily affected by AGB stars, that are extremely luminous in the NIR and whose contribution to this part of the spectrum is in this work widely investigated with and without dusty shells around AGBs. In Pessev et al. (2008) these data have been combined with new photometry in such a way to get nine additional objects: all these data form the largest database of integrated near-NIR magnitudes and colors of LMC/SMC star clusters. Moreover, the 2MASS data have been merged with optical photometry originating from the work of Bica et al. (1996) and the compilation of van den Bergh (1981). The sample provides optimal coverage of the age-metallicity parameter space of LMC/SMC star clusters. For addiction information about the sample selection, data acquisition and reduction, see the papers from Pessev et al. (2006) and Pessev et al. (2008).

We want now to compare the predictions of our SSP models and the observed clusters colors as a function of age. In such a way we should be able to evaluate the performance of our models, to eventually determine the ages at which discrepancies between data and models can occur. From these ages is then easy to recognize the responsible stages of stellar evolution and the model ingredients that need further attention and refinements. We will not have as main target to derive the properties of the observed star clusters. Indeed, when a comparison between observations of star clusters and theoretical predictions is performed, it is important to keep in mind that the theory of SSPs assumes that clusters are massive enough that all the stellar evolutionary phases are well sampled. Predictions of any model based on these assumptions will match the observations only in the limit of a sufficiently large number

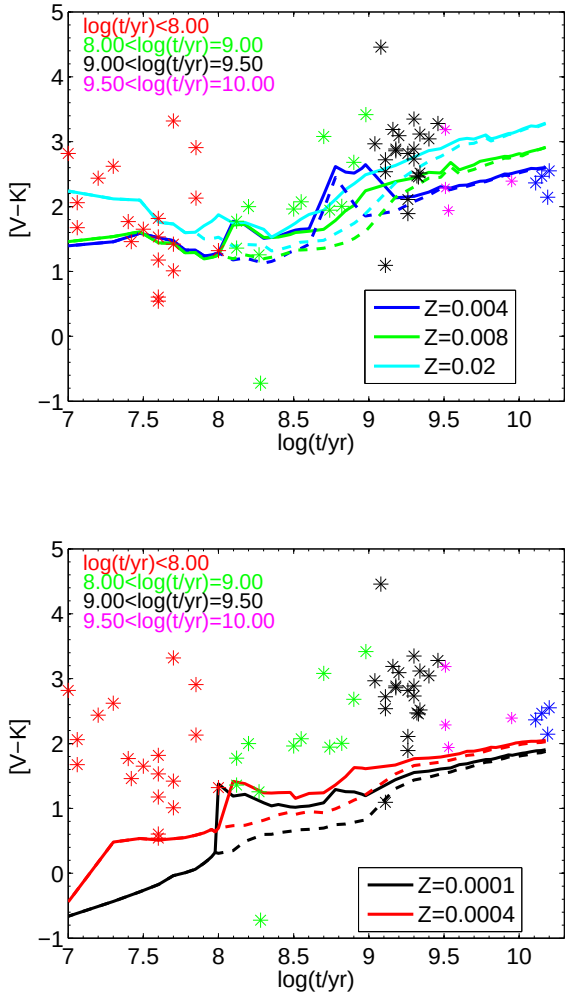

Figure 3.9: **Upper panel**: theoretical [V − K] colors of our SSPs, with (continuous lines) and without (dotted lines) the contribution of circumstellar dust shell around AGB stars, as a function of the age (from 0.01 until 15 Gyr). The following values of metallicity are considered as indicated: Z=0.004 (blue lines), Z=0.008 (green lines), Z=0.02 (cyan lines). The SSPs are superimposed to integrated colors of LMC star clusters, taken from the compilation of Pessev et al. (2006) and Pessev et al. (2008); the data are plotted in different colors according to the age of the cluster, as indicated in the figure. **Lower panel**: as in the **upper panel**, but we superimposed to the data SSPs of metallicity Z=0.0001 (black lines) and Z=0.0004 (red lines).

of observed stars. In this sense, the spread in the intrinsic colors of clusters with similar ages and metallicities can be ascribed to stochastic fluctuations in the number of bright stars residing in low population clusters. As already pointed out, the star clusters of the Magellanic Clouds have a population of stars numerous enough that their integrated colors are less sensitive to stochastic effects when compared

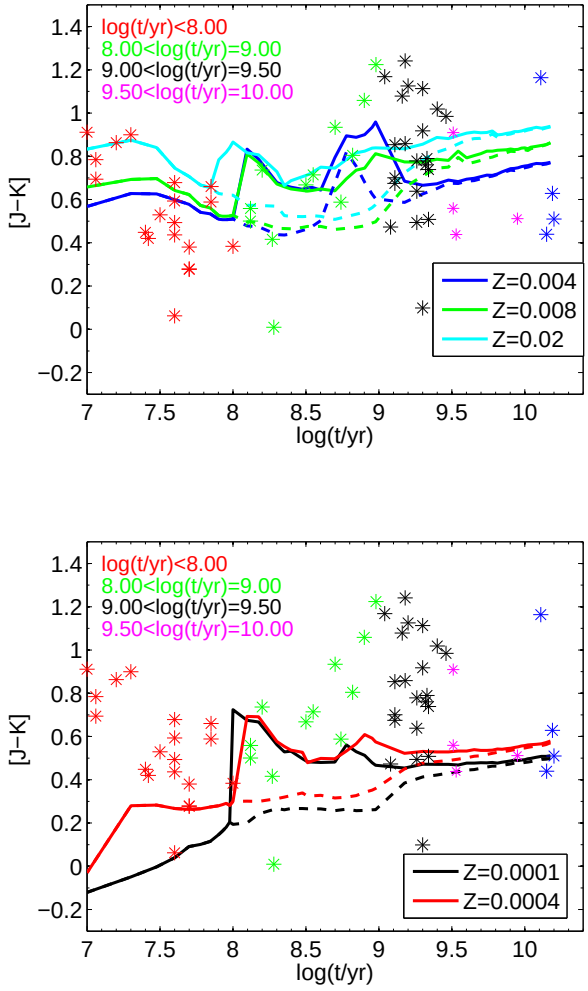

Figure 3.10: The same as in Fig. 3.9, but in this case we show the theoretical and integrated [J − K] color for both SSPs and the star clusters' sample.

to galactic open clusters. The [V − K] color is presented in the Fig. 3.9: while on the **upper panel** we superimposed to the data the SSPs of Z=0.004, Z=0.008 and Z=0.02, on the **lower panel** we show the SSPs of Z=0.0001 and Z=0.0004. In Fig. 3.10, we do the same but now considering the [J − K] color. The data have been selected (and hence plotted with different colors) according to their age (estimated from the CMDs of the clusters, see the cited papers for further information) and their metallicity: we decided to divided them into four age ranges (as shown in both panels). All these clusters have $[Fe/H] > -1.71$, thus their are classified as *metal-rich* clusters. The distribution of the individual points around the model tracks is reasonably tight; there is a good agreement between the properties of the clusters

and the model predictions, in particular if we consider the **upper panels** of both figures, where appropriate metallicities for the Large Magellanic Cloud clusters' are taken into account. As it can be seen, there is a considerable difference between dusty colors and no dust colors, as already discussed in Sect. 3.2.3; this discrepancy starts when the first AGB appears, as expected, and it is more evident when looking at the Fig. 3.10, where the infrared color is shown. Moreover, we can observe two 'bumps' toward redder colors: the first is located at about 0.1 Gyr and it is due to the pronounced effect of the AGB phase transition (which starts at a few hundred Myr); the step increases the predicted colors since the increased flux in the near-IR pass-bands. The second 'bump' is located between 1 and 2 Gyr, and it is likely due to the development of the RGB; this is more evident when a higher values of the SSP metallicities are taken into account.

3.2.5 The color-color diagrams

We compared the time evolution of theoretical colors for SSPs with and without the contribution of dusty AGB stars and the observed clusters colors as a function of the age. It might be interesting now to compare and mix the integrated broad-band colors of SSPs, whose AGB stars are enshrouded in dust shells, to those of a sample of star clusters. Because of this we have analyzed the colors of young globular clusters of the Magellanic Clouds.

Pietrzynski & Udalski (2000) presented age determinations for about 600 star clusters belonging to the central part of the LMC. They are all younger than 1.2 Gyr and hence the majority of them belong to the age range in which the AGB phase can develop significantly contributing to the integrate light of the clusters. Moreover, following the work of Piovan et al. (2003), we selected a small sample in which the contribution to the total light by AGB stars is particulary strong. These photometric data are derived from the *2MASS Second Incremental Data Release* and the *Image Atlas*, which contains 1.9 millions of images in the infrared bands J, H, K_s. The integrated magnitudes have been calculated by Pretto (2002) and they are available to us. We also considered the IR colors for the LMC and SMC clusters by Persson et al. (1983) used by Mouhcine (2002). The Figs. 3.11, 3.12 and 3.13 show the two color diagrams (respectively, [H-K] vs. [J-H], [H-K] vs. [V-K] and [J-K] vs. [V-K]). In each diagram we show the data of Persson et al. (1983) for LMC (open circles) and SMC (black stars), the data from Pretto (2002) (cross-shaped points). All the data have been reddening corrected. The **upper panel** of the three figures show the new SSPs with (continuous lines) and without (dotted lines) the contribution of the dust shells, while on the **lower panel** we superimposed the classical SSPs (Bertelli's ones). For both kinds of SSP models, different metallicities are presented, namely

Z=0.02 (magenta lines), Z=0.004 (cyan lines) and Z=0.008 (green lines), while the age range is from 100 Myr (when the contribution of AGB stars begin to contribute to the integrated light of the stellar population) until 15 Gyr (when all the intermediate and massive stars already evolved long ago from the AGB phase).
It is evident from the figures that the new dusty SSPs span the range of data much better than both the old SSPs of Bertelli and the new SSPs with *no dust around the AGB stars*: indeed the color obtained by the old SSPs are too red in [J-H] and they span a narrower range, above all in [H-K]. On the contrary the new SSPs have bluer [J-H] and [V-K] colors. The [V-K] color is particularly suitable to study this evolutionary phase of the stellar populations: indeed the AGB phase transition (occurring between the age of ∼200 Myr and ∼1 Gyr, that is log(t/yr)=8.30 and log(t/yr)=9.17) causes abrupt changes in the near-infrared luminosity of the clusters while producing only small changes in the optical. Our new SSPs extend toward blu colors, approximately like the SSPs by Mouhcine (2002), as shown in Piovan et al. (2003). The differences between our SSPs and the models of Mouhcine (2002) are due to the adoption, in their models, of empirical spectra for O and C stars. In our work, instead, we use theoretical models of M stars which are not able to reproduce the empirical spectra as well as the empirical ones. More work is required to improve the theoretical spectra of cool stars to be included in population synthesis studies.

It is also interesting to compare data and theory looking at the colors that can help to break the well-known age-metallicity degeneracy while delivering photometry with adequate signal-to-noise ratios, even if it is not our main target the precise determination of the age and metallicity of the clusters.
For this reason, following the ideas fromPessev et al. (2008), we show a couple of figures now considering the color combination [B-J] vs. [J-K], that have been proved by Puzia et al. (2007) to be very good in age resolution, through the [B-J] color, while the [J-K] is more sensible to the metallicity (except for the small age interval when the AGB phase transition occurs, since [J-K] can show a modest age dependence). We use the database by Pessev et al. (2006) and Pessev et al. (2008), that was presented in Sect. 3.2.4. In this case we superimpose only the new dusty SSPs, but now for all the available values of metallicities, as the legend on the panels indicates. The age range for the SSPs is now from 10 Myr (there are not clusters younger than this age) up to 15 Gyr. The age of the SSPs grow moving from left to right, when looking at a single value of the metallicity. We do not consider here *only* the young clusters of the LMC and SMC, as in the previous analysis, but we divide the sample into two groups: the young clusters ($t < 0.95$ Gyr) and the old ones. Moreover, we subdivide the clusters into *metal-rich* clusters (if [Fe/H] > -1.71), and *metal-poor* ones.

The following symbols have been adopted:

- the open circles represents clusters younger than $t < 0.95$ Gyr; the contrary when a stars is used;
- the black symbols refer to metal-poor objects while the red ones to metal-rich clusters.

The **upper panel** of the Fig. 3.14 shows the two color diagram for the star clusters in the LMC, while the data for the SMC are plotted in the **lower panel**. While for the LMC we can appreciate all the combinations between age and metallicity (with the exception of young metal poor clusters), for the SMC the database offers only metal-rich clusters for various ages and no metal poor objects. The separation between the different age and metallicity ranges is evident: we can observe how our SSPs are able to cover the data, particulary when looking at the region of the youngest metal-rich clusters. Instead, our models fail in reproducing the old clusters of the LMC (situated between $0.3 \lesssim [B-J] \lesssim 0.6$ and $2 \lesssim [J-K] \lesssim 5$) that are mostly older and metal-poor objects (even if some metal-rich clusters appear in this region). We encountered some problem also in the region situated between $1 \lesssim [B-J] \lesssim 1.3$ and $2 \lesssim [J-K] \lesssim 3$, populated by the oldest and metal-rich clusters. Of course this partial disagreement with the observations suggests that some of the ingredients of the models can be improved, for example about the cool stars part of the library of stellar spectra in use. But it is important to remember, as already pointed out, that stochastic fluctuations in the number of giant stars will cause the spread in cluster colors at any ages and metallicity. This effect is obviously greater when the SMC data are taken into account, considering that we are analyzing *only* a very small number of clusters. The stochastic fluctuations can explain the disagreement between data and theory in the mentioned range of colors; to exclude this, it will be necessary to overcome this problem and to calculate *composite* cluster colors for different age intervals.

3.3 Comparison with data: M31

To conclude this chapter we present a comparison between theoretical models and data for M31.

M31, the *Andromeda* galaxy, is one of the galaxies of the Local Group and it is located at around 778 kpc from the MW. Its distance modulus is 24.47 (Holland 1998; Stanek & Garnavich 1998; McConnachie et al. 2005); M31 is an ideal local galaxy to study Globular Clusters (GCs), since it is near and contains more GCs than all

the other Local Group galaxies combined together (Battistini et al. 1987; Racine 1991; Harris 1991; Fusi Pecci et al. 1993). The globular cluster system of M31 has been studied since the beginning of extragalactic astronomy, by Hubble, in 1932: he also presented the first catalogue of 140 GC candidates in this galaxy. After Hubble, numerous lists of M31 GC candidates were published. For more details about this, see the paper of Ma (2011): we only remember here the Bologna catalogue, which contains 827 objects, classified into five groups by the authors' degree of confidence. Up to now, we focused on the central region of the LMC, besides the SMC. For M31, instead, clusters belonging to the outer regions of the galaxy have been analyzed. They can be useful to trace the substructures supposed to form in the outer region of their parent galaxy. Indeed, the popular Λ cold dark matter model for galaxy formation, forecast the presence of substructures located in the outer region, that continue to grow from the accretion and the disruption of companions satellite.

We started from the photometric data in J, H and K from 2MASS imaging of 10 classical globular clusters in the outermost regions of M31, analyzed by Ma (2011) (for more details about the data reduction see this paper). These data have been combined with the V and I photometry. The sample of M31 halo globular clusters is originally from Mackey et al. (2006), Mackey et al. (2007), who estimated the metallicities, distance modulus and reddening values from their observed color-magnitude diagrams built using the deep images obtained with ACS/*HST*. For what concerns the ages of these clusters, they have been determined comparing the integrated photometric data with high resolution SSP models using the Padova-2000 metal poor evolutionary tracks and a Salpeter (1955) IMF, since their metallicities are $-2.14 < [Fe/H] < -0.70$. In this section we use their age determinations and uncertainties as a function of both $[V-I]$ and $[J-K]$ and we superimpose our new dusty SSPs for all the available values of metallicity. The **upper panel** of the Fig. 3.15 shows the theoretical evolution of the [V-I] color of our SSPs as a function of the age, while on the **lower panel** we focus on the [J-K] color. It is clear from the figure that the $[V-I]$ color is the most appropriate to reproduce the age and the metallicity of these M31 clusters, since it varies steeply for ages older than 1 Gyr when the metallicity (as in this case) is fixed. Moreover, the uncertainties associated with the observational data are lower when looking at this color with respect at the $[J-K]$. The last consideration we can do is that some clusters, according with the age proposed in Ma (2011), show a very old age, that our SSPs can not reproduce, since our models stop at 15 Gyr, chosen in such a way to agree with the current age of the universe 13.7 Gyr plus some margin.

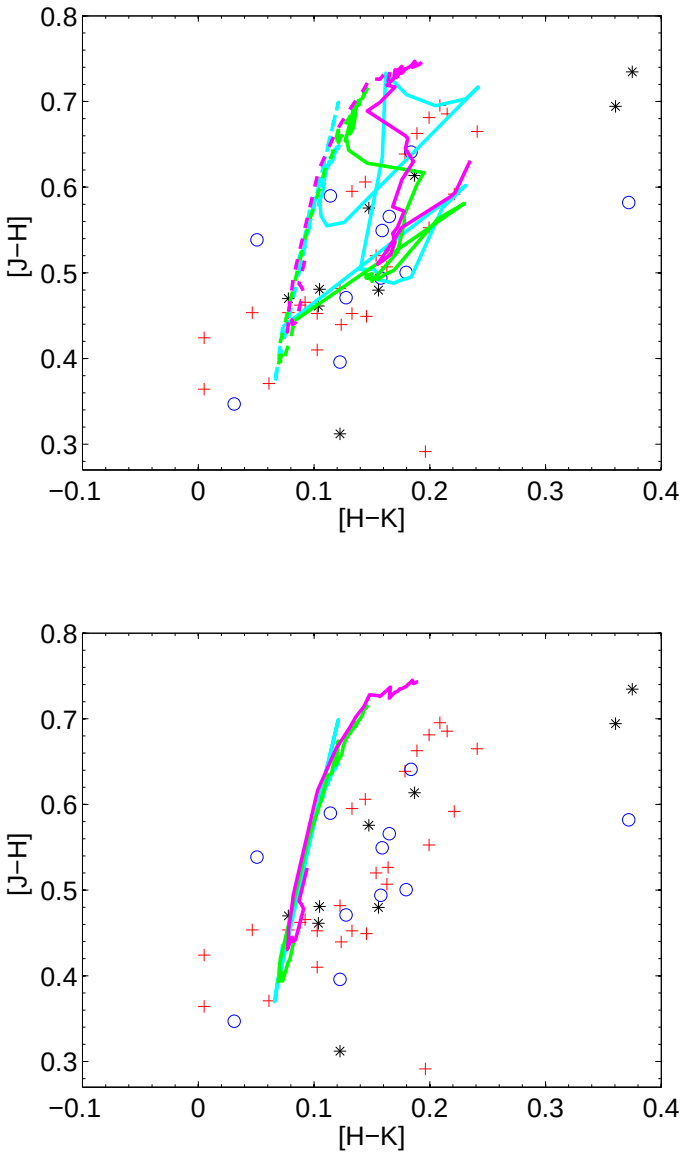

Figure 3.11: The *two color diagram* [H − K] vs. [J − H] for young star clusters of the Magellanic Clouds. The open circles are the LMC clusters selected by Mouhcine (2002) from the catalogue of Persson et al. (1983), while the black stars indicate the same but for the SMC. The cross-shaped points are few LMC clusters whose IR colors have been collected by Pretto (2002) using 2MASS data. All the data have been properly reddening corrected. In the upper figure, the lines show the color range spanned by the new SSPs with (continuous lines) and without (dotted lines) the contribution of circumstellar dusty shell around AGB stars. Different values of the metallicity are represented: Z=0.02 (magenta), Z=0.004 (cyan) and Z=0.008 (green). The range of ages for the SSPs is from 100 Myr up to 15 Gyr. On the lower figure, we superimposed to the data the old SSPs as computed by Bertelli et al. (1994) isochrones (hence without considering the new improvements as explained in Chap. 1), for the same values of the metallicity and with the same age range as the new SSPs.

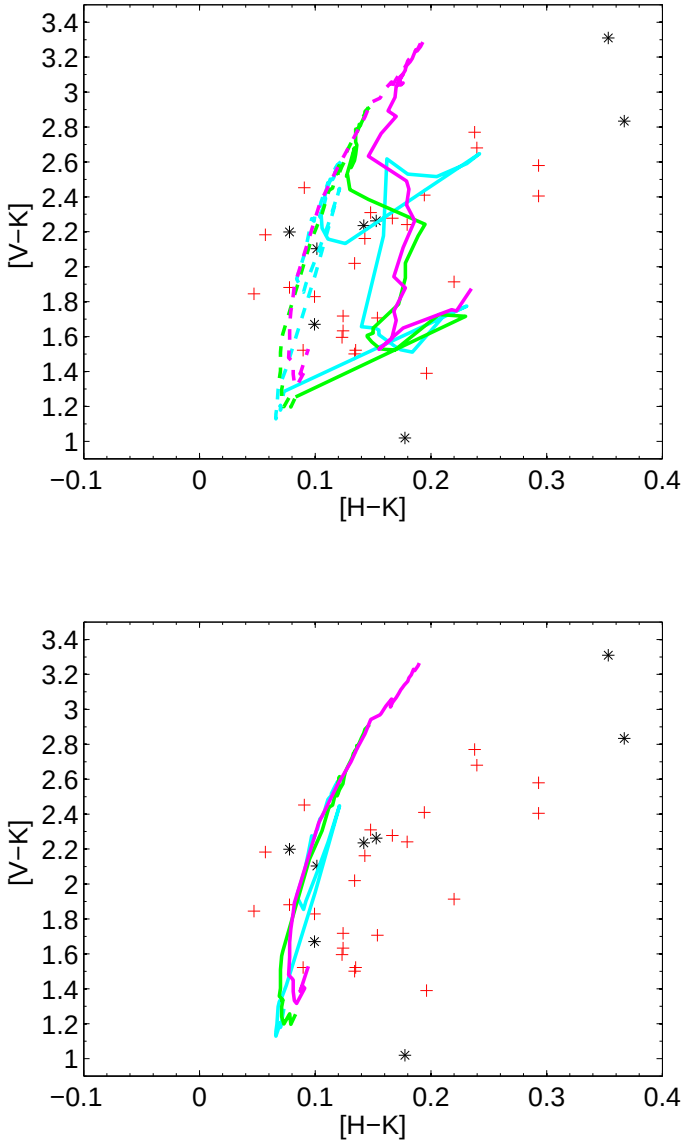

Figure 3.12: The same as in Fig. 3.11, but for [H − K] vs. [V − K] colors. The meaning of the symbol is the same as in the Fig. 3.11.

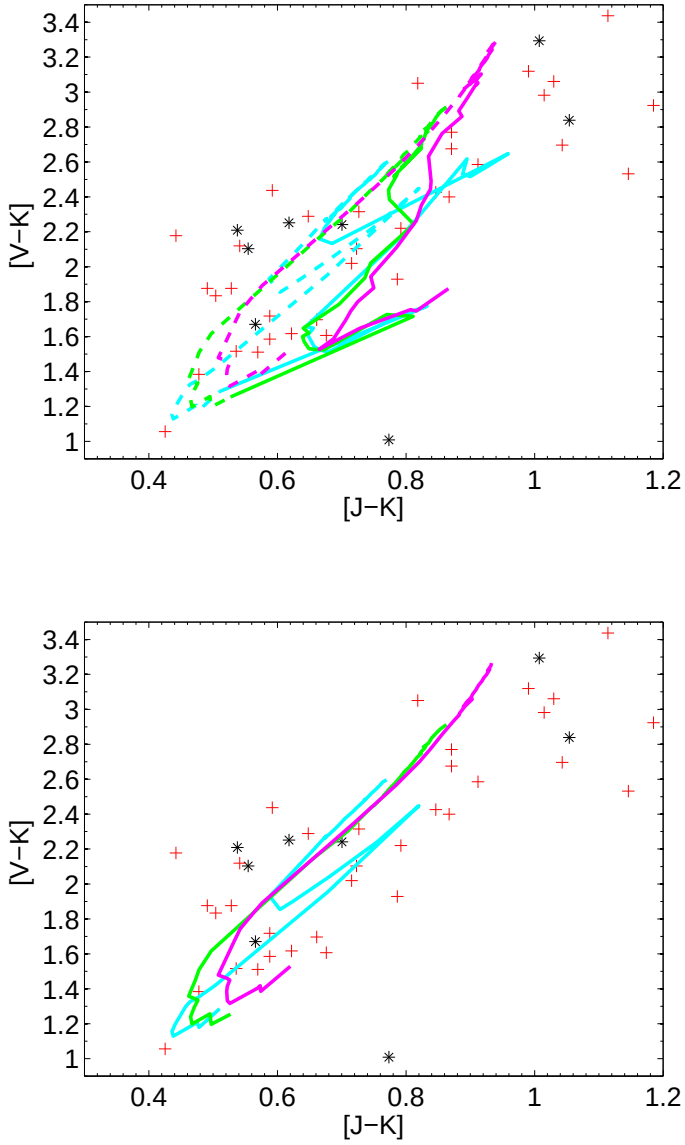

Figure 3.13: The same as in Fig. 3.11, but for [J − K] vs. [V − K] colors. The meaning of the symbol is the same as in the Fig. 3.11.

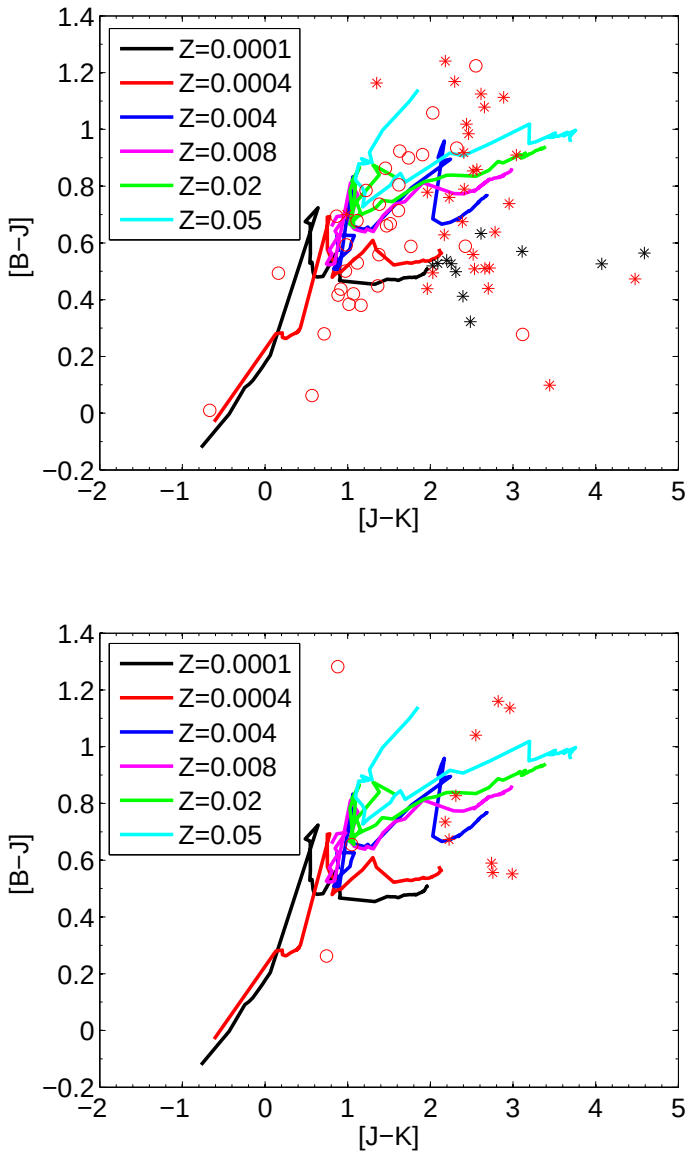

Figure 3.14: [B-J] vs. [J-K] color-color diagram for the star clusters of the LMC (**upper panel**) and SMC (**lower panel**). Three combinations of age and metallicity are taken into account: the open red circles represent young ($t < 0.95$ Gyr) and metal-rich ($[Fe/H] > -1.71$) clusters, the red stars represent old and metal-rich ones, finally, the black stars stand for old and metal-poor objects. Superimposed to the data we show the new SSPs for different values of the metallicity, as the legend indicates.

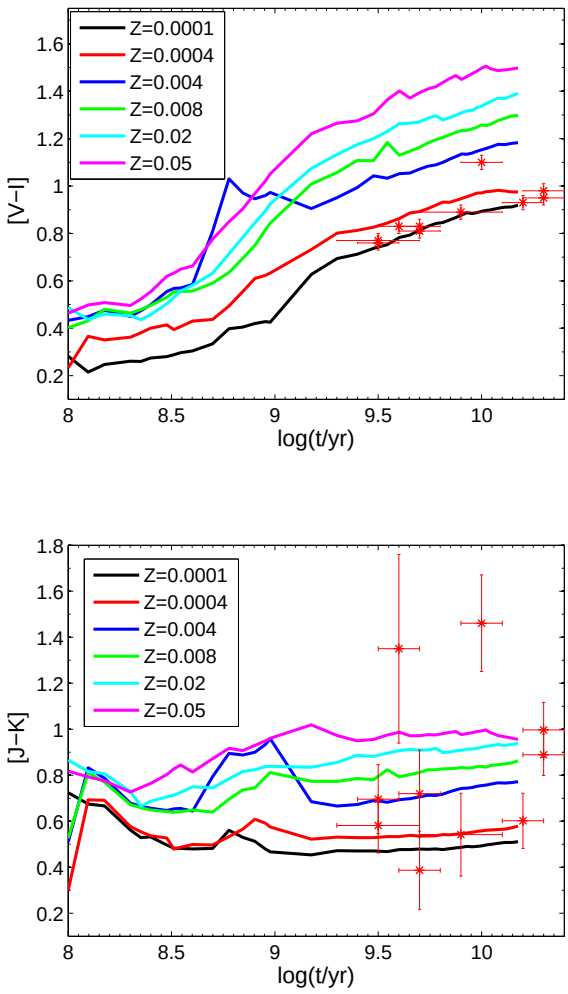

Figure 3.15: Theoretical evolution of the [V-I] color of our SSPs as a function of the age (**upper panel**) and of the [J-K] color (**lower panel**) again as a function of the age. SSPs for different values of the metallicity are shown, as the legend indicates. The data and their uncertainties are from Ma (2011).

Chapter 4

Galaxies

4.1 SED of galaxies of different morphological types

4.1.1 Physical components of galactic models

The most refined dusty galactic models available in literature contain three physical components, following a classical scheme introduced in Silva et al. (1998) and then adopted in many EPS models with dust Bressan et al. (2002), Piovan et al. (2006b), Galliano et al. (2008), Popescu et al. (2011):

- the diffuse ISM, made of gas and dust; the model for the ISM adopted in this thesis is described in detail in Piovan et al. (2006a) and includes a state-of-art description of a three component ISM made by graphite, silicates and PAHs, the most widely adopted scheme for a dusty ISM.

- the large complexes of MCs in which active star formation occurs. In our model we do not take HII regions and nebular emission into account. Very young stars are totally or partially embedded in these parental MCs and the SEDs emitted by these stars are severely affected by the dusty MCs environment around them and skewed toward the IR. The library of dusty MCs for which a ray-tracing radiative transfer code has been adopted is presented in (Piovan et al. 2006a) at varying the input parameters.

- The populations of stars that are no longer embedded in their parental MCs. These stars can be subdivided in the intermediate age AGB stars (with age from about 0.1 Gyr to 1-2 Gyr) that are intrinsically obscured by their own dust shells (Piovan et al. 2003; Marigo et al. 2008), and the old stars which shine as bare objects, which radiation crosses only the diffuse galactic ISM and there is no more local extinction. The effect of dust around AGB stars has

been included ex-novo in our code in this thesis and is described in detail in Chaps. 1 and 3, where new SEDs of SSPs have been presented and tested.

One of the three physical components, the stars already free from their dusty parental environments, is always present, with the exception of extremely young models where all stars are heavily obscured in the clouds where they are born. The galaxy models stand on a robust model of chemical evolution that assuming a suitable prescription for gas infall, IMF, star formation rate and stellar ejecta provides the total amounts of gas and stars present at any age together with their chemical history (Chiosi 1980; Tantalo et al. 1996; Tantalo et al. 1998; Portinari et al. 1998; Portinari & Chiosi 1999; Portinari & Chiosi 2000; Piovan et al. 2006b). In Chap. 1 we already introduced the new set of IMF now available in the galactic code. It is obvious that the IMF in usage must be the same in all the part of the model, starting from the isochrones and SEDs to the chemical model. In particular, the chemical models have been tailored (see later Chap. 6) in such a way to match the gross properties of galaxies of different morphological type. In order to describe the interaction between stars and ISM in building up the total SED of a galaxy, one has to know the spatial distribution of gas and stars. This is made adopting a simple geometrical model for each type of galaxy. The total gas and star mass provided by the chemical model are distributed over the whole volume by means of suitable density profiles, one for each component and depending on the galaxy type (spheroidal, disk and disk plus bulge). The galaxy is then split in suitable volume elements to each of which the appropriate amounts of stars, MCs and ISM are assigned. Each elemental volume bin is at the same time source of radiation from the stars inside and absorber and emitter of radiation from and to all other volume bins and the ISM in between. They are the elemental seeds to calculate the total SED.

4.1.2 The spatial distribution of stars and ISM

In the classical EPS that do not consider the presence of dust,the SED of a galaxy is simply obtained by convolving the SSPs spectra with the SFH (Arimoto & Yoshii 1987; Bressan et al. 1994; Tantalo et al. 1998). In the most refined models of intermediate type galaxies with disk and bulge (and maybe even a halo), the galaxy structure is mimicked by considering different SFHs for the various morphological types and/or components of a galaxy, e.g. bulge and disk (Buzzoni 2002; Buzzoni 2005). This simple convolution is no longer suitable to be used when the ISM and the absorption and IR/sub-mm emission by dust should be taken taken into account. In particular, the emission requires a spatial description, whereas the only treatment of the extinction could be simulated by applying a suitable extinction curve. In the general case with dust extinction/emission (Silva et al. 1998; Piovan et al. 2006b)

the spatial distribution of the ISM, dust and stars in the galaxy should be specified. To this aim we start from the observational evidence that the spatial distribution of stars and ISM depends on the galaxy morphological type of galaxy. The galaxy classification starts from the Hubble sequence, and can be roughly simplified to three main types: ellipticals, pure disks and disk plus bulge galaxies at varying the relative weight played by the disk and the bulge. One has to consider therefore a different geometrical description for various physical components. In our models we consider three prototype distributions, i.e. a pure disk, a spheroid and combination of the two to simulate: late-type galaxies (with no bulge), early-type galaxies (ellipticals), and intermediate-type (with a more or less prominent bulge) galaxies, respectively. All these models are characterized by a regular star formation history. No bursts of star formation are included into the chemical model (for some examples of models of starburst galaxies see Piovan et al. (2006b)).

Disk Galaxies

The mass density distribution of stars, ρ_*, diffuse ISM, ρ_M, and MCs, ρ_{MC}, inside a disk galaxy (or in the same way in the disk component of a disk+bluge model) can be represented by a double decreasing exponential laws so that the mass density decreases moving away from the equatorial plane and the galactic center or both. Taking a system of polar coordinates with origin at the galactic center [r, θ, ϕ], the height above the equatorial plane is $z = rcos\theta$ and the distance from the galactic center along the equatorial plane is $R = rsin\phi$; ϕ is the angle between the polar vector r and the z-axis perpendicular to the galactic plane passing through the center. The azimuthal symmetry rules out the angle ϕ and therefore the density laws for the three components are:

$$\rho_i = \rho_{0i} \exp\left(\frac{-r\sin\theta}{R_d^i}\right) \exp\left(\frac{-r|\cos\theta|}{z_d^i}\right) \tag{4.1.1}$$

where "i" can be "$*$", "M", "MCs", that is stars, diffuse ISM and star forming MCs. R_d^*, R_d^{MC}, R_d^M are the radial scale lengths of stars, MCs and ISM, respectively, whereas z_d^*, z_d^{MC}, z_d^M are the corresponding scale heights above the equatorial plane. To a first approximation, we assume the same distributions for stars and star forming MCs so that $R_d^* = R_d^{MC}$ and $z_d^* = z_d^{MC}$, thus reducing the number of scale parameters. Distributions with different scale parameters for the three components are, however, possible. The scale parameters are chosen taking into account on the observations, depending on the objects one wants to model. For example, for the disk of a typical massive galaxy like the MW one, one can assume that $z_d \simeq 0.3 - 0.4kpc$, and derive R_d from observations about the distribution of gas and stars, or from empirical relations, like the Im et al. (1995), $\log(R_d/kpc) \sim -0.2M_B - 3.45$, where

M_B is the absolute blue magnitude. Typical values for R_d are around $5kpc$.

The constants ρ_i vary with the time step. Let us indicate now with t_G the age of the galaxy to be modelled. For the gaseous components only the normalization constants $\rho_{0MC}(t_G)$ and $\rho_{0M}(t_G)$ are required as both loose memory of their past history and what we need is only the amount and chemical composition of gas at the present time. This is not the case for the stellar component for which $\rho_{0*}(t)$ is needed at each time $0 < t < t_G$. In other words to calculate the stellar emission we need to properly build the mix of stellar populations of any age $\tau' = t_G - t$, as result of the history of star formation. The normalization constants are derived by integrating the density laws over the volume and by imposing the integrals to equal the mass obtained from the chemical model. In general, the mass of each component $M_i(t)$ is given by:

$$M_i = \int_V \rho_{0i} \exp\left(-\frac{r\sin\theta}{R_d^i}\right) \exp\left(-\frac{r|\cos\theta|}{z_d^i}\right) dV. \tag{4.1.2}$$

The mass of stars born at the time t is given by $\Psi(t)$,, and therefore $\rho_{0*}(t)$ will be obtained by using $M_*(t) = \Psi(t)$. $M_{GAS}(t) = \Psi(t)$, total mass of gas, is the result of gas accretion, star formation and gas restitution by dying stars. The current total mass $M_{MC}(t_G)$ is a fraction of $M_{GAS}(t)$ and the remain $M_{GAS}(t)$ will form $M_M(t)$. The double integral (in r and θ) is numerically solved for $\rho_{0i}(t)$ to be used in Eq. 4.1.1. The galaxy radius R_{gal} is left as a free parameter of the model, thus allowing for systems of different sizes and distributions of the components.

There is a final technical point to examine, i.e. how to subdivide the whole volume of a disk galaxy into a number of sub-volumes so that the energy source inside each of these can be approximated to a point source located in their centers. This requires that the coordinates (r, θ, ϕ) are divided in suitable intervals. As far as the radial coordinate is concerned, test experiments have indicated that subdividing the galaxy radius in a number of intervals n_r = 40-60 would meet the condition, secure the overall energy balance among the sub-volumes, speed up the computational time and yield numerically accurate results. The number of radial intervals is derived by imposing that the mass density among two adjacent sub-volumes scales by a fixed ratio $\rho_j/\rho_{j+1} = \zeta$, with constant ζ. Upon simple manipulations the above relation becomes $r_{j+1} = r_j + \eta$. Therefore, the radial grid is equally spaced in constant steps given by R_{gal}/n_r (Silva 1999; Piovan et al. 2006b). The grid for the angular coordinate θ is chosen in such a way that spacing gets thinner approaching the equatorial plane, thus allowing for more sub-volumes in regions of higher mass density. We split the angle θ going from 0 to π in n_θ sub-values. We need an odd value for n_θ so that we have (n_θ - 1) /2 sub-angles per quadrant. Following Silva (1999), the angular distance α_1 between the two adjacent values of the angular grid

is chosen in such a way that R_{gal} subtends a fraction $f < 1$ of the disk scale height (z_d); in other words $\alpha_1 = \arcsin(f z_d / R_{gal})$. Logarithmic angular steps are then imposed $\Delta \log\theta = [2/(n_\theta - 3)] \log(\pi/2\alpha_1)$ where n_θ is determined by the condition that the second angular bin near the equatorial plan is $g\alpha_1$, with $g < 3$.. This implies $n_\theta = 2\log(\pi/2\alpha_1)/\log g + 3$. The grid for the angular coordinate ϕ is chosen to be suitably finely spaced near $\phi = 0$ and to get progressively broader and broader moving away clockwise and counterclockwise from $\phi = 0$. The angular steps are spaced on the logarithm scale. As a matter of fact, thanks to the azimuthal symmetry it is sufficient to calculate the radiation field impinging on the volume $V(r_k, \theta_k, \phi_k = 0)$ from all other volumes $V(r_k, \theta_k, \phi_k)$. A grid thinner at $\phi \simeq 0$ than elsewhere guarantees the approximation of point like energy sources at the center of the volume elements and the conservation of the total energy in turn.

Early-type Galaxies

The luminosity distribution of early-type galaxies can be described by the density profiles of Hubble, de Vaucouleurs and King (Kormendy (1977)). However, following Fioc & Rocca-Volmerange (1997), we use a density profile slightly different from the King law in order to secure a smooth behavior at the galaxy radius R_{gal}. We suppose that the mass density profiles for stars, MCs, and diffuse ISM are represented by the laws

$$\rho_i = \rho_{0i} \left[1 + \left(\frac{r}{r_c^i} \right)^2 \right]^{-\gamma_i} \tag{4.1.3}$$

where again "i" can be "$*$", "M", "MCs" (stars, diffuse ISM and MCs). r_c^*, r_c^{MC}, r_c^M are the core radii of the distributions of stars, MCs, and diffuse ISM, respectively. The exponents γ_* and γ_{MC} can be 1.5 (Piovan et al. 2006b), while γ_{ISM} is not well known. Froehlich (1982), Witt et al. (1992), Wise & Silva (1996) suggest to adopt, for the elliptical galaxies, $\gamma_M \simeq 0.5 - 0.75$ (coming from $\rho_M \propto \rho_*^n$ with $n \simeq 0.5 - 0.3$); it means that the ISM is less concentrated toward the center with respect to the stars. Here, we consider $\gamma_M = 0.75$. The density profile has to be truncated at the galactic radius R_{gal}, which is a free parameter of the model. This would prevent the mass $M(r) \to \infty$ for $r \to \infty$. In analogy to what already made for disk galaxies, the constants $\rho_{0*}(t)$, $\rho_{0MC}(t_G)$, $\rho_{0M}(t_G)$ can be found by integrating the density law over the volume and by equating this value of the mass to the correspondent one derived from the global chemical model:

$$\rho_{0i} = \frac{M_i}{4\pi (r_c^i)^3 \int_0^{R_{gal}/r_c^i} [x^2/(1+x^2)^\gamma] dx} \tag{4.1.4}$$

where $x = r/r_c^i$ while ρ_{0i} and M_i have the same meaning as in Sect. 4.1.2. The integral is numerically evaluated and solved for ρ_{0i}. Like in the case of disk galaxies, the last step is to fix the spacing of the coordinate grid (r, θ, ϕ). The problem will be simpler and the calculations will be faster than in the previous case because of the spherical symmetry. The spacing of the radial grid is made keeping in mind the energy conservation constrain. Also in this case we take a sufficiently large number of grid points $n_r \simeq 40 - 60$. The condition on the density ratio between adjacent volumes, $\rho_j/\rho_{j+1} = \xi$, will be constant, imply that:

$$r_i = r_c \sqrt{\left[1 + \left(\frac{R_{gal}}{r_c}\right)^2\right]^{i/n_r} - 1}, \tag{4.1.5}$$

where usually $r_c = r_*$.The coordinate ϕ is subdivided into an equally spaced grid, with n_ϕ elements in total, and $\phi_1 = 0$, $\phi_1 = 0$. Since the distribution is spherically symmetric, we do not need a thinner grid toward the equatorial plane. For the azimuthal coordinate θ we adopt the same grid we have presented for disk galaxies.

Intermediate-type galaxies

Intermediate-type galaxies are characterized by the relative proportions of their bulge and disk: they go from the early S0 and Sa where the bulge is big, to the late Sc and Sd where the bulge is small or negligible. In our models, we take all this into account by means of different SFHs for the disk and the bulge. Furthermore, both in the bulge and disk we consider the three components (ISM, MCs and stars) in a realistic way. In analogy to what already made for purely disk galaxies we adopt a system of polar coordinates with origin at the galactic center (r, θ, ϕ) Azimuthal symmetry rules out the coordinate ϕ. In the disk, the density profiles for the three components are the double decreasing exponential laws of Eq. 4.1.1. Accordingly, we introduce the scale lengths $R^*_{d,B}$, $R^M_{d,B}$, $R^{MC}_{d,B}$, $z^*_{d,B}$, $z^M_{d,B}$, $z^{MC}_{d,B}$ where the suffix B indicates that now the scale lengths are referred to the *disk-bulge composite model*. In the bulge the three components are distributed according to the King-like profiles defined in Eq. 4.1.3, where now the core radii $r^*_{c,B}$, $r^M_{c,B}$, $r^{MC}_{c,B}$ are referred to the bulge. The constants of normalization are derived in the same way described in Sects. 4.1.2 and 4.1.2. The two SFHs of disk and bulge are assumed to be independent and are simply obtained from the chemical models where the mass of disk and bulge are specified. The content in stars, MCs and ISM in a given point of the galaxy will be simply given by the sum of the contributions for the disk and bulge. Owing to the composite shape of the galaxy (a sphere plus a disk), we have to define *a new mixed grid sharing the properties of both components*, i.e. those described in Sects. 4.1.2 and 4.1.2. Let us indicate with R_B the bulge radius and with R_{gal} the galaxy radius. The radial

grid is defined in the following way. We build two grids of radial coordinates, $r_{B,i}$ and $r_{D,i}$, one for the disk and one for the bulge, in analogy to what we did in Sects. 4.1.2 and 4.1.2. As the grid of the bulge is not equally spaced, but thicker toward the center of the galaxy, we take the coordinates $r_{i,B}$ of the bulge grid if $r_i < R_B$, while if $r_i > R_B$, we take the coordinates of the disk $r_{D,i}$ until R_{gal}. For the angular coordinate θ we proceed in the same way. We build $\theta_{i,B}$ and $\theta_{D,i}$, as in Sects. 4.1.2 and 4.1.2. In this case the disk grid is thinner toward the equatorial plane of the galaxy whereas the bulge grid is equally spaced, so we take the coordinates $\theta_{D,i}$ of the disk as long as $\theta_{D,i+1} - \theta_{D,i} < \theta_{B,i+1} - \theta_{B,i}$ and $\theta_{B,i}$ elsewhere. The azimuthal grid is chosen in the same way both for the disk and the bulge, since it is not related to the distributions, both having azimuthal symmetry.

The elemental volume grid

Assigned the geometrical shape of the galaxies, the density distributions of the three main components, and the coordinate grid (r, θ, ϕ) (the number of grid points for the three coordinates is $n_r + 1, n_\theta + 1, n_\phi$), the galaxy is subdivided into (n_r, n_θ, n_ϕ) small volumes V, each of which identified by the coordinates of the center $r_{iV} = (r_i + r_{i+1})/2$, $\theta_{jV} = (\theta_j + \theta_{j+1})/2$, $\phi_{kV} = (\phi_k + \phi_{k+1})/2$. Thereinafter the volume $V(r_{iV}, \theta_{jV}, \phi_{kV})$ will be simply indicated as $V(i, j, k)$. The mass of stars, MCs, and diffuse ISM in each volume are easily derived from the corresponding density laws $\rho_i(i, j, k) \times V(i, j, k)$, where the pedix i stands for stars, MCs, and ISM in turn. By doing this, we neglect all local gradients in ISM and MCs (gradients inside each elemental volume). Since the elemental volumes have been chosen sufficiently small, the approximation is fairly reasonable.

4.2 The spectral energy distribution

Given the main physical components of a model galaxy, their spatial distribution, the coordinate system and the grid of elemental volumes, to proceed further one has to model the interaction among stars, dusty ISM and MCs to simulate the total SED emerging from the galaxy. Let us consider a generic volume $V' = V(i', j', k')$ of the galaxy: it will receive the radiation coming from all other elemental volumes $V = V(i, j, k)$. The radiation traveling from one volume to another interacts with the ISM comprised between any two generic volumes. Therefore one has to take into account the energy that is both absorbed and emitted by the ISM under the interaction with the radiation field. Two simplifying hypotheses are worth being made here:

1. the dust contained in a generic volume V does not contribute to the radiation

field impinging on the volume $V^{'}$. This approximation stands on the notion that, in first approximation, owing to the low optical depths of the diffuse ISM in the MIR/FIR, dust can not effectively absorb in significant amount the radiation it emits, except for high density regions such as complex of MCs, for which dust self-absorption has already been taken into account (Piovan et al. 2006a). Therefore, only stars and MCs will contribute to the incoming radiation.

2. The radiative transfer from a generic volume V to $V^{'}$ is simply calculated by means of the so-called effective optical depth defined by:

$$\tau_{eff} = \sqrt{\tau_{abs}(\tau_{abs} + \tau_{sca})} \tag{4.2.1}$$

The above relation stands on the following considerations: scattering increases the absorption, however as photons are not destroyed, the effective optical depth must be lower than the sum of the optical depths by scattering and absorption but higher than the one by sole absorption (Rybicki & Lightman 1979). Although this expression for τ_{eff} has been derived for photons randomly traveling across an absorbing diffusive medium, so that it would strictly apply only to an infinite, homogeneous, isotropically scattering medium, we make use of it here. This approximation has been shown to be acceptable, depending on the view angle of the galaxy (Silva et al. 1998).

The total radiation field incident on V' is:

$$J(\lambda, V') = \sum_{i=1}^{n_r} \sum_{j=1}^{n_\theta} \sum_{k=1}^{n_\phi} \frac{V[j^{MC}(\lambda, V) + j^*(\lambda, V)]}{r^2(V, V')} \times e^{[-\tau^{eff}(\lambda, V, V')]} \tag{4.2.2}$$

where the summations are carried over the whole ranges of i, j, k with $i \neq i'$ $j \neq j'$ $k \neq k'$; $r^2(V, V')$ is the value averaged over the volume of the square of the distance between the volumes V and V'; τ_{eff} as defined by Eq. 4.2.2, that becomes:

$$\tau_{eff}(\lambda, V, V') = \sqrt{\sigma_{abs}(\lambda)[\sigma_{abs}(\lambda) + \sigma_{sca}(\lambda)]} \times \int_{V(i,j,k)}^{V(i',j'k')} n_H(l) dl \tag{4.2.3}$$

This integral represents the number of H atoms contained in the cylinder between V and V'. The two terms $j^{MC}(\lambda, V)$ and $j^*(\lambda, V)$ are the emission by MCs and stars per unit volume of $V(i, j, k)$. They are evaluated at the center of the volume element. Let us now define two kinds of SSPs:

- *classical free SSPs*: they are already free of the parental cloud. For these SSPs we do not take into account the local effects of absorption/emission due to

dust in the local ISM. However, we introduced and calculated in these SEDs the effects of the the dust shells around AGB stars. With the exception of this additional point, they correspond to classical SSPs whose spectra have been calculated using the isochrones and the spectral libraries. Here we stress that they are not *dusty free*. Indeed, when dealing with *galaxy models with dust*, different kinds of dust effects should be considered. For what concerns the local dust, we consider: (a) the parental clouds in which very young stars are embedded and (b) the circumstellar dust shells around low and intermediate mass stars, during the AGB phase, when they form an outer dust-rich shell of material obscuring and reprocessing the radiation emitted by underneath stars. This latter effect of AGB stars has been properly included and analyzed, see Chap. 1.

- *SSPs embedded in dusty MCs*. In the early stages of their evolution we can consider stars as still heavily obscured by their parental dusty MCs. The libraries of these SSPs have been presented in Piovan et al. (2006a) as a function of four parameters: (1) optical depth τ, (2) metallicity Z, (3) PAHs ionization state (three possibilities, that is, PAHs ionized with full calculations of the ionization state, neutral PAHs and ionization state of the PAHs as in a mixture of Cold Neutral Matter, Warm Neutral Matter and Warm Ionized Matter in the same relative proportions as in the MW) and, finally, (4) the abundance of Carbon in very small grains. For these SSPs we adopt the library by Piovan et al. (2006a) that for the input SEDs in the radiative transfer Ray-Tracing code did not consider the contribution of dust around AGB stars. In principle, we should calculate again with the Ray-Tracing technique new dusty SEDs, now adopting as input the SEDs of this thesis with dust around AGB stars. In practice, as first approximation, we can safely adopt the old database and we do not expect that much difference because: (1) the region of the input flux interested by AGB stars is not the region of the spectrum most involved in the interaction with dust; (2) what matters is more the total luminous budget of the stellar population underneath, than some differences in the shape of the spectral input distribution (due in this case to the amount of energy transferred in the FIR from the NIR); (3) even if the self-absorption of dust is included, it plays a secondary effect unless very high optical depths are chosen for the cloud.

Let us denote with f_d the fraction of the SSP luminosity that is reprocessed by dust and with t_0 the time scale for this to occur, in such a way that:

$$f_d = \begin{cases} 1 & t \leq t_0 \\ 2 - t/t_0 & t_0 < t \leq 2t_0 \\ 0 & t \geq 2t_0 \end{cases} \tag{4.2.4}$$

where t_0 is a suitable parameter determining the evaporation time of the parental MCs. Up to t_0, young stars are completely embedded in the MC, then, when $t_0 < t \leq 2t_0$ they are partially embedded and this effect is simulated increasing the amount of light that leaves stars and reach the observer without interact with the dusty environment. Finally, when $t_0 \geq 2t_0$, the stellar light is free from the surrounding dust (Silva et al. 1998). Accordingly, the fraction of SSP luminosity that escapes without interacting with dust is $f_f = 1 - f_d$. The parameter t_0 will likely depend on the properties of the ISM and type of galaxy in turn. Plausibly, t_0 will be of the order of the lifetime of massive stars. The monochromatic luminosity of a free SSP of given age $\tau' = t_G - t$, born at t, and metallicity Z for unit of SSP mass is therefore:

$$L^f_\lambda(\tau', Z) = \frac{\int_{M_L}^{M_U} \Phi(M) f_\lambda(M, \tau', Z) dM}{\int_{M_L}^{M_U} \Phi(M) dM} \tag{4.2.5}$$

Knowing the the monochromatic luminosity of the naked SSPs $L^f_\lambda(\tau', Z)$, the monochromatic luminosity of the dust enshrouded SSPs $L^d_\lambda(\tau', Z)$ has been derived as described in Piovan et al. (2006a). The emission of stars and MCs per unit volume, $j^{MC}(\lambda, V)$ and $j^*(\lambda, V)$ respectively, are given by:

$$j^*(\lambda, V) = \int_{2t_0}^{t_G} \rho_*(t) L^f_\lambda(\tau', Z) dt + \int_{t_0}^{2t_0} \left(\frac{t}{t_0} - 1 \right) \rho_*(t) L^f_\lambda(\tau', Z) dt \tag{4.2.6}$$

e da:

$$j^{MC}(\lambda, V) = \int_0^{t_0} \rho_*(t) L^d_\lambda(\tau', Z) dt + \int_{t_0}^{2t_0} \left(2 - \frac{t}{t_0} \right) \rho_*(t) L^d_\lambda(\tau^{'}, Z) dt \tag{4.2.7}$$

It is worth noticing that the luminosity of the MCs depends only on the luminosity of the young embedded stars and not on the mass of the molecular gas in the MCs. The factors $(2 - t/t_0)$ and $(1 - (2 - t/t_0)) = (t/t_0 - 1)$ follows from the relations 4.2.5 and the definition of ff. Once calculated the incident radiation field $J(\lambda, V')$ we can obtain the emission per unit volume from the dusty ISM. At this point the azimuthal and spherical symmetries of the galaxy models become very important. The emission per unit volume from the dusty ISM calculated at the center of the volume elements is the same everywhere, independently of the coordinate ϕ. Therefore it is enough

to calculate the dust emission at $\phi = 0$ for all the possible values of r and θ on this "galaxy slice". It is obvious that the symmetry will be lost when considering the total emission from a certain volume element because owing to the adopted spacing of the galaxy the elemental volumes are not equal. However, as long as we refer to the emission per unit volume, the symmetry properties above allows us to avoid tedious and lengthy numerical calculations. The total radiation field for unit volume emitted by a single element is:

$$j^{TOT}(\lambda, V) = j^{MC}(\lambda, V) + j^{*}(\lambda, V) + j^{ISM}(\lambda, V), \tag{4.2.8}$$

where $j^{ISM}(\lambda, V)$ is the radiation outgoing from a unit volume of the dusty diffuse ISM and is given by the sum of the contributions from silicates, graphite and PAHs. The total outgoing emission from the volume V is therefore given by $j^{TOT}(\lambda, V) \times V$, obviously different from volume to volume. The radiation emitted by each elemental volume (n_r, n_θ, n_ϕ) has to travel across a certain volume of the galaxy itself before reaching the edge, escaping from the galaxy, and being detected by an external observer. While finding its way out, the radiation is absorbed and diffused by the ISM. The external observer will see the galaxy along a direction fixed by the angle Θ, where $\Theta = 0$ means that the galaxy is seen *face-on*, whereas $\Theta = \pi/2$ means that the galaxy is seen *edge-on*. To this aim, we need to determine the properties of the cylinders of matter from the center of each element V to the edge of the galaxy, along the direction Θ in order to calculate the amount of radiation emitted by the galaxy along this direction. Therefore, the monochromatic luminosity measured by an external observer is:

$$L(\lambda, \Theta) = 4\pi \sum_{i=1}^{n_r} \sum_{j=1}^{n_\theta} \sum_{k=1}^{n_\phi} V j^{TOT}(\lambda, V) e^{[-\tau_{eff}(\lambda, V, \Theta)]}, \tag{4.2.9}$$

where $\tau_{eff}(\lambda, V, \Theta)$ is the effective optical depth between $V(i, j, k)$ and the galactic edge along the direction. For more details, see Piovan et al. (2006b).

4.3 Evaporation of Molecular Clouds

Before using the dusty SSPs SED in order to calculate the SED of the modelled galaxy, we need to know how much time is needed at the MCs to evaporate and transfer their gaseous matter to the surrounding ISM. As already described, the "Ray Tracing" method has been used to solve the equation of radiative transfer and to calculate extended libraries of SSP SEDs, taking into account the absorption and scattering of the light due to the dust of the molecular clouds. However, this is not an evolutionary model but a static one (once fixed a set of input parameters), since

we can not follow the evolution of the cloud. In the real case, however, the clouds are destroyed on a timescale of the order of 10 Myr on average, typical lifetime of the molecular clouds (Dwek 1998; Zhukovska et al. 2008). This is the expected trend from an energetic point of view: the MC is swept away from the radiation emitted by the underneath stars, that is from the energy coming from the SNe explosions and stellar winds of massive stars. A simple way to simulate this process is to assume that as the time goes on, the SSPs fluxes reprocessed by dust decrease, while on the opposite the amount of flux not reprocessed and free of dust increases. It would be interesting to consider in detail these physical effects and to relate them to the amount of gas residing in the cloud, however it is beyond the purposes of this thesis. For this reason we assume t_0 as the time scale for the evaporation of the MC: it will depend for example from the properties of the ISM and from the details of the star formation process happening in the cloud. The combination between the density of the surrounding medium, the young stars and the amount of energy they produce determine the time scale. We expect it to be of the same order of the lifetime of massive stars (the age range going from 3 up to 50-100 Myr), as indeed is the typical MCs lifetime. Maybe, t_0 will be near to the lowest value, the lifetime of the most massive stars of the population, if we consider a low-density environment with a moderate rate of star formation, as for instance it may happen in a typical spiral galaxy. This kind of environment should be easy to be disrupted. On the contrary, we expect t_0 to be near to the upper value when we take into account a high-density environment, like for example in star-burst galaxies, where a very obscured star formation can occur in a high density ISM, more difficult to destroy.

The figures 4.3 and 4.2, show the gradual transition of SSPs of different metallicities: in the early stages of their evolution stars are embedded in the parental molecular clouds and then they gradually start shining freely from the dust. The ages represented in the plot are t=10, 20, 29.5 and 35 Myr and t_0= 15 Myr. For more information about the modelling of the SSPs, we refer to Piovan et al. (2006a). Briefly, the following trend occurs:

- when t=10 Myr stars are totally embedded in the MC (dotted lines in both figures). Of course this depends upon the selected timescale t_0. In this case it is fixed at 15 Myr and dusty SSPs are therefore used until that age of the SSP;

- when t=35 Myr SSPs are completely out of the MCs and the resulting SED has a classical shape without the contribution of dust in emission and extinction (dash-dotted lines);

- for the other two ages the SEDs are a mix of the previous cases with a contribution of both stars and dust. The dynamical process of a population of stars

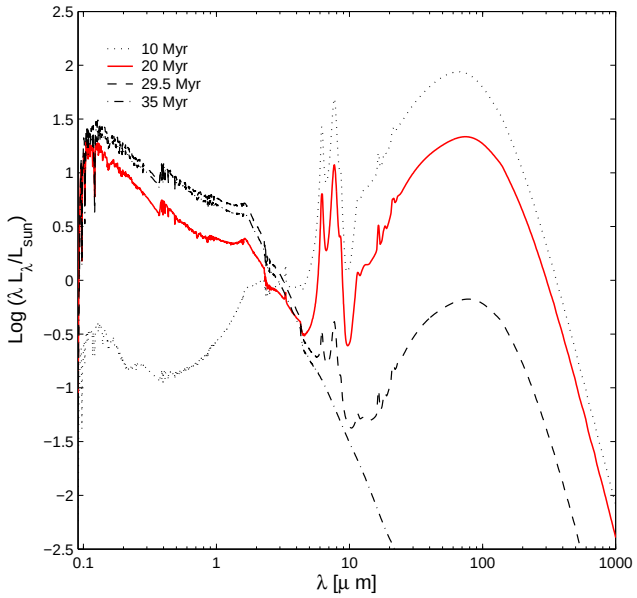

Figure 4.1: SSPs SEDs for Z=0.02 and t_0= 15 Myr from t=10 Myr (dotted line) up to 35 Myr (dash-dotted line). Two intermediate ages are also shown, that are 20 Myr (continuous line) and 35 Myr (dashed line).

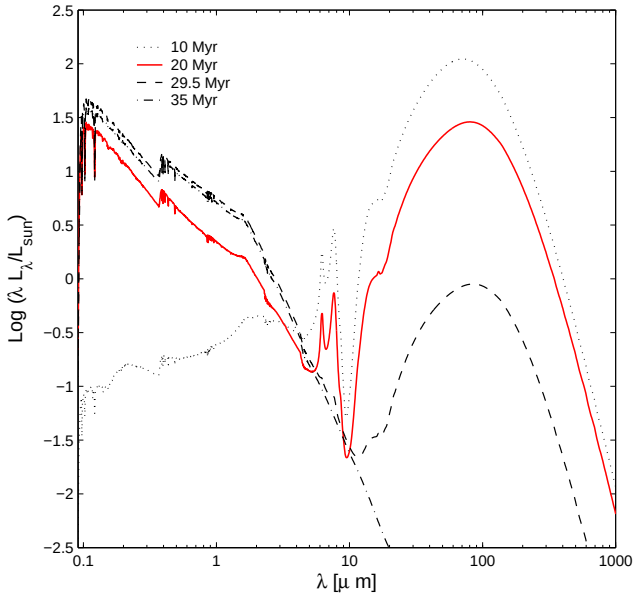

Figure 4.2: The same SSPs in Fig. 4.3 but for $Z = 0.004$.

from obscured to free is simulated with a suitable proportion of free and dusty SEDs as described above (continuous and dashed lines).

4.4 The Fortran Code

Our code, elaborated in Fortran 77 and now adjourned in Fortran 90, allows, as just explained, the calculation of spectrophotometric models of galaxies of different morphological type. The role of dust in the formation and evolution of galaxies is taken into account in a state-of-art way, with the inclusion of the effects of dust at different levels, going from shells of dust around AGB stars to dusty MCs and diffuse ISM. The original version of the code was developed, presented and used to reproduce some sample galaxies belonging to the local universe in Piovan et al. (2006a): more in detail, it allowed to model the SED of a disk, elliptical and starburst galaxy, in the local universe (that is, for $z \sim 0$). The idea to develop further the code, however, was to (1) build a code able to compute population synthesis models with dust not only at the current age *but* also able to analyze the *evolution* of SEDs and (2) to extend the morphological types to intermediate types made by disk and bulge. Now, with the improvement introduced in this thesis, we are able to calculate models of galaxies of many different morphological type, including the presence of dust in all its effects, starting from the redshift of formation $z = z_{form}$ up to $z = 0$, taking into account the modern cosmology. The code is made up of a series of routines and every subroutine deals with a specific part of the galactic models. It worth to spend some time in the description of the code, to underline the improvement added in this thesis work in order to reduce the computational time and widen the number of options available. Also, it is intention of the authors to make in the near future this code publicly available for scientific use as an open source project. All the routines are called by a main file (`Galaxy2012.f90`), that, at the beginning of the simulation, reads the input parameters of the model (for example, the final age of the galaxy, corresponding at $z = 0$, which change at varying the adopted cosmological frameworks, the radius of the galaxy, the length scales of both stars and gas, the amount of diffuse gas and the timescale of evaporation of the molecular clouds).

In this section we shortly present the main routines, remembering that the following steps are executed:

1. reading of the input chemical information (SFH and metallicity);

2. reading of the input SSPs fluxes (free SEDs and dusty SEDs);

3. calculations of the geometric grids (they change depending on the morphological type of the modelled galaxy, as explained in Sects. 4.1.2, 4.1.2 and 4.1.2);

4. calculations of the normalized cylinder of matters between the elemental volumes.

5. calculation of the composite fluxes for each elemental volume and the fluxes incident on the single volume elements;

6. calculation of the emission of dust, subdivided into PAHs, graphite and silicate;

7. calculation of the effects of the extinction and of the final radiation flux outgoing toward the observer, for different inclinations of the object.

4.4.1 Main subroutines

Let us analyze briefly the main routines, following the order of call:

- **READSTARFO**: this subroutine reads the information coming from the chemical code, some of which are used as input of spectrophotometric simulations. Here we remember:
  - M_{12}: the baryonic asymptotic galactic mass, expressed in $10^{12} M_{\odot}$;
  - DM: the ratio between the masses of luminous M_L and dark matter M_D;
  - R_L/R_D: the ratio between scale radii of luminous and dark matter;
  - τ: the infall time scale;
  - ζ: fraction of total stellar mass greater that 1 $M_{\odot}$: it determines the lower mass of the IMF (the upper value is 100 $M_{\odot}$) if this option is selected. Otherwise, it is possible to fix the lower limit to a value of 0.1 or 0.01 $M_{\odot}$ depending on the IMF (Piovan et al. 2011b), since now several options for the IMF are available. See also Sect. 1.1.4 for a detailed discussion of this topic.
  - ν: the SFR efficiency (related to the time scale of stellar formation $t_{SF} \propto 1/\nu$);
  - t_{Gal}: the final age of the model. This age is fixed once the cosmological frameworks is established. Since the normalization in the chemical code depends on the final asymptotic mass and the star formation is adjusted with an infall law normalized from 0 Gyr to t_{Gal}, it is necessary to correctly specify the final age, when the galactic model will reach M_{12} as asymptotic mass of primordial material accreted by infall;
  - finally the following quantities, for every age of the chemical model: time (expressed in Gyr), amount of gas (normalized at the asymptotic final mass), metallicity of the gas, star formation rate, potential energy of the gas, mass of living stars, total asymptotic mass, integral of the SFR, rate of SNe (both types I and II, expressed in $Gyr^{-1} M_{\odot}^{-1}$) and, finally, mass of remnants.

The subroutine calculates the *amount of molecular and diffuse gas in the galaxy* for every galactic age calculated by the chemical simulation. We deal with an interstellar medium characterized by diffuse ISM and dense molecular clouds, but up to now we do not have a physical description able to calculate step by step the amount of gas *singularly* in both phases. The subdivision of the amount of gas is a free parameter: clearly, this is a rude approximation but this is the best actually one can do, till the possibility to follow the evolution of the gas in dense and diffuse phases will be introduced. To keep realistic the proportion of the two components we proceed in the following way: the input parameter fixes the fraction of molecular gas at the peak of star formation. According to this value, the amount of molecular gas in different ages with a different star formation rate is scaled proportionally: indeed we assume plausibly that the amount of molecular gas is proportional to the activity of star formation at that time. Next, the total mass of the SSPs is calculated (as the integral of the IMF between the upper and the lower mass values) and this value is used as normalization factor for the SSPs fluxes.

- **READFLUSSI**: It reads both kind of SSPs fluxes from the database, for dusty e dust free SSPs, according to the selected IMF, it normalizes the fluxes and checks for the conservation of the energy.

- **GRID**: The geometrical characteristics of the modelled galaxy are taken into account: a three-dimensional (r, θ, ϕ) grid is built, according to the morphological type. In the case of disc model, a double-exponential distribution is used (see Sect. 4.1.2): the grid for the angular coordinate θ is chosen in such a way that spacing gets thinner approaching the equatorial plane, thus allowing for more sub-volumes in regions of higher mass density. In the case of early-type galaxies, a equally spaced θ grid is used. For the intermediate type galaxies, it has been necessary to build a new mixed geometric grid sharing the properties of both components (a central sphere surrounded by a disk). So two grids of angular coordinates have been built: one for the disc ($\theta_{B,i}$) and one for the bulge, ($\theta_{D,i}$). After this, we consider $\theta_{D,i}$ when $|\theta_{D,i+1} - \theta_{D,i}| < |\theta_{B,i+1} - \theta_{B,i}|$ and $\theta_{B,i}$ elsewhere. For more a detailed explanation of the geometric grids, please refer to Sect. 4.1.2.
  The **CIL** subroutine is included in **GRID**, in order to build the cylinders of matter from each volume in the bulge or disk to the edge of galaxies along the direction of view, in order to calculate the amount of extinguished radiation emitted by the galaxy toward the observer.

- **BIRTH**: With this routine the SFR, the mass of stars, the metallicity Z and

the mass of molecular and diffuse gas are calculated, for the simulated age, interpolating the information from the output file of the chemical code, read by **READSTARFO**.

- **NORMALIZZO**: All these distributions of matter are normalized, that is calculated for ρ/ρ_0. For a given instant of time, this subroutine calculates the normalization constants $\rho_{0,i}$ of the matter, for gas and stars respectively. The distribution of the matter depends on the galaxy models, as shown in Sect. 4.1.2: for an elliptical galaxy (or the bulge, for an intermediate type galaxy) the subroutine **ELLINTEGRAL** is used, while for the disk **DISKINTEGRAL** is called.

- **SILICATI**: This subroutine calculates the properties of absorption and scattering of silicate grains. The files of optical properties of silicates are read, and the cross sections are calculated. This subroutine and the next one need a *flag* in order to choose between different extinction curves, according to the abundance of carbon or silicates. The subroutine **GRAIN_DISTR** is used – kindly made available by J. Weingartner in his webpage (`http://physics.gmu.edu/joe/`) – (Weingartner & Draine 2001a). With this routine the abundance of grains of a given size a is established and used to calculate the cross sections.

- **GRAFITE**: This subroutine calculates the absorption and scattering properties of graphite grains, similarly to the routine **SILICATE**. An important parameter is the upper limit of the PAH distribution, which is coincident with the lower limit of the graphite distribution: the two populations do not overlap as in Li & Draine (2001, Draine & Li (2001) and the PAHs are considered as the small-size tail of the carbonaceous grains. The transition size has been fixed at 56 Å thus allowing both PAHs and small, thermally fluctuating, graphite grains to concur to shape the SED in the MIR. This limit is chosen in agreement with the dimension at which Li & Draine (2001) set the transition mixing the optical properties of PAHs and graphite. The exact value of the transition size has in practice no influence on the extinction curve thanks to the similar UV-optical properties of PAHs and small graphite grains. The same considerations do not clearly apply to the IR emission, where a large population of PAHs will produce a stronger emission in the MIR bands. We want to stress that our approach is different from Weingartner & Draine (2001a) and Li & Draine (2001), where PAHs and graphite grains are included in a single family of the so called "carbonaceous grains", where the smallest grains have the PAHs optical properties, the biggest grains have the graphite properties, and for the intermediate dimensions a smooth transition from PAHs to graphite properties

is adopted. Our treatment is necessary since our emission model deal separately with PAHs and graphite, in order to speed up calculations Piovan et al. (2006a).

- **PAHs**: This routine, similarly to the previous two, calculates the cross sections of PAHs. They can be either neutral and ionized: the relative percentage will depend on the chemical composition of the ISM and on the incident radiation field. For the purposes of this thesis, we follow the subdivision adopted by Li & Draine (2001), that can reproduce the properties of the Milky Way. This is achieved by a suitable combination of the ionization state of PAHs in the *Cold Neutral Matter* (CNM), *Warm Ionized Matter* (WIM) *Neutral and Warm Matter* (WNM). For consistency with the diffuse ISM, also in the case of dusty SSPs, the model of mean ionization state of PAHs assumed is the one of the Milky Way.
  It should be noticed, finally, that the ionization state of the PAHs has no influence on the extinction in the UV /optical range and on the emission in the FIR since (assuming the same distribution of the grains) the optical properties do not depend on the state of ionization, at these wavelengths. The profiles of the emission lines in the MIR, however, are affected by the adopted approximation (Piovan et al. 2006a).

- **KERNEL**: This is the fundamental routine of the spectro-photometric code. Here we calculate:

  - the radiation emitted, per unit volume, in the volumes of the sample slice at $\phi = 0$ (indeed we are getting advantage of the azimuthal symmetry), for the stellar populations *free* from their parental MCs;
  - the radiation emitted, per unit volume, in the volumes of the sample slice at $\phi = 0$, for the stellar populations *still embedded* in their parental MCs;
  - the total radiation emitted, for unit volume, in the volumes of the sample slice at $\phi = 0$, for stellar population free from any kind of dust (in order to calculate the original EPS without dust);
  - the radiation incident on the sample slice at $\phi = 0$, that comes from all the other volumes of the galaxy;

  Following the chemical evolution of the galaxy, the grid of SSPs is built. For this purpose, we use the evolutionary history indicated by the chemical code that will be characterized by different values of age and metallicity, corresponding to different sets of SSPs.

- **EQUILIBRIOSIL**: Once the incident flux per unit volume is calculated, the silicate emission is obtained, distinguishing between small and large grains. A separation size between these two categories of grains has been considered: smaller grains are subjected to temperature fluctuations, while larger grains assumes an average temperature in equilibrium, due to their large heat capacity. They re-emit the energy absorbed from the radiation field in the MIR/FIR. Since the silicates, as well as graphite, have a "smoothed" and extremely regular emission profile, this has been calculated initially for a small set of wavelengths – in the UV / optical wavelength, since no dust emission is detected here –, while fully treated in the MIR/FIR/sub-mm, where the emission of dust is mostly concentrated.

- **EQUILIBRIOGRA**: This routine calculates the emission due to graphite grains, in the same way the **EQUILIBRIOSIL** does for silicate grains.

- **EMISSIONEPAH**: As already stated, we need to distinguish between neutral and ionized PAHs. Their state ultimately depends on the physical and chemical properties of the interstellar medium (temperature, hydrogen atoms density, electron density and carbon atoms density). Then, the emission of PAHs is calculated.

- **EXTINCTION**: This routine calculates the outgoing galaxy luminosity, along four inclinations. These are:

  - the galaxy is seen *face-on*;
  - the galaxy is observed at an angle of 30° respect to the z axis, perpendicular to the equatorial plane of the galaxy, or 60° if measured respect to the galactic equatorial plane;
  - the galaxy is observed at an angle of 60° respect to the z axis, perpendicular to the equatorial plane of the galaxy, or 30° is measured respect to the galactic equatorial plane;
  - the galaxy is seen *edge-on*.

  The following monochromatic luminosity are calculated; they will be the output:

  - the total luminosity of the galaxy, taking into account all the extinction/emission effects of the dust;
  - the luminosity of the stars only, taking into account *only* the extinction effect due to the dust obscuring OB stars in the MCs;

  - the luminosity of the stars, without considering the effects of extinction/emission due to the interstellar dust: this is the classical evolutionary populations synthesis without dust, often very useful for the sake of comparison;
  - the luminosity of young and obscured stars in the regions of star formation;
  - the luminosity of the diffuse interstellar medium, taking into account the contribution of graphite grains and silicates only;
  - the luminosity of the PAHs, both neutral and ionized ones.
  - For the intermediate model (disk+bulge), the total luminosity of the *bulge*, taking into account all the extinction/emission effects of the dust;
  - For the intermediate model (disk+bulge), the luminosity of the stars of the *bulge*, taking into account *only* the extinction effect due to the dust obscuring OB stars in the MCs;
  - For the intermediate model (disk+bulge), the luminosity of the stars of the *bulge*, without considering the effects of extinction/emission due to the interstellar dust (classical EPS);
  - For the intermediate model (disk+bulge), the total luminosity of the *disk*, taking into account all the extinction/emission effects of the dust;
  - For the intermediate model (disk+bulge), the luminosity of the stars of the *disk*, taking into account *only* the extinction effect due to the dust obscuring OB stars in the MCs;
  - For the intermediate model (disk+bulge), the luminosity of the stars of the *disk*, without considering the effects of extinction/emission due to the interstellar dust (classical EPS);

- **SCRITTURA**: This last subroutine writes the outputs on formatted files.

4.4.2 Other subroutines

Beyond these subroutines, which are the building blocks of the galactic code, and which are called directly from the main file, we need to use other subroutine. In this section we briefly examine some of these:

- **BRACKET**: this is a one-dimensional numerical interpolation subroutine, used in combination with the **STEFFEN** one.

- **STEFFEN**: This subroutine works jointly with the **BRACKET** one, and performs one-dimensional non-linear interpolation of a function according to Steffen (1990).

- **GRAIN_DISTR**: It calculates the distribution of dust grains using the Weingartner & Draine (2001a) law, once that the extinction curve and the size of the grains for which we want to get the abundance are specified. In addition, the distribution allows for possible changes in metallicity, using the *dust-to-gas* ratio: since we still do not include in our simulations the model described in the last chapter of this work, we simply scale the abundance of dust with the metallicity (Piovan et al. 2006a). In particular, for solar and sub-solar metallicities we can rely on the hints from the LMC and SMC about graphite/silicates partition on a give metallicity. For metallicities higher than the solar one, the amount of dust follows the law $\delta = \delta_{\odot}\,(Z/Z_{\odot})$, keeping the solar partition between carbonaceous grains and silicates (see Chap. 6).

- Then, there is a group of routines used to calculate the ionization state of PAHs. For all the details about the physics included in these routines see Draine & Sutin (1987), Bakes & Tielens (1994) and Weingartner & Draine (2001c):

  - **JPZETA**: it calculates the rate of photo-emission;
  - **JIZETA**: it calculates the growth rate of positive ions;
  - **JEZETA**: it calculates the growth rate of electrons;
  - **HNUPDTcalc**: calculation of $E = h\nu_{pdt}$, photo-detachment threshold energy
  - **Ygrande**: it calculates the yield due to photoelectric effect $Y(h\nu, Z, a)$, which depends on the energy of the incident photons, the atomic number Z and the size of the grains a.
  - **HNUPETcalc**: calculation of $E = h\nu_{pdt}$, photo-emission threshold energy.

- **ZERBIS**: This is a numerical routines from the *Numerical Recipes* (Press et al. 1992); it applies the bisection method to compute the zeros of a function.

- **FLUXMETAL**: This subroutine interpolate the SSPs fluxes, considering both age and metallicity.

- **INTEGRANDO**: This subroutine multiplies the local star formation rate by the local distribution of matter (considering the density at the center of the volume as a constant throughout the volume, and multiplying by the volume, instead of integrated on the volume itself) and the normalization constant calculated with **NORMALIZZO**. In this way, we get the amount of newly born stars in a given volume . Depending on the age of the stellar population and in agreement with the evaporation/escaping time t_0, dusty or dust-free SSPs are then used.

4.5 Improvements of the code

The original version of the code have been changed and improved in order to account for our new purposes. A simple set of population synthesis models with dust, based on Piovan et al. (2006a), Piovan et al. (2006b), has been developed in the past (Cassarà 2008). As already stated, we simulated the spectral energy distribution (SED) for galaxies of various morphological types, following the evolution of the SED from the redshift of galaxies formation $z = z_{form}$ to the current $z = z_0$, taking into account modern cosmology. The main target in Cassarà (2008) concerned spectrophotometric models for only two basic types of galaxies, elliptical and disk ones, with rough approximations for the main input parameters of the code. However, a more detailed and systematic study of intermediate type galaxies was lacking, whereas these latter ones are made up of a bulge and a disc with *different masses and SFHs*. The central bulge contributes in a fundamental way to the whole galaxy emission and can be either small or big along the Hubble sequence.
At the purpose to extend the model to disk+bulge galaxies, the galactic code have been re-wrote and re-organized in order to obtain theoretical SEDs for intermediate type galaxies, very time consuming from the computational point of view. The evolution and star formation history of the stellar populations of the bulge has been simulated similarly to an elliptical galaxy, characterized by a short and significant period of star formation activity, while for the disk we gathered the information coming from the simulations of late-type galaxies (Piovan et al. 2006b). It was necessary to build a new mixed geometric grid sharing the properties of both components (a central sphere surrounded by a disk) and to build the cylinders of matter from each volume in the bulge to the edge of galaxies along the direction of view, in order to calculate the amount of radiation emitted by the galaxy toward the observer.
We remind here two important assumptions that allow to compute grids of coordinates and fluxes of the SSPs *a priori*, before to run the full set of simulations from $z=z_{form}$ to $z=z_0$:

- the IMF does not vary over time;
- the geometry of the galaxy remains the same.

Obviously, the scale radius of the baryonic matter can change over time; however, this approximation is acceptable since the chemical evolution of the galaxy is calculated *without* assuming a geometric structure of the galaxy. Our input chemical models do not supply information about the spatial distribution of stars and gas: the galaxy is simulated as a mass point (Chiosi 1980). Some more advanced models have been and are being developed (Tantalo et al. 1998; Portinari et al. 1998; Piovan et al. 2011a; Piovan et al. 2011b; Piovan et al. 2011c), in particular to include a chemical

description of the abundance of dust. They will be described in detail in the last part of this thesis, but they are still not interfaced with the galactic code, in order to improve the description of the dust component. Also, it is likely that only coupling the spectrophotometric code with *n-body* dynamical simulations the spatial evolution of the distributions of scale radii can be followed. For our purposes, the invariance of the geometric grid is adopted: we will just vary the normalization constants of the distributions of stars and gas according to their time evolution. As for the IMF, we can choose now between 9 different prescriptions, following what have been done for the isochrones and SSPs (see Sect. 1.1.4 and Chap. 3 for a detailed analysis about this point). Since at first, we want to check our models and compare them with observations in order to validate them, we will not focus at the level of galaxies simulations with the variation of the IMF, but we will stick on the Salpeter one eventually varying the ζ parameter. The calculations of galactic models with different IMFs will be treated in future works. Since we are dealing with evolutionary models, the age of the galaxy is updated at each cycle depending on:

- the difference between the current value of the SFR and the value of the SFR at the age immediately before, in order to calculate more models when the star formation history changes steeply, and vice-versa;
- the time interval to which the current age of the galaxy belongs: the time steps are *a priori* set to be more crowded within the first 0.5 Gyr, since the star formation is peaked here and to a small age range, a large redshift range corresponds.

In *evolutionary* sequences of galaxy models with dust, the computational speed and the accuracy are no longer a secondary issue. So, the numerical part of the code have been improved: (1) introducing, where possible, the *Numerical Recipes* routines (Press et al. 1992); (2) using power-laws fits in order to calculate the emission temperature of the big dust grains in thermal equilibrium with the incident radiation filed. This temperature of equilibrium does not depend on the spectral shape of the incident radiation field, but just upon the total budget of energy impinging on the grains. This property allowed to introduce power-laws as a function of the grain dimension and the impinging total energy; (3) the storage matrices S (Piovan et al. 2006b) to calculate the emission of the PAHs have been recalculated and better stored, in order to fasten the calculation of the emission of the PAHs; (4) most of the matrices are now dynamical and can adapt to the grids of age, elemental volumes and wavelengths.

To conclude this section, we present a flow diagram (4.3) which shows the different routines of the galactic code, in order of appearance, to summarize all the discussion.

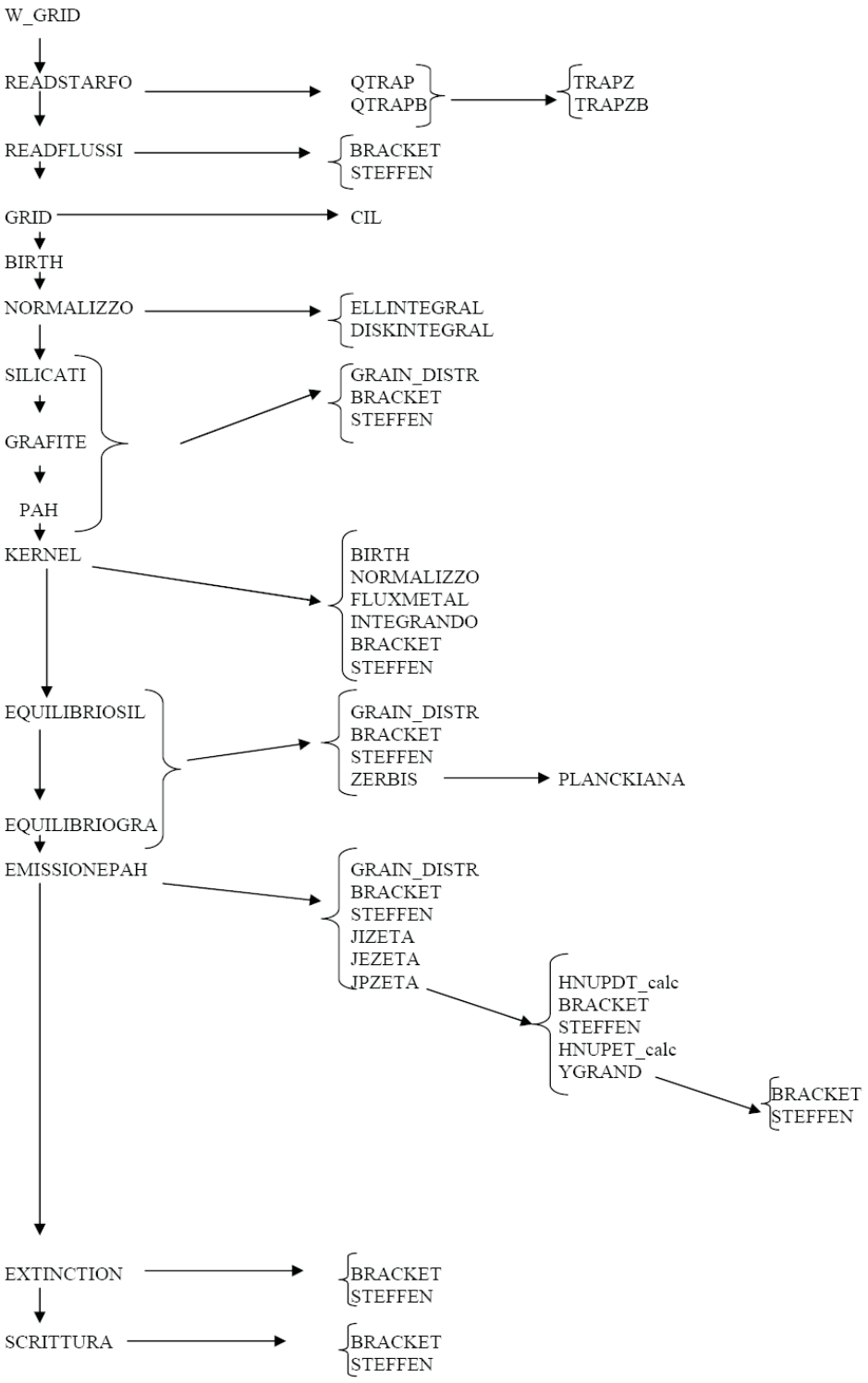

Figure 4.3: Flow diagram: it schematizes the sequence call of the routines used in the evolutionary population synthesis code with their dependence.

Chapter 5

Models of galaxies of different morphological types

5.1 The composition of dust

In this chapter we present our models of galaxies of different morphological types, taking into account the effects of dust emission and extinction, both for the local and high redshift universe. To introduce this topic it is worth a quick summary about the dust properties and the mixture adopted into the models: for a much more extended analysis of this point and all the details about the calculations of the emission/extinction effects, see Piovan et al. (2006a).

The physical properties of the interstellar grains are derived mostly analyzing the dust extinction curves in the UV/optical region of the spectra and the emission spectra in the infrared bands (from the near up to the far infrared), in different physical environments. From the amount of information that can be obtained looking at the effects of extinction and emission related to dust grains, it is possible to derive in particular the features useful to constrain and define a quasi-standard model of interstellar dust, made up of three components.
From the characteristic broad bump of the extinction curve in the UV at 2175 $\AA$ and from the absorption features at 9.7μm and 18μm (Draine 2003), one can infer that a two components model made of graphite and silicates is required.

The study of the emission adds further constraints. A population of VSGs has been invoked to reproduce the emission observed by IRAS in the pass-bands at 12μm and 25μm. Indeed, the VSGs temperatures can fluctuate well above 20 K if their energy content is small compared to the energy of the absorbed photons (Leger & Puget 1984; Desert et al. 1986; Dwek 1986; Guhathakurta & Draine 1989; Siebenmorgen & Kruegel 1992; Draine & Li 2001; Li & Draine 2001).

Excluding that VSGs are made of silicates simply because the 10μm emission

feature of silicates is not detected in diffuse clouds (Mattila et al. 1996; Onaka et al. 1996), most likely they are made of carbonaceous material with broad ranges of shapes, dimensions, and chemical structures (see also Desert et al. (1986) and Li & Mayo Greenberg (2002), for a discussion of this topic).

Emission lines at 3.3, 6.2, 7.7, 8.6, and 11.3 μm, originally named unidentified infrared bands (UIBs), have been first observed in luminous reflection nebulae, planetary HII regions and nebulae (Sellgren et al. 1983; Mathis 1990) and subsequently also in the diffuse ISM with IRTS (Onaka et al. 1996; Tanaka et al. 1996) and ISO (Mattila et al. 1996). There is nowadays general consensus that these lines owe their origin to the presence of PAH molecules, vibrationally excited by the absorption of a UV-optical photon (Leger & Puget 1984; Li & Draine 2001). Currently these spectral features are commonly referred to as the aromatic IR bands (AIBs).

Based on these considerations, any realistic model of a dusty ISM, to be able to explain the UV-optical extinction and the IR emission of galaxies, has to include at least three components, i.e. graphite, silicates, and PAHs. Furthermore, while it may treat the big grains as in thermal equilibrium with the radiation field, it has to allow the VSGs to have temperatures above the mean equilibrium value. In order to obtain the properties of a mixture of grains, we have to specify their cross sections, their dimensions, and the kind of interaction with the local radiation field. For more informations see Piovan et al. (2006a). We only summarize here the models that inspired our three dust components ISM, with graphite, silicates and PAHs. The cross sections for graphite are from Draine & Lee (1984), for silicates are from Laor & Draine (1993) and PAHs are from Li & Draine (2001), taking the latest releases from the B. T. Draine webpage. The extinction curves and the distribution of dust grains as a function of their dimension are taken from Weingartner & Draine (2001a). The emission of graphite and silicates, both for thermally fluctuating VSGs and big grains in thermal equilibrium, is based upon the classical paper Guhathakurta & Draine (1989), while for PAHs we adapted Puget et al. (1985). Finally, the ionization state of PAHs is calculated with the physical models by Draine & Sutin (1987, Bakes & Tielens (1994, Weingartner & Draine (2001c).

5.2 The adopted chemical model: an introduction

A chemical code supporting EPS is needed to describe the evolution of the SFR and the enrichment of the ISM in metallicity (and eventually in dust). The chemical evolution of the galaxy is described using a classical chemical *infall* model (Lynden-Bell 1975; Tinsley 1980b), originally developed in Padova by Chiosi (1980) in its latest version one-zone with infall, for elliptical galaxies and disks Tantalo et al. (1998, Piovan et al. (2006b). It has long been known that the closed-box model applied

to study the chemical history of the solar vicinity fails to explain the metallicity distribution observed among the old field stars, giving rise to the so-called G-Dwarf Problem (Tinsley 1980b; Tinsley 1980a). The solution of the G-Dwarf dilemma are models with infall, in which the total mass of the disk is let increase with time at a convenient rate starting from a much lower value. With the current law of star formation (proportional to the gas mass) the competition between gas accretion by infall and gas depletion by star formation gives rise to a non monotonic time dependence of the star formation rate which instead of steadily decreasing from the initial stage as in the closed-box model starts small, increases to a peak value, and then declines over a time scale which is a sizable fraction of the infall time scale. The advantage of the infall model with respect to the closed-box one, is that the metallicity increases faster, and few stars are formed at very low metallicity. Since the excess of very low-metal stars is avoided, the G-Dwarf Problem is naturally solved. In the following sections we will illustrate the main features and equations of the infall models that support our spectro-photometric simulations.

5.2.1 Main features: elliptical galaxies or bulge of the intermediate types

Applied to an elliptical galaxy, the infall model of chemical evolution can *mimic* the collapse of the parental proto-galaxy from a very extended size to the one we see today. As the gas falls into the gravitational potential well at a suitable rate and the galaxy shrinks, the gas density increases so that star formation begins. As more gas flows in, the more efficient star formation gets. Eventually, the whole gas content is exhausted and turned into stars, thus quenching further star formation. Like in the disk, the star formation rate starts small, rises to a maximum, and then declines. Because of the more efficient chemical enrichment of the infall model, the initial metallicity for the bulk of star forming activity is significantly different from zero. It must be underlined that the collapse of the proto-galactic cloud can not be modelled in a realistic dynamical way using a traditional chemical code: to simulate the gas dynamics other technique must be used (see for instance Chiosi & Carraro (2002), Springel et al. (2005), Merlin & Chiosi (2007), Gibson et al. (2007), Merlin et al. (2010)). However, these models require a lot of computational time and do not allow to easy explore the space of the parameters, even if they are very promising as support of spectro-photometric simulations Tantalo et al. (2010). Hence our chemical model will be a *static* one: it aims at simulating in a simple fashion the formation of the galaxy by collapse of primordial gas in presence of dark matter. The galaxy is simulated as a mass point (Chiosi 1980): the model does not supply information about the spatial distribution of stars and gas, that will be distributed according to

suitable laws (see Chap. 4, where the distribution laws and the normalizations of the physical quantities are explained in detail for the different morphological types).

Galaxies are described as one-zone open models made of two components, luminous material of mass $M_L(t)$ embedded in a halo of dark matter of mass M_D, whose presence affects only the gravitational potential of the galaxy and the binding energy of the gas. In the infall scheme the mass of the luminous component increases with time according to:

$$\frac{dM_L(t)}{dt} = \dot{M}_0 \exp(-t/\tau) \tag{5.2.1}$$

where τ is the accretion time scale: the time dependence of $M_L(t)$ is

$$M_L(t) = \frac{M_L(T_G)}{[1-\exp(-T_G/\tau)]}[1-\exp(-t/\tau)] \tag{5.2.2}$$

The spatial distribution of the dark component with respect to the luminous one is supposed to obey the dynamical models of Bertin et al. (1992) and Saglia et al. (1992): the mass and radius of the dark component, M_D and R_D, respectively, are related to those of the luminous material, M_L and R_L, by the relation:

$$\frac{M_L(t)}{M_D} \geq \frac{1}{2\pi}(\frac{R_L(t)}{R_D})[1+1.37(\frac{R_L(t)}{R_D})] \tag{5.2.3}$$

The mass of the dark component is assumed be constant in time and equal to $M_D = \beta M_L(T_G)$ with $\beta = 5$. Furthermore, the binding gravitational energy of the gas is given by :

$$\Omega_g(t) = -\alpha_L G\frac{M_g(t)M_L(t)}{R_L(t)} - G\frac{M_g(t)M_D}{R_L(t)}\Omega'_{LD} \tag{5.2.4}$$

where $M_g(t)$ is the current value of the gas mass, α_L is numerical factor $\simeq 0.5$, and

$$\Omega'_{LD} = \frac{1}{2\pi}(\frac{R_L(t)}{R_D})[1+1.37(\frac{R_L(t)}{R_D})] \tag{5.2.5}$$

is the contribution to the gravitational energy given by the presence of dark matter. Following Bertin et al. (1992) and Saglia et al. (1992), we assume $M_L/M_D = 0.2$ and $R_L/R_D = 0.2$. Using these values for M_L/M_D and R_L/R_D, the contribution to gravitational energy by the dark matter is $\Omega'_{LD} = 0.04$ and the total correction to the gravitational energy of the gas (Eq. 5.2.4) does not exceed 0.3 of the term for the luminous mass. Assuming that at each stage of the infall process the amount of luminous mass that has already accumulated gets soon virialized and turned into stars, the total gravitational energy and radius of the material already settled onto the equilibrium configuration can be approximated with the relations for the total gravitational energy and radius as function of the mass (Saito 1979a; Saito 1979b) for

elliptical galaxies whose spatial distribution of stars is such that the global luminosity profile obeys the $R^{1/4}$ law. In such a case the relation between $R_L(t)$ and $M_L(t)$ is:

$$R_L(t) = 26.1 \times (M_L(t)/10^{12} M_\odot)^{(2-\eta)} \ \ \text{kpc} \tag{5.2.6}$$

with $\eta = 1.45$ - see also Arimoto & Yoshii (1987) -. Another useful quantity is the volume density of gas $\rho_g(t)$ given by:

$$\rho_g(t) = \frac{3M_g(t)}{4\pi R_L(t)^3} \tag{5.2.7}$$

It is worth recalling that if dark and luminous matter are supposed to have the same spatial distribution, Eqs. 5.2.4 and 5.2.5 are no longer required: the binding energy of the gas can be simply obtained from:

$$\Omega_g(t) = \Omega_{L+D}(t) M_g(t)[2 - M_g(t)]. \tag{5.2.8}$$

Basic equations

The complete formalism describing the chemical evolution of galaxies used to support the photometric code, can be found in Tantalo et al. (1996). In the last chapter of this thesis (see Chap. 6), this formulation will be expanded to a multi-zone system with dust, in order to build a model of dust formation and evolution in galaxies. Here we show only the final equation for the chemical evolution of the ISM considered as the sum of dust and gas, and therefore simulated as a single component. The evolution of the normalized abundance G_i of the i-th element is given by:

$$\begin{aligned}
\frac{d}{dt}G_i(t) &= -\chi_i(t)\,\psi(t) + \int_0^{t-\tau_{M_{B,l}}} \psi(t') \left[\phi(M)\, R_i(M) \left(-\frac{dM}{d\tau_M}\right)\right]_{M(t-t')} dt' + \\
&+ (1-A) \int_{t-\tau_{M_{B,l}}}^{t-\tau_{M_{B,u}}} \psi(t') \left[\phi(M)\, R_i(M) \left(-\frac{dM}{d\tau_M}\right)\right]_{M(t-t')} dt' + \\
&+ \int_{t-\tau_{M_{B,u}}}^{t-\tau_{M_u}} \psi(t') \left[\phi(M)\, R_i(M) \left(-\frac{dM}{d\tau_M}\right)\right]_{M(t-t')} dt' + \\
&+ A \int_{t-\tau_{M_{1,min}}}^{t-\tau_{M_{1,max}}} \psi(t') \left[f(M_1)\, R_i(M_1) \left(-\frac{dM_1}{d\tau_{M_1}}\right)\right]_{M_1(t-t')} dt' + \\
&+ R_{SNI} E_{SNI,i} + \left[\frac{d}{dt}G_i(t)\right]_{inf} - \left[\frac{d}{dt}G_i(t)\right]_{out}.
\end{aligned} \tag{5.2.9}$$

The first term at the r.h.s. is the depletion of the ISM because of the star formation process that consumes the interstellar matter; the following three terms at r.h.s. are the contributions of single stars to the enrichment of the element i, the fifth term

is the contribution by the primary star of a binary system, the sixth term is the contribution of type Ia SNe, the following term describes the infall of primordial material, and finally the last one takes into account the eventual outflow of matter at the onset of the galactic wind in elliptical galaxies. $f(M_1)$ is the distribution function of the primary M_1 mass in a binary system, between $M_{1,min} = M_{B,l}/2$ and $M_{1,max} = M_{B,u}$. R_{SNI} is the rate of type Ia SNe rate , while $E_{SNI,i}$ is the ejecta of the chemical element i always in type Ia SNe. Further details on the calculation of yields and the adopted formalism can be found in Chiosi & Maeder (1986), Matteucci & Greggio (1986) and Portinari et al. (1998). For further analysis of this equation of the chemical evolution, see Chap. 6 of this thesis where the model is expanded specifically for disks. We conclude this section remembering that:

- As for the IMF, we can choose now between 9 different prescriptions, following what have been done for the isochrones and SSPs (see Sect. 1.1.4 and Chap. 3 for a detailed analysis about this point). Since at first, we want to check our models and compare them with observations in order to validate them, we will not focus at the level of galaxies simulations with the variation of the IMF, but we will stick on the Salpeter one, eventually varying the ζ parameter. The calculations of galactic models with different IMFs will be performed in future works.

- As for the Star Formation Rate, we adopt the classical Schmidt function (Schmidt 1959). Other prescriptions can be used: for a more detailed discussion of this topic and a list of typical star formation laws, please refer to Chap. 6.

5.2.2 Main features: disk galaxies or disk of the intermediate types

In the same way as for ellipticals, for disk galaxies or for the disks of intermediate type galaxies, we adopt an open model, with continuous infall of primordial gas that builds the disk gradually, as suggested by dynamical studies (Larson 1976; Burkert et al. 1992). The galactic disk is not divided into concentric cylindrical shells, which evolve independently, as for instance in Portinari & Chiosi (1999, Portinari & Chiosi (2000). For the purposes of this analysis, where the chemical code essentially supports the population synthesis, one-zone formulation is enough: the radial dependence is no longer present and the disk is modelled as an adimensional object, without a spatial extension in the radial direction (Talbot & Arnett 1971). Galactic disks are comfortably described in terms of surface mass density $\sigma(t)$, which depends on time t, since in each ring the surface density is growing in time due to gradual infall of gas. If we indicate with $\sigma_g(t)$ the surface gas density, the gas fraction at any time

t is the ratio: $\sigma_g(t)/\sigma(t)$ while the surface star density is $\sigma_s(t) = \sigma(t) - \sigma_g(t)$. In closed models the total surface density is constant and the other quantities can be normalized with respect to it; in open models it is suitable to normalize with respect to the total surface density at the present age of the Galaxy t_G, i.e. at the final age of the model. So the normalized surface gas density is introduced:

$$G(t) = \frac{\sigma_g(t)}{\sigma(t_G)} \tag{5.2.10}$$

In each ring the gas is assumed to be chemically homogeneous, and the normalized gas density for each chemical species i is:

$$G_i(t) = X_i(t)G(t) \tag{5.2.11}$$

where X_i is the fractionary mass abundance of species i; $\sum_i X_i = 1$ by definition. The chemical evolution of the ISM is the evolution of the set of the G_is (for the complete formalism, we refer to Portinari et al. (1998)). For disk galaxies, the infall term is expressed using the mass surface density $\sigma(t)$, gradually increasing due to the infall of gas with rate $\dot{\sigma_{inf}}(t)$. The contribution of the infalling gas to the evolution of the (normalized) gas fraction $G(t)$ is:

$$\left[\frac{d}{dt}G(t)\right]_{inf} = \frac{\sigma_{inf}(t)}{\sigma(t_G)} \tag{5.2.12}$$

and, for each single chemical species i :

$$\left[\frac{d}{dt}G_i(t)\right]_{inf} = \frac{\sigma_{inf}(t)X_{i,inf}}{\sigma(t_G)} \tag{5.2.13}$$

The rate of infall exponentially decreases with the time scale τ:

$$\dot{\sigma_{inf}}(t) = Ae^{-\frac{t}{\tau}} \tag{5.2.14}$$

This formulation well reproduces the results of dynamical models (Larson 1976; Burkert et al. 1992; Carraro et al. 1998), with the exception of the radial flows of gas. The A term is obtained integrating with respect to time t and imposing that when $t = t_{Gal}$ the surface mass density $\sigma(t_G)$ is:

$$A\left(1 - e^{-\frac{t_G}{\tau}}\right)\tau = \sigma(t_G) \tag{5.2.15}$$

For the complete formalism and the whole set of chemical equations, we refer to Portinari et al. (1998).

5.3 Models parameters for the bulges

Primary parameters of the elliptical models (or of the bulge component of intermediate type models) are:

1. The galactic mass $M_L(t_{Gal})$. In the infall models it represents the asymptotic value which the inflowing material reaches at the final galaxy age. The age t_{Gal} is one of the input of the spectro-photometric code, and it is fixed once the cosmological framework, and in particular the age of galaxy formation, is established. In any case, galactic winds, halting the star formation process, in practice fix the galactic stellar mass to the value already stored in stars at the age of the gas ejection. For a detailed description of the galactic wind process and effects on the masses of gas and stars, see Cassarà (2008). Our models have been calculated for the following values of $M_L(t_{Gal})$, to account for different values of the L_{Bulge}/L_{Tot} ratio, needed to compare theoretical galaxy colors with the observed ones:

   - $0.01765 \times 10^{12} M_\odot$;
   - $0.03510 \times 10^{12} M_\odot$;
   - $0.04500 \times 10^{12} M_\odot$;
   - $0.05500 \times 10^{12} M_\odot$;
   - $0.06450 \times 10^{12} M_\odot$;
   - $0.07260 \times 10^{12} M_\odot$;
   - $0.08160 \times 10^{12} M_\odot$;
   - $0.08450 \times 10^{12} M_\odot$;
   - $0.11800 \times 10^{12} M_\odot$;

   The only model calculated as a *full* elliptical galaxy is the last one: the previous values of mass are intended as the masses of the bulges of the intermediate type galaxies. The corresponding disk masses are listed in Sect. 5.4. The final mass value, for each models, is $\sim 1 \times 10^{11} M_\odot$, trying to follow the prescriptions of Buzzoni (2005) to create a sample of models of disk+bulge galaxies.

2. The ratios R_L/R_D and M_L/M_D which fix the gravitational potential and the effect of dark matter; as already described in Sect. 5.2.2, its value is 5;

3. The exponent k of the Schmidt function: all models have been calculated using $k = 1$;

4. The efficiency ν of the star formation rate. All bulge models have $\nu = 5$, in order to reduce the number of free parameters. Even if different values of ν at varying the galactic mass can be used (Tantalo et al. 1996; Tantalo et al. 1998), we decided to fix it. It is worth noticing that in some way the effect of the ν parameter is not expected to be as strong as in (Tantalo et al. 1996; Tantalo et al. 1998) models, because the mass range that we are taking into account is not as large as it was in those works. We are just taking what could be an average mass of 10^{11} $M_{\odot}$ for our galaxy models: not too big and not too small.

5. The initial mass function (slope and ζ). The slope is kept constant at the classical value of Salpeter, whereas $\zeta = 0.5$. As pointed in Tantalo et al. (1996), this is a good choice in order to get models with M/L_B ratios in agreement with the observational data and it allows also to be consistent with the super-solar metallicities suggested in Buzzoni (2005) for the bulges in intermediate type galaxies spectro-photometric models.

6. The infall time scale τ. Although the time scale of mass accretion is often considered as a free parameter of the models, we assume $\tau = 0.3$ for all the models in order to reduce the number of free parameters.

7. The final age t_{Gal}: considering the ΛCDM model and the redshift of galaxy formation $z = z_{form} = 8$, we get $t_{Gal} = 13.09$ Gyr.

5.4 Models parameters for the disks

For disk galaxies or for the disk component in the intermediate types, we use the following prescriptions:

1. The galactic mass $M_L(t_{Gal})$. Models have been calculated for the following values of $M_L(t_{Gal})$, linked at the corresponding values of the bulge masses presented in Sect. 5.3, in order to obtain a global mass for the intermediate type galaxies of $M_{disk} + M_{Bulge} \simeq 10^{11} M_{\odot}$ (see Sect. 5.3). It is worth noticing that disk galaxies do not experience galactic winds, hence the star formation is still active at the present age. We refer to Cassarà (2008) for a more detailed analysis of the chemical evolution, in particular for what concerns the different star formation histories which characterize both elliptical and disk galaxies.

   - $0.08700 \times 10^{12} M_{\odot}$;
   - $0.07360 \times 10^{12} M_{\odot}$;
   - $0.06650 \times 10^{12} M_{\odot}$;

- $0.05660 \times 10^{12} M_{\odot}$;
- $0.04716 \times 10^{12} M_{\odot}$;
- $0.04600 \times 10^{12} M_{\odot}$;
- $0.03400 \times 10^{12} M_{\odot}$;
- $0.02690 \times 10^{12} M_{\odot}$;
- $0.09450 \times 10^{12} M_{\odot}$;

As for the elliptical case, we have only one *pure* disc galaxy (last case): the previous values of mass are intended as the masses of the disks for the intermediate cases.

2. The exponent k of the Schmidt function: all models have been calculated using $k = 1$;

3. The efficiency ν of the star formation rate. All disc models have $\nu = 0.35$; in Portinari et al. (1998), $\nu = 0.50$. We have decided to reduce slightly this value in order to account for the adopted disc metallicity in Buzzoni (2005). If more elaborate star formation laws would be used to reproduce the star formation in disc galaxies (Portinari & Chiosi 2000), this value would change in order to keep the desired metallicity.

4. The initial mass function (slope and ζ). The slope is kept constant at the classical value of Salpeter, whereas $\zeta = 0.17$. This low value of the $\zeta = 0.17$ parameter is necessary again in order to obtain the metallicities suggested in Buzzoni (2005) for the disk, that is assumed with a metallicity equal or even lower that the typical LMC one, that is $Z \lesssim 0.008$. Buzzoni (2005) assumes $Z \approx 0.006$.

5. The infall time scale τ. We assume $\tau = 3$ in order to account for a more time-extended star formation in disk galaxies (Portinari & Chiosi 1999; Portinari & Chiosi 2000).

6. The final age t_{Gal}: considering the ΛCDM model and the redshift of galaxy formation $z = z_{form} = 8$ we get in the same way as for the disks $t_{Gal} = 13.09$.

5.5 SEDs of galaxies of different morphological types: parameters

Details about the spectro-photometric code and the models of galaxies of different morphological type, calculated by means of evolutionary population synthesis, can

be found in Chap. 4, while for what concerns the meaning of all the input parameters read by the main file of the spectro-photometric code `Galaxy2012.f90`, we refer to Cassarà (2008). Here we summarize and discuss only the most important parameters, distinguishing, as usual, between the bulge component of an intermediate type galaxy (or the elliptical galaxy) and the disk component (or the disk galaxy):

Bulge component or Elliptical galaxy

- r_c^M: scale radius of the interstellar medium in King law, see Sect. 4.1.2: its value is 0.5 kpc. Before the onset of the galactic wind, the gas is made up of molecular clouds with active star formation *and* diffuse interstellar medium. Indeed, we need the length scales of MCs, diffuse ISM and stars, which, for the sake of simplicity, have the same value of 0.5 Kpc. For the effects related to the variation of scale radii, see Piovan et al. (2006a).

- r_c^*/r_c^M: this parameter allows for the splitting up between the distribution of gas and stars on two different scale radii. For our purposes, we suppose that both components have the same spatial distribution; however, it could be plausible a different distribution of diffuse gas after the onset of the galactic wind (indeed it would be located more externally with respect to stars, see Cassarà (2008) and Chiosi & Carraro (2002)).

- γ_*: 1.5, see Sect. 4.1.2;

- γ_{MC}: 1.5, see Sect. 4.1.2;

- γ_{gas}: 0.75, see Sect. 4.1.2;

- `fgasmol`: 0.8; this parameter fixes the amount of molecular gas present in the galaxy at the age with the peak of star formation, with respect to the total gas. This value is then used to scale proportionally the amount of MCs at different ages of the evolution of the galaxy. Indeed, we assume that star formation occurs in the cold MCs and therefore they should be dominant in the ISM at the peak of SFR. For elliptical galaxies or bulges it has been used *only* before the onset of the galactic wind, after which the star formation process halts. After, no more star formation occurs.

- t_0: $30 \times 10^6 yr$; we adopt this value since it is plausible that MCs in ellipticals and bulges, where the star formation occurs, are embedded in a primordial high-density environment. In consequence of this hence requiring more time to disrupt this dense environment, respect to MCs of disk galaxies (Sect. 4.3).

- `ellfracgas`: 0.015, as explained in details in Cassarà (2008).

Disk component or disk galaxy

- z_d^*: 0.4 kpc, see Sect. 4.1.2;
- z_d^{gas}: 0.4 kpc, see Sect. 4.1.2;
- R_d^*: 5 kpc, see Sect. 4.1.2;
- R_d^{gas}: 5 kpc, see Sect. 4.1.2;
- `fgasmol`: 0.6; as already explained, this parameter indicates the amount of molecular gas (and then the amount of molecular clouds) present in the galaxy at the age of the peak of star formation. We use this value following Piovan et al. (2006b), who took into account estimates of the masses of H_2 and HI/HII obtained from observations of late-type galaxies in the local universe;
- t_0: $6 \times 10^6 yr$, Sect. 4.3; for the disk components or disk galaxies, we consider a shorter evaporation time scale than the one for elliptical galaxies, assuming that the environment of star formation never reaches such high-densities. Again, we follow the prescription of Piovan et al. (2006b) and we use the approximation that the evaporation time scale of galaxies in the local universe will be the same along the whole galaxies evolution. Indeed, the regular star formation of disk galaxies suggests a time scale with small variation along the hubble time.

5.6 SEDs of galaxies of different morphological types: results

5.6.1 SEDs at the $t_{Gal} = 13.09$ Gyr

In this section we present theoretical SEDs for galaxies of various morphological types, taking into account the contribution of the different physical components to the whole galaxy emission. The analyzed age is the final age of the models, that it, $t = t_{Gal} = 13.09$ Gyr, calculated considering as redshift of formation $z_{form} = 8$, in the current cosmological framework.

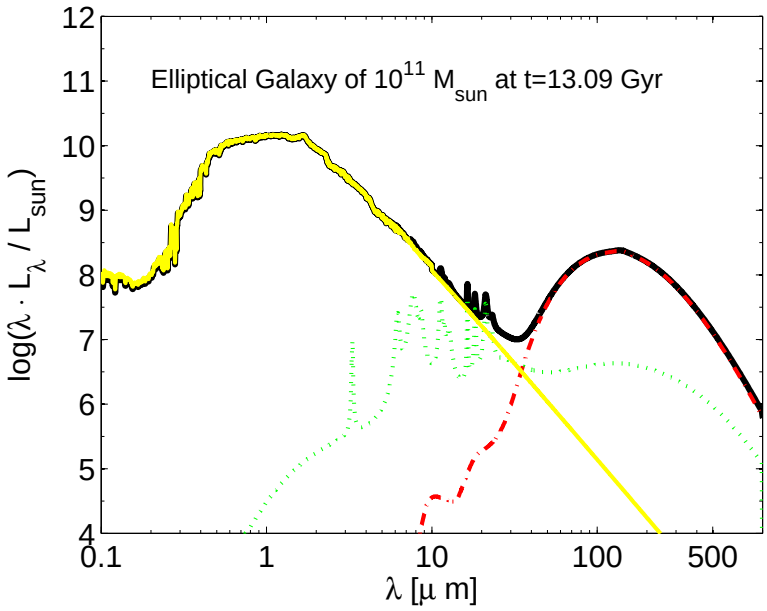

Figure 5.1: SED of the model *elliptical galaxy* of $M = 10^{11} M_{\odot}$ (black continuous line). We represent also the emission of both graphite and silicate grains (red dot-dashed line), the emission of PAHs (green dotted line), and the SED where only the extinction effect of the MCs is included (yellow continuous line).

Respectively, these figures show:

- Fig. 5.1: SED of the model elliptical galaxy of $10^{11} M_{\odot}$(black continuous line). We represent also the emission of both graphite and silicate grains (red dot-dashed line), the emission of PAHs (green dotted line), and the old stellar population extinguished *only* for the MCs effect (yellow continuous line);

- Fig. 5.2: SED of the model S0a galaxy, with $M_{Bulge} = 0.045 \times 10^{11} M_{\odot}$ and $M_{Disk} = 0.0665 \times 10^{11} M_{\odot}$: as in the following section will be explained, the morphological classification of our intermediate models have been done considering the theoretical $[B - V]$ and $[U - B]$ colors. The luminosity of the same physical components as in Fig. 5.1 is represented; for this model and the following three intermediate ones we can observe the contribution of the emission of MCs (blue dashed line) due to the star formation still active in the disk. This effect can not be appreciate in the case of an elliptical galaxy since the galactic wind swept off the ISM hence stopping the star formation.

- Fig. 5.3: SED of the model Sbc-Sab galaxy, with $M_{Bulge} = 0.0351 \times M_{\odot}$ and $M_{Disk} = 0.0736 \times M_{\odot}$. As in the previous figure, together with the global EPS with the contribution of dust, we observe the emission of graphite and silicate

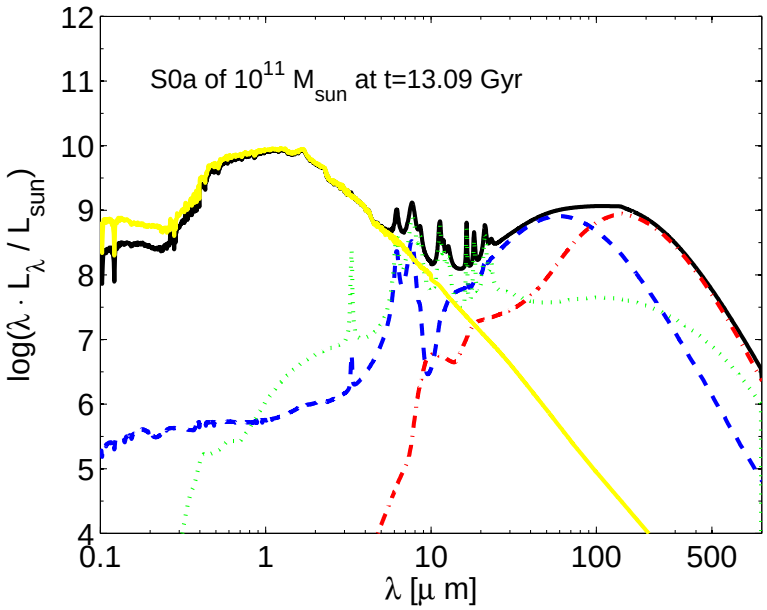

Figure 5.2: As in Fig. 5.1, but for a *S0a galaxy* of $M_{tot} = 10^{11} M_{\odot}$. The meaning of the lines is the same as in Fig. 5.1, but for S0a we can also appreciate the emission of MCs (blue dashed line), which is lacking in the previous case since the onset of the galactic wind halted the star formation.

grains, the emission of PAHs, the old stellar population extinguished *only* for the MCs effect (and not for the effect of extinction of the diffuse interstellar dust) and, finally, the emission of MCs.

- Fig. 5.4: SED of the model disk galaxy of $10^{11} M_{\odot}$ with the contribution of the different physical components at the whole galaxy emission.

It is evident that the shape of the SEDs of the various components gradually changes passing from the elliptical model to the disk model: few differences can be observed comparing the two intermediate galaxy types. These considerations hold for the models at 13.09 Gyr (z=0):

- For the elliptical model: the global emission (black continuous line) shows a peak in the UV (thus reproducing the ultraviolet excess observed in elliptical galaxies) and a weak IR peak, which is clearly due to a poor amount of dust grains in the diffuse medium (there is no contribution of the molecular clouds at the emission in the IR region since star formation has stopped). The extinction effect is weak since at the final age of the galaxy small amounts of gas and dust are present.

- For the disk model: both the environments with the presence of dust, namely

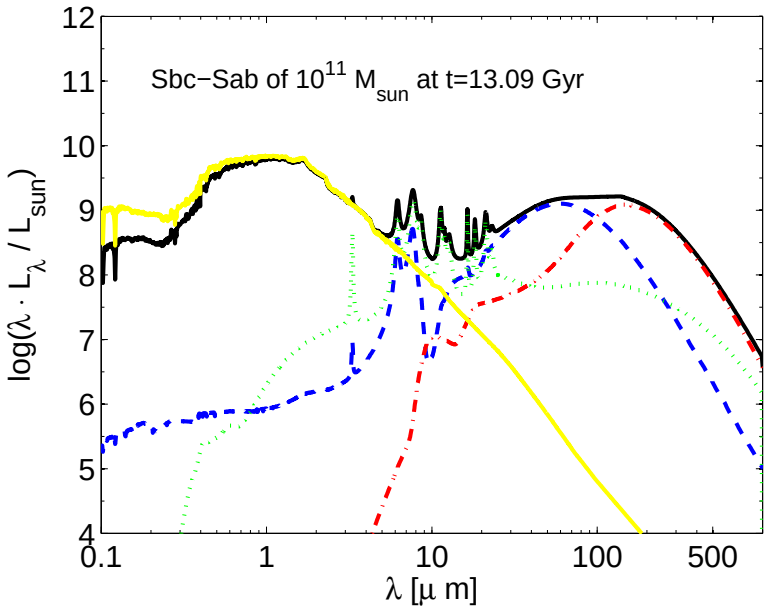

Figure 5.3: The same as in Fig. 5.1, but for a *Sbc-Sab galaxy* of $M_{tot} = 10^{11} M_{\odot}$. The meaning of the lines is the same as in Figs. 5.1 and 5.2.

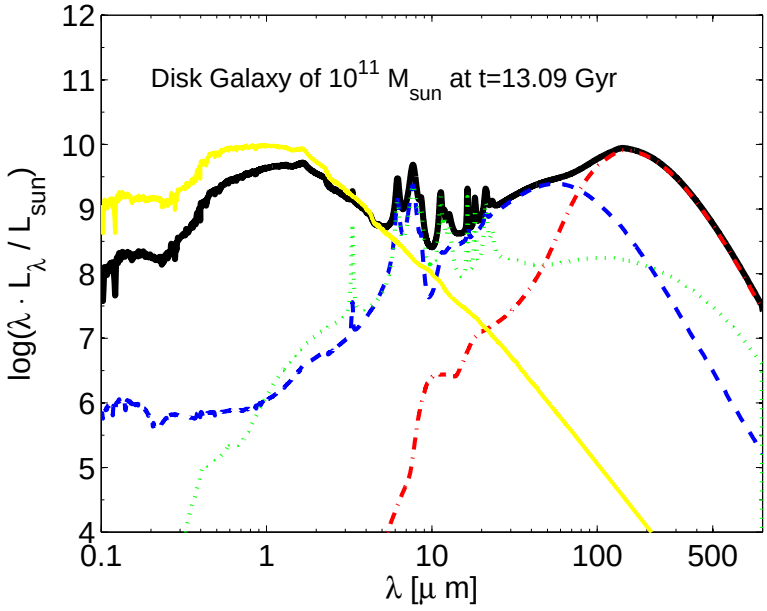

Figure 5.4: The same as in Fig. 5.1, but for a disk galaxy of $M = 10^{11} M_{\odot}$. The meaning of the lines is the same as in Figs. 5.1 and 5.2

the diffuse interstellar medium and the star forming regions, contribute to the IR luminosity in significant amount and both play a role in the extinction of the UV/optical radiation;

- For the intermediate types (disk plus bulge): the emission of the different components is quite similar to those of the disk model. However, in the UV region, the SED where the stellar population is extinguished *only* for the MCs effect (yellow lines - taking into account only the effect of obscuration of young stars) and the total emission (black lines) are in practice indistinguishable for $\lambda \gtrsim 0.5\mu m$, while as shown in Fig. 5.4 for disk model they are clearly separate. This is ultimately due to the smaller amount of gas still present in the intermediate model compared to the disk only model. Indeed in the former case the galactic wind swept away all the gas in the bulge, whereas in the disk the galactic wind is not active.

The contribution of the PAHs, silicates and graphite grains grows going from the elliptical model to the disk model; this effect is due, as already pointed out, to the small amount of dust and gas present in the elliptical galaxy at the final age, whereas in disk galaxies (assuming, as already noted, the infall model and the Schmidt law for star formation) the star formation continues until the present age. As a consequence of this, at every age, spectro-photometric models will contain *all* the physical components, as we have just seen: newly born stars still embedded in their parental molecular cloud, stars of various ages and metallicities free from molecular clouds and, finally, a substantial contribution of the diffuse ISM.

Some considerations about the galactic wind

When the thermal energy of the gas in the galaxy, heated by the SNe explosions, by stellar winds and UV radiation from massive stars and cooled by radiative cooling processes, equals or exceeds its gravitational potential energy:

$$E_{th}(t) \geq \Omega_g(t) \tag{5.6.1}$$

the phenomenon known as *galactic wind* occurs: in the chemical simulations, when the thermal energy exceeds the binding potential energy, the star formation is stopped and all the remaining gas at that time in the galaxy is ejected. This is obviously a rude approximation of the real situation, since it implicitly assumes that:

- the energy is immediately stored and distributed homogeneously in the gas;
- the condition expressed by Eq. 5.6.1 occurs contemporaneously on the whole gas content.

This is not completely accurate because:

1. it is plausible that cavities and tunnels of hot gas can be formed (Matthews & Baker 1971), and the distribution of energy injected into the gas is not homogeneous;

2. the galaxy is a three-dimensional object, the gas is distributed throughout the galactic volume: the onset of galactic wind will therefore be a *gradual* phenomenon, which will concern particularly the gas located in the outer part of the galaxy. The amount of gas which leaves the galaxy is therefore a fraction of the total amount and it gradually leaves the galaxy in a continuous *loss-process* rather than in a single episode.

***When* the galactic wind occurs?**

Some assumptions about the distribution of baryonic and dark matter are required, together with the efficiency of different heating and cooling processes, in order to correctly (a) evaluate the total gravitational potential and (b) describe the thermal evolution of the galaxy. The models in literature show that galactic winds typically occur for $t_{gw} < 1$ Gyr, later in massive elliptical galaxies and earlier in low mass galaxies (Arimoto & Yoshii 1987; Bressan et al. 1994; Gibson & Matteucci 1997; Tantalo et al. 1996; Tantalo et al. 1998; Chiosi et al. 1998). In our models of elliptical galaxies, the star formation is virtually complete within the first Gyr when the onset of the galactic wind occurs, in agreement with the values proposed in literature. Indeed, the peak of star formation occurs, depending on the mass, within 0.50 Gyr - 1.0 Gyr. After the onset of the galactic wind we have no more star formation and no more young stars embedded in MCs contributing to the total SED. Anyway, the amount of gas still rise, because of the mass loss of AGB and RGB stars, but star formation is in practice completed.

Disk galaxy: the effect of inclinations

Disk galaxies can be observed along different inclinations toward the observer. In our models four inclinations are available and obviously, we expect the final SED to be different according to the viewing angle. The available angles in the code are described in Chap. 4. The choice of these values is arbitrary, but we wanted anyway to cover with different cases the range between face-on and edge-on galaxies, extreme cases included.

Differently from what happens for the models of elliptical galaxies which are subjected to the spherical symmetry, the luminosity emitted from an edge-on spiral galaxy will be heavily absorbed due to the equatorial dust lane between the stars

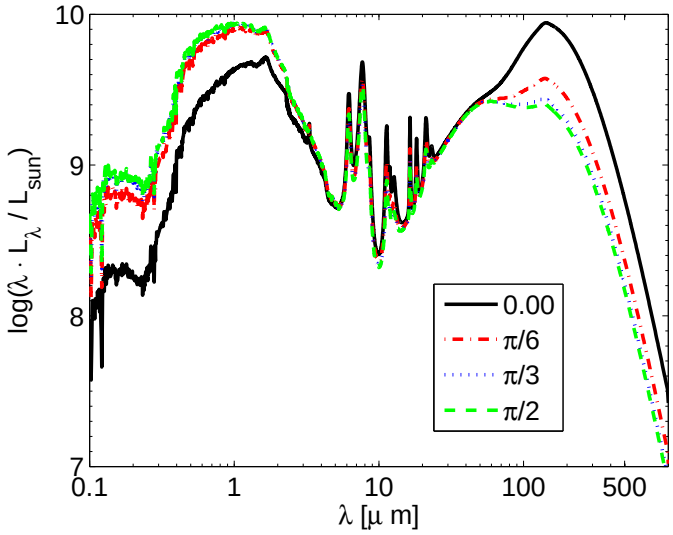

Figure 5.5: SED of the model disk galaxies of $M = 10^{11} M_{\odot}$ for different viewing angles.

and the observer, and will present a pronounced peak in the IR region of the spectrum. The same galaxy seen face-on will show a less intense FIR emission and a more intense emission in the UV/optical region compared to the edge-on model. The Fig. 5.5 shows the total emission of the model disk galaxy of $10^{11} M_{\odot}$ according to different inclinations. The SEDs for this galaxy show as expected, the opposite trend of the IR emission and extinction in the UV-optical region (for the sake of illustrations, the range of the y-axis in this figure is shorter than the y-axis of the corresponding Fig. 5.4). For $\lambda \geq 150 \mu m$, the edge-on emission of the dust is greater than the emission at all the other inclinations. Vice-versa in the UV-optical region: as expected, for the edge-on galaxy, the emission is lower than for the other inclinations. It is clear that every time that we consider SEDs, colors or magnitudes of dust-rich galaxies that are not spherically symmetric, thus introducing the dependence on the viewing angle, the results are significantly different depending on the angle. For the same model they span a range of possible SED and magnitudes.

5.6.2 Evolutionary models

While in Sect. 5.6.1 we analyzed the SEDs of modelled galaxies at the final age, now we present *evolutionary* models, still considering galaxies of various morphological types, namely elliptical, E-S0, S0, Sab, Sab-Sbc and disk (Sd) models. The panels of Fig. 5.6 - **upper panel**: elliptical galaxy; **middle panel**: E-S0 galaxy; **lower panel**: S0 galaxy - and 5.7 - **upper panel**: Sab galaxy; **middle panel**: Sab-Sbc galaxy; **lower panel**: disk galaxy (Sd) - show how the total EPS emission of the models

changes at varying the age along the Hubble time according to the morphological type, assuming a redshift of formation of the galaxies $z_{for} = 8$ (corresponding to 13.09 Gyr at $z = 0$ with the current cosmological model).

As we can see, for the elliptical model at t=0.085 Gyr, the emission is strongly concentrated in the IR region of the spectrum: the large amount of dust present in the galaxy at this age absorbs the young stars emission in the UV/optical region, and it re-emits this luminosity in the IR. These young stars play a key role in the early stages of galaxy evolution, because of intense star formation heavily obscured. Immediately after the onset of the galactic wind, (which, we stress, it is supposed to occur *simultaneously* for the *entire* gas content of the galaxy), the gas is swept away and the star formation is halted. One can assume that the star formation is virtually complete when $t = t_{gw}$. We can therefore explain the SEDs of the elliptical galaxy for the ages 2.55, 5.66 and 13.09 Gyr: they represent the aging of a stellar population becoming older and older with a small diffuse gas and dust content. The diffuse medium absorbs the stellar radiation in small amount, while the majority of the emission is due to cool stars in the NIR region. For the S0 models, the presence of a small disk component allows star formation to never stop. It follows that, even if for t=0.085 Gyr the SED is quite similar to the elliptical galaxy model and dominated from dust emission, for the other ages the SED is very different and the diffuse ISM significantly contributes to the MIR/FIR emission. It is also interesting to observe that the PAHs features appear only after a significant enrichment in metals: this is due to the choice of the Weingartner & Draine (2001a) extinction curves. At low metallicity we adopt their SMC flat curve with a poor or negligible contribution of the PAHs. Finally, the UV emission is much stronger than in ellipticals, as expected, since in S0 models there is a component (the small disk) never ending star formation. In the Sab, Sab-Sbc and Sd (disk) model, we see that, since the disk mass is growing, the amount of dust is growing as well and its effects are more and more pronounced. The total emission increases with time, reaches a maximum in correspondence of the peak of the star formation (both in the optical region and in the IR) and then decreases with the decrease of the star formation rate, according to the typical SFH . used as input for disks (Piovan et al. 2006b; Cassarà 2008). As already pointed out, the star formation does not fall sharply as for elliptical galaxies: it reaches a peak and then slowly declines, but it proceeds until the present age. It is worth noticing that for t=0.085 Gyr, the spectral energy distribution is *strongly* located in two peaks (FIR and UV); at increasing the age, the trend is smoothed since intermediate-age and old stars contribute significantly to the $1\mu m$ emission. For the late type models it is even more evident than for the S0, the behaviour of the PAHs features with the metallicity: the low Z extinction curves introduced in our models and based upon the SMC curve, produce high-z models with PAHs features not strong. Finally, for the full disk model, there is not a phase in the early stages of the evolution where the galaxy is dominated by the FIR emission. Indeed, we miss in this case the strong and heavily obscured burst of star formation of the bulge. Along the whole evolution

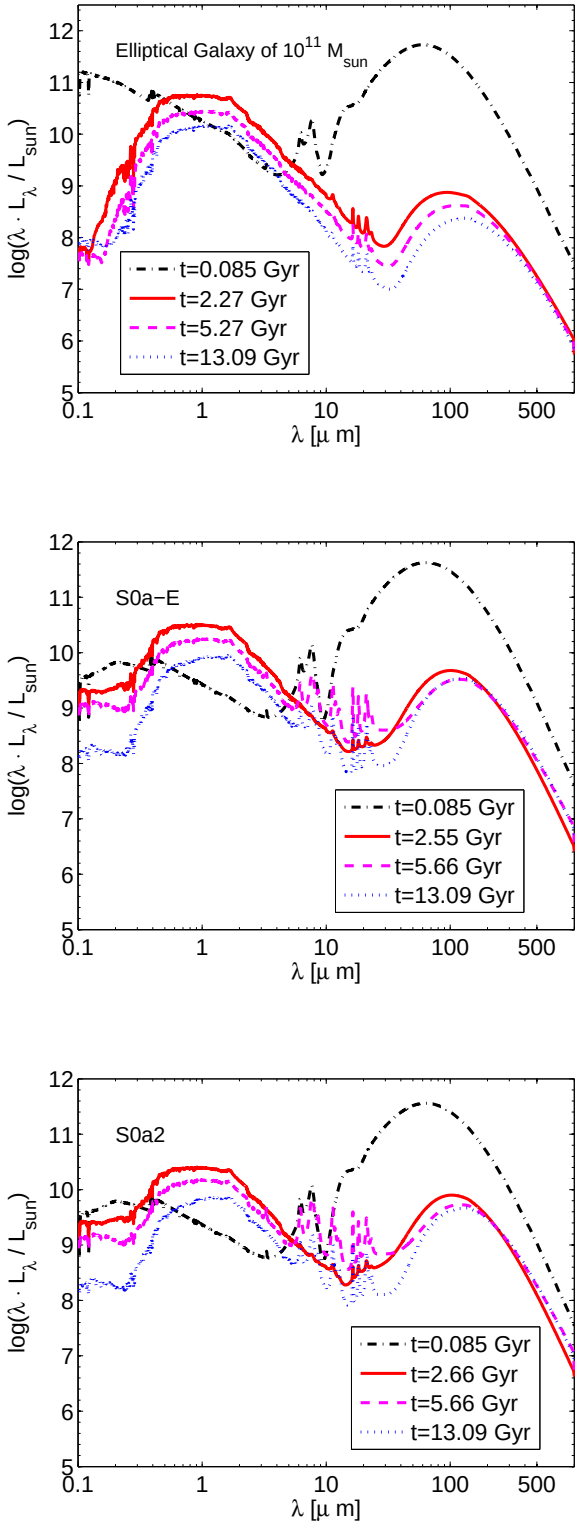

Figure 5.6: Time evolution of the SED of modelled galaxies of early morphological types - **upper figure**: elliptical; **middle figure**: E-S0; **lower figure**: S0 - of $M = 10^{11} M_{\odot}$ for four significative ages, as the legend indicates.

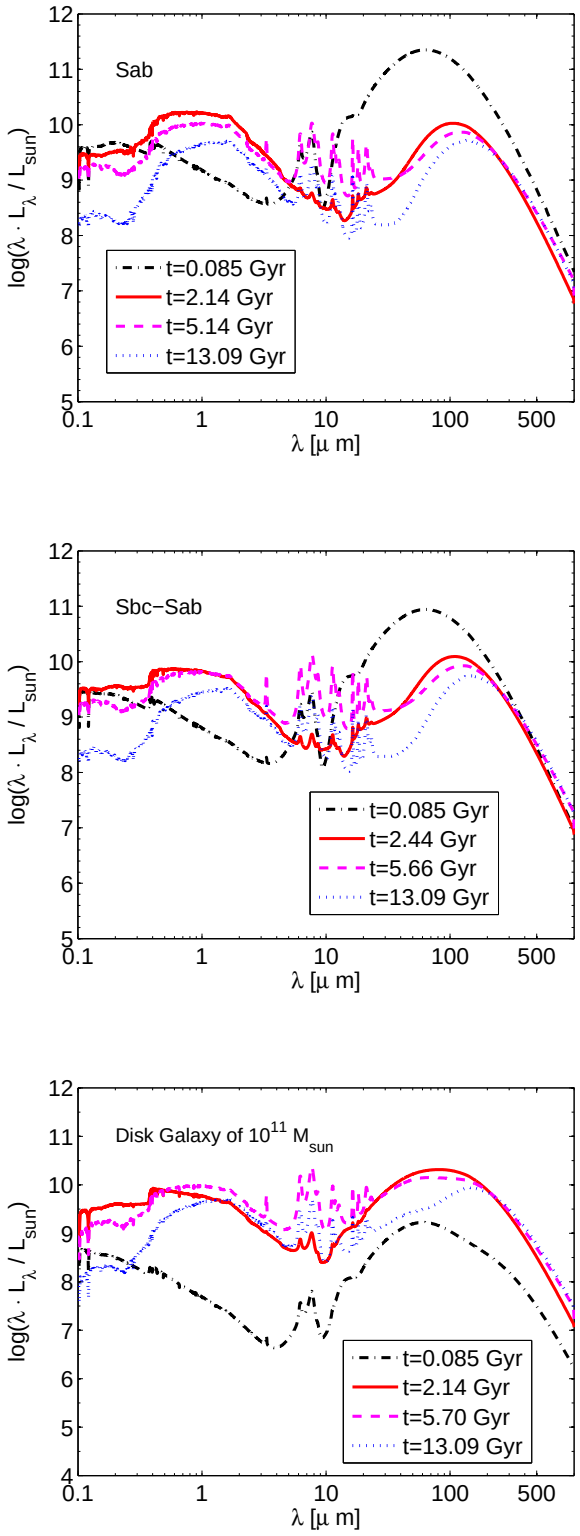

Figure 5.7: Time evolution of the SED of modelled galaxies of late morphological types - **upper figure**: Sab; **middle figure**: Sab-Sbc; **lower figure**: Sd-Irr (disk), of $M = 10^{11} M_{\odot}$ for four significative ages, as the legend indicates.

a more regular process of star formation unrolls.

5.7 Theoretical and observed galaxies colors

In this section we examine the theoretical colors obtained from SEDs of galaxies of different morphological types and we compare our results with some observational data available in literature.
In Buzzoni (2005), a set of evolutionary population synthesis models for template galaxies along the Hubble morphological sequence has been presented. The models account for the individual evolution of bulge, disk and halo components and they provide basic morphological features, along with bolometric luminosity and color evolution, between 1 and 15 Gyr.

Indeed, a tight relation exists between integrated colors and morphological type, through the relative contribution of bulge and disk stellar populations (Arimoto & Jablonka 1991). Ongoing star formation, in particular, is a key mechanism to modulate galaxy colors, especially at short wavelength (Larson & Tinsley 1978; Kennicutt 1998), while visual and infrared luminosity are better sensitive to the global star formation history (Quirk & Tinsley 1973; Sandage 1986; Gavazzi & Boselli 1996). The models of Buzzoni (2005) especially deal with the stellar component, which is obviously the prevailing contributor to galaxy luminosity in the UV-optical region. Residual gas acts more selectively on the SED by enhancing monochromatic emission, like for the Balmer lines. However, as far as galaxy broad-band colors are concerned, in the present age range, its influence is negligible and can be treated apart. Internal dust could play, on the contrary, a more important role, especially at short wavelength ($\lambda \lesssim 3000$ Å).

Metallicity and stellar birth rate are constrained by comparing with observations and other theoretical studies. For other details about operational tools and models set-up see Buzzoni (2005).

As presented in the previous sections and chapters of this thesis, our models are quite different from the Buzzoni ones: first of all, we do not consider the contribution of the halo component, since only disk and bulge are included. However, this point should not be a point of strong disagreement, because the halo plays a secondary role in the mass and luminosity budget. Moreover, our models consider the contribution of dust at different levels, (see Chap. 4), even if, as already pointed out, we still kept the opportunity to calculate the so-called classical EPS, hence excluding the contribution of dust to the galaxy emission that will be a stars-only spectrum. This is useful in order to compare eventually the models with classical EPS (Bressan et al. 1994; Buzzoni 2002; Buzzoni 2005).

Another difference with Buzzoni (2005) is that we do not simply adopt a law of

star formation, but the models stand on a robust code of chemical evolution that assuming a suitable prescription for gas infall, IMF, star formation rate and stellar ejecta provides the total amounts of gas and stars present at any age together with their chemical history (Chap. 6) (Chiosi 1980; Tantalo et al. 1996; Tantalo et al. 1998; Portinari et al. 1998; Portinari & Chiosi 1999; Portinari & Chiosi 2000; Piovan et al. 2006b). We already discussed the pros and cons of the chemical code, which, we remember, is a *one-zone* model. Another important difference between the two population synthesis techniques is the adopted star formation rate: we use the classical Schmidt law, (see Sect. 5.2.2), while in Buzzoni (2005) a power law such $SFR = Kt^{-\eta}$ with $\eta < 1$ is used (we refer to the original papers for more details).

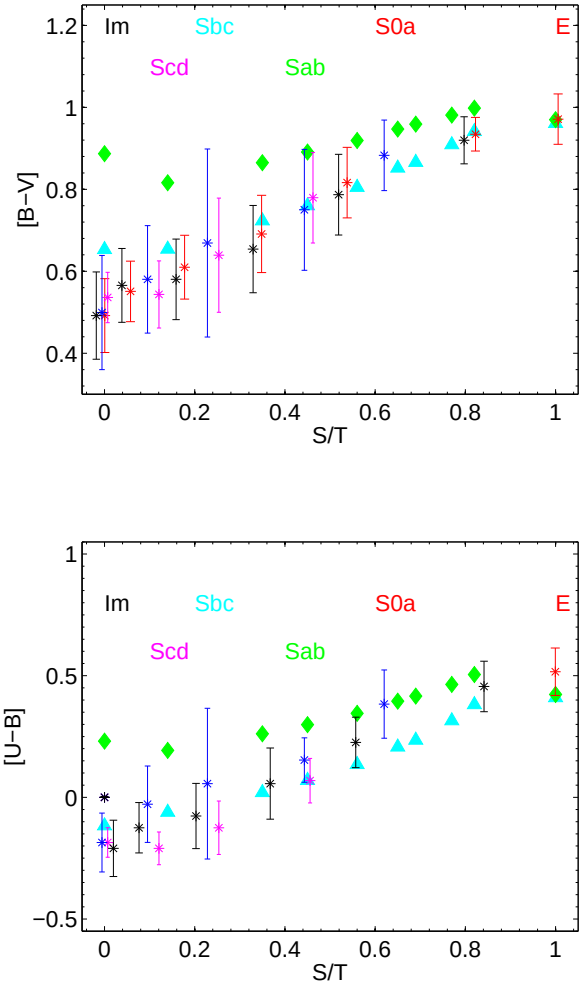

Figure 5.8: Galaxy color distribution (**upper panel**: [B-V] vs. bolometric morphological parameter S/T=L_{Bulge}/L_{Tot}; **lower panel**: [U-B] vs. bolometric morphological parameter S/T=L_{Bulge}/L_{Tot}). Data are from Pence (1976) (magenta stars), Gavazzi et al. (1991) (blue stars), Roberts & Haynes (1994) (red stars) and Buta et al. (1994) (black stars). All the data have been properly corrected by dust extinction. The red star located at $\sim$ S/T= 1 represents the mean color for ellipticals (Buzzoni 1995). Our theoretical colors are indicated with green diamonds and cyan triangles: they have been calculated, respectively, by means of the EPS with dust and EPS corrected for the contribution of dust.

As already mentioned, we choose to fix the chemical parameters for the modelled galaxies in order to account for the required L_{Bulge}/L_{Tot}, as explained below. Buzzoni (2005) calibrated, for each Hubble type, a morphological parameter defined as S/T = L(spheroid)/L(tot). As the S/T calibration does not vary much at infrared wavelength, he fixed the I luminosity as a reference for the model setup.

In our simulations, this ratio can not be determined *a priori*; indeed, we start from the spectral energy distribution of a certain modelled galaxy (obtained using the galactic spectro-photometric code), for which we fixed *a priori* the asymptotic infall mass, and then the resulting SED becomes the input of the photometric code, which calculate colors and magnitudes in different photometric systems (see Chap. 2 for a complete treatment of the subject). We also introduced the possibility to calculate and obtain not only magnitudes and colors, but also luminosities, since in literature data sometimes are available as luminosities, for example in studies of the fundamental plane. In particular, in our case this output luminosity, for disk and bulge, is used *a posteriori* to get clues about the initial asymptotic mass that should be used as input. Carefully proceeding in this way, it is possible to finally obtain the correct initial values for disk and bulge in order to be consistent with the S/T ratios for the different morphological types.
If all the parameters have been fixed, in particular the metallicity (hence ζ, τ, ν, see Sects. 5.3 and 5.4), we found that there is an *almost-linear* relation between the mass of the bulge component (the mass of the corresponding disk follow from $M_{disk,\odot} = 10^{11} - M_{bulge,\odot}$, since all the intermediate types have the same total mass of $10^{11} M_{\odot}$) and luminosity.

As explained in Buzzoni (2005), observations of the central bulge of the Milky Way show that it mostly consists of metal-rich stars (Frogel 1988; Frogel 1999) and this seems a quite common situation also for external galaxies (Jablonka et al. 1996; Goudfrooij et al. 1999; Davidge 2001). The exact average value of the bulge metallicity, however, has been subject to continual revision in the recent years, ranging from a marked metal overabundance (i.e. [Fe/H] $\sim +0.2$, (Whitford & Rich 1983; Rich 1990; Geisler & Friel 1992)) to less prominent values, actually consistent with a standard or even slightly sub-solar metallicity (Tiede et al. 1995; Sadler et al. 1996; Zoccali et al. 2003; Origlia et al. 2005). According to these arguments, for the bulge component in his intermediate type galaxies Buzzoni (2005) adopts an SSPs with [Fe/H]$= +0.22$. He chose to maintain a super-solar metallicity for the bulge component, in better agreement with the observations of external galaxies. For the disk component, relying on the observed colors of present-day galaxies (Buzzoni 2005) adopted $[\mathrm{Fe/H}]_{\mathrm{disk}} = -0.5$ dex as a luminosity-weighted representative value for his models. As pointed out in Buzzoni (2002), this value roughly agrees with the Milky Way stellar population in the solar neighborhood (Edvardsson et al. 1993), and is in line with the Arimoto & Jablonka (1991) theoretical estimates, suggesting a mean luminosity-weighted $[\mathrm{Fe/H}]_{\mathrm{disk}} \sim -0.3$ dex for their disk-dominated galaxy models.

In order to account for the prescription of Buzzoni (2005), two different sets of galactic models have been prepared: their parameters have been discussed in Sects. 5.3 and 5.4. The only difference between the sets concerns the final metallicity.

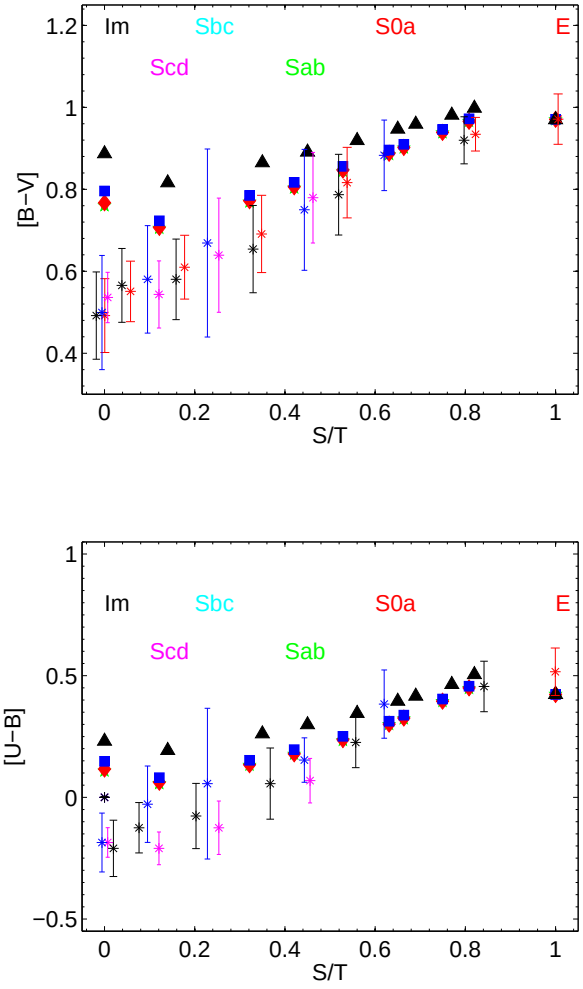

Figure 5.9: The same as in Fig. 5.8, but now only theoretical colors for EPS with dust are shown: the different symbols and colors indicate different viewing angles. Black triangles: galaxy seen *edge-on*; blue squares: galaxy observed at an angle of 60° measured respect to the galactic equatorial plane; red diamonds: galaxy observed at an angle of 30° measured respect to the galactic equatorial plane; green stars: galaxy seen *face-on*.

Indeed, our chemical code does not allow (unless we force the input parameters to extreme values) to reach a super-solar metallicity for the bulge components, in particular at decreasing the mass. For realistic inputs, our bulges reach solar or only slightly super-solar metallicities. Also for the disk component, we can not reach easily the low value suggested by Buzzoni (2005): the metallicity of our disks tends to be slightly higher. The fundamental parameters that must be varied in order to play with the final metallicities of disk and bulge is the ζ parameter. Slightly super-solar

metallicity (for the bulge) and a bit less than the average LMC metallicity (for the disk) are the best values that can be obtained for plausible ζ for Salpeter IMF with total asymptotic mass 10^{11}. We kept these values in order to maintain the general property that in any case the bulge ($Z \gtrsim 0.02$) is more metal rich than the disk ($Z \lesssim 0.008$). In order to evaluate the effect due to different values of the metallicity for the two galaxy components, disk and bulge, we decided to calculate two different set of models:

- the first set stands on the parameters already discussed in the previous sections. In this case, the galactic code, performing the EPS, will interpolate between SEDs of SSPs taking for each of them the metallicity predicted by the chemical code at the time when that stellar population was born.
- the second set stand on the same parameters, but in this case we forced the galactic code by fixing the metallicities of disk and bulge according to same values adopted in Buzzoni (2005). In this case there is no interpolation on the SEDs of SSPs in metallicity, because it is fixed for both disk and bulge.

The results of our simulations, together with the observed colors, are shown in the Figs. 5.8, 5.10 and 5.9. They represent galaxy color distribution, that is (**upper panel**: [B-V] vs. bolometric morphological parameter S/T=L_{Bulge}/L_{Tot}; **lower panel**: [U-B]) vs. bolometric morphological parameter S/T=L_{Bulge}/L_{Tot}. Data are taken from Pence (1976) (magenta stars), Gavazzi et al. (1991) (blue stars), Roberts & Haynes (1994) (red stars) and Buta et al. (1994) (black stars). The red star located at $\sim$ S/T= 1 is the mean color for elliptical galaxies (Buzzoni 1995). All the data have been reddening corrected by the respective authors. In Fig. 5.8, our theoretical colors are indicated with green diamonds and cyan triangles: they have been calculated, respectively, considering EPS with dust and EPS corrected for the extinction of dust, namely the classical bare EPS. These colors are obtained fixing, as already explained, the metallicity of both disk and bulge components. In Fig. 5.10, our theoretical colors are instead indicated with green stars and red diamonds: again, they have been calculated considering EPS with dust and the classical EPS without the contribution of dust. For for these models we only fixed the chemical parameters as discussed in Sects. 5.3 and 5.3, thus leaving the spectro-photometric code free to correctly interpolate in metallicity, following the input pattern obtained with the chemical simulations. Finally, in Fig. 5.9, only theoretical colors starting from SEDs of EPS models *with dust* have been plotted, but taking into account the effect of the viewing angle (see Sect. 5.6.1).
The agreement of our simulations with the data is good and the following considerations hold:

- as expected, in all the figures, the theoretical colors that best stand on the region of the data, that are corrected for extinction, are the dust-free ones: between the classical EPS and the EPS with dust there is a difference of ~ 0.2 for both colors. This difference can be easily explained since the colors in the plots are all in the optical region, thus being all absorbed by dust, with more extinction for the bands at shorter wavelengths. A stronger difference would be observed in optical - near IR colors, since the near IR radiation is less absorbed by dust.

- the effect of dust is more evident in late-type galaxies, more rich of gas and dust; for the elliptical model, at the present age (all these models have been calculated from z=z_{for} to z=0, that is $t_G = 13.09$ Gyr) only a small amount of dust is still present (see for example the previous discussion, Sect. 5.6.1). Colors obtained using EPS with or without dust are in practice indistinguishable, while the differences increase going from early-type toward late-type galaxies;

- the effect of the metallicity is evident *but* not so remarkable: the same trend is followed by the theoretical colors, for both cases with fixed and not fixed metallicity, Figs. 5.8 and 5.10. This suggests that the our realistic model, where we simply took the chemical model as EPS input without artificial input hypothesis, well behave in reproducing the observations.

- the effect of the inclination of the disk component in the intermediate type models is obviously the same already discussed in Sect. 5.6.1: the absorption due to dust is more spectacular when the galaxies are observed edge-on.

5.8 Evolutionary and Cosmological Corrections

In this section we want to present some preliminary results obtained extending our colors and magnitudes to redshift z>0 and comparing our models with some available observational data. When we consider a source observed at redshift z, we need to take into account that the photon is observed at a wavelength λ_0, but it was emitted by the source at a wavelength λ_e, and these two are related by:

$$\lambda_e = \lambda_0/(1+z). \tag{5.8.1}$$

A source that has an apparent magnitude m, observed through a photometric pass-band, is related to its absolute magnitude M, in the emitted-frame pass-band, and to the K-correction, K_{corr}, in the following way:

$$m = M + DM + K_{corr}, \tag{5.8.2}$$

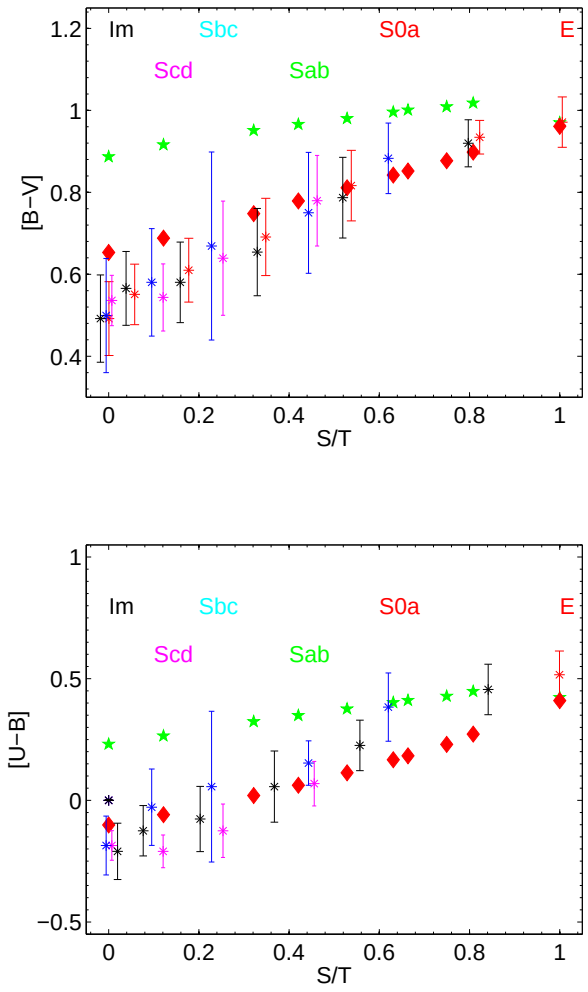

Figure 5.10: As in Fig. 5.8, but here the metallicity of the models is *not fixed* as in Fig. 5.8 (see the text for more details about this point).

where DM is the distance modulus, defined by

$$DM = 5log_{10}\left(\frac{D_L(z)}{10pc}\right), \tag{5.8.3}$$

being $D_L(z)$ the luminosity distance and $1pc = 3.086 \times 10^{18} cm$.

If the source is at redshift z, then its luminosity is related to its spectral density flux (energy per unit time per unit area per unit wavelength) by

$$L(\lambda_e) = 4\pi(1+z)D_L^2 f(\lambda_0), \tag{5.8.4}$$

where $f(\lambda_0)$ is the monochromatic flux of a galaxy (for all the details about the

flux in the calculation of magnitudes and colors see Chap. 2). The K-correction is defined as:

$$K_{corr} = 2.5log_{10}(1+z) + 2.5log_{10}\left[\frac{L(\lambda_0)}{L(\lambda_e)}\right]. \tag{5.8.5}$$

or by the equivalent formula in frequency:

$$K_{corr} = -2.5log_{10}(1+z) + 2.5log_{10}\left[\frac{L(\nu_0)}{L(\nu_e)}\right] \tag{5.8.6}$$

In order to take a fair comparison between the samples at different redshifts, we must correct the photometric properties of our observed galaxies (magnitudes, colors, etc.) into rest-frame quantities by applying K-corrections. Moreover, we must also correct these rest-frame quantities for the expected evolutionary changes over the redshift range studied. These evolutionary corrections are performed adopting our modelled galaxies of different morphological types (elliptical, intermediate types, disk) presented in Sect. 5.6.2 for the galaxy spectral energy distribution (SED) and its evolution with redshift. The K- and E-corrections are generated taking advantage of the SEDs calculated with the stellar EPS technique. In this way we can recover the evolution of the absolute magnitudes, colors and luminosities as a function of the redshift z, including the effect of the K- and E-corrections on the SED of our model galaxies.

For galaxies, the cosmological $K(z)$ and evolutionary $E(z)$ corrections are conventionally given in terms of magnitude differences:

$$K(z) = M(z,t_0) - M(0,t_0), \tag{5.8.7}$$

$$E(z) = M(z,t_z) - M(z,t_0), \tag{5.8.8}$$

where $M(0,t_0)$ is the absolute magnitude in a pass-band derived from the *rest frame* spectrum of the galaxy at the current time, $M(z,t_0)$ is the absolute magnitude derived from the spectrum of the galaxy *at the current time but redshifted at* z, and $M(z,t_z)$ is the absolute magnitude obtained from the spectrum of the galaxy *at time* t_z *and redshifted at* z.

The absolute magnitude, $M(z)$, in some broadband filter and at redshift z, is given by:

$$M(z) = -2.5\log L(z,t(z)), \tag{5.8.9}$$

and, passing to apparent magnitudes,

$$m(z) = M(z) + E(z) + K(z) + DM(z). \tag{5.8.10}$$

Obviously, the relation between the cosmic time t and redshift z, $t(z)$, of a stellar population formed at a given initial redshift z_f, depends on the cosmology considered and the parameters adopted. Since we will simply check our SEDs with the luminosities of the Takeuchi et al. (2010) database (T. T. Takeuchi - provate communication 2012), it is useful to remind how to get the luminosities back from the apparent AB, ST and Vega magnitudes. We have that the luminosity in a pass-band is:

$$L(\nu_0)\,\Delta\nu_0 = L(\lambda_0)\,\Delta\lambda_0 = 10^{0.4K(z)} 4\pi D_L^2(z) \cdot 10^{-0.4(m_{AB}+48.60)} \Delta\nu_0 \qquad (5.8.11)$$

since $\nu_0 \cdot f_{\nu_0} = \lambda_0 \cdot f_{\lambda_0}$, $\nu_0 \cdot f_{\nu_0} = \nu_e L(\nu_e)/(4\pi D_L^2(z))$ and $\lambda_0 \cdot f_{\lambda_0} = \lambda_e L(\lambda_e)/(4\pi D_L^2(z))$. $\Delta\nu_0$ and $\Delta\lambda_0$ are the integrals of the filter over the pass-band. A similar equation holds for Vega and ST system, just using the correct photometric constants and remembering that from ST and VEGA we get a monochromatic flux for Angstrom and not for Hz. The database by Takeuchi et al. (2010) in particular is available in monochromatic fluxes normalized to the pivotal wavelength and not corrected for E(z) and K(z). That is, simply:

$$\nu_e L(\nu_e) = 4\pi D_L^2(z)\, f(\nu_0)\, \nu_0 \qquad (5.8.12)$$

when required, we will stick to their observed quantity, without introducing the E and K-corrections.

5.9 Comparison with the observations

Huge surveys, from earth or space, allow nowadays to obtain a big amount of data at different redshifts and in different wavelengths, from the UV to the FIR. The main characteristic of these deep photometric surveys detecting a large number of galaxies is that a significant fraction of the detected objects appear as a point source. They can nor be easily distinguished from single stars, neither easily classified from a morphological point of view. It follows that the photometric study of their properties is crucial, also in order to produce some morphological classification. In this thesis, first we took into account two *deep catalogues*, COSMOS e GOODS, over which Tantalo et al. (2010) selected an extended sample of early type galaxies. For more details about these surveys see Chap. 2. This morphological selection can be done with an automatic pipeline able to separate the objects by means of their bi-dimensional distribution of the light: this is the case of the first catalogue COSMOS. In the GOODS database, however, it is possible to select in a more appropriate way by means of a correlation between a catalogue of spectroscopic and photometric redshifts and a morphological catalogue. For all the details about the GOODS and COSMOS samples see Cassarà (2008), Tantalo et al. (2010). In Figs. 5.11 and 5.12 the selected

COSMOS sample is represented (**bottom panels**), where we distinguishes Early-Type galaxies by means of a parameter T_{phot} which for the galaxies of interest is $T_{phot} \leq 1.1$ (Tantalo et al. 2010). In Figs. 5.13, 5.14 and 5.15 (**bottom panels**) we show the sample of early-type galaxies obtained from the GOODS survey, where ellipticals have been selected with a cross-correlation between various catalogues. In particular Early-Type Galaxies with photometric estimate of the redshift are represented in a different way (blue filled circles) than the objects for which there is a spectroscopic estimate (light blue empty circles).

In Figs. 5.11 and 5.12, **upper panels**, we represent the evolution with the redshift of the COSMOS colors $B_J - r^+$ e $K_S - r^+$ for our models of galaxies of different morphological types. We represent three cases, in order to take into account the whole range of morphological types: (1) an elliptical galaxy, for which two masses $10^{10} M_\odot$ and $10^{12} M_\odot$ have been calculated, since the selected data sample is made by early type galaxies: (2) an Sab model, thus characterized by disk and bulge in significant fraction, with total mass $10^{11} M_\odot$ and, finally, (3) a disk galaxy (Sd model) representing the extreme case with no bulge contribution. We also represented the evolution of the colors with (continuous lines) and without dust contribution (dashed lines). The agreement with the data for the elliptical galaxy models is good, at least until $z \sim 1 - 1.5$. It is first of all interesting to compare our models with the ones by Tantalo et al. (2010), that have been obtained with a different technique and from chemo-dynamical n-body simulations, by adding the contribution of all the star particles. In the redshift interval $0 < z < 1$, where most of the Early Type galaxies is concentrated, our color presents a better agreement with the observational data, respect to the model n-body based. The reason for this can be that these n-body simulations have not been calculated with a number of particles large enough. This lack of a thin mass resolution produces star particles that are like small dwarf-galaxies, more than small clusters as it would be desirable. For a statistical effect, every time that one of the gas particles is converted into stars, in practice we have a huge amount of newly born stars. The ultimate effect is that there is often a not negligible contribution to the total integrated light due to young stars and that tends to keep the colors bluer.
In our simulations, the galactic wind, stops abruptly the process of star formation and therefore the galaxy evolves almost passively from the redshift of the wind $z = z_{twind}$ until $z = 0$. The lack of young objects makes our colors redder than in Tantalo et al. (2010).

For intermediate-high redshift $1 < z < 3$, the difference between our colors and n-body EPS colors is significant. We can notice as our colors, much redder, in particular for the most massive galaxy $10^{12} M_\odot$ extend toward the region with the blue circles representing ellipticals. This interval, however, is delicate for our models because in the chemical simulations supporting the EPS code, the galactic wind starting at $z \sim 3$ is an instantaneous process emptying the galaxy of gas; a more gradual process as we expect to happen in real galaxies would be more suitable allowing to avoid fluctuations in the calculated color due to the discontinuity in the evolution of the gas mass. For redshift higher than $z \sim 3$, about corresponding to the onset of the galactic wind, we have no data to test the agreement between observations and theoretical colors. We can notice, however, the effect of the dust, by comparing the dashed (without dust) and continuous lines (with dust). Dust absorbs stellar

radiation stronger in the band B_J than r^+. Both magnitudes grow, but, since the B_J band is more absorbed, the color becomes redder. As expected the color by Tantalo et al. (2010) is bluer, similar to our color dust-free.
In the Figs. 5.13, 5.14 and 5.15 we represent the fit of our models with the GOODS data. Again in the lower panels we see the colors from n-body simulations plus adapted EPS technique. Again, the agreement of our colors with the simulations is quite good, at least up to the redshift where the data are available, about $z \sim 1.5$. The irregular behaviour of the colors after the onset of the galactic wind is due to the approximated treatment of the wind, as already discussed and also to a grid of galaxy models at varying the redshift that should be more refined in z. In these colors it is possible to see again the difference between results obtained with dust-free models and dusty models.

Finally we can analyze the behaviour of the colors for intermediate type and disk models. The results for COSMOS are quite interesting: the colors tend to stay in the region occupied by the yellow points, exactly where there are not ellipticals. In particular for the $B_J - r^+$ the result is good with a clearly different path in the color-redshift plane followed by the different morphological types. In the $K_S - r^+$-redshift plane, again the disk pattern develops in the region of the yellow dots, while the intermediate type models moves in between the two extreme cases. For the GOODS data we have just ellipticals and we can not say anything on the other morphological types, even if it can be noticed that in general they tend to stay bluer compared to the ellipticals, For $z > 2.5 - 3$ the colors overlap and the situation is more confused.

In Figs. 5.9 and 5.9, to conclude this section, we present a simple comparison of the luminosities of our models with a sample of data of 607 galaxies of various morphological type by Takeuchi et al. (2010) observed in different photometric systems. Of course this sample contains data of objects with a wide range of masses and morphological types and to properly study these data we would need to calculate many galaxy models and distribute them in mass. This is beyond the purposes of this thesis and we leave this to future work. For now we want to use the sample to simply check that our models are consistent with the luminosity range expected from the observations. At this purpose we plot the evolution of the monochromatic luminosity of our models for three massive galaxies (elliptical, intermediate and disk) of about 10^{12} $M_\odot$ as asymptotic mass. Since the redshift range of the data, from z=0 up to z=0.16, is small we do not expect for a single mass of our models a significant evolution in luminosity. This is well verified looking at Figs. 5.9 and 5.9. However, our average models stay in the range of the observations in all bands, with a range covered by the different inclinations of the disk. This effect is in particular relevant for the UV luminosities. For Akari, since dust does not absorb its own radiation there is no difference between different inclinations and the two lines, continuous

and dashed one, are coincident. As expected the elliptical galaxy model, present a low luminosity due to the low content of dust, while the dust-rich morphological types better agree with the observations.

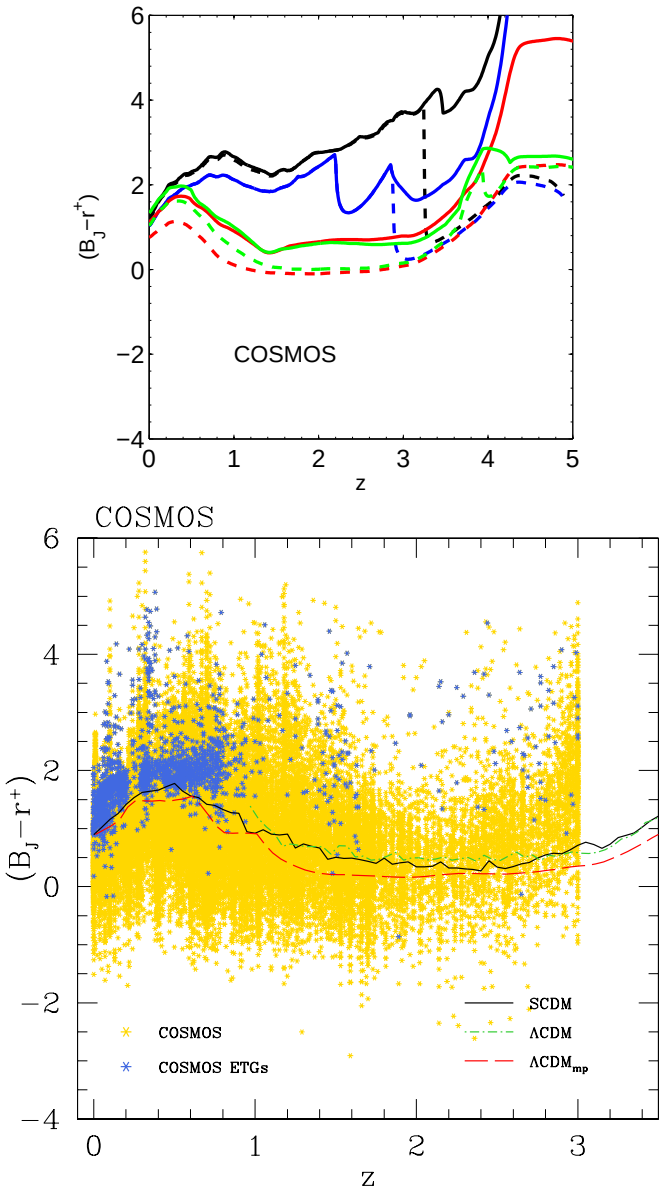

Figure 5.11: Cosmological evolution with the redshift for the $B_J - r^+$ of the survey COSMOS (both filters are pass-bands of the Subaru telescope). **Lower panel**: the sample of galaxies represented is taken from the catalogue of galaxies observed in the COSMOS survey and selected in Tantalo et al. (2010). The total sample of galaxies is represented in *yellow*, while the Early Type Galaxies are represented in *blu*. The evolution of three models by Tantalo et al. (2010) obtained with a EPS applied to n-body simulations are also represented for some cosmological scenarios. **Upper panel**: evolution of the color $B_J - r^+$ for three models presented in this thesis work or ad-hoc calculated for this redshift evolution, namely: (1) two elliptical galaxies with masses $10^{10} M_\odot$ and $10^{12} M_\odot$ and with the same choice of the input parameters as in Sect. 5.6.2 (black and blue lines); (2) an intermediate type model Sab of $10^{11} M_\odot$ (green line) and (3) a disk galaxy (Sd) of $10^{11} M_\odot$ (red line). In all the cases we show the evolution of the color taking into account our dusty EPS (continuous lines) and classical EPS without dust (dotted lines).

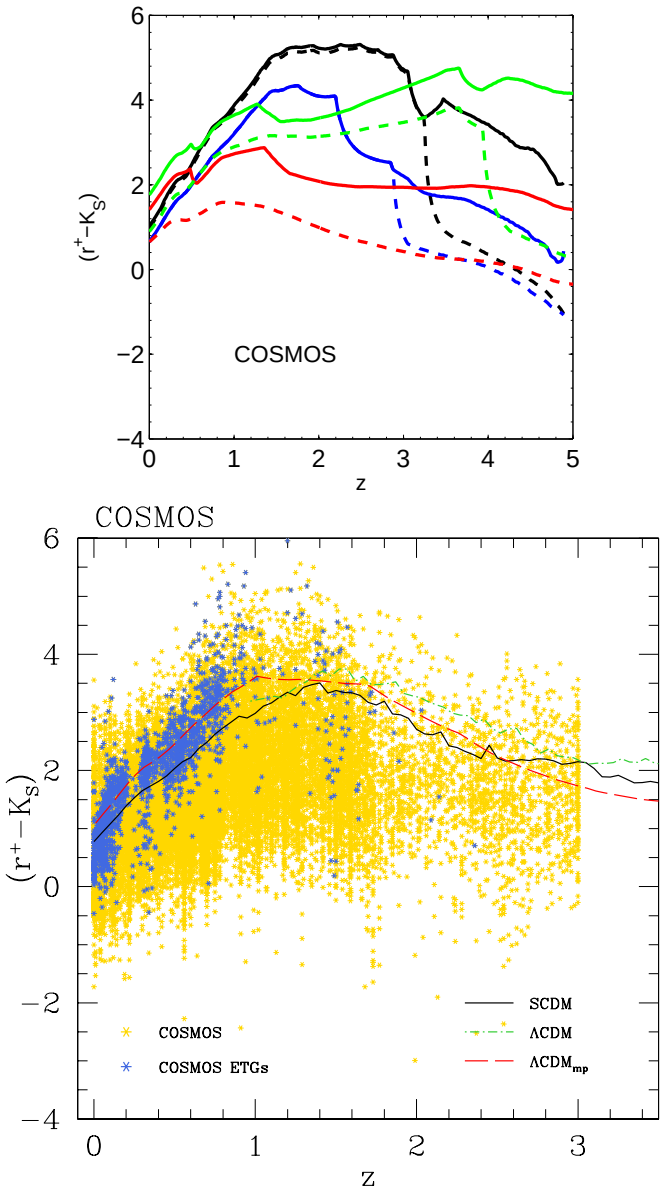

Figure 5.12: Cosmological evolution with the redshift for the $K_S - r^+$ of the survey COSMOS (r^+ is a filter of the Subaru telescope, while K_S is from the Kitt Peak national Observatory). **Lower panel**: the sample of galaxies represented is taken from the catalogue of galaxies observed in the COSMOS survey and selected in Tantalo et al. (2010). The total sample of galaxies is represented in *yellow*, while the Early Type Galaxies are represented in *blue*. The evolution of three models by Tantalo et al. (2010) obtained with a EPS applied to n-body simulations are also represented for some cosmological scenarios. **Upper panel**: evolution of the color $K_S - r^+$ for three models presented in this thesis work or ad-hoc calculated for this redshift evolution, namely: (1) two elliptical galaxies with masses $10^{10} M_\odot$ and $10^{12} M_\odot$ and with the same choice of the input parameters as in Sect. 5.6.2 (black and blue lines); (2) an intermediate type model Sab of $10^{11} M_\odot$ (green line) and (3) a disk galaxy (Sd) of $10^{11} M_\odot$ (red line). In all the cases we show the evolution of the color taking into account our dusty EPS (continuous lines) and classical EPS without dust (dotted lines).

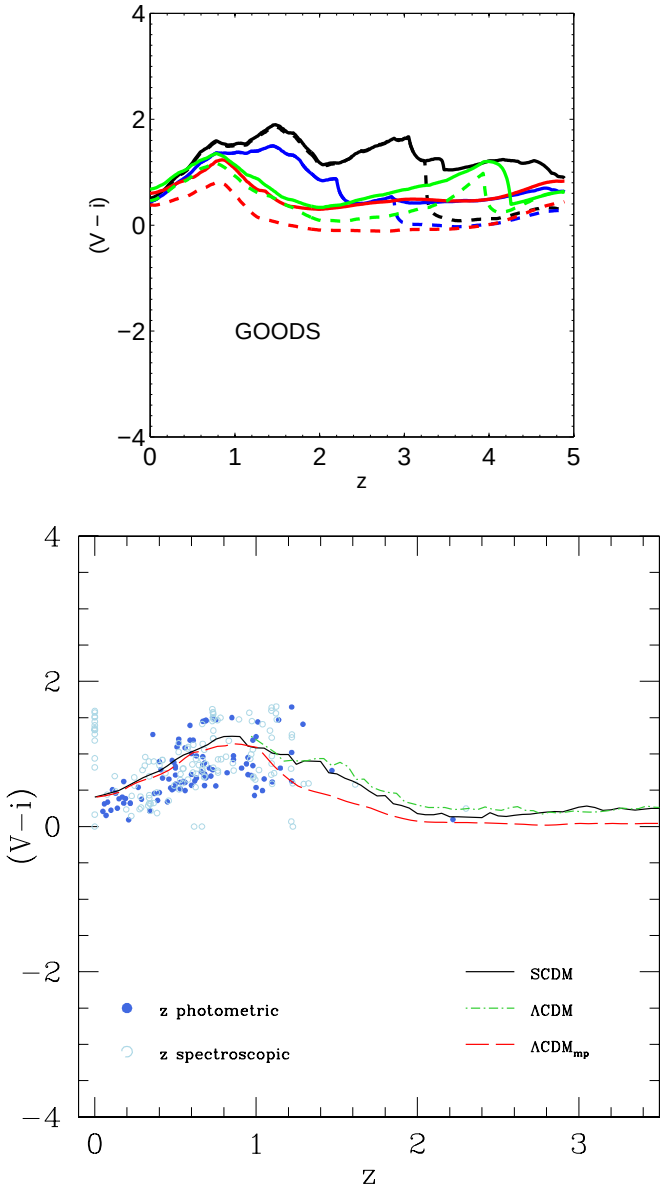

Figure 5.13: Cosmological evolution with the redshift for the color $V(F606W) - i(FTT5W)$ of the survey GOODS (bands ACS-HST). **Lower panel**: the sample of galaxies represented has been selected in Tantalo et al. (2010) and it is built with Early-Type Galaxies with photometric estimate of the redshift (blue filled circles) o spectroscopic estimate (light blue empty circles). The evolution of the color $V(F606W) - i(FTT5W)$ is shown for three EPS models from n-body simulations in different cosmological scenarios. See Tantalo et al. (2010) for more details. **Upper panel**: the evolution of the color $V(F606W) - i(FTT5W)$ for three models presented in this thesis work or ad-hoc calculated for this redshift evolution, namely: (1) two elliptical galaxies with masses $10^{10} M_{\odot}$ and $10^{12} M_{\odot}$ and with the same choice of the input parameters as in Sect. 5.6.2 (black and blue lines); (2) an intermediate type model Sab of $10^{11} M_{\odot}$ (green line) and (3) a disk galaxy (Sd) of $10^{11} M_{\odot}$ (red line). In all the cases we show the evolution of the color taking into account our dusty EPS (continuous lines) and classical EPS without dust (dotted lines).

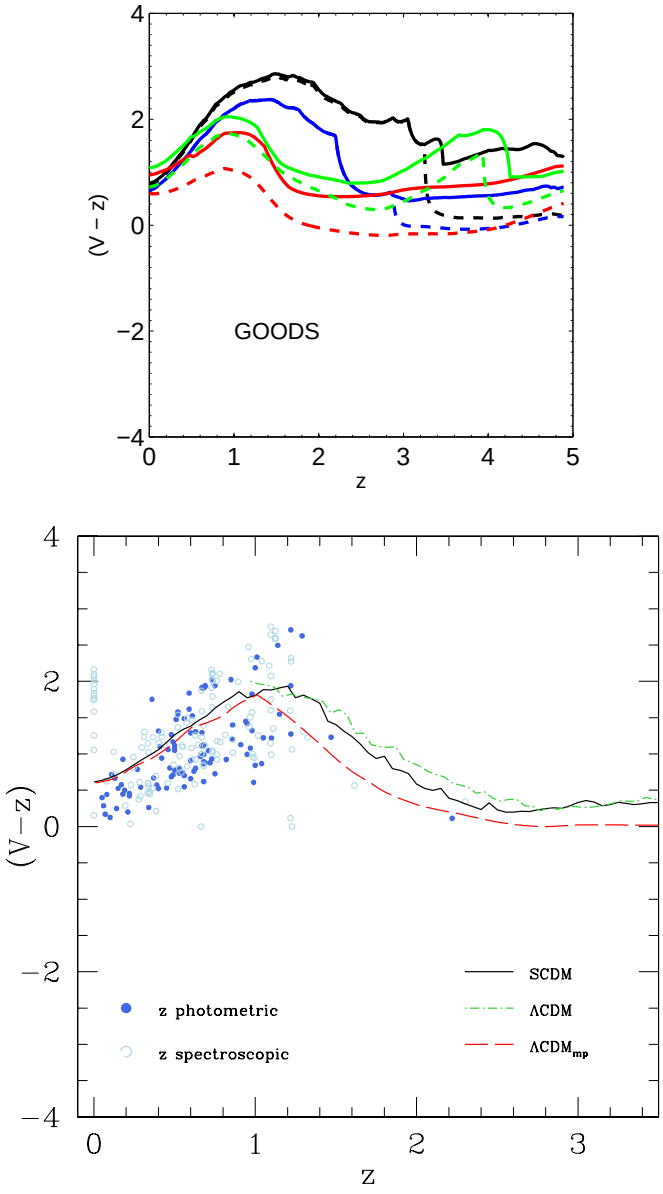

Figure 5.14: Cosmological evolution with the redshift for the color $V(F606W) - z(F850LP)$ of the survey GOODS (bands ACS-HST). **Lower panel**: the sample of galaxies represented has been selected in Tantalo et al. (2010) and it is built with Early-Type Galaxies with photometric estimate of the redshift (blue filled circles) o spectroscopic estimate (light blue empty circles). The evolution of the color $V(F606W) - z(F850LP)$ is shown for three EPS models from n-body simulations in different cosmological scenarios. See Tantalo et al. (2010) for more details. **Upper panel**: the evolution of the color $V(F606W) - z(F850LP)$ for three models presented in this thesis work or ad-hoc calculated for this redshift evolution, namely: (1) two elliptical galaxies with masses $10^{10} M_{\odot}$ and $10^{12} M_{\odot}$ and with the same choice of the input parameters as in Sect. 5.6.2 (black and blue lines); (2) an intermediate type model Sab of $10^{11} M_{\odot}$ (green line) and (3) a disk galaxy (Sd) of $10^{11} M_{\odot}$ (red line). In all the cases we show the evolution of the color taking into account our dusty EPS (continuous lines) and classical EPS without dust (dotted lines).

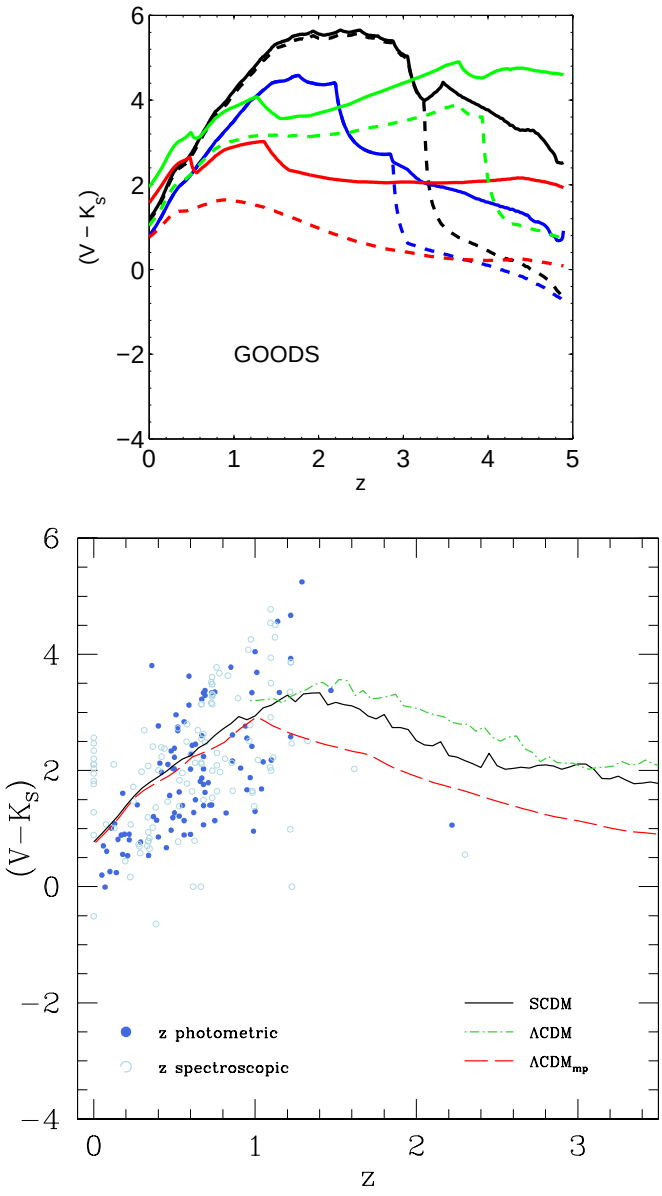

Figure 5.15: Cosmological evolution with the redshift for the color $V(F606W) - K_S$ of the survey GOODS (V band from ACS-HST, while K_S from VLT-ISAAC). **Lower panel**: the sample of galaxies represented has been selected in Tantalo et al. (2010) and it is built with Early-Type Galaxies with photometric estimate of the redshift (blue filled circles) o spectroscopic estimate (light blue empty circles). The evolution of the color $V(F606W) - K_S$ is shown for three EPS models from n-body simulations in different cosmological scenarios. See Tantalo et al. (2010) for more details. **Upper panel**: the evolution of the color $V(F606W) - K_S$ for three models presented in this thesis work or ad-hoc calculated for this redshift evolution, namely: (1) two elliptical galaxies with masses $10^{10} M_\odot$ and $10^{12} M_\odot$ and with the same choice of the input parameters as in Sect. 5.6.2 (black and blue lines); (2) an intermediate type model Sab of $10^{11} M_\odot$ (green line) and (3) a disk galaxy (Sd) of $10^{11} M_\odot$ (red line). In all the cases we show the evolution of the color taking into account our dusty EPS (continuous lines) and classical EPS without dust (dotted lines).

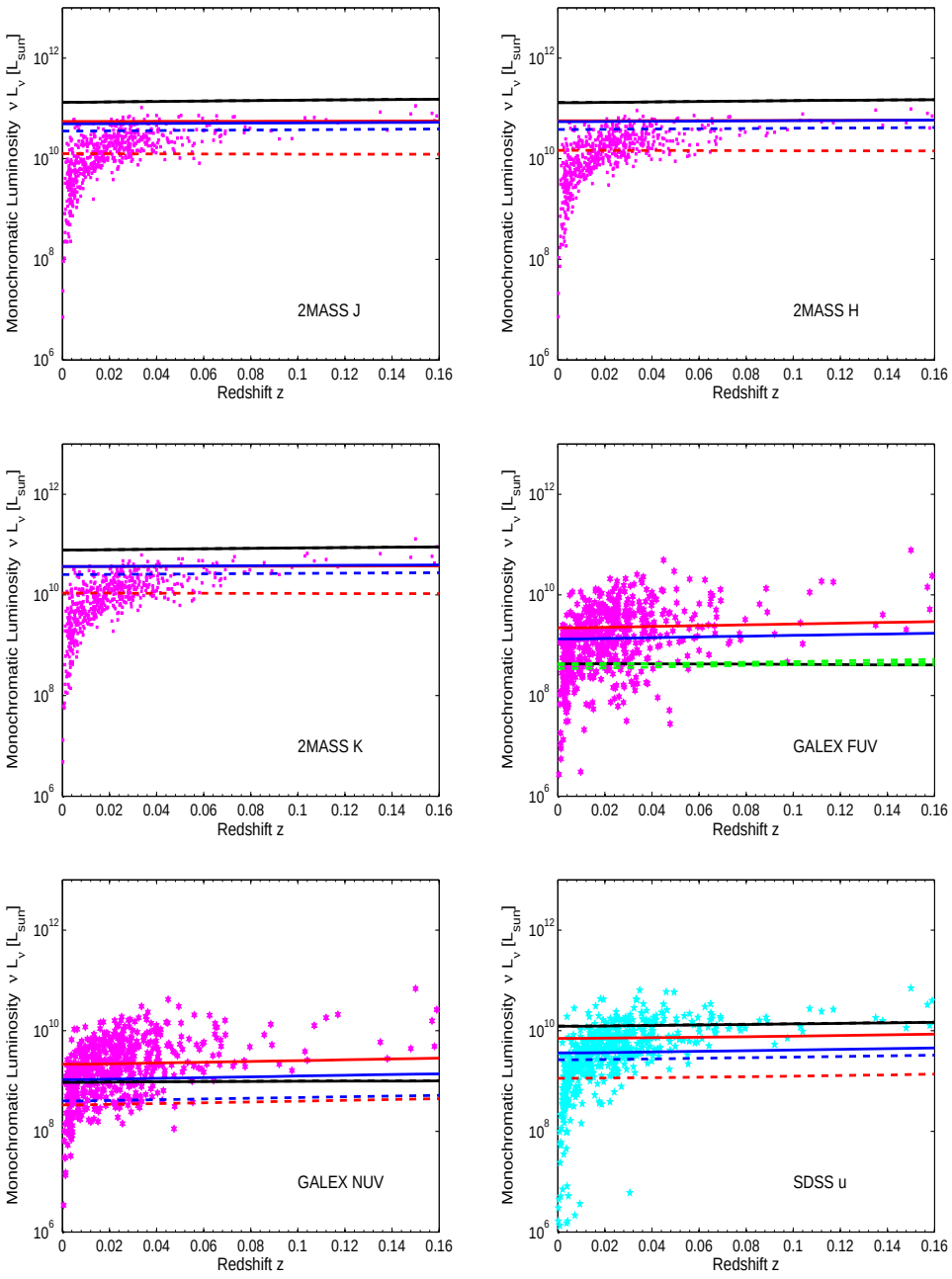

Figure 5.16: A comparison of the monochromatic luminosities $\nu \cdot L(\nu)$ of 3 models with asymptotic mass 10^{12} $M_{\odot}$ with a sample of of galaxies of various morphological types and masses by Takeuchi et al. (2010). We represent an elliptical galaxy (black lines), an intermediate type galaxy (blue lines) and a disk galaxy (red lines). Continuous lines represent the edge-on model, more affected by the ISM extinction, while dashed lines represent the face-on model. We represent the J, H and K bands of 2MASS, FUV and NUV from Galex and the u-band from SDSS.

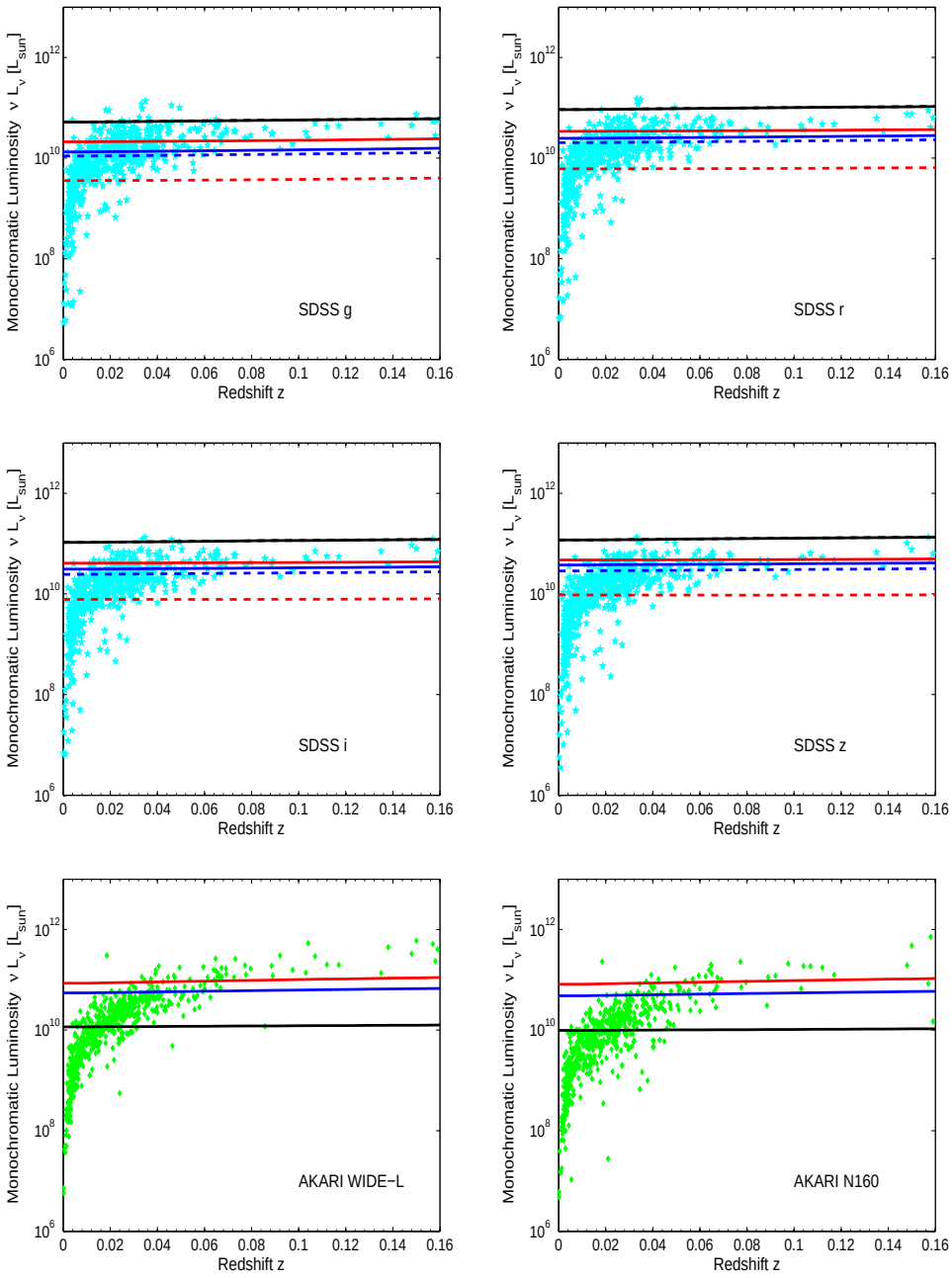

Figure 5.17: The same as in Fig. 5.9, but for different bands, namely g, r, i, z for SDSS and two AKARI bands WIDE-L and N160 in the far infrared.

Chapter 6

A chemical model for the evolution of dust in the ISM

[1]

6.1 Dust in spectro-photometric models

As shown in Chaps. 4 and 5, our galactic models consider the contribution of dust. For this reason we need to know, or to hypothesize in some way, two basic properties of the dust, that is: (1) the amount of dust in the ISM, namely we need the dust-to-gas ratio and (2) the relative proportion of carbonaceous grains (PAHs plus graphite grains) and silicates. This latter point is valid assuming, as we did, a classical ISM made by three components, *silicate* grains, *graphite* grains, and *polycyclic aromatic hydrocarbons* (PAHs), but of course more complex models of ISM could be built. As we have already seen in Chap. 5, a chemical code supporting the EPS is needed to describe the evolution of the SFR and the enrichment of the ISM in metals, in order to follow the mass and metallicity of the different generations of stars. Even if most of classical models are able to follow in detail the evolution of the abundances of the various elements in the ISM, still only few models are able to follow the evolution of the dusty component (Dwek 1998; Calura et al. 2008; Zhukovska et al. 2008), and in few cases they have been applied to population synthesis models with dust (Pipino et al. 2011). Once we do some hypothesis about the number of dust components

[1] This chapter of the thesis is based upon the papers *L. Piovan, C. Chiosi, E. Merlin, T. Grassi, R. Tantalo, U. Buonomo and L. P. Cassarà, "Formation and Evolution of the Dust in Galaxies. I. The Condensation Efficiencies.", 2011, submitted to A&A; "Formation and Evolution of the Dust in Galaxies. II. The Solar Neighbourhood"* and *"Formation and Evolution of the Dust in Galaxies. III. The Disk of the Milky Way"*. See for more details Piovan et al. (2011a), Piovan et al. (2011b) and Piovan et al. (2011c), submitted to A&A and in the process of revision.

included, in a more or less realistic way, we need to know how much dust should be put in the model galaxy.

One possibility, adopted in our simulations, is to simply assume that the amount of dust (formed with elements like C, Si, Mg, Fe) is proportional to the metallicity:

$$\delta = \delta_{\odot} \cdot Z/Z_{\odot} \tag{6.1.1}$$

where $\delta = M_d/M_H$ is the ratio between the mass in dust M_d and the mass of hydrogen M_H respectively. If m_i is the total mass of the i-th type of grain then $M_d = \sum_i m_i$, with m_i obtained integrating over the whole distribution of grains at varying their dimension. So, once known the amount of gas in the modelled galaxy (which is correlated to its age through the chemical model), the amount of dust in the ISM depends on δ.

For sub-solar metallicities, this assumption can rely upon the sequence MW-LMC-SMC decreasing in metallicity and with the same *dust-to-gas* ratio trend: models of the MW normally assume $\delta = 0.01$, for the Large Magellanic Cloud $\delta = 0.00288$, and for the Small Magellanic Cloud $\delta = 0.00184$. This three mean ratios are proportional (1: 1/5: 1/10), going from MW to SMC (Pei 1992), and this trend is correlated with the abundances of heavy elements into this three galaxies (1: 1/3: 1/8).

These simple relations about dust-to-gas ratio implies that in first approximation $\delta \propto Z$ and consequently $\delta = \delta_{\odot}(Z/Z_{\odot})$. Indeed, the most dust-rich galaxies are also the most metal-rich ones, because dust is made by metals. This relation is also in agreement with Dwek (1998), Dwek (2005), based on evolutionary models for the composition and abundance of gas and dust in the MW. Nevertheless, this remains just an approximation. The problem remains crucial for galaxies with metallicities higher than the MW (because,for example, of a strong star formation quickly enriching the ISM): in this case we do not have enough information in order to constrain the dust component. Even if as a first approximation one can assume that the dust content scale with the metallicity, what about the relative proportions of the various elements? Which amount should we consider for each component? It may happen that the relative proportion for the MW is conserved or not. The solution is to adopt or develop a chemical model, not only able to follow the enrichment and the distribution of the elements in mass into the gas, but *also into the dust*. In this way, the composition of dust and the chemical evolution of the galaxies will be connected. This model would be able then to constrain, for each dust component included, the amount and distribution of this component. In this chapter we will present in detail the effort that has been done in order to include a state-of-art description of the evolution and formation of dust in galaxies. This description should be then used to support the spectro-photometric models of galaxies with a more advanced chemical

interface. In particular, the Milky Way (MW) has been chosen as the ideal laboratory to study the dust cycle (Zhukovska et al. 2008) and its impact on the wider subject of galaxy formation, with the target to later (1) extend the dusty chemical model to ellipticals and (2) interface it to out spectro-photometric code. For obvious reasons, the MW provides plenty of observational data to which we can compare theoretical predictions, thus setting useful constraints on theoretical simulations and highlighting the role of the most important physical quantities leading the whole problem. Once this important step is accomplished, our modelling of the role played by dust could be extended to other galaxies such as spheroidals , high-z galaxies and QSOs.

Therefore, we simulated the formation, evolution and composition of dust in the MW, both locally in the Solar Ring and radially along the Galactic Disk. We built up a detailed dusty chemical model starting from the pioneering study by Dwek (1998) and taking into account the more recent ones by Zhukovska et al. (2008), Calura et al. (2008), Valiante et al. (2009), Gall et al. (2011a), Gall et al. (2011b), Mattsson (2011), Valiante et al. (2011), Kemper et al. (2011) and Dwek & Cherchneff (2011). The theoretical model we are building up stems from the basic one with infall by Chiosi (1980), however updated to the more recent version with radial flows of matter and presence of a central bar developed by Portinari & Chiosi (2000). The stellar yields of chemical elements in form of gas are those calculated by Portinari et al. (1998). The model follows the evolution of the abundances of a number of elements composing the ISM gas, includes the formation/destruction and evolution of dust and, finally, follows in detail also the abundances of those elements that are embedded in the dust grains. To this aims, the model makes use of the best prescriptions available in literature concerning dust accretion, destruction and condensation in the AGB winds and SNe explosions.

The main observational test will be the data on element depletion provided by the Solar Ring of the MW to which we will compare our results. At the same time, obviously, classical constraints about abundances in stars, SNa rate, surface densities, radial gradients and so on should be satisfied in a fully consistent picture.

6.2 Extending the chemical model equations

In classical models of chemical evolution, the Disk of the MW is subdivided in N concentric circular rings of a certain thickness Δr, where r is the galacto-centric distance, in the case of plane geometry or N concentric cylindrical shells if the third dimension is considered. Each ring or shell is identified by the mid radius r_k with $k = 1, ..., N$. In most cases, radial flows of interstellar gas and dust are neglected, so that each ring / shell evolves independently from the others. The physical quantity

used to describe the Disk is the surface mass density as a function of the radial coordinate r and time t: $\sigma(r_k, t)$ is the mass surface density at radius r_k and time t. Depending on the model, σ can refer to the ISM ($\sigma^{\mathcal{M}}$), in turn split into dust or gas (σ^D or σ^G respectively), to the stars (σ^*) or to the total mass (simply σ). At every radius r_k, the surface mass density is supposed to slowly grow by infall of either primordial or already enriched gas and to fetch at the present age t_G the mass density profile across the Galactic Disk for which an exponential profile is best suited to represent the surface mass density distribution: $\sigma(r_k, t_G) \propto \exp(-r_k/r_d)$, where r_d is the scale radius of the Galactic Disk, that is typically estimated of the order of $4 - 5$ kpc. Since the final density profile is *a priori* known, one may normalize to it the current total surface mass density of the ISM "$\mathcal{M}$" (sum of gas and dust),

$$\mathcal{M}(r_k, t) = \frac{\sigma^{\mathcal{M}}(r_k, t)}{\sigma(r_k, t_G)}. \tag{6.2.1}$$

Introducing the fractional mass of the i-th generic element we have:

$$\mathcal{M}_i(r_k, t) = \frac{\sigma_i^{\mathcal{M}}(r_k, t)}{\sigma(r_k, t_G)} = \chi_i(r_k, t)\,\mathcal{M}(r_k, t) \tag{6.2.2}$$

and therefore the fractional mass abundance $\chi_i(r_k, t) = \mathcal{M}_i(r_k, t)/\mathcal{M}(r_k, t)$, with $\sum_i \chi_i(r_k, t) = 1$.

Similar expressions can be derived for the dust (indicated by "D") and the gas (indicated by "G")

$$D(r_k, t) = \frac{\sigma^D(r_k, t)}{\sigma(r_k, t_G)} \tag{6.2.3}$$

$$G(r_k, t) = \frac{\sigma^G(r_k, t)}{\sigma(r_k, t_G)} \tag{6.2.4}$$

with $\sigma^{\mathcal{M}}(r_k, t) = \sigma^G(r_k, t) + \sigma^D(r_k, t)$ and $\sigma(r_k, t) = \sigma^{\mathcal{M}}(r_k, t) + \sigma^*(r_k, t)$, where $\sigma^*(r_k, t)$ is the surface mass density of stars. For single chemical elements we may write:

$$D_i(r_k, t) = \frac{\chi_i^D(r_k, t)\,\sigma_D(r_k, t)}{\sigma(r_k, t_G)} = \chi_i^D(r_k, t)\,D(r_k, t) \tag{6.2.5}$$

$$G_i(r_k, t) = \frac{\chi_i^G(r_k, t)\,\sigma_G(r_k, t)}{\sigma(r_k, t_G)} = \chi_i^G(r_k, t)\,G(r_k, t) \tag{6.2.6}$$

with $\sum_i \left[\chi_i^D(r_k, t) + \chi_i^G(r_k, t)\right] = 1$, from which it follows that $\sum_i \chi_i^D(r_k, t) \neq 1$ and $\sum_i \chi_i^G(r_k, t) \neq 1$.

The fundamental equation describing the evolution of the ISM in absence of radial flows of matter between contiguous shells (Portinari & Chiosi 2000) and processes of dust accretion/destruction (Dwek 1998) is:

$$\begin{aligned}\frac{d}{dt}\mathcal{M}_i\left(r_k,t\right) &= -\chi_i\left(r_k,t\right)\psi\left(r_k,t\right)+\int_{M_l}^{M_u}\psi\left(r_k,t-\tau_M\right)R_i\left(M\right)\phi\left(M\right)dM \\ &+ \left[\frac{d}{dt}\mathcal{M}_i\left(r_K,t\right)\right]_{inf} \end{aligned} \tag{6.2.7}$$

where $\phi\left(M\right)$ is the IMF and M_l and M_u are the lower and upper limits for the stellar masses, $\psi\left(r_k,t-\tau_M\right)$ is the star formation rate (SFR) at the radius r_k and at the time $t'=t-\tau_M$, $R_i\left(M\right)=E_{iM}/M$ (Portinari et al. 1998) is the fraction of a star of initial mass M ejected back in form of the chemical species i. The three terms at the r.h.s. represent the depletion of the ISM due to star formation, its increase by stellar ejecta, and the increase by infall of external gas (either primordial or already enriched).

Adding supernovae and radial flows. Type Ia supernovae originate in binary systems and have a fundamental role, in particular concerning the iron enrichment. The supernovae rate and the adopted formalism are the ones of Greggio & Renzini (1983) and the formulation of equation describing chemical evolution of the ISM is modified following Matteucci & Greggio (1986). The contribution of single stars, corresponding to a fraction $(1-A)$ of the total, is separated from the contribution of binary system, a fraction A of the total. Inserting the contribution of type Ia supernovae and integrating in time, instead that in mass, the equation for the evolution of the i-th component of the ISM is,

$$\begin{aligned}\frac{d}{dt}\mathcal{M}_i\left(r_k,t\right) = -\chi_i\psi + + \int_0^{t-\tau_{M_{B,l}}}\psi\left[\phi\left(M\right)R_i\cdot\left(-\frac{dM}{d\tau_M}\right)\right]_{M(\tau)}dt' + (1-A)\cdot \\ \cdot\int_{t-\tau_{M_{B,l}}}^{t-\tau_{M_{B,u}}}\psi\left[\phi R_i\cdot\left(-\frac{dM}{d\tau_M}\right)\right]_{M(\tau)}dt' + \int_{t-\tau_{M_{B,u}}}^{t-\tau_{M_u}}\psi\left[\phi R_i\cdot\left(-\frac{dM}{d\tau_M}\right)\right]_{M(\tau)}dt' + \\ + A\int_{t-\tau_{M_{1,min}}}^{t-\tau_{M_{1,max}}}\psi\left[f(M_1)\,R_{i,1}\cdot\left(-\frac{dM_1}{d\tau_{M_1}}\right)\right]_{M_1(\tau)}dt' + R_{SNI}\cdot E_{SNI,i} + \\ + \left[\frac{d}{dt}\mathcal{M}_i\left(r_k,t\right)\right]_{inf} - \left[\frac{d}{dt}\mathcal{M}_i\left(r_k,t\right)\right]_{out} + \left[\frac{d}{dt}\mathcal{M}_i\left(r_k,t\right)\right]_{rf}\end{aligned} \tag{6.2.8}$$

where $\psi=\psi\left(r_k,t'\right)$, $\phi=\phi\left(M\right)$, $\chi=\chi_i\left(r_k,t\right)$, $R_i=R_i\left(M\right)$, $R_{i,1}=R_i\left(M_1\right)$ and $M\left(t-t'\right)=M\left(\tau\right)$. The first term at the r.h.s. is as usual the one describing the depletion of interstellar material because of the process of star formation and it depends from the star formation rate and from the abundance of the i-th element considered. The next three terms represent the contribution of single stars to the

enrichment of the i-th element. The fifth term is the contribution of the primary star in a binary system (assumed to be independent from the secondary star as far as it concerns the chemical yields). The sixth term is the contribution of type Ia SNe. Finally, the last three terms are the infall rate of external gas, the outflow rate of matter due for example to the onset of galactic winds powered by supernovæ explosions, and the radial flows of gas that determine the ISM exchange between contiguous shells (Portinari & Chiosi 2000), respectively. Furthermore, $f(M_1)$ is the distribution function of the mass of the primary star M_1 in a binary system, between $M_{1,min} = M_{B,l}/2$ and $M_{1,max} = M_{B,u}$, where $M_{B,l}$ and $M_{B,u}$ are the lower and upper limit of the binary systems assumed respectively $3M_\odot$ and $12M_\odot$. R_{SNI} is the rate of type Ia SNe and $E_{SNI,i}$ their ejecta of the i-th chemical species. $M(\tau) = M(t - t')$ is the mass of a star of lifetime τ, born at t'. It is worth noticing that various quantities depend on the metallicity $Z(t)$ as well as on M: $M(\tau) = M(t - t') = M(t - t', Z(t - t'))$ and $R_i(M) = R_i(M, Z(t - t'))$ as stellar lifetimes and ejecta depend on metallicity. $R_i(M)$ are calculated on the base of the detailed stellar yields from Portinari et al. (1998) and keep track of finite stellar lifetimes (no instantaneous recycling approximation). Eqs. 6.2.8 govern the evolution of the ISM.

Separating gas from dust. For our purposes we need to formulate the equations governing the evolution of the dust in the ISM. Separating the ISM in gas and dust, the equations governing the evolution of the generic elemental species i in the dust are

$$\begin{aligned}
\frac{d}{dt}D_i(r_k,t) = &-\chi_i^D\psi + \int_0^{t-\tau_{M_{B,l}}} \psi\left[\phi\delta_{c,i}^w R_i\cdot\left(-\frac{dM}{d\tau_M}\right)\right]_{M(\tau)} dt' + \\
&+ (1-A)\int_{t-\tau_{M_{B,l}}}^{t-\tau_{M_{SNe}}} \psi\left[\phi\delta_{c,i}^w R_i\cdot\left(-\frac{dM}{d\tau_M}\right)\right]_{M(\tau)} dt' + (1-A)\cdot \\
&\cdot\int_{t-\tau_{M_{SNe}}}^{t-\tau_{M_{B,u}}} \psi\left[\phi\delta_{c,i}^{II} R_i\cdot\left(-\frac{dM}{d\tau_M}\right)\right]_{M(\tau)} dt' + \int_{t-\tau_{M_{B,u}}}^{t-\tau_{M_u}} \psi\left[\phi\delta_{c,i}^{II} R_i\cdot\left(-\frac{dM}{d\tau_M}\right)\right]_{M(\tau)} dt' + \\
&+ A\int_{t-\tau_{M_{SNe}}}^{t-\tau_{M_{1,max}}} \psi\left[f(M_1)\,\delta_{c,i}^{II} R_{i,1}\cdot\left(-\frac{dM_1}{d\tau_{M_1}}\right)\right]_{M(\tau)} dt' + \\
&+ A\int_{t-\tau_{M_{1,min}}}^{t-\tau_{M_{SNe}}} \psi\left[f(M_1)\,\delta_{c,i}^{w} R_{i,1}\cdot\left(-\frac{dM_1}{d\tau_{M_1}}\right)\right]_{M(\tau)} dt' + R_{SNI}E_{SNI,i}\delta_{c,i}^I + \\
&- \left[\frac{d}{dt}D_i(r_k,t)\right]_{out} + \left[\frac{d}{dt}D_i(r_k,t)\right]_{rf} + \left[\frac{d}{dt}D_i(r_k,t)\right]_{accr} - \left[\frac{d}{dt}D_i(r_k,t)\right]_{SN}
\end{aligned} \tag{6.2.9}$$

where $\chi_i^D = \chi_i^D(r_k, t)$. The first term at the r.h.s. of Eq. 6.2.9 is the depletion of dust because of star formation that consumes both gas and dust (uniformly mixed in the ISM). The second term is the contribution by stellar winds from low mass stars to the enrichment of the i-th component of the dust. Following Dwek (1998), we introduce the so-called condensation coefficients $\delta_{c,i}^w$ that determines the fraction of material

in stellar winds that goes into dust with respect to that in gas (local condensation). The third term is the contribution by stars not belonging to binary systems and not going into type II SNe (the same coefficients $\delta^w_{c,i}$ are used). The fourth term is the contribution by stars not belonging to binary systems, but going into type II SNe. For the condensation efficiency in the ejecta of type II SNe we introduce the coefficients $\delta^{II}_{c,i}$, the analog of $\delta^w_{c,i}$. The possible choices for these coefficients are discussed in the following of the chapter. The fifth term is the contribution of massive stars going into type II SNe. The sixth and seventh term represent the contribution by the primary star of a binary system, distinguishing between those becoming type II SNe from those failing this stage and using in each situation the correct coefficients. The eighth term is the contribution of type Ia SNe, where again we introduced the condensation coefficients $\delta^I_{c,i}$ to describe the mass fraction of the ejecta going into dust. The last four terms describe: (1) the outflow of dust due to galactic winds (in the case of disk galaxies this term can be set to zero); (2) the radial flows of matter between contiguous shells; (3) the accretion term describing the accretion of grain onto bigger particles in cold clouds; (4) the destruction term taking into account the effect of the shocks of SNe on grains, obviously giving a negative contribution. The infall term in the case of dust can be neglected because we can safely assume that the material entering the galaxy is made by gas only without a solid dust component mixed to it.

Finally, from the equation for $D_i(r_k,t)$ we can get the equation describing the evolution of the gaseous component $G_i(r_k,t)$, where $G_i(r_k,t) = \mathcal{M}_i(r_k,t) - D_i(r_k,t)$:

$$\begin{aligned}
\frac{d}{dt}G_i(r_k,t) = &-\chi_{G,i}\psi + (1-A)\int_{t-\tau_{M_{B,l}}}^{t-\tau_{M_{SNe}}} \psi\left[\phi\left(1-\delta^w_{c,i}\right)R_i\cdot\left(-\frac{dM}{d\tau_M}\right)\right]_{M(\tau)}dt' + \\
&+ (1-A)\int_{t-\tau_{M_{SNe}}}^{t-\tau_{M_{B,u}}} \psi\left[\phi\left(1-\delta^{II}_{c,i}\right)R_i\cdot\left(-\frac{dM}{d\tau_M}\right)\right]_{M(\tau)}dt' + \\
&+ \int_{0}^{t-\tau_{M_{B,l}}} \psi\left[\phi\left(1-\delta^w_{c,i}\right)R_i\cdot\left(-\frac{dM}{d\tau_M}\right)\right]_{M(\tau)}dt' + \\
&+ \int_{t-\tau_{M_{B,u}}}^{t-\tau_{M_u}} \psi\left[\phi(M)\left(1-\delta^{II}_{c,i}\right)R_i\cdot\left(-\frac{dM}{d\tau_M}\right)\right]_{M(\tau)}dt' + \\
&+ A\int_{t-\tau_{M_{SNe}}}^{t-\tau_{M_{1,max}}} \psi\left[f(M_1)\left(1-\delta^{II}_{c,i}\right)R_{i,1}\cdot\left(-\frac{dM_1}{d\tau_{M_1}}\right)\right]_{M(\tau)}dt' + \\
&+ A\int_{t-\tau_{M_{1,min}}}^{t-\tau_{M_{SNe}}} \psi\left[f(M_1)\left(1-\delta^w_{c,i}\right)R_{i,1}\cdot\left(-\frac{dM_1}{d\tau_{M_1}}\right)\right]_{M(\tau)}dt' + \\
&+ R_{SNI}E_{SNI,i}\left(1-\delta^I_{c,i}\right) + \left[\frac{d}{dt}G_i(r_k,t)\right]_{inf} + \\
&- \left[\frac{d}{dt}G_i(r_k,t)\right]_{out} + \left[\frac{d}{dt}G_i(r_k,t)\right]_{rf} - \left[\frac{d}{dt}D_i(r_k,t)\right]_{accr} + \left[\frac{d}{dt}D_i(r_k,t)\right]_{SN}
\end{aligned} \tag{6.2.10}$$

where again the outflow term $-\left[\frac{d}{dt}G_i(r_k,t)\right]_{out}$ will be fixed to zero because we do not have galactic wind for spirals with continuous star formation. Since the primordial

material is likely dust-free we have $\left[\frac{d}{dt}\mathcal{M}_i\left(r,t\right)\right]_{in} = \left[\frac{d}{dt}G_i\left(r,t\right)\right]_{in}$.

It is worth noticing the following point: the stellar models, upon which are based our yields, predict that stars with mass higher than $6M_\odot$ go into SNe, whereas those with mass lower than $6M_\odot$ first become AGB stars and later White Dwarfs. We must therefore split the third and the fifth member of Eq. 6.2.8)in two parts, both in Eqs. 6.2.10 and 6.2.9, because the minimum mass dividing the intervals of AGB and/or SNe belongs to the mass interval $(3-12M_\odot)$ describing binary systems going into type Ia SNe[1].

To summarize. Indicating the contribution to the yields by stellar winds and type Ia and II SNe with the symbols $W_{i,D}\left(r_k,t\right)$, $W_{i,G}\left(r_k,t\right)$ and $W_{i,\mathcal{M}}\left(r_k,t\right)$ (they can easily be reconstructed by comparison) and neglecting the outflow term, Eqs. 6.2.8, 6.2.9 and 6.2.10)become:

$$\begin{aligned}\frac{d}{dt}\mathcal{M}_i\left(r_k,t\right) &= -\chi_i^{\mathcal{M}}\left(r_k,t\right)\psi\left(r_k,t\right) + +W_{i,\mathcal{M}}\left(r_k,t\right)\\ &+\left[\frac{d}{dt}\mathcal{M}_i\left(r_k,t\right)\right]_{rf}\end{aligned} \tag{6.2.11}$$

[1]For example in Eq. 6.2.9, using $\delta_{c,i}$ to indicate the generic condensation coefficient we have the following split:

$$\left(1-A\right)\int_{t-\tau_{M_{B,l}}}^{t-\tau_{M_{B,u}}}\psi\left[\phi\delta_{c,i}R_i\left(M\right)\left(-\frac{dM}{d\tau_M}\right)\right]_{M(\tau)}dt'$$

is divided into:

$$\begin{aligned}&\left(1-A\right)\int_{t-\tau_{M_{B,l}}}^{t-\tau_{M_{SNe}}}\psi\left[\phi\delta_{c,i}^{w}R_i\left(-\frac{dM}{d\tau_M}\right)\right]_{M(\tau)}dt'\\ &+\left(1-A\right)\int_{t-\tau_{M_{SNe}}}^{t-\tau_{M_{B,u}}}\psi\left[\phi\delta_{c,i}^{II}R_i\left(-\frac{dM}{d\tau_M}\right)\right]_{M(\tau)}dt'\end{aligned}$$

where M_{SNe} is the separation mass that tell us if we must use the condensation coefficients of stellar winds (condensation of dust in the envelopes of AGB stars) in the mass interval between $M_{B,l}$ and M_{SNe} or the condensation coefficients of supernovæ between M_{SNe} e $M_{B,u}$. In the same way:

$$A\int_{t-\tau_{M_{1,min}}}^{t-\tau_{M_{1,max}}}\psi\left[f(M_1)\,\delta_{c,i}R_{i,1}\left(-\frac{dM_1}{d\tau_{M_1}}\right)\right]_{M_1(\tau)}dt'$$

splits itself into:

$$\begin{aligned}&A\int_{t-\tau_{M_{SNe}}}^{t-\tau_{M_{1,max}}}\psi\left[f(M_1)\,\delta_{c,i}^{II}R_{i,1}\left(-\frac{dM_1}{d\tau_{M_1}}\right)\right]_{M(\tau)}dt'\\ &+A\int_{t-\tau_{M_{1,min}}}^{t-\tau_{M_{SNe}}}\psi\left[f(M_1)\,\delta_{c,i}^{w}R_{i,1}\left(-\frac{dM_1}{d\tau_{M_1}}\right)\right]_{M(\tau)}dt'.\end{aligned}$$

$$\frac{d}{dt}D_i\left(r_k,t\right) = -\chi_i^D\left(r_k,t\right)\psi\left(r_k,t\right) + +W_{i,G}\left(r_k,t\right) + \left[\frac{d}{dt}D_i\left(r_k,t\right)\right]_{accr} - \left[\frac{d}{dt}D_i\left(r_k,t\right)\right]_{SN} + \left[\frac{d}{dt}D_i\left(r_k,t\right)\right]_{rf} \quad (6.2.12)$$

$$\frac{d}{dt}G_i\left(r_k,t\right) = -\chi_{G,i}\left(r_k,t\right)\psi\left(r_k,t\right) + W_{i,G}\left(r_k,t\right) - \left[\frac{d}{dt}D_i\left(r_k,t\right)\right]_{accr} + \left[\frac{d}{dt}D_i\left(r_k,t\right)\right]_{SN} + \left[\frac{d}{dt}G_i\left(r_k,t\right)\right]_{inf} + \left[\frac{d}{dt}G_i\left(r_k,t\right)\right]_{rf}. \quad (6.2.13)$$

It is soon evident that the dust creation/destruction and the radial flows make the system of differential equations much more complicated than the original one by Talbot (1975) for a one-zone closed-box model. As the ISM is given by the sum of gas and dust, only two of these equations are required, furthermore Eq. 6.2.11 can be used only if gas and dust flow with the same velocity. To proceed further we must now specify the law of star formation, the IMF, the stellar ejecta and the various rates describing gas infall, dust accretion/destruction, and radial flows/bar effect. No details will be given about these ones. They are included into the model and they are mainly useful in order to reproduce the radial gradients of abundance in the MW. The reader should refer to Portinari & Chiosi (2000) for all the details.

6.3 The Star Formation Laws and Initial Mass Functions

Star Formation. The law of Star Formation (SF) is a key ingredient of any model of galaxy formation and evolution. Unfortunately it is poorly known, so that many prescriptions for the SF rate can be found in literature. We have considered several well known SF laws adopted for the MW (see Portinari & Chiosi (1999) for more details). A very popular prescription is the Schmidt (1959) law. In our formalism it becomes:

$$\Psi(r_k,t) = -\left[\frac{dG(r_k,t)}{dt}\right]_* = \nu\left[\frac{\sigma(r_k,t_G)}{\sigma(r_\odot,t_G)}\right]^{\kappa-1} G^\kappa(r_k,t) \quad (6.3.1)$$

where the normalization factor is $\sigma(r_\odot,t_G)^{-(\kappa-1)}$ and ν is in $[t^{-1}]$. Following Portinari & Chiosi (1999) we adopt $\kappa = 1.5$.

This simple dependence of the SFR can be complicated by including other physical effects. For instance, the SF suited to spiral galaxies such as the MW, may include the effect of gas compression by density waves (Roberts 1969; Shu et al. 1972; Wyse

& Silk 1989; Prantzos & Silk 1998) or gravitational instabilities (Wang & Silk 1994). We have:

$$\Psi(r_k,t) = \nu \left[\frac{r}{r_\odot}\right]^{-1} \left[\frac{\sigma(r_k,t_G)}{\sigma(r_\odot,t_G)}\right]^{\kappa-1} G^\kappa(r_k,t) \tag{6.3.2}$$

where ν is always in $[t^{-1}]$ and $k = 1$ (Kennicutt 1998; Portinari & Chiosi 1999). Another possibility is to describe the SF as a balance between cooling and heating processes, that is the gravitational settling of the gas onto the Disk and the energy injection from massive stars (Talbot 1975; Dopita 1985; Dopita & Ryder 1994). In our formalism, we have

$$\Psi(r_k,t) = \nu \left[\frac{\sigma^n(r_k,t)\,\sigma^{m-1}(r_k,t_G)}{\sigma(r_\odot,t_G)^{n+m-1}}\right] G^m(r_k,t) \tag{6.3.3}$$

where $n = 1/3$, $m = 5/3$ (Portinari & Chiosi 1999) and ν in $[t^{-1}]$. This formulation is similar to the original one by Talbot (1975) thus leading to similar results (Portinari et al. 1998).

Initial Mass Function. The same IMFs described in Sect. 1.1.4 are adopted in the chemical model with dust.

6.4 Growth dust grains in the ISM

Dust grains form by a number of physical processes (see below) and once in the ISM they may grow in mass by accreting a number of atoms or molecules. In the following we examine in some detail the accretion mechanisms for which two different models are proposed adapted from the literature.

6.4.1 The Dwek (1998) model or case A

Dwek (1998) view of grain growth can be summarized as follows. Let us consider an ISM whose dust component is formed by grains made of a single element i-th with mass $m_{gr,i}$. Let m_i be the mass of an atom (or molecule) of the element i-th in the gaseous phase. N_i is the number of atoms (molecules) of the element i-th locked up into the mono-composition grains that we are considering and $n_{gr,i}$ the density of grains of i-th type in the ISM, considered in this model as *a single phase*, without distinction between diffuse ISM and cold molecular clouds. Let now α_i be the sticking coefficient, telling us the probability that an atom (molecule) of the element i in the gaseous phase binds to the grains increasing the number of atoms/molecules on it. Finally $n_{gas,i}$ is the number density the gas made of atoms (molecules) of type i-th

and $\overline{v} = \left(\frac{8K_BT}{\pi m_i}\right)^{\frac{1}{2}}$ is the mean thermal velocity of the particles of the element i in the gaseous phase with respect to the dust grains. We get:

$$\frac{dN_i}{dt} = \alpha_i \pi a^2 n_{gr,i} n_{gas,i} \overline{v}\,. \tag{6.4.1}$$

Multiplying both members of the equation by the constant mass m_i, multiplying and dividing the second member by the mass of one grain $m_{gr,i}$, introducing the mean thermal velocity $\overline{v}$ and using the following relation [3] (Dwek 1998):

$$m_i n_{gas,i} = 2 m_H n_{H_2} \left(1 - \frac{\sigma_i^D}{\sigma_i^{\mathcal{M}}}\right) \tag{6.4.2}$$

where $\sigma_i^D\,(r,t)$ and $\sigma_i\,(r,t)$ are functions of position and time, we obtain:

$$\frac{d\sigma_i^D}{dt} = \frac{\sigma_i^D}{\tau_{i,0}} \left(1 - \frac{\sigma_i^D}{\sigma_i^{\mathcal{M}}}\right). \tag{6.4.3}$$

For the dimensional consistency of the equation, the multiplying quantity has the dimension of the inverse of a time indicated by $\tau_{i,0}$

$$\frac{1}{\tau_{i,0}} = 2 n_{H_2} \alpha_i \frac{\pi a^2}{A_i} \left(\frac{8K_BT}{\pi m_i}\right)^{\frac{1}{2}}\,. \tag{6.4.4}$$

It may be worth of interest to give an estimate of the involved timescale: by means of typical values of the involved quantities, Dwek (1998) obtains $\sim 3 \times 10^4$ yrs. It is possible now to define the accretion time scale of our i-th element onto the grains as:

$$\frac{1}{\tau_{i,accr}} = \frac{1}{\tau_{0,i}} \cdot \left(1 - \frac{\sigma_i^D}{\sigma_i^{\mathcal{M}}}\right) \tag{6.4.5}$$

that is the inverse of $\tau_{0,i}$ multiplied by the fraction of the i-th element in the gaseous phase. Again, we drop the dependence from r and t. Dwek (1998) adopting the ratio $\sigma_i^D/\sigma_i^{\mathcal{M}} \approx 0.7$ gets $\tau_{i,accr} \approx 10^5$ yrs which turns out to be significantly shorter than the lifetime of molecular clouds where accretion takes place. This lifetime is estimated to be of the order of $t_{MC} \sim 2 - 3 \times 10^6 - 10^7$ yrs. The lifetime of a molecular cloud is comparable to the lifetime of the most massive stars born in it. These stars indeed injecting great amounts of energy by stellar winds and SNæ explosions eventually disrupt the cloud. Similar estimates have been made in studies on the temporal evolution of dust in the ISM by Calura et al. (2008), $\sim 5 \cdot 10^7$ yrs, and Zhukovska et al. (2008), $\sim 10^7$ yrs, and are consistent with observational and

[3] The above relation says that the mass of the element i-th in the gaseous phase can be expressed by means of the density of the molecular clouds, i.e. the site in which the grains grow. $2 m_H n_{H_2}$ is the mass of the molecular cloud, $\left(1 - \sigma_i^D/\sigma_i^{\mathcal{M}}\right)$ is the fraction of the element i-th in the gaseous phase as a function of the abundance of the same element in the dust and ISM.

theoretical estimates of the lifetimes of molecular clouds (see for example Matzner (2002), Krumholz et al. (2006) and Blitz et al. (2007)). One may argue that we are comparing two different timescales, i.e. with $t_{i,accr} \ll t_{MC}$. However, inside molecular clouds there are many physical processes continuously stripping atoms and and molecules from the grains, like UV radiation and cosmic rays. The net effect of it could be that $\tau_{i,accr}$ is considerably lengthened (Dwek 1998), likely up to $6 \cdot 10^7$ yrs, so that $t_{i,accr} \simeq t_{MC}$. Furthermore, all the dust grains are in cold molecular clouds where the growing occurs. The simplest way to take this into account is to divide the above estimate for $t_{i,accr}$ by the fraction of dust in molecular clouds. The resulting accretion timescale would be $t_{i,accr} \sim 1 - 2 \times 10^8$ yrs.

There is another important point to consider on which indeed several studies of the ISM evolution are based: both the destruction timescale (driven by SNe explosions) and the accretion timescale $t_{i,accr}$ have the same dependence on the star formation rate ψ and surface mass density σ_i. SNæ rate can be expressed as $\tau_{i,snr} \propto \sigma/\psi$. The lower the star formation rate, the lower is the number of supernovae explosions and finally the longer the destruction time of grains due to shocks. We clearly expect $\tau_{i,accr}$ to vary over the evolutionary history of the Galaxy: Dwek (1998) divides the accretion timescale by σ^{MC}/σ and reasonably assumes that $\psi \propto \sigma^{MC}$. In this way, $\tau_{i,accr} \propto \sigma\psi$. Since both $\tau_{i,accr}$ and $\tau_{i,snr}$ have the same dependence from σ^{ISM}/ψ Dwek (1998) suggests that the ratio between the two timescales is constant: $\tau_{i,accr}/\tau_{i,snr} = 1/2$. If now we consider the accretion/destruction terms in Eq. 6.2.12 we have:

$$\begin{aligned} \left(\frac{d\sigma_i^D}{dt}\right)_{accr} + \left(\frac{d\sigma_i^D}{dt}\right)_{snr} &= \frac{\sigma_i^D}{\tau_{i,accr}} - \frac{\sigma_i^D}{\tau_{i,snr}} = \\ &= 2 \cdot \frac{\sigma_i^D}{\tau_{i,snr}} - \frac{\sigma_i^D}{\tau_{i,snr}} = \frac{\sigma_i^D}{\tau_{i,snr}} \,. \end{aligned} \tag{6.4.6}$$

The contribution of the creation/destruction terms is greatly simplified and the numerical solution of the differential equations describing the dust evolution becomes very simple. More refined is the solution adopted by Calura et al. (2008). In brief, (i) only $\tau_{0,i}$ is fixed and $\tau_{i,accr}$ remains an explicit function of the ratio σ_i^D/σ_i; (ii) no *a priori* correlation between $\tau_{i,accr}$ and $\tau_{i,snr}$ is supposed to exist, the two timescales are defined independently, and both plays a role in the σ_i^D evolution. In our model we adopt the same strategy.

6.4.2 The Zhukovska et al. (2008) model or case B

A step forward in modelling grain accretion has been made by Zhukovska et al. (2008). In brief: (i) grain accretion is tightly related to molecular clouds and a

multi-phase description of the ISM would be required; (ii) the evolution of chemical elements is calculated in presence of some typical dust compounds that are representative of the grain families growing inside the cold regions of the ISM or ejected by the stars, namely silicates, carbonaceous grains, iron grains, and silicon carbide. This model has two important advantages. First, it allows for different physical situations each of which implying different timescales for each elements and different relationships between $\tau_{i,accr}$ and $\tau_{i,snr}$ which are independent; second, accretion in cold regions is described in a realistic way; third, the model can be easily incorporated in a multi-phase description of the ISM to estimate the amounts of gas in the warm and cold phases.
Let us now examine some of the key points and basic equations of the model and how they are adapted to our description, where contrary to what made in Zhukovska et al. (2008) we track the evolution *abundances of single elements in dust* instead of *ad-hoc* families of dust grains.

The growth of the generic type of grains j is driven by the least abundant element indicated as element i (otherwise called the *key element*) among those forming the grain. All the other elements concurring to form the j-th compound adapt their abundances to that of the *key element*. For a mixture of accreting grains made of silicates (pyroxenes and olivines, i.e. magnesium-iron sulfates), carbonaceous and iron grains, the key elements are Mg, Si or Fe for silicates, depending on which has the lowest abundance, C for carbon grains, and Fe for iron grains. Most of these elements accrete some specific atomic or molecular species called *growth species*. The growth in mass of a single j-th grain type is:

$$\frac{dm_j}{dt} = S_j \alpha_j v_j^{gw} A_j^D m_H \frac{\nu_{i,j}^{gw}}{\nu_{i,j}^D} n_j^{gw} \tag{6.4.7}$$

where m_j is the mass of one grain of the j-th type, S_j is the surface area, α_j is the sticking coefficient, v_j^{gw} is the relative velocity of the accreting species with respect to the grain, $A_j^D m_{\rm H}$ is the mass of one atom (or molecule) that is accreting on the grain type j, n_j^{gw} is the number density of the growth species j, and finally $\nu_{i,j}^{gw}/\nu_{i,j}^D$ is the ratio between the number of atoms of the i-th key element in the growth species for the j-th dust type and the number of atoms of the element i we need to build one grain of dust type j.

After some substitutions and simplifications for which all the details can be found in Zhukovska et al. (2008), it comes out:

$$\frac{df_{i,j}}{dt} = \frac{1}{\tau_j^{gr}} f_{i,j} \left(1 - f_{i,j}\right) \tag{6.4.8}$$

where $f_{i,j} \propto \rho_j^D$ is the fraction of the key element i that is already condensed onto the dust type j, called degree of condensation. $1 - f_{i,j}$ is therefore the fraction of

the key element i still in the gaseous phase and available to form growth species for the j-th dust component. An explicit formula for τ_j^{gr} as a function of all the relevant quantities (Zhukovska et al. 2008, see Eq. 31) is:

$$\tau_j^{gr} = 46 \frac{(A_j^{gw})^{1/2} \nu_{i,j}^D}{A_j^D} \left(\frac{\rho_j^C}{3}\right) \left(\frac{10^3}{n_H}\right) \left(\frac{3.5 \cdot 10^{-5}}{\epsilon_{i,j}}\right) \mathrm{Myr}\,. \tag{6.4.9}$$

Integrating Eq. 6.4.8 with the initial conditions $f_{i,j} = f_{0,i,j}$ for $t = 0$ we get the final equation describing the evolution of the condensed fraction:

$$f_{i,j}\,(t) = \frac{f_{0,i,j} e^{t/\tau_j^{gr}}}{1 - f_{0,i,j} + f_{0,i,j} e^{t/\tau_j^{gr}}}\,. \tag{6.4.10}$$

As in real conditions the grain accretion takes place in cold MCs with a finite lifetime τ_{MC}, the above accretion time scale must be compared with τ_{MC}. As already discussed for model A of accretion, the molecular lifetime constrains the real time interval during which the exchange of matter between cold clouds and surrounding medium can happen. It is the interplay between the accretion/disruption timescales to determine if and how much material can be condensed inside the cloud before it dissolves into the surrounding ISM. If $f_{0,i,j}$ is the initial degree of condensation of the key element i of the grains j and the molecular cloud will be destroyed after a lifetime t we have that the effective amount of material that is given back to the ISM after the cloud dissolution is:

$$M_j^{MC}\,(t) = (f_{i,j}\,(t) - f_{0,i,j})\,\chi_{j,max}^D M_{MC} \tag{6.4.11}$$

where $f_{i,j}\,(t) - f_{0,i,j}$ is the fraction of key element condensed with respect to the initial condensation fraction, $\chi_{j,max}^D$ is the maximum possible fraction of the j-th dust type that can be formed in the molecular cloud and that would exist if all the material is condensed in dust type j. Multiplying by the mass of the cloud we get the mass of newly formed material M_j^{MC} returned to the ISM. The fraction $\chi_{j,max}^D$ is given by

$$\chi_{j,max}^D = \frac{A_j^D \epsilon_{i,j}}{(1 + 4\epsilon_{He})\,\nu_{i,j}^D} \tag{6.4.12}$$

as shown in the footnote below [4].

[4]The number density n_{H} of hydrogen atoms is given by $n_{\mathrm{H}} = \rho_{MC}/\left[(1 + 4\epsilon_{He})\,m_{\mathrm{H}}\right]$ which in turn follows from the series of equalities: $\rho_{MC} = m_{\mathrm{H}} n_{\mathrm{H}} + 4 m_{\mathrm{H}} n_{\mathrm{He}} = m_{\mathrm{H}} n_{\mathrm{H}} + 4 m_{\mathrm{H}} n_{\mathrm{H}} \epsilon_{\mathrm{He}} = m_{\mathrm{H}} n_{\mathrm{H}} (1 + 4\epsilon_{He})$, where $\epsilon_{He} = n_{\mathrm{He}}/n_{\mathrm{H}}$. The fraction $\chi_{j,d,max}$ is given by $\chi_{j,max}^D = \frac{\rho_{j,max}^D}{\rho_{MC}} = \frac{A_j^D m_{\mathrm{H}} (\epsilon_{i,j} n_{\mathrm{H}})}{\nu_{i,j}^D \cdot m_{\mathrm{H}} n_{\mathrm{H}} (1 + 4\epsilon_{He})} = \frac{A_j^D \epsilon_{i,j}}{(1 + 4\epsilon_{He}) \nu_{i,j}^D}$. The explanation is quite simple: dividing the number of atoms $\epsilon_{i,j} n_{\mathrm{H}}$ of the key element available in the molecular cloud by the number of atoms $\nu_{i,j}^D$ of the

Not all the MCs have the same lifetime: therefore there is a certain probability $P(t)$ that a molecular cloud is destroyed in the time interval $t - t + dt$. According to Zhukovska et al. (2008) the probability is well represented by an exponential law with time scale τ_{MC}. The instantaneous condensation fraction at the time t of the key element i relative to the dust compound j is derived from integrating over time and considering for each cloud of lifetime x, born at $t - x$ the condensation fraction holding at the time of birth $f_{0,i,j}(t - x)$. Since the lifetime distribution function quickly decays over time, only the MCs born some τ_{MC} before t will contribute in practice. The instantaneous condensation fraction is

$$f_{i,j}(t) = \frac{1}{\tau_{MC}} \int_0^t \frac{f_{0,i,j}(t-x) e^{x/\tau_j^{gr}} e^{-x/\tau_{MC}}}{1 - f_{0,i,j}(t-x)(1 - e^{x/\tau_j^{gr}})} dx \,. \tag{6.4.13}$$

This procedure is however time consuming when applied in practice. A much simpler approach is provided by using the average restitution mass $\overline{R}_j^{MC}$ and the average condensation fraction $\overline{f}_{i,j}$ assuming $f_{0,i,j}$ as a constant. Using Eq. 6.4.11 and integrating between 0 and $t = \infty$ we obtain the mean value of $f_{i,j}$:

$$\overline{f}_{i,j} = \frac{1}{\tau_{MC}} \int_0^\infty \frac{f_{0,i,j} e^{t/\tau_j^{gr}}}{1 - f_{0,i,j} + f_{0,i,j} e^{t/\tau_j^{gr}}} e^{-t/\tau_{MC}} dt \,. \tag{6.4.14}$$

Inserting Eq. 6.4.14 into Eq. 6.4.11 we get $\overline{M}_{j,MC}$, that is the time averaged mass of dust type j returned to the ISM. However, this is only part of the story, because the molecular clouds have also different mass, so we need to evaluate their mean mass $\overline{M}_{MC}$ and use this instead of M_{MC}.

Fractional mass of dust grains of j-type. With aid of Eq. 6.4.14 we can derive the fractional mass of dust type j produced by the accretion of grains in cold clouds per unit area and unit time:

$$\left(\frac{d\sigma_i^D}{dt}\right)_{accr} = \frac{1}{\tau_{MC}} \left(\overline{f}_{i,j} - f_{0,i,j}\right) \cdot \chi_{j,max}^D \sigma_{MC} \,. \tag{6.4.15}$$

Looking at Eq. 6.4.15, it requires to know the amount of molecular gas of the galaxy we are going to model. To do this, a multi-phase description of the ISM taking into account the exchange of matter between cold and warm phases would be required. This is not possible with the present model because Eqs. 6.2.8, 6.2.9, and 6.2.10 have been formulated for the single phase description and without a description of the gas exchange between cold and warm phases. To overcome this limitation some adjustment of the model are needed. Introducing $\chi_{MC} = \sigma^{MC}/\sigma^{\mathcal{M}}$ as the fraction

same key element that are tied up when we form one dust grain, we get the maximum number of dust grains that we can form per unit volume. Knowing the mass of a single dust grain, $A_j^D m_{\rm H}$, the the mass density $\rho_{j,max}^D$ immediately follows.

of molecular gas and with some passages (Zhukovska et al. 2008) the final equation for grain growth in MCs in the frame of a single-phase ISM.

$$\left(\frac{d\sigma_i^D}{dt}\right)_{accr} = \frac{\chi_{MC}}{(1-\chi_{MC})\,\tau_{MC}} \left(\overline{f}_{i,j}\sigma_{j,max}^D - \sigma_j^D\right) . \tag{6.4.16}$$

We need however to fix χ_{MC}: in Zhukovska et al. (2008) this fraction is fixed to 0.2 in agreement to the observations for the Solar Ring at the current time. However this approximation could not probably hold for other phases of the evolution of the Solar Ring or other regions of the MW. Since in our one-phase chemical model no description is available for a multi-phase ISM, it is unavoidable to estimate from time to time (possibly related to the physical properties of the system) the amount mass in cold molecular clouds (MCs) in each ring. The partition between MCs and diffuse ISM (the remaining part of the ISM) crucially enters the accretion term in Eqs. 6.2.11, 6.2.12 and 6.2.13 and drives the evolution of the dust budget. In this formulation the fraction, χ_{MC}, of ISM locked up in MCs is a parameter. For this reason we have included two possibilities for χ_{MC}. In the first one, as already stated we take $\chi_{MC} = 0.2$, and assume that it has remained constant from the formation of the MW to the present. Therefore, a constant value is adopted during the entire evolution of the Solar Ring. The second description for χ_{MC} is presented below and it stands on the data for the MW Disk. In practice, it correlates the fraction of MCs to the SFR and the local gas density. Both recipes produce similar results for the Solar Vicinity, but in the case of a constant fraction χ_{MC} the amount of dust could be underestimated and overestimated in the innermost and outermost regions of the MW disk, respectively. If compared to other more physically sounded prescriptions, a constant χ_{MC} would give rise to a flatter "gradient in dust". We expect however that the local physical conditions affect the accretion process and the fraction of MCs varies with time and space. This strongly favors the second prescription for a varying fraction of MCs.

Fig. 6.1 shows the radial dependence across the MW Disk of the current surface density profiles of H_2, HI and total gas (upper panel) of the MW and the current SFR normalized to the solar value SFR/SFR$_\odot$ (lower panel)indicated by the observational data. Superposed to the data we show some typical SF laws presented in Sect. 6.3. It is worth recalling that the total gas surface density includes also the contribution by helium (Boissier & Prantzos 1999; Yin et al. 2009). With the aid of this, we look at the correlations between SFR/SFR$_\odot$, $\sigma^G(r_k,t)$ (one of quantities followed by the chemical model), and $\sigma_{H_2}(r_k,t)$ (related to the parameter χ_{MC}).

To this aim, first we derive the best fit for the three quantities: the results (obtained using the MATLAB *Curve Fitting Toolbox*) are indicated by the solid lines

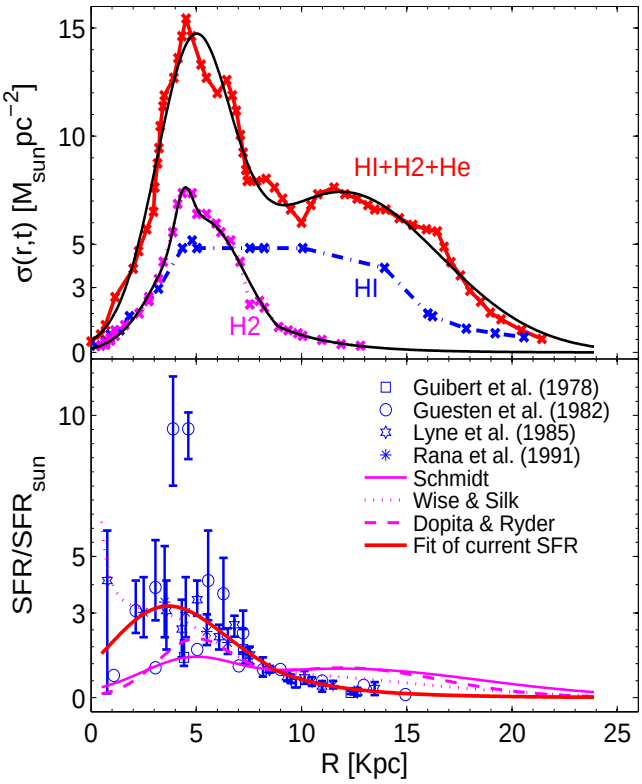

Figure 6.1: **Upper panel**: present-day radial profiles across the MW Disk for molecular hydrogen $\sigma_{H_2}(r, t_G)$, neutral hydrogen $\sigma_{HI}(r, t_G)$, and total amount of gas $\sigma^G(r, t_G)$ obtained taking into account helium correction (Boissier & Prantzos 1999; Yin et al. 2009). **Lower panel**: present-day radial profile of star formation across the MW Disk, according to the data by Guibert et al. (1978) (squares), Guesten & Mezger (1982) (circles), Lyne et al. (1985) (hexagons), Rana (1991) (stars). Superposed to the data are three theoretical SF laws (Schmidt - continuous line, Wyse & Silk - dotted line, Dopita & Ryder - dashed line) and an exponential best fit, all referring to the present age t_G of the MW.

in the top panel and the thick line in the bottom panel of Fig. 6.1. Second, using the best fits we derive the 3D correlation between the H_2 mass, the star formation rate, and total gas mass. They are shown in the three panels of Fig. 6.2. To reproduce the 3D data and extrapolate the results to unknown regions of the parameter space, we use the Artificial Neural Networks technique (hereafter ANNs) modelled from biological nervous systems: ANNs are like a network of neurons linked together by synapses (numerical weights). The network in usage here is taken from Grassi et al. (2011) to whom the reader should refer for all details. It contains two layers of hidden neurons whose number is $n_h = 5$ and $n_g = 25$, respectively and has two input neurons, i.e. (SFR/SFR$_\odot$ and and $\sigma^G(r_k, t_G)$) (plus the bias input that is always set to a constant value) and one output neuron, i.e. $\sigma_{H_2}(r_k, t_G)$. The evolution of the RMS is monotonic and decreases to approximately RMS $= 10^{-3}$ after 10^6 iterations.

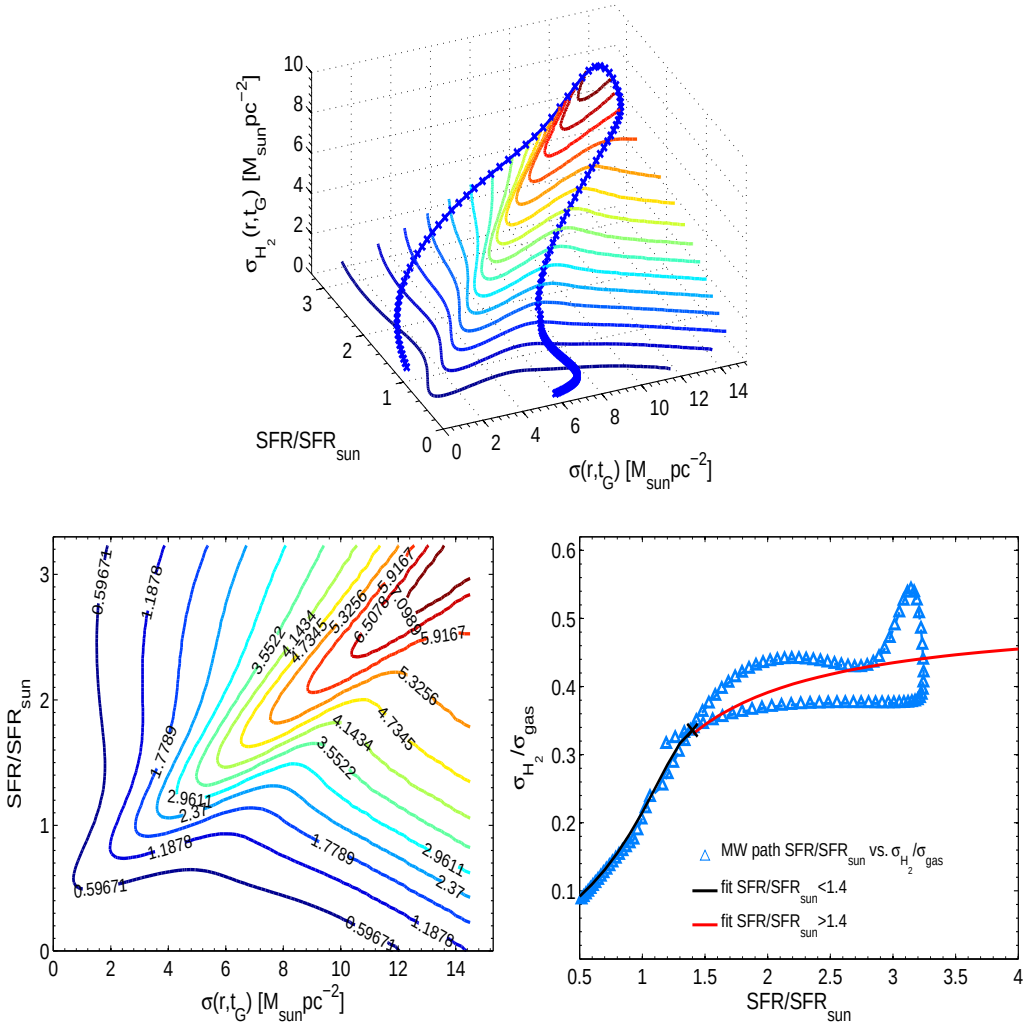

Figure 6.2: **Left Panel**: 3D plot of $\sigma_{H_2}(r, t_G)$ as a function of SFR/SFR$_\odot$ and $\sigma^G(r, t_G)$ for the present-day radial profiles across the MW Disk (crosses). The solid line superposed to the data is the fit from the ANNs. Contour isolines obtained by extrapolating the ANNs weights to the regions uncovered by the data are also shown. **Middle Panel**: The same as in the Left Panel but showing only the 2D contour levels of $\sigma_{H_2}(r, t_G)$ in the SFR/SFR$_\odot$ vs. $\sigma^G(r, t_G)$ plane. **Right Panel**: 2D plot with the radial SFR/SFR$_\odot$ vs $\sigma_{H_2}(r, t_G)/\sigma^G(r, t_G)$ relationship for the MW (triangles) and a two-piece fit of the data. The region of interest is the one for SFR higher than solar.

In the left panel of Fig. 6.2 we show the fit found by the ANNs (solid line) compared with the data (crosses). We suppose now that the correlation between the three parameters established from the present-day data remains the same as a function of the Galaxy age and therefore we drop the dependence on time. Furthermore, adopting the same ANN weights, we extrapolate the ANN predictions to the whole space of the parameters SFR/SFR$_\odot$, $\sigma^G(r,t)$ and $\sigma_{H_2}(r,t)$. The contours and isolines describing the extrapolated regions are shown in left and middle panels of Fig. 6.2.

Some comments are worth being made here. First, we have no warranty that the behaviour in the extrapolated region is so regular as predicted by the ANNs. In the huge gaps uncovered by the experimental data for the MW, we could for example have valleys and peaks so that to cast light on this problem a complete coverage of the parameter space with observational data for spiral galaxies in general would be required. However, this goes beyond the aims of this study. It suffices here to check that extrapolating the MW data does not lead to un-physical results. The predictions seem to be reasonable: for low SFR or low gas amount, the H_2 mass is low. For high SFR and gas mass we have a reasonable amount of H_2. Even if we look only at the region where the SFR is high but the total amount of gas is low, the prediction for H_2 is also reasonable. Even if the correlation between H_2 and SFR is not clear and somewhat in contradictions with the expectations, stars are seen to form from the cold molecular gas (Kennicutt 1998) and a significant amount of H_2 is physically acceptable when SFR is significant.

Second, the region covered by the ANN is bounded by the limits $[(\mathrm{SFR}/\mathrm{SFR}_\odot)_{min}$, $(\mathrm{SFR}/\mathrm{SFR}_\odot)_{max}]$ and $[\sigma^G(r,t)_{min}, \sigma^G(r,t)_{max}]$. This may be a problem in particular with high SFRs, because the limits for the ANN have been set basing upon data for the SFR in the innermost regions of the Disk where the uncertainty is high. To cope with this point of embarrassment, when the SFR is higher than about $3\times\mathrm{SFR}_\odot$, we replace the predictions based on the ANNs with a simpler fit based on $\sigma_{H_2}(r,t_G)$ versus SFR data and we keep the fraction χ_{MC} in the interval $0.4-0.5$. All of this is shown in the right panel of Fig. 6.2.

Degree of condensation. Another critical parameter to be examined with accuracy is the condensation degree $\overline{f}_{i,j}$. It depends on the comparison between τ_{MC}, the average lifetime of the MC, and the typical accretion time of grains τ_j^{gr} of Eq. 6.4.9. If $\tau_j^{gr} \gg \tau_{MC}$ then we expect that only small amounts of dust are produced because the cold clouds will be destroyed before that dust has enough time to grow. On the contrary, if $\tau_j^{gr} \ll \tau_{MC}$, we expect the condensation of dust grains to occur almost completely and consequently dust to increase. Zhukovska et al. (2008) propose an analytical expression for the condensation degree as a function of the ratio τ_j^{gr}/τ_{MC} (assuming a constant $f_{0,i,j}$):

$$\overline{f}_{i,j} = \left[\frac{1}{f_{0,i,j}^2 \left(1 + \frac{\tau_{MC}}{\tau_j^{gr}}\right)^2} + 1 \right]^{-\frac{1}{2}} . \qquad (6.4.17)$$

According to Zhukovska et al. (2008), this expression is no longer valid only for very small values of $f_{0,i,j}$. The situation for our models is more complicated because we are dealing with large variations of $f_{0,i,j}$ and τ_j^{gr}. To clarify the issue, we checked in advance whether or nor the above relation can be still used. To this aim we have calculated the differences between $\overline{f}_{i,j}$ from t Eq. 6.4.17 and the relation of Eq. 6.4.14. This comparison is made for $\tau_j^{gr} < 1000\tau_{MC}$ and $\tau_j^{gr} > \tau_{MC}/50$. If $\tau_j^{gr} > 1000\tau_{MC}$ or $\tau_j^{gr} < \tau_{MC}/50$ we use the Taylor expansion suggested by Zhukovska et al. (2008) deal with the extreme cases of very slow or very fast accretion time.

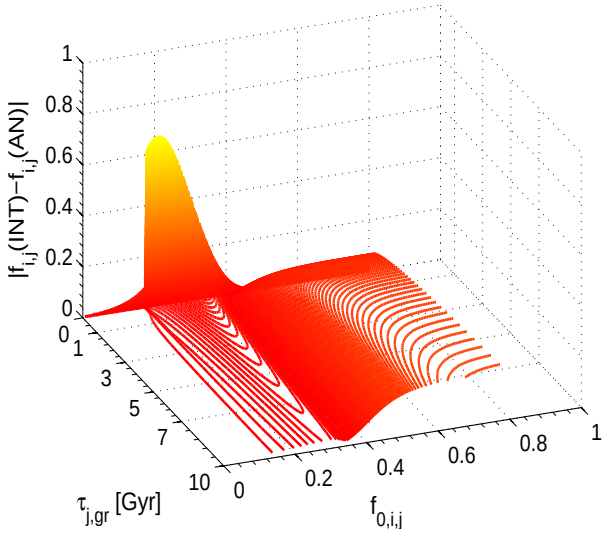

Figure 6.3: Absolute value of the differences between the $\overline{f}_{i,j}$ calculated integrating and averaging on the MCs lifetimes as in Eq. 6.4.14 and the same quantity derived from the analytical formula of Eq. 6.4.17 suggested by Zhukovska et al. (2008). A grid of 200×200 suitably discrete values of $f_{0,i,j}$ and τ_j^{gr} has been considered.

The results are presented in Fig. 6.4.2 for a 200×200 grid of models with uniform spacing of $f_{0,i,j}$ and τ_j^{gr} growing linearly from low to high values. The error can be significant, in particular for very low $f_{0,i,j}$ and very short τ_j^{gr} or high τ_j^{gr} and average $f_{0,i,j}$.

As we discussed in Sect. 6.4.1, the same accretion term in Dwek (1998) and Calura et al. (2008) is

$$\left(\frac{d\sigma_i^D}{dt}\right)_{accr} = \frac{\sigma_i^D}{\tau_{i,accr}} = \frac{\sigma_i^D}{\tau_{0,i}} \cdot \left(1 - \frac{\sigma_i^D}{\sigma_i^{\mathcal{M}}}\right) . \tag{6.4.18}$$

The basic difference between the two approaches is that while Dwek (1998) and Calura et al. (2008) describe the evolution of the abundance of the element i in the dust, Zhukovska et al. (2008) follow the evolution of the abundance of the j-th dust type in a given sample molecule considered to represent the situation of the ISM. To adapt the equations to our formulation for single elements (see Sect. 6.2), we start from:

$$\sigma_i^G = \sigma_i^{\mathcal{M}} - \sigma_i^D \tag{6.4.19}$$

which summing up all the dust types j in which the i-th element is locked up (independently on whether or not it is a key element for that kind of molecule) becomes:

$$\sigma_i^G = \sigma_i^{\mathcal{M}} - \sum_j \nu_{i,j}^D \frac{A_{i,j}}{A_j^D} \sigma_j^D \tag{6.4.20}$$

with

$$\sigma_i^D = \sum_j \nu_{i,j}^D \frac{A_{i,j}}{A_j^D} \sigma_j^D \tag{6.4.21}$$

where as usual σ_i^D is the surface mass density of the i-th element in dust, while σ_j^D is the surface mass density of the j-th type dust. The above relations says that the amount of element i contained in the dust is given by the sum of the contributions by all the j-th kinds of dust in which i is involved. For each one of the j-th dust types, we divide σ_j^D by the unit mass $A_j^D m_{\rm H}$ of one species j and find the number density of dust type j. Then, for each one of these molecules j we have $\nu_{i,j}^D$ atoms of the element i. Finally, we multiply by the atomic mass $A_{i,j} m_{\rm H}$ of the element i to get the mass of the element i coming from the j-th type dust. If we derive respect to time we obtain

$$\left(\frac{d\sigma_i^D}{dt}\right)_{TOT} = \sum_j \nu_{i,j}^D \frac{A_{i,j}}{A_j^D} \left(\frac{d\sigma_j^D}{dt}\right)_{TOT} \tag{6.4.22}$$

where the total evolution of dust is given by the sum of the variations due to the star formation, the stardust injected in the ISM, the destruction of the grains by SN shocks, and the accretion process in the cold regions. Taking into account only this last one:

$$\left(\frac{d\sigma_i^D}{dt}\right)_{accr} = \sum_j \nu_{i,j}^D \frac{A_{i,j}}{A_j^D} \left(\frac{d\sigma_j^D}{dt}\right)_{accr} \tag{6.4.23}$$

The amount of element i contained in dust is given by the sum of the contributions by all the jth kinds of dust in which i is involved. For each dust type j, we divide σ_j^D

by the unit mass $A_j^D m_{\rm H}$ of one species j of dust and find the number density of the j-th dust type. For each dust type j we have $\nu_{i,j}^D$ atoms of the element i. Finally, we multiply by the atomic mass $A_{i,j} m_{\rm H}$ of the element i to get the mass of this coming from the j-th type dust. Inserting the expression for $\left(d\sigma_j^D/dt\right)_{accr}$ we have:

$$\left(\frac{d\sigma_i^D}{dt}\right)_{accr} = \sum_j \nu_{i,j}^D \frac{A_{i,j}}{A_j^D} \left(\frac{d\sigma_j^D}{dt}\right)_{gg} =$$
$$= \sum_j \frac{\nu_{i,j}^D A_{i,j}}{A_j^D} \frac{\chi_{MC}}{(1-\chi_{MC})\,\tau_{MC}} \left(\overline{f}_{k,j}\sigma_{j,max}^D - \sigma_j^D\right) . \tag{6.4.24}$$

Let's now introduce $\sigma_{j,max}^D$, which is related to the amount of key-element k in the j-th dust type present in the ISM, i.e. $\sigma_k^{\mathcal{M}}$. We can express σ_j^D by means of the k-th key-element of the j-th dust type that is locked up into the j-th component itself. This quantity is not known and not tracked by our model. All we know is how much of a given element is locked up into dust, but *we do not know how much of that element is locked in every kind of dust.* For example we are able to follow how much silicon is locked up into dust, but not how much silicon is stored in pyroxene, olivine and quartz. Doing the substitution we have:

$$\left(\frac{d\sigma_i^D}{dt}\right)_{accr} = \sum_j \frac{\nu_{i,j}^D A_{i,j}}{A_j^D \tau_{MC}} \frac{\chi_{MC}}{(1-\chi_{MC})} \cdot$$
$$\cdot \left[\overline{f}_{k,j} \frac{A_j^D}{A_{k,j}\nu_{k,j}^D} \sigma_{k,j}^{\mathcal{M}} - \frac{A_j^D}{A_{k,j}\nu_{k,j}^D} \sigma_{k,j}^D\right] \tag{6.4.25}$$

$$\left(\frac{d\sigma_i^D}{dt}\right)_{accr} = \frac{\chi_{MC}}{(1-\chi_{MC})\,\tau_{MC}} \sum_j \frac{A_{i,j}\nu_{i,j}^D}{A_{k,j}\nu_{k,j}^D} \cdot$$
$$\cdot \left[\overline{f}_{k,j}\sigma_{k,j}^{\mathcal{M}} - \sigma_{k,j}^D\right] \tag{6.4.26}$$

Posing $K = \chi_{MC}/\left(\tau_{MC}\,(1-\chi_{MC})\right)$, we have:

$$\left(\frac{d\sigma_i^D}{dt}\right)_{accr} = K \left[\sum_{j,i=k} \left(\overline{f}_{i,j}\sigma_{i,j}^{\mathcal{M}} - \sigma_{i,j}^D\right) + \right.$$
$$\left. + \sum_{j,i\neq k} \frac{A_{i,j}\nu_{i,j}^D}{A_{k,j}\nu_{k,j}^D} \left(\overline{f}_{k,j}\sigma_{k,j}^{\mathcal{M}} - \sigma_{k,j}^D\right)\right] \tag{6.4.27}$$

where k indicates the key element of the dust type j, because it may occur that a dust molecule contains the i-th element of which we tracking the evolution, but *not*

the key element that could be of another type. For example, we could be following the evolution of carbon and considering the silicon carbide that contains carbon, but not as key-element. As a consequence of this, the above has been split in two parts: in the first one we include the part of the j-th dust type in which the element i is locked *as key-element*; in the second part we have the dust molecules containing the i-th element but *not as key element*, which instead corresponds to the element k. Therefore the summation goes for all the $k \neq i$. The notation $\sigma^D_{k,j}$ is meant to indicate the surface mass density of the k-th element locked up into the dust compounds j.

6.5 Dust accretion rates for a few important elements

At this stage we need to specify the dust accretion rate given by Eq. 6.4.27 for some specific elements whose evolution we intend to study. The model follows 16 elements (Portinari et al. 1998): H, ^{4}He, ^{12}C, ^{13}C, ^{14}N, ^{15}N, ^{16}O, ^{17}O, ^{18}O, ^{22}Ne, ^{20}Ne, ^{24}Mg, ^{28}Si, ^{32}S, ^{40}Ca, ^{56}Fe.

Four families of dust can be identified and tracked by the model: they are the silicates, carbonaceous and iron grains, and silicon carbide (it is worth clarifying that SiC does not form by accretion in MCs). We must distribute the 16 elements followed by the model in the four families of dust. First of all, H, ^{4}He, ^{20}Ne, ^{22}Ne are noble gases not involved into the dust formation process by accretion. Second, since the hydrogen is by far the most abundant element in the Universe, even if it may be contained in many dust molecules (such as for instance the PAHs), its abundance in the ISM gas will not be significantly affected by dust. For what concern ^{16}O, ^{17}O, ^{18}O, ^{24}Mg, ^{28}Si, ^{56}Fe, according to the simplified Zhukovska et al. (2008) scheme, they are involved in silicates (all of them) and iron grains (just some of them). For ^{14}N, ^{15}N, ^{32}S and ^{40}Ca there is no specific dust family to associate them. However, the observations tell us that they are or could be depleted –see for instance the case of Calcium (Whittet 2003; Tielens 2005)–, so we must set a plausible yet simple scheme to describe them. Finally, ^{12}C and ^{13}C are both involved into the formation of carbonaceous grains and silicon carbide. In the following we will examine the case of ^{12}C, ^{13}C, ^{16}O, ^{17}O, ^{18}O, ^{24}Mg, ^{28}Si and ^{56}Fe in some detail.

6.5.1 Carbon

Carbon is present in dust as key constituent of many molecules containing carbon (C-molecules), otherwise named carbonaceous grains. It is also part of important dust molecules like silicon carbide (SiC) where, however, the key element ruling the process is silicon. SiC grains are mainly related to AGB carbon stars and for them

there is no process of accretion in cold clouds of the ISM. Finally, the problem of the formation of SiC in the ejecta of supernovæ is still debated.

Nozawa et al. (2003), studying dust formation in population III supernovæ argues that they cannot form SiC grains with radii comparable to the pre-solar SiC grains identified as supernova condensates, because silicon and carbon are firstly locked into other carbonaceous grains or silicates before the formation of SiC grains can take place. However, we observe a small but significant percentage of X-type SiC grains (one of the minor types A, B, X, Y and Z, that is believed to be formed in the ejecta of type II SNe because of the isotopic signature) with respect to the mainstream SiC (about 90% of the total and whose origin is attributed to AGB C-stars, because of their similar $^{12}C/^{13}C$ ratio, signatures of s-processes and the 11.3 SiC μm feature in C-stars). The ratio between X-type and mainstream type can be quantified in about 0.01 (Hoppe et al. 2000). Therefore, as proposed by Deneault et al. (2003), special conditions and/or chemical pathways might have to be considered in order to realize the formation in type II SNe of SiC grains. To reproduce the observed X-type over mainstream ratio, Zhukovska et al. (2008) considers a small formation of SiC in Type II SNe, however this is just an *ad-hoc* recipe based on meteorites and does not throw light over the uncertain amount of dust, and X-type SiC, produced by SNe.

The equation describing the accretion of carbonaceous grains of the ISM is:

$$\left(\frac{d\sigma_C^D}{dt}\right)_{accr} = K\left\{\overline{f}_{C,C}\left(1-\xi_{CO}\right)\sigma_{C,C}^{\mathcal{M}} - \sigma_{C,C}^D\right\} \tag{6.5.1}$$

where $\sigma_{\rm C,C}^{\mathcal{M}}$ is the amount of the available carbon, $\xi_{\rm CO}$ a factor accounting for the carbon embedded in molecules like CO that do not take part to the accretion process, $\sigma_{\rm C,C}^D$ is the carbon already condensed into dust, and $\overline{f}_{\rm C,C}$ is the average condensation factor (see Sect. 6.4 model B). The accretion of C-molecules in molecular clouds happens according to a time scale defined by Eq. 6.4.9 which for the specific case of carbon is:

$$\tau_C^{gr} = 46\frac{(A_C^{gw})^{\frac{1}{2}}\nu_{C,C}^D}{A_C^D}\left(\frac{\rho_C^D}{3}\right)\left(\frac{10^3}{n_H}\right)\left(\frac{3.5\cdot10^{-5}}{\epsilon_{C,C}}\right)Myr\,. \tag{6.5.2}$$

This relation deserves some comments. First of all $\nu_{\rm C,C}^{\rm D}=1$ because carbon is present in the cold regions of molecular clouds as single atoms or molecules with typically one atom of carbon. Second, $\rho_C^D = 2.26$ g cm^{-3} (Li & Draine 2001). To determine A_C^D we should average the masses of the various type of molecules present in the molecular clouds. Carbon is embedded in CO (with a percentage easily up to 20 or 40%). There are also lots of C-molecules like: $CO_2, H_2CO, HCN, CS, CH_4$, C_2H_2, C_2H_6, $HCOOH, OCS, ...$ We consider $\rm A_C^D = 28$ corresponding to CO as a sort of mean value fairly representing the above group. $A_{\rm C}^{\rm gw}=12$ assuming single atoms

as the typical accreting species. Finally, we need to specify $\epsilon_{\rm C,C}$ the abundance by number with respect to H of the key-species C driving the process of accretion of dusty C-molecules. We have:

$$\epsilon_{C,C} = (1 - \xi_{CO}) \, \frac{\sigma_C^{\mathcal{M}} - \sigma_C^D}{12 \sigma_H^{\mathcal{M}}} \, . \tag{6.5.3}$$

In this relation, the factor $(1 - \xi_{CO})$ takes into account that fact that the carbon already in CO is not available to the accretion process. This correction is not negligible. Second, we subtract from the carbon atoms available for accretion, those ones already embedded in dust or belonging to unreactive species like SiC. Finally, we obtain for the typical accretion time:

$$\tau_C^{gr} = \frac{1.80}{(1 - \xi_{CO}) \, n_H} \left(\frac{\sigma_H^{\mathcal{M}}}{\sigma_C^{\mathcal{M}} - \sigma_C^D} \right) Myr \, . \tag{6.5.4}$$

A similar relation is assumed for ^{13}C, in which the only difference is the 2.03 instead of 1.80. This assumption stands on the notion that ^{13}C, much less abundant than ^{12}C, undergoes the same kind of accretion processes and forms similar C-molecules. Clearly this is a simplified view of the subject, however sustained by the fact that, on average, the mean N(^{12}CO)/N(^{13}CO) ratio in diffuse clouds is close or compatible with the local interstellar isotope ratio ^{12}C/^{13}C, even if the N(^{12}CO)/N(^{13}CO) can be easily enhanced or reduced by a factor of two with a large spread (Liszt 2007; Visser et al. 2009). This allows to think that the relative percentage of carbon isotopes in molecules and dust should not be on average too different.

To practically use Eq. 6.5.1, we need $f_{0,C,C}$ to get the average condensation factor $\overline{f}_{C,C}$: $f_{0,C,C}$ is the initial condensation of the key-element C of the carbonaceous dust compound. If $\widetilde{\chi}_j^D$ is the mass fraction of dust type j contained in the part of the ISM that is not stored in cold clouds, we have:

$$f_{0,C,C} \approx \frac{\widetilde{\chi}_C^D}{\chi_{C,max}^D} \approx \frac{\chi_C^D}{\chi_{C,max}^D} \approx \frac{\sigma_{C,C}^D}{\sigma_{C,C}^{\mathcal{M}}} \tag{6.5.5}$$

where to derive it, we simply replaced the mass fraction of dust in the ISM not belonging to cold regions with the mass fraction embedded in the cold ones: $\widetilde{\chi}_C^D \approx \chi_C^D$. This simply means that after every cycle of MCs there is complete restitution and mixing with the ISM, so that on the average the ISM dust content always mirrors the initial mass-fraction already condensed at the formation of the MC.

6.5.2 Silicon

Silicon is present in many types of grains generically referred to as silicates, one of the most complicated families of minerals. We consider only some kinds of silicates, commonly used in models of dust formation. First of all, we list the pyroxenes that are

inosilicates (i.e. a family containing single chain and double chain silicates) in general indicated by $XY(Si,Al)_2O_6$, where X represents ions such as calcium, sodium, iron^{2+} and magnesium, whereas Y represents ions of smaller size such as chromium, aluminum, iron^{+3}, magnesium. Aluminum, while commonly replacing in other silicates, does not often do it in pyroxenes. Typical pyroxenes used in dust models are the end members of the enstatite-hypersthene-ferrosilite series described by $Mg_xFe_{1-x}SiO_3$ with $0 < x < 1$ determining the partition between the two possibilities. Enstatite is the magnesium end-member $MgSiO_3$ of the series, while ferrosilite is the iron end-member $FeSiO_3$: both are found in iron and stony meteorites. Second, we have the olivines. They are a series of minerals falling in between two end-members, fayalite and forsterite. They can be described by $[Mg_xFe_{1-x}]_2SiO_4$ with $0 < x < 1$ determining the partition. Fayalite is the iron-rich member with Fe_2SiO_4. Forsterite is the magnesium-rich member with Mg_2SiO_4. The two minerals form a series where the iron and magnesium can be interchanged without much effect, also difficult to detect, on the crystal structure. Olivine can be found for example in many meteorites like the iron-nickel ones, in the tails of comets, and in the disks of dust around young stars. Both pyroxenes and olivines are expected to exist in the interstellar dust because they form from magnesium and iron that are abundant. In addition to this and limited to the calculation of stellar dust yields, we included quartz, the most common mineral on the surface of the Earth, composed by SiO_2 and silicon carbide, SiC. Silicon carbide in expected to form in the ejecta of carbon-rich stars and type II SNe, but not by accretion in cold clouds.

Two parameters control the pyroxene-olivine mixture: the Mg fraction x, assumed to be the same for pyroxenes an olivines, and the abundance ratio between the amount of magnesium and silicon bound in dust A^D_{Mg}/A^D_{Si}. This latter determines the fraction of silicates with olivine stoichiometry $F_{Ol} = A^D_{Mg}/(A^D_{Si} \cdot x) - 1$, while for pyroxenes we can define $F_{Pyr} = 1 - F_{Ol}$. The two parameters are fixed and chosen according to present day observations of IR emission and abundances in the diffuse ISM (Dwek et al. 1997; Whittet 2003; Dwek 2005), i.e. $x = 0.8$ and $A^D_{Mg}/A^D_{Si} = 1.06 - 1.07$. Varying these parameters does not significantly affect the total efficiency of dust production by the MCs (Zhukovska et al. 2008). For the purposes of this study, they can be kept fixed. The equation describing the evolution of silicon is nearly the same no matter whether or not silicon *is the key-element* for pyroxenes and olivines.

The Mg/Fe case. Let us first suppose that the key-element is magnesium/iron and not silicon. Using Eq. 6.4.27 we get:

$$\left(\frac{d\sigma^D_{Si}}{dt}\right)_{accr} = K\frac{A_{Si,Pyr}\nu^D_{Si,Pyr}}{A_{i,Pyr}\nu^D_{i,Pyr}} \cdot \{\overline{f}_{i,Pyr}\sigma^{\mathcal{M}}_{i,Pyr} - \\ - \sigma^D_{i,Pyr}\} + K\frac{A_{Si,Ol}\nu^D_{Si,Ol}}{A_{i,Ol}\nu^D_{i,Ol}}\{\overline{f}_{i,Ol} \cdot \\ \cdot \sigma^{\mathcal{M}}_{i,Ol} - \sigma^D_{i,Ol}\} \tag{6.5.6}$$

where $\overline{f}_{i,Pyr}$ and $\overline{f}_{i,Ol}$ are the average condensation fractions of pyroxenes and olivines, obtained according to the procedure described in Sect. 6.4. Furthermore, $\nu^D_{Si,Pyr}$ is the number of silicon atoms needed for one molecule of pyroxene, i.e. $\nu^D_{Si,Pyr} = 1$. Since for each molecule we have just one Si atom, $\nu^D_{Si,Pyr} \cdot A_{Si,Pyr} = 28$. The quantity $A_{i,Pyr} = 24$ or 56 (magnesium or iron). We must also define $\nu^D_{i,Pyr}$ (a number between 0 and 1). Assuming a fixed partition x: $\nu^D_{Mg,Pyr} = 0.8$ and $\nu^D_{Fe,Pyr} = 0.2$. Finally, we have the physical constants for olivines: $\nu^D_{Si,Ol} = 1$, $A_{Si,Ol} = 28$, $A_{Mg,Ol} = 24$, $A_{Fe,Ol} = 56$, $\nu^D_{Mg,Ol} = 1.6$, finally $\nu^D_{Fe,Ol} = 0.4$. Since F_{Pyr} and F_{Ol} are the fractions of pyroxenes and olivines in which silicates are subdivided, we have the following partition of magnesium in dust $\sigma^D_{Mg} = \sigma^D_{Mg,Ol} + \sigma^D_{Mg,Pyr} = (x \cdot F_{Pyr})/(x \cdot F_{Pyr} + 2x \cdot F_{Ol})\sigma^D_{Mg} + (2x \cdot F_{Ol})/(x \cdot F_{Pyr} + 2x \cdot F_{Ol})\sigma^D_{Mg} = Mg_{Pyr}\sigma^D_{Mg} + Mg_{Ol}\sigma^D_{Mg}$ and of iron in silicates (once subtracted the iron embedded in iron grains) $\sigma^D_{Fe,Sil} = \sigma^D_{Fe} - \sigma^D_{Fe,Fe} = \sigma^D_{Fe,Ol} + \sigma^D_{Fe,Pyr} = (1-x) \cdot F_{Pyr}/((1-x) \cdot F_{Pyr} + 2(1-x) \cdot F_{Ol})\sigma^D_{Fe,Sil} + 2(1-x) \cdot F_{Ol}/((1-x) \cdot F_{Pyr} + 2(1-x) \cdot F_{Ol})\sigma^D_{Fe,Sil} = Fe_{Pyr}\sigma^D_{Fe,Sil} + Fe_{Ol}\sigma^D_{Fe,Sil}$.

It is worth also noting that the dust compounds of which we follow the accretion, i.e. pyroxenes/olivines for silicates, carbonaceous grains and iron grains, are fewer in number than the dust molecules considered by the stellar yields of dust in the most detailed models calculated by CNT theory. The number and variety of the dust molecules injected into the ISM are wider than the number of accreting species. For this reason, before splitting σ^D_{Mg}, $\sigma^D_{Fe,Sil}$ and σ^D_{Si} (see below) between pyroxenes/olivines, we need to keep memory of the evolution of the other dust species injected by AGB/SNe (also eventually swept up and destroyed by shocks in the ISM), which are not included in the accretion scheme.

The Si case. In alternative, silicon can be the key-element for olivines and pyroxenes:

$$\left(\frac{d\sigma^D_{Si}}{dt}\right)_{accr} = K\{\overline{f}_{Si,Pyr}\sigma^{\mathcal{M}}_{Si,Pyr} - \sigma^D_{Si,Pyr}\} \\ + K\{\overline{f}_{Si,Ol}\sigma^{\mathcal{M}}_{Si,Ol} - \sigma^D_{Si,Ol}\} \tag{6.5.7}$$

where again $\overline{f}_{Si,Pyr}$ and $\overline{f}_{Si,Ol}$ are the average condensation fractions of silicon in pyroxenes and olivines. The corresponding partition of silicon in dust is $\sigma^D_{Si} = \sigma^D_{Si,Pyr} + \sigma^D_{Si,Ol} = F_{Pyr}\sigma^D_{Si} + F_{Ol}\sigma^D_{Si}$. We need to calculate the accretion time scales of pyroxenes and olivines, to be compared with the lifetime of molecular clouds and included into the integrations for $\overline{f}_{Mg,Pyr}$, $\overline{f}_{Mg,Ol}$, $\overline{f}_{Si,Pyr}$ and $\overline{f}_{Si,Ol}$. Applying Eq. 6.4.9 we get:

$$\tau^{gr}_{Pyr} = 46\frac{(A^{gw}_{Pyr})^{1/2}\nu^D_{i,Pyr}}{A^D_{Pyr}}\left(\frac{\rho^D_{Pyr}}{3}\right)\left(\frac{10^3}{n_H}\right)\left(\frac{3.5\cdot10^{-5}}{\epsilon_{i,Pyr}}\right) = \\ = \frac{\tau^{gr}_{0,Pyr,i}}{\sigma^{\mathcal{M}}_i}\frac{\sigma^{\mathcal{M}}_H}{n_H} \tag{6.5.8}$$

$$\tau^{gr}_{Ol} = 46\frac{(A^{gw}_{Ol})^{1/2}\nu_{i,d,Ol}}{A_{d,Ol}}\left(\frac{\rho_{d,Ol}}{3}\right)\left(\frac{10^3}{n_H}\right)\left(\frac{3.5\cdot10^{-5}}{\epsilon_{i,Ol}}\right) = \\ = \frac{\tau^{gr}_{0,Ol,i}}{\sigma^{\mathcal{M}}_i}\frac{\sigma^{\mathcal{M}}_H}{n_H} \tag{6.5.9}$$

where $\tau^{gr}_{0,Pyr,i}$ and $\tau^{gr}_{0,Ol,i}$ are two constants that depend on the key-element. $\tau^{gr}_{0,Pyr,i}$ is equal to 2.05, 1.30 and 1.16 for the key-elements Si, Mg and Fe respectively, while $\tau^{gr}_{0,Ol,i}$ is equal to 2.05, 2.60 and 2.32 again for Si, Mg and Fe. A^{gw}_{Ol} and A^{gw}_{Pyr} are the atomic weight of the growing species. Finally, $A_{d,Ol} = A_{d,Pyr} = 121.41$. It is important to note that in the calculation of the abundances of species available for dust accretion, we do not subtract the amount of dust already formed σ^D_i from the total ISM abundance $\sigma^{\mathcal{M}}_i$; this is equivalent to assume that the grains of silicates already formed act as reactive species in the accretion process. Dropping this assumption (and simplification), the accretion process would be too slow. There is one exception though in the case of iron as the key-element for the mixture of silicates mixture. In such a case we subtract from $\sigma^{\mathcal{M}}_i$ the amount of iron already embedded in the iron dust grains (that do not react with silicates), thus obtaining $\sigma^{\mathcal{M}}_i = \sigma^{\mathcal{M}}_{Fe} - \sigma^D_{Fe,Fe}$. The initial condensation fractions $f_{0,i,Pyr}$, $f_{0,i,Ol}$ needed to derive $\overline{f}_{i,Pyr}$, $\overline{f}_{i,Ol}$ can be obtained as in Eq. 6.5.5.

6.5.3 Oxygen

Oxygen is much more abundant than the refractory elements Si, Fe, Mg, Ca and S. Therefore, oxygen (at least the most abundant isotope ^{16}O) will never become a key-element determining the growth of the typical dust grains in the ISM. The equation describing the evolution of the mass abundance of the ^{16}O is obtained from Eq. 6.4.27, dropping the terms giving the contribution of the O as key-element. Therefore, considering the accretion of pyroxenes and olivines, the temporal evolution of the ^{16}O abundance (we drop the mass number of the isotope) is:

$$\left(\frac{d\sigma_O^D}{dt}\right)_{accr} = K\frac{A_{O,Pyr}\nu_{O,Pyr}^D}{A_{i,Pyr}\nu_{i,Pyr}^D}\left\{\overline{f}_{i,Pyr}\sigma_{i,Pyr}^{\mathcal{M}} - \right.$$
$$\left. - \sigma_{i,Pyr}^D\right\} + K\frac{A_{O,Ol}\nu_{O,Ol}^D}{A_{i,Ol}\nu_{i,Ol}^D}\left\{\overline{f}_{i,Ol}\sigma_{i,Ol}^{\mathcal{M}} - \right.$$
$$\left. - \sigma_{i,Ol}^D\right\} \tag{6.5.10}$$

where once again the key-element could be Mg, Si or Fe, depending on which has the lowest abundance. The subscript i indicates a generic key-element. As usual, $\overline{f}_{i,Pyr}$ and $\overline{f}_{i,Ol}$ are the average condensation fractions when the MC is dispersed, and $\sigma_{i,Pyr}^D$ and $\sigma_{i,Ol}^D$ are defined as in Sect. 6.5.2. Introducing the Dirac delta function notation we have: $A_{i,Pyr} = 28\delta\left(A_i - 28\right) + 24\delta\left(A_i - 24\right) + 56\delta\left(A_i - 56\right)$ where A_i is the mass number of the key-element i. Furthermore, $A_{O,Pyr} = 16$ and, since in pyroxenes we have sulfite SiO_3 with 3 oxygen atoms, $\nu_{O,Pyr}^D = 3$, $\nu_{i,Pyr}^D = 1\delta\left(A_i - 28\right) + 0.8\delta\left(A_i - 24\right) + 0.2\delta\left(A_i - 56\right)$, and $A_{O,Ol} = 16$. Similarly, $\nu_{O,Ol}^D = 4$ because in the olivines we have sulfate SiO_4, $A_{i,Ol} = 28\delta\left(A_i - 28\right) + 24\delta\left(A_i - 24\right) + 56\delta\left(A_i - 56\right)$, and $\nu_{i,Ol}^D = 1\delta\left(A_i - 28\right) + 1.6\delta\left(A_i - 24\right) + 0.4\delta\left(A_i - 56\right)$. The accretion time scales τ_{Pyr}^{gr} and τ_{Ol}^{gr} that we need for $\overline{f}_{i,Pyr}$ and $\overline{f}_{i,Ol}$, the elemental abundances of the key-elements and the initial condensation fractions are the same as in Sect. 6.5.2.
In this context, we need also a simple description for ^{17}O and ^{18}O. First of all let us examine how they behave in the inert CO molecule. The way in which the isotopes of O and C combine to form many isotopologues other than $^{12}C^{16}O$ is very complicated and thoroughly studied, because of the importance of CO molecule, its easy detection and chemical stability (van Dishoeck & Black 1988; Liszt 2007; Visser et al. 2009). The photo-dissociation of CO is a line process and consequently subject to self-shielding that in turn depends on the column density. Therefore, isotopologues other than $C^{16}O$ are not self-shielded unless located very deeply into the molecular clouds due to the much lower abundance of ^{17}O and ^{18}O (Clayton 2003; Lee et al. 2008; Visser et al. 2009). Looking at the case of the Sun, where the isotopic ratios are about $^{16}O/^{18}O \approx 500$ and $^{16}O/^{17}O \approx 2600$ (Lodders et al. 2009; Asplund et al. 2009), the regions with abundances of the isotopologues different than $C^{16}O$ significantly reduced with respect to other isotopologues are located very deeply in the atmosphere. Basing on these considerations, we set the reduction factor of ^{17}O and ^{18}O, ξ'_{CO}, equal to 1/3 of the reduction factor assumed for CO in Eq. 6.5.3. All this agrees with the observational ratios $C^{16}O/C^{17}O$ and $C^{16}O/C^{18}O$ in ζ Oph, > 5900 and ≈ 1550 respectively (Savage & Sembach 1996).

Another point to note is that the ratios ^{16}O to ^{17}O and ^{18}O in the interstellar dust could be different from the same ratios in the ISM (Clayton 1988; Leshin et al.

1997). The subject is a matter of debate, because the above ratios strongly depend on the site where those isotopes condense into dust (Meyer 2009). Consequently, we should not simply scale to ^{17}O and ^{18}O the results obtained for ^{16}O. However, a detailed analysis of this issue is far beyond the purposes of this paper and we leave it to future improvements of our model. For the time being, basing on the following considerations we adopt a simple recipe. As in the dust grains, ^{17}O and ^{18}O are much less abundant than other elements, consider them as the key element of the dust accretion process. Therefore, Eq. 6.4.27 applied to ^{17}O and ^{18}O (briefly indicated as $^{\mathrm{n}}$O) becomes:

$$\left(\frac{d\sigma^D_{(^nO)}}{dt}\right)_{accr} = K\left\{\overline{f}_{(^nO),Pyr}\left(1-\xi'_{CO}\right)\sigma^{\mathcal{M}}_{(^nO),Pyr} - \sigma^D_{(^nO),Pyr}\right\} + K\left\{\overline{f}_{(^nO),Ol}\left(1-\xi'_{CO}\right)\sigma^{\mathcal{M}}_{(^nO),Ol} - \sigma^D_{(^nO),Ol}\right\} \tag{6.5.11}$$

where ξ'_{CO} takes into account that not all ^{17}O and ^{18}O in the ISM can be used to form new grains because part of them are locked in the CO. The relative amounts of ^{17}O and ^{18}O available to form silicates are $\epsilon_{(^nO),Sil} = (1-\xi'_{CO})\left(\sigma^{\mathcal{M}}_{(^nO)}\right)/(A_{(^nO)}\sigma^{\mathcal{M}}_H)$ and the accretion timescales for ^{17}O and ^{18}O are:

$$\tau^{gr}_{^{17}O} = \frac{0.97}{\left(1-\xi'_{CO}\right)n_H}\left(\frac{\sigma^{\mathcal{M}}_H}{\sigma^{\mathcal{M}}_{^{17}O}}\right)Myr \tag{6.5.12}$$

$$\tau^{gr}_{^{18}O} = \frac{1.00}{\left(1-\xi'_{CO}\right)n_H}\left(\frac{\sigma^{\mathcal{M}}_H}{\sigma^{\mathcal{M}}_{^{18}O}}\right)Myr \tag{6.5.13}$$

where we have considered a typical silicate in which just one atom of ^{17}O and/or ^{18}O is involved in the accretion process.

6.5.4 Magnesium

In our simple picture of the the grain accretion process, magnesium intervenes in pyroxenes and olivines, often as the key-element. Furthermore, magnesium is present also in other dust compounds such as MgO contained in the SNe yields of dust. In analogy to the case of Si, the set of equations governing the temporal evolution of the Mg abundance is different depending on whether or not Mg is the key, similarly to silicon. If Mg is a key element:

$$\left(\frac{d\sigma^D_{Mg}}{dt}\right)_{accr} = K\cdot\left\{\overline{f}_{Mg,Pyr}\sigma^{\mathcal{M}}_{Mg,Pyr} - \sigma^D_{Mg,Pyr}\right\} + K\cdot\left\{\overline{f}_{Mg,Ol}\sigma^{\mathcal{M}}_{Mg,Ol} - \sigma^D_{Mg,Ol}\right\} \tag{6.5.14}$$

with the usual meaning of the symbols. The accretion time scales and the initial condensation fractions of Mg can be obtained in the same way as in Sect. 6.5.2, following Eqs. 6.5.8, 6.5.9 and 6.5.5. If Mg is not the key-element, but Si or Fe are playing the role, we have the following equation for the Mg accretion:

$$\left(\frac{d\sigma^D_{Mg}}{dt}\right)_{accr} = K \cdot \frac{A_{Mg,Pyr}\nu^D_{Mg,Pyr}}{A_{i,Pyr}\nu^D_{i,Pyr}} \left\{\overline{f}_{i,Pyr}\sigma^{\mathcal{M}}_{i,Pyr} - \sigma^D_{i,Pyr}\right\} + K\frac{A_{Mg,Ol}\nu^D_{Mg,Ol}}{A_{i,Ol}\nu^D_{i,Ol}} \cdot \left\{\overline{f}_{i,Ol}\sigma^{\mathcal{M}}_{i,Ol} - \sigma^D_{i,Ol}\right\} \tag{6.5.15}$$

in which $A_{Mg,Pyr} = 24$, $\nu^D_{Mg,Pyr} = 0.8$, $A_{i,Pyr} = 28$ or 56 (silicon/iron), $\nu^D_{Si,Pyr} = 1$, $\nu^D_{Fe,Pyr} = 0.2$, $A_{Mg,Ol} = 48$, $\nu^D_{Mg,Ol} = 1.6$, $A_{Si,Ol} = 28$, $\nu^D_{Si,Ol} = 1$ and $\nu^D_{Fe,Ol} = 0.4$. The time scales for accretion of pyroxenes/olivines and the initial condensation fractions are again from Eqs. 6.5.8, 6.5.9 and 6.5.5. For $\sigma^D_{i,Pyr}$ and $\sigma^D_{i,Ol}$ see Sect. 6.5.2.

6.5.5 Iron

Even considering the small number of accreting compounds included in our model, iron can be locked up in grains of various type thanks to accretion processes in cold regions of the ISM. First of all, iron is locked up in iron grains that act as the key element. Second, iron is also present in pyroxene and olivine grains. In such a case, iron may or may not be the key element. In any case it is removed from the gaseous phase and stored in grains. The existence of two channels for locking up iron into grains leads to a rather complicated equation for the evolution of the iron. There are the main terms to consider: in the first and second, iron participates to the formation of silicates (pyroxenes and olivines) *as or not a key-element*, and in the third one iron plays the role of a *key-element* for the formation of iron grains. Furthermore, the equation will be slightly different depending on whether magnesium, silicon or iron is the key-element for the formation of pyroxenes/olivines. The final equation is

$$\begin{aligned}\left(\frac{d\sigma^D_{Fe}}{dt}\right)_{accr} = {} & K\frac{A_{Fe,Pyr}\nu^D_{Fe,Pyr}}{A_{i,Pyr}\nu^D_{i,Pyr}} \left\{\overline{f}_{i,Pyr}\sigma^{\mathcal{M}}_{i,Pyr} - \sigma^D_{i,Pyr}\right\} + K\frac{A_{Fe,Ol}\nu^D_{Fe,Ol}}{A_{i,Ol}\nu^D_{i,Ol}} \left\{\overline{f}_{i,Ol}\sigma^{\mathcal{M}}_{i,Ol} - \right. \\ & \left. - \sigma^D_{i,Ol}\right\} + K\left\{\overline{f}_{Fe,Fe}\left(\sigma^{\mathcal{M}}_{Fe} - \sigma^D_{Fe,Sil}\right) - \right. \\ & \left. - \left(\sigma^D_{Fe} - \sigma^D_{Fe,Sil}\right)\right\}\end{aligned} \tag{6.5.16}$$

where the subscript i stands for Si, Mg or Fe itself. Using the Dirac delta function notation, we have $A_{i,Pyr} = 28{\cdot}\delta\,(A_i - 28){+}24{\cdot}\delta\,(A_i - 24){+}56{\cdot}\delta\,(A_i - 56)$. The same expression holds good for $A_{i,Ol}$. We have also: $A_{Fe,Pyr} = A_{Fe,Ol} = 56$, $\nu^D_{Fe,Pyr} = 0.2$ (according to $\mathrm{Mg_xFe_{1-x}SiO_3}$ with $x = 0.8$), $\nu^D_{i,Pyr} = 1{\cdot}\delta\,(A_i - 28){+}0.8{\cdot}\delta\,(A_i - 24){+}$ $0.2{\cdot}\delta\,(A_i - 56)$, $\nu^D_{Fe,Ol} = 0.4$ (according to $[\mathrm{Mg_xFe_{1-x}}]_2\,\mathrm{SiO_4}$ with $x = 0.8$) and finally $\nu^D_{i,Ol} = 1 \cdot \delta\,(A_{i,Ol} - 28) + 1.6 \cdot \delta\,(A_{i,Ol} - 24) + 0.4 \cdot \delta\,(A_{i,Ol} - 56)$. Also, with the usual meaning, $\overline{f}_{i,Pyr}$, $\overline{f}_{i,Ol}$ and $\overline{f}_{Fe,Fe}$ are the average condensations before cloud dispersion.

For internal consistency, the system of equations must take into account that the iron abundance used to describe the evolution of the iron grains should be corrected for the iron already condensed into pyroxenes and olivines, subtracting it from $\sigma^{\mathcal{M}}_{Fe}$ and σ^D_{Fe}. If the key-element is magnesium, the amount of iron $\sigma^D_{Fe,Sil}$ embedded into pyroxenes and olivines is given by:

$$\sigma^D_{Fe,Sil} = \frac{\sigma^D_{Mg} A_{Fe}}{24}\left(\frac{\nu^D_{Fe,Ol}}{\nu^D_{Mg,Ol}} Mg_{Ol} + \frac{\nu^D_{Fe,Pyr}}{\nu^D_{Mg,Pyr}} Mg_{Pyr}\right) \tag{6.5.17}$$

where A_{Fe} is the atomic weight of the iron and Mg_{Ol} and Mg_{Pyr} are defined in Sect. 6.5.2. Doing the correct substitution we get

$$\sigma^D_{Fe,Sil} = \sigma^D_{Mg}\,(0.583 \cdot Mg_{Ol} + 0.583 \cdot Mg_{Pyr}) \tag{6.5.18}$$

In a similar way, if the role of key element is played by silicon we have:

$$\sigma^D_{Fe,Sil} = \sigma^D_{Si}\,(0.8 \cdot F_{Ol} + 0.4 \cdot F_{Pyr}) \tag{6.5.19}$$

where F_{Ol} and F_{Pyr} have been defined in Sect. 6.5.2. If iron is the key element for silicates, we simply have:

$$\sigma^D_{Fe,Sil} = \sigma^D_{Fe} - \sigma^D_{Fe,Fe} \tag{6.5.20}$$

This clearly requires to keep track of the accretion/destruction and injection of the iron grains by SNe and AGB stars. The accretion time scales for pyroxenes/olivines are the same as in Eqs. 6.5.8 and 6.5.9, whereas for iron grains:

$$\begin{aligned}\tau^{gr}_{Fe} &= 46\frac{(A^{gw}_{Fe})^{1/2}\nu^D_{Fe,Fe}}{A^D_{Fe}}\left(\frac{\rho^{Fe}_D}{3}\right)\left(\frac{10^3}{n_H}\right)\cdot \\ &\cdot\left(\frac{3.5\cdot 10^{-5}}{\epsilon_{Fe,Fe}}\right) = \frac{31.56}{n_H}\frac{\sigma_H}{\left(\sigma^{\mathcal{M}}_{Fe} - \sigma^D_{Fe,Sil}\right)} Myr.\end{aligned} \tag{6.5.21}$$

where $\nu^D_{Fe,Fe} = 1$ and $\rho^D_{Fe} = 7.86\,\mathrm{g\,cm^{-3}}$. Concerning the accreting elements we consider the simplest case in which they are in form of atoms. The initial condensation fractions for magnesium/silicon as key-elements ca be obtained as already described for carbon, while for iron we have:

$$f_{0,Fe,Fe} = \frac{\chi^D_{Fe}}{\chi^D_{Fe,max}} = \frac{\sigma^D_{Fe} - \sigma^D_{Fe,Sil}}{\sigma^{\mathcal{M}}_{Fe} - \sigma^D_{Fe,Sil}}. \tag{6.5.22}$$

where we subtract the amount of iron already locked up in silicates and therefore not available to form iron grains.

6.5.6 Calcium

This element has a complicate behaviour difficult to follow. First of all it is usually heavily depleted in the ISM (Whittet 2003; Tielens 2005), and its abundance in the solar system is quite low. The difficult arises from the total condensation efficiency and the big fluctuations generated by the low abundance, compared to other refractory elements. Second there is not an average molecule that could be used to represent typical calcium grains in a simple theoretical description. Furthermore, the measurements of depletion cannot be easily derived from observational data: in principle the ionization equilibrium equation should be solved to derive the Ca abundance from the observations of Ca II. Possible estimates of Ca abundances by electron densities and strengths of the ionizing radiation fields are not easy and relying on ratios of ionization and recombination rates between different elements (like CaII to those of NaI or KI for instance) is a cumbersome affair (Weingartner & Draine 2001b). For all these reasons, (Jenkins (2009) - private communication) leaved Ca (and also Na and K) aside. Trying to overcome this difficulty, we simplify the problem as follows. Thanks to its low abundance, we consider Ca as the key-element of the associated grains of dust; the equation for the evolution of Ca is:

$$\left(\frac{d\sigma^D_{Ca}}{dt}\right)_{accr} = K\left\{\overline{f}_{Ca,Ca}\sigma^{\mathcal{M}}_{Ca}(Ca) - \sigma^D_{Ca}(Ca)\right\} \tag{6.5.23}$$

where all the symbols have their usual meaning. To derive the accretion time scale τ^{gr}_{Ca} we do not refer to a typical Ca dust grain but simply take *the shortest* timescale among those of refractory elements that are most depleted, i.e. Mg, Si and Fe ($\tau^{gr}_{Si}, \tau^{gr}_{Mg}, \tau^{gr}_{Fe}$), and a timescale $\tau^{gr}_{Ca,Ca}$ for the formation of dust silicates-like molecules with one calcium atom as key atom. This last-named timescale is multiplied for a correction factor Ca_X, eventually allowing for a fast accretion. Therefore $\tau^{gr}_{Ca} = \min\{\tau^{gr}_{Si}, \tau^{gr}_{Mg}, \tau^{gr}_{Fe}, Ca_X \cdot \tau^{gr}_{Ca,Ca}\}$. The initial condensation fraction at the MC formation is as usual $f_{Ca,Ca} = \sigma^D_{Ca}/\sigma^{\mathcal{M}}_{Ca}$.

6.5.7 Sulfur

Sulfur is a very important element: it is often used as a reference case of nearly zero depletion in studies of local and distant objects (Jenkins 2009). However the real depletion efficiency of this element is a matter of debate and the assumption of nearly zero depletion cannot be safe. Calura et al. (2009) reviews data and theoretical interpretations gathered over the past years to convincingly show that S can be depleted in considerable amounts. Jenkins (2009) points out the depletion of sulfur can be significant along some lines of sight. We take Jenkins (2009) results into account to set upper and lower limits to the sulfur depletion. Considering sulfur as a refractory element, its evolution in dust is given by

$$\left(\frac{d\sigma_S^D}{dt}\right)_{accr} = K\left\{\overline{f}_{S,S}\sigma_S^{\mathcal{M}}(S) - \sigma_S^D(S)\right\} \tag{6.5.24}$$

where all the symbols have their usual meaning. Current observations do allow us to choose a grain as representative of the accretion process. In analogy to what made for calcium, the accretion time $\tau_{S,gr}$ is supposed to be *the longest* between the timescales of the refractory elements, i.e. Mg, Si and Fe, and a timescale $\tau_{S,S}^{gr}$ for the formation of dust silicates-like molecules with one sulfur atom as key atom, allowing therefore for a slow accretion. We also introduce a multiplying scaling factor S_X to eventually correct this timescale. Therefore $\tau_S^{gr} = S_X \cdot \max\{\tau_{Si}^{gr}, \tau_{Mg}^{gr}, \tau_{Fe}^{gr}, \tau_{S,S}^{gr}\}$. The initial condensation fraction for $\overline{f}_{S,S}$ is $f_{S,S} = \sigma_S^D/\sigma_S^{\mathcal{M}}$.

6.5.8 Nitrogen

Nitrogen is known to be poorly depleted and if not depleted at all (Whittet 2003; Tielens 2005). Jenkins (2009) suggests that depletion is independent from the line of sight depletion strength factor and that in any case depletion is very low, thus confirming the poor ability of nitrogen to condense into dust grains. As nitrogen is included in our list of elements (both ^{14}N and ^{15}N), the evolution of both isotopes in dust is governed by:

$$\left(\frac{d\sigma_N^D}{dt}\right)_{accr} = K\left\{\overline{f}_{N,N}\sigma_N^{\mathcal{M}}(N) - \sigma_N^D(N)\right\} \tag{6.5.25}$$

where for the accretion time we simply take the *longest* between C and O and the accretion timescale with one nitrogen atom as growing species for a nitrogen molecule. Carbon and oxygen are the nearest elements, both do not show a strong depletion and, finally, similarly to nitrogen both indicate (at least along some lines of sight) low values of depletion. Taking the longest timescale, we implicitly assume that nitrogen very slowly accretes onto dust. As usual $f_{N,N} = \sigma_N^D/\sigma_N^{\mathcal{M}}$.

6.6 Supernovae: the destruction term

As we have seen in Sect. 6.2, we are dealing not only with the accretion of dust, but also with a term taking into account the effects of destruction of the interstellar dust, thus restituting heavy elements to the gaseous component. Dust grains in the ISM can be destroyed by physical process such as the passage of shock waves by supernovæ explosions. The destruction time scale of the element i-h in dust grains in the ISM because of the shocks by local SNe is defined as the ratio between the available amount of that element locked up into dust (the surface mass density $\sigma_i^D(r,t)$, at a given radius and evolutionary time) and the rate at which grains containing that element are destroyed refueling the gaseous phase :

$$\tau_{SNR,i} = \sigma_i^D \Big/ \left(\frac{d\sigma_i^D}{dt}\right)_{SNR} \tag{6.6.1}$$

as usual, we drop the dependence from r and t. The destruction time scale can be expressed as follows:

$$\left(\frac{d\sigma_i^D}{dt}\right)_{SNR} = M_i^{destr} \cdot R_{SN} \tag{6.6.2}$$

where $M_i^{destr} = M_i^{destr}(r,t)$ is the amount of mass destroyed by a single SN event, while $R_{SN} = R_{SN}(r,t)$ is the global rate of SNe, obtained by adding together the rate of Type I and II SNe. Multiplying numerator and denominator by σ_i^D and combining together Eqs. 6.6.1 and 6.6.2 it follows:

$$\tau_{SNR,i} = \sigma_i^D \Big/ \left(\frac{d\sigma_i^D}{dt}\right)_{SNR} = \frac{1}{R_{SN}} \frac{\sigma_i^D}{M_i^{destr}} \,. \tag{6.6.3}$$

The amount of mass destroyed by the interstellar shocks can be defined as the amount of mass swept by the SN shock, multiplied by the fraction of dust mixed with the ISM (in this way we get the total swept up mass of dust) and finally by a factor of dust destruction ϵ_i that depends on the element we are taking into account:

$$M_i^{destr} = \frac{\sigma_i^D}{\sigma_i^{\mathcal{M}}} \cdot M_{swept} \cdot \epsilon_i \,. \tag{6.6.4}$$

Inserting this expression into Eq. 6.6.3 we have:

$$\tau_{SNR,i} = \frac{1}{R_{SN}} \frac{\sigma_i^D}{M_i^{destr}} = \frac{1}{M_{swept}\epsilon_i} \left(\frac{\sigma_i^{\mathcal{M}}}{R_{SN}}\right) . \tag{6.6.5}$$

We need now to get an estimate of the mass swept up by a SN shock propagating through the ISM. To describe the evolution of the SN remnant we follow Cioffi et al. (1988) and Gibson (1994). In brief, the evolution of the remnant after the SNa explosion is subdivided into three main phases: (i) free expansion that lasts until the

mass of the swept up material is comparable to the mass of the expelled material; (ii) adiabatic expansion, or so-called Sedov-Taylor phase, lasting until when the radiative cooling time of the shocked gas is about equal to the expansion time of the remnant; (iii) radiative expansion, with the formation of a cold and dense shell behind the shock front, starting when at least some sections of the shocked gas have radiated most of their thermal energy (Ostriker & McKee 1988). Phase (i) has a simple solution that can be obtained using the obvious relation $(4/3)\,\pi R^3 \rho_0 = M_{SN}$ where M_{SN} is the mass of the expelled material. The duration of the phase is $\tau = R/v \approx 200$ years (very short indeed). For the phase (ii) we have the classical auto-similar adiabatic solution of Sedov-Taylor (Ostriker & McKee 1988);

$$R_s\,(t) = 1.15 \left(\frac{E_0}{\rho_g\,(t)}\right)^{1/5} t^{2/5} \tag{6.6.6}$$

where E_0 is the energy of the blast wave in units of 10^{50} erg and $\rho_g\,(t)$ is the density of the environment. The radiative cooling leads to the formation of a thin and dense shell at t_{sf}:

$$t_{sf} = 3.61 \cdot 10^4 \cdot \varepsilon_0^{3/14} n_H^{-4/7} \left(\frac{Z}{Z_\odot}\right)^{-5/14} \tag{6.6.7}$$

$n_{\rm H}$ is the number density of hydrogen atoms, Z the metallicity of the ISM and $Z_\odot$ the solar value. ε_0 is the energy in units of 10^{51} erg. The blast wave decelerates until when the radiative losses start dominating. At about $t_{PDS} \approx 0.37 t_{sf}$, the remnant enters the so-called Pressure Driven Snowplow phase (PDS) lasting or Phase (iii). In the early stages of the PDS phase, the radius of the remnant changes according to the following equation (where $t_{SN} = t - t'$):

$$R_S\,(t_{SN}) = R_{PDS} \left(\frac{4}{3}\frac{t_{SN}}{t_{PDS}} - \frac{1}{3}\right)^{3/10} \tag{6.6.8}$$

where the radii are in parsec. R_{PDS} is the radius at the start of the PDS phase:

$$R_{PDS} = 14 \cdot \varepsilon_0^{2/7} n_0^{3/7} \left(\frac{Z}{Z_\odot}\right). \tag{6.6.9}$$

The inner side of the shock continuously looses energy because of the radiative cooling and it pushes forward the shell in the ISM. At the time t_{merge}, given by:

$$t_{merge} = 21.1 \cdot t_{sf} \varepsilon_0^{5/49} n_0^{10/49} \left(\frac{Z}{Z_\odot}\right)^{15/49}. \tag{6.6.10}$$

The remnant and the ISM loose their identity as single entities and merge together. Subsequently, in the time interval for $t_{merge} \leq t_{SN} \leq t_{cool}$ the radius of the shell is given by:

$$R_{merge} = 3.7 R_{PDS} \varepsilon_0^{3/98} n_0^{3/49} \left(\frac{Z}{Z_\odot} \right)^{9/98} \tag{6.6.11}$$

in parsec, where the time scale t_{cool} is:

$$t_{cool} = 203 t_{sf} \left(\frac{Z}{Z_\odot} \right)^{-9/14} \tag{6.6.12}$$

in years. There are four time intervals, with the corresponding radii, to consider:

$$\begin{aligned}
&R_S\left(t_{SN}\right) = 1.15 \left(\tfrac{E_0}{\rho_g(t)}\right)^{\frac{1}{5}} t_{SN}^{\frac{2}{5}} && 0 \le t_{SN} < t_{PDS};\\
&R_S\left(t_{SN}\right) = R_{PDS} \left(\tfrac{4}{3}\tfrac{t_{SN}}{t_{PDS}} - \tfrac{1}{3}\right)^{\frac{3}{10}} && t_{PDS} \le t_{SN} < 1.17 t_{sf};\\
&R_S\left(t_{SN}\right) = R_{PDS} \left(\tfrac{4}{3}\tfrac{t_{SN}}{t_{PDS}} - \tfrac{1}{3}\right)^{\frac{3}{10}} && 1.17 t_{sf} \le t_{SN} < t_{merge};\\
&R_S = 3.7 R_{PDS} \varepsilon_0^{\frac{3}{98}} n_0^{\frac{3}{49}} \left(\tfrac{Z}{Z_\odot}\right)^{\frac{9}{98}} && t_{merge} \le t_{SN} < t_{cool}\,.
\end{aligned} \tag{6.6.13}$$

To obtain the shock velocity in the various time intervals, we need the R_S as functions of time. Approximating $\rho_g\left(t\right) \approx \overline{\rho}_g$, we get:

$$\begin{aligned}
&v_S\left(t_{SN}\right) = \tfrac{2}{5}\tfrac{R_S(t)}{t} && 0 \le t_{SN} < t_{PDS};\\
&v_S\left(t_{SN}\right) = \tfrac{2}{5}\tfrac{R_{PDS}}{t_{PDS}} \left(\tfrac{4}{3}\tfrac{t}{t_{PDS}} - \tfrac{1}{3}\right)^{-\frac{7}{10}} && t_{PDS} \le t_{SN} < 1.17 t_{sf};\\
&v_S\left(t_{SN}\right) = \tfrac{2}{5}\tfrac{R_{PDS}}{t_{PDS}} \left(\tfrac{4}{3}\tfrac{t}{t_{PDS}} - \tfrac{1}{3}\right)^{-\frac{7}{10}} && 1.17 t_{sf} \le t_{SN} < t_{merge};\\
&v_S\left(t_{SN}\right) = 0 && t_{merge} \le t_{SN} < t_{cool}\,.
\end{aligned} \tag{6.6.14}$$

After t_{merge} there is no longer expansion and we simply have $v_S\left(t_{SN}\right) = 0$. How do we proceed in the chemical simulation? First of all we need n_{H}, the number density of hydrogen atoms. This is a spatial density, in atoms per cubic centimeter; we must derive it from the surface mass density of hydrogen in our flat geometry. This is done assuming as parameters the scale height and thickness of the disk suggested by the observational data. Once n_{H} is known, we derive the time scales t_{sf}, t_{PDS} and t_{merge}, and finally the radii of the remnant and velocity of the shock at the beginning and end of the three evolutionary phases we have described. At this point we must fix the velocity v_{low} setting the limit at which the shock stops disrupting the dust grains. A typical value is about 50 km/s (see for a thorough discussion of this point Nozawa et al. (2006) and Nozawa et al. (2007)). Knowing the limit velocity, we can soon determine the time in which the remnant expanding at the limit velocity covers a distance equal to its own radius. The swept up mass is:

$$M_{swept} = \frac{4}{3}\pi R \left(v_{low}\right)^3 n_H\,. \tag{6.6.15}$$

The other factors of Eq. 6.6.5 are the ratio $\sigma_i^{\mathcal{M}}/R_{SN}$ and the coefficients ϵ_i that describe the fraction of the element i condensed into dust that is destroyed by the shock. While the ratio $\sigma_i^{\mathcal{M}}/R_{SN}$ is simply provided by the chemical model in use, to

calculate ϵ_i we refer to the studies by Nozawa et al. (2006) and Nozawa et al. (2007). In brief, the Nozawa et al. (2006) data are used in the first evolutionary phases of the galaxies to derive the destruction coefficients for the ISM dust. From Tab. (6) of Nozawa et al. (2006) we take the a_i and b_i to be used in:

$$\epsilon_j = a_j E_{51}^{b_j} \tag{6.6.16}$$

where E_{51} is the energy of the supernova in units of 10^{51} erg. For simplicity we assume $E_{51} = 1$, typical energy of the explosion of SNe of mass not too high, that according to the IMF are also the most numerous. In this way we get the coefficients to be used for destruction by forward shocks in the ISM. Furthermore, the results by Nozawa et al. (2007) are used to constrain the yields by the SNe progenitors, before dust is injected into the ISM where it will interacts with the shocks generated by the surrounding SNe. Therefore we take into account the amount of material injected into the ISM (Nozawa et al. 2003) corrected for the effect of the internal reverse shock.

6.7 Yields of star-dust

As we described in Sect. 6.2, one of the key ingredients of the equations describing the evolution of the abundances of the elements in gas and dust are the condensation efficiencies: they allow to take into account the amount of dust injected in the ISM by the main dust factories, SNe and AGB stars. A careful treatment of them is necessary, in particular according to the recent interest in the high-z universe.

Indeed, current observations unveiled the existence of a high-z universe heavily obscured by large quantities of dust (Shapley et al. 2001; Carilli et al. 2001; Bertoldi et al. 2003; Robson et al. 2004; Wang et al. 2008; Wang et al. 2008; Michałowski et al. 2010; Michałowski et al. 2010). Once established the presence of dust, some key questions still remain about the physical origin of this dust, its chemical composition and its influence on the starlight in high-z galaxies. These questions are hardly debated in literature, in order to understand if SNe can account, da sole, for these dust (Gall et al. 2011b), if the contribution of increased dust in the interstellar medium can be neglected or not (Dwek et al. 2009; Draine 2009; Mattsson 2011) and what is the role played by the more massive AGB stars (Valiante et al. 2009).

The concept of duty cycle for the dust must be introduced to suitably describe the formation and evolution of dust in high-z and local galaxies, and to simultaneously infer precious clues on when and how galaxies formed and evolved. The cyclic history of the interstellar dust is described in detail by Zhukovska et al. (2008) and nicely illustrated in the classical diagram by Jones (2004). In brief, low and intermediate

AGB stars thanks to mass loss by stellar winds, and massive stars thanks to the Core Collapse SNa explosions (CCSNe), inject refractory elements in the ISM: most of this material is in gaseous form, but important amounts of it condense into the so-called *star-dust*. Once mixed in the turbulent ISM, star-dust grains are subjected to destructive processes that restitute the material to the gaseous phase. The competition between this process and the one of dust accretion onto the so-called seeds in dense and cold molecular clouds determines the total budget of dust in the ISM and the observed depletion of the refractory elements by formation of new dust grains. In the MCs, where dust accretes and cools down the region, star formation takes place generating new stars that in turn evolve and die, thus more and more enriching the ISM with new metals and star-dust.

It is soon evident that some key agents must intervene to drive the evolution of dust. They are some grains or grain families with given composition and properties, the physical mechanisms of formation/accretion and destruction of dust in the ISM, and finally the yields of dust by stars.
Dealing with star-dust to be included in the equations for chemical evolution of the ISM, the best way to account for it is to use a compilation of condensation efficiencies δ (Dwek 1998; Calura et al. 2008) to be applied to the masses of *single elements* restituted by stars to the ISM. In other words, starting from the classical compilations of the gas mass in form of a given element ejected by each star during its life back into the ISM, we provide a compilation of coefficients giving the dust-to-gas ratio for that specific ejecta.

Many different recipes are proposed to deal with the two main factories of star-dust (AGB stars and SNe): some of them consider only the total amount of dust that is injected and neglect its composition, others adopt simple schemes to follow the evolution of a group of elements and/or molecules taken as representative of the dust in the ISM. In Tab. 6.7 we list all the prescriptions we have adopted based on the most recent models of dust formation and destruction.
In this section the best theoretical recipes available nowadays in literature to estimate the amount of dust produced by SNe and AGB stars are discussed and for SNe compared to the observations to get clues on the problem. The condensation efficiencies have been then analyzed in the context of our model of dust formation and evolution in the Solar Ring and Galactic Disk.

6.7.1 Yields of dust by SNe

SNe are primary sites of dust formation. The direct evidence began with the pioneering observations of the SN 1987A (Danziger et al. 1991; Dwek et al. 1992; McCray

Table 6.1: Prescriptions taken from literature to model the star-dust contribution to the ISM.

Work	AGB stars	SNe
Calura et al. (2008)[1]	Dwek (1998)	Dwek (1998)
Zhukovska et al. (2008)[2]	Ferrarotti & Gail (2006)	Its own δ^{SN} scheme
Valiante et al. (2009)[3]	Ferrarotti & Gail (2006)	Bianchi & Schneider (2007)
Pipino et al. (2011)[4]	Dwek (1998)	revised Dwek (1998)
Yamasawa et al. (2011)[5]	no AGB stars	Nozawa et al. (2003), Nozawa et al. (2007)
Gall et al. (2011a, Gall et al. (2011b)[6]	Ferrarotti & Gail (2006)	Todini & Ferrara (2001), Nozawa et al. (2003), Nozawa et al. (2006)
Dwek & Cherchneff (2011)[7]	Dwek (1998)	Its own δ^{SN} scheme

[1]The same condensation efficiencies δ proposed by Dwek (1998) are adopted. [2]Low and constant condensation efficiencies are proposed and adopted for SNe. [3]The original model by Todini & Ferrara (2001) for dust formation in SNe is extended to a wider set of initial conditions and model assumptions. [4]Condensation efficiencies δ by Dwek (1998) are lowered to match the observation of dust in CCSNe, thus including in some way the uncertainties of the destructive reverse shock effects. [5]Only SNe are included as dust factories because the study is limited to the very early universe. [6]Average coefficients are obtained in order to study the evolution of the total dust mass in star-burst galaxies and QSOs. [7]Only the average total amount of dust formed in SNe and WR is considered.

1993; Bautista et al. 1995; Dwek 1998) until the recent and deep observations of the SN 1987A itself and other SNe. These new data are obtained by means of the new generation of IR and sub-mm instruments, like Spitzer (Bouchet et al. 2006; Meikle et al. 2007; Rho et al. 2008; Rho et al. 2009; Kotak et al. 2009; Rho et al. 2009), Akari (Sakon et al. 2009), SCUBA and PACS/SPIRE onboard Herschel Space Observatory (for a global summary about these instruments, see Chap. 2).
Given these premises, some questions arise:

- How much dust is produced by a single SNa (according to the observational data)?
- What is the condensation efficiency of the different refractory elements during the evolution of the SNa remnants, when the effects of forward and reverse shocks are taken into account (Nozawa et al. 2006; Nozawa et al. 2007; Kozasa et al. 2009)?
- Do SNe produce enough dust to significantly contribute to the obscuration of primordial galaxies or a substantial amount of that dust is due to nucleation

Table 6.2: Observational data on the dust formation in the ejecta and remnants of CCSNe and in the Kepler SNa, the progenitor of which is still controversial.

SNe[1]	Galaxy[2]	Type[3] ($M_\odot$)	$M_{*,prog}$[4] ($M_\odot$)	M_d[5]
SN 1987A	LMC	II-peculiar	$20^{(25)}$	$2\cdot10^{-4}-1.3\cdot10^{-3\,(25)}$, 0.4-0.7$^{(27)}$
SN 1999em	NGC1637	II-P$^{(6)}$	$12-14^{(6)}$	$>10^{-4\ (6)}$
SN 2003gd	M74	II-P$^{(7)}$	8^{+4}_{-2} $^{(9)}$	$10^{-4\ (7)}-0.02\ ^{(9)}$
Kepler	MW	Ia$^{(10,12)}$,Ib$^{(11)}$,II-L$^{(11)}$	$8\ ^{(10)}-\ >10\ ^{(11)}$	$0.09\ ^{(13)}-0.14\ ^{(13)}$; $<1.2^{(13)}$
SNR1E0102.2-7219	SMC	Ib,Ic,II-L$^{(17)}$	$25^{(14)}$	$8\cdot10^{-4\,(15)}$ - $0.014^{(16)}$
Cassiopeia A	MW	IIn$^{(21)}$-IIb$^{(20)}$	13-30$^{(18,20)}$	$0.02-0.054^{(19)}$; $<1.0^{(26)}$
SN 2005af	NGC 4945	II-P$^{(22)}$	13-35$^{(22)}$	$4\cdot10^{-4\,(23)}$
N 132D	LMC	Ib$^{(24)}$	30-35$^{(24)}$	$>8\cdot10^{-3\,(24)}$

[1]Identification name of the SNe and remnants. [2]Galaxy in which the supernova has been observed. [3]Classification of the CCSNe and thermonuclear SNe according to the observational scheme: almost all of the tabulated objects are CCSNe, only for Kepler SNa the classification is still debated. [4]Estimated mass of the progenitor in solar masses. [5]Estimated mass of dust condensed in the remnant. [6]Elmhamdi et al. (2003). [6]Meikle et al. (2007). [8]Hendry & Smartt (2005). [9]Sugerman et al. (2006). [10]Reynolds et al. (2007). [11]Bandiera (1987). [12]Cassam-Chenaï et al. (2004). [13]Gomez et al. (2009). The estimated mass depends strongly on the absorption coefficient κ. The adopted value is the one appropriate for SNa dust according to Dunne et al. (2009). But for different κ the estimate could grow until $1.2M_\odot$ or even more (Gomez et al. 2009). . [14]Sandstrom et al. (2009). [15]Stanimirović et al. (2005). [16]Rho et al. (2009), but according to the estimate by Sandstrom et al. (2009), up to $0.6M_\odot$ of cold dust could be present. [17]Finkelstein et al. (2004). [18]Young (2006). [19]Rho et al. (2008). [20]Krause et al. (2008). [21]Chevalier & Oishi (2003). [22]Kotak et al. (2006). [23]Kotak (2008). [24]Rho et al. (2009). [25]Ercolano et al. (2007). [26]Dunne et al. (2009) [27]Matsuura et al. (2011).

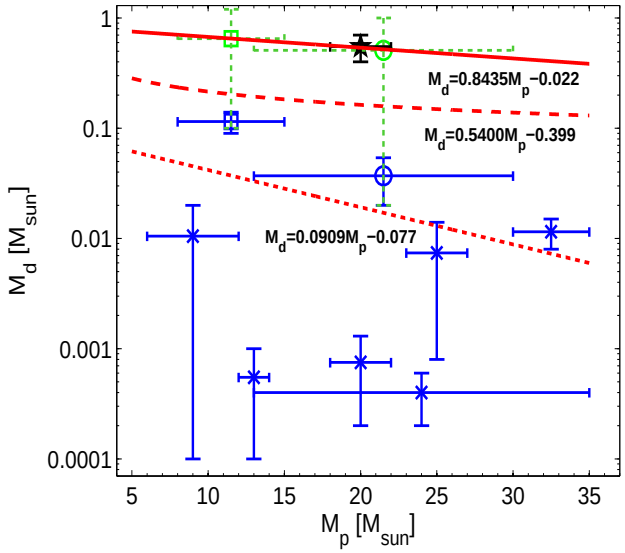

Figure 6.4: Observational estimates of the masses of newly formed dust M_d in the CCSNe (four-points stars and solid line error bars) as a function of the progenitor mass M_p, both expressed in solar units. The recent estimates of the amount of newly formed dust in Kepler SNa (square with dotted line error bars), Cas A (circle with dotted line error bars) obtained by sub-mm observations, and in SN 1987A (five-pointed star with continuous line error bars) with the PACS/SPIRE onboard the Herschel Space Observatory are also displayed. Three fits are shown: the dotted line represents the best fit obtained from using only the masses of dust determined by NIR/MIR observations; the dashed line represents the best fit to all the data; finally, the continuous line represents the best fit only to the amounts of dust derived from FIR/sub-mm data.

in the ISM with SNe mainly providing the seeds on which dust grains of the ISM grow (Dwek et al. 2009; Draine 2009)

- Do current theoretical models of dust formation (Todini & Ferrara 2001; Nozawa et al. 2003; Schneider et al. 2004; Kozasa et al. 2009) agree with the observational data (Rho et al. 2008; Rho et al. 2009; Kozasa et al. 2009; Rho et al. 2009; Matsuura et al. 2011)?

- Above all, which kind of SNe produce dust?

Which kind of SNe produce dust?

From the entries of Tab. 6.2 we note that nearly all SNa types are dust producers. The only exception are type Ia SNe in which no dust has been detected (Borkowski et al. 2006; Draine 2009), even if the classification of Kepler SNa is still uncertain and can suggest a type Ia SNa. In addition to this, in meteorites no pre-solar grains formed in type Ia thermonuclear SNe explosions have been found (Clayton & Nittler

2004). Therefore, it is most likely that type Ia SNe have almost zero condensation efficiency. Recently, Kozasa et al. (2009) calculated some models of dust formation in CCSNe, based upon the same formalism of Nozawa et al. (2003), but using different underlying models of SNe. The aim was to investigate the effects on dust nucleation of a different amount of hydrogen in the envelope at the onset of the collapse. In Fig. 6.5 (left panel) the total yields of dust by Kozasa et al. (2009) compared to Nozawa et al. (2003) yields, are shown. When the hydrogen-rich envelope at the onset of the collapse is thick, the models agree each other, and the total amount of dust produced is about the same. On the contrary, the effect of the hydrogen-rich envelope on the amount of dust produced is significant: for type IIb SNe it drops by a factor of about three, from $\sim 0.45 M_{\odot}$ to $0.167 M_{\odot}$. This fact suggests that in chemical models of galaxies it would be interesting to distinguish the contribution by different types of CCSNe, e.g. because of different mass loss histories a different onion-like structures of the progenitor (Kozasa et al. 2009; Gall et al. 2011a). The effect of the varying hydrogen envelope could modify our view of the types of SNe able to produce significant amounts of dust.

How much dust can a single supernova inject into the ISM?

Since the early observations of the SNa 1987A, this question has long been debated with controversial answers. Indeed: (1) The sample of observed SNe with ongoing dust formation is small, hence it is almost impossible to get some reliable clues about the link between mass and metallicity of the progenitor and the amount of produced dust; (2) The MIR-NIR observations could miss the presence of a significant amount of cold and very cold dust. Only with SCUBA-2, ALMA, and Herschel Space Observatory we might be able to highlight this issue (Gomez et al. 2007; Rho et al. 2008; Nozawa et al. 2008; Dunne et al. 2009; Gomez et al. 2009). The very recent discovery of a significant amount of very cold dust grains in SN 1987A (Matsuura et al. 2011) seems to strengthen this point; (3) It is not clear if and how much dust is embedded in a thin envelope or in thick clumpy regions, thus making quantitative estimates highly uncertain (Ercolano et al. 2007), if the assumption that the radiation emitted by dust comes from an optically thin region (Kozasa et al. 2009; Meikle et al. 2007); (4) It is always a cumbersome affair to discriminate between contamination by foreground dust and dust residing and forming locally in the observed SNa (Dunne et al. 2003; Krause et al. 2004; Wilson & Batrla 2005; Rho et al. 2008).

The Tab. 6.2 summarize the most significant observations of dust formation in SNe and the available information about the progenitor mass and the SNa type: because of the uncertainties and the poor statistics, it is not possible to disentangle the

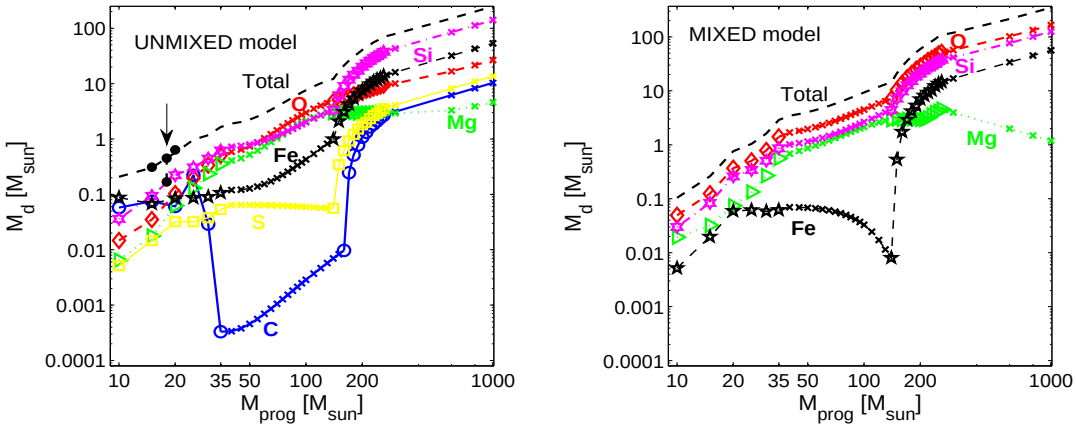

Figure 6.5: Yields of dust for C, O, Mg, Si, S and Fe, calculated from the list of dust compounds of Nozawa et al. (2003) and the *unmixed* (**Left Panel**) and *mixed* (**Right Panel**) models of ejecta as a function of the progenitor mass. All quantities on display are expressed in solar masses. Small crosses represent extrapolations from the data of Nozawa et al. (2003) to other mass ranges. The legend is as follows: C (empty circles and continuous line); O (diamonds and dashed line); Mg (triangles and dotted line); Si (six-pointed stars and dot-dashed line); S (squares and continuous line) and Fe (five-pointed stars and dashed line). The dashed line without markers represents the total amount of dust left over by the shocks in the SNR. We also show (filled circles) the total yields of dust by Kozasa et al. (2009) for the unmixed 15, 18 and 20$M_\odot$ models. The effect of a different hydrogen-rich envelope on the amount of dust formed by a 18$M_\odot$ model is also indicated by the arrow.

complex dependence of the observed ongoing dust formation on physical parameters like the mass and metallicity of the progenitor star and the density of the underlying environment where the explosion took place. For Kepler and Cas A SNe we show also the estimates derived from taking into account recent sub-mm determinations of the cold dust contribution (Dunne et al. 2009; Gomez et al. 2009). If we consider all the objects whose estimates of the dust content is based *only* upon observations of warm dust in the NIR/MIR, the analytical fit yields about 0.006-0.05 $M_\odot$ of dust per SNa, depending on the progenitor mass. Clearly, this is only a mean lower limit because we are neglecting the cold dust emitting at longer wavelengths, which could easily increase the average estimate by one or even two orders of magnitude, i.e. up to 0.1-0.2 $M_\odot$ of dust per SNa (dashed line in Fig. 6.4). If we consider only the observations taking into account FIR/sub-mm data, we get 0.4-0.7 $M_\odot$ per SNa: in this case SNe would be very efficient dust factories! However, with a sample of only three data drawing any conclusion would be premature. More sub-mm data from SCUBA-2, ALMA, and Herschel Space Observatory are needed to solve the problem.

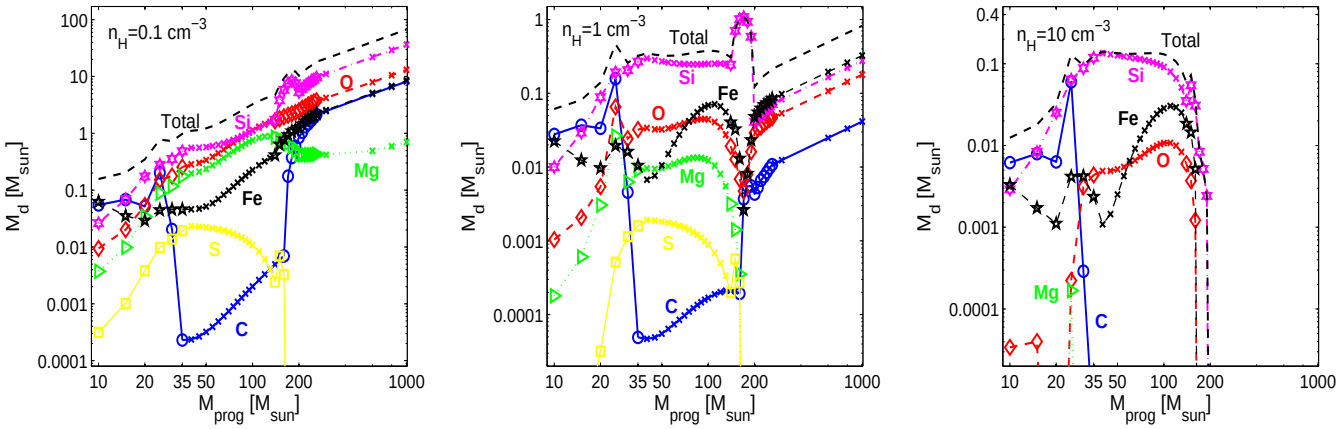

Figure 6.6: Masses of C, O, Mg, Si, S and Fe, hidden in the dust and left over by the reverse shocks in SNRs (Nozawa et al. 2007) as a function of the progenitor mass, for the *unmixed* grain model of Nozawa et al. (2003) and at varying the hydrogen number density n_H. All quantities on display are expressed in solar masses. Small crosses represent extrapolations from the dust yields calculated by Nozawa et al. (2003) to other mass ranges. The legend is as follows: C (empty circles and continuous line); O (diamonds and dashed line); Mg (triangles and dotted line); Si (six-pointed stars and dot-dashed line); S (squares and continuous line) and Fe (five-pointed stars and dashed line). The dashed line without markers represents the total amount of dust survived to the shocks in the SNR. **Left Panel**: Masses of C, O, Mg, Si, S and Fe in dust survived to reverse shocks for $n_H = 0.1\,cm^{-3}$. **Middle Panel**: The same as in left panel but for $n_H = 1\,cm^{-3}$. **Right Panel**: The same as in left panel but for $n_H = 10\,cm^{-3}$.

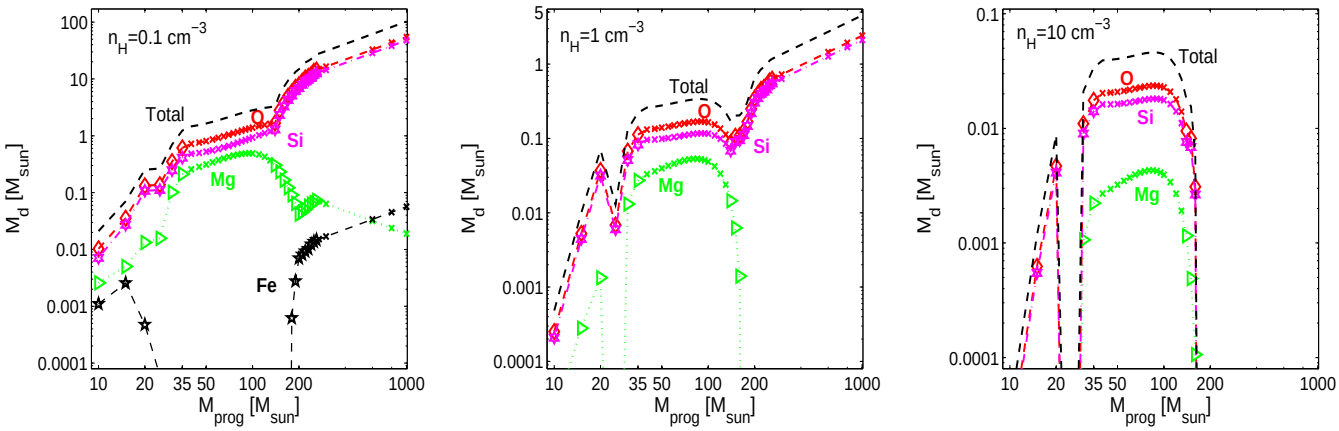

Figure 6.7: The same as in Fig. 6.6 but for the *mixed* grain model by Nozawa et al. (2003). The meaning of all the symbols is the same as in Fig. 6.6. **Left Panel**: The masses of O, Mg, Si and Fe in dust that survived to the reverse shocks for $n_H = 0.1\,cm^{-3}$. **Middle Panel**: The same as in left panel but for $n_H = 1\,cm^{-3}$. **Right Panel**: The same as in left panel but for $n_H = 10\,cm^{-3}$.

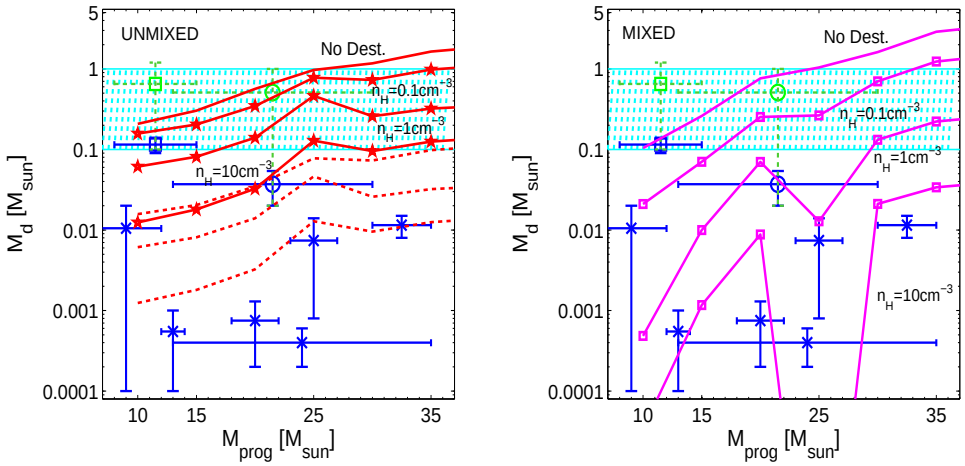

Figure 6.8: Comparison between theoretical models and observational data. The amount of dust surviving destruction is shown for three ambient number densities $n_H = 0.1\,cm^{-3}$, $n_H = 1\,cm^{-3}$ and $n_H = 10\,cm^{-3}$. Also, the original undestroyed yields by Nozawa et al. (2003) are displayed. The crosses, circles, squares and five-pointed star represent observational data from Tab. 6.2 relative to freshly formed dust in SNRs, as in Fig. 6.4, with the same meaning of the symbols. The hatched area in both panels represent the amount of dust per SNa needed to explain the obscured high-z quasars, according to the estimates by Dwek et al. (2009). **Left panel** Theory vs. observation for the *unmixed* model. The solid line without marks shows the undestroyed yields. The continuous lines from top to bottom show the yields at increasing n_H. Dotted lines represent the three n_H re-scaled by a factor of 10. **Right panel** Theory vs. observation for the *mixed* model. The continuous lines have the same meaning as in the left panel.

How the empirical data compare with the theoretical models?

Until now, an handful of studies have tried to theoretically model dust (Todini & Ferrara 2001; Nozawa et al. 2003; Schneider et al. 2004; Kozasa et al. 2009) and molecules (Cherchneff & Lilly 2008; Cherchneff & Dwek 2009; Cherchneff & Dwek 2010) formation in SNe, coupling a more or less refined classical nucleation theory (CNT) or kinetic theory. Some of these studies have been dedicated to Population III SNe but their results can be applied to SNe with progenitors of different metallicities, even with super-solar values. Indeed, according to Todini & Ferrara (2001) and Nozawa et al. (2003), dust formation in the ejecta is almost insensitive to the metallicity of the progenitor stars. The processes of dust destruction and cooling in the surrounding ISM are also scarcely dependent on the ISM metallicity (Nozawa et al. 2007; Nozawa et al. 2008). The most complete compilation of dust yields is by Nozawa et al. (2003): they modelled the formation of dust in CCSNe from 13 to 30 $M_\odot$ and Pair-Instability SNe (PISNe) from 170 to 200 $M_\odot$ for both unmixed and mixed He cores. From the database of Nozawa et al. (2003) one can derived the mass of each element embedded in the dust components. In Fig. 6.5 we show

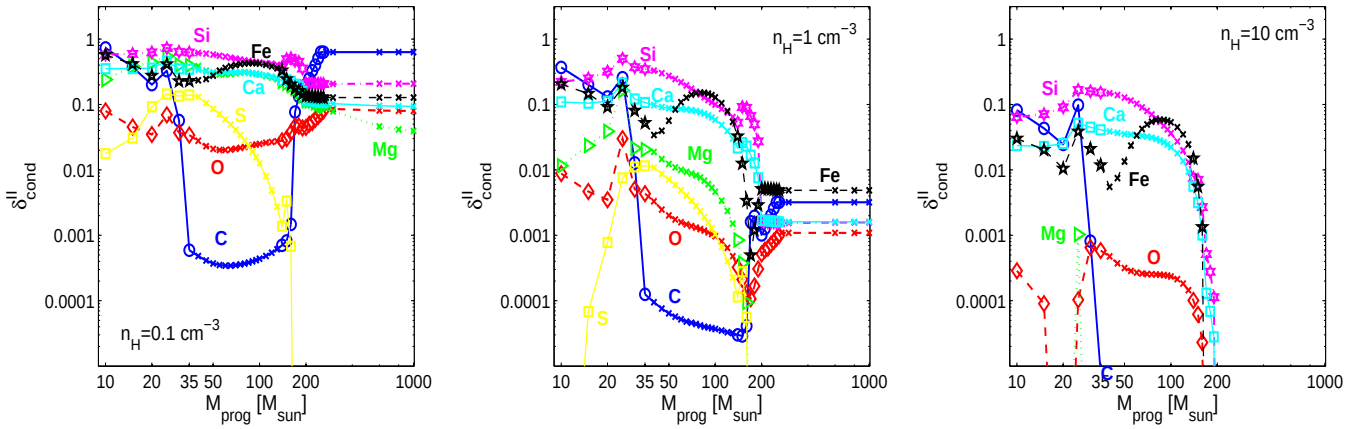

Figure 6.9: Condensation efficiencies of the elements C, O, Mg, Si, Ca, S and Fe in SNRs as a function of the progenitor mass, according to the *unmixed* grain models of Nozawa et al. (2003), Nozawa et al. (2007) and at varying the hydrogen number density n_H. The small crosses represent extrapolations of the yields of dust by Nozawa et al. (2003) to other mass ranges. We plot: C (empty circles and continuous line); O (diamonds and dashed line); Mg (triangles and dotted line); Si (six-pointed stars and dot-dashed line); S (squares and continuous line); Ca (squares and continuous line) and Fe (five-pointed stars and dashed line). **Left Panel**: Condensation efficiencies of C, O, Mg, Si, S and Fe in dust survived to reverse shocks in a medium with $n_H = 0.1\,cm^{-3}$. **Middle Panel**: The same as in left panel but for $n_H = 1\,cm^{-3}$. **Right Panel**: The same as in left panel, only for $n_H = 10\,cm^{-3}$.

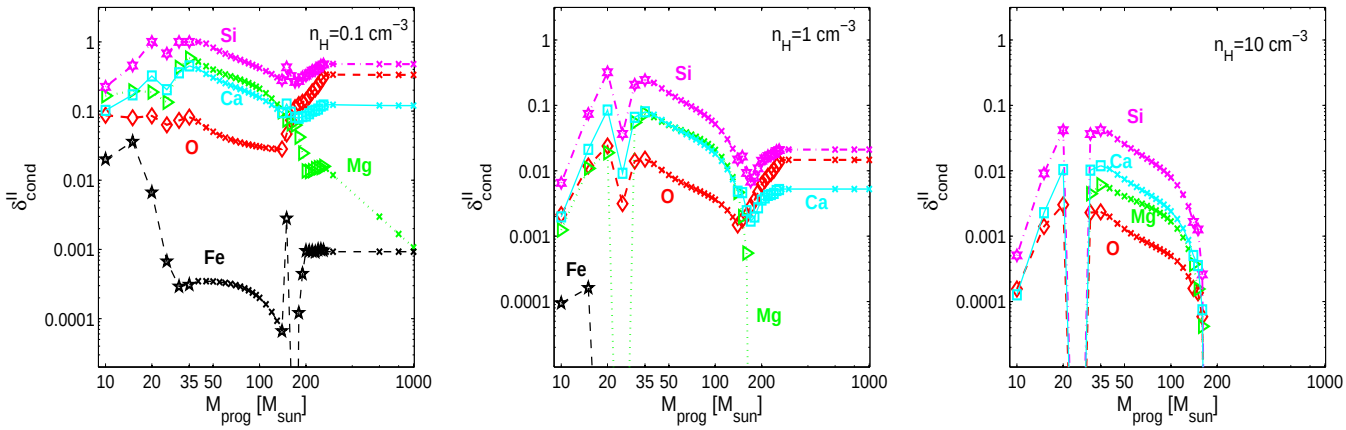

Figure 6.10: The same as in Fig. 6.9 but for the *mixed* grain model of Nozawa et al. (2003), Nozawa et al. (2007). The meaning of all the symbols is the same as in Fig. 6.9. **Left Panel**: Condensation efficiencies of O, Mg, Si, Ca and Fe for $n_H = 0.1\,cm^{-3}$. **Middle Panel**: The same as in left panel but for $n_H = 1\,cm^{-3}$. **Right Panel**: The same as in left panel but for $n_H = 10\,cm^{-3}$.

the yields of dust for each element and the total yield, for both unmixed (left panel) and mixed (right panel) cases. The progenitor masses in the grid do not cover the whole range of possible values, so some interpolation/extrapolation of the data have been applied, which, owing to the coarse coverage of large mass intervals, may be affected by large uncertainties. In general, in the case of unmixed cores, many dusty compounds form: the general trend of all the elements is quite regular, with just some exceptions, like carbon (in the unmixed model) and iron (in the mixed model): the yields grow at growing mass of the progenitor. Before comparing theory and observations, we have taken into account the dynamical evolution of the dust and its destruction in SNRs, in particular due to the passage of the reverse shock (Nozawa et al. 2007; Bianchi & Schneider 2007). Basing on previous studies by Nozawa et al. (2003) and Nozawa et al. (2006), Nozawa et al. (2007) calculated the dust yields and sizes of dust grains surviving destruction. Starting from this yields, new yields can be derived, as a functions of the ambient numerical density n_H. These resulted are presented in Figs. 6.6 (unmixed model) and 6.7 (mixed model). In both mixed and unmixed cases, the higher the ambient density n_H, the higher is the amount of dust destroyed and the smaller the yields. Some elements, like S or Mg in the unmixed case or Fe in the mixed one, are completely destroyed in high density environments.

Finally, in Fig. 6.8 we compare the theoretical yields with the observational data, for both the unmixed and mixed models. The yields based on the unmixed models marginally agree with the observational data obtained from the MIR observations. To get a satisfactory agreement one would need to re-scale the yields from unmixed models by at least a factor of 10. However, these yields much better agree with the estimates if the last ones come from FIR/sub-mm observations. The yields based on mixed models, because of the stronger destruction of dust grains in the SNRs, better agree with the MIR observations, but considering the contribution of cold dust they fail to match the FIR/sub-mm data unless the SNa explosion takes place in a low density environment.
More recent observations seem suggest unmixed models instead of mixed ones.

Condensation efficiencies

Once the original total yields from the SNe models are known, one can derive the condensation efficiencies of the various elements. However, the SNa models by Umeda & Nomoto (2002), whose the study by Nozawa et al. (2003) is based on, are not publicly available. To overcame this problem, the up-to-date nucleosynthesis calculations by Nomoto et al. (2006) and Tominaga et al. (2007) more similar to those of Umeda & Nomoto (2002) (with similar mass-cut, progenitor mass, Ye and explosion energy ratios from the gaseous yields) are used, in order to obtain the dust-to-gas

ratio from the gaseous yields.

In Figs. 6.9 and 6.10 we show the condensation efficiencies of C, O, Mg, Si, S and Fe for the unmixed model and O, Mg, Si, Ca and Fe for the mixed one, both at varying the ambient density n_H. For the highest densities, more grains are destroyed before being injected into the ISM and therefore the condensation efficiencies are lower. For the condensation efficiencies of Ca, not included in Nozawa et al. (2003), For the condensation efficiency of Ca we adopt the mean value of the other refractory elements (Mg, Si, S and Fe). Basing on observations of the Cas A remnant (Ennis et al. 2006), Kozasa et al. (2009) prefer to use unmixed models. Furthermore, the unmixed model: (i) better reproduces the extinction curves observed in high-z quasars (Hirashita et al. 2005); (ii) it is exactly in the range suggested by Dwek et al. (2009) to cope with the high-z obscured universe and, (iii) SNe have to produce some amount of carbonaceous grains according to observations of pre-solar dust, whereas the mixed model is not able to produce C-based dust. It seems therefore that the unmixed model condensation efficiencies should be preferred.

Even if the Nozawa et al. (2003) is the most available database, other prescriptions for the efficiency of dust condensation in SNRs can be found. First of all the simple formulation by Dwek (1998) and Calura et al. (2008) who for type II SNe adopt a set of condensation efficiencies *independent* from the mass/metallicity of the star or the density of the parental environment. No distinction is made for the condensation efficiencies between type II CCSNe and thermonuclear type Ia SNe. The values for the condensation efficiencies are somewhat arbitrary (Dwek 1998); they are simply meant to indicate the effect of condensation with some destruction. One of the most controversial issues is the assumption made by Dwek (1998) and Calura et al. (2008) about Type Ia SNe: the condensation efficiencies are assumed to be high despite the fact that no dust formation has been observed in Type Ia SNRs (Draine 2009). This contradictory assumption has been recently corrected in Pipino et al. (2011), even if the arbitrary choice between the condensation efficiencies make them as free parameters.

Another prescription for dust condensation in SNe worth being examined is the one by Zhukovska et al. (2008). They assume that SNe are poor producers of dust, introduce condensation factors independent from both mass of the progenitor and/or metallicity. In their models, type Ia SNe can produce only small amount of iron. According to Zhukovska et al. (2008), the uncertainties on dust formation in SNe are still so large that purely theoretical yields cannot be safely used. For all these considerations, it appears that the more detailed set of condensation efficiencies based on Nozawa et al. (2003), Nozawa et al. (2006) and Nozawa et al. (2007) is more safe and of general use to be adopted into theoretical models. It relies on detailed models that are still the most handy available in literature thanks to the number of modelled

masses, to the included effects of the reverse shock and environmental density on the surviving mass of dust grains (salterei il perche i modelli CNT non vanno bene). Nevertheless, as long as models at varying those parameters are not available, the current estimates of the condensation efficiencies by Nozawa et al. (2003), Nozawa et al. (2006) and Nozawa et al. (2007) can be safely used in chemical models.

How these yields of dust and corresponding condensation efficiencies compare with the amount of dust that is estimated to explain the obscured objects at high redshift?

The question is still open and vividly debated: it is not clear whether SNe play a major role as dust producers in high-z, very young galaxies, when AGB stars still have not yet started contributing to the total budget (Sugerman et al. 2006; Bianchi & Schneider 2007; Nozawa et al. 2008), or grain accretion in the ISM dominate leaving to SNRs the role of seed producers over which accretion should take place (Dwek et al. 2009; Draine 2009). Dwek et al. (2009) argue that $0.1 - 1 M_{\odot}$ of dust is produced by every SNa to fully explain high-z obscured objects, the dust being originating in SNRs. In Fig. 6.8, the hatched area indicates the $0.1 - 1 M_{\odot}$ region. The theoretical yields agree with the values falling into the hatched region, and the recent observations in FIR/sub-mm seem confirm this scenario. unmixed case. Because of it, Dwek et al. (2009), Draine (2009) favored the accretion in the ISM as the dominant source of dust in high-z quasars. The dust accretion in the ISM requires that some enrichment in metals has already occurred so that some delay is unavoidable. For very high SFR such as in QSOs, the delay can be very short (Gall et al. 2011a; Gall et al. 2011b), thus further complicating the whole picture. However, more detailed observations of cold dust in some SNRs significantly increase the dust contribution by SNe, that becomes high enough to overwhelm the ISM accretion in the early stages. The issue is still debated.

6.8 Yields of dust from AGB stars

Apart of SNe, low and intermediate mass stars in the asymptotic giant branch (AGB) phase are long known to safely be strong injectors of dust in the ISM. It is worth noting that dust formation in the red giant branch (RGB) and even early asymptotic giant branch (E-AGB) stars can be ignored because the physical properties of their stellar winds do not favour dust formation and the rates of mass loss are very low (Gail et al. 2009). Only the thermally pulsing AGB (TP-AGB) stars are expected to form dust in significant amounts (see Chap. 1).

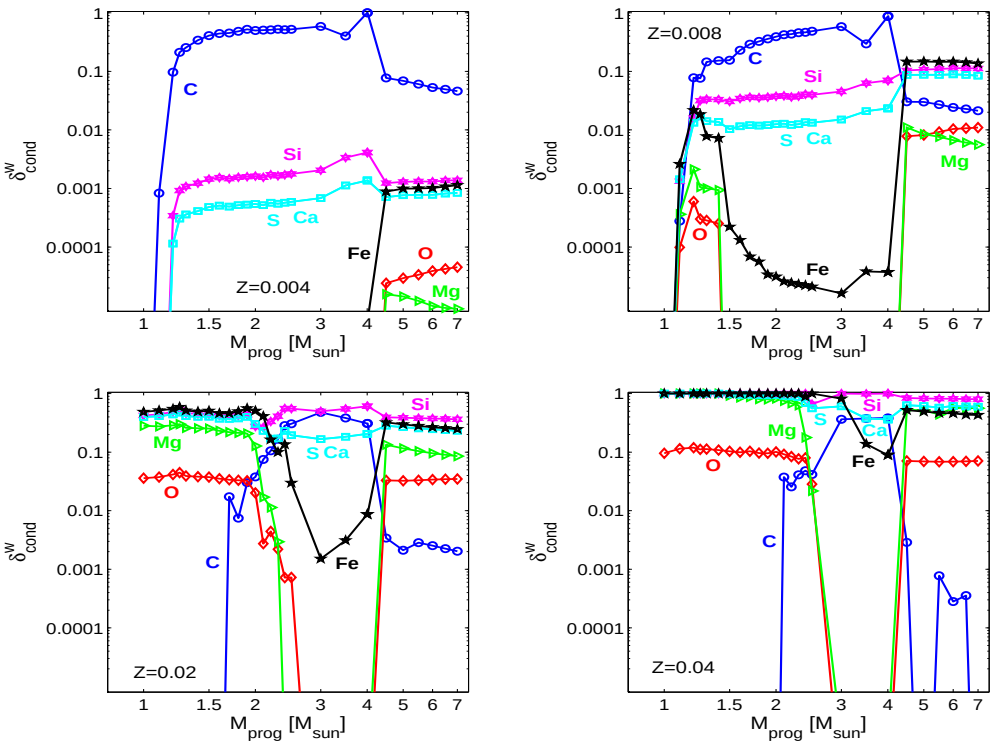

Figure 6.11: Condensation efficiencies for the elements C, O, Mg, Si, Ca, S and Fe in SNRs as a function of the progenitor mass at varying the metallicity Z. We plot: C (empty circles and continuous line); O (diamonds and dashed line); Mg (triangles and dotted line); Si (six-pointed stars and dot-dashed line); S and Ca (squares and continuous line) and Fe (five-pointed stars and dashed line).

TP-AGB stars have been the subject of an impressive number of studies based on the theory of stellar evolution and going from synthetic models (Marigo et al. 1996; Wagenhuber & Groenewegen 1998; Marigo 2002; Izzard & Poelarends 2006; Marigo & Girardi 2007) to full calculations of evolutionary, even hydrodynamical, models (Herwig et al. 1997; Karakas et al. 2002; Ventura et al. 2002; Herwig 2004; Weiss & Ferguson 2009). Moreover, dust formation in AGB stars has been the subject of more and more refined and detailed models (Gail et al. 1984; Gail & Sedlmayr 1985; Gail & Sedlmayr 1987; Dominik et al. 1993; Gail & Sedlmayr 1999; Ferrarotti & Gail 2002; Ferrarotti & Gail 2006; Gail et al. 2009), able to calculate the amount of newly formed dust in M-stars, S-stars and C-stars, along a sequence of growing C/O ratio. This ratio determines the dust mixtures formed in the outflows (Piovan et al. 2003; Ferrarotti & Gail 2006; Gail et al. 2009), as investigated and analyzed in Sect. 1.4. Recently, Ferrarotti & Gail (2006) presented a detailed database of dust yields from AGB stars, that was later extended by Zhukovska et al. (2008). Ferrarotti & Gail (2006) models are obtained applying the schemes for dust formation to synthetic

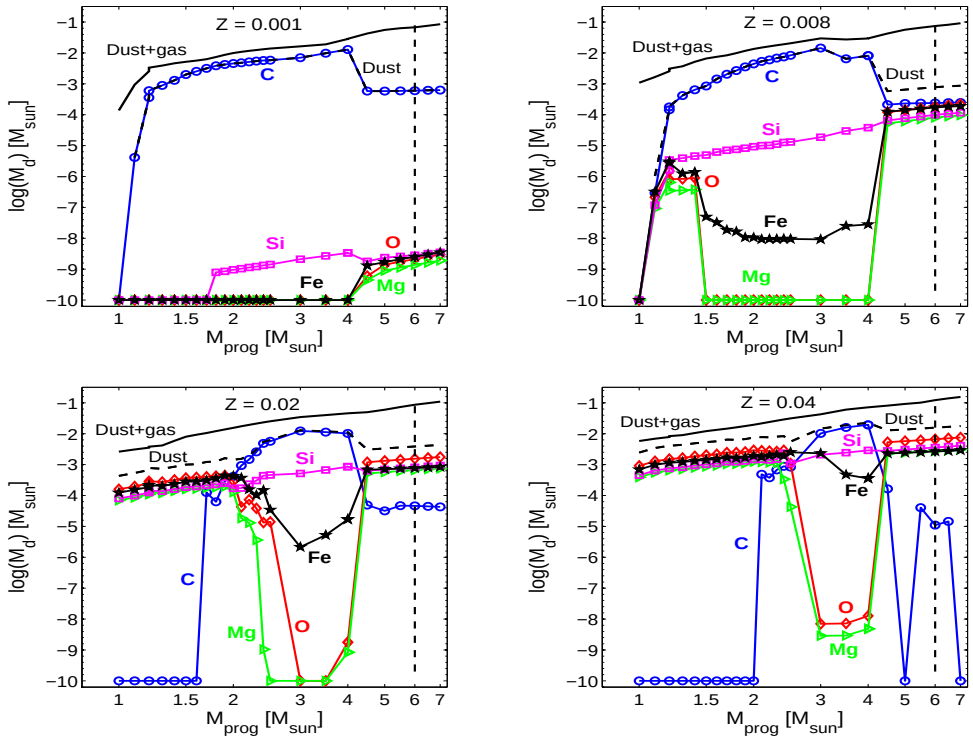

Figure 6.12: Dust ejecta for C, O, Mg, Si, and Fe, calculated by means of dust compounds of Ferrarotti & Gail (2006) and Zhukovska et al. (2008) for AGB stars as a function of the progenitor mass. Four metallicities are considered. The legend is as follows: C (empty circles and continuous line); O (diamonds and dashed line); Mg (triangles and dotted line); Si (six-pointed stars and dot-dashed line); S (squares and continuous line) and Fe (five-pointed stars and dashed line). The dashed line without markers is the total amount of dust in the ejecta. The vertical dashed line represents the 6 $M_{\odot}$ upper AGB limit according to our set of yields Marigo et al. (1996), Marigo et al. (1998), Portinari et al. (1998). Finally, the continuous line shows the total ejected mass in dust and gas for what concerns the five elements we have considered in the plot according to van den Hoek & Groenewegen (1997).

AGB models standing on van den Hoek & Groenewegen (1997) and Marigo et al. (1996). Also, for some elements the results by Karakas & Lattanzio (2003) have been used. To obtain the dust condensation coefficients $\delta^{w}_{c,i}$ for every element i-th of our set, the first step is to calculate the amount of each element embedded in newly formed dust.

In Fig. 6.12, for the elements C, O, Mg, Si, Fe, we show the total amount $M_{i,d}\,(M, Z)$ of dust formed in the outflows of AGB stars, according to the previous cited models. Moreover, for each AGB star, we show the total amount of ejected dust and compare it to the total amount of lost material. The following remarks can be made. First, as shown in the top panels, the dust produced by low metallicity AGB stars of any mass is carbon dominated. This point seems to agree with the

suggested high-z scenario in which the appearance of the PAH features and graphite extinction bump in the UV are both connected to the delayed injection of carbon by AGB stars, as shown by observations of galaxies of different metallicity (Dwek 2005; Galliano et al. 2008; Dwek et al. 2009). Second, at growing metallicity, silicate dust starts to be formed in significant amount, however there is always some injection of carbon dust from stars around $3M_{\odot}$. Third, the following questions arise: At which mass do This recipe is strictly classical and follows the one adopted by Portinari et al. (1998) to calculate the chemical yields, since the idea is to base simulations upon the latest release of those yields. Below 6 solar masses we have stars ending as WDs through the AGB channel; for masses between 6 and $8M_{\odot}$ (Portinari et al. 1998) assumed $1.3M\odot$ of remnant, either WD or NS, and the overlying layers expelled either by an explosion or a TP-AGB phase; for masses $M> 8M_{\odot}$ we have stars developing an iron core and exploding as CCSNe. However, other mass limits would be possible considering all the uncertainties affecting the evolution of stars in the mass range 6 to $12M_{\odot}$. For instance Zhukovska et al. (2008), Gail et al. (2009) and Calura et al. (2008) extend the AGB stars to stars with initial mass of $8M_{\odot}$, thus shifting part of the dust emission from SNe to AGB stars.

Once the masses of dust ejecta are defined, the condensation efficiencies for the element i-th during the TP-AGB phase can be obtained. In Fig. 6.11 we show the condensation efficiencies at growing metallicity. While the condensation efficiency of carbon keeps quite high, for oxygen and other refractory elements it grows at increasing metallicity. For metallicity two times solar, for some elements like Si and some stellar masses, almost all the material is condensed into dust. Another possibility for the condensation efficiencies of AGB stars is proposed by Dwek (1998): their models depend on the final C/O ratio in the ejecta, without following the evolution of the star along the AGB (as in the complex dust nucleation model by Ferrarotti & Gail (2006)) and they are also *independent* from the metallicity of the stars.

6.9 Models of the ISM with dust: results

The chemical model for disk galaxies we are proposing extends the the original dust-free, multi-zone model with radial flows developed by the Padova group over the years (Chiosi 1980; Chiosi & Maeder 1986; Portinari et al. 1998; Portinari & Chiosi 1999; Portinari & Chiosi 2000; Portinari et al. 2004; Portinari et al. 2004b) to which the reader should refer for all the details not mentioned here. The model is quite complicate and obviously contains many parameters. Therefore it would be wise to suitably select the parameters to vary, guided by some general considerations to be kept in mind: (i) This study is mainly devoted to highlight the role of dust in chemical models rather than perfectly reproducing the properties of gas and stars of

the MW in the local pool. For this reason various recipes for dust formation and evolution in the ISM must be tested. (ii) A reasonable agreement between model results and observational data for gas, dust and stars (both in the solar vicinity and across the galactic disk) must be reached for the sake of physical consistency of the whole model. (iii) Finally, we will take advantage of the results already obtained by Chiosi (1980, Chiosi & Maeder (1986, Portinari et al. (1998, Portinari & Chiosi (1999, Portinari & Chiosi (2000, Portinari et al. (2004, Portinari et al. (2004b) as far as the fine tuning of several important parameters is concerned.

In the following each model is identified by a string of nine letters (the number of parameters) in italic face whose position in the string and the alphabet corresponds to a particular parameter and choice for it. The position in the string is the same as in the list below. Let's now shortly comment on the parameters we have considered and the choices we have made for each of them together with the identification code.

(1) The IMF with its lower and upper limits and the fraction ζ of stars with mass $M > 1M_{\odot}$. Eight IMF are considered as described in Sect. 1.1.4: Salpeter ($\mathcal{A}$), Larson ($\mathcal{B}$), Kennicutt ($\mathcal{C}$), Kroupa original ($\mathcal{D}$), Chabrier ($\mathcal{E}$), Arimoto ($\mathcal{F}$), Kroupa 2002-2007 ($\mathcal{G}$), Scalo ($\mathcal{H}$) and, finally, Larson adapted to the Solar Ring ($\mathcal{I}$). Since some of them are similar, we will examine in particular only the results obtained for some interesting cases useful to understand the influence of the IMF. The upper and lower mass limits (and ζ) are selected according to the default values already given in Sect. 1.1.4.

(2) The Star Formation law. Five SFR are considered (Sect. 6.3: constant SFR ($\mathcal{A}$), Schmidt law ($\mathcal{B}$), Talbot & Arnett (T&A - $\mathcal{C}$), Dopita & Ryder (D&R - $\mathcal{D}$) and, finally, Wyse & Silk (W&S - $\mathcal{E}$).

(3) The fraction of MCs in which dust accretion takes place. This quantity must be specified because the chemical model in use does not contain a real multi-phase description of the ISM. Two cases are included: a constant fraction ($\mathcal{A}$) based on the Solar Ring data ($\chi_{MC} = 0.2$) and a varying χ_{MC} ($\mathcal{B}$) related to the local SFR and total gas density (see Sect. 6.4.2).

(4) The model for the accretion of grains in cold molecular regions. Two choices are available: the simple model by Dwek (1998) based on typical accretion timescales for dust grains as modified by Calura et al. (2008) (see Sect. 6.4.1) ($\mathcal{A}$) and the recent and more refined model by Zhukovska et al. (2008) (see Sect. 6.4.2) ($\mathcal{B}$).

(5) The condensation efficiencies for dust in Type Ia SNe. Two cases are possible as already described: Dwek (1998) ($\mathcal{A}$) and Zhukovska et al. (2008) ($\mathcal{B}$). In the

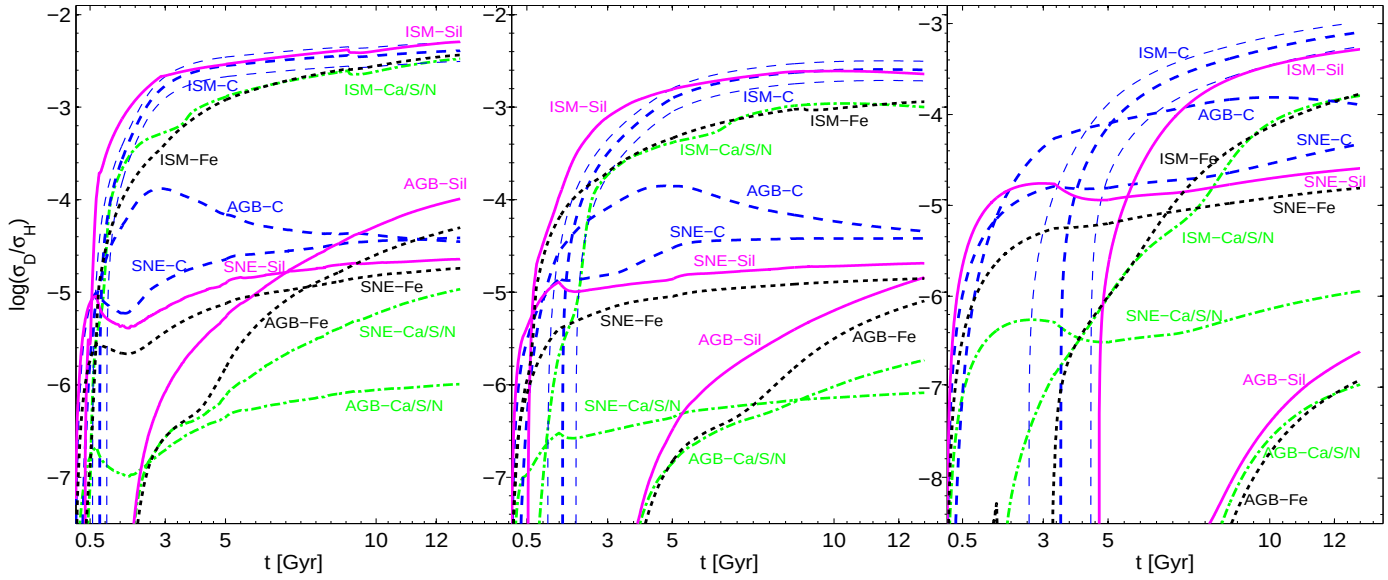

Figure 6.13: Temporal evolution of the contribution to the abundance of dust by the four types of grain (on which we distributed the single elements) and the three sources. All the contributions have been properly corrected for the destruction of dust. **Left panel**: results for an inner ring of the MW centered at 2.3 kpc. We show: silicates (continuous lines), carbonaceous grains (dashed lines), iron dust (dotted lines) and, finally, other grains bearing S, Ca and N (dot-dashed lines). For each group we distinguish the net contributions from the ISM accretion, AGB and SNe, that is: ISM-C, AGB-C and SNe-C for carbon grains, ISM-Sil, AGB-Sil and SNe-Sil for silicates, ISM-Fe, AGB-Fe and SNe-Fe for the iron dust and finally, ISM-Ca/S/N, AGB-Ca/S/N and SNe-Ca/S/N for the other grains. The two thin dashed lines represent the same $\mathcal{GDABBCBBB}$ model but with 15% (upper dashed line) and 45% (lower dashed line) of CO. In all cases $\xi_{\rm CO} = 0.30$ as default value. **Central panel**: the same as in the left panel but for the Solar Ring at 8.5 kpc. **Right panel**: the same as in the left panel but for an outer ring at 15.1 kpc. Since the ratio σ_D/σ_H is lower, the scale of the y-axis is shifted respect to the scales for the inner region and the Solar Ring in the left and central panels.

former they contribute to the dust budget in a away comparable to that of Type II SNe, whereas in the latter their role is negligible except for a small amount of iron in agreement with the observations.

(6) The condensation efficiencies for dust in Type II SNe. Three choices are possible. The first one by Dwek (1998) who suggests a high condensation efficiency ($\mathcal{A}$), the efficiencies by Nozawa et al. (2003, Nozawa et al. (2006, Nozawa et al. (2007) based on dust nucleation models and taking into account the effects of the reverse and forward shocks ($\mathcal{B}$), and finally those by Zhukovska et al. (2008) who favor a low condensation efficiency in SNe based upon pre-solar grain observations.

(7) The condensation efficiencies for dust from AGB stars. Two choices are available: the simple recipes by Dwek (1998) ($\mathcal{A}$) and the condensation efficiencies obtained by full calculations of dust formation in synthetic AGB models by Ferrarotti & Gail (2006) ($\mathcal{B}$).

(8) The age at which a bar is introduced to reproduce the radial distribution of the gas in the Galactic disk, in particular in the region of the molecular ring around 4 kpc. For the purposes of this work we do not play with the bar effect: the pattern of velocity to simulate the bar effect in the radial flows mechanism is simply taken from Portinari & Chiosi (2000),(to which the reader should refer for all the details) and is suitably chosen for every SFR law. There is no bar-effect on the Solar Ring, for this reason between the three cases included (no bar effect ($\mathcal{A}$), an onset of the bar 4 Gyr ago ($\mathcal{B}$) and 1 Gyr ago ($\mathcal{C}$), we will simply just fix the bar effect at the case ($\mathcal{B}$).

(9) The parameters of the SFR laws: these are chosen according to the discussion by (Portinari & Chiosi 1999). While the exponents k or m and n are fixed (see Sect. 6.3) we let the efficiency of the star formation ν vary and assume three values more or less in the ranges suggested by (Portinari & Chiosi 1999) for every SF law. The minimum value for ν_{min} is case $\mathcal{A}$ and the maximum value for ν_{max} is case $\mathcal{C}$). The average case is $\mathcal{B}$.

The Tab. 6.3 summarizes the parameters we have just described together with their associated identification code: the sequence must be read from top to bottom. For example, the string $\mathcal{DBAABABAB}$ corresponds to Kroupa 1998 IMF, Schmidt SFR, ANN model for χ_{MC}, Dwek (1998) accretion model, Zhukovska et al. (2008) type Ia SNe recipe for dusty yields, Dwek (1998) condensation efficiencies for type II SNe, Ferrarotti & Gail (2006) yields for AGB stars, no bar and high efficiency ν of the

Table 6.3: Parameters of the models. Column (1) is the parameter number, column (2) the associated physical quantity, and column (3) the source and the italic symbols are the identification code we have adopted. See the text for some more details.

n^o	Parameter	Source and identification label
1	IMF	Salpeter[1] ($\mathcal{A}$), Larson[2] ($\mathcal{B}$), Kennicutt[3] ($\mathcal{C}$) Kroupa orig.[4] ($\mathcal{D}$), Chabrier[5] ($\mathcal{E}$), Arimoto[6] ($\mathcal{F}$), Kroupa 2007[7] ($\mathcal{G}$), Scalo[8] ($\mathcal{H}$), Larson SN[9] ($\mathcal{I}$)
2	SFR law	Constant SFR ($\mathcal{A}$), Schmidt[10] ($\mathcal{B}$), Talbot & Arnett[11] ($\mathcal{C}$), Dopita & Ryder[12] ($\mathcal{D}$), Wyse & Silk[13] ($\mathcal{E}$)
3	χ_{MC} model	Artificial Neural Networks model[14] ($\mathcal{A}$), Constant χ_{MC} as in the Solar Neigh.[15] ($\mathcal{B}$)
4	Accr. model	Modified Dwek (1998) and Calura et al. (2008) ($\mathcal{A}$); adapted Zhukovska et al. (2008) model ($\mathcal{B}$)
5	SNe Ia model	Dust injection adapted from: Dwek (1998), Calura et al. (2008) ($\mathcal{A}$), Zhukovska et al. (2008) ($\mathcal{B}$)
6	SNe II model	Dust injection adapted from: Dwek (1998) ($\mathcal{A}$), Zhukovska et al. (2008) ($\mathcal{B}$), Nozawa et al. (2003, Nozawa et al. (2006, Nozawa et al. (2007) ($\mathcal{C}$)
7	AGB model	Dust injection adapted from: Dwek (1998) ($\mathcal{A}$), Ferrarotti & Gail (2006) ($\mathcal{B}$)
8	Galactic Bar[16]	No onset ($\mathcal{A}$), onset at $t_G - 4$ Gyr ($\mathcal{B}$), onset at $t_G - 1$ Gyr ($\mathcal{C}$)
9	Efficiency SFR[17]	Low efficiency ($\mathcal{A}$), medium efficiency ($\mathcal{B}$) , high efficiency ($\mathcal{C}$)

[1]Salpeter (1955). [2]Larson (1986),Larson (1998). [3]Kennicutt (1983), Kennicutt et al. (1994). [4]Kroupa (1998). [5]Chabrier (2001). [6]Arimoto & Yoshii (1987). [7]Kroupa (2002a),Kroupa (2007). [8]Scalo (1986). [9]Larson (1986, Scalo (1986, Portinari et al. (2004). [10]Schmidt (1959). [10]Talbot (1975). [11]Talbot (1975). [12]Dopita & Ryder (1994). [13]Wyse & Silk (1989). [14]Piovan et al. (2011c). [15]Zhukovska et al. (2008). [16]Portinari & Chiosi (2000). [16]Piovan et al. (2011b).

SFR. If not otherwise specified radial flows and bar effect will always be included by default.

Obviously, these are not the only parameters of chemical models: even the classical ones are themselves very rich of parameters and when including also radial flows, bars and dust formation/evolution the parameter space acquires many more dimensions so that a full exploration of it is a cumbersome affair. However, it may happen that: (1) some variables play a secondary role, thus not influencing that much the results (in particular we focus on the effects related to dust, the target of the work) and just adding second order corrections; (2) some variables, even if playing an important role and influencing significantly the results, have a well defined and/or restricted sphere of influence therefore are not of much interest here because their effect is clear. The

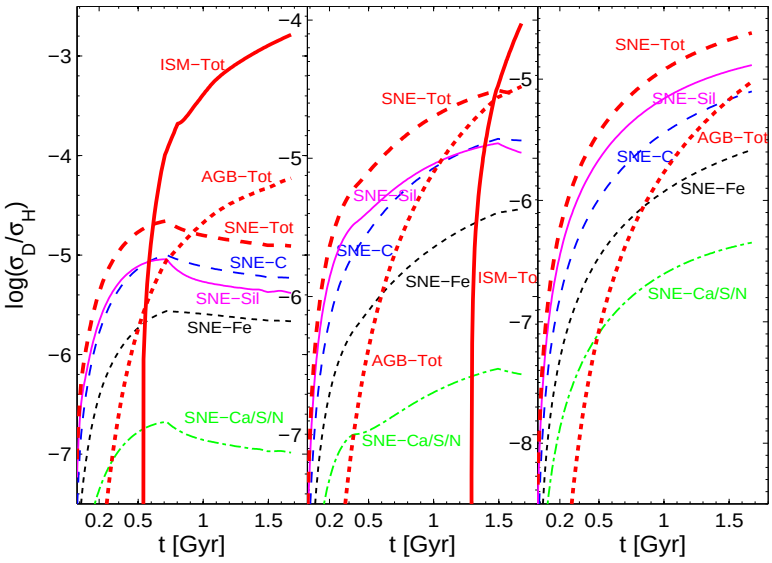

Figure 6.14: Temporal evolution of the contribution to the abundance of dust during the *first 1.5 Gyr-2 Gyr*. All the contributions have been properly corrected for the destruction of dust. **Left panel**: results for the inner ring of the MW at 2.3 kpc. We show for the SNe injection: silicates (thin continuous line SNe-Sil), carbonaceous grains (thin dashed line, SNe-C), iron dust (thin dotted line, SNe-Fe) and, finally, other grains bearing S, Ca and N (thin dot-dashed line, SNe-Ca/S/N). The *thick* lines represent the total contribution from one source to the dust budget sub-divided in: SNe (thick dashed line, SNe-tot), ISM (thick continuous line) and AGB (thick dotted line). **Central panel**: the same as in the left panel but for the Solar Ring at 8.5 kpc. **Right panel**: the same as in the left panel but for the outer ring at 15.1 kpc.

parameters belonging to these two classes are not varied in the models, but kept fixed to a suitable value. In the following we examine the effect of some primary and secondary parameters and the general behaviour of the dust model. To this purpose we adopt the $\mathcal{GDAB\mathcal{B}C\mathcal{B}B\mathcal{B}}$ model as the 'default' one, with radial flows and bar included (Portinari & Chiosi 2000) as the reference case. This model uses the most detailed theoretical recipes for the yields of dust and the amounts of MCs, while the SFR and the IMF are simply selected between the available ones.

6.10 The effect of different yields of dust

By choosing a set of plausible parameters for the MW, simulations can be realized. We use them in order to test the different choices for the star-dust yields just discussed. Therefore, in these simulations, all the physical ingredients are fixed: *only* the choices for star-dust yields are varied, in order to understand the differences between one set or another. It has been adopted:

1. the IMF from Kroupa (2007) (see Sect. 1.1.4);

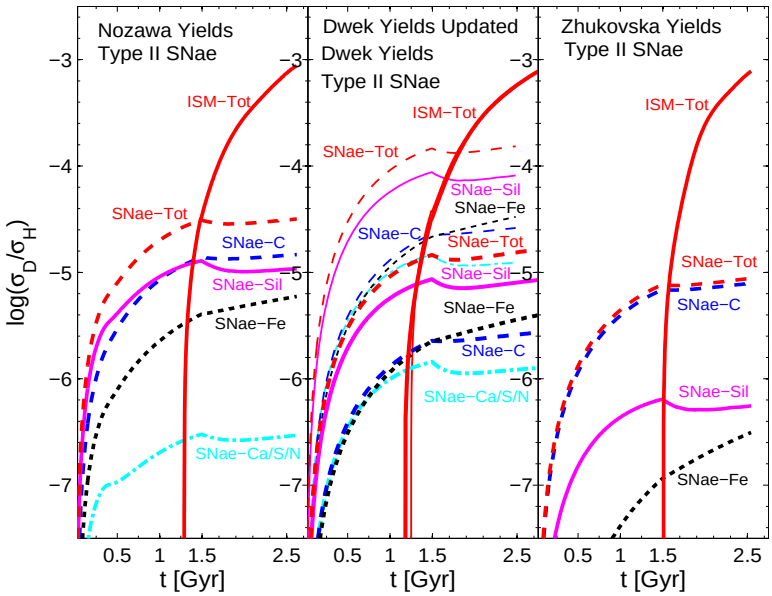

Figure 6.15: Temporal evolution of the contribution to the dust budget in the Solar Neighborhood during the *first 1.5 Gyr-2.5 Gyr* by type II SNe according to three different prescriptions for the dust condensation efficiencies. All the contributions are already corrected for the effect of dust destruction. We show: the contribution by accretion of dust grains in the ISM (ISM-tot, continuous line); the total contribution by SNe dust yields (SNe-tot, dashed line); the contributions by the different kind of SNa dust grains, that is Silicates (SNe-Sil, continuous line), carbonaceous grains (SNe-C, dashed line), iron dust grains (SNe-Fe, dotted line) and Ca/S/N generic dust grains (SNe-Ca/S/N, dot-dashed line). **Left panel**: the results based on the Nozawa et al. (2003),Nozawa et al. (2006), Nozawa et al. (2007) condensation efficiencies. **Central panel**: the same as in the left panel but for the Dwek (1998) condensation efficiencies and for the Pipino et al. (2011) efficiencies. **Right panel**: the same as in the left panel but for the Calura et al. (2008) condensation efficiencies.

2. the SFR fromDopita & Ryder (1994) with $\nu = 0.55$;

3. a fraction of molecular clouds χ_{MC}, where the accretion of dust as a function of the local SFR and gas mass occurs;

4. the accretion dust model proposed by Zhukovska et al. (2008);

5. the radial gas flows and the effect of the galactic bar from Portinari & Chiosi (2000).

These are plausible choices commonly adopted in the literature to simulate the disk of MW and Solar Ring. Let us analyze now the effect of varying the condensation efficiencies (and hence the production of stardust) for CCSNe, SN Ia and AGB stars.

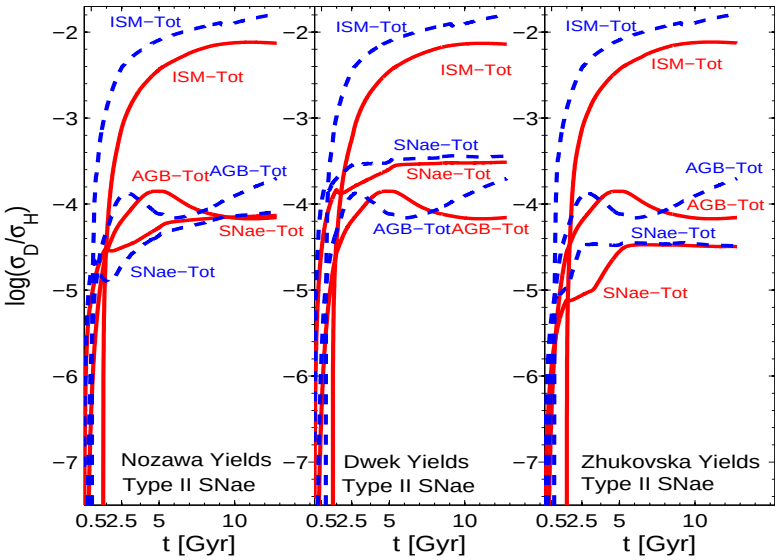

Figure 6.16: Temporal evolution of the contribution to the dust budget by type II SNe according to three different prescriptions for the dust condensation efficiencies. The data refer to the Solar Ring (continuous lines) and the innermost region of the MW (dashed lines). All the contributions are already corrected for the effect of dust destruction. We show: the contribution by accretion of dust grain in the ISM (ISM-tot) and the total contributions by SNe (SNe-tot) and AGB stars (AGB-tot). **Left panel**: the results for the Nozawa et al. (2003), Nozawa et al. (2006), Nozawa et al. (2007) condensation efficiencies. **Central panel**: the same as in the left panel but for the Dwek (1998) and Calura et al. (2008) condensation efficiencies. **Right panel**: the same as in the left panel but for the Zhukovska et al. (2008) condensation efficiencies.

6.10.1 The effect of varying the yields of dust for CCSNe

Let us evaluate the effect of varying the amount of star-dust injected from type II SNe. We compare three cases: (a) high condensation efficiencies by Dwek (1998) and Calura et al. (2008); (b) the set based upon the CNT models for Type II SNe and PISNe by Nozawa et al. (2003), Nozawa et al. (2006) and Nozawa et al. (2007) and (c) the low SNæ condensation efficiencies proposed by Zhukovska et al. (2008). We also included the recently revised Dwek (1998) efficiencies, as proposed by Pipino et al. (2011) in order to reproduce the observational constraints: the coefficients for type II SNe are lowered by a factor of 10. The results of the corresponding chemical models, with every parameter fixed except the use of different CCSNe efficiencies, are presented in Fig. 6.15 where for simplicity we divided the contribution by SNe grouping the elements in some typical grain families, silicates (like olivines, pyroxenes and quartz, depleting the gas of magnesium, silicon, iron and oxygen), carbonaceous grains, iron dust and other grains involving S/Ca/N. The simulated region is the Solar Ring. Even if the Solar Ring region is not interested by an intense star formation activity, nevertheless in the early phases of the evolution, before that dust accretion

in the ISM becomes significant, different efficiencies have a strong impact on the early evolution of the dust content. The CNT models present a contribution that is in the middle between low efficiencies by Zhukovska et al. (2008) and the high efficiencies by Dwek (1998). The corrected contribution by Pipino et al. (2011), scaled in such a way to agree with the observations, tends to produce similar total amount of dust as the CNT models, even if the relative contribution to the total mass budget of the elements embedded into dust grains is quite different. The level of carbonaceous grains formed adopting the Zhukovska et al. (2008) coefficient for carbon is similar to the one predicted by the revised ad-hoc efficiencies by Pipino et al. (2011) and the CNT models by Nozawa et al. (2003). This agreement seems satisfactory and it suggests some confidence in the carbon coefficient by Nozawa et al. (2003). For the refractory elements involved into the formation of silicates, the small number of detections of pre-solar grains does not allow a safe constraint. Zhukovska et al. (2008) assume a very low efficiency of condensation as working hypothesis, while CNT models forecast a higher efficiency for these elements. According to the results by Matsuura et al. (2011) and the measured abundances found in SN 1987A with Herschel, this latter choice seems to be the most realistic one. The kind of mixture of silicates, anyway is strongly model dependent, as shown by Fig. 6.16, and quite different partitions of grains are formed, depending on the adopted δ.

While the influence of different yields of dust by SNe can be very important in the early stages of the evolution, once the accretion process in the ISM becomes the dominant dust factory and the SFR declines, there is in practice no influence on the relative dust budget compared to the gas amount at the current age, as clearly shown in Fig. 6.16. This figure show the evolution until the current time of three region of the MW, that are an inner ring around 2.3 Kpc (left panel), the Solar Ring at 8.5 Kpc (middle panel) and an outer ring at 15.1 Kpc (right panel). The three regions,from left to right, can be taken in some way as representative of three environments where a high/average/low star formation, respectively, occurred. The poor influence of the different recipes on the current total mass budget is true even for the innermost regions of the MW with higher SFR.

6.10.2 The effect of varying the yields of dust for type Ia SNe

We turn now to examine the contribution to the dust content by Type Ia SNe. Two different evaluations have been included: (a) high efficiency of dust formation by type Ia SNe (Dwek 1998; Calura et al. 2008) and (b) very low efficiency, in closer agreement with observations. In Fig. 6.17 we present the evolution in the first Gyrs of the star-dust injected by the SNe in three different regions of the MW Disk as before. The contribution by SNe is in turn split according to the different types of grains that

have been considered and on which the single elements have been suitably grouped together. As expected, Type Ia SNe do not affect the dust evolution during the first 0.5-1 Gyr, simply according to the current scenario for the origin of these objects since they still have to come in significant numbers. Furthermore, in the innermost regions, with high SFR and fast ISM enrichment, the dust accretion process starts to dominate early on the dust production and when type Ia SNe come into play, it is already too late to have a significant role. However, in regions with low SFR such as the solar vicinity or, even more significantly, the outermost regions, it may happen that Type Ia SNe significantly affect the dust enrichment, simply because the ISM accretion mechanism is delayed because of the poor enrichment in metals. This effect gets clearly stronger at lowering the SFR.

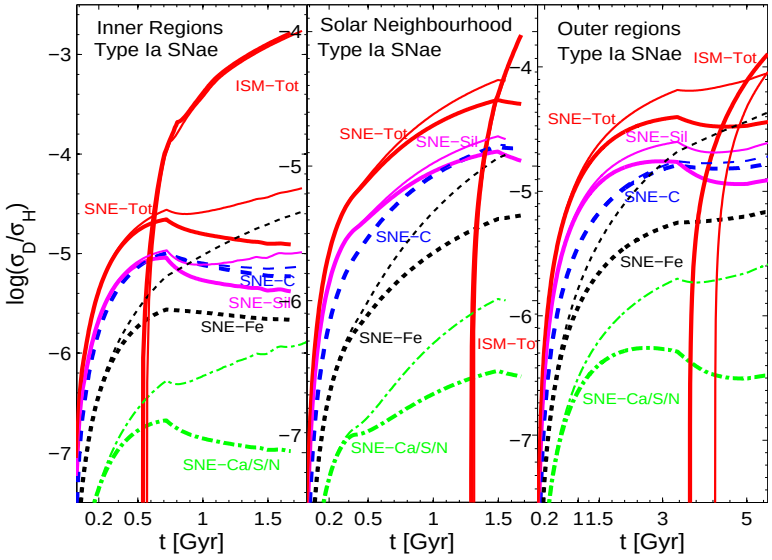

Figure 6.17: Temporal evolution of the contribution to the dust budget during the *first 1.5 Gyr-2.5 Gyr* by type Ia SNe for two prescriptions of dust ejecta and three different regions of the MW: an inner ring at 2.3 Kpc, the Solar Ring, and an outer ring at 15.1 Kpc. The results for prescription based on Dwek (1998), Calura et al. (2008) are represented with thin lines, whereas those for case based on Zhukovska et al. (2008) are shown with thick lines. All the contributions are already corrected for the effect of dust destruction. We show: the contribution by accretion of dust grain in the ISM (ISM-tot, continuous lines); the total contribution by SNe dust yields (SNe-tot, type Ia + type II SNe - continuous line); the contributions by the different kind of SNa dust grains, that is silicates (SNe-Sil, continuous lines), carbonaceous grains (SNe-C, dashed lines), iron dust grains (SNe-Fe, dotted lines) and Ca/S/N based dust grains (SNe-Ca/S/N, dot-dashed lines). **Left panel**: the results for the inner ring. **Central panel**: the same as in the left panel but for the Solar Ring. **Right panel**: the same as in the left panel but for the outer ring.

Do different choices for the Type Ia SNe condensation efficiencies influence the final depletion of the elements into dust at the current age? We show in Fig. 6.18 the evolution of the dust budget for our two different recipes for Type Ia SNe: there is

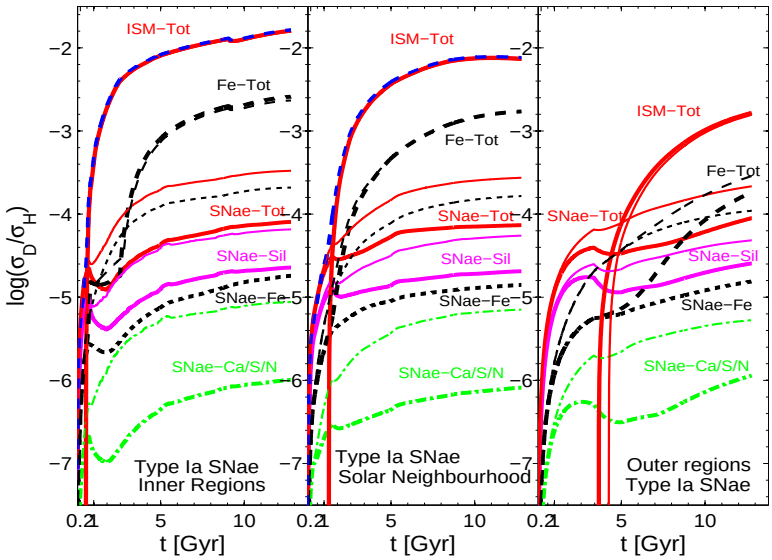

Figure 6.18: Temporal evolution up to 13 Gyr of the contribution to the dust budget by type Ia SNe for two prescriptions of dust ejecta and three different regions of the MW. We show: the contribution by accretion of dust grain in the ISM (ISM-tot, continuous lines); the total evolution of the iron-dust (Fe-tot, dashed lines); the contributions by some of the SNa dust grains, that is silicates (SNe-Sil, continuous lines), iron dust grains (SNe-Fe, dotted lines) and Ca/S/N based dust grains (SNe-Ca/S/N, dot-dashed lines). **Left panel**: the results for the inner ring. **Central panel**: the same but for the Solar Ring. **Right panel**: the same but for the outer ring.

no difference in the ISM accretion process even for the low SFR environment. Even if the two recipes for the dust condensation in Type Ia SNe produce very different amount of dust, this has no influence on the ISM process that mainly depends on the global amount of metals available in the ISM: some differences in the iron-dust budget, when a low-star-forming environment is considered. In this case the final depletion is due to type Ia SNe, that are the main iron polluters. In the solar vicinity, on the contrary, at the present time no effect can be seen.

6.10.3 The effect of varying the yields of dust for AGB stars

Finally, we examine the role played by AGB stars. In the very early stages of the evolution the contribution by AGB stars is negligible: since the most massive AGB star that we included in our models has 6 $M_{\odot}$, it takes some time before AGB stars start polluting the ISM. Depending on the condensation efficiency of the SNe dust, if this latter is low it may happen that there could be a possibility for AGB stars to contribute significantly before the ISM accretion process starts dominating. In Fig. 6.19 we show the evolution of the AGB dust budget for the three regions of the MW disk for the δ of Dwek (1998) and the set obtained from Ferrarotti & Gail (2006) The difference between the models is less striking than for SNe, with some exception

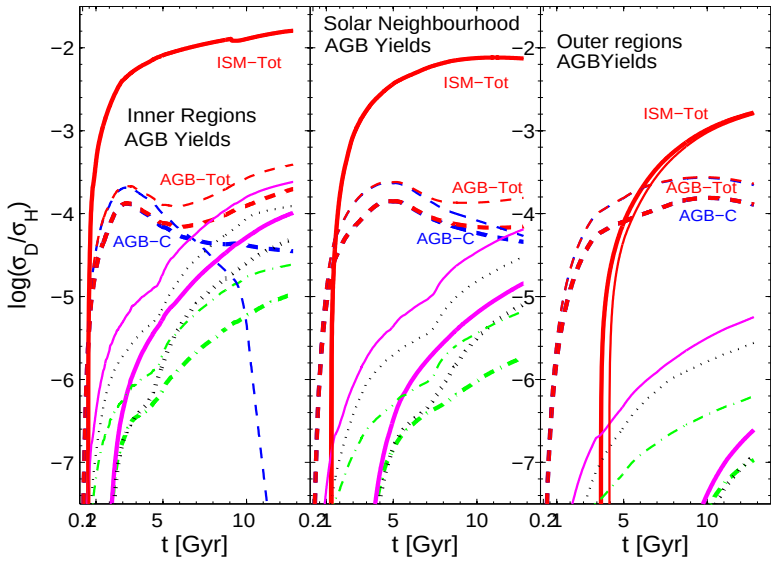

Figure 6.19: Temporal evolution of the contribution from AGB stars to the dust budget calculated until the present age. All the contributions have been properly corrected for the effect of dust destruction. Three regions of the MW Disk are considered as usual: the inner ring (left panel), the Solar Ring (middle panel), and the outer region (right panel). Thick lines represent our model $\mathcal{A}$ based upon Dwek (1998), whereas the thin lines represent model $\mathcal{B}$ based upon Ferrarotti & Gail (2006). We show: the total contribution by accretion of dust grain in the ISM (continuous lines) and the total contribution by AGB stars (dashed lines); the contributions by the various kinds of AGBs dust grains, in the specific: the iron-stardust (dotted lines); the silicates (continuous lines), the carbonaceous grains (dashed lines) and Ca/S/N based dust grains (dot-dashed lines). **Left panel**: The results for the inner ring. **Central panel**: the same as in the left panel but for the Solar Ring. **Right panel**: the same as in the left panel but for the outer ring.

like carbon evolution at high metallicities (left panel). Once more, dust production by ISM accretion overwhelms that by stars: for low SFR we see a temporal window where AGB could produce some effect before the ISM accretion process becomes predominant. In any case we consider more reliable the use of the Ferrarotti & Gail (2006) models, that includes the effect of the metallicity on the development of the Carbon rich phase in the AGB, while the simple recipe by Dwek (1998), Calura et al. (2008), Pipino et al. (2011) do not take into account this point. The condensation factors are divided considering the effect of both metallicity and/or progenitor mass. The approach by which dust formation is simulated in the circumstellar envelope of AGB stars, is more reliable than the hypotheses assumed for dust formation in SNe (Cherchneff & Dwek 2010). The inclusion of the metallicity effect allows to respect an important characteristic of the dust mixture:low metallicity stars more easily enter the carbon rich phase and produce more carbon dust, while high metallicity stars, mainly avoiding or briefly entering the C-rich part of the evolution mainly contribute with silicates.

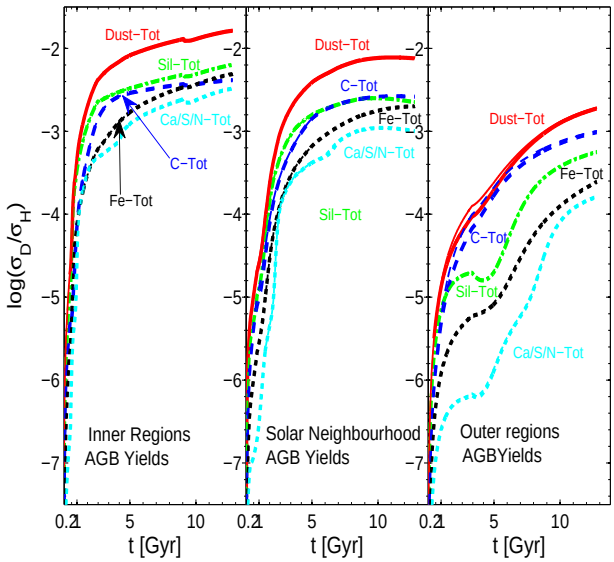

Figure 6.20: Temporal evolution of the contribution from AGB stars to the dust budget calculated until the present age. Three regions of the MW Disk are considered as usual: the inner ring (left panel), the Solar Ring (middle panel), and the outer region (right panel). Thick lines represent the model based upon Dwek (1998), while thin lines represent the model based upon Ferrarotti & Gail (2006). We show: the total amount of dust grains in the ISM (continuous lines) and the total amount of the various grain families, where with total we mean AGB stardust plus SNe stardust plus accreted dust in the ISM. In detail we show: the iron-stardust (dotted lines); the silicates (dot-dashed lines), the carbonaceous grains (dashed lines) and Ca/S/N based dust grains (dotted lines). **Left panel**: The results for the inner region of the MW Disk. **Central panel**: the same as in the left panel but for the Solar Ring. **Right panel**: the same as in the left panel but for the outer ring.

Does the different possible recipes for AGB star-dust lead to some differences in the evolution of the dust content in the ISM? In Fig. 6.20 the evolution of the *total* normalized abundance of the various dust grains families for the prescriptions for the AGB stars (always for the three regions of the disk), is shown. Only in the outer regions with very low star formation rates and low metallicities we can notice a difference between one model of dust nucleation and injection by AGB stars and another. In the other regions, there is in practice no difference at varying the AGB condensation efficiencies. This simply means that in the early stages, with the typical SF laws for the MW, AGB stars dust factory is dominated by SNe (unless a very low condensation efficiencies by SNe are assumed), and later by the accretion process in the ISM. Obviously AGB stars play a fundamental role in refueling the ISM with metals and seeds, but the dust factory of the ISM accretion mechanism is the starring actor. Of course, if some peculiar dust grains (like SiC) are injected by AGBs and not formed by accretion in the ISM, in that case AGB stars play a crucial role in

determining the evolution of that kind of dust.

6.11 Solar System Abundances

To validate now the results of our model applying it to the MW we need a reference set of chemical abundances. They are also known as the *cosmic reference abundances*. Usually, the Solar System abundances provide the comparison set of values, but other choices are possible (Savage & Sembach 1996; Asplund et al. 2009; Whittet 2010). Since the solar system abundances can not be determined directly from measurements of the ISM, because of the depletion of the elements accreted into dust, two main sources of information are usually adopted: spectroscopic data inferred from the Sun and Meteoritic Abundances.

Photospheric abundances of the Sun can not be determined directly, but only by means of a model atmosphere of the solar spectrum. The model must be able to calculate lines formation (classical 1D or hydrodynamical 3D), and takes into account radiative transfer and non-LTE processes (see for a review about solar abundances obtained from spectroscopy Basu & Antia (2008)). However, since there are no lines of noble gases in the solar photosphere, coronal lines, energetic particles or solar wind are also studied, in particular to determine the crucial abundances of He and Ne.

Between the tens of thousands meteorites fell on the earth, only five are C1 carbonaceous chondrites (Lodders et al. 2009). They form the only group of meteorites allowing us to determine the abundances in the proto-solar environment that match the solar ones, and keep some memory of the original proto-environment. However, volatile elements and noble gases like H, He, C, N, O, and Ne, therefore including the most abundant elements, are heavily depleted in these meteorites. We can not rely on mass spectrometry to safely determine their abundances, but an additional source of information must be adopted.

It is common practice to combine photospheric and meteoritic measurements to get the compilations of abundances commonly used in literature and continuously updated year after year (Anders & Grevesse ; Grevesse & Noels 1993; Grevesse & Sauval 1998; Lodders 2003; Asplund et al. 2005; Grevesse et al. 2007; Lodders et al. 2009; Asplund et al. 2009).

Two points are worth of mention. (i) According to the most recent models, the present photospheric abundances of the Sun are lower than the bulk abundances of the proto-Sun formed about 4.6 Gyr ago because of the physical processes taking place in the deep convective region under the solar surface. The effects of thermal diffusion, gravitational settling due to differential gravity and radiative acceleration (Turcotte & Wimmer-Schweingruber 2002) allow helium and heavy elements to deposit in the interiors of the Sun. The decay of radioactive elements affects the isotopic

Table 6.4: Chemical abundances for the Sun at the present age according to the classical compilation by Grevesse & Sauval (1998) (GS98 - photospheric solar abundances) and the more recent ones by Asplund et al. (2009) (AGSS09 - photospheric solar abundances) and Lodders et al. (2009) (LPG09 - photospheric and meteoritic abundances compilation). Finally, in the last column we present the abundances we have adopted in this study. The Abundance A(X) of the element X is in units of $\log_{10}(\mathrm{N(X)/N(H)}) + 12$. Only the elements included in our chemical model are reported and discussed

Element	GS98	AGSS09	LPG09	This work
H	12.00	12.00	12.00	12.00
He	10.93±0.004	10.93±0.01	10.93±0.02	10.93±0.02
C	8.52±0.06	8.43±0.05	8.39±0.04[1]	8.50±0.06[7]
N	7.92±0.06	7.83±0.05	7.86±0.12[2]	7.83±0.05
O	8.83±0.06	8.69±0.05	8.73±0.07[3]	8.73±0.06
Ne	8.08±0.06	7.93±0.10	8.05±0.10[4]	7.99±0.10
Mg	7.58±0.05	7.60±0.04	7.54±0.06[5]	7.57±0.05
Si	7.55±0.05	7.51±0.03	7.53±0.01[6]	7.53±0.01
S	7.33±0.11	7.12±0.03	7.16±0.02[5]	7.14±0.03
Ca	6.36±0.02	6.34±0.04	6.31±0.02[6]	6.34±0.04
Fe	7.50±0.05	7.50±0.04	7.46±0.08[5]	7.50±0.04
Z/X	0.0231±0.018	-	-	-

[1]This is the same low photosphere value as in Lodders (2003), selected from Allende Prieto et al. (2002), and confirmed in Asplund et al. (2005) and Scott et al. (2006). [2]N is taken from Caffau et al. (2009), from solar photospheric models. [3]The O abundance is an average from solar photospheric models by Caffau et al. (2008), Ludwig & Steffen (2008), Meléndez & Asplund (2008). [4]Ne abundance is an average from Morel & Butler (2008, Landi et al. (2007). [5]Average between solar and meteoritic values. [6]Meteoritic value. [7]Caffau et al. (2010).

compositions (Piersanti et al. 2007; Lodders et al. 2009). The correction needed to obtain the unfractioned abundances of the proto-Sun is of about 0.05 dex for He and 0.04 dex for heavier elements (Asplund et al. 2009) or slightly higher of 0.01 dex for both corrections (Lodders et al. 2009). With these corrections there is agreement with the abundances observed in nearby B stars by Przybilla et al. (2008). (ii) The He and Ne abundances determined with coronal lines or solar wind suffer from the FIP effect. Therefore the most precise method to determine the He abundance is helioseismology and the adiabatic index Γ_1, whereas for Ne abundance are the photospheric ratios Ne/O and Ne/Mg together with their systematic errors (Basu & Antia 2008).

Starting from Allende Prieto et al. (2001, Allende Prieto et al. (2002), the widely used compilation of abundances by Grevesse & Sauval (1998) has been the subject of

a continuous revision of the photospheric C, N, O abundances toward a significantly lower value, i.e. about 0.2 dex lower than before (Asplund et al. 2004; Asplund et al. 2005; Asplund et al. 2005). These new values, derived from 3D hydrodynamical models with updated input physics and no macro- and micro-turbulence, bring the Sun to better agree with the metal content of the Galactic neighbourhood (Turck-Chièze et al. 2004). They are also in good agreement with recent determinations of B-star abundances (Nieva & Przybilla 2008b; Nieva & Przybilla 2008a) and carbonaceous C1 chondrites for many elements (Asplund et al. 2005; Lodders et al. 2009; Asplund et al. 2009). There is also a better agreement between different diagnostics(OI, [OI] and OH vibrational and roto-vibrational bands for Oxygen, CI, [CI], CH, C_2 and CO for Carbon), but a strong disagreement with the helioseismological models (Antia & Basu 2005; Bahcall et al. 2005; Bahcall et al. 2005; Antia & Basu 2006; Basu & Antia 2008). In brief, the position of the base of the convective zone, the helium abundance, sound speed and density profiles are all affected by the revised abundances (Basu & Antia 2008). Many suggestions have been advanced to solve this discrepancy, e.g. increased input opacities, increased abundances of neon or other elements, fine tuning of the diffusion process, inclusion of other additional physical processes etc. All this, however, without removing the discrepancy. The recent revision of the abundance compilation by Asplund et al. (2009), reversed the trend toward higher abundances, thus in closer agreement with helioseismology, even if the differences are still significant. Also, a series of models calculated over the past few years (all based on the so-called CO^{5}BOLD 3D hydrodynamical code) go toward a reconciliation with helioseismology (Caffau et al. 2008; Caffau & Ludwig 2008; Caffau et al. 2009; Ludwig et al. 2009; Maiorca et al. 2009; Caffau et al. 2010). Anyway, as pointed out in Caffau et al. (2010), results from different 3D hydrodynamical simulations may still mutually differ by as much as 0.1 dex, suggesting that better validation of the hydrodynamical models and more and more updated solar models are needed (Turck-Chièze et al. 2008).

In Tab. 6.4 we show the classical set of abundances by Grevesse & Sauval (1998) (GS98), the two most recent compilations available in literature by Asplund et al. (2009) (AGSS09) and Lodders et al. (2009) (LPG09) and, finally, in the last column, our adopted reference set for the present-day solar abundances. The abundances by number of the various elements are indicated by A(X) which stands for $\log_{10}(\mathrm{N(X)/N(H)}) + 12$.

Let us now examine in some detail the choice we made for the abundances of the various elements included in our model:

Carbon: the carbon abundance is A(C)=8.50±0.06 according to Caffau et al. (2010). It corresponds to a weak efficiency of the collisions with neutral hydrogen atoms ($S_H = 1/3$). The uncertainty is the sum of statistical (0.02) and systematic

(0.04) errors. This value is similar to the old GS98 determination and very close to the average estimate of the carbon abundance during the past thirty years (see Tab. 4 in Caffau et al. (2010)).

Nitrogen: the abundance of Nitrogen determined by AGSS09 does not much differ from that by LPG09, but it is significantly lower than GS98. We adopt the value by AGSS09 A(N)=7.83±0.05. As this is derived from both atomic and molecular lines, the error is minimized.

Oxygen: Oxygen, together with Neon, are the most debated and uncertain elements (Asplund et al. 2009). LPG09 adopted the average value between the estimate from CO^{5}BOLD atmosphere models by Caffau et al. (2008) (8.76±0.07), that by Ludwig & Steffen (2008) (8.72±0.06), and the one by Meléndez & Asplund (2008) (8.71±0.02). AGSS09 recommends 8.69±0.05 obtained from atmosphere models with updated physics and taking the mean value of estimates based on [OI], OI, OH vibration-rotation and OH pure rotation. Whittet (2010) adopts 8.76±0.03 based upon observations of nearby B-stars (Przybilla et al. 2008). Averaging all these values, we adopt 8.73±0.06.

Neon: the abundance of Neon proposed by AGSS09 (7.93±0.10) is determined from their O abundance and the Ne/O ratio. LPG09 (8.05±0.10) takes the mean value between measurements in B-type stars and UV-flares. The proposed values are very different. We adopt the average value of 7.99±0.10. The corresponding Ne/O ratio is 0.182 in very good agreement with Schmelz et al. (2005).

Magnesium: magnesium gf-values for the two ionization stages MgI and MgII suffer of well know uncertainties, as underlined in AGSS09. For this reason we adopt the weighed average between the LPG09 meteoritic abundance 7.55±0.01 and the AGSS09 value, obtaining 7.55±0.05.

Silicon: silicon is the element linking meteoritic and photospheric measurements. Since H is very depleted in C1 chondrites, meteoritic abundances are usually expressed in the cosmochemical scale as number of atoms per 10^6 Si atoms. If the abundance by number of Si is known, we may easily obtain the abundance by number of any element in the usual scale $\mathrm{A(X)} = \log_{10}(\mathrm{N(X)/N(H)}) + 12$. The various estimates of the Si abundance listed in Tab. 6.4 agree quite well each other. Therefore we can adopt the estimate by LPG09 that is the average between the solar photospheric and meteoritic values.

Sulfur: the sulfur abundance has been revised by AGSS09, including additional lines and NLTE corrections. We take the mean between this value and the meteoritic abundance by LPG09 (see their Tab. 4).

Calcium: for the abundance of Calcium we choose the value proposed by AGSS09, which is in good agreement with LPG09 and GS98 and is based upon recent NLTE abundance corrections by Mashonkina et al. (2007).

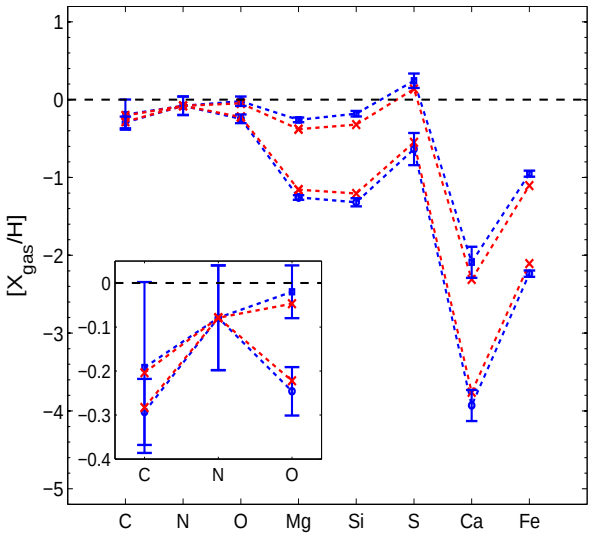

Figure 6.21: The range of depletions is shown for those elements in our list that intervene in the dust formation or are present in the ejecta by AGB stars and SNe (C, N, O, Ms, Si, S, Ca and Fe). The insert shows in detail the depletions for C, N and O. Four values are plotted for each element. Filled squares and circles represent the smallest and largest depletion, respectively. The crosses determine the range for the depletion in the Warm and Cool components of the Galactic Disk, according to Jenkins (2009) and Savage & Sembach (1996). See Tab. 6.5 for more details.

Iron: we adopt the value given by AGSS09, in excellent agreement with the meteoritic measurement by LPG09 and GS98.

Once the reference abundances are assigned, we can tackle the element depletion in the ISM, that is the under-abundance of some elements compared to the corresponding reference value, because a fraction of the element under consideration is locked up in the interstellar dust. The depletion of the element X in the ISM is measured in the following way. Following Jenkins (2009) and Whittet (2010) we define

$$[X_{gas}/H] = log\left[N\left(X\right)/N\left(H\right)\right] - log\left(X/H\right)_{ISM} \tag{6.11.1}$$

where $\mathrm{N(X)}$ is the column density of the element X and $\mathrm{N(H) = N(HI) + N(H_2)}$ the same for hydrogen and, finally, and $\mathrm{(X/H)_{ISM}}$ the assumed reference abundance. If part of the element X is locked up into dust grains ($\mathrm{[X_{gas}/H] \leq 0}$), the fractional abundance of the element depleted into dust is

$$(X_{dust}/H) = (X/H)_{ISM} \cdot \left(1 - 10^{[X_{gas}/H]}\right) . \tag{6.11.2}$$

Usually, establishing the degree of depletion of an element is a cumbersome affair, because the choice of the reference abundance is a difficult task and errors and

inconsistencies affect the measurements (Whittet 2003; Whittet 2010). Recently, Jenkins (2009) presented a thorough study of the depletion for 17 elements along 243 lines of sight, trying to focus on the rates of depletion and leaving aside the problem of the reference abundance. He was able to characterize the degree of depletion according to three parameters: one describes the overall level of depletion along a particular line of sight; the other two are related to the depletion of each element along that line. Once adopted the reference abundances proposed by Lodders (2003) for the proto-sun, Jenkins (2009) presents the depletion parameters for the smallest and largest depletion efficiencies (his parameter F_*), thus bracketing the region to be matched by any theoretical model. In the context of the present study, to correctly make use of the Jenkins (2009) results, the following remark is appropriate. Jenkins (2009) analysis stems from the Lodders (2003) present reference abundances (see his Tab. 1) which is different from the one we have adopted (see the entries of Tab. 1.1. Therefore, a suitable shift has to be applied. Furthermore, the Lodders (2003) reference abundances for the proto-solar environment have been obtained from the present-day solar+meteoritic ones by adding ~ 0.07, which is likely too a correction (Jenkins 2009; Lodders et al. 2009; Przybilla et al. 2008). Therefore, we derive our present-day reference abundances applying the more realistic correction suggested by (Asplund et al. 2009).

Tab. 6.5 shows the reference abundances for the Solar Ring used by Jenkins (2009) and those adopted in our set for the proto-solar environment, together with the upper and lower limits for the smallest ($F_* = 0$) and heaviest ($F_* = 1$) depletion efficiencies adapted from Jenkins (2009) to our case. Calcium deserves some remarks. It is not included in the Jenkins (2009) list, whereas we take it into account. Furthermore, as this element is heavily depleted in the ISM (Whittet 2003; Tielens 2005), we consider the values proposed by Crinklaw et al. (1994) for the smallest and heaviest depletion. The value proposed by Whittet (2003) for the diffuse clouds falls in the middle.

In Fig. 6.11.1 we finally show the range of depletions adopted in our work to test the simulations versus the Solar Ring. Since the depletion is line-of-sight dependent, we show for each element the range allowed taking into account the smallest and largest depletion with relative error bars. The values of depletion for cool and warm disk are also shown. For the sake of clarity, we expanded the depletion range for C, N, O in the lower left corner of the figure.

6.11.1 Fraction of CO in the ISM

As already discussed in Sects. 6.5.1 and 6.5.3, a percentage from 20% to 40% of the Carbon and up to 20% of the Oxygen is locked in the CO molecules (see van Dishoeck et al. (1993) and van Dishoeck & Blake (1998)). This affects the amount of Carbon

Table 6.5: In column (1) we list the elements we have considered. In columns (2) and (3) we show the chemical abundances for the proto-solar environment, according to the Lodders (2003) compilation adopted by Jenkins (2009) and the values we have adopted. In columns (4) and (5) we give $[\mathrm{X_{gas}/H}]_0$ and $[\mathrm{X_{gas}/H}]_1$, the smallest and largest depletion values for the various elements are obtained from Jenkins (2009), with a correction to account for the difference between the reference set of elemental abundances. In column (6) we list the abundances in the ISM and in columns (7) and (8) we show the abundances of elements in dust in units of 10^6 ($\mathrm{X_{dust}/H}$), for the smallest and largest depletions, respectively. Finally columns (9) and (10) show the abundances for the Warm Disk and the Cool Disk, according to the fit made by Jenkins (2009) of the Savage & Sembach (1996) data.

Element	$A(X)^1$	$A(X)^2$	$\left[\frac{X_{gas}}{H}\right]_0$	$\left[\frac{X_{gas}}{H}\right]_1$	$\left(\frac{X_{ISM}}{H}\right)_\odot$ ($\cdot 10^6$)	$\left(\frac{X_{dust}}{H}\right)_0$ ($\cdot 10^6$)	$\left(\frac{X_{dust}}{H}\right)_1$ ($\cdot 10^6$)	$\left[\frac{X_{gas}}{H}\right]_{WD}$	$\left[\frac{X_{gas}}{H}\right]_{CD}$
(1)	(2)	(3)	(4)	(5)	(6)	(7)	(8)	(9)	(10)
H	12.00	12.00	-	-	10^6	-	-	-	-
He	10.984±0.02	10.98±0.02	-	-	$9.5{\cdot}10^4$	-	-	-	-
C	8.46±0.04	8.54±0.06	-0.192±0.194	-0.293±0.075	347	124^{+80}_{-124}	170^{+28}_{-33}	-0.204	-0.283
N	7.90±0.11	7.87±0.05	-0.079±0.119	-0.079±0.119	74	12^{+15}_{-19}	12^{+15}_{-19}	-0.079	-0.079
O	8.76±0.05	8.77±0.05	-0.020±0.060	-0.246±0.055	588	27^{+73}_{-82}	255^{+40}_{-45}	-0.047	-0.222
Ne	8.08±0.06	7.97±0.10	-	-	93	-	-	-	-
Mg	7.62±0.02	7.61±0.05	-0.260±0.030	-1.257±0.029	41	18^{+2}_{-2}	38^{+1}_{-1}	-0.380	-1.157
Si	7.61±0.02	7.57±0.01	-0.180±0.035	-1.319±0.052	37	13^{+2}_{-2}	35^{+1}_{-1}	-0.320	-1.205
S	7.26±0.04	7.18±0.03	0.243±0.092	-0.635±0.206	15	-11^{+63}_{-6}	12^{+2}_{-2}	0.137	-0.548
Ca	6.41±0.03	6.38±0.04	-2.090±0.200	-3.930±0.200	2.4	2.38	2.398	-2.311	-3.746
Fe	7.54±0.03	7.54±0.04	-0.951±0.038	-2.236±0.041	35	31^{+1}_{-1}	34^{+0}_{-0}	-1.105	-2.107

Abundances $A(X)$ of the element X are in units of $\log_{10}(\mathrm{N(X)/N(H)}) + 12$. [1]Proto-solar abundances adopted in (Jenkins 2009). [2]Proto-solar abundances adopted in this work. [3]The positive depletion of sulfur means that instead of observing a depletion of the element the gas seems to be enriched of sulfur atoms respect to the reference set.

available as key-element for the growth process owing to the lowered abundance of this element in the gaseous phase. Furthermore, in the dense and cold regions of the ISM, CO tends to condense onto dust grains (Goldsmith 2001; Bacmann et al. 2002; Whittet 2010), leaving the gas phase and sticking efficiently to dust (Whittet 2010). The depletion of the CO can reach in pre-stellar cores even a factor of 10 (Tafalla et al. 2002; Walmsley et al. 2004). All this is parameterized by the fraction $\zeta_{\rm CO}$ of CO. The effect of $\zeta_{\rm CO}$ on the key-elements ^{12}C and ^{13}C (and of $\zeta'_{\rm CO}$ on ^{17}O and ^{18}O) is straightforward: the higher is the amount in CO, the lower is the amount of free atoms in the gas-phase available for the growth, thus implying longer timescales and slower dust formation. Therefore, we expect a lower contribution by the accretion to the dust budget of the ISM when high values of $\zeta_{\rm CO}$ are adopted.

In Fig. 6.13, we present the time evolution of the contributions to the dust budget for three regions of the MW: a central region (r_k = 2.3kpc), the Solar Ring (r_k = 8.5kpc) and an outer region (r_k = 15.1kpc). First of all, we do not show the temporal evolution of the single elements, but of important groups of elements representative of the main typical ISM dust types. These are the silicates (olivines+pyroxenes+quartz+silicon in SiC), carbonaceous grains (carbon grains plus carbon in SiC), iron grains and, finally, other grains containing S, N and Ca. All the dust abundances have been normalized to the local hydrogen density and corrected for dust destruction so as to represent the effective net contribution to the dust budget. The contributions are split in three main sources: AGBs, SNe and ISM accretion. In order to explore the effect of CO, in the $\mathcal{GDABBCBBB}$ model we vary the CO abundance from 15% up to 45%: the two thin dashed lines in Fig. 6.13 bracket the region of variation of the ISM contribution. Carbon accretion in the ISM is the only process varying with the CO abundance: the lower $\xi_{\rm CO}$ the higher is the ISM contribution. This effect can be significant and we cannot easily get rid of it when evaluating carbon depletion: however, it is clear and straightforward and limited to the only carbon. Even if ^{16}O is a component of the CO molecule, due to its high abundance and never being a key-element, it is scarcely affected by variations of $\xi_{\rm CO}$. The same holds true for ^{17}O and ^{18}O but in this case due to their low abundance: their budget depends on $\xi_{\rm CO}$, but their contribution to the global budget is negligible. Therefore, the variations of $\xi_{\rm CO}$ do not affect the silicates budget.

From the analysis of Fig. 6.13 we can notice several general features of the dust evolution common to all the models that are worth to be underlined: (i) the main contribution to the dust enrichment during most of the Galaxy lifetime is due to the accretion process in the ISM. Furthermore, dust production is much higher in the inner regions of the Galactic Disk compared to the outer ones where the weight of the ISM gets smaller so that during many Gyr the stardust injected from AGB stars and SNe drives the total yields. This is ultimately due to the low number densities

of metals that do not favour the accretion process; (ii) the inner regions reach higher metallicities than the outer ones: therefore, all physical processes depending on the metallicities are much enhanced in the central regions of the Galaxy, e. g. the yields of dust from oxygen rich M-stars; (iii) even if some sources (like AGB-C stars in the inner regions) may vary their contributions with time, in general the *total* amount of dust keeps growing monotonically. In some way, this mirrors the metallicity enrichment of the ISM and the fact that dust formation is very sensitive to metals.

In Fig. 6.14 we show in detail the evolution of the contributions of AGB stars, SNe and ISM to the total budget of dust during the first 1.5-2 Gyr for the three selected regions of the Galactic disk. For AGB, SNe and ISM we show the total budget. However, limited to SNe, we also distinguish the various types of grains. During the early stages, stardust dominates the scene: going from the innermost to the outermost regions it takes more and more time for the ISM accretion to overcome the stellar contribution. This is ultimately due to the higher densities and metal content of the inner regions that favors the onset of accretion. For the outer regions, with low density and low SFR, the ISM starts to be important only at t>4 Gyr (see Fig. 6.13). It is interesting to note how the dust-to-gas ratio for net yield by SNe is nearly constant going from the innermost regions (left panels of Fig. 6.14 and 6.13) to the external ones (right panels of the same figures), even if the associated timescales are much different. Toward the center of the Galaxy, we have more hydrogen, higher SFR, higher SNe rate and higher yields of dust. Both gas (via infall) and SNe dust (via infall, SFR and SNe explosions) grow in absolute value moving from outside to inside, whereas their ratio does not change in the same proportions (considered that in any case the yields of dust by SNe do not depend on the metallicity, at least according the the kind of theoretical results to our disposal).

6.11.2 The effect of the IMF

Different IMFs influence in a crucial way the injection of dust into the ISM. For every generation of stars, the relative amount of newly born massive objects able to produce dust via the SN channel and the amount of low and intermediate mass stars refueling the ISM with the dust produced through the TP-AGB phase, both depend on the IMF. This last one also determines the timescales of stardust injection and the relative contribution by SNe and AGB stars.

In Fig. 6.22 we compare the degree of dust enrichment obtained using nine different IMFs chosen among those widely used in literature. The reference case is always given by the model $\mathcal{GDABBCBBB}$. All the others are obtained from this by varying the first parameter of the list from case $\mathcal{A}$ to case $\mathcal{I}$. First of all, let us examine the effects of the IMF during the first evolutionary stages, when the dust enrichment is

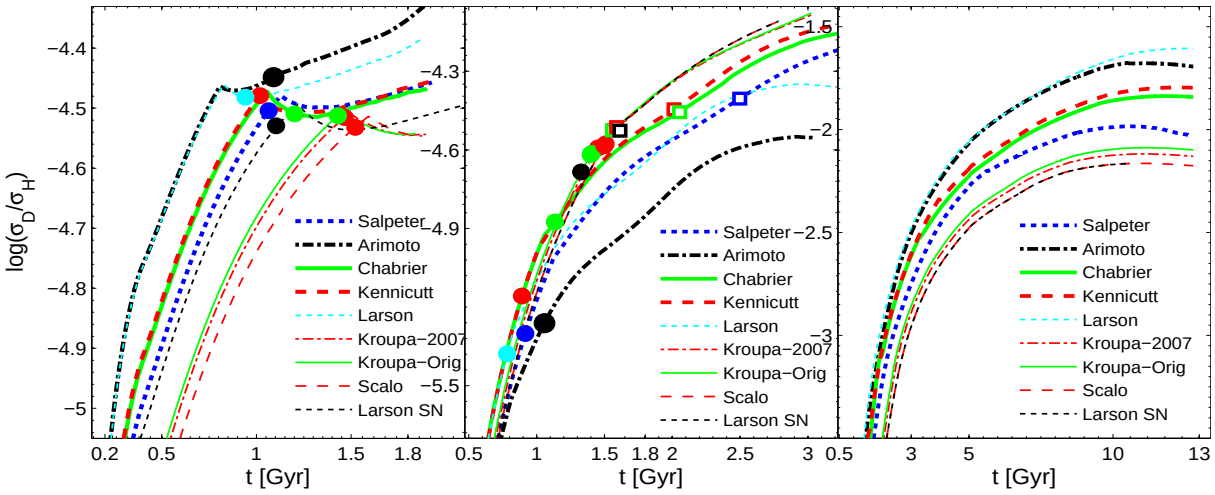

Figure 6.22: Temporal evolution of the contribution to the abundance of dust during the *first 2 Gyr-3 Gyr* in the Solar Ring at 8.5 kpc and for *different IMFs*. All the contributions have been corrected for the destruction of dust. Nine IMFs have been considered: Salpeter (thick dotted line), Arimoto (thick dot dashed line), Chabrier (thick continuous line), Kennicutt (thick dashed line), Larson (thin dotted line), Kroupa-2007 (thin dot-dashed line), Kroupa original (thin continuous line), the Scalo IMF (thin dashed line) and, finally, the Larson IMF adapted to the Solar Ring (thin dashed line). See Sect. 6.3 for more details. **Left panel**: temporal evolution of the total contribution to the dust budget by SNe in the MW Solar Ring. The filled symbols represent the instant when the contribution by ISM accreted dust *equalizes* the SNe injected dust amount. **Middle panel**: time evolution of the total contribution to the dust budget by AGB stars for the MW Solar Ring. The filled symbols represent the instant when the contribution by AGB injected dust *equalizes* the ISM dust production by accretion, while the empty symbols represent the instant (if eventually it happens) when AGB dust equalizes the SNe injected dust. **Right panel**: time evolution of the total dust budget for different IMFs.

mainly due to SNe, which also supply the seeds and metals for the accretion process in the ISM. We begin with the the solar vicinity displayed in the left panel of Fig. 6.22. We note that, at varying the IMF and keeping fixed all the other parameters of the model, the age at which the dust enrichment by the accretion in the ISM becomes comparable to that by SNe can vary by about ~ 0.5 Gyr. The time difference can be easily explained as due to the different percentage of massive stars exploding as SNe (and thus refueling the ISM) with the different IMF (see the entries of Tab. 1.2 in Chap. 1).

Some IMFs (like those by Kroupa, Larson Solar Ring and Scalo) predict a small number of SNe compared to others (like those by Larson, Kennicutt or Chabrier) that are more generous in the number of massive stars and hence Type II SNe. Therefore, in the former case a small injection of dust by SN explosions and a slow accretion (fewer seeds to disposal) are expected. The opposite holds true with the latter case case favouring the formation of massive stars. Furthermore, with the former case the

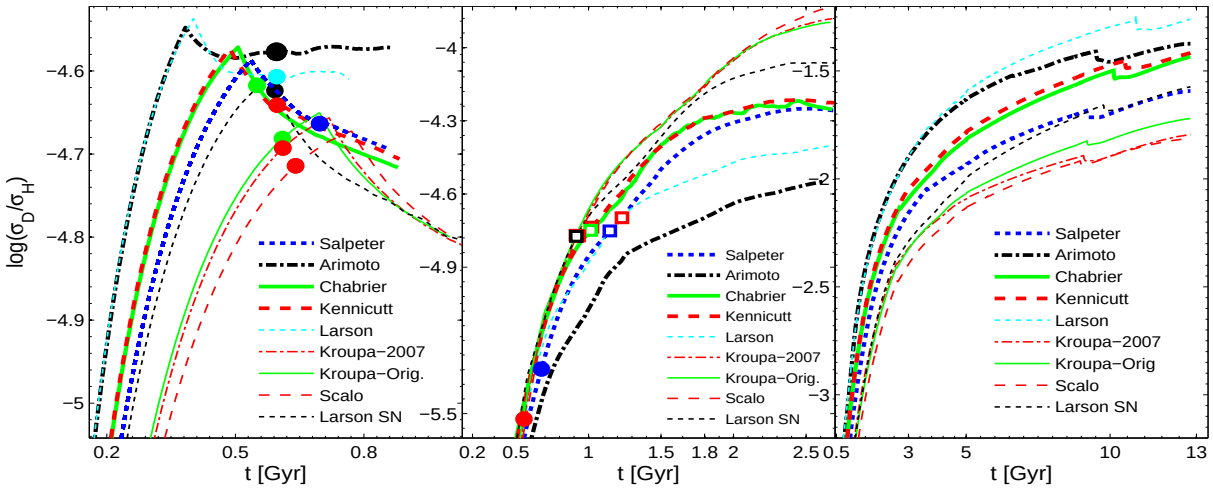

Figure 6.23: Temporal evolution of the contribution to the abundance of dust during the *first 1-2 Gyr* in the *inner part* of the MW disk at 2.3 kpc from the centre and for *different IMFs*. All the contributions have been corrected for the destruction of dust. Nine IMFs have been considered as in Fig. 6.22. See Sect. 6.3 for more details. The meaning of all the symbols is the same as in Fig. 6.22.

time at which the ISM gets dust-rich by accretion is delayed with respect to the other case. This is also shown in the panels of Fig. 6.22 where the time when the ISM accretion equalizes the dust enrichment by SNe at decreasing the relative percentage of massive stars in the IMF is marked. It is also evident that IMFs skewed toward massive stars produce much more dust of stellar origin. Consequently, before accretion in the ISM starts driving the evolution of the dust, large differences brought by the IMF are possible.

So far we have examined the solar vicinity with a relatively mild star formation efficiency. What about the innermost region of the MW characterized by a much higher SFR? The situation is shown in the left panel of Fig. 6.23 which displays the dust enrichment due to SNe as in Fig. 6.22. Compared to the solar vicinity, we note that SNe produce many more seeds and metals, accretion in the ISM develops faster and becomes important very earlier on. However, in the ISM the dust production by accretion becomes more or less comparable to that by SNe at the same time *independently* of the IMF (see the large dots marked in the left panel of Fig. 6.23). In the case of the solar vicinity, the cross-over stage hardly occurred below 1 Gyr extending up to 1.5 Gyr, whereas now they all fall in the age range 0.6-0.7 Gyr. In a medium rich of seeds, dust accretion grows faster and the effect of the IMF somehow loses importance.

The differences both in the amounts of dust of stellar origin injected and the timescale of earlier enrichment in dust by SNe are very large. In general, the effects induced

by variations in the IMF can be very large during the earliest stages of evolution. Along this line of thought, we can expect that in high-redshift obscured galaxies with high SFR (easily even higher than the early SFR of the inner regions of the MW) some IMFs may not be able to produce the amounts of observed dust of stellar origin before the dust accretion process has become significant. The immediate implication of this for primeval galaxies can be easily foreseen. According Draine (2009), some accretion in the ISM to explain the amount of dust in observed primeval galaxies is required. The picture should be as follows: (i) before dust by accretion in the ISM and dust injected by stars become comparable, the effect of the IMF prevails and determines the amounts of dust present in the Galaxy; (ii) if the SFR is high, the IMF does not play an important role in determining the onset of the dust accretion process in the ISM, whereas if (iii) the SFR is low, different IMFs cause an important spread in the ages at which dust by accretion becomes important.

We pass now to examine the role played by AGB stars. In the middle panels of Figs. 6.22 and 6.23 we see for the same regions of the left panels the contribution of the AGB stars to the total dust budget. The AGB stars contribute significantly over a longer time-scale: the filled symbols show the age at which dust produced by AGB stars and dust accreted in the ISM become comparable, whereas the empty ones show the same but for AGB stars versus SNe. In both cases the age is marked when and if the equality among the three contributions can be established. There are indeed some extreme IMFs, where massive stars are favored with respect to the intermediate mass ones progenitors of AGB stars (like the Arimoto IMF), in which during the first Gyrs AGB stars never reach SNe in the inner MW regions (Fig. 6.23 - middle panel). Furthermore, IMFs richer in intermediate mass stars produce bigger amounts of dust by AGB stars. This may somehow be correlated with the delayed appearance in a galaxy spectral energy distribution of the PAHs features: the delay may depend on efficiency of dust injection by AGB stars.

Finally, in the right panels of Figs. (6.22) and (6.23) we show the evolution of the total dust content in the ISM: it is interesting to note how the differences between the various IMFs in the early stages are the same as those expected (observed) at the present age, keeping constant all other parameters. The IMFs producing more dust by SNe (and of course seeds for accretion) in the early stages are the same for which we get higher amounts of dust at the current age. The differences among the various IMFs can be significant. Indeed, a fast enrichment of dust during the early stages caused by SNe, (keeping fixed all other parameters, the condensation coefficients in particular) goes together with a strong enrichment in metals. More metals means more atoms available for dust to grow in the ISM. For this reason IMFs skewed toward massive stars favor the accretion of dust in the ISM and lead to higher final contents of dust.

6.11.3 The effect of the SF law

As presented in Sect. 6.3, four SF laws have been considered. The results are shown in the four panels of Fig. 6.24 limited to the early stages of the evolution. The reference model is $\mathcal{GDAABBCBBB}$, in which the SFR is changed as indicated.

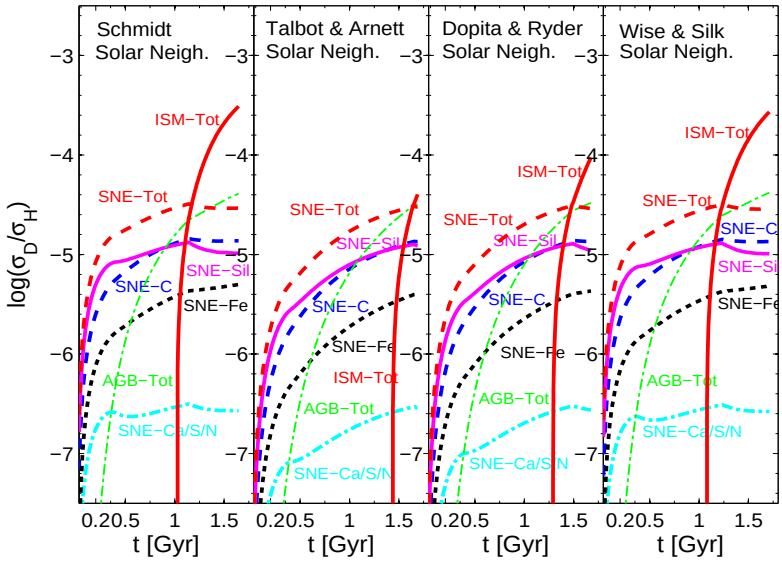

Figure 6.24: Temporal evolution of the dust budget in the Solar Ring during the early stages until 1.5-2.5 Gyr. Four SF laws are shown in the four panels: Schmidt, Talbot & Arnett, Dopita & Ryder and Wyse & Silk. We display: the amount of dust grains accreted in the ISM (continuous lines), the amount of dust injected by AGB stars (thin dot-dashed line), the total amount of SNe stardust (dashed line) also subdivided into the various grain families, respectively, i.e. dotted line (iron-dust), silicates (continuous line), carbonaceous grains (dashed line), and S/Ca/N based grains (dot-dashed line). **Left panel**: Temporal evolution of the dust budget injected in the Solar Ring by the various sources and the Schmidt law. **Central-left panel**: the same as in the left panel but for the Talbot & Arnett law. **Central-Right panel**: the same as in the left panel but for the Dopita & Ryder SF law. **Right panel**: the same as in the left panel but for the Wyse & Silk SF law.

The parameters k and ν of the SFR are chosen in agreement with the analysis made by Portinari & Chiosi (1999), in such a way that the sole effect of the SFR law is isolated. All other parameters of the model are kept fixed. At given k and ν, the different SF laws widely adopted for the MW disk produce a similar dust budget. Some differences can be noted (i) in the amount of dust before the onset of the ISM accretion, with the Schmidt and/or Wyse & Silk laws favouring a higher amount of dust by SNe and (ii) in the age at which the production of dust by accretion in the ISM becomes more important than that by SNe. Depending on the SF law, the time interval in which SNe dominate the total dust budget gets short or long.

Given that the specific expression for the SF law is not of primary importance here (at least choosing among the ones we included in this study), we turn the attention

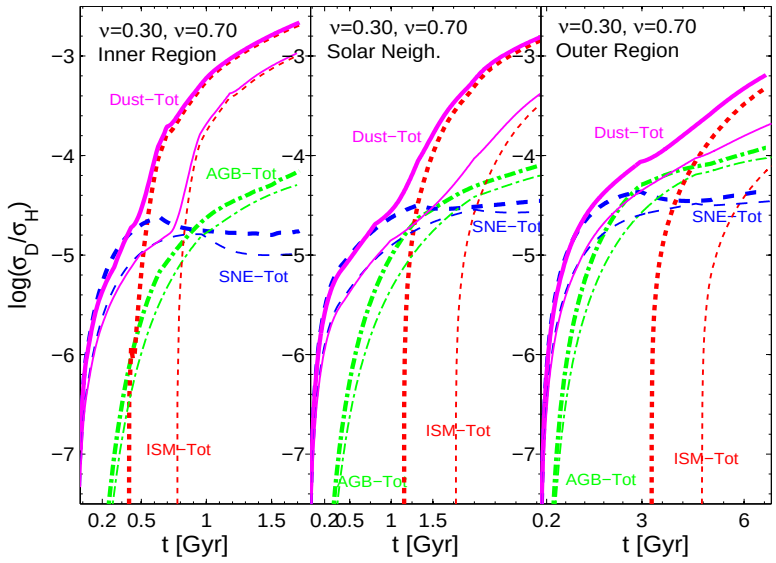

Figure 6.25: Temporal evolution of the contribution to the dust budget during the first Gyrs at varying the coefficient ν of the star formation law, namely the Dopita & Ryder SF law, for *three regions* of the MW. The thin line is $\nu = 0.30$ (low efficiency), while the thick line is for $\nu = 0.70$ (high efficiency). We show: the total amount of dust (from accretion in the ISM plus dust ejected by SNe and AGB stars - continuous line); the contribution by accretion of dust grain in the ISM (dotted line); the total contribution by SNe (dashed line); the contribution by AGB stars (dot-dashed line). **Left panel**: the results for an inner ring of the MW. **Central panel**: the same as in the left panel but for the Solar Ring. **Right panel**: the same as in the left panel but for an outer ring of the MW.

to the efficiency of SF represented by the parameter ν. In Fig. 6.25 we show the contribution to the dust budget in the usual three significant rings of the MW at varying ν from $\nu = 0.30$ to $\nu = 0.70$. As expected lower values of ν imply a smaller rate of SNe and number of AGB stars, therefore a delay in the ISM dust accretion process because there are less seeds/metals injected by stars into the ISM from the stars, and finally a lower total production of dust. As expected, varying the SF parameters affects the system in the early phases of the evolution when the SF is strong. This can be noticed once comparing thin and thick lines in Fig. 6.25.

Does the efficiency ν affect also the dust budget at the present epoch? In Fig. 6.26 we show the evolution of the same three regions of Fig. 6.25 up to the present age of the MW. As we can see, in the inner regions and the solar vicinity, even if there is a significant difference in the past, at the present time the difference gets negligible, whereas in the outer regions the difference in the dust budgets (both total and partial ones) remains remarkable. This is an effect of the adopted SF laws that are all scaled to the current star formation at the solar ring and for this reason tend to ultimately produce the same result as the evolution proceeds. However, we expect that if the SF law is not tied up to normalization or scaling factor, the adoption of different SF

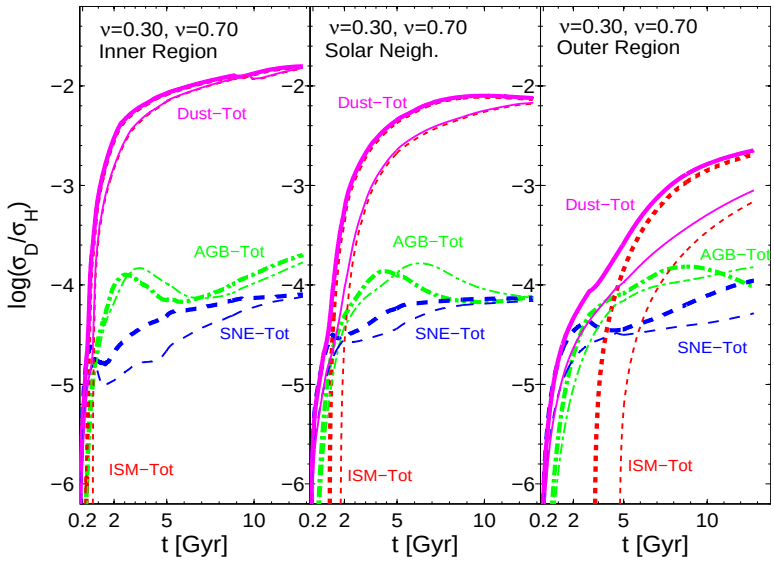

[h]

Figure 6.26: Temporal evolution of the contribution to the dust budget up to the present age at varying the coefficient ν of the star formation law from 0.30 to 0.70. The meaning of the symbols is the same as in Fig. 6.25. **Left panel**: the results for an inner ring of the MW. **Central panel**: the same as in the left panel but for the Solar Ring. **Right panel**: the same as in the left panel but for an outer MW ring.

laws would have a strong impact on the whole evolution. The difference in the outer regions is explained by the long delay in onset of the ISM dust accretion process in the case of low efficiencies ν (very low star forming environment): when eventually the ISM accretion process becomes important, there is not enough time to reach the dust budget produced in the high ν case. This behaviour is also strengthened by the inward radial flows that remove gas from the outermost regions.

6.11.4 The effects of different models for dust accretion in the ISM

In this study we consider two models of dust accretion in the ISM (see Sects. 6.4.1, 6.4.2 and 6.5 for details): model $\mathcal{A}$ based on Dwek (1998) where accretion is simply included with a general timescale depending on the destruction timescale. Indeed, the accretion timescale is half of the destruction timescale, and the same value is used for all the elements (Dwek 1998; Calura et al. 2008). Model $\mathcal{B}$ based on Zhukovska et al. (2008) in which a different timescale for each element is adopted and the evolution of the dust abundances for a number of elements, supposedly contained in a several species of dust grains, is followed. Furthermore, there is no *a priori* connection between the destruction and accretion timescales.

In Fig. 6.27, we show the evolution of the dust budget for the two accretion models. The amounts of dust produced by SNe and AGB stars and all the other

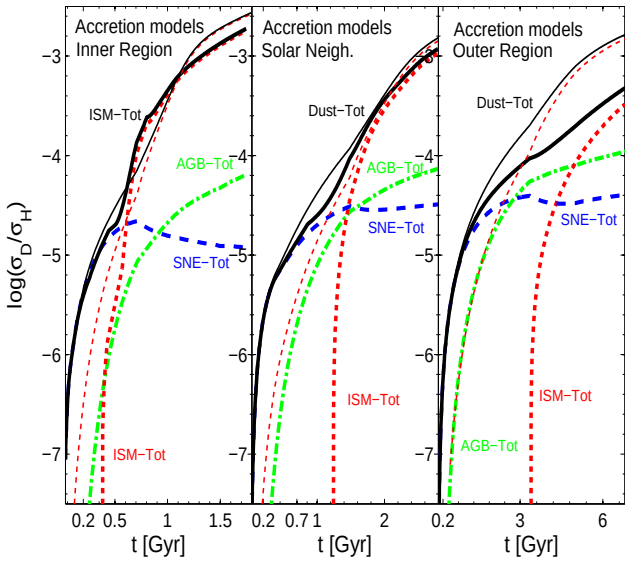

Figure 6.27: Temporal evolution of the dust production during the early phases of the MW evolution at varying the accretion model used to describe dust formation in the ISM. Three regions have been considered as usual: an inner one (left panel), the Solar Ring (middle panel), and an outer region (right panel). Thick lines represent model $\mathcal{A}$ based upon Dwek (1998) and Calura et al. (2008), whereas thin lines represent model $\mathcal{B}$ based upon Zhukovska et al. (2008). For AGB (dot-dashed line) and SNe (dashed line) we only show one line as the contribution is fixed. We show: the total amount of dust grains in the ISM (continuous lines) and the total amount of accreted dust in the ISM (dotted lines). **Left panel**: The results for an inner region. **Central panel**: The results for the Solar Ring. **Right panel**: The results for an outer region.

parameters are kept fixed. In particular, the description of the dust destruction process is the same in both cases: therefore we can examine the sole effect of accretion. In the very early stages there is no difference: the budget is dominated by SNe. The accretion process however starts to be significant very fast in model $\mathcal{A}$, because it simply depends on the adopted timescale, while in model $\mathcal{B}$ it is more sensitive to the physical conditions of the environment: in general it tends to slow down at decreasing SFR and densities (i.e. passing from the innermost to the outermost regions). Even if there is some difference between model $\mathcal{A}$ and $\mathcal{B}$, the behaviour of the *total* dust budget is similar. This finding means that if we are interested in the total amount of dust produced, we can do it simply choosing a suitable timescale for dust formation. This holds everywhere but the outer regions where for model $\mathcal{A}$ we probably need a longer timescale of dust formation to closely agree with model $\mathcal{B}$. This sounds reasonable because it is likely that the accretion timescale varies with the environment. In any case even the simple model of dust accretion with constant timescale is fully adequate to follow the evolution of the *total* dust budget in the early stages of evolution.

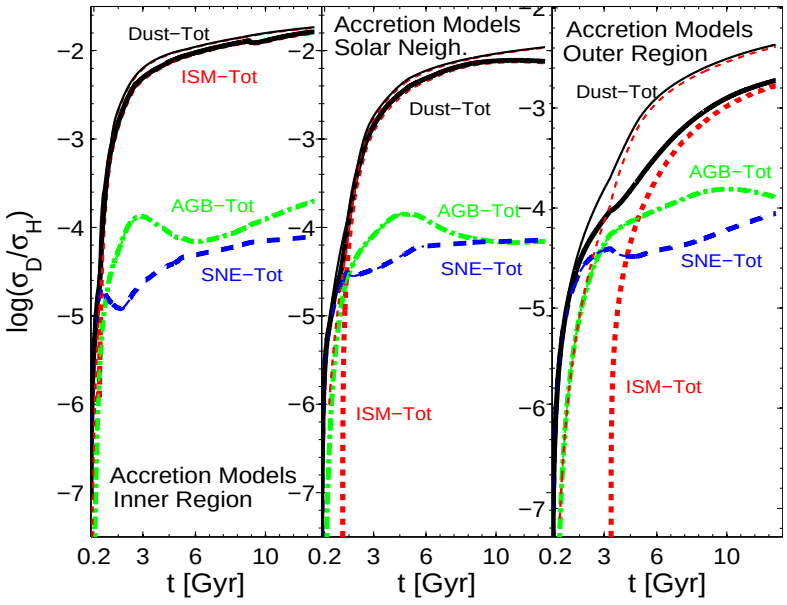

[h]

Figure 6.28: Temporal evolution of the dust production in the MW up to the present age at varying the accretion model used to describe dust formation in the ISM. **Left panel**: The results for the inner ring. **Central panel**: The same but for the Solar Neighborhood. **Right panel**: The same but for the outer ring.

In Fig. 6.28 we extend the evolution up to the present time: in the inner regions and solar vicinity of the MW the differences between the two models are quite small, whereas as expected they are large in the external regions of the disk. In brief, in model $\mathcal{A}$ the accretion in the ISM starts very early independently from the environment and consequently it gives rise to a higher dust content compared to model $\mathcal{B}$.

A deeper insight of the differences brought by the models of dust accretion is possible looking at the evolution of the single elements composing the dust. In Fig. 6.29 we show the evolution of some depleted elements up to the present time, namely C, O, Mg, Si and Fe. As expected there is a strong disagreement between the two accretion models in all the regions. In the case of oxygen the difference is striking: model $\mathcal{A}$ with a fixed timescale produces a lot of oxygen in dust. Since there is no description of how the various elements enter the different dust grains, with a fixed timescale the most abundant element is also the most abundant in dust. With a simple model we can not follow, for instance, the different ways in which oxygen is bound in silicates, or iron is bound both in iron-dust and silicates. Of course, only the comparison with the observational depletion factors can highlight the issue. Most likely, model $\mathcal{B}$ taking into account the physical conditions of the medium and following in detail the evolution of typical dust grains should better reproduce the

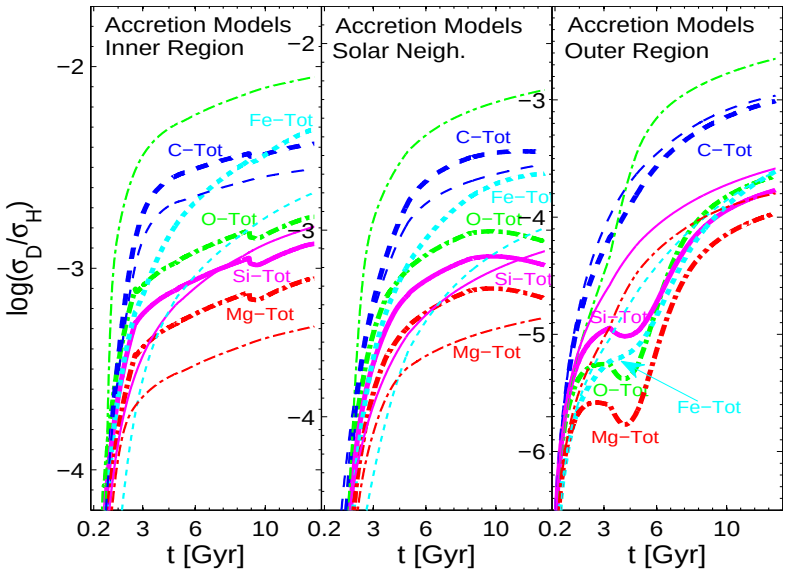

Figure 6.29: Temporal evolution of the dust production in the MW up to the present age at varying the accretion model used to describe dust formation in the ISM. In this plot we put into elements the contribution of individual element to the total dust budget. **Left panel**: The results for an inner ring of the MW. **Central panel**: The same but for the Solar Ring. **Right panel**: The same but for an outer ring of the MW.

observational depletion factors.

6.11.5 A final note on the model parameters

We have just discussed the main parameters entering the problem of the calculation of the dust enrichment of the ISM. However we must underline the following point: classical chemical models are widely used in literature to follow the metal enrichment in galaxies of different morphology. They are already complicated because of the many physical ingredients entering the problem, like the law of SF, the IMF, the stellar yields and the geometrical description of the galaxy. When the dust is added to the problem, the parameter space literally blows up, because in addition to the classical parameters we have to consider also those governing the dust content. The amount of dust of stellar origin injected in the ISM, the way in which the dust content increases/decreases by accretion/destruction and other physical processes, all these concur to extend the list of parameters. All our models includes radial flows of matter and the effects of a galactic bar. All the details and typical parameters are taken from Portinari & Chiosi (1999) and Portinari & Chiosi (2000). Radial flows and bar have been taken into account to better reproduce a wide number of properties of the MW disk, in particular to simultaneously reproduce the radial gradients and the peak of gas observed around 4 kpc. The main motivation for including the radial flows and

the bar is therefore the consistency between theory and observation as far as the depletion factors, radial/local abundances and gas masses are concerned. However, the bar influences the innermost properties of the MW and it is of no interest in this work. Again, the influence of the radial flows of matter mainly applies to the radial properties of the disk. If limited to the Solar Ring, their effect could be mimicked with a slightly different choice of the parameters. Concerning the radial flows, it must be finally observed that in principle the pattern of velocities of gas and dust could be different. For the sake of simplicity, we assume here that gas and dust are moving with the same velocities. Thanks to this gas and dust should have similar radial behaviour.

6.12 Models and observations

The final step of our study is to compare the theoretical results with the data in the Solar Vicinity, thus ultimately validating the model we have built up to describe the dust enrichment of the ISM. As we already discussed, the model has many parameters, which together with the many observational data to match would make the search of best-fit solution a huge task to be accomplished. However, pursuing this strategy would not lead us to get a deeper physical insight of the dust formation in the MW Disk and Solar Vicinity in particular. Therefore, instead of looking for the absolute best-fit model, we are more interested in the model response to thoughtful choices of the parameters and in the comparison of model results with data on element depletion, local abundances. The following observational data for the MW are taken in consideration:

(1) The depletion of the elements in the local ISM (see Sect. 6.11) is the main check for a dust accretion model. This one to be physically consistent must reproduce the observational depletion of many elements. Obviously the depletion is line-of-sight dependent and we can only estimate the range of plausible values (See Fig. 6.11.1).

(2) The local evolution of the elemental abundances in the Solar Vicinity. This is observationally indicated by many diagnostic planes such as [El/H] vs. [Fe/H] and [El/Fe] vs. [Fe/H] for some elements that are also involved in the dust formation process, derived from large samples of F and G stars. The models need to match those diagnostic planes. This allows us to check that not only the process of dust formation/injection is properly simulated but also that the total enrichment process, as observed in the different generations of stars, is realistically reproduced.

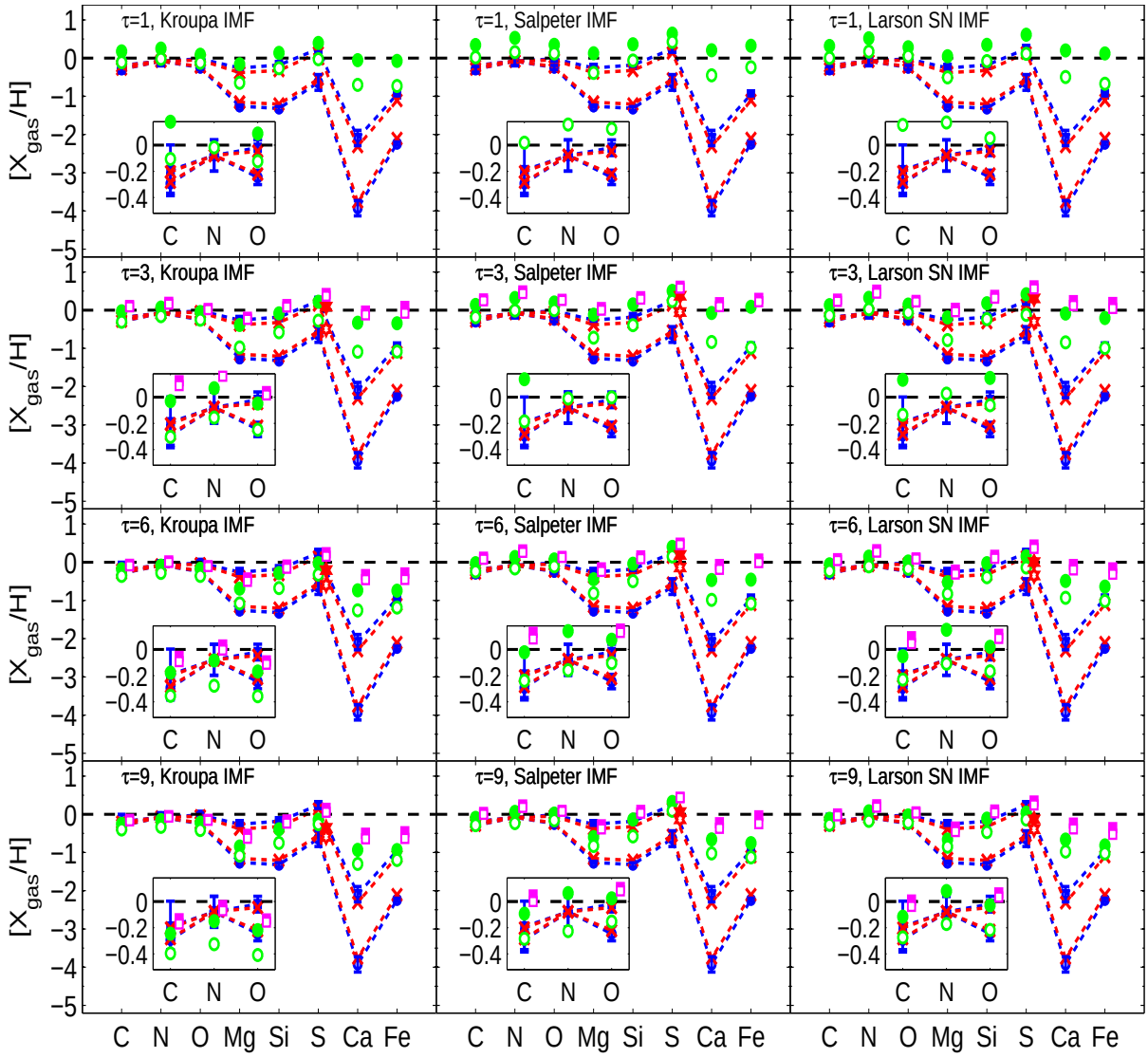

Figure 6.30: Depletion of C, N, O, Mg, Si, S, Ca and Fe in the ISM as observed in the Solar Ring. The observations are compared with the models at varying three important parameters, namely the IMF, the SF efficiency ν, and the mass accretion time scale τ. For the IMF we consider : the recent Kroupa IMF (left panels), the classical Salpeter one (central panels) and the Larson IMF adapted to the Solar Ring (right panels). These IMFs are all described in Sect. 6.3). Four cases are considered for ν, that is $\nu = 0.30$ (empty circles), $\nu = 0.70$ (filled circles), $\nu = 1.10$ (empty squares) and $\nu = 1.50$ (filled squares). Finally, four values are used for the accretion time scale, namely $\tau = 1$, $\tau = 3$, $\tau = 6$ and $\tau = 9$ Gyr , from the top line to the bottom line of each panel.

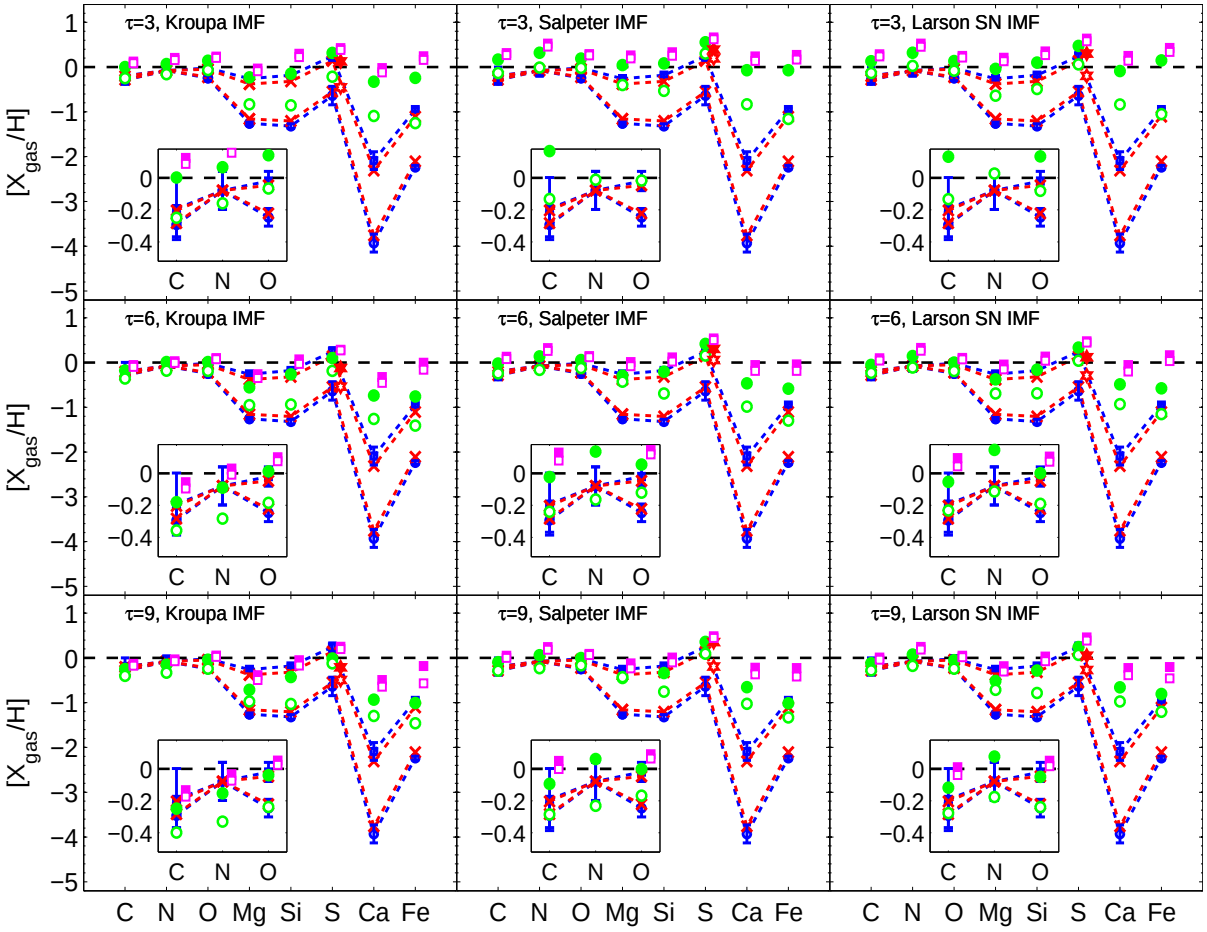

Figure 6.31: Depletion of C, N, O, Mg, Si, S, Ca and Fe in the ISM as observed in the Solar Ring compared with models calculated with enhanced yields of Mg. The observational data is compared with the models at varying of the IMF (three choices), the efficiency of the star formation ν (four choices) and the infall timescale τ (three choices). The meaning of the symbols is the same as in Fig. 6.11.1.

(3) The large scale properties of the MW in the Solar Vicinity like the surface densities of stars and gas, rate of SNe, dust-to-gas ratio, and present day SFR must be reproduced.

(4) The age-metallicity relation in the [Fe/H] vs. Age plane as observed in stars of the Solar Vicinity.

(5) The metallicity of the Sun at the current age and of the proto-Sun about 4.56 Gyr ago.

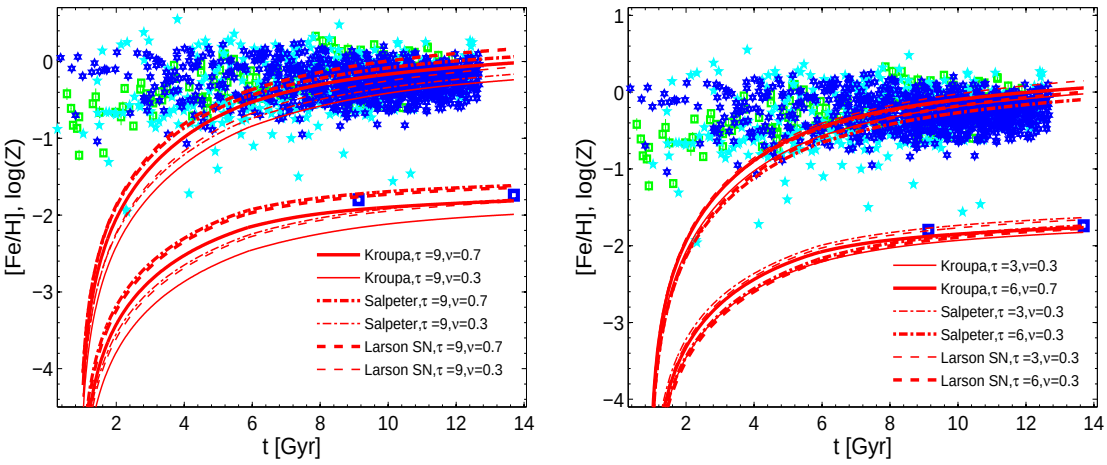

Figure 6.32: Temporal evolution of the metallicity Z and the iron abundance [Fe/H] in the Solar Neighborhood for a wide sample of models. Data are taken from Ibukiyama & Arimoto (2002) (dark stars: photometric [Fe/H]; light stars: spectroscopic [Fe/H]), Ramírez et al. (2007) (squares: sample of thin and thick disk stars). Open squares represent the metallicity of the solar system and of present-day ISM (Gail et al. 2009). **Left panel**: six models are represented, at varying the IMF, the efficiency of the star formation ν and the infall timescale between the values $\tau = 3$ and $\tau = 6$ Gyr. **Right panel**: six models are shown at varying the IMF and the efficiency ν between 0.3 and 0.7 with a fixed infall timescale $\tau = 9$ Gyr.

The reference model is always $\mathcal{GDAABBCBBB}$ according to the parameter list contained in Tab. 6.3 and it includes the radial flows and the bar. The main parameters we are going to play with are the star formation efficiency ν, the infall timescale τ and the IMF. For this latter we consider those by Kroupa, Larson (however adapted to the Solar Vicinity in the high mass tail as discussed in Sect. 6.3) and by Salpeter (usually taken as the reference case for comparison). As already listed in Tab. 1.2, we limit ourselves to the IMFs that do not predict a high number of SNe. IMFs of this type are perhaps more suited to other dust-rich environments, like starburst galaxies or ellipticals (Valiante et al. 2009; Gall et al. 2011a; Gall et al. 2011b; Pipino et al. 2011). The MW disk and the Solar Vicinity in particular seem to require IMFs somewhat poor in massive stars (Dwek 1998; Calura et al. 2008; Zhukovska et al. 2008).

Four infall timescales are considered, that is $\tau = 1$, $\tau = 3$, $\tau = 6$ and $\tau = 9$, from the shortest to the longest, and four values of the star formation efficiency, $\nu = 0.3$, $\nu = 0.7$, $\nu = 1.1$ and $\nu = 1.5$, from the lowest to the highest efficiencies.

The results of these models are presented in the various panels of Fig. 6.30. In general, moving from the upper right to the bottom left corner of the figure, the depletion of the elements gets easier to obtain. We find that: (i) in the case with the Kroupa IMF the observational range of abundances is easily reproduced over ample ranges for the remaining two parameters (ν and τ); (ii) models with the other two IMFs lead good results only if the infall timescale τ and the efficiency ν are properly chosen. About the depletion of the individual elements we note what follows:

Carbon: carbon depletion is simulated assuming that the fraction of carbon hidden in the CO molecules amounts to 0.3. This parameter plays a key role as shown in Fig. 6.13. At varying ξ_{CO} it is possible to allow for less or more dust embedded in C grains, whose accretion depends on the C atoms free to accrete. Carbon depletion is, in any case, well reproduced for the most common sets of the parameters.

Nitrogen: to reproduce the small depletion of nitrogen we find that the simple choice of the longest timescale between the oxygen and carbon, and the use of a mean nitrogen dust grain were not enough to keep low the amount of nitrogen condensed into dust. To this aim, we introduce a multiplicative factor N_X for the accretion time scale $\tau^{gr}_{N,N}$ that enters Eq. 6.5.25 and tune it so that the low observational depletion is reproduced. The results shown in Figs. 6.30 and 6.31 include the scaling factor N_X. We get that $N_X \gtrsim 10$ is required to fetch the small accretion of nitrogen.

Magnesium and Silicon: magnesium is embedded into dust thank to the presence of olivines/pyroxenes and in our best simulations it is found to be easily very depleted. The preference goes toward the maximum allowed depletion rather than the minimum one. The opposite happens for silicon which is more often found close to the minimum depletion limit (see Fig. 6.30). This common behavior for Mg and Si can be explained with the under-production of Mg characterizing the SNe yields by Portinari et al. (1998) that are ultimately based on Woosley & Weaver (1995): This is a long known problem (Timmes et al. 1995; François et al. 2004) that becomes crucial in our case, because Mg is one of the possible key elements driving the accretion process of the silicates. If the amount of Mg atoms available to form dust is under-abundant, this will set up an upper limit to the amount of olivines/pyroxenes that can be formed. In this study, first we calculate models with the original yields by Portinari et al. (1998)[1] (filled and empty circles and squares in Fig. 6.30). This

[1]The latest version of the yields is used in which the under-abundance of Mg is partially corrected (Portinari, 2011 private communication).

Table 6.6: Comparison of the properties of the MW in the Solar Ring with model results[1] and with the Zhukovska et al. (2008) model from which the observational data is taken:

Observable	Observed	ZGT08[2]	This work	Reference
Total surface density $\sigma(r_\odot, t_G)$ $\left[\mathrm{M_\odot pc^{-2}}\right]$	50 - 62	56	52	Holmberg & Flynn (2004)
ISM surface density $\sigma_{\mathcal{M}}(r_\odot, t_G)$ $\left[\mathrm{M_\odot pc^{-2}}\right]$	7 - 13	9.7	10 - 19.5	Dickey (1993)
	~ 8	9.7	10 - 19.5	Dame (1993)
	13 - 14	9.7	10 - 19.5	Olling & Merrifield (2001)
Gas fraction $\sigma_{\mathcal{M}}(r_\odot, t_G)/\sigma(r_\odot, t_G)$	0.05 - 0.2	0.17	0.2 - 0.39	
Surface density of visible stars $\sigma_*(r_\odot, t_G)$ $\left[\mathrm{M_\odot pc^{-2}}\right]$	30 - 40	38.6	23 - 35	Gilmore et al. (1989)
Surface density of stellar remnants $\left[\mathrm{M_\odot pc^{-2}}\right]$	2 - 4	7.7	6 - 10	Mera et al. (1998)
Star Formation Rate $\left[\mathrm{M_\odot pc^{-2} Gyr^{-1}}\right]$	3.5 - 5	3.1	1.6 - 4	Rana (1991)
SNe II rate $\left[\mathrm{pc^{-2} Gyr^{-1}}\right]$	0.009-0.0326	0.016	0.01 - 0.04	Tammann et al. (1994)
SNe Ia rate $\left[\mathrm{pc^{-2} Gyr^{-1}}\right]$	0.0015-0.0109	0.0024	0.0035 - 0.0078	Tammann et al. (1994)
Infall Rate $\left[\mathrm{M_\odot pc^{-2} Gyr^{-1}}\right]$	0.5 - 5	1.45	0.25 - 1.80	Braun & Thilker (2004)

[1]The range of values for the entries of column (4) refers to the models discussed in this section, for the case with no correction to Mg abundance. Of all the models shown in Fig. 6.30, we select only the twelve models presented in Fig. 6.32. [2]Zhukovska et al. (2008).

choice leads to a dust mixture where Mg (already under-abundant) is usually more depleted than Si. The case is well illustrated in Fig. 6.30. According to Zhukovska et al. (2008), the yields of Mg based on Woosley & Weaver (1995) could be suited to reproduce the Milky Way once scaled by a factor of 2-3 in order to obtain Mg/Si/Fe ratios in agreement with the observational ones for the MW, thus leading to a dust mixture closer to reality. Keeping in mind this suggestion, we calculate the same models of Fig. 6.30 slightly modifying the yields of Mg for Type II SNe, in practice changing the tabulations of Portinari et al. (1998) according to the suggestion by Zhukovska et al. (2008). These new calculations allow us to test the model response to variations of the Mg yields. The results are shown in Fig. 6.31 where we note that the agreement with the observational data is better for all the IMFs, in particular with the Kroupa IMF the results are very good. Furthermore, the whole range of observational depletions is now better covered by varying the star formation efficiency than with the original yields of Mg: changing ν from 0.3 to 0.7 all the range of observational values is obtained. However, as in the previous case of Fig. 6.30, the highest star formation rates enrich too much the ISM in metals and the process of dust formation is hardly able to deplete the ISM. The models clarify that the process of dust formation *crucially* depends on the the amounts of metals injected by the stars via mass loss and/or SNe. They also make clear that the set of abundances at the base of the theoretical models for metal enrichment and dust production of the ISM must be strictly identical, otherwise there would be no consistency between the two descriptions (consistency is of course always secured in reality).

Iron: in normal circumstances iron is highly depleted. In most of the models in Fig. 6.30 the best we can obtain at varying the parameters is to reach the upper limit of the observational depletion range, i.e. $-2 \leq [\mathrm{Fe_{gas}}/H] \leq -1$. Even if two possible processes for the formation of dust (iron dust and silicates) are included, the mechanism of iron formation in cold regions of our models is not able to reach such lower values. Probably a more complex model, for instance with a spectrum of MCs with different lifetimes and/or some processes of accretion in other parts of the ISM different from MCs, is needed to reach the severe -2 depletion limit. With the modified Mg abundances, the results improve a bit due to the higher amount of silicates and hidden iron, but still we are not able to fully span the interval from -1 to -2.

Calcium: some of the considerations we made for the iron apply to calcium, for which the observed depletion is even more severe than that of iron. For calcium, there is no overlap at all with the observational interval. As described in Sect. 6.5.6, we introduce a multiplicative factor Ca_X in the accretion time scale $\tau^{gr}_{Ca,Ca}$ and try to calibrate it against the observational values. Even using $Ca_X \lesssim 0.05$ it is not possible to describe the strong depletion of Ca. The results presented in Figs. 6.30

and 6.31 are for a small scaling factor ~ 0.1.

Sulfur: sulfur can be very depleted along some lines of sight, much less along other. Since a typical sulfur dust grain is not available to simulate the accretion process, we used a simple prescription for the average accretion with sulfur atoms accreting on themselves (see Sect. 6.5.7 for more details). A multiplicative factor S_X has been introduced to calibrate the timescale τ_S^{gr}, the longest between the timescales of the refractory elements and the accretion of sulfur atoms on themselves. The results displayed in Figs. 6.30 and 6.31 show the sulfur depletion with (filled and empty hexagons) and without (filled and empty circles) the effect of S_X on the accretion time scale τ_S^{gr}. With S_X going from 1 (no correction - circles) to 0.6-0.4 (small correction - hexagons) the theory fairly agrees with observational data.

Oxygen: this element does not participate as a key-element in any accretion process of dust formation. However it takes part to the formation of the silicates and it is an ingredient of the dust yields from stars of different masses. Because of its high abundance, the depletion is small, even if lots of oxygen atoms are contained in olivines/pyroxenes. In Figs. 6.30 and 6.31 we can see that the theoretical predictions well reproduce the observational data, in particular when Mg is corrected for under-abundance in the yields. The agreement simply follows from using the correct Mg/Si ratio.

6.12.1 Abundances and Depletions in the Solar Vicinity

To check the internal consistency of the depletion models, we must secure that the theoretical evolution of the abundances of the various elements in the Solar Neighborhood is able to reproduce the observational data. It would be a point of strong contradiction if the models can reproduce the elemental abundances in the dust, but fail to reproduce the pattern of abundances in the gas and stars. In Fig. 6.32 we show the evolution of the metallicity Z and iron abundance [Fe/H] for a wide selection of models, taking into account more or less the combinations of IMF, ν and τ that best reproduce the depletion measured in the Solar Ring. In such a case, one should discard the models with $\tau = 1$ that hardly fit the data for depletion in the Solar Ring. Most of the remaining models fairly agree with the observational data with the exception of the case with the Kroupa IMF, slow infall ($\tau = 9$), and low SFR ($\nu = 0.3$) that is not able to grow fast enough in metals. In Tab. 6.6 we present the check of the minimum/maximum values obtained in our models vs. the observations in the Solar Ring of various physical quantities of interest. The same simulations presented in Fig. 6.32 are compared with both the results obtained by Zhukovska et al. (2008) and the observational data. The general agreement between our results and the observations is good and it allows to conclude that we are em-

ploying a correct modelling of the Solar Ring. Once that the more general quantities, like the mass of stars, gas, the SN rates and the total surface mass are satisfactorily reproduced we can proceed to examine the evolution of the abundances of the single elements in the Solar Ring and how they match up with the local data.
In the panels of Fig. 6.33 we show the time evolution in the Solar Neighborhood of the abundances of six elements heavily involved in dust formation, namely C, O, Mg, Si, S and Ca, in the diagnostic planes [A/Fe] vs. [Fe/H]. The observational data refers to F and G stars (see Fig. 6.33 for more details on the data and associated legend). Twelve models are displayed at varying the IMF (Larson Solar Ring, Salpeter and Kroupa), efficiency of star formation ($\nu = 0.3$ and 0.7), and the infall timescale τ (3, 6 and 9 Gyr). Not all the cases are shown for $\tau = 3$ and $\tau = 6$ but only the most interesting ones as far as the degree of depletion is concerned (see Figs. 6.30 and 6.31). In general, the agreement is good for $\tau = 3$ and $\tau = 6$, while for $\tau = 9$, during the first 2 Gyr (in practice until [Fe/H] ~ -1.5) the enrichment in metals is too slow with respect to the observations. The only exception is carbon which always agrees with the observations. It must be pointed out that we are using infall models with a single timescale. This simplified picture leads to models that in the [A/Fe] vs. [Fe/H] planes cannot reach regions of very low or very high [Fe/H]. In reality, during the lifetime of the MW different time scales could be involved in the evolution of the describe the Solar Neighborhood, e.g. a fast early enrichment followed by a much slower one. Double infall models (Chiosi 1980; Chiappini et al. 1997) or more complicated scenarios are however beyond the aims of this study. Finally, it is worth noticing: (i) the under-abundance of Mg in the top right panel; (ii) the marginal agreement of the models with sulfur evolution.

In Fig. 6.34 we show the evolution of the Mg abundance in the Solar Ring once corrected for the under-abundance problem. The same models already presented in Fig. 6.33 are shown, but for the correction of the Magnesium abundance. With this correction not only we have a better pattern of depletions (See Fig. 6.31), but also a better reproduction of the local data.

To enforce the argument we examine the evolution of the most important elements involved in the dust formation process looking at the [A/Fe] vs. [Fe/H] diagrams relative to the Solar Ring. The most striking points of disagreement with the observational data are the under-abundance of Mg and the evolution of Sulphur. For the sake of comparison, we also show the models by Zhukovska et al. (2008), calculated after revising the yields by Woosley & Weaver (1995) and Nomoto et al. (2006). In both cases the yields of Sulphur do not lead to a good fit of the observations. The yields by Nomoto et al. (2006) give indeed the worst model. Our yields produce similar results in the sense that they tend to keep the abundance of Sulphur too high. Fortunately, this has no effect on the overall production of dust as Sulphur drives its

own accretion efficiency (See Sect. 6.5.7) and does not affect other channels of dust production. Apart from these minor uncertainties, the observational data and theoretical abundances fairly agree and consequently dust formation stands on a realistic description of the evolution of the elemental abundances in the Solar Ring.

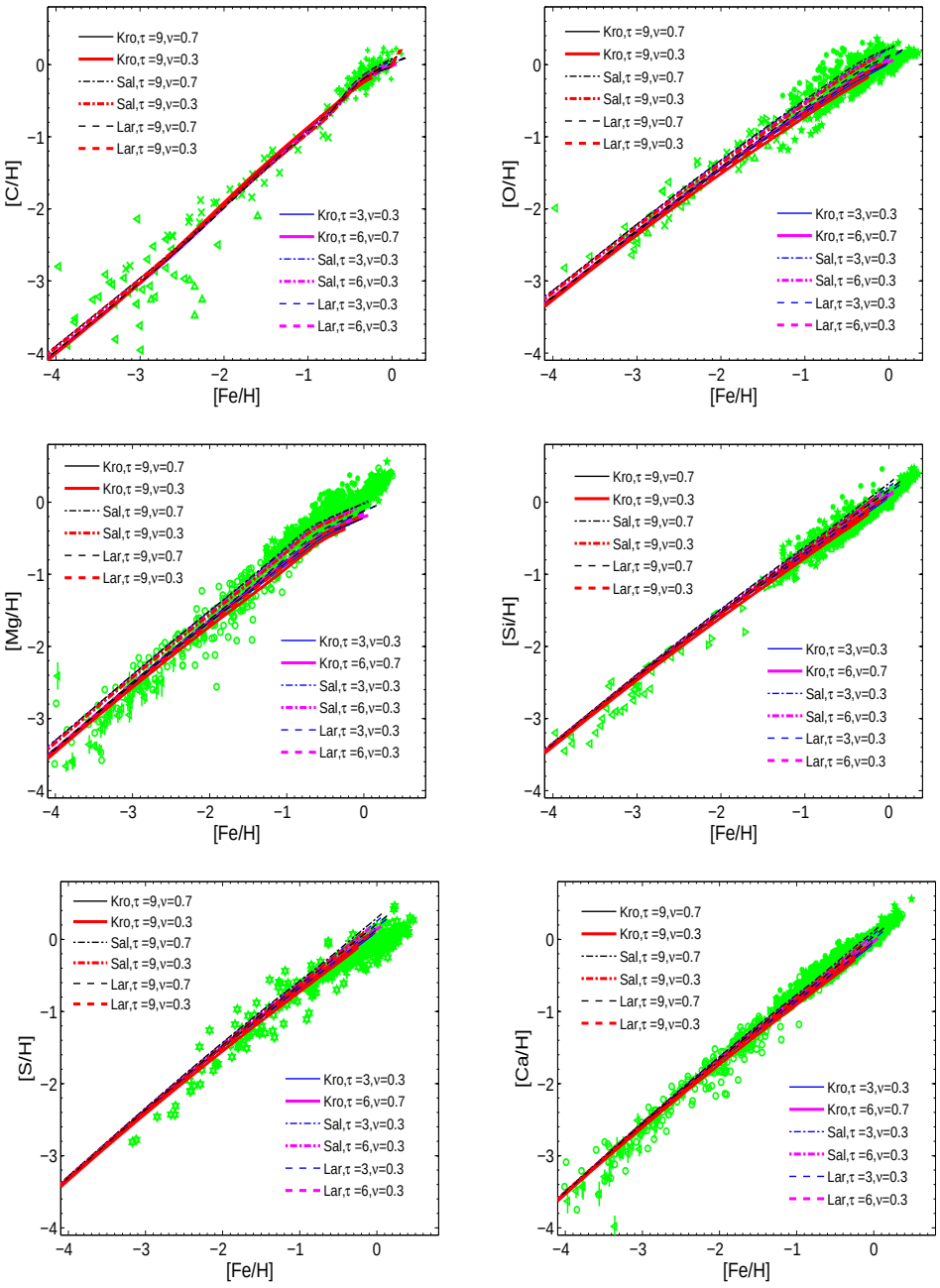

Figure 6.33: Evolution of the elemental abundances in the Solar Ring as measured by a sample of F and G stars vs the simulations. The evolution of [A/H] vs. [Fe/H] is represented for C, O, Mg, Si, S and Ca. Data from: **O** from Chen et al. (2000) , Meléndez & Barbuy (2002), Reddy et al. (2003), Gratton et al. (2003), Akerman et al. (2004), Cayrel et al. (2004), Jonsell et al. (2005), Soubiran & Girard (2005); **C** from Meléndez & Barbuy (2002), Reddy et al. (2003), Akerman et al. (2004), Cayrel et al. (2004); **Mg** from Chen et al. (2000), Gratton et al. (2003), Reddy et al. (2003), Soubiran & Girard (2005) and Venn et al. (2004) (circle); **Si** from Chen et al. (2000), Gratton et al. (2003), Reddy et al. (2003), Cayrel et al. (2004), Jonsell et al. (2005), Soubiran & Girard (2005); **S** from Reddy et al. (2003) and Caffau et al. (2005) (six-point star) and, finally, **Ca** from Chen et al. (2000), Gratton et al. (2003), Reddy et al. (2003), Venn et al. (2004), Cayrel et al. (2004), Soubiran & Girard (2005), Jonsell et al. (2005). Twelve models are superposed to the data, at varying the IMF (Kroupa, Salpeter and Larson adapted to the Solar Ring), the efficiency of the star formation ν (two values: $\nu = 0.3$ and $\nu = 0.7$) and the infall timescale τ (three values: $\tau = 3$, $\tau = 6$ and $\tau = 9$ Gyr). Only the most interesting combinations are shown (Figs. 6.30 and 6.31).

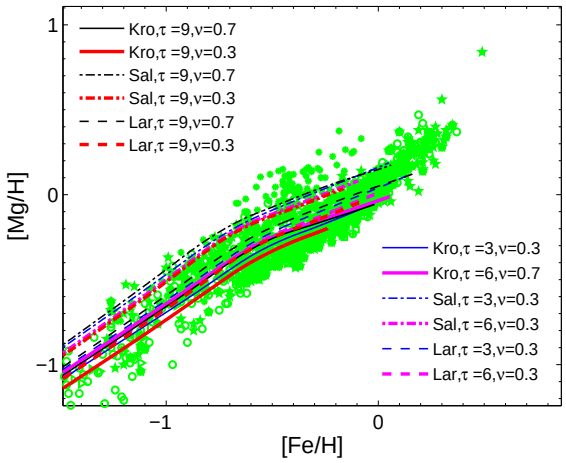

Figure 6.34: Evolution of the Mg abundance in the Solar Neighborhood as measured in a sample of F and G stars. The yields have been slightly corrected for the Mg under-abundance. This corrected abundance is the same as in Fig. 6.31.

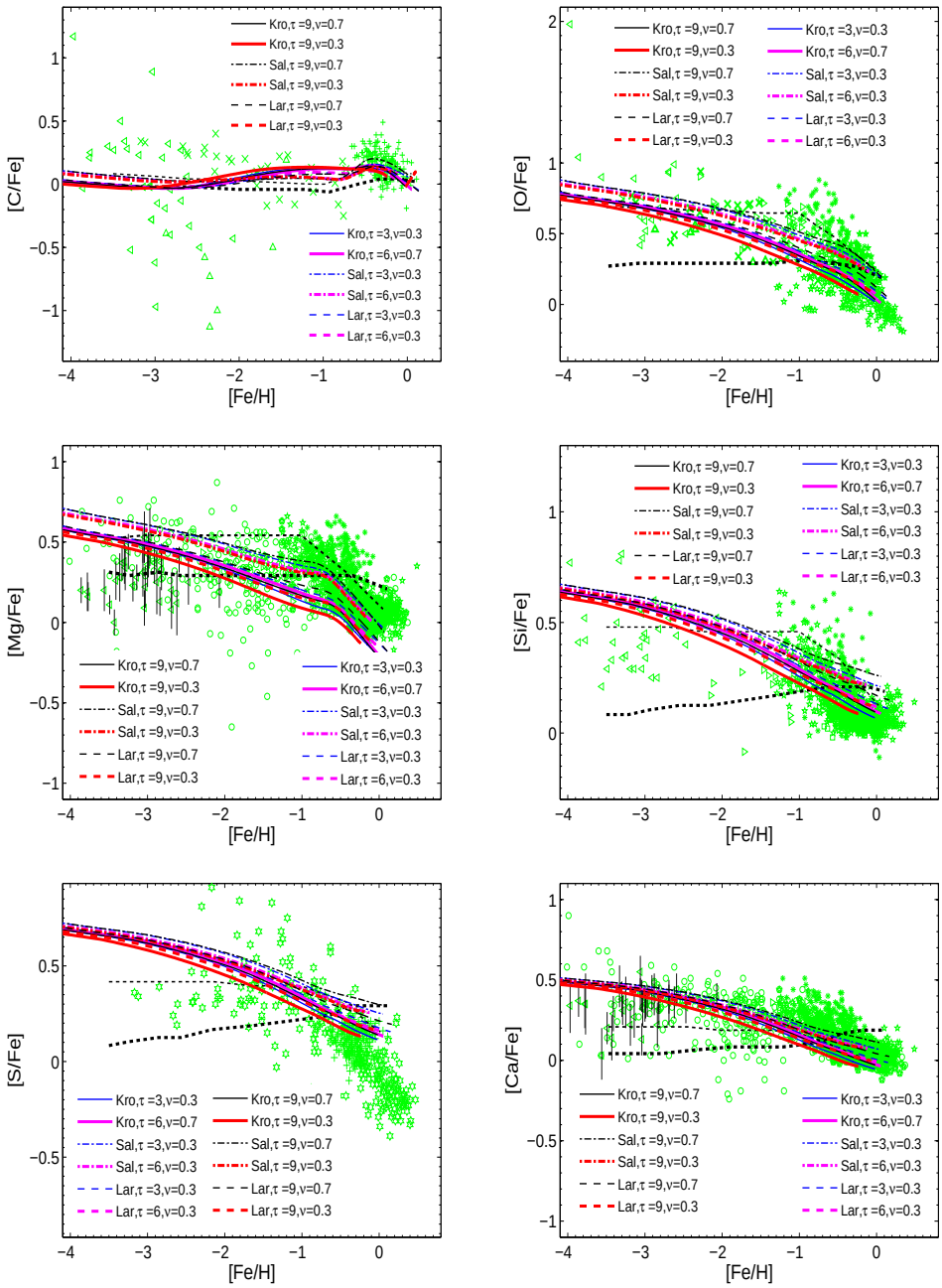

Figure 6.35: Evolution of the elemental abundances in the Solar Neighborhood as measured in a sample of F and G stars. The evolution of [A/Fe] vs. [Fe/H] is shown for six elements of interest, that is C, O, Mg, Si, S and Ca. For the sake of comparison we plot the results by Zhukovska et al. (2008) for the SN yields by Woosley & Weaver (1995) where Mg and Fe have been corrected to get a better agreement with the observations (the thick dotted line), and the yields by Nomoto et al. (2006), the thin dotted line. The meaning of the symbols for the observational data is the same as in Fig. 6.33.

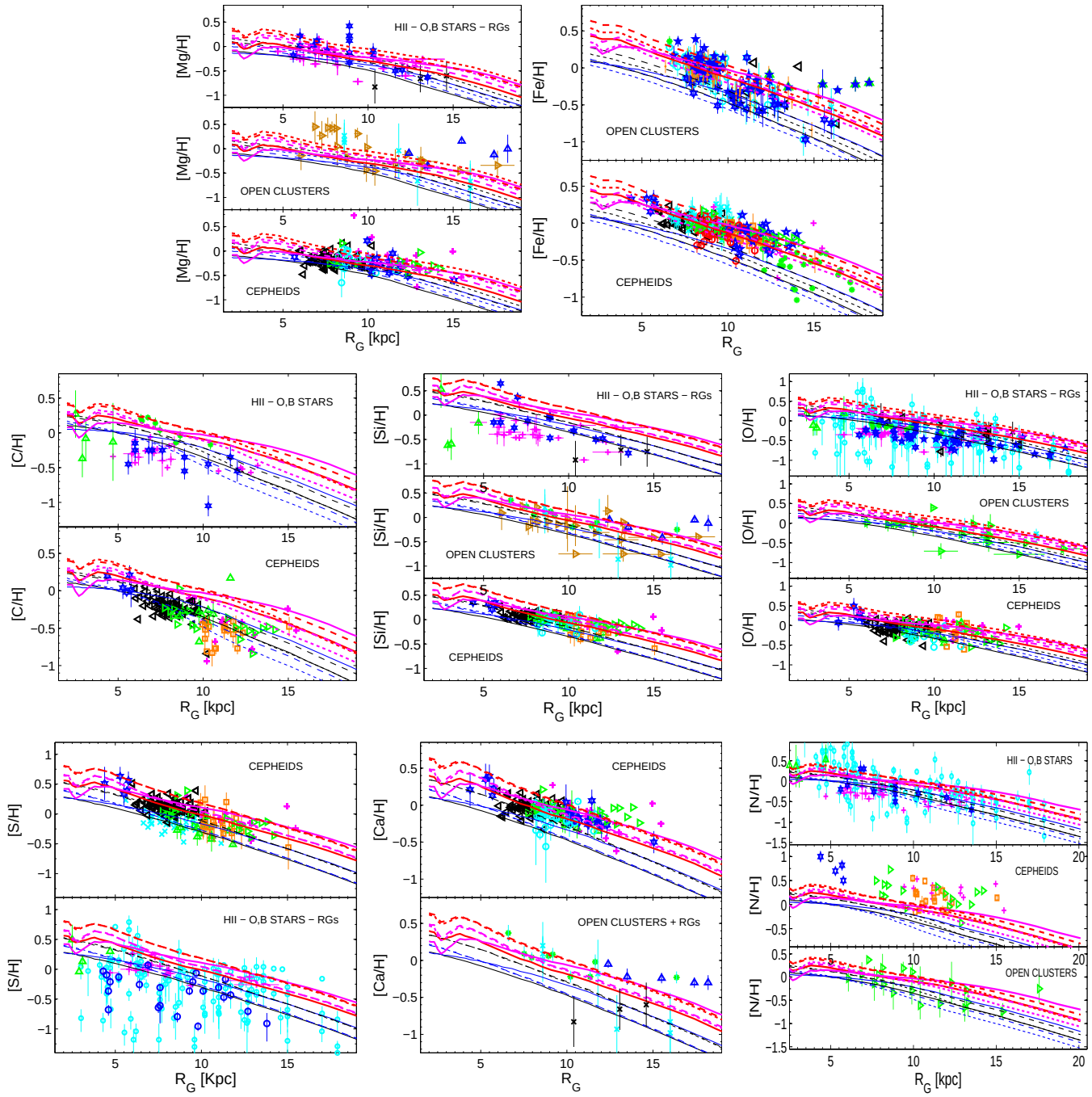

Figure 6.36: Evolution of the Galactic abundances of [Mg/H], [Fe/H], [C/H], [Si/H], [O/H], [S/H], [Ca/H] and [N/H] as a function of the galacto-centric distance for different types of abundance indicators. In all the diagrams we present the evolution of the radial gradient from the age at which the Sun was formed (thin lines) to the current age (thick lines). The elemental abundances are measured in the following sources: O and B stars, Field Red Giants (RGs), HII regions, open clusters and Cepheid variables. The sources have been divided into two or three groups/panels, depending on the available ones for that element, in such a way to examine the gradients from different sources. The following models are considered: Kroupa IMF, $\tau = 3$ and $\nu = 0.3$ (continuous thin black and thick red lines); Kroupa IMF, $\tau = 6$ and $\nu = 0.7$ (continuous thin blue and thick magenta lines); Salpeter IMF, $\tau = 3$ and $\nu = 0.3$ (dotted thin black and thick red lines); Salpeter IMF, $\tau = 6$ and $\nu = 0.3$ (dotted thin blue and thick magenta lines); Larson Solar Ring IMF, $\tau = 3$ and $\nu = 0.3$ (dashed thin black and thick red lines), and finally Larson Solar Ring IMF, $\tau = 6$ and $\nu = 0.3$ (dashed thin blue and thick magenta lines).

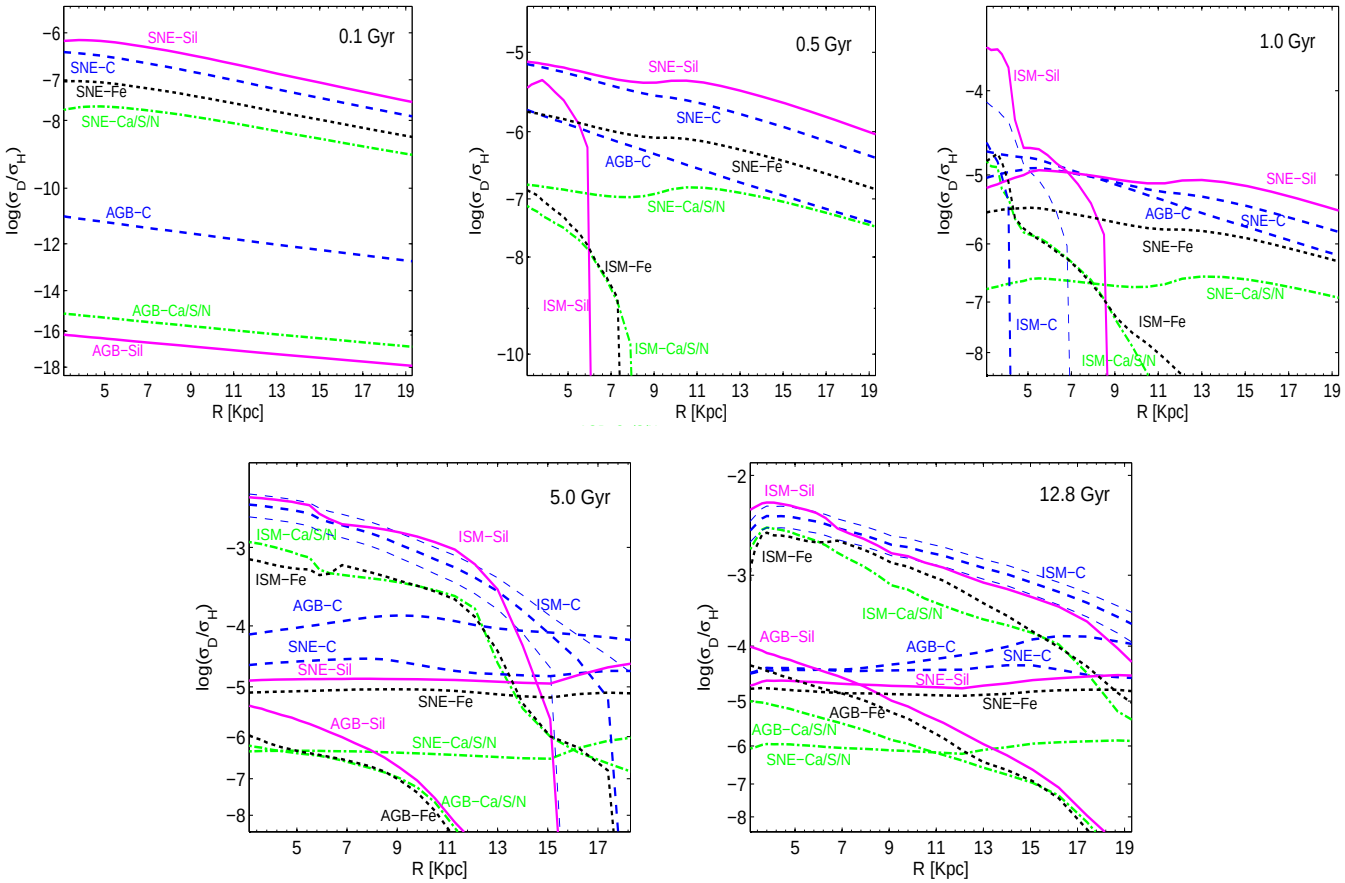

Figure 6.37: Temporal evolution of the radial contribution to the abundance of dust by the four types of grain among which we distributed the single elements (that is silicates, carbonaceous grains, iron dust grains and generic grains embedding Ca, N or S) and the three sources of dust, namely SNe, AGB stars and accretion in the ISM. All the contributions have been properly corrected for the destruction of dust. Five ages are represented from the early stages to the current time. **Upper left panel**: the radial contribution of the four types of dust grains to the total dust budget at 0.1 Gyr. We show: silicates (continuous lines), carbonaceous grains (dashed lines), iron dust (dotted lines) and, finally, generic grains containing S, Ca and N (dot-dashed lines). For each group we distinguish the net contributions from the ISM accretion, AGB and SNe, that is: ISM-C, AGB-C and SNe-C for carbonaceous grains, ISM-Sil, AGB-Sil and SNe-Sil for silicates, ISM-Fe, AGB-Fe and SNe-Fe for the iron dust and finally, ISM-Ca/S/N, AGB-Ca/S/N and SNe-Ca/S/N for the other grains. In all cases the abundance of CO is fixed to $\xi_{\rm CO} = 0.30$ taken as the reference value. For the last two ages we also show for the ISM the results for $\xi_{\rm CO} = 0.15$ and $\xi_{\rm CO} = 0.45$. **Upper Central panel**: the same as in the upper left panel but for 0.5 Gyr. **Upper Right panel**: the same as in the upper left panel but for 1.0 Gyr. **Lower Left panel**: the same as in the upper left panel but for 5.0 Gyr. **Lower Right panel**: the same as in the upper left panel but for 12.8 Gyr. Since the ratio σ_D/σ_H grows at varying age, the scale of the y-axis is continuously shifted according to the value of the plotted data.

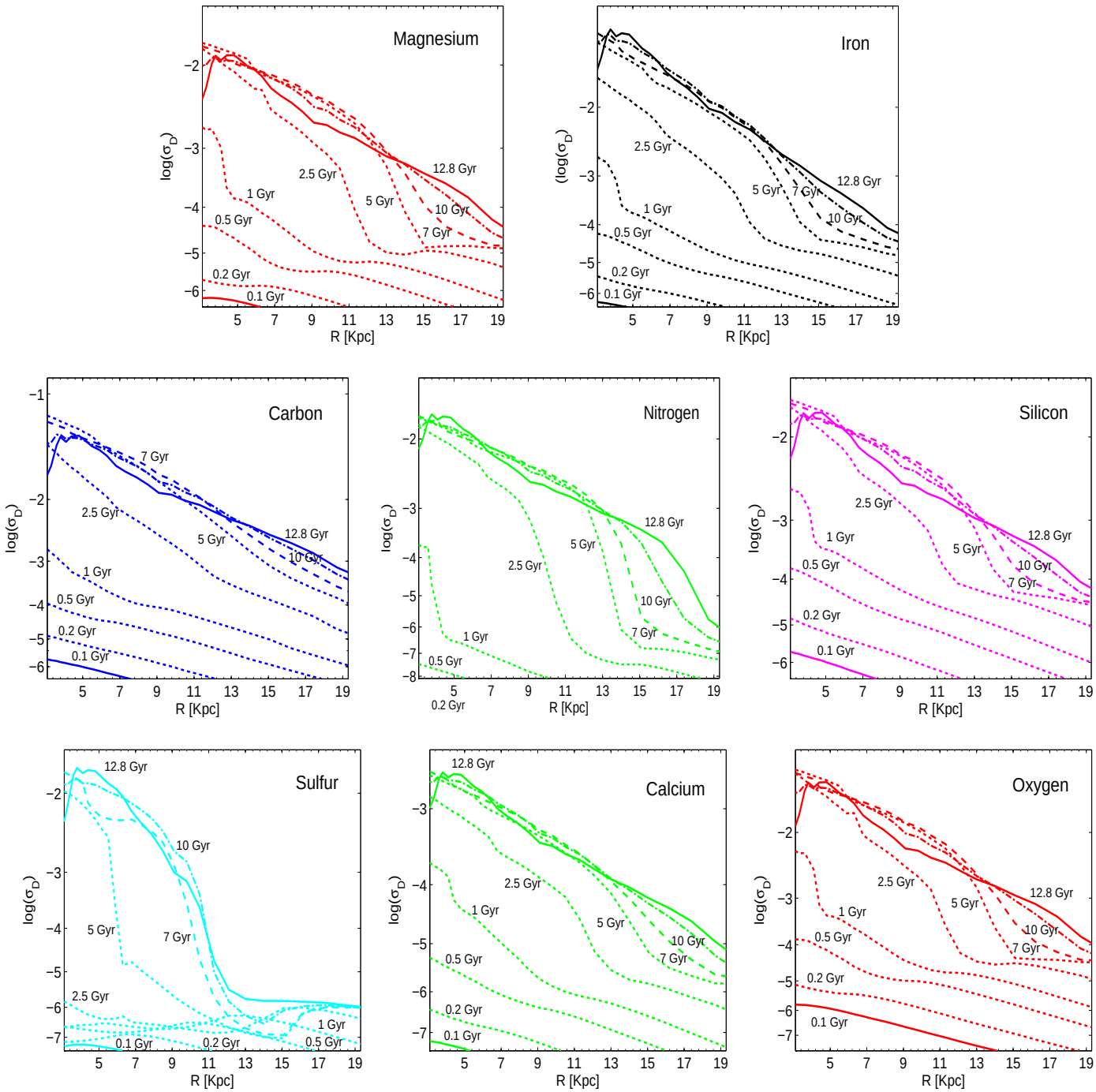

Figure 6.38: Temporal evolution of the logarithmic radial abundance of dust $\sigma_i^D(r_k, t)$, in $[M_\odot pc^{-2}]$, for all the elements belonging to our set and involved into the process of dust formation, that is C, N, O, Mg, Si, S, Ca and Fe. All the contributions have been properly corrected for the dust destruction. Nine ages are represented from the early stages to the current time, that is 0.1, 0.2, 0.5, 1, 2.5, 5, 7, 10 and 12.8 Gyr, assuming that the formation of the MW started when the Universe was ∼0.9 Gyr old (Gail et al. 2009). **Upper panels**: from left to right the time evolution of the radial abundance σ^D for Mg and Fe. **Central panels**: the same as in the upper panels but for C, N and Si, from left to right. **Lower panels**: the same as in the central panels, but for S, Ca and O. Since the abundance σ_i^D changes at varying the age in a different range for each element, the scale of the y-axis is continuously shifted according to the represented range of values.

6.13 Radial gradients in element abundances

Studying the properties of dust in the Solar Ring is by far easier than across the Disk of the MW: indeed the data to our disposal for the Disk are much fewer and of poorer quality than those for the Solar Ring. For instance, we cannot estimate the depletion of elements at different distances from the Solar Ring toward the Galactic Center and/or the outermost regions of the Disk. However, we can compare the radial gradients in element abundances, as indicated by Cepheid stars, Open Clusters, HII regions and O,B stars. In the case of a satisfactory agreement between the observations and theoretical predictions for the element abundances, we may argue with some confidence that the predictions for radial variation of the dust properties are reasonably good. In relation to this see the case of the relative abundances of Mg and Si and how they would affect the formation of silicates in the dust and depletion of these elements.

In the following, we examine the radial variations of the elemental abundances to check if our multi-shells model, in presence of radial flows of gas and inner bar, is able to reproduce in a satisfactory way at least the main radial properties of the MW. As already said we are not looking for the best model in absolute sense but only the a general agreement with observational data so that our predictions for dust formation and evolution stand on solid ground.

[7] **Magnesium**. O and B stars: Gummersbach et al. (1998) (Gu98), Smartt et al. (2001) (Sm01), Daflon & Cunha (2004) (Da04); Field Red Giants: Carney et al. (2005) (Ca05); Open Clusters: Rolleston et al. (2000) (Ro00), Carraro et al. (2004) (Ca04), Carraro et al. (2007) (Ca05), Yong et al. (2005) (Yo05); Cepheid stars: Andrievsky et al. (2002) (An02a), Andrievsky et al. (2002) (An02b), Andrievsky et al. (2002) (An02c), Andrievsky et al. (2002) (An02d), Luck et al. (2003) (Lu03), Kovtyukh et al. (2005) (Ko05), Luck et al. (2006) (Lu06), Yong et al. (2006) (Yo06), Lemasle et al. (2007) (Le07). **Iron**. Open Clusters: Twarog et al. (1997) (Tw97), Carraro et al. (1998) (Ca98), Hou et al. (2002) (Ho02), Chen et al. (2003) (Ch03), Ca04, Yo05, Ca07, Sestito et al. (2008) (Se08), Magrini et al. (2009) (Ma09); Cepheid stars: An02a, An02b, An02c, An02d, Lu03, Ko05, Lu06, Yo06, Le07 and Lemasle et al. (2008) (Le08). **Carbon**. O and B stars (Gu98, Sm01, Da04); HII regions: Esteban et al. (2005) (Es05); Cepheid stars: An02a, An02b, An02c, An02d, Lu03, Ko05 and Andrievsky et al. (2004) (An04). **Silicon**. O and B stars Gu98, Sm01, Da04; Field Red Giants: Ca05; Open Clusters: Ro00, Ca04, Ca07, Yo05, Se08; Cepheid stars: An02a, An02b, An02c, An02d, Lu03, An04, Ko05, Lu06, Yo06, Le07. **Sulfur**. Cepheid stars: An02a, An02b, An02c, An02d, Lu03, An04, Ko05, Lu06; O and B stars: Sm01, Da04; HII regions Martín-Hernández et al. (2002) (Ma02), Rudolph et al. (2007) (Ru07); Open Clusters: Ca04, Ca07, Yo05, Se08; Field Red Giants: Ca05; Cepheid stars: An02a, An02b, An02c, An02d, Lu03, An04, Ko05, Lu06, Yo06, Le07. **Calcium**. Open Clusters: Ca04, Ca07, Yo05, Se08; Field Red Giants: Ca05; Cepheid stars: An02a, An02b, An02c, An02d, Lu03, An04, Ko05, Lu06, Yo06, Le07. **Oxygen**: HII regions Deharveng et al. (2000) (De00), Es05, Ru07; O and B stars: Smartt & Rolleston (1997) (Sm97), Da04, Sm01; Field Red Giants: Ca05; Open Clusters: Ro00, Ca04, Yo05; Cepheid stars: An02a, An02b, An02c, An02d, Lu03, An04, Ko05, Le07. **Nitrogen**: HII regions: Ru07; O and B stars: Gu98, Da04, Sm01; Open Clusters: Ro00; Cepheid stars: An02b, An02c, Lu03, Ko05.

Two important observational constraints must be satisfied and reproduced by the models, namely: (i) the radial distribution of the gas and (ii) the radial gradients in those elements that are involved in the dust formation. In Fig. 6.42, we compare the density profiles for models calculated with different IMF, efficiency of the star formation ν and the infall timescale τ. Twelve models are shown. This sample is taken from the wider grid of models calculated by to reproduce the depletion of the elements observed in the Solar Ring [2]. The twelve models are shown in Fig. 6.42. They are with original stellar yields by Portinari et al. (1998) (no correction to the Mg abundance is applied). Since we have no data for the element depletion as a function of the radial distance, the slight under-abundance of Mg is less of a problem here. Furthermore, selecting the twelve cases, very short infall timescales have been excluded because the models would not reproduce the element depletions observed in the Solar Ring. Finally, since we have no hints on the observational error associated to the mass density profile $\sigma_g(r)$ as a function of the galacto-centric distance, at each distance we apply an error derived from the ratio $\Delta\sigma_g/\sigma_g$ for the Solar Ring, and assumed to remain constant. Indeed, already in the Solar Ring, there is a significant uncertainty in the local gas density, the estimates of which go from 7-13 $M_{\odot}pc^{-2}$ (Dickey 1993), to ~ 8 (Dame 1993) up to 13-14 (Olling & Merrifield 2001).

It is soon evident that while some models fairly agree with the observational data for σ_g, others significantly deviate from it in particular for the innermost regions: models with long infall timescale and low star formation efficiency (such as the model with $\tau = 9$ Gyr and $\nu = 0.3$) do not consume enough gas. In literature the problem is often solved either introducing a suitable radial dependence for τ or changing the IMF in such a way that the low-mass long-lived stars are favored. However, for the purposes of the present study, we prefer to keep both τ and IMF constant with the galacto-centric distance. Finally, it is worth noting the crucial contribution of the bar whose presence nicely reproduces the gas density distribution in the innermost regions, simulating the bump at about 5 kpc.

In Fig. 6.36 we show the gradients across the Galactic Disk in the abundance ratios [Mg/H], [Fe/H], [C/H], [Si/H], [O/H], [S/H], [Ca/H] and [N/H]. All these elements are also involved in dust formation and evolution. For each element we group the observational data according to the source of the abundances, namely O and B

[2]The whole sample contains model for four vτ ($\tau = 1$, $\tau = 3$, $\tau = 6$ and $\tau = 9$ Gyr), three IMFs (Salpeter, Kroupa multi-power law and Larson adapted to the SN), four values of the efficiency of the star formation ν ($\nu = 0.3$, $\nu = 0.7$, $\nu = 1.1$ and $\nu = 1.5$), and two cases for the stellar yields of elements, the original ones by Portinari et al. (1998) and a revised version taking into account a correction for a slight under-abundance in Mg.

stars, field Red Giants (RGs), HII regions, Cepheid variables and open clusters. The references for the observational data are listed in the footnote[7]. Only models with intermediate values of τ ($1 < \tau < 9$) are compared with the data. Since most likely different sources trace the gradients at different galactic ages, we plot the gradients as they were at the time the Sun was born (about 4.5 Gyr ago, the thin blue and black lines) and at the present age (thick red and magenta lines). Most objects under examination should fall into the region spanned by the gradients during this time interval. In general, theoretical predictions and data fairly agree with minor discrepancies that can be, in some cases, attributed to the yields, such as the slight Mg under-abundance and/or C and S over-abundance (Portinari et al. 1998). Other major discrepancies between the theoretical and observational abundance gradients that depend on the type of source under consideration are expected and can be taken to indicate the performance of the models. For instance, following Kovtyukh et al. (2005), in intermediate mass stars the C under-abundance (carbon is deficient at about $[C/H] = -0.4$) and the N over-abundance (nitrogen is enhanced at about $[N/H] = +0.4$) has been predicted by Luck (1978) and Luck & Lambert (1981) and confirmed in studies of Cepheids and non-variable super-giants (Andrievsky et al. 1996; Kovtyukh et al. 1996). This is more or less what we observe when the evolution of theoretical element abundances C and N along the Disk are superposed to the measurements of C and N abundances in Cepheids (intermediate mass stars of 3 to 9 $M_{\odot}$). Finally, comparing theory and data, one should keep in mind that models do not take star dynamics and kinematics into account and the stars always remain in the same region where they are born: the radial flows act only on gas and dust.

6.13.1 Radial gradients in dust

Assessed that the radial gradients, in the gaseous element abundances and total gaseous density, reasonably agree with the observational data, at least for some combinations of the input parameters, we examine the radial formation and evolution of dust in the MW Disk being confident that it is grounded on a realistic evolution of the global abundances in the ISM. In Fig. 6.37 we show for five selected ages, from the early stages to the current time, the time evolution of the radial abundance of four typical grain families, that is silicates, carbonaceous grains, iron grains and generic grains formed with Ca, N and S. We grouped these last three elements into a single group for the sake of simplicity because of their low abundance. The contributions to each one of the four groups have been split among the three sources of dust, that is star-dust from SNe and AGB stars and accretion in the cold regions of the ISM. The amount of dust in all the regions continuously grows following the

enrichment in metals produced by the many generations of stars. In the early stages of the evolution, at 0.1 Gyr, star-dust from SNe is the main source of dust across the whole disk. At 0.5 Gyr the accretion of dust in the ISM starts to be significant in the innermost regions and slowly becomes the dominating source in the whole Disk, earlier for the innermost regions and later for the outermost ones. AGB stars contribute mostly with carbon-rich grains in the early evolution at low metallicity Z and only when a significant metallicity is reached they start enriching the ISM in silicates. It is worth noting here that the evolutionary scheme across the Disk we have just outlined is a consequence of the role played by the star-dust from SNe in the early stages. Reducing the yields of dust by SNe would obviously change the the above results for the early stages.

In Fig. 6.38 we present the evolution with time of the radial dependence of the logarithm of the dust abundance $\sigma_i^D(r_k,t)$ for all the elements in our list taking part to dust formation, namely C, N, O, Mg, Si, S, Ca and Fe. Nine ages are represented from the early stages to the current time. All the elements more or less follow the same evolutionary trend, and eventually reach a typical profile with a bump at 4-5 kpc in agreement with the gas density profile (as expected). It is interesting to note that while for the innermost-central rings of the disk the enrichment in dust already reaches a maximum at about 5 Gyr, for the outermost regions the dust budget keeps growing until the present age. The reason for that can be easily attributed to the delayed contribution by accretion in the ISM occurring in the outer regions with low star formation. In brief, as accretion of dust grains in the ISM gets important only when and if some enrichment in metals has taken place, in the outer regions of low star formation this is inhibited by the low metal content that can be reached over there.

It is interesting to examine not only the abundance evolution of each element in the dust, but also the relative abundance of each element embedded into dust (or the relative fraction of each dust grain family) with respect to the total dust budget. For this reason in Fig. 6.39 we show the evolution of the radial *mass fraction of each element embedded into dust* $\sigma_i^D(r_k,t)/\sigma^D(r_k,t)$, *normalized to the total dust budget*, for some of the elements in our list and/or some families of grains. In particular, we show the fraction of silicates (which means Mg, Si, Fe and O embedded into quartz/pyroxenes/olivines by accretion in the ISM or star-dust) and carbonaceous grains (this latter is nearly coincides with the amount of C, once subtracted the amount of C belonging to the silicon carbide). Let us examine the behaviour of silicates and carbonaceous grains in some detail. At the beginning of the evolution, where only the most massive SNe contribute, the mass of dust in silicates is a bit larger than in carbon based grains. This is in agreement with the recent observations of SN 1987A with the Herschel Space Observatory (Matsuura et al. 2011): the sig-

nificant emission by a population of cold dust grains observed by PACS and SPIRE can be reproduced only with a mixture of both carbonaceous grains and silicates with these latter more abundant than the C-based dust grains. This is indeed what is shown in Fig. 6.37 at the age of 0.1 Gyr, when SNe play the major role. As soon as AGB stars start to contribute (at low/sub-solar metallicities a 5-6 solar masses has a lifetime of the order of 0.1 Gyr) the mixture of SNe and low-Z AGB stars slowly increases the fraction of carbonaceous grains and reduces that of silicates. Indeed, low-Z AGB stars are easily C-star and mainly inject carbon in the ISM. At ages in the range 0.5-1 Gyr, at least in the innermost regions, the formation of dust grains in the cold ISM starts to be a very efficient process and strongly influences the total budget. Our silicates are made by Mg, Si, O and Fe: the timescale for the formation of silicates in the early evolution, when SNe enriched the ISM with all of these elements, is therefore shorter than the one for carbonaceous grains (carbon is also partially locked in the unreactive CO).

Carbon is injected by SNe (plus a significant contribution by low-Z AGB stars), but in any case carbon is less than the sum of all the other refractory elements involved in silicates. Their total number density in the ISM, compared to the one of carbon atoms, favors the formation of silicates during the early evolution. This can be seen in the upper right panel of Fig. 6.37; the fraction of carbon locked up in CO also plays an important role. In the panels of Fig. 6.39 for the carbonaceous grains and silicates, one can note that, as a consequence of the behaviour described above, the fraction of silicates in the innermost regions grows until the age of about 1 Gyr is reached, while the fraction of C-rich dust decreases. Afterwards, as AGB stars join SNe to increase the number density of Carbon atoms in the ISM, the accretion of carbon in cold MCs becomes also efficient, and the silicates/carbonaceous grains ratio slowly decreases again. A different behaviour takes place in the outermost regions: at the beginning there is a ratio similar to the inner regions, but the fraction silicates/carbonaceous grains keeps decreasing because (i) the accretion in the ISM has long timescales and starts late due to the low densities and Z; (ii) the strong contribution of C-based dust, due to the low-Z AGB stars, dominates in a significant window between SNe and start of the ISM accretion. The final result is the high fraction of carbon dust with respect to silicates in the outer region. It is interesting now to compare our results with the evolution of the gradient in Carbon predicted by Zhukovska & Gail (2009). Since in their case SNe are very poor factories of silicates, but significant injectors of Carbon-rich dust, Zhukovska & Gail (2009) adopt for the early evolutionary stages in the inner regions, a mixture almost totally made by Carbon-based dust. In our case, on the contrary, we obtain in the inner Disk that the partition between the two main dust types is more balanced and both play a comparable role. In any case, in the outer regions we find results very close to those

by Zhukovska & Gail (2009). In brief, at the current age we all find that the final gradient in relative mass fraction of carbonaceous grains has a similar positive slop reaching in the outermost region a value as high as 70% of the dust mass embedded in carbonaceous grains.

The behaviour of iron dust has the opposite trend: it starts very flat and at the current time we have a negative gradient, with iron dust significantly contributing to the dust mass in the center of the MW. In the early stages, we have some contribution to the iron budget by SNe (however less than for silicates and carbonaceous grains, see top panels in Fig. 6.37) and because of the low metallicities a negligible contribution by low-Z AGB stars. As time goes on, the sum of the contributions from (i) CCSNe, (ii) accretion in the ISM that for iron dust starts to be significant at t$> 1-2$ Gyr, (iii) AGB stars that reach solar metallicities in the inner regions and start to inject iron dust, and, finally, (iv) type Ia SNe. The sum of all of these contributions yields a gradient with negative slope.

6.13.2 Radial gradients in element depletion

Once examined the results for the radial gradients in element abundances both in the gas and dust, we discuss the corresponding gradient in element depletion due to dust formation. First, we concentrate on the innermost and outermost regions of the Disk. In Fig. 6.40 we show the results for the depletion of r C, N, O, Mg, Si, S, Ca and Fe in the ISM in an inner ring of the MW Disk centered at 2.3 Kpc. This is a region of high density and high star formation in turn. The results are shown for both the original (upper panel) and corrected Mg yields (lower panel). Indeed, a small correction to the original yields for the Mg under-abundance leads to different (better) results for the dust mixture as the Mg to Si ratio affects the formation of silicates and the final results for the Solar Ring. The same group of models presented and used to study the depletion in the Solar Ring are shown for the inner and outer regions, but limited to those with the coefficient of star formation efficiency $\nu = 0.3$ and $\nu = 0.7$. The infall time scale is varied between 1 and 9 Gyr (or between 3 and 9 Gyr in the Mg-corrected models) and three IMFs are examined, namely the Kroupa multi power-law IMF, the Larson IMF adapted to the Solar Ring and, finally, the Salpeter one for the sake of comparison. We also show the un-depleted (no dust formation) abundances of the gas (i.e. the gas+dust total abundance). The abundances referring to the same models are connected by a line (dashed or continuous for $\nu = 0.3$ and $\nu = 0.7$ respectively) to better show how the elemental abundances fall down because of the dust formation. As expected, all the elements exhibit a lower abundance in the gas. Some common features are: (i) models with corrected yields

of Mg (bottom panels) show a stronger depletion because they form more silicates, due to the more balanced ratio between Mg and Si; (ii) Mg is much more depleted than Si because of the higher abundance $\Delta[X_{gas}/H]$ of Si (actually $\Delta[X_{gas}/H]$ of Si and Mg are nearly the same but the total starting abundance of Si is higher); (iii) compared to the depletion in the Solar Ring, there is a less significant difference between the models with $\nu = 0.3$ and $\nu = 0.7$, with the exception of the case with $\tau = 1$ Gyr. The reason for this can be tracked in the fast onset of the ISM accretion phase in both cases. Very early on, accretion drives the dust budget and tends to smooth differences due to injections of stardust; (iv) the IMFs with higher number of SNe produce a stronger enrichment than the case with a smaller population of SNe, but the $\Delta[X_{gas}/H]$ caused by the depletion is quite similar.

The situation for a companion outermost region of low density and low star formation centered at 15 kpc is presented in Fig. 6.41. The meaning of the symbols is the same as before. In this Figure we applied a small to the right for the case $\nu = 0.7$ to avoid superposition of the models. Comparing the data displayed in Fig. 6.40 and Fig. 6.41 we note that: (i) in general the innermost regions form more dust with a higher reduction of the gas abundance $\Delta[X_{gas}/H]$. This is the result of forming dust in a medium richer in metals and denser in which the accretion process is favored; (ii) the effect of the different efficiencies of star formation (parameterized by ν) is more evident in the low density/low SFR regions because it makes more evident the effect of metals and ISM enrichment on dust formation; (iii) in the outermost regions almost all the elements suffer a comparable depletion $\Delta[X_{gas}/H]$, simply because the accretion process is very weak over there.

Finally, in the six panels of Fig. 6.43 we show the abundances of [Mg/H], [Fe/H], [C/H], [Si/H], [S/H] and [Ca/H] in the gas as a function of the galacto-centric distance. To single out the difference between models with and without dust depletion, in all the diagrams we show the radial gradient at the current age for the ISM as a whole (that is gas+dust, left sub-panels in each plot) and for the gaseous component *alone* (right sub-panels in each plot) including the effect of depletion. Twelve combinations of the parameters IMF, ν and τ are shown for both the un-depleted (left panels) and depleted (right panels) cases. For each group of four panels we have therefore six un-depleted cases on the top left sub-panel and six on the bottom left sub-panel. The same six plus six cases are shown for the depleted gas in the top and bottom right sub-panels. As expected, dust globally lowers the amount of elements in the gas across the whole disk, but also in some cases alters significantly what would be the slope of the gradient in absence of dust. In particular, in the innermost regions, where a higher density of heavy atoms is available to accrete on the seeds, the regularity of the gradient breaks more strikingly than in the outermost regions

where the gradient keeps roughly the original slope. The innermost regions, that are also affected by the bar ($r < 5\,kpc$), present a even more irregular behaviour, in particular for the elements most depleted and participating to the complex process of silicates formation, like Magnesium and Silicon. Indeed, Carbon keeps a regular gradient as in our model no other heavy elements are supposed to participate to the accretion process of carbonaceous grains. Iron is also very irregular in the innermost regions, since it participates both to the formation of silicates and iron dust grains.

6.14 Final remarks and conclusions

The main conclusions can be summarized as follows:

- We described the database of condensation efficiencies for the main elements that form the dust emitted by the most important dust factories in nature, SNe and AGB stars. See Piovan et al. (2011a) for organized tables containing the condensation efficiencies for the refractory elements C, O, Mg, Si, S, Ca and Fe in AGB stars and SNe. The condensation efficiencies, multiplied by the gaseous ejecta provide an estimate of the amount of each element trapped into dust that is injected into the ISM. This compilation stands upon the *theoretical* work by Ferrarotti & Gail (2006), Zhukovska et al. (2008) for the AGB stars, in order to take into account the different metallicity of AGB stars and hence the different dust production, according to the C/O ratio. Moreover, Nozawa et al. (2003), Nozawa et al. (2006), Nozawa et al. (2007) have been chosen for SNe, because: (1) they include the effect of the different density of the environment in which the SNa explosion occurs which crucially determines the final amount of dust surviving to the shocks; (2) their models produces amounts of carbonaceous grains that agree with the estimate required by the pre-solar dust grains; (3) they product significant amounts of silicates that seem to be necessary to reproduce very recent cold dust emission spectra in the SN 1987A and (4) the CNT unmixed model agrees well with both the FIR/sub-mm estimates of newly formed dust in SNe and the amount of dust required to explain high-z obscured objects with the SNe playing a decisive role. Despite many uncertainties still exist, both theoretically and observationally, this set of models allows some confidence in the calculation of condensation efficiencies, to simulate the production of star-dust.

- The CO molecules influence the formation of C-based dust, thus introducing into the estimates an unavoidable uncertainty. The higher the amount of carbon embedded into CO, the slower is the accretion process and the smaller the amount of carbonaceous grains that are formed.

- During most of the MW evolutionary history, the main process enriching the ISM in dust is the accretion in the cold regions. Only in the very early stages, SNe dominate, and the duration of this phase tends to shorten in regions of high star formation and fast enrichment in metals (innermost regions of the MW). The opposite for the regions of low star formation (the outskirts of the MW), where the accretion in the ISM becomes significant much later so that for many Gyr SNe govern the total dust budget. In this case, AGB stars play an important role, because there is enough time for them to significantly contribute to the dust budget, without being overwhelmed by the SNe (earlier phases) or the ISM accretion (later phases). The time interval during which SNe are the main dust producer can slightly change at varying the upper mass limit of stars undergoing the AGB phase.

- The conclusions for the MW Disk can be extended to galaxies characterized by continuous star formation on the notion that the outer regions of the MW Disk might correspond to low star forming galaxies and the inner ones to high star forming objects. Very high values of SFR (See for example Gall et al. (2011a, Gall et al. (2011b) for detailed simulations of starburst galaxies and QSOs), which are not reached in the MW, not even in the early phases of the evolution in the inner regions, somehow elude this simple scheme. In any case, star-dust dominates the mild SF environments for a long period of time. This time scale tends to decrease in environments with IMFs skewed toward the mass interval in which the star-dust/metals factories (AGB stars and SNe) are important, thus helping the onset of the accretion phase in the ISM.

- In the high SFR/high metallicity regions AGB stars mainly produce silicates, whereas in the low SFR/low metallicity ones, carbon stars can contribute significantly to the C-based dust.

- The IMF plays a fundamental role because it controls the relative amounts of low, intermediate and massive stars (see the entries of Tab. 1.2). We found that IMFs skewed toward massive stars are not suitable to reproduce the properties of dust in the MW, the Solar Ring in particular, (see also Dwek (1998, Zhukovska et al. (2008, Calura et al. (2008), whereas it seems that for starburst galaxies (Gall et al. 2011a), ellipticals (Pipino et al. 2011) and QSOs (Gall et al. 2011b; Valiante et al. 2011) IMFs more biased toward higher mass stars are required, because otherwise it would be more difficult to reproduce the amount of dust observed already on site in very high-z objects. The alternative is to introduce very high condensation efficiencies in SNe. This possibility is somehow supported by the recent FIR/sub-mm observations on

the SN 1987A by Matsuura et al. (2011). In such a case normal IMFs in high-z galaxies and QSOs cannot be excluded. The use of different IMFs for different galaxies in order to reproduce dust properties is a subject of vivid debate, and tightly related to the wider question about the universality of the IMF. The debate seems to favour an IMF sensitive to the initial conditions of star formation (see for instance the recent Elmegreen (2009, Bastian et al. (2010, Myers et al. (2011, Gunawardhana et al. (2011, Kroupa (2011) to mention a few). This possibility was suggested long ago by Chiosi et al. (1998) to solve the apparent contradiction between the spectral and chemical properties of early type galaxies. Similar conclusions are reached by Valiante et al. (2011), trying to match the observed properties of the QSOs SDSS J1148+5251, where a top-heavy IMF allow a more coherent match between different observations. Finally, when the SFR is high (inner regions), the effect of the IMF on the dust budget tends to disappear at the current time, because the accretion in the ISM becomes dominant early on in the evolution, while if the SFR is low we can see the effect of different IMFs spreading until the current time.

- Lower efficiencies ν of the SF, in the range adopted for the Solar Ring, correspond to a slower onset of the accretion in the ISM and a lower final dust budget.

- We tested different descriptions of the process of dust accretion in the ISM. A simple approach adopts an average time-scale of accretion to estimate the *total* dust budget at least in the early stages and for normal star forming environments. More complicated descriptions are require to follow the evolution of the abundance of single elements in dust or low star forming regions.

- The range of depletions observed for most of the elements, that is C, N, O, Mg, Si and S, is nicely reproduced by reasonable combinations of the parameters. IMFs with the classical slope in the high mass range, more easily fit the data for depletion. The only exceptions are: (i) iron, for which probably a more complex mechanism of accretion in the ISM than the simple one on cold regions is required (Zhukovska et al. 2008); (ii) calcium whose extreme depletion can not be reproduced by our model.

- The ratio between the abundances of Mg and Si is crucial in the formation of silicates and it is important to tune it according to the ratio expected from models. We had to correct the slightly under-abundance of the Mg in our gaseous yields, to obtain a better agreement with the observed depletion for the refractory elements involved into the silicates formation.

- For plausible combinations of the parameters, the same that allowed to nicely reproduce the properties of the Solar Ring, both for gas and dust, we find a good general agreement with the mass gradients observed in the MW Disk, both for the total gas mass and the single element abundances. These latter have been compared with the abundances observed in different types of objects, like Cepheids, open clusters, HII regions, O and B stars and Red Giants. Some striking differences between models and observations for C and N can be easily explained by means of the stellar evolution theories.

- The evolutionary scheme for dust formation and evolution across the Disk, emerging from the simulations, is as follows: SNe dominate the dust budget in the early stages in the whole disk. As time goes on, AGB stars enter the game: they contribute to the C-based dust budget if the metallicity keeps low, switch to O-rich dust as soon as the metallicity is near solar or super-solar. For this reason AGB stars behave in a different way in the inner regions where the metallicity quickly increases and in the outer regions where the metallicity keeps low for long time. The ISM accretion is the main contributor to the dust budget across the whole disk. It starts very early on in the innermost regions due to the faster enrichment and the highest number densities of the elements involved in dust and much later in the outer regions where metallicity and density are lower and where AGB stars of low-Z can be very important for many Gyr. It is clear from this trend that a crucial role is played by the SNe: the faster they enrich the ISM in metals, the faster the ISM starts to play a decisive role. Furthermore, the higher the condensation efficiencies, the higher is the amount of dust that can be injected during the time interval before the ISM dominates. The uncertainties on the efficiency of dust condensation in SNe (Piovan et al. 2011a) could clearly change the picture during the early evolutionary phases (Zhukovska et al. 2008; Gall et al. 2011a; Gall et al. 2011b).

- The radial distribution of the dust mass follows the behaviour of the gas showing a bump in the inner zone and a negative slope at the present time. It decreases moving outwards. The fractional radial mass of silicates has also a *negative* slope, whereas the carbonaceous grains have a *positive* slope. They also play a more and more important role as we move toward the outskirts. This is ultimately due to the combined effect of several causes : (i) the yield from SNæ that enrich the ISM with elements involved in silicates and dust where star formation is more active; (ii) the long time interval during which low-Z AGB stars inject carbon in the outskirts of the Disk, and (iii) the delay in the onset of the ISM accretion in the outer regions.

- The depletion of the elements is more significant in the inner regions, with the highest star formation and densities, while in the outskirts we have less depletion due to lower efficiency of dust accretion and star-dust injection.

- As expected, the depletion significantly alters the radial gradients in the gas abundances, in particular for the elements involved in silicates, for which (at least in our simplified model) many elements enter the process and the key element driving the process can vary with time, making the whole thing more irregular.

According to the results obtained for the Solar Ring and the MW Disk, we are confident that the model developed and tested in this thesis work should be suitable to simulate the evolution of dust in pure Disks and in the Disks of intermediate model made by disk and bulge. To complete the interface with the spectrophotometric code the model should be extended to spheroidals with a simple spherical geometry, in order to be applied to pure ellipticals and bulges. A multi-zone model of this kind is actually under development. Once the support of the chemical evolution of dust will be integrated into the code, we guess that the composition and amount of dust could be simulated in a more realistic way, in particular for primordial and high-z galaxies.

To conclude, the classical chemical models nicely reproduce the observed depletion and properties of the Solar Ring. The theoretical ingredients, like condensation coefficients and accretion models, behave in a satisfactory way. What can be improved? Clearly the major weak point is the one-phase description of the ISM. At least a two-phases ISM is required. Finally, work is in progress to introduce a multi-phase description of the ISM with dust in N-Body-TSPH simulations of galaxies.

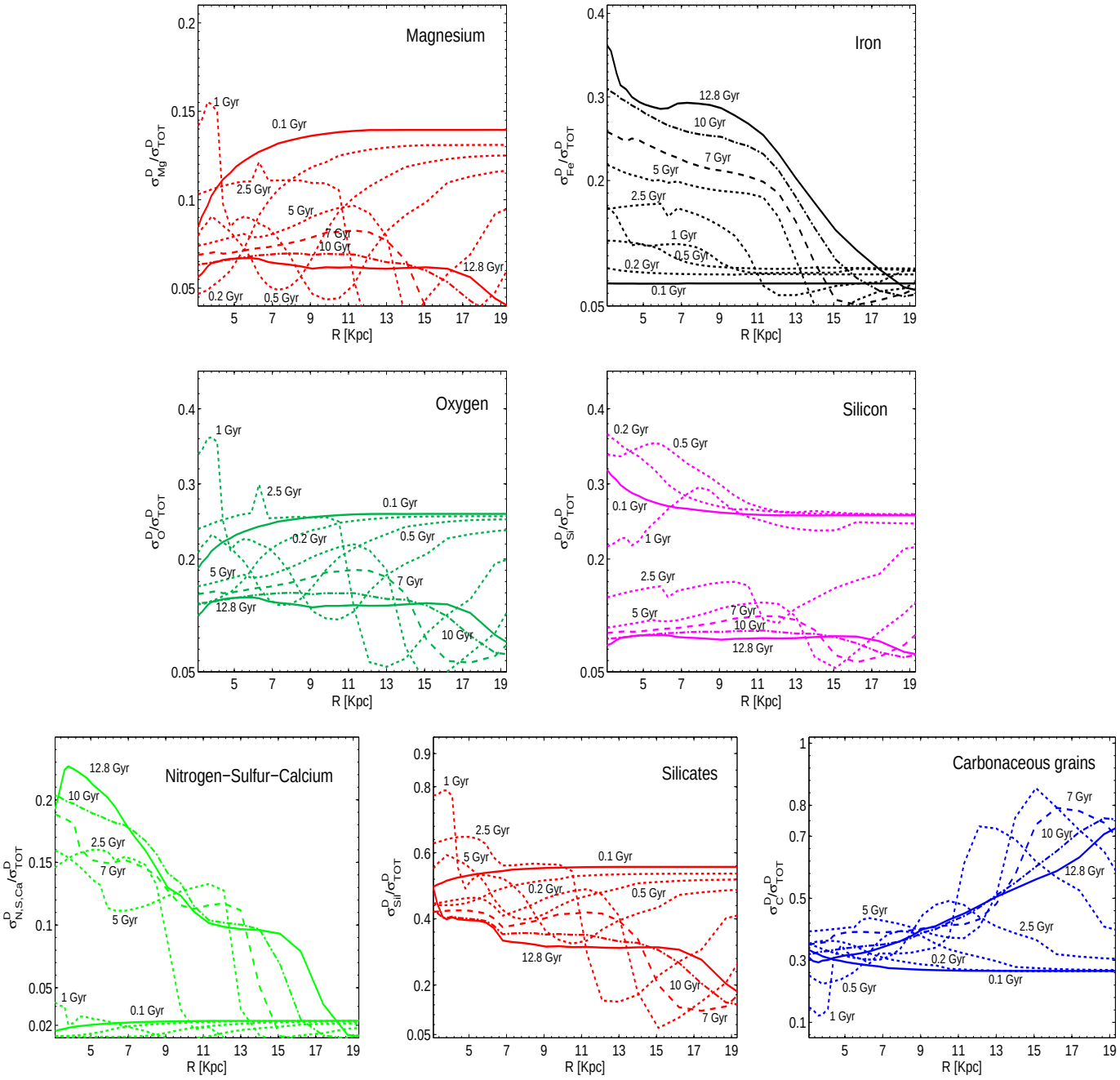

Figure 6.39: Temporal evolution of the radial *mass fraction of single elements or grain families embedded into dust* $\sigma_i^D(r_k,t)/\sigma^D(r_k,t)$, *normalized to the total dust budget*, for some of the elements belonging to our set and involved in the process of dust formation (that is C, N, O, Mg, Si, S, Ca and Fe) and some grain types (silicates, carbonaceous grains, iron grains and Ca/N/S). All the contributions have been properly corrected for the dust destruction. Nine ages are represented as in Fig. 6.38, from the early stages to the current time, that is 0.1, 0.2, 0.5, 1, 2.5, 5, 7, 10 and 12.8 Gyr, assuming that the formation of the MW started when the Universe was ∼0.9 Gyr old (Gail et al. 2009). **Upper panels**: from left to right the time evolution of the radial mass fraction of Mg and Fe, normalized to the total dust mass. **Central panels**: the same as in the upper panels but for O and Si, from left to right. **Lower panels**: the same as in the central panels, but for S, N and Ca (lumped together) and O, silicates (that is the mass fraction of Mg, Si, Fe and O involved into quartz/pyroxenes/olivines) and C (that in practice, once subtracted the carbon embedded in SiC, forms the carbonaceous grains).

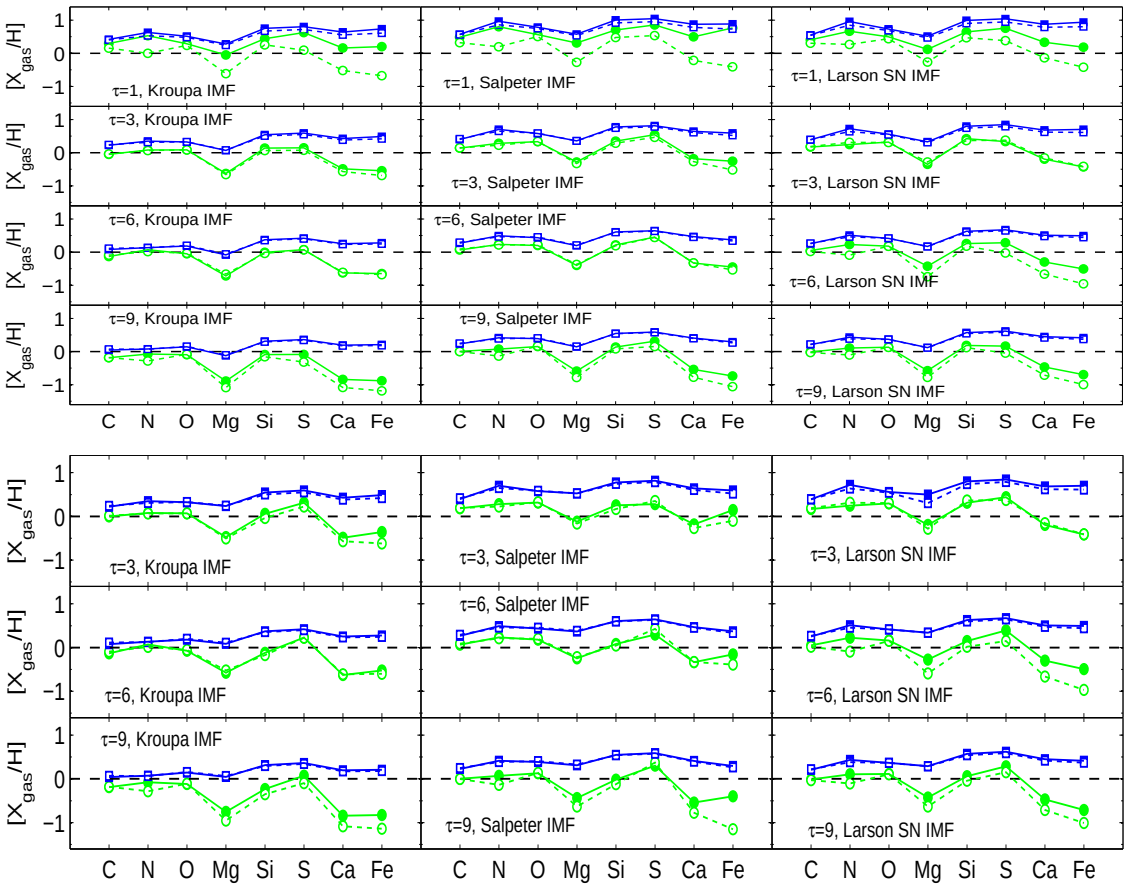

Figure 6.40: Depletion of the elements C, N, O, Mg, Si, S, Ca and Fe in the ISM for an *inner ring* of the MW centered at 2.3 Kpc. **Top panels**: the element depletions are obtained using the original yields, *no correction for the Mg under-abundance is applied*. The same combinations of the parameters adopted to simulate the depletion in the Solar Ring are considered, that is three IMF (Salpeter, Kroupa multi power-law and Larson adapted to the Solar Ring) and four infall time scales ($\tau = 1$, $\tau = 3$, $\tau = 6$ and $\tau = 9$). In each panel the global ISM abundance (gas+dust) is shown. The values of the abundances are connected with continuous lines for the case $\nu = 0.7$ (filled squares and circles), while for $\nu = 0.3$ (open squares and circles) we use dashed lines. The squares represent the global ISM abundance, while the circles the depleted gas abundance. For each panel there is a label showing the combination IMF/infall timescale we have adopted. **Bottom panels**: the same as in the top panel but with the original yield corrected for the Mg under-abundance. Only three infall timescales are shown ($\tau = 3$, $\tau = 6$ and $\tau = 9$).

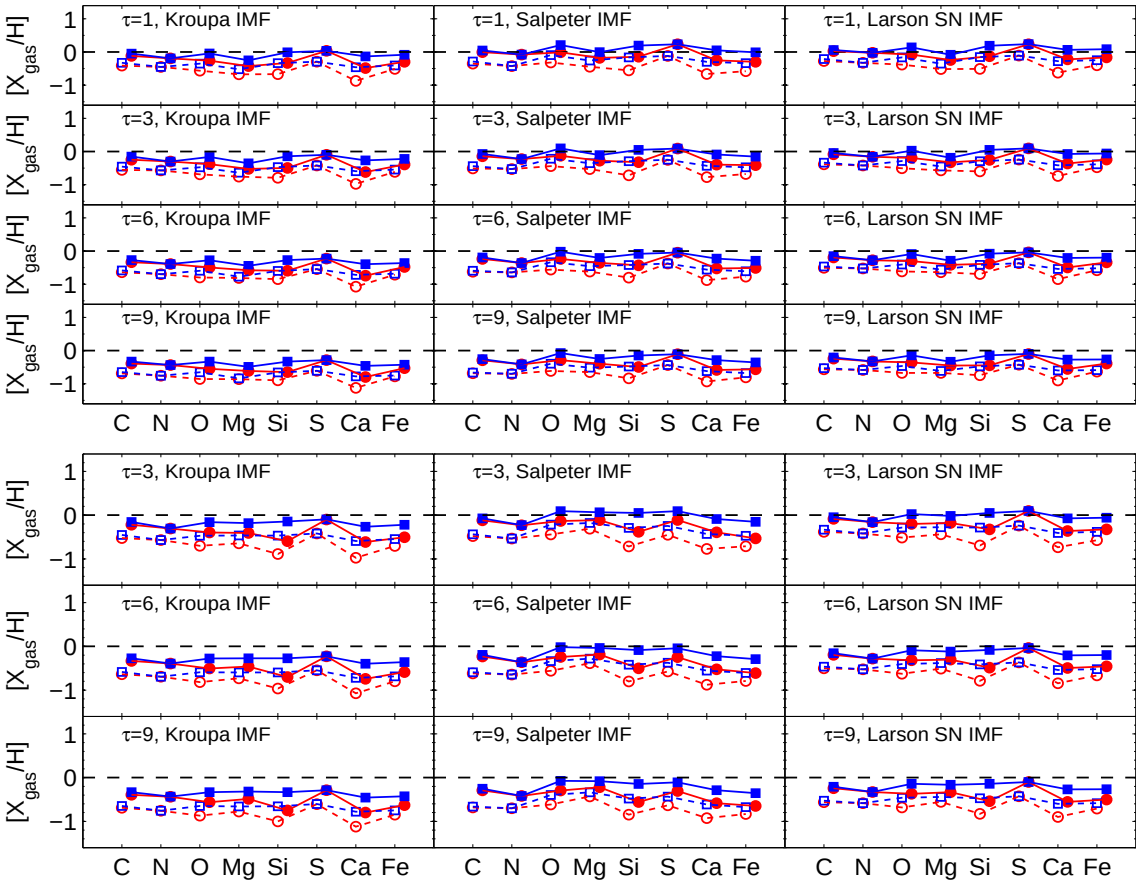

Figure 6.41: Depletion of the elements C, N, O, Mg, Si, S, Ca and Fe in the ISM for an *outer ring* of the MW at 15.0 Kpc. **Top panels**: the element depletions are obtained using the original yields, *no correction for the Mg under-abundance is applied*. The choice of the parameters and the meaning of the symbols are the same as for Fig. 6.40. For the sake of a better representation of the data, the case with $\nu = 0.7$ *is slightly shifted to the right* in such a way to avoid the superposition with $\nu = 0.3$. As in Fig. 6.40, the dashed lines connect the un-depleted and depleted gas abundances for the $\nu = 0.3$ case. **Bottom panels**: the same of the top panel, but with the original yield corrected for the Mg under-abundance. The same timescales of Fig. 6.40 are used.

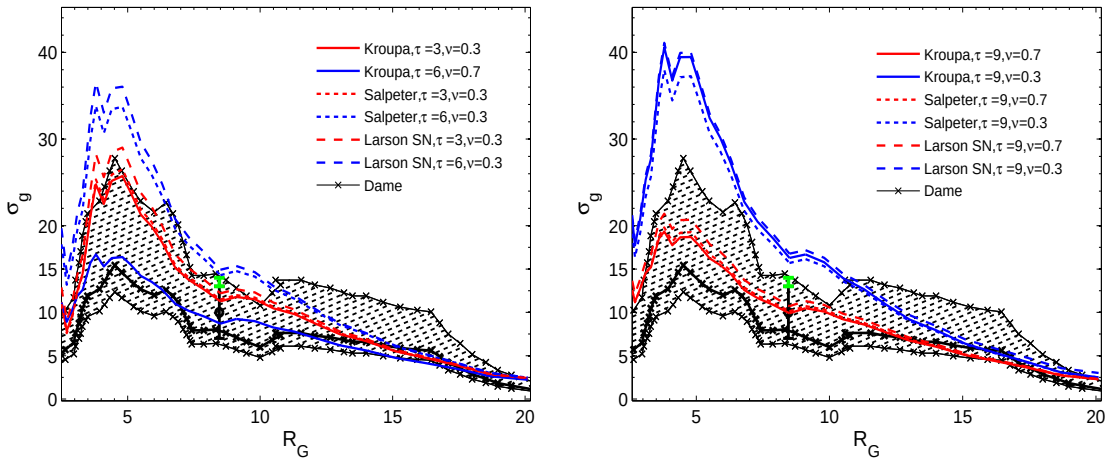

Figure 6.42: Radial surface density profile of the gas in the MW for twelve models taken from the set used to reproduce the element depletion. The models differ for the parameters: IMF (Larson SoNe, Salpeter, Kroupa multi power law), infall timescale τ (3, 6 and 9 Gyr), the efficiency ν (0.3 and 0.7). Not all the combinations have been represented, but only the most significant ones. Data for the SoNe are taken from Dame (1993) and the hatched area represents the confidence region taking into account the errors in the observational estimates. Data for the SoNe gas mass density are from Dickey (1993, Dame (1993) and Olling & Merrifield (2001).

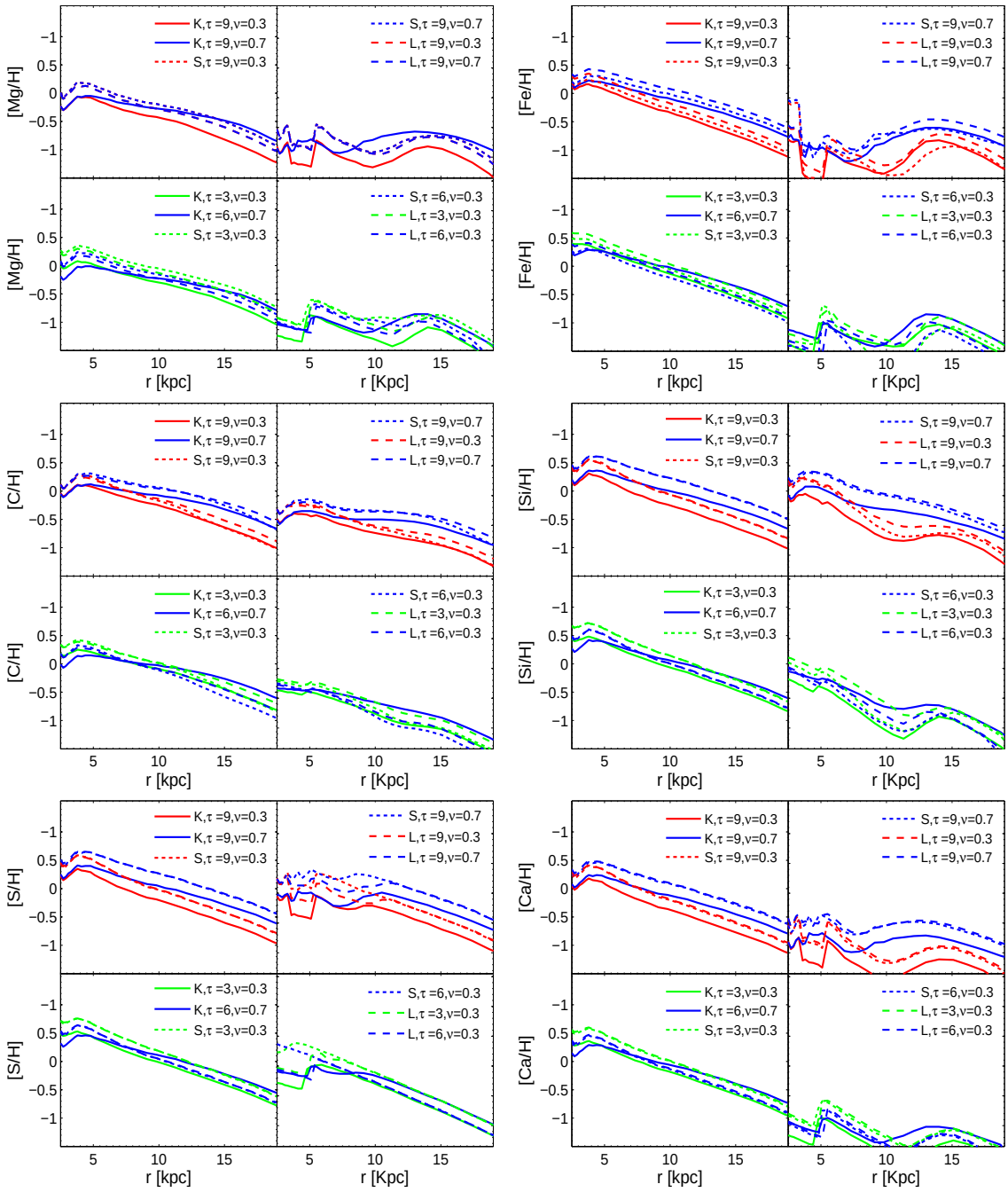

Figure 6.43: The Galactic abundances of [Mg/H], [Fe/H], [C/H], [Si/H], [S/H] and [Ca/H] in the gas as a function of the galacto-centric distance. In all diagrams we present the radial gradient at the current age for both the ISM component as a whole (that is gas+dust, left panels in each plot) and the gaseous component *alone* (right panels in each plot) taking into account the depletion of the elements due to the presence of dust. Twelve combinations of the parameters are considered for both the un-depleted (left panels) and depleted (right panels) cases. *The legend has been split between left and right panels for the sake of clarity.* The following cases are shown. Kroupa IMF: $(\tau, \nu) = (3, 0.3)$ (continuous green line), $(\tau, \nu) = (6, 0.7)$ (continuous blue line), $(\tau, \nu) = (9, 0.3)$ (continuous red line) and $(\tau, \nu) = (9, 0.7)$ (continuous blue line); Salpeter IMF: $(\tau, \nu) = (3, 0.3)$ (dotted green line), $(\tau, \nu) = (6, 0.3)$ (dotted blue line), $(\tau, \nu) = (9, 0.3)$ (dotted red line), and $(\tau, \nu) = (9, 0.3)$ (dotted blue line); Larson Solar Ring IMF: $(\tau, \nu) = (3, 0.3)$ (dashed green line), $(\tau, \nu) = (6, 0.3)$ (dashed blue line), $(\tau, \nu) = (9, 0.7)$ Gyr (dashed green line) and $(\tau, \nu) = (8, 0.3)$ (dashed blue line). All theses cases are also examined for the Solar Ring in this chapter.

Discussion

In this thesis the effects of dust on galaxies have been deeply studied and considered in both chemical and spectro-photometric simulations of galaxies of different morphological types at many different levels, trying to improve the treatment of dust extinction, emission, formation and evolution in our models.
The main results of this study are summarized here:

1. We introduced and studied the effects of dust in isochrones and SEDs of SSPs with an improved state-of-art treatment of the AGB phase in intermediate and low mass stars, taking into account circumstellar dust shells around them. The agreement with observations of AGB stars in the LMC and SMC and with integrated colors of clusters is generally good. We have been able to reproduce the tails of AGB stars in CMD toward low temperatures.

2. We developed and tested state-of-art models of galaxies of different morphological types, E, S0, Sa, Sb, Sc, Sd and disks, with the inclusion of all the local and global effects of dust extinction and emission. We have been able to reproduce the colors of local galaxies at varying the morphological type and of ellipticals at varying the redshift, in many different photometric systems. The evolution of the SEDs of the various galaxy types is consistent with the evolution of the dust content.

3. in order to improve upon the information supplied by the chemical code to the EPS, we developed and presented a state-of-art description of the evolution and formation of dust in spiral galaxies, with a complete treatment of dust yields and dust accretion/destruction processes. This refined model should be in future used to support the spectro-photometric models with a more advanced chemical interface. In particular, the Milky Way has been chosen as the ideal laboratory to study the dust cycle. The depletion of the elements in the solar ring has been successfully reproduced while satisfying the constraints obtained from many other observations of the MW. The effect on dust formation and evolution of the IMF, SF law, mechanism of accretion, star-dust yields and other parameters has been examined.

Several improvements are in progress to overcome some of the weak points of the simulations:

- as already explained, our new chemical model should be in future used to support the spectro-photometric models of disk galaxies and developed in order to support other morphological types. The amount and composition of dust for these galaxies will be obtained by chemical simulations of formation and evolution of dust taking into account star-dust injection, dust accretion and destruction in the ISM.

- The SFH, gas content, star & gas distributions for elliptical galaxies will be obtained by means of high resolution N-body tree-SPH simulations in order to get a realistic description of the galactic wind process and the gas content of the galaxy after the wind;

- another important aspect when building theoretical SEDs for galaxies of different morphological type is the library used for these kinds of models. Up till now, in the galactic code, we use the libraries taken from Piovan et al. (2006b) and the new dusty AGB library presented in this thesis work, but libraries of photometric models using high resolution spectra should be calculated in the future.

- a huge amount of data from the most advanced telescopes and satellites is more and more available. In order to test and get clues about galaxies from all these information, new methods of analysis should be developed, like neural networks.

- a fundamental task will be to compare the simulations with observations, particularly with high redshift data, in order to constrain the parameters used to calculate the evolution of the SEDs, to understand experimental data and to get clues about the evolution of galaxies by means of the EPS method.

- Finally, we are working to make all our codes freely available to the scientific community, in order to expand the number of the people using them, working on them and contributing to their improvement.

References

Hempel , M. & M. Kissler-Patig (2004, June). Extragalactic globular clusters in the near infrared. IV. Quantifying the age structure using Monte-Carlo simulations. *A&A 419*, 863–876.

Akerman, C. J., L. Carigi, P. E. Nissen, M. Pettini, & M. Asplund (2004, February). The evolution of the C/O ratio in metal-poor halo stars. *A&A 414*, 931–942.

Allard, F. & P. H. Hauschildt (1995, May). Model atmospheres for M (sub)dwarf stars. 1: The base model grid. *ApJ 445*, 433–450.

Allende Prieto, C., D. L. Lambert, & M. Asplund (2001, July). The Forbidden Abundance of Oxygen in the Sun. *ApJ 556*, L63–L66.

Allende Prieto, C., D. L. Lambert, & M. Asplund (2002, July). A Reappraisal of the Solar Photospheric C/O Ratio. *ApJ 573*, L137–L140.

Alongi, M., G. Bertelli, A. Bressan, C. Chiosi, F. Fagotto, L. Greggio, & E. Nasi (1993, March). Evolutionary sequences of stellar models with semiconvection and convective overshoot. I - Z = 0.008. *A&AS 97*, 851–871.

Anders, E. & N. Grevesse. Abundances of the elements - Meteoritic and solar.

Andrievsky, S. M., D. Bersier, V. V. Kovtyukh, R. E. Luck, W. J. Maciel, J. R. D. Lépine, & Y. V. Beletsky (2002, March). Using Cepheids to determine the galactic abundance gradient. II. Towards the galactic center. *A&A 384*, 140–144.

Andrievsky, S. M., V. V. Kovtyukh, R. E. Luck, J. R. D. Lépine, D. Bersier, W. J. Maciel, B. Barbuy, V. G. Klochkova, V. E. Panchuk, & R. U. Karpischek (2002, January). Using Cepheids to determine the galactic abundance gradient. I. The solar neighbourhood. *A&A 381*, 32–50.

Andrievsky, S. M., V. V. Kovtyukh, R. E. Luck, J. R. D. Lepine, W. J. Maciel, & Y. V. Beletsky (2002, September). Galactic abundance gradient. III. (Andrievsky+, 2002). *VizieR Online Data Catalog 339*, 20491–+.

Andrievsky, S. M., V. V. Kovtyukh, R. E. Luck, J. R. D. Lépine, W. J. Maciel, & Y. V. Beletsky (2002, September). Using Cepheids to determine the galactic abundance gradient. III. First results for the outer disc. *A&A 392*, 491–499.

Andrievsky, S. M., V. V. Kovtyukh, & I. A. Usenko (1996, January). The chemical composition of the s-Cepheids. II. *A&A 305*, 551–+.

Andrievsky, S. M., R. E. Luck, P. Martin, & J. R. D. Lépine (2004, January). The Galactic abundance gradient from Cepheids. V. Transition zone between 10 and 11 kpc. *A&A 413*, 159–172.

Antia, H. M. & S. Basu (2005, February). The Discrepancy between Solar Abundances and Helioseismology. *ApJ 620*, L129–L132.

Antia, H. M. & S. Basu (2006, June). Determining Solar Abundances Using Helioseismology. *ApJ 644*, 1292–1298.

Arimoto, N. & P. Jablonka (1991, September). Evolutionary method of population synthesis for bulge-disc systems - Optical-infrared colour-magnitude relation of spiral galaxies. *A&A 249*, 374–388.

Arimoto, N. & Y. Yoshii (1987, February). Chemical and photometric properties of a galactic wind model for elliptical galaxies. *A&A 173*, 23–38.

Aringer, B., L. Girardi, W. Nowotny, P. Marigo, & M. T. Lederer (2009, September). Synthetic photometry for carbon rich giants. I. Hydrostatic dust-free models. *A&A 503*, 913–928.

Asplund, M., N. Grevesse, & A. J. Sauval (2005, September). The Solar Chemical Composition. In T. G. Barnes III & F. N. Bash (Ed.), *Cosmic Abundances as Records of Stellar Evolution and Nucleosynthesis*, Volume 336 of *Astronomical Society of the Pacific Conference Series*, pp. 25–+.

Asplund, M., N. Grevesse, A. J. Sauval, C. Allende Prieto, & R. Blomme (2005, February). Line formation in solar granulation. VI. [C I], C I, CH and C_2 lines and the photospheric C abundance. *A&A 431*, 693–705.

Asplund, M., N. Grevesse, A. J. Sauval, C. Allende Prieto, & D. Kiselman (2004, April). Line formation in solar granulation. IV. [O I], O I and OH lines and the photospheric O abundance. *A&A 417*, 751–768.

Asplund, M., N. Grevesse, A. J. Sauval, & P. Scott (2009, September). The Chemical Composition of the Sun. *ARA&A 47*, 481–522.

Aufdenberg, J. P., A. Mérand, V. Coudé du Foresto, O. Absil, E. Di Folco, P. Kervella, S. T. Ridgway, D. H. Berger, T. A. ten Brummelaar, H. A. McAlister, J. Sturmann, L. Sturmann, & N. H. Turner (2006, July). First Results from the CHARA Array. VII. Long-Baseline Interferometric Measurements of Vega Consistent with a Pole-On, Rapidly Rotating Star. *ApJ 645*, 664–675.

Bacmann, A., B. Lefloch, C. Ceccarelli, A. Castets, J. Steinacker, & L. Loinard (2002, July). The degree of CO depletion in pre-stellar cores. *A&A 389*, L6–L10.

Bahcall, J. N., S. Basu, M. Pinsonneault, & A. M. Serenelli (2005, January). Helioseismological Implications of Recent Solar Abundance Determinations. *ApJ 618*, 1049–1056.

Bahcall, J. N., A. M. Serenelli, & S. Basu (2005, March). New Solar Opacities, Abundances, Helioseismology, and Neutrino Fluxes. *ApJ 621*, L85–L88.

Bakes, E. L. O. & A. G. G. M. Tielens (1994, June). The photoelectric heating mechanism for very small graphitic grains and polycyclic aromatic hydrocarbons. *ApJ 427*, 822–838.

Bandiera, R. (1987, August). The origin of Kepler's supernova remnant. *ApJ 319*, 885–892.

Bastian, N., K. R. Covey, & M. R. Meyer (2010, September). A Universal Stellar Initial Mass Function? A Critical Look at Variations. *ARA&A 48*, 339–389.

Basu, S. & H. M. Antia (2008, March). Helioseismology and solar abundances. *457*, 217–283.

Battistini, P., F. Bonoli, A. Braccesi, L. Federici, F. Fusi Pecci, B. Marano, & F. Borngen (1987, February). Search for (globular) clusters in M31. IV - Candidates in a 3 X 3-deg square field centred on M31. *A&AS 67*, 447–481.

Bautista, M. A., D. L. Depoy, A. K. Pradhan, J. H. Elias, B. Gregory, M. M. Phillips, & N. B. Suntzeff (1995, February). Near infrared spectra of SN 1987A: Days 936 to 1445. *AJ 109*, 729–736.

Bedijn, P. J. (1987, November). Dust shells around Miras and OH/IR stars - Interpretation of IRAS and other infrared measurements. *A&A 186*, 136–152.

Begemann, B., J. Dorschner, T. Henning, H. Mutschke, J. Guertler, C. Koempe, & R. Nass (1997, February). Aluminum Oxide and the Opacity of Oxygen-rich Circumstellar Dust in the 12–17 Micron Range. *ApJ 476*, 199.

Bertelli, G., A. Bressan, C. Chiosi, F. Fagotto, & E. Nasi (1994, August). Theoretical isochrones from models with new radiative opacities. *A&AS 106*, 275–302.

Bertelli, G., L. Girardi, P. Marigo, & E. Nasi (2008, June). Scaled solar tracks and isochrones in a large region of the Z-Y plane. I. From the ZAMS to the TP-AGB end for 0.15-2.5 M_{sun} stars. *A&A 484*, 815–830.

Bertin, G., R. P. Saglia, & M. Stiavelli (1992). *ApJ 384*, 423.

Bertoldi, F., C. L. Carilli, P. Cox, X. Fan, M. A. Strauss, A. Beelen, A. Omont, & R. Zylka (2003, July). Dust emission from the most distant quasars. *A&A 406*, L55–L58.

Bessell, M. S. (1990). *PASP 102*, 1181.

Bessell, M. S. & J. M. Brett (1988). *PASP 100*, 1134.

Bessell, M. S., J. M. Brett, & M. W. P. R. Scholz (1991, August). Colors and stratifications of extended static model photospheres of M stars located on the FGB, AGB and supergiant branch. *A&A 89*, 335–366.

Bessell, M. S., J. M. Brett, P. R. Wood, & M. Scholz (1989, January). Colors of extended static model photospheres of M giants. *A&AS 77*, 1–30.

Bianchi, S. & R. Schneider (2007, July). Dust formation and survival in supernova ejecta. *MNRAS 378*, 973–982.

Bica, E., J. J. Claria, H. Dottori, J. F. C. Santos, Jr., & A. E. Piatti (1996, January). Integrated UBV Photometry of 624 Star Clusters and Associations in the Large Magellanic Cloud. *ApJS 102*, 57.

Blanco, A., A. Borghesi, S. Fonti, & V. Orofino (1998, February). Circumstellar emission from dust envelopes around carbon stars showing the silicon carbide feature. *A&A 330*, 505–514.

Blitz, L., Y. Fukui, A. Kawamura, A. Leroy, N. Mizuno, & E. Rosolowsky (2007). Giant Molecular Clouds in Local Group Galaxies. In B. Reipurth, D. Jewitt, & K. Keil (Eds.), *Protostars and Planets V*, pp. 81–96.

Bloecker, T. (1995, May). Stellar evolution of low and intermediate-mass stars. I. Mass loss on the AGB and its consequences for stellar evolution. *A&A 297*, 727–+.

Blommaert, J., R. Siebenmorgen, A. Coulais, L. Metcalfe, M.-A. Miville-Deschênes, K. Okumura, S. Ott, A. Pollack, M. Sauvage, & J.-L. Starck (Eds.) (2003, November). *The ISO Handbook Volume II: CAM - The ISO Camera (v 2.0)*, Volume 1262 of *ESA Special Publication*.

Blommaert, J. A. D. L., M. A. T. Groenewegen, K. Okumura, S. Ganesh, A. Omont, J. Cami, I. S. Glass, H. J. Habing, M. Schultheis, G. Simon, & J. T. van Loon (2006, December). ISO mid-infrared spectroscopy of Galactic Bulge AGB stars. *A&A 460*, 555–563.

Blum, R. D., J. R. Mould, K. A. Olsen, J. A. Frogel, M. Werner, M. Meixner, F. Markwick-Kemper, R. Indebetouw, B. Whitney, M. Meade, B. Babler, E. B. Churchwell, K. Gordon, C. Engelbracht, B.-Q. For, K. Misselt, U. Vijh, C. Leitherer, K. Volk, S. Points, W. Reach, J. L. Hora, J.-P. Bernard, F. Boulanger, S. Bracker, M. Cohen, Y. Fukui, J. Gallagher, V. Gorjian, J. Harris, D. Kelly, A. Kawamura, W. B. Latter, S. Madden, A. Mizuno, N. Mizuno, A. Nota, M. S. Oey, T. Onishi, R. Paladini, N. Panagia, P. Perez-Gonzalez, H. Shibai, S. Sato, L. Smith, L. Staveley-Smith, A. G. G. M. Tielens, T. Ueta, S. Van Dyk, & D. Zaritsky (2006, November). Spitzer SAGE Survey of the Large Magellanic Cloud. II. Evolved Stars and Infrared Color-Magnitude Diagrams. *AJ 132*, 2034–2045.

Bohlin, R. C., A. W. Harris, A. V. Holm, & C. Gry (1990, July). The ultraviolet calibration of the Hubble Space Telescope. IV - Absolute IUE fluxes of Hubble Space Telescope standard stars. *ApJS 73*, 413–439.

Boissier, S. & N. Prantzos (1999, August). Chemo-spectrophotometric evolution of spiral galaxies - I. The model and the Milky Way. *MNRAS 307*, 857–876.

Boissier, S. & N. Prantzos (2000, February). Chemo-spectrophotometric evolution of spiral galaxies - II. Main properties of present-day disc galaxies. *MNRAS 312*, 398–416.

Bolatto, A. D., J. D. Simon, S. Stanimirović, J. T. van Loon, R. Y. Shah, K. Venn, A. K. Leroy, K. Sandstrom, J. M. Jackson, F. P. Israel, A. Li, L. Staveley-Smith, C. Bot, F. Boulanger, & M. Rubio (2007, January). The Spitzer Survey of the Small Magellanic Cloud: S^3MC Imaging and Photometry in the Mid- and Far-Infrared Wave Bands. *ApJ 655*, 212–232.

Bonatto, C., E. Bica, & L. Girardi (2004, February). Theoretical isochrones compared to 2MASS observations: Open clusters at nearly solar metallicity. *A&A 415*, 571–576.

Borkowski, K. J., B. J. Williams, S. P. Reynolds, W. P. Blair, P. Ghavamian, R. Sankrit, S. P. Hendrick, K. S. Long, J. C. Raymond, R. C. Smith, S. Points, & P. F. Winkler (2006, May). Dust Destruction in Type Ia Supernova Remnants in the Large Magellanic Cloud. *ApJ 642*, L141–L144.

Bouchet, P., E. Dwek, J. Danziger, R. G. Arendt, I. J. M. De Buizer, S. Park, N. B. Suntzeff, R. P. Kirshner, & P. Challis (2006, October). SN 1987A after 18 Years: Mid-Infrared Gemini and Spitzer Observations of the Remnant. *ApJ 650*, 212–227.

Braun, R. & D. A. Thilker (2004, April). The WSRT wide-field H I survey. II. Local Group features. *A&A 417*, 421–435.

Bressan, A., C. Chiosi, & F. Fagotto (1994, August). Spectrophotometric evolution of elliptical galaxies. 1: Ultraviolet excess and color-magnitude-redshift relations. *ApJS 94*, 63–115.

Bressan, A., F. Fagotto, G. Bertelli, & C. Chiosi (1993, September). Evolutionary sequences of stellar models with new radiative opacities. II - Z = 0.02. *A&AS 100*, 647–664.

Bressan, A., G. L. Granato, & L. Silva (1998, April). Modelling intermediate age and old stellar populations in the Infrared. *A&A 332*, 135–148.

Bressan, A., L. Silva, & G. L. Granato (2002, September). Far infrared and radio emission in dusty starburst galaxies. *A&A 392*, 377–391.

Bruzual, G. & S. Charlot (2003, October). Stellar population synthesis at the resolution of 2003. *MNRAS 344*, 1000.

Bruzual A., G. & S. Charlot (1993, March). Spectral evolution of stellar populations using isochrone synthesis. *ApJ 405*, 538–553.

Burkert, A., J. W. Truran, & G. Hensler (1992, June). The collapse of our Galaxy and the formation of the Galactic disk. *ApJ 391*, 651–658.

Buta, R., S. Mitra, G. de Vaucouleurs, & H. G. Corwin, Jr. (1994, January). Mean morphological types of bright galaxies. *AJ 107*, 118–134.

Buzzoni, A. (1995). In A. Buzzoni, A. Renzini, & A. Serrano (Eds.), *Fresh Views of Elliptical Galaxies*, ASP Conf Ser. 86, pp. 189.

Buzzoni, A. (2002, March). Ultraviolet Properties of Primeval Galaxies: Theoretical Models from Stellar Population Synthesis. *AJ 123*, 1188–1199.

Buzzoni, A. (2005, August). Broad-band colours and overall photometric properties of template galaxy models from stellar population synthesis. *MNRAS 361*, 725–742.

Caffau, E., P. Bonifacio, R. Faraggiana, P. François, R. G. Gratton, & M. Barbieri (2005, October). Sulphur abundance in Galactic stars. *A&A 441*, 533–548.

Caffau, E. & H. Ludwig (2008, October). 3D model atmospheres and the solar photospheric oxygen abundance. In L. Deng & K. L. Chan (Ed.), *IAU Symposium*, Volume 252 of *IAU Symposium*, pp. 35–39.

Caffau, E., H. Ludwig, P. Bonifacio, R. Faraggiana, M. Steffen, B. Freytag, I. Kamp, & T. R. Ayres (2010, February). The solar photospheric abundance of carbon.Analysis of atomic carbon lines with the CO5BOLD solar model. *ArXiv e-prints*.

Caffau, E., H. Ludwig, M. Steffen, T. R. Ayres, P. Bonifacio, R. Cayrel, B. Freytag, & B. Plez (2008, September). The photospheric solar oxygen project. I. Abundance analysis of atomic lines and influence of atmospheric models. *A&A 488*, 1031–1046.

Caffau, E., E. Maiorca, P. Bonifacio, R. Faraggiana, M. Steffen, H. Ludwig, I. Kamp, & M. Busso (2009, May). The solar photospheric nitrogen abundance. Analysis of atomic transitions with 3D and 1D model atmospheres. *A&A 498*, 877–884.

Calura, F., M. Dessauges-Zavadski, J. X. Prochaska, & F. Matteucci (2009, March). Constraining the Star Formation Histories of Gamma-Ray Burst Host Galaxies from their Observed Abundance Patterns. *ApJ 693*, 1236–1249.

Calura, F., A. Pipino, & F. Matteucci (2008, March). The cycle of interstellar dust in galaxies of different morphological types. *A&A 479*, 669–685.

Capak, P., H. Aussel, M. Ajiki, H. J. McCracken, B. Mobasher, N. Scoville, P. Shopbell, Y. Taniguchi, D. Thompson, S. Tribiano, S. Sasaki, A. W. Blain, M. Brusa, C. Carilli, A. Comastri, C. M. Carollo, P. Cassata, J. Colbert, R. S. Ellis, M. Elvis, M. Giavalisco, W. Green, L. Guzzo, G. Hasinger, O. Ilbert, C. Impey, K. Jahnke, J. Kartaltepe, J.-P. Kneib, J. Koda, A. Koekemoer, Y. Komiyama, A. Leauthaud, O. Le Fevre, S. Lilly, C. Liu, R. Massey, S. Miyazaki, T. Murayama, T. Nagao, J. A. Peacock, A. Pickles, C. Porciani, A. Renzini, J. Rhodes, M. Rich, M. Salvato, D. B. Sanders, C. Scarlata, D. Schiminovich, E. Schinnerer, M. Scodeggio, K. Sheth, Y. Shioya, L. A. M. Tasca, J. E. Taylor, L. Yan, & G. Zamorani (2007, September). The First Release COSMOS Optical and Near-IR Data and Catalog. *ApJS 172*, 99–116.

Caputi, K. I., G. Lagache, L. Yan, H. Dole, N. Bavouzet, E. Le Floc'h, P. I. Choi, G. Helou, & N. Reddy (2007, May). The Infrared Luminosity Function of Galaxies at Redshifts z = 1 and z ˜ 2 in the GOODS Fields. *ApJ 660*, 97–116.

Carilli, C. L., F. Bertoldi, M. P. Rupen, X. Fan, M. A. Strauss, K. M. Menten, E. Kreysa, D. P. Schneider, A. Bertarini, M. S. Yun, & R. Zylka (2001, July). A 250 GHz Survey of High-Redshift Quasars from the Sloan Digital Sky Survey. *ApJ 555*, 625–632.

Carney, B. W., D. Yong, M. L. Teixera de Almeida, & P. Seitzer (2005, September). Elemental Abundance Ratios in Stars of the Outer Galactic Disk. II. Field Red Giants. *AJ 130*, 1111–1126.

Carraro, G., F. Bresolin, S. Villanova, F. Matteucci, F. Patat, & M. Romaniello (2004, October). Metal Abundances in Extremely Distant Galactic Old Open Clusters. I. Berkeley 29 and Saurer 1. *AJ 128*, 1676–1683.

Carraro, G., D. Geisler, S. Villanova, P. M. Frinchaboy, & S. R. Majewski (2007, December). Old open clusters in the outer Galactic disk. *A&A 476*, 217–227.

Carraro, G., Y. K. Ng, & L. Portinari (1998, June). On the Galactic disc age-metallicity relation. *MNRAS 296*, 1045–1056.

Cassam-Chenaï, G., A. Decourchelle, J. Ballet, U. Hwang, J. P. Hughes, R. Petre, & et al. (2004, February). XMM-Newton observation of Kepler's supernova remnant. *A&A 414*, 545–558.

Cassarà, L. P. (2008). Evolutionary spectral synthesis in 3d models with dust of galaxies along the hubble sequence. Master's thesis, University of Padova, Italy.

Castellani, M. & A. Tornambe (1991, November). Advanced evolutionary phases of large-metallicity low-mass stars and the problem of the ultraviolet excess of elliptical galaxies. *ApJ 381*, 393–408.

Castelli, F. & R. L. Kurucz (1994, January). Model atmospheres for VEGA. *A&A 281*, 817–832.

Cayrel, R., E. Depagne, M. Spite, V. Hill, F. Spite, P. François, B. Plez, T. Beers, F. Primas, J. Andersen, B. Barbuy, P. Bonifacio, P. Molaro, & B. Nordström (2004, March). First stars V - Abundance patterns from C to Zn and supernova yields in the early Galaxy. *A&A 416*, 1117–1138.

Chabrier, G. (2001, June). The Galactic Disk Mass Budget. I. Stellar Mass Function and Density. *ApJ 554*, 1274–1281.

Chabrier, G. (2002, March). The Galactic Disk Mass Budget. II. Brown Dwarf Mass Function and Density. *ApJ 567*, 304–313.

Chabrier, G. (2003, July). Galactic Stellar and Substellar Initial Mass Function. *PASP 115*, 763–795.

Chen, L., J. L. Hou, & J. J. Wang (2003, March). On the Galactic Disk Metallicity Distribution from Open Clusters. I. New Catalogs and Abundance Gradient. *AJ 125*, 1397–1406.

Chen, Y. Q., P. E. Nissen, G. Zhao, H. W. Zhang, & T. Benoni (2000, February). Chemical composition of 90 F and G disk dwarfs. *A&AS 141*, 491–506.

Cherchneff, I. & E. Dwek (2009, July). The Chemistry of Population III Supernova Ejecta: I - Formation of Molecules in the Early Universe. *ArXiv:astro-ph/0907.3621*.

Cherchneff, I. & E. Dwek (2010, April). The Chemistry of Population III Supernova Ejecta. II. The Nucleation of Molecular Clusters as a Diagnostic for Dust in the Early Universe. *ApJ 713*, 1–24.

Cherchneff, I. & S. Lilly (2008, August). Primordial Massive Supernovae as the First Molecular Factories in the Early Universe. *ApJ 683*, L123–L126.

Chevalier, R. A. & J. Oishi (2003, August). Cassiopeia A and Its Clumpy Presupernova Wind. *ApJ 593*, L23–L26.

Chiappini, C., F. Matteucci, & R. Gratton (1997, March). The Chemical Evolution of the Galaxy: The Two-Infall Model. *ApJ 477*, 765–+.

Chiappini, C., F. Matteucci, & P. Padoan (1997). *MNRAS*. submitted, SISSA preprint 41/97/A.

Chiosi, C. (1980, March). Chemical evolution of the galactic disk - The inflow problem. *A&A 83*, 206–216.

Chiosi, C., A. Bressan, L. Portinari, & R. Tantalo (1998, November). A new scenario of galaxy evolution under a universal Initial Mass Function. *A&A 339*, 355–381.

Chiosi, C. & G. Carraro (2002, September). Formation and evolution of elliptical galaxies. *MNRAS 335*, 335–357.

Chiosi, C. & A. Maeder (1986). *ARA&A 24*, 329.

Cioffi, D. F., C. F. McKee, & E. Bertschinger (1988). *ApJ 334*, 252.

Cioni, M.-R. L., L. Girardi, P. Marigo, & H. J. Habing (2006, March). AGB stars in the Magellanic Clouds. II. The rate of star formation across the LMC. *A&A 448*, 77–91.

Clayton, D. D. (1988, November). Isotopic anomalies - Chemical memory of Galactic evolution. *ApJ 334*, 191–195.

Clayton, D. D. & L. R. Nittler (2004, September). Astrophysics with Presolar Stardust. *ARA&A 42*, 39–78.

Clayton, R. N. (2003, December). Oxygen Isotopes in Meteorites. *Treatise on Geochemistry 1*, 129–142.

Cohen, M., W. A. Wheaton, & S. T. Megeath (2003, August). Spectral Irradiance Calibration in the Infrared. XIV. The Absolute Calibration of 2MASS. *AJ 126*, 1090–1096.

Cordier, D., A. Pietrinferni, S. Cassisi, & M. Salaris (2007, February). A Large Stellar Evolution Database for Population Synthesis Studies. III. Inclusion of the Full Asymptotic Giant Branch Phase and Web Tools for Stellar Population Analyses. *AJ 133*, 468–478.

Coupon, J., O. Ilbert, M. Kilbinger, H. J. McCracken, Y. Mellier, S. Arnouts, E. Bertin, P. Hudelot, M. Schultheis, O. Le Fèvre, V. Le Brun, L. Guzzo, S. Bardelli, E. Zucca, M. Bolzonella, B. Garilli, G. Zamorani, A. Zanichelli, L. Tresse, & H. Aussel (2009, June). Photometric redshifts for the CFHTLS T0004 deep and wide fields. *A&A 500*, 981–998.

Crinklaw, G., S. R. Federman, & C. L. Joseph (1994, April). The depletion of calcium in the interstellar medium. *ApJ 424*, 748–753.

Daflon, S. & K. Cunha (2004, December). Galactic Metallicity Gradients Derived from a Sample of OB Stars. *ApJ 617*, 1115–1126.

Dame, T. M. (1993). The distribution of neutral gas in the Milky Way. In S. S. Holt & F. Verter (Ed.), *Back to the Galaxy*, Volume 278 of *American Institute of Physics Conference Series*, pp. 267–278.

Danziger, I. J., L. B. Lucy, P. Bouchet, & C. Gouiffes (1991). Molecules Dust and Ionic Abundances in Supernova 1987A. In S. E. Woosley (Ed.), *Supernovae*, pp. 69.

David, P. & R. Papoular (1990, October). The circumstellar silicate dust as seen by IRAS. I - Opacity and temperature. *A&A 237*, 425–435.

David, P. & B. Pegourie (1995, January). The complex dielectric function for circumstellar silicate grains based on the IRAS data. *A&A 293*, 833–839.

Davidge, T. J. (2001, September). The Brightest Asymptotic Giant Branch Stars in the Inner Bulge of M31. *AJ 122*, 1386–1396.

Deharveng, L., M. Peña, J. Caplan, & R. Costero (2000, January). Oxygen and helium abundances in Galactic Hii regions - II. Abundance gradients. *MNRAS 311*, 329–345.

Deneault, E., D. D. Clayton, & A. Heger (2003, September). Supernova Reverse Shocks: SiC Growth and Isotopic Composition. *ApJ 594*, 312–325.

Desert, F. X., F. Boulanger, & S. N. Shore (1986, May). Grain temperature fluctuations - A key to infrared spectra. *A&A 160*, 295–300.

Dickey, J. M. (1993, January). Gas as a Tracer of Galactic Structure. In R. M. Humphreys (Ed.), *The Minnesota Lectures on the Structure and Dynamics of the Milky Way*, Volume 39 of *Astronomical Society of the Pacific Conference Series*, pp. 93–+.

Dijkstra, C., A. K. Speck, R. B. Reid, & P. Abraham (2005, November). The 10 μm Feature of M-Type Stars in the Large Magellanic Cloud and the Dust Condensation Sequence. *ApJ 633*, L133–L136.

Dominik, C., E. Sedlmayr, & H. Gail (1993, October). Dust formation in stellar winds. VI. Moment equations for the formation of heterogeneous and core-mantle grains. *A&A 277*, 578–+.

Dopita, M. (1985). *ApJ 295*, L5.

Dopita, M. & S. D. Ryder (1994). *ApJ 430*, 163.

Dotter, A., B. Chaboyer, D. Jevremović, V. Kostov, E. Baron, & J. W. Ferguson (2008, September). The Dartmouth Stellar Evolution Database. *ApJS 178*, 89–101.

Draine, B. T. (2003). Interstellar Dust Grains. *ARA&A 41*, 241–289.

Draine, B. T. (2009, March). Interstellar Dust Models and Evolutionary Implications. *ArXiv:astro-ph/0903.1658*.

Draine, B. T. & H. M. Lee (1984, October). Optical properties of interstellar graphite and silicate grains. *ApJ 285*, 89–108.

Draine, B. T. & A. Li (2001, April). Infrared Emission from Interstellar Dust. I. Stochastic Heating of Small Grains. *ApJ 551*, 807–824.

Draine, B. T. & B. Sutin (1987, September). Collisional charging of interstellar grains. *ApJ 320*, 803–817.

Dunne, L., S. Eales, R. Ivison, H. Morgan, & M. Edmunds (2003, July). Type II supernovae as a significant source of interstellar dust. *424*, 285–287.

Dunne, L., S. J. Maddox, R. J. Ivison, L. Rudnick, T. A. Delaney, B. C. Matthews, C. M. Crowe, H. L. Gomez, S. A. Eales, & S. Dye (2009, April). Cassiopeia A: dust factory revealed via submillimetre polarimetry. *MNRAS 394*, 1307–1316.

Dwek, E. (1986, March). Temperature fluctuations and infrared emission from dust particles in a hot gas. *ApJ 302*, 363–370.

Dwek, E. (1998, July). The Evolution of the Elemental Abundances in the Gas and Dust Phases of the Galaxy. *ApJ 501*, 643.

Dwek, E. (2005, April). Interstellar dust: what is it, how does it evolve, and what are its observational consequences? In C. C. Popescu & R. J. Tuffs (Eds.), *The Spectral Energy Distributions of Gas-Rich Galaxies: Confronting Models with Data*, Volume 761 of *American Institute of Physics Conference Series*, pp. 103.

Dwek, E., R. G. Arendt, D. J. Fixsen, T. J. Sodroski, N. Odegard, J. L. Weiland, W. T. Reach, M. G. Hauser, T. Kelsall, S. H. Moseley, R. F. Silverberg, R. A. Shafer, J. Ballester, D. Bazell, & R. Isaacman (1997, February). Detection and Characterization of Cold Interstellar Dust and Polycyclic Aromatic Hydrocarbon Emission, from COBE Observations. *ApJ 475*, 565–+.

Dwek, E. & I. Cherchneff (2011, February). The Origin of Dust in the Early Universe: Probing the Star Formation History of Galaxies by Their Dust Content. *ApJ 727*, 63.

Dwek, E., F. Galliano, & A. Jones (2009, February). The Cycle of Dust in the Milky Way: Clues from the High-Redshift and Local Universe. *ArXiv:astro-ph/0903.0006*.

Dwek, E., S. H. Moseley, W. Glaccum, J. R. Graham, R. F. Loewenstein, R. F. Silverberg, & R. K. Smith (1992, April). Dust and gas contributions to the energy output of SN 1987A on day 1153. *ApJ 389*, L21–L24.

Edvardsson, B., J. Andersen, B. Gustafsson, D. L. Lambert, P. E. Nissen, & J. Tomkin (1993, August). The Chemical Evolution of the Galactic Disk - Part One - Analysis and Results. *A&A 275*, 101.

Elitzur, M. & Ž. Ivezić (2001, October). Dusty winds - I. Self-similar solutions. *MNRAS 327*, 403–421.

Elmegreen, B. G. (2009, January). The Stellar Initial Mass Function in 2007: A Year for Discovering Variations. In *The Evolving ISM in the Milky Way and Nearby Galaxies*.

Elmhamdi, A., I. J. Danziger, N. Chugai, A. Pastorello, M. Turatto, E. Cappellaro, G. Altavilla, S. Benetti, F. Patat, & M. Salvo (2003, February). Photometry and spectroscopy of the Type IIP SN 1999em from outburst to dust formation. *MNRAS 338*, 939–956.

Ennis, J. A., L. Rudnick, W. T. Reach, J. D. Smith, J. Rho, T. DeLaney, H. Gomez, & T. Kozasa (2006, November). Spitzer IRAC Images and Sample Spectra of Cassiopeia A's Explosion. *ApJ 652*, 376–386.

Epchtein, N., B. de Batz, E. Copet, P. Fouque, F. Lacombe, T. Le Bertre, G. Mamon, D. Rouan, D. Tiphene, W. B. Burton, E. Deul, H. Habing, J. Boersenberger, M. Dennefeld, A. Omont, J. C. Renault, B. Rocca-Volmerange, S. Kimeswenger, I. Appenzeller, R. Bender, T. Forveille, F. Garzon, J. Hron, P. Persi, M. Ferrari-Toniolo, & I. Vauglin (1994, July). DENIS: A Deep Near-Infrared Survey of the southern sky. *Ap&SS 217*, 3–9.

Ercolano, B., M. J. Barlow, & B. E. K. Sugerman (2007, March). Dust yields in clumpy supernova shells: SN 1987A revisited. *MNRAS 375*, 753–763.

Esteban, C., J. García-Rojas, M. Peimbert, A. Peimbert, M. T. Ruiz, M. Rodríguez, & L. Carigi (2005, January). Carbon and Oxygen Galactic Gradients: Observational Values from H II Region Recombination Lines. *ApJ 618*, L95–L98.

Fagotto, F., A. Bressan, G. Bertelli, & C. Chiosi (1994a, April). Evolutionary sequences of stellar models with new radiative opacities. III. Z=0.0004 and Z=0.05. *A&AS 104*, 365–376.

Fagotto, F., A. Bressan, G. Bertelli, & C. Chiosi (1994b, May). Evolutionary sequences of stellar models with new radiative opacities. IV. Z=0.004 and Z=0.008. *A&AS 105*, 29–38.

Fagotto, F., A. Bressan, G. Bertelli, & C. Chiosi (1994c, May). Evolutionary sequences of stellar models with very high metallicity. V. Z=0.1. *A&AS 105*, 39–45.

Ferguson, J. W., D. R. Alexander, F. Allard, T. Barman, J. G. Bodnarik, P. H. Hauschildt, A. Heffner-Wong, & A. Tamanai (2005, April). Low-Temperature Opacities. *ApJ 623*, 585–596.

Ferraro, F. R., F. Fusi Pecci, V. Testa, L. Greggio, C. E. Corsi, R. Buonanno, D. M. Terndrup, & H. Zinnecker (1995, January). Globular clusters in the Magellanic Clouds - II. IR-array photometry for 12 globular clusters and contributions to the integrated cluster light. *MNRAS 272*, 391–422.

Ferrarotti, A. S. (2003). *Staubbildung in Sternwinden*. Ph. D. thesis, PhD Thesis, Naturwissenschaftlich-Mathematische Gesamtfakultät der Universität Heidelberg, Germany. III + 143 pp. (2003).

Ferrarotti, A. S. & H. Gail (2002, January). Mineral formation in stellar winds. III. Dust formation in S stars. *A&A 382*, 256–281.

Ferrarotti, A. S. & H.-P. Gail (2001, May). Mineral formation in stellar winds. II. Effects of Mg/Si abundance variations on dust composition in AGB stars. *A&A 371*, 133–151.

Ferrarotti, A. S. & H.-P. Gail (2006, February). Composition and quantities of dust produced by AGB-stars and returned to the interstellar medium. *A&A 447*, 553–576.

Finkelstein, S. L., J. A. Morse, J. C. Green, & COS Science (2004, December). HST Proper-Motion Measurements of the Supernova Remnant E0102-7219. In *Bulletin of the American Astronomical Society*, Volume 36 of *Bulletin of the American Astronomical Society*, pp. 1510.

Fioc, M. & B. Rocca-Volmerange (1997, October). PEGASE: a UV to NIR spectral evolution model of galaxies. Application to the calibration of bright galaxy counts. *A&A 326*, 950–962.

Fluks, M. A., B. Plez, P. S. The, D. de Winter, B. E. Westerlund, & H. C. Steenman (1994, June). On the spectra and photometry of M-giant stars. *A&AS 105*, 311–336.

Fouqué, P., L. Chevallier, M. Cohen, E. Galliano, C. Loup, C. Alard, B. de Batz, E. Bertin, J. Borsenberger, M. R. Cioni, E. Copet, M. Dennefeld, S. Derriere, E. Deul, P.-A. Duc, D. Egret, N. Epchtein, T. Forveille, F. Garzón, H. J. Habing, J. Hron, S. Kimeswenger, F. Lacombe, T. Le Bertre, G. A. Mamon, A. Omont, G. Paturel, S. Pau, P. Persi, A. C. Robin, D. Rouan, M. Schultheis, G. Simon, D. Tiphène, I. Vauglin, & S. J. Wagner (2000, January). An absolute calibration of DENIS (deep near infrared southern sky survey). *A&AS 141*, 313–317.

François, P., F. Matteucci, R. Cayrel, M. Spite, F. Spite, & C. Chiappini (2004, July). The evolution of the Milky Way from its earliest phases: Constraints on stellar nucleosynthesis. *A&A 421*, 613–621.

Froehlich, H.-E. (1982). Dusty King spheres. *Astronomische Nachrichten 303*, 97–103.

Frogel, J. A. (1988). The Galactic nuclear bulge and the stellar content of spheroidal systems. *ARA&A 26*, 51–92.

Frogel, J. A. (1999, July). A Brief History of Star Formation and Chemical Enrichment in the Bulge of the Milky way. *Ap&SS 265*, 303–309.

Fukugita, M., T. Ichikawa, J. E. Gunn, M. Doi, K. Shimasaku, & D. P. Schneider (1996, April). The Sloan Digital Sky Survey Photometric System. *AJ 111*, 1748.

Fusi Pecci, F., C. Cacciari, L. Federici, & A. Pasquali (1993, January). The M31 Globular Clusters: Status of the Search, Photometry and Spatial Distribution, and HST Observations. In G. H. Smith & J. P. Brodie (Ed.), *The Globular Cluster-Galaxy Connection*, Volume 48 of *Astronomical Society of the Pacific Conference Series*, pp. 410.

Gail, H., R. Keller, & E. Sedlmayr (1984, April). Dust formation in stellar winds. I - A rapid computational method and application to graphite condensation. *A&A 133*, 320–332.

Gail, H. & E. Sedlmayr (1985, July). Dust formation in stellar winds. II - Carbon condensation in stationary, spherically expanding winds. *A&A 148*, 183–190.

Gail, H. & E. Sedlmayr (1999, July). Mineral formation in stellar winds. I. Condensation sequence of silicate and iron grains in stationary oxygen rich outflows. *A&A 347*, 594–616.

Gail, H., S. V. Zhukovska, P. Hoppe, & M. Trieloff (2009, June). Stardust from Asymptotic Giant Branch Stars. *ApJ 698*, 1136–1154.

Gail, H. P. & E. Sedlmayr (1987, January). Dust formation in stellar winds. III - Self-consistent models for dust-driven winds around C-stars. *A&A 171*, 197–204.

Gall, C., A. C. Andersen, & J. Hjorth (2011a, April). Genesis and evolution of dust in galaxies in the early Universe. I. Modelling dust evolution in starburst galaxies. *A&A 528*, A13+.

Gall, C., A. C. Andersen, & J. Hjorth (2011b, April). Genesis and evolution of dust in galaxies in the early Universe. II. Rapid dust evolution in quasars at z ¿ 6. *A&A 528*, A14+.

Gallerani, S., R. Maiolino, Y. Juarez, T. Nagao, A. Marconi, S. Bianchi, R. Schneider, F. Mannucci, T. Oliva, C. J. Willott, L. Jiang, & X. Fan (2010, November). The extinction law at high redshift and its implications. *A&A 523*, A85+.

Galliano, F., E. Dwek, & P. Chanial (2008, January). Stellar Evolutionary Effects on the Abundances of Polycyclic Aromatic Hydrocarbons and Supernova-Condensed Dust in Galaxies. *ApJ 672*, 214–243.

Galliano, F., S. C. Madden, A. G. G. M. Tielens, E. Peeters, & A. P. Jones (2008, May). Variations of the Mid-IR Aromatic Features inside and among Galaxies. *ApJ 679*, 310–345.

Gavazzi, G. & A. Boselli (1996). A UBVJHK Photometric Catalogue of 1022 Galaxies in nearby clusters (Special Issue). *Astrophysical Letters Communications 35*, 1.

Gavazzi, G., A. Boselli, & R. Kennicutt (1991, April). Multifrequency windows on spiral galaxies. I - UBV and H-alpha aperture photometry. *AJ 101*, 1207–1230.

Geisler, D. & E. D. Friel (1992, July). The metallicity distribution of G and K giants in Baade's window. *AJ 104*, 128–143.

Gibson, B. K. (1994, December). On the Influence of Supernova Remnant Thermal Energy in Powering Galactic Winds. *88*, 383.

Gibson, B. K. & F. Matteucci (1997, January). On Dwarf Galaxies as the Source of Intracluster Gas. *ApJ 475*, 47.

Gibson, B. K., P. Sánchez-Blázquez, S. Courty, & D. Kawata (2007). Chemodynamical Simulations of Elliptical Galaxies. In E. Emsellem, H. Wozniak, G. Massacrier, J.-F. Gonzalez, J. Devriendt, & N. Champavert (Ed.), *EAS Publications Series*, Volume 24 of *EAS Publications Series*, pp. 133–138.

Gilman, R. C. (1969, March). On the Composition of Circumstellar Grains. *ApJ 155*, L185.

Gilman, R. C. (1972, December). On the Coupling of Grains to the Gas in Circumstellar Envelopes. *ApJ 178*, 423–426.

Gilmore, G., R. F. G. Wyse, & K. Kuijken (1989). Stellar dynamics and Galactic evolution. In J. E. Beckman & B. E. J. Pagel (Ed.), *Evolutionary Phenomena in Galaxies*, pp. 172–200.

Girardi, L., G. Bertelli, A. Bressan, C. Chiosi, M. A. T. Groenewegen, P. Marigo, B. Salasnich, & A. Weiss (2002, August). Theoretical isochrones in several photometric systems. I. Johnson-Cousins-Glass, HST/WFPC2, HST/NICMOS, Washington, and ESO Imaging Survey filter sets. *A&A 391*, 195–212.

Girardi, L., A. Bressan, G. Bertelli, & C. Chiosi (2000, February). Evolutionary tracks and isochrones for low- and intermediate-mass stars: From 0.15 to 7 M_{sun}, and from Z=0.0004 to 0.03. *A&AS 141*, 371–383.

Girardi, L., A. Bressan, C. Chiosi, G. Bertelli, & E. Nasi (1996, May). Evolutionary sequences of stellar models with new radiative opacities. VI. Z=0.0001. *A&AS 117*, 113–125.

Girardi, L., E. K. Grebel, M. Odenkirchen, & C. Chiosi (2004, July). Theoretical isochrones in several photometric systems. II. The Sloan Digital Sky Survey ugriz system. *A&A 422*, 205–215.

Girardi, L. & P. Marigo (2007, November). Towards Simulating the Photometry, Chemistry, Mass Loss and Pulsational Properties of AGB Star Populations in Resolved Galaxies. In F. Kerschbaum, C. Charbonnel, & R. F. Wing (Ed.), *Why Galaxies Care About AGB Stars: Their Importance as Actors and Probes*, Volume 378 of *Astronomical Society of the Pacific Conference Series*, pp. 20.

Goldsmith, P. F. (2001, August). Molecular Depletion and Thermal Balance in Dark Cloud Cores. *ApJ 557*, 736–746.

Gomez, H. L., L. Dunne, R. J. Ivison, E. M. Reynoso, M. A. Thompson, B. Sibthorpe, S. A. Eales, T. M. Delaney, S. Maddox, & K. Isaak (2009, August). Accounting for the foreground contribution to the dust emission towards Kepler's supernova remnant. *MNRAS 397*, 1621–1632.

Gomez, H. L., S. A. Eales, & L. Dunne (2007, February). Smoking supernovae. *International Journal of Astrobiology 6*, 159–167.

Goudfrooij, P., M. V. Alonso, C. Maraston, & D. Minniti (2001, November). The star cluster system of the 3-Gyr-old merger remnant NGC 1316: clues from optical and near-infrared photometry. *MNRAS 328*, 237–256.

Goudfrooij, P., J. Gorgas, & P. Jablonka (1999, December). Line Strengths and Line Strength Gradients in Bulges along the Hubble Sequence. *Ap&SS 269*, 109–116.

Grassi, T., P. Krstic, E. Merlin, U. Buonomo, L. Piovan, & C. Chiosi (2010, December). ROBO: a Model and a Code for the Study of the Interstellar Medium. *ArXiv e-prints*.

Grassi, T., E. Merlin, L. Piovan, U. Buonomo, & C. Chiosi (2011, March). MaNN: Multiple Artificial Neural Networks for modelling the Interstellar Medium. *ArXiv e-prints*.

Gratton, R. G., E. Carretta, R. Claudi, S. Lucatello, & M. Barbieri (2003, June). Abundances for metal-poor stars with accurate parallaxes. I. Basic data. *A&A 404*, 187–210.

Grebel, E. K. & W. J. Roberts (1995, February). Heterochromatic extinction. I. Dependence of interstellar extinction on stellar temperature, surface gravity, and metallicity. *A&AS 109*, 293–312.

Greggio, L. & A. Renzini (1983). *A&A 118*, 217.

Greggio, L. & A. Renzini (1990, November). Clues on the hot star content and the ultraviolet output of elliptical galaxies. *ApJ 364*, 35–64.

Grevesse, N., M. Asplund, & A. J. Sauval (2007, June). The Solar Chemical Composition. *Space Science Reviews 130*, 105–114.

Grevesse, N. & A. Noels (1993). Atomic data and the spectrum of the solar photosphere. *Physica Scripta Volume T 47*, 133–138.

Grevesse, N. & A. J. Sauval (1998, May). Standard Solar Composition. *Space Science Reviews 85*, 161–174.

Groenewegen, M. A. T. (1993). *On the evolution and properties of AGB stars*. Ph. D. thesis, , Univ. of Amsterdam (1993).

Groenewegen, M. A. T. (1995, January). Dust shells around infrared carbon stars. *A&A 293*, 463–478.

Groenewegen, M. A. T. (2006, March). The mid- and far-infrared colours of AGB and post-AGB stars. *A&A 448*, 181–187.

Groenewegen, M. A. T. & T. de Jong (1993, January). Synthetic AGB evolution. I - A new model. *A&A 267*, 410–432.

Groenewegen, M. A. T., P. A. Whitelock, C. H. Smith, & F. Kerschbaum (1998, January). Dust shells around carbon Mira variables. *MNRAS 293*, 18.

Guesten, R. & P. G. Mezger (1982). Star formation and abundance gradients in the galaxy. *Vistas in Astronomy 26*, 159–224.

Guhathakurta, P. & B. T. Draine (1989, October). Temperature fluctuations in interstellar grains. I - Computational method and sublimation of small grains. *ApJ 345*, 230–244.

Guibert, J., J. Lequeux, & F. Viallefond (1978, August). Star formation in interstellar gas density in our Galaxy. *A&A 68*, 1–15.

Gummersbach, C. A., A. Kaufer, D. R. Schaefer, T. Szeifert, & B. Wolf (1998, October). B stars and the chemical evolution of the Galactic disk. *A&A 338*, 881–896.

Gunawardhana, M. L. P., A. M. Hopkins, R. G. Sharp, S. Brough, E. Taylor, J. Bland-Hawthorn, C. Maraston, R. J. Tuffs, C. C. Popescu, D. Wijesinghe, D. H. Jones, S. Croom, E. Sadler, S. Wilkins, S. P. Driver, J. Liske, P. Norberg, I. K. Baldry, S. P. Bamford, J. Loveday, J. A. Peacock, A. S. G. Robotham, D. B. Zucker, Q. A. Parker, C. J. Conselice, E. Cameron, C. S. Frenk, D. T. Hill, L. S. Kelvin, K. Kuijken, B. F. Madore, B. Nichol, H. R. Parkinson, K. A. Pimbblet, M. Prescott, W. J. Sutherland, D. Thomas, & E. van Kampen (2011, April). Galaxy And Mass Assembly (GAMA): The star formation rate dependence of the stellar initial mass function. *ArXiv e-prints*.

Habing, H. J. (1996). Circumstellar envelopes and asymptotic giant branch stars. *ARA&A 7*, 97–207.

Habing, H. J., J. Tignon, & A. G. G. M. Tielens (1994, June). Calculations of the outflow velocity of envelopes of cool giants. *A&A 286*, 523–534.

Hackwell, J. A. (1972, November). Long wavelength spectrometry and photometry of M, S and C-stars. *A&A 21*, 239.

Harris, W. E. (1991). Globular cluster systems in galaxies beyond the Local Group. *ARA&A 29*, 543–579.

Hayes, D. S. (1985). Stellar absolute fluxes and energy distributions from 0.32 to 4.0 microns. In D. S. Hayes, L. E. Pasinetti, & A. G. D. Philip (Ed.), *Calibration of Fundamental Stellar Quantities*, Volume 111 of *IAU Symposium*, pp. 225–249.

Hayes, D. S. & D. W. Latham (1975, March). The MT. Hopkins Calibration of the Spectral Energy Distribution of VEGA. In A. G. D. Philip, D. S. Hayes, & D. C. Crawford (Ed.), *Multicolor Photometry and the Theoretical HR Diagram*, pp. 215.

Hendry, M. A. & S. J. Smartt (2005, December). SN 2003gd: A Normal Type II-P Supernova? In M. Turatto, S. Benetti, L. Zampieri, & W. Shea (Eds.), *1604-2004: Supernovae as Cosmological Lighthouses*, Volume 342 of *Astronomical Society of the Pacific Conference Series*, pp. 341.

Heras, A. M. & S. Hony (2005, August). Oxygen-rich AGB stars with optically thin dust envelopes. *A&A 439*, 171–182.

Herwig, F. (2004, December). Evolution and Yields of Extremely Metal-poor Intermediate-Mass Stars. *ApJS 155*, 651–666.

Herwig, F., T. Bloecker, D. Schoenberner, & M. El Eid (1997, August). Stellar evolution of low and intermediate-mass stars. IV. Hydrodynamically-based overshoot and nucleosynthesis in AGB stars. *A&A 324*, L81–L84.

Hewett, P. C., S. J. Warren, S. K. Leggett, & S. T. Hodgkin (2006, April). The UKIRT Infrared Deep Sky Survey ZY JHK photometric system: passbands and synthetic colours. *MNRAS 367*, 454–468.

Hirashita, H., T. Nozawa, T. Kozasa, T. T. Ishii, & T. T. Takeuchi (2005, March). Extinction curves expected in young galaxies. *MNRAS 357*, 1077–1087.

Holland, S. (1998). *The Globular Clusters and Halo of M31*. Ph. D. thesis, THE UNIVERSITY OF BRITISH COLUMBIA (CANADA).

Holmberg, J. & C. Flynn (2004, August). The local surface density of disc matter mapped by Hipparcos. *MNRAS 352*, 440–446.

Holtzman, J. A., C. J. Burrows, S. Casertano, J. J. Hester, J. T. Trauger, A. M. Watson, & G. Worthey (1995, November). The Photometric Performance and Calibration of WFPC2. *PASP 107*, 1065.

Hony, S., L. B. F. M. Waters, & A. G. G. M. Tielens (2002, August). The carrier of the "30" mu m emission feature in evolved stars. A simple model using magnesium sulfide. *A&A 390*, 533–553.

Hoppe, P., R. Strebel, P. Eberhardt, S. Amari, & R. S. Lewis (2000, November). Isotopic properties of silicon carbide X grains from the Murchison meteorite in the size range 0.5-1.5 μm. *Meteoritics and Planetary Science 35*, 1157–1176.

Hou, J., R. Chang, & L. Chen (2002, February). Abundance Gradient from Open Clusters and Implications for the Galactic Disk Evolution. *Chinese Journal of Astronomy and Astrophysics 2*, 17–32.

Hou, J. L., J. Yin, S. Boissier, N. Prantzos, R. X. Chang, & L. Chen (2008, July). Properties and Chemical Evolution of the M31 Disk: Comparison with the Milky Way. *ArXiv:astro-ph/0807.2492*.

Ibukiyama, A. & N. Arimoto (2002, November). HIPPARCOS age-metallicity relation of the solar neighbourhood disc stars. *A&A 394*, 927–941.

Iglesias, C. A. & F. J. Rogers (1996, June). Updated Opal Opacities. *ApJ 464*, 943–+.

Im, M., S. Casertano, R. E. Griffiths, K. U. Ratnatunga, & J. A. Tyson (1995, March). A test of galaxy evolutionary models via angular sizes. *ApJ 441*, 494–504.

Ivezic, Z. & M. Elitzur (1997, June). Self-similarity and scaling behaviour of infrared emission from radiatively heated dust - I. Theory. *MNRAS 287*, 799–811.

Izzard, R. G. & A. J. T. Poelarends (2006). Synthetic super-AGB stars. *Memorie della Societa Astronomica Italiana 77*, 840.

Jablonka, P., N. Arimoto, & P. Martin (1996). The Overabundance of Magnesium Over Iron in the Bulges of Spiral Galaxies. In R. Bender & R. L. Davies (Ed.), *New Light on Galaxy Evolution*, Volume 171 of *IAU Symposium*, pp. 395.

Jaeger, C., F. J. Molster, J. Dorschner, T. Henning, H. Mutschke, & L. B. F. M. Waters (1998, November). Steps toward interstellar silicate mineralogy. IV. The crystalline revolution. *A&A 339*, 904–916.

Jenkins, E. B. (2009, August). A Unified Representation of Gas-Phase Element Depletions in the Interstellar Medium. *ApJ 700*, 1299–1348.

Johnson, H. L. (1966). Astronomical Measurements in the Infrared. *ARA&A 4*, 193.

Jones, A. P. (2004, May). Dust Destruction Processes. In A. N. Witt, G. C. Clayton, & B. T. Draine (Ed.), *Astrophysics of Dust*, Volume 309 of *Astronomical Society of the Pacific Conference Series*, pp. 347–+.

Jonsell, K., B. Edvardsson, B. Gustafsson, P. Magain, P. E. Nissen, & M. Asplund (2005, September). Chemical abundances in 43 metal-poor stars. *A&A 440*, 321–343.

Jonsson, P., B. A. Groves, & T. J. Cox (2010, March). High-resolution panchromatic spectral models of galaxies including photoionization and dust. *MNRAS 403*, 17–44.

Karakas, A. I. & J. C. Lattanzio (2003). Production of Aluminium and the Heavy Magnesium Isotopes in Asymptotic Giant Branch Stars. *Publications of the Astronomical Society of Australia 20*, 279–293.

Karakas, A. I., J. C. Lattanzio, & O. R. Pols (2002). Parameterising the Third Dredge-up in Asymptotic Giant Branch Stars. *Publications of the Astronomical Society of Australia 19*, 515–526.

Kemper, F., A. J. Markwick, & P. M. Woods (2011, May). The crystalline fraction of interstellar silicates in starburst galaxies. *MNRAS 413*, 1192–1199.

Kennicutt, Jr., R. C. (1983, September). The rate of star formation in normal disk galaxies. *ApJ 272*, 54–67.

Kennicutt, Jr., R. C. (1998, May). The Global Schmidt Law in Star-forming Galaxies. *ApJ 498*, 541–+.

Kennicutt, Jr., R. C., P. Tamblyn, & C. E. Congdon (1994, November). Past and future star formation in disk galaxies. *ApJ 435*, 22–36.

Kormendy, J. (1977, December). Brightness distributions in compact and normal galaxies. II - Structure parameters of the spheroidal component. *ApJ 218*, 333–346.

Kotak, R. (2008, June). Core-Collapse Supernovae as Dust Producers. In F. Bresolin, P. A. Crowther, & J. Puls (Eds.), *IAU Symposium*, Volume 250 of *IAU Symposium*, pp. 437–442.

Kotak, R., P. Meikle, D. Farrah, C. Gerardy, R. Foley, S. van Dyk, C. Fransson, P. Lundqvist, J. Sollerman, R. Fesen, A. Filippenko, S. Mattila, A. Andersen, P. Hoeflich, M. Pozzo, & J. C. Wheeler (2009, April). Dust and the type II-plateau supernova 2004et. *ArXiv:astro-ph/0904.3737*.

Kotak, R., P. Meikle, M. Pozzo, S. D. van Dyk, D. Farrah, R. Fesen, A. V. Filippenko, R. J. Foley, C. Fransson, C. L. Gerardy, P. A. Höflich, P. Lundqvist, S. Mattila, J. Sollerman, & J. C. Wheeler (2006, November). Spitzer Measurements of Atomic and Molecular Abundances in the Type IIP SN 2005af. *ApJ 651*, L117–L120.

Kovtyukh, V. V., S. M. Andrievsky, I. A. Usenko, & V. G. Klochkova (1996, December). The chemical composition of the s-Cepheids. III. *A&A 316*, 155–163.

Kovtyukh, V. V., G. Wallerstein, & S. M. Andrievsky (2005, November). Galactic Cepheids. I. Elemental Abundances and Their Implementation for Stellar and Galactic Evolution. *PASP 117*, 1173–1181.

Kozasa, T., T. Nozawa, N. Tominaga, H. Umeda, K. Maeda, & K. Nomoto (2009, March). Dust in Supernovae; Formation and Evolution. *ArXiv:astro-ph/0903.0217*.

Krause, O., S. M. Birkmann, G. H. Rieke, D. Lemke, U. Klaas, D. C. Hines, & K. D. Gordon (2004, December). No cold dust within the supernova remnant Cassiopeia A. *432*, 596–598.

Krause, O., S. M. Birkmann, T. Usuda, T. Hattori, M. Goto, G. H. Rieke, & K. A. Misselt (2008, May). The Cassiopeia A Supernova Was of Type IIb. *320*, 1195–.

Kroupa, P. (1998, July). On the binary properties and the spatial and kinematical distribution of young stars. *MNRAS 298*, 231–242.

Kroupa, P. (2001). The Local Stellar Initial Mass Function. In S. Deiters, B. Fuchs, A. Just, R. Spurzem, & R. Wielen (Ed.), *Dynamics of Star Clusters and the Milky Way*, Volume 228 of *Astronomical Society of the Pacific Conference Series*, pp. 187–+.

Kroupa, P. (2002a). The Initial Mass Function and Its Variation (Review). In E. K. Grebel & W. Brandner (Ed.), *Modes of Star Formation and the Origin of Field Populations*, Volume 285 of *Astronomical Society of the Pacific Conference Series*, pp. 86–+.

Kroupa, P. (2002b, January). The Initial Mass Function of Stars: Evidence for Uniformity in Variable Systems. *Science 295*, 82–91.

Kroupa, P. (2007, March). The initial mass function of simple and composite stellar populations. *ArXiv Astrophysics e-prints*.

Kroupa, P. (2011, April). The universality hypothesis: binary and stellar populations in star clusters and galaxies. In J. Alves, B. G. Elmegreen, J. M. Girart, & V. Trimble (Ed.), *IAU Symposium*, Volume 270 of *IAU Symposium*, pp. 141–149.

Kroupa, P., C. A. Tout, & G. Gilmore (1993, June). The distribution of low-mass stars in the Galactic disc. *MNRAS 262*, 545–587.

Krumholz, M. R., C. D. Matzner, & C. F. McKee (2006, December). The Global Evolution of Giant Molecular Clouds. I. Model Formulation and Quasi-Equilibrium Behavior. *ApJ 653*, 361–382.

Kurucz, R. L. (1993, October). Model Atmospheres (Kurucz, 1979). *VizieR Online Data Catalog 6039*, 0.

Landi, E., U. Feldman, & G. A. Doschek (2007, April). Neon and Oxygen Absolute Abundances in the Solar Corona. *ApJ 659*, 743–749.

Laor, A. & B. T. Draine (1993, January). Spectroscopic constraints on the properties of dust in active galactic nuclei. *ApJ 402*, 441–468.

Larson, R. B. (1976). *MNRAS 166*, 585.

Larson, R. B. (1986). *MNRAS 218*, 409.

Larson, R. B. (1998, December). Early star formation and the evolution of the stellar initial mass function in galaxies. *MNRAS 301*, 569–581.

Larson, R. B. & B. M. Tinsley (1978, January). Star formation rates in normal and peculiar galaxies. *ApJ 219*, 46–59.

Le Floc'h, E., C. Papovich, H. Dole, E. F. Bell, G. Lagache, G. H. Rieke, E. Egami, P. G. Pérez-González, A. Alonso-Herrero, M. J. Rieke, M. Blaylock, C. W. Engelbracht, K. D. Gordon,

D. C. Hines, K. A. Misselt, J. E. Morrison, & J. Mould (2005, October). Infrared Luminosity Functions from the Chandra Deep Field-South: The Spitzer View on the History of Dusty Star Formation at $0 < z < 1$. *ApJ 632*, 169–190.

Lebzelter, T., T. Posch, K. Hinkle, P. R. Wood, & J. Bouwman (2006, December). Tracing the Development of Dust around Evolved Stars: The Case of 47 Tuc. *ApJ 653*, L145–L148.

Lee, J., E. A. Bergin, & J. R. Lyons (2008, November). Oxygen isotope anomalies of the Sun and the original environment of the solar system. *Meteoritics and Planetary Science 43*, 1351–1362.

Leger, A. & J. L. Puget (1984, August). Identification of the 'unidentified' IR emission features of interstellar dust? *A&A 137*, L5–L8.

Lejeune, T., F. Cuisinier, & R. Buser (1997). *A&AS 125*, 299.

Lejeune, T., F. Cuisinier, & R. Buser (1998). *A&AS 130*, 65.

Lejeune, T. & D. Schaerer (2001, February). Database of Geneva stellar evolution tracks and isochrones for $(UBV)_J(RI)_C$ JHKLL'M, HST-WFPC2, Geneva and Washington photometric systems. *A&A 366*, 538–546.

Lemasle, B., P. François, G. Bono, M. Mottini, F. Primas, & M. Romaniello (2007, May). Detailed chemical composition of Galactic Cepheids. A determination of the Galactic abundance gradient in the 8-12 kpc region. *A&A 467*, 283–294.

Lemasle, B., P. François, A. Piersimoni, S. Pedicelli, G. Bono, C. D. Laney, F. Primas, & M. Romaniello (2008, November). Galactic abundance gradients from Cepheids. On the iron abundance gradient around 10-12 kpc. *A&A 490*, 613–623.

Leshin, L. A., A. E. Rubin, & K. D. McKeegan (1997, February). The oxygen isotopic composition of olivine and pyroxene from CI chondrites. *61*, 835–845.

Li, A. & B. T. Draine (2001, June). Infrared Emission from Interstellar Dust. II. The Diffuse Interstellar Medium. *ApJ 554*, 778–802.

Li, A. & J. Mayo Greenberg (2002). In dust we trust: an overview of observations and theories of interstellar dust. In V. Pirronello & J. Krelowski (Eds.), *Solid State Astrochemistry*, pp. 1–45. Kluwer.

Liszt, H. S. (2007, December). Formation, fractionation, and excitation of carbon monoxide in diffuse clouds. *A&A 476*, 291–300.

Lodders, K. (2003, July). Solar System Abundances and Condensation Temperatures of the Elements. *ApJ 591*, 1220–1247.

Lodders, K., H. Palme, & H. Gail (2009, January). Abundances of the elements in the solar system. *ArXiv e-prints*.

Lorenz-Martins, S., F. X. de Araújo, S. J. Codina Landaberry, W. G. de Almeida, & R. V. de Nader (2001, February). Modeling of C stars with core/mantle grains: Amorphous carbon + SiC. *A&A 367*, 189–198.

Lorenz-Martins, S. & J. Lefevre (1994, November). SiC grains and evolution of carbon stars. *A&A 291*, 831–841.

Lorenz-Martins, S. & L. Pompeia (2000, July). Modelling of oxygen-rich envelopes using corundum and silicate grains. *MNRAS 315*, 856–864.

Luck, R. E. (1978, January). The chemical composition of late-type supergiants. III - Carbon, nitrogen, and oxygen abundances for 19 G and K Ib stars. *ApJ 219*, 148–164.

Luck, R. E., W. P. Gieren, S. M. Andrievsky, V. V. Kovtyukh, P. Fouqué, F. Pont, & F. Kienzle (2003, April). The galactic abundance gradient from Cepheids. IV. New results for the outer disc. *A&A 401*, 939–949.

Luck, R. E., V. V. Kovtyukh, & S. M. Andrievsky (2006, August). The Distribution of the Elements in the Galactic Disk. *AJ 132*, 902–918.

Luck, R. E. & D. L. Lambert (1981, May). The abundances of carbon, nitrogen, and oxygen in the atmospheres of Cepheid variables - Evidence for helium enrichment. *ApJ 245*, 1018–1034.

Ludwig, H., E. Caffau, M. Steffen, P. Bonifacio, B. Freytag, & R. Cayrel (2009, November). Solar abundances and 3D model atmospheres. *ArXiv e-prints*.

Ludwig, H. & M. Steffen (2008). Hydrodynamical Model Atmospheres and 3D Spectral Synthesis. In N. C. Santos, L. Pasquini, A. C. M. Correia, & M. Romaniello (Ed.), *Precision Spectroscopy in Astrophysics*, pp. 133–138.

Lynden-Bell, D. (1975). The chemical evolution of galaxies. *Vistas in Astronomy 19*, 299–316.

Lyne, A. G., R. N. Manchester, & J. H. Taylor (1985, April). The galactic population of pulsars. *MNRAS 213*, 613–639.

Ma, J. (2011, November). 2MASS photometry and age estimate of globular clusters in the outer halo of M31. *ArXiv e-prints*.

Mackey, A. D., A. Huxor, A. M. N. Ferguson, N. R. Tanvir, M. Irwin, R. Ibata, T. Bridges, R. A. Johnson, & G. Lewis (2006, December). ACS Photometry of Extended, Luminous Globular Clusters in the Outskirts of M31. *ApJ 653*, L105–L108.

Mackey, A. D., A. Huxor, A. M. N. Ferguson, N. R. Tanvir, M. Irwin, R. Ibata, T. Bridges, R. A. Johnson, & G. Lewis (2007, February). ACS Photometry of Newly Discovered Globular Clusters in the Outer Halo of M31. *ApJ 655*, L85–L88.

Magrini, L., P. Sestito, S. Randich, & D. Galli (2009, January). The evolution of the Galactic metallicity gradient from high-resolution spectroscopy of open clusters. *A&A 494*, 95–108.

Maiorca, E., E. Caffau, P. Bonifacio, M. Busso, R. Faraggiana, M. Steffen, H. Ludwig, & I. Kamp (2009, September). The Solar Photospheric Nitrogen Abundance: Determination with 3D and 1D Model Atmospheres. *Publications of the Astronomical Society of Australia 26*, 345–350.

Maíz Apellániz, J. (2006, February). A Recalibration of Optical Photometry: Tycho-2, Strömgren, and Johnson Systems. *AJ 131*, 1184–1199.

Marigo, P. (2002, May). Asymptotic Giant Branch evolution at varying surface C/O ratio: effects of changes in molecular opacities. *A&A 387*, 507–519.

Marigo, P., A. Bressan, & C. Chiosi (1996, September). The TP-AGB phase: a new model. *A&A 313*, 545–564.

Marigo, P., A. Bressan, & C. Chiosi (1998, March). TP-AGB stars with envelope burning. *A&A 331*, 564–580.

Marigo, P. & L. Girardi (2001, October). Coupling emitted light and chemical yields from stars: A basic constraint to population synthesis models of galaxies. *A&A 377*, 132–147.

Marigo, P. & L. Girardi (2007, July). Evolution of asymptotic giant branch stars. I. Updated synthetic TP-AGB models and their basic calibration. *A&A 469*, 239–263.

Marigo, P., L. Girardi, A. Bressan, M. A. T. Groenewegen, L. Silva, & G. L. Granato (2008, May). Evolution of asymptotic giant branch stars. II. Optical to far-infrared isochrones with improved TP-AGB models. *A&A 482*, 883–905.

Martín-Hernández, N. L., E. Peeters, C. Morisset, A. G. G. M. Tielens, P. Cox, P. R. Roelfsema, J. Baluteau, D. Schaerer, J. S. Mathis, F. Damour, E. Churchwell, & M. F. Kessler (2002, January). ISO spectroscopy of compact H II regions in the Galaxy. II. Ionization and elemental abundances. *A&A 381*, 606–627.

Mashonkina, L., A. J. Korn, & N. Przybilla (2007, January). A non-LTE study of neutral and singly-ionized calcium in late-type stars. *A&A 461*, 261–275.

Mathis, J. S. (1990). Interstellar dust and extinction. *ARA&A 28*, 37–70.

Matsuura, M., E. Dwek, M. Meixner, M. Otsuka, & e. a. Babler, B. (2011, July). Herschel Detects a Massive Dust Reservoir in Supernova 1987A. *ArXiv e-prints*.

Matteucci, F. & P. François (1989, August). Galactic chemical evolution - Abundance gradients of individual elements. *MNRAS 239*, 885–904.

Matteucci, F. & L. Greggio (1986). *A&A 154*, 279.

Matthews, W. G. & J. C. Baker (1971). *ApJ 170*, 241.

Mattila, K., D. Lemke, L. K. Haikala, R. J. Laureijs, A. Leger, K. Lehtinen, C. Leinert, & P. G. Mezger (1996, November). Spectrophotometry of UIR bands in the diffuse emission of the galactic disk. *A&A 315*, L353–L356.

Mattsson, L. (2011, March). Dust in the early Universe: evidence for non-stellar dust production or observational errors? *MNRAS*, 451–+.

Matzner, C. D. (2002, February). On the Role of Massive Stars in the Support and Destruction of Giant Molecular Clouds. *ApJ 566*, 302–314.

McConnachie, A. W., M. J. Irwin, A. M. N. Ferguson, R. A. Ibata, G. F. Lewis, & N. Tanvir (2005, January). Distances and metallicities for 17 Local Group galaxies. *MNRAS 356*, 979–997.

McCray, R. (1993). Supernova 1987A revisited. *ARA&A 31*, 175–216.

McDonald, I., J. T. van Loon, G. C. Sloan, A. K. Dupree, A. A. Zijlstra, M. L. Boyer, R. D. Gehrz, A. Evans, C. E. Woodward, & C. I. Johnson (2011, April). Spitzer spectra of evolved stars in omega Centauri and their low-metallicity dust production. *ArXiv e-prints*.

McGregor, P., J. Hart, M. Downing, D. Hoadley, & G. Bloxham (1994, March). CASPIR: A cryogenic array spectrometer/imager for the MSSSO 2.3 M telescope. *Experimental Astronomy 3*, 139–140.

Meikle, W. P. S., S. Mattila, A. Pastorello, C. L. Gerardy, R. Kotak, J. Sollerman, S. D. Van Dyk, D. Farrah, A. V. Filippenko, P. Höflich, P. Lundqvist, M. Pozzo, & J. C. Wheeler (2007, August). A Spitzer Space Telescope Study of SN 2003gd: Still No Direct Evidence that Core-Collapse Supernovae are Major Dust Factories. *ApJ 665*, 608–617.

Meixner, M., K. D. Gordon, R. Indebetouw, J. L. Hora, B. Whitney, R. Blum, W. Reach, J.-P. Bernard, M. Meade, B. Babler, C. W. Engelbracht, B.-Q. For, K. Misselt, U. Vijh, C. Leitherer, M. Cohen, E. B. Churchwell, F. Boulanger, J. A. Frogel, Y. Fukui, J. Gallagher, V. Gorjian, J. Harris, D. Kelly, A. Kawamura, S. Kim, W. B. Latter, S. Madden, C. Markwick-Kemper, A. Mizuno, N. Mizuno, J. Mould, A. Nota, M. S. Oey, K. Olsen, T. Onishi, R. Paladini, N. Panagia, P. Perez-Gonzalez, H. Shibai, S. Sato, L. Smith, L. Staveley-Smith, A. G. G. M. Tielens, T. Ueta, S. van Dyk, K. Volk, M. Werner, & D. Zaritsky (2006, December). Spitzer Survey of the Large Magellanic Cloud: Surveying the Agents of a Galaxy's Evolution (SAGE). I. Overview and Initial Results. *AJ 132*, 2268–2288.

Meléndez, J. & M. Asplund (2008, November). Another forbidden solar oxygen abundance: the [O I] 5577 Å line. *A&A 490*, 817–821.

Meléndez, J. & B. Barbuy (2002, August). Keck NIRSPEC Infrared OH Lines: Oxygen Abundances in Metal-poor Stars down to [Fe/H] = -2.9. *ApJ 575*, 474–483.

Mera, D., G. Chabrier, & R. Schaeffer (1998, February). Towards a consistent model of the Galaxy. I. Kinematic properties, star counts and microlensing observations. *A&A 330*, 937–952.

Merlin, E., U. Buonomo, T. Grassi, L. Piovan, & C. Chiosi (2010, April). EvoL: the new Padova Tree-SPH parallel code for cosmological simulations. I. Basic code: gravity and hydrodynamics. *A&A 513*, A36.

Merlin, E. & C. Chiosi (2007, October). Simulating the formation and evolution of galaxies: multi-phase description of the interstellar medium, star formation, and energy feedback. *A&A 473*, 733–745.

Meyer, B. S. (2009, September). Oxygen Isotope Evolution in Interstellar Dust. *Meteoritics and Planetary Science Supplement 72*, 5340–+.

Michałowski, M. J., E. J. Murphy, J. Hjorth, D. Watson, C. Gall, & J. S. Dunlop (2010, November). Dust grain growth in the interstellar medium of 5 ¡ z ¡ 6.5 quasars. *A&A 522*, A15+.

Michałowski, M. J., D. Watson, & J. Hjorth (2010, April). Rapid Dust Production in Submillimeter Galaxies at z ¿ 4? *ApJ 712*, 942–950.

Mobasher, B., P. Capak, N. Z. Scoville, T. Dahlen, M. Salvato, H. Aussel, D. J. Thompson, R. Feldmann, L. Tasca, O. Le Fevre, S. Lilly, C. M. Carollo, J. S. Kartaltepe, H. McCracken, J. Mould, A. Renzini, D. B. Sanders, P. L. Shopbell, Y. Taniguchi, M. Ajiki, Y. Shioya, T. Contini, M. Giavalisco, O. Ilbert, A. Iovino, V. Le Brun, V. Mainieri, M. Mignoli, & M. Scodeggio (2007, September). Photometric Redshifts of Galaxies in COSMOS. *ApJS 172*, 117–131.

Morel, T. & K. Butler (2008, August). The neon content of nearby B-type stars and its implications for the solar model problem. *A&A 487*, 307–315.

Moro , D. & U. Munari (2000, December). The Asiago Database on Photometric Systems (ADPS). I. Census parameters for 167 photometric systems. *A&AS 147*, 361–628.

Mouhcine, M. (2002). Modelling of intermediate age stellar populations III. Effects of dust-shells around AGB stars. *A&A 394*, 125–135.

Myers, A. T., M. R. Krumholz, R. I. Klein, & C. F. McKee (2011, February). Metallicity and the Universality of the IMF. *ArXiv e-prints*.

Narayanan, D., A. Dey, C. C. Hayward, T. J. Cox, R. S. Bussmann, M. Brodwin, P. Jonsson, P. F. Hopkins, B. Groves, J. D. Younger, & L. Hernquist (2010, September). A physical model for z ˜ 2 dust-obscured galaxies. *MNRAS 407*, 1701–1720.

Neugebauer, G., H. J. Habing, R. van Duinen, H. H. Aumann, B. Baud, C. A. Beichman, D. A. Beintema, N. Boggess, P. E. Clegg, T. de Jong, J. P. Emerson, T. N. Gautier, F. C. Gillett, S. Harris, M. G. Hauser, J. R. Houck, R. E. Jennings, F. J. Low, P. L. Marsden, G. Miley, F. M. Olnon, S. R. Pottasch, E. Raimond, M. Rowan-Robinson, B. T. Soifer, R. G. Walker, P. R. Wesselius, & E. Young (1984, March). The Infrared Astronomical Satellite (IRAS) mission. *ApJ 278*, L1–L6.

Nieva, M. F. & N. Przybilla (2008a, August). Accurate Quantitative Spectroscopy of OB Stars: C and N abundances near the Main Sequence. In *Revista Mexicana de Astronomia y Astrofisica Conference Series*, Volume 33 of *Revista Mexicana de Astronomia y Astrofisica Conference Series*, pp. 35–37.

Nieva, M. F. & N. Przybilla (2008b, April). Carbon abundances of early B-type stars in the solar vicinity. Non-LTE line-formation for C II/III/IV and self-consistent atmospheric parameters. *A&A 481*, 199–216.

Nomoto, K., N. Tominaga, H. Umeda, C. Kobayashi, & K. Maeda (2006, October). Nucleosynthesis yields of core-collapse supernovae and hypernovae, and galactic chemical evolution. *Nuclear Physics A 777*, 424–458.

Nozawa, T., T. Kozasa, & A. Habe (2006, September). Dust Destruction in the High-Velocity Shocks Driven by Supernovae in the Early Universe. *ApJ 648*, 435–451.

Nozawa, T., T. Kozasa, A. Habe, E. Dwek, H. Umeda, N. Tominaga, K. Maeda, & K. Nomoto (2007, September). Evolution of Dust in Primordial Supernova Remnants: Can Dust Grains

Formed in the Ejecta Survive and Be Injected into the Early Interstellar Medium? *ApJ 666*, 955–966.

Nozawa, T., T. Kozasa, H. Umeda, H. Hirashita, K. Maeda, K. Nomoto, N. Tominaga, A. Habe, E. Dwek, T. T. Takeuchi, & T. T. Ishii (2008, December). Origin and Nature of Dust in the Early Universe. *ArXiv e-prints*.

Nozawa, T., T. Kozasa, H. Umeda, K. Maeda, & K. Nomoto (2003, December). Dust in the Early Universe: Dust Formation in the Ejecta of Population III Supernovae. *ApJ 598*, 785–803.

Oke, J. B. (1964, August). Photoelectric Spectrophotometry of Stars Suitable for Standards. *ApJ 140*, 689–+.

Olling, R. P. & M. R. Merrifield (2001, September). Luminous and dark matter in the Milky Way. *MNRAS 326*, 164–180.

Omont, A., P. Cox, F. Bertoldi, R. G. McMahon, C. Carilli, & K. G. Isaak (2001, August). A 1.2 mm MAMBO/IRAM-30 m survey of dust emission from the highest redshift PSS quasars. *A&A 374*, 371–381.

Onaka, T., I. Yamamura, T. Tanabe, T. L. Roellig, & L. Yuen (1996, October). Detection of the Mid-Infrared Unidentified Bands in the Diffuse Galactic Emission by IRTS. *PASJ 48*, L59–L63.

Ordal, M. A., R. J. Bell, R. W. Alexander, L. A. Newquist, & M. R. Querry (1988, March). Optical properties of Al, Fe, Ti, Ta, W, and Mo at submillimeter wavelengths. *Applied Optics 27*, 1203–1209.

Origlia, L., E. Valenti, & R. M. Rich (2005, February). High-resolution infrared spectra of NGC 6342 and 6528: two moderately reddened bulge globular clusters. *MNRAS 356*, 1276–1282.

Ostriker, J. P. & C. F. McKee (1988). *Rev. Mod. Phys. 60*, 1.

Pagel, B. E. J. (1997, October). *Nucleosynthesis and Chemical Evolution of Galaxies*. Nucleosynthesis and Chemical Evolution of Galaxies, by Bernard E. J. Pagel, pp. 392. ISBN 0521550610. Cambridge, UK: Cambridge University Press, October 1997.

Pégourié, B. (1988, April). Optical properties of alpha silicon carbide. *A&A 194*, 335–339.

Pei, Y. C. (1992, August). Interstellar dust from the Milky Way to the Magellanic Clouds. *ApJ 395*, 130–139.

Pence, W. (1976, January). K-corrections for galaxies of different morphological types. *ApJ 203*, 39–51.

Persson, S. E., M. Aaronson, J. G. Cohen, J. A. Frogel, & K. Matthews (1983, March). Photometric studies of composite stellar systems. V - Infrared photometry of star clusters in the Magellanic clouds. *ApJ 266*, 105–129.

Pessev, P. M., P. Goudfrooij, T. H. Puzia, & R. Chandar (2006, August). A Database of 2MASS Near-Infrared Colors of Magellanic Cloud Star Clusters. *AJ 132*, 781–800.

Pessev, P. M., P. Goudfrooij, T. H. Puzia, & R. Chandar (2008, April). A comparison of optical and near-infrared colours of Magellanic Cloud star clusters with predictions of simple stellar population models. *MNRAS 385*, 1535–1560.

Piersanti, L., O. Straniero, & S. Cristallo (2007, February). A method to derive the absolute composition of the Sun, the solar system, and the stars. *A&A 462*, 1051–1062.

Pietrinferni, A., S. Cassisi, M. Salaris, & F. Castelli (2004, September). A Large Stellar Evolution Database for Population Synthesis Studies. I. Scaled Solar Models and Isochrones. *ApJ 612*, 168–190.

Pietrinferni, A., S. Cassisi, M. Salaris, & F. Castelli (2006, May). A Large Stellar Evolution Database for Population Synthesis Studies. II. Stellar Models and Isochrones for an α-enhanced Metal Distribution. *ApJ 642*, 797–812.

Pietrzynski, G. & A. Udalski (2000, September). The Optical Gravitational Lensing Experiment. Ages of about 600 Star Clusters from the LMC. *50*, 337–354.

Piovan, L., C. Chiosi, E. Merlin, T. Grassi, R. Tantalo, U. Buonomo, & L. P. Cassarà (2011a, July). Formation and Evolution of the Dust in Galaxies. I. The Condensation Efficiencies. *ArXiv e-prints*.

Piovan, L., C. Chiosi, E. Merlin, T. Grassi, R. Tantalo, U. Buonomo, & L. P. Cassarà (2011b, July). Formation and Evolution of the Dust in Galaxies. II. The Solar Neighbourhood. *ArXiv e-prints*.

Piovan, L., C. Chiosi, E. Merlin, T. Grassi, R. Tantalo, U. Buonomo, & L. P. Cassarà (2011c, July). Formation and Evolution of the Dust in Galaxies. III. The Disk of the Milky Way. *ArXiv e-prints*.

Piovan, L., R. Tantalo, & C. Chiosi (2003, September). Shells of dust around AGB stars: Effects on the integrated spectrum of Single Stellar Populations. *A&A 408*, 559–579.

Piovan, L., R. Tantalo, & C. Chiosi (2006a, March). Modelling galaxy spectra in presence of interstellar dust - I. The model of interstellar medium and the library of dusty single stellar populations. *MNRAS 366*, 923–944.

Piovan, L., R. Tantalo, & C. Chiosi (2006b, August). Modelling galaxy spectra in presence of interstellar dust - II. From the ultraviolet to the far-infrared. *MNRAS 370*, 1454–1478.

Pipino, A., X. L. Fan, F. Matteucci, F. Calura, L. Silva, G. Granato, & R. Maiolino (2011, January). The chemical evolution of elliptical galaxies with stellar and QSO dust production. *A&A 525*, A61.

Popescu, C. C., R. J. Tuffs, M. A. Dopita, J. Fischera, N. D. Kylafis, & B. F. Madore (2011, March). Modelling the spectral energy distribution of galaxies. V. The dust and PAH emission SEDs of disk galaxies. *A&A 527*, A109+.

Portinari, L. & C. Chiosi (1999, October). On star formation and chemical evolution in the Galactic disc. *A&A 350*, 827–839.

Portinari, L. & C. Chiosi (2000, March). On radial gas flows, the Galactic Bar and chemical evolution in the Galactic Disc. *A&A 355*, 929–948.

Portinari, L., C. Chiosi, & A. Bressan (1998, June). Galactic chemical enrichment with new metallicity dependent stellar yields. *A&A 334*, 505–539.

Portinari, L., A. Moretti, C. Chiosi, & J. Sommer-Larsen (2004, April). Can a "Standard" Initial Mass Function Explain the Metal Enrichment in Clusters of Galaxies? *ApJ 604*, 579–595.

Portinari, L., J. Sommer-Larsen, & R. Tantalo (2004a, January). On the mass-to-light ratio and the initial mass function in disc galaxies. *MNRAS 347*, 691.

Portinari, L., J. Sommer-Larsen, & R. Tantalo (2004b, January). On the mass-to-light ratio and the initial mass function in disc galaxies. *MNRAS 347*, 691–719.

Prantzos, N. & S. Boissier (2000, April). Chemo-spectrophotometric evolution of spiral galaxies - III. Abundance and colour gradients in discs. *MNRAS 313*, 338–346.

Prantzos, N. & J. Silk (1998, November). Star Formation and Chemical Evolution in the Milky Way: Cosmological Implications. *ApJ 507*, 229–240.

Press, W. H., S. A. Teukolsky, W. T. Vetterling, & B. P. Flannery (1992). *Numerical recipes in FORTRAN. The art of scientific computing*.

Pretto, T. (2002). Master's thesis, University of Padova, Italy.

Przybilla, N., M. Nieva, & K. Butler (2008, December). A Cosmic Abundance Standard: Chemical Homogeneity of the Solar Neighborhood and the ISM Dust-Phase Composition. *ApJ 688*, L103–L106.

Puget, J. L., A. Leger, & F. Boulanger (1985, January). Contribution of large polycyclic aromatic molecules to the infrared emission of the interstellar medium. *A&A 142*, L19–L22.

Puzia, T. H., B. Mobasher, & P. Goudfrooij (2007, October). Evidence for the Evolution of Young Early-Type Galaxies in the GOODS/CDF-S Field. *AJ 134*, 1337–1347.

Puzia, T. H., S. E. Zepf, M. Kissler-Patig, M. Hilker, D. Minniti, & P. Goudfrooij (2002, August). Extragalactic globular clusters in the near-infrared. II. The globular clusters systems of NGC 3115 and NGC 4365. *A&A 391*, 453–470.

Quirk, W. J. & B. M. Tinsley (1973, January). Star Formation and Evolution in Spiral Galaxies. *ApJ 179*, 69–84.

Racine, R. (1991, March). Globular clusters in the halo of M31. *AJ 101*, 865–872.

Ramírez, I., C. Allende Prieto, & D. L. Lambert (2007, April). Oxygen abundances in nearby stars. Clues to the formation and evolution of the Galactic disk. *A&A 465*, 271–289.

Rana, N. C. (1991). Chemical evolution of the Galaxy. *ARA&A 29*, 129–162.

Reddy, B. E., J. Tomkin, D. L. Lambert, & C. Allende Prieto (2003, March). The chemical compositions of Galactic disc F and G dwarfs. *MNRAS 340*, 304–340.

Reimers, D. (1975). Circumstellar absorption lines and mass loss from red giants. *Memoires of the Societe Royale des Sciences de Liege 8*, 369–382.

Renzini, A. & A. Buzzoni (1986). Global properties of stellar populations and the spectral evolution of galaxies. In C. Chiosi & A. Renzini (Ed.), *Spectral Evolution of Galaxies*, Volume 122 of *Astrophysics and Space Science Library*, pp. 195–231.

Reynolds, S. P., K. J. Borkowski, U. Hwang, J. P. Hughes, C. Badenes, J. M. Laming, & J. M. Blondin (2007, October). A Deep Chandra Observation of Kepler's Supernova Remnant: A Type Ia Event with Circumstellar Interaction. *ApJ 668*, L135–L138.

Rho, J., T. Kozasa, W. T. Reach, J. D. Smith, L. Rudnick, T. DeLaney, J. A. Ennis, H. Gomez, & A. Tappe (2008, January). Freshly Formed Dust in the Cassiopeia A Supernova Remnant as Revealed by the Spitzer Space Telescope. *ApJ 673*, 271–282.

Rho, J., W. T. Reach, A. Tappe, U. Hwang, J. D. Slavin, T. Kozasa, & L. Dunne (2009, July). Spitzer Observations of the Young Core-Collapse Supernova Remnant 1E0102-72.3: Infrared Ejecta Emission and Dust Formation. *ApJ 700*, 579–596.

Rho, J., W. T. Reach, A. Tappe, L. Rudnick, T. Kozasa, U. Hwang, M. Andersen, H. Gomez, T. DeLaney, L. Dunne, & J. Slavin (2009, January). Dust Formation Observed in Young Supernova Remnants with Spitzer. *ArXiv:astro-ph/0901.1699*.

Rich, R. M. (1990). *ApJ 362*, 604.

Roberts, M. S. & M. P. Haynes (1994). Physical Parameters along the Hubble Sequence. *ARA&A 32*, 115–152.

Roberts, W. W. (1969, October). Large-Scale Shock Formation in Spiral Galaxies and its Implications on Star Formation. *ApJ 158*, 123–+.

Robson, I., R. S. Priddey, K. G. Isaak, & R. G. McMahon (2004, June). Submillimetre observations of z ¿ 6 quasars. *MNRAS 351*, L29–L33.

Rolleston, W. R. J., S. J. Smartt, P. L. Dufton, & R. S. I. Ryans (2000, November). The Galactic metallicity gradient. *A&A 363*, 537–554.

Romano, D., F. Matteucci, P. Salucci, & C. Chiappini (2000, August). The Mass Surface Density in the Local Disk and the Chemical Evolution of the Galaxy. *ApJ 539*, 235–240.

Rowan-Robinson, M. (1980, November). Radiative transfer in dust clouds. I - Hot-centered clouds associated with regions of massive star formation. *ApJS 44*, 403–426.

Rowan-Robinson, M. & S. Harris (1982, July). Radiative transfer in dust clouds. II - Circumstellar dust shells around early M giants and supergiants. *MNRAS 200*, 197–215.

Rudolph, A. L., M. Fich, G. R. Bell, T. Norsen, J. P. Simpson, M. R. Haas, & E. F. Erickson (2007, January). Abundance gradients in the Galaxy (Rudolph+, 2006). *VizieR Online Data Catalog 216*, 20346.

Rybicki, G. B. & A. P. Lightman (1979). *Radiative processes in astrophysics*. New York, Wiley-Interscience, 1979. 393 p.

Sadler, E. M., R. M. Rich, & D. M. Terndrup (1996, July). K Giants in Baade's Window. II. The Abundance Distribution. *AJ 112*, 171.

Saglia, R. P., G. Bertin, & M. Stiavelli (1992). *ApJ 384*, 433.

Saito, M. (1979a). *PASJ 31*, 181.

Saito, M. (1979b). *PASJ 31*, 193.

Sakon, I., T. Onaka, T. Wada, Y. Ohyama, H. Kaneda, D. Ishihara, T. Tanabé, T. Minezaki, Y. Yoshii, N. Tominaga, K. Nomoto, & T. e. a. Nozawa (2009, February). Properties of Newly Formed Dust by SN 2006JC Based on Near- to Mid-Infrared Observation With AKARI. *ApJ 692*, 546–555.

Salpeter, E. E. (1955, January). The Luminosity Function and Stellar Evolution. *ApJ 121*, 161–+.

Sandage, A. (1986). *A&A 161*, 89.

Sandstrom, K. M., A. D. Bolatto, S. Stanimirović, J. T. van Loon, & J. D. T. Smith (2009, May). Measuring Dust Production in the Small Magellanic Cloud Core-Collapse Supernova Remnant 1E0102.27219. *ApJ 696*, 2138–2154.

Savage, B. D. & K. R. Sembach (1996). Interstellar Abundances from Absorption-Line Observations with the Hubble Space Telescope. *ARA&A 34*, 279–330.

Scalo, J. M. (1986, May). The stellar initial mass function. *Fund. Cosmic Phys. 11*, 1–278.

Schmelz, J. T., K. Nasraoui, J. K. Roames, L. A. Lippner, & J. W. Garst (2005, December). Neon Lights up a Controversy: The Solar Ne/O Abundance. *ApJ 634*, L197–L200.

Schmidt, M. (1959, March). The Rate of Star Formation. *ApJ 129*, 243.

Schneider, R., A. Ferrara, & R. Salvaterra (2004, July). Dust formation in very massive primordial supernovae. *MNRAS 351*, 1379–1386.

Schönberner, D. & M. Steffen (2007, November). On the Mass-Loss History at the Tip of the AGB. In F. Kerschbaum, C. Charbonnel, & R. F. Wing (Ed.), *Why Galaxies Care About AGB Stars: Their Importance as Actors and Probes*, Volume 378 of *Astronomical Society of the Pacific Conference Series*, pp. 343–+.

Schutte, W. A. & A. G. G. M. Tielens (1989, August). Theoretical studies of the infrared emission from circumstellar dust shells - The infrared characteristics of circumstellar silicates and the mass-loss rate of oxygen-rich late-type giants. *ApJ 343*, 369–392.

Scott, P. C., M. Asplund, N. Grevesse, & A. J. Sauval (2006, September). Line formation in solar granulation. VII. CO lines and the solar C and O isotopic abundances. *A&A 456*, 675–688.

Sellgren, K., M. W. Werner, & H. L. Dinerstein (1983, August). Extended near-infrared emission from visual reflection nebulae. *ApJ 271*, L13–L17.

Sestito, P., A. Bragaglia, S. Randich, R. Pallavicini, S. M. Andrievsky, & S. A. Korotin (2008, September). Open clusters as key tracers of Galactic chemical evolution. III. Element abundances in Berkeley 20, Berkeley 29, Collinder 261 and Melotte 66. *A&A 488*, 943–958.

Shapley, A., G. Fabbiano, & P. B. Eskridge (2001, November). A Multivariate Statistical Analysis of Spiral Galaxy Luminosities. I. Data and Results. *ApJS 137*, 139–199.

Shu, F. H., V. Milione, W. Gebel, C. Yuan, D. W. Goldsmith, & W. W. Roberts (1972, May). Galactic Shocks in an Interstellar Medium with Two Stable Phases. *ApJ 173*, 557–+.

Siebenmorgen, R. & E. Kruegel (1992, June). Dust model containing polycyclic aromatic hydrocarbons in various environments. *A&A 259*, 614–626.

Silva, L. (1999). *Modelling the SED Evolution of Dusty Galaxies and Applications*. Ph. D. thesis, SISSA.

Silva, L., G. L. Granato, A. Bressan, & L. Danese (1998, December). Modeling the Effects of Dust on Galactic Spectral Energy Distributions from the Ultraviolet to the Millimeter Band. *ApJ 509*, 103–117.

Sirianni, M., M. J. Jee, N. Benítez, J. P. Blakeslee, A. R. Martel, G. Meurer, M. Clampin, G. De Marchi, H. C. Ford, R. Gilliland, G. F. Hartig, G. D. Illingworth, J. Mack, & W. J. McCann (2005, October). The Photometric Performance and Calibration of the Hubble Space Telescope Advanced Camera for Surveys. *PASP 117*, 1049–1112.

Smartt, S. J. & W. R. J. Rolleston (1997, May). The Galactic Oxygen Abundance Gradient. *ApJ 481*, L47.

Smartt, S. J., K. A. Venn, P. L. Dufton, D. J. Lennon, W. R. J. rolleston, & F. P. Keenan (2001, February). Chemical abundances of 5 Galactic disk B stars (Smartt+, 2001). *VizieR Online Data Catalog 336*, 70086.

Sommer-Larsen, J. (1996, January). On the Star Formation Rate, Initial Mass Function, and Hubble Type of Disk Galaxies and the Age of the Universe. *ApJ 457*, 118.

Soubiran, C. & P. Girard (2005, July). Abundance trends in kinematical groups of the Milky Way's disk. *A&A 438*, 139–151.

Springel, V., T. Di Matteo, & L. Hernquist (2005, February). Black Holes in Galaxy Mergers: The Formation of Red Elliptical Galaxies. *ApJ 620*, L79–L82.

Stanek, K. Z. & P. M. Garnavich (1998, August). Distance to M31 with the Hubble Space Telescope and HIPPARCOS Red Clump Stars. *ApJ 503*, L131.

Stanimirović, S., A. D. Bolatto, K. Sandstrom, A. K. Leroy, J. D. Simon, B. M. Gaensler, R. Y. Shah, & J. M. Jackson (2005, October). Spitzer Space Telescope Detection of the Young Supernova Remnant 1E 0102.2-7219. *ApJ 632*, L103–L106.

Steffen, M. (1990, November). A Simple Method for Monotonic Interpolation in One Dimension. *A&A 239*, 443.

Sugerman, B. E. K., B. Ercolano, M. J. Barlow, A. G. G. M. Tielens, G. C. Clayton, A. A. Zijlstra, M. Meixner, A. Speck, T. M. Gledhill, N. Panagia, M. Cohen, K. D. Gordon, M. Meyer, J. Fabbri, J. E. Bowey, D. L. Welch, M. W. Regan, & R. C. Kennicutt (2006, July). Massive-Star Supernovae as Major Dust Factories. *313*, 196–200.

Suh, K.-W. (1999, April). Optical properties of the silicate dust grains in the envelopes around asymptotic giant branch stars. *MNRAS 304*, 389–405.

Suh, K. W. (2000, July). Optical properties of the carbon dust grains in the envelopes around asymptotic giant branch stars. *MNRAS 315*, 740–750.

Suh, K. W. (2002, May). Crystalline silicates in the envelopes and discs around oxygen-rich asymptotic giant branch stars. *MNRAS 332*, 513.

Tafalla, M., P. C. Myers, P. Caselli, C. M. Walmsley, & C. Comito (2002, April). Systematic Molecular Differentiation in Starless Cores. *ApJ 569*, 815–835.

Takeuchi, T. T., V. Buat, S. Heinis, E. Giovannoli, F.-T. Yuan, J. Iglesias-Páramo, K. L. Murata, & D. Burgarella (2010, May). Star formation and dust extinction properties of local galaxies from the AKARI-GALEX all-sky surveys . First results from the most secure multiband sample from the far-ultraviolet to the far-infrared. *A&A 514*, A4.

Talbot, R. J. & W. D. Arnett (1971, December). The Evolution of Galaxies. I. Formulation and Mathematical Behavior of the One-Zone Model. *ApJ 170*, 409.

Talbot, Jr., R. J. (1975, September). Evolution of Spiral Galaxies. In *Bulletin of the American Astronomical Society*, Volume 7 of *Bulletin of the American Astronomical Society*, pp. 550–+.

Tammann, G. A., W. Loeffler, & A. Schroeder (1994, June). The Galactic supernova rate. *ApJS 92*, 487–493.

Tanaka, M., T. Matsumoto, H. Murakami, M. Kawada, M. Noda, & S. Matsuura (1996, October). IRTS Observation of the Unidentified 3.3-Micron Band in the Diffuse Galactic Emission. *PASJ 48*, L53–L57.

Tantalo, R., S. Chinellato, E. Merlin, L. Piovan, & C. Chiosi (2010, July). Formation and evolution of early-type galaxies: spectro-photometry from cosmo-chemo-dynamical simulations. *A&A 518*, A43+.

Tantalo, R., C. Chiosi, A. Bressan, & F. Fagotto (1996, July). Spectro-photometric evolution of elliptical galaxies. II. Models with infall. *A&A 311*, 361–383.

Tantalo, R., C. Chiosi, A. Bressan, P. Marigo, & L. Portinari (1998, July). Spectro-photometric evolution of elliptical galaxies. III. Infall models with gradients in mass density and star formation. *A&A 335*, 823–846.

Tiede, G. P., J. A. Frogel, & D. M. Terndrup (1995, March). Deep JHK Photometry and the Infrared Luminosity Function of the Galactic Bulge. In *American Astronomical Society Meeting Abstracts #186*, Volume 27 of *Bulletin of the American Astronomical Society*, pp. 884.

Tielens, A. G. G. M. (1990). Towards a circumstellar silicate mineralogy. In M. O. Mennessier & A. Omont (Ed.), *From Miras to Planetary Nebulae: Which Path for Stellar Evolution?*, pp. 186–200.

Tielens, A. G. G. M. (2005, September). *The Physics and Chemistry of the Interstellar Medium*.

Timmes, F. X., S. E. Woosley, & T. A. Weaver (1995, June). Galactic chemical evolution: Hydrogen through zinc. *apjs 98*, 617–658.

Tinsley, B. M. (1980a). *ApJ 5*, 287.

Tinsley, B. M. (1980b). *ApJ 241*, 41.

Todini, P. & A. Ferrara (2001, August). Dust formation in primordial Type II supernovae. *MNRAS 325*, 726–736.

Tominaga, N., H. Umeda, & K. Nomoto (2007, May). Supernova Nucleosynthesis in Population III 13-50 $M_\odot$ Stars and Abundance Patterns of Extremely Metal-poor Stars. *ApJ 660*, 516–540.

Turck-Chièze, S., S. Couvidat, L. Piau, J. Ferguson, P. Lambert, J. Ballot, R. A. García, & P. Nghiem (2004, November). Surprising Sun: A New Step Towards a Complete Picture? *Physical Review Letters 93*(21), 211102–+.

Turck-Chièze, S., P. A. Phi Nghiem, & S. Mathis (2008, October). Solar structure models. *Journal of Physics Conference Series 118*(1), 012030–+.

Turcotte, S. & R. F. Wimmer-Schweingruber (2002, December). Possible in situ tests of the evolution of elemental and isotopic abundances in the solar convection zone. *Journal of Geophysical Research (Space Physics) 107*, 1442–+.

Twarog, B. A., K. M. Ashman, & B. J. Anthony-Twarog (1997, December). Some Revised Observational Constraints on the Formation and Evolution of the Galactic Disk. *AJ 114*, 2556–+.

Umeda, H. & K. Nomoto (2002, January). Nucleosynthesis of Zinc and Iron Peak Elements in Population III Type II Supernovae: Comparison with Abundances of Very Metal Poor Halo Stars. *ApJ 565*, 385–404.

Valiante, R., R. Schneider, S. Bianchi, & A. C. Andersen (2009, August). Stellar sources of dust in the high-redshift Universe. *MNRAS 397*, 1661–1671.

Valiante, R., R. Schneider, S. Salvadori, & S. Bianchi (2011, June). The origin of dust in high redshift QSOs: the case of SDSS J1148+5251. *ArXiv e-prints*.

van den Bergh, S. (1981, October). UBV observations of globular clusters in the Magellanic Clouds. *A&AS 46*, 79–87.

van den Bergh, S. & G. L. Hagen (1968). UBV Photometry of Star Clusters in the Magellanic Clouds. *Astronomical Journal, Vol. 73, p. 206 73*, 206.

van den Hoek, L. B. & M. A. T. Groenewegen (1997, June). New theoretical yields of intermediate mass stars. *A&A 123*, 305–328.

van Dishoeck, E. F. & J. H. Black (1988, November). The photodissociation and chemistry of interstellar CO. *ApJ 334*, 771–802.

van Dishoeck, E. F. & G. A. Blake (1998). Chemical Evolution of Star-Forming Regions. *ARA&A 36*, 317–368.

van Dishoeck, E. F., G. A. Blake, B. T. Draine, & J. I. Lunine (1993). The chemical evolution of protostellar and protoplanetary matter. In E. H. Levy & J. I. Lunine (Ed.), *Protostars and Planets III*, pp. 163–241.

van Loon, J. T., M. Cioni, A. A. Zijlstra, & C. Loup (2005, July). An empirical formula for the mass-loss rates of dust-enshrouded red supergiants and oxygen-rich Asymptotic Giant Branch stars. *A&A 438*, 273–289.

van Loon, J. T., I. McDonald, J. M. Oliveira, A. Evans, M. L. Boyer, R. D. Gehrz, E. Polomski, & C. E. Woodward (2006, April). The first 8-13 μm spectra of globular cluster red giants: circumstellar silicate dust grains in 47 Tucanae (NGC 104). *A&A 450*, 339–343.

Vassiliadis, E. & P. R. Wood (1993, August). Evolution of low- and intermediate-mass stars to the end of the asymptotic giant branch with mass loss. *ApJ 413*, 641–657.

Venn, K. A., M. Irwin, M. D. Shetrone, C. A. Tout, V. Hill, & E. Tolstoy (2004, September). Stellar Chemical Signatures and Hierarchical Galaxy Formation. *AJ 128*, 1177–1195.

Ventura, P., F. D'Antona, & I. Mazzitelli (2002, October). Yields from low metallicity, intermediate mass AGB stars:. Their role for the CNO and lithium abundances in Globular Cluster stars. *A&A 393*, 215–223.

Ventura, P. & P. Marigo (2009, October). Evolution and chemical yields of AGB stars: effects of low-temperature opacities. *MNRAS 399*, L54–L58.

Visser, R., E. F. van Dishoeck, & J. H. Black (2009, August). The photodissociation and chemistry of CO isotopologues: applications to interstellar clouds and circumstellar disks. *A&A 503*, 323–343.

Wachter, A., K.-P. Schröder, J. M. Winters, T. U. Arndt, & E. Sedlmayr (2002, March). An improved mass-loss description for dust-driven superwinds and tip-AGB evolution models. *A&A 384*, 452–459.

Wagenhuber, J. & M. A. T. Groenewegen (1998, December). New input data for synthetic AGB evolution. *A&A 340*, 183–195.

Walmsley, C. M., D. R. Flower, & G. Pineau des Forêts (2004, May). Complete depletion in prestellar cores. *A&A 418*, 1035–1043.

Wang, B. & J. Silk (1994, June). Gravitational instability and disk star formation. *ApJ 427*, 759–769.

Wang, R., C. L. Carilli, J. Wagg, F. Bertoldi, F. Walter, K. M. Menten, A. Omont, P. Cox, M. A. Strauss, X. Fan, L. Jiang, & D. P. Schneider (2008, November). Thermal Emission from Warm Dust in the Most Distant Quasars. *ApJ 687*, 848–858.

Wang, R., J. Wagg, C. L. Carilli, D. J. Benford, C. D. Dowell, F. Bertoldi, F. Walter, K. M. Menten, A. Omont, P. Cox, M. A. Strauss, X. Fan, & L. Jiang (2008, April). SHARC-II 350 μm Observations of Thermal Emission from Warm Dust in z ¿ 5 Quasars. *AJ 135*, 1201–1206.

Waters, L. B. F. M. & F. G. Molster (1999). Crystalline silicates in AGB and post-AGB stars. In *IAU Symp. 191: Asymptotic Giant Branch Stars*, Volume 191, pp. 209.

Waters, L. B. F. M., F. J. Molster, T. de Jong, D. A. Beintema, C. Waelkens, A. C. A. Boogert, D. R. Boxhoorn, T. de Graauw, S. Drapatz, H. Feuchtgruber, R. Genzel, F. P. Helmich, A. M. Heras, R. Huygen, H. Izumiura, K. Justtanont, D. J. M. Kester, D. Kunze, F. Lahuis, H. J. G. L. M. Lamers, K. J. Leech, C. Loup, D. Lutz, P. W. Morris, S. D. Price, P. R. Roelfsema, A. Salama, S. G. Schaeidt, A. G. G. M. Tielens, N. R. Trams, E. A. Valentijn, B. Vandenbussche, M. E. van den Ancker, E. F. van Dishoeck, H. Van Winckel, P. R. Wesselius, & E. T. Young (1996, November). Mineralogy of oxygen-rich dust shells. *A&A 315*, L361–L364.

Weingartner, J. C. & B. T. Draine (2001a, February). Dust Grain-Size Distributions and Extinction in the Milky Way, Large Magellanic Cloud, and Small Magellanic Cloud. *ApJ 548*, 296–309.

Weingartner, J. C. & B. T. Draine (2001b, December). Electron-Ion Recombination on Grains and Polycyclic Aromatic Hydrocarbons. *ApJ 563*, 842–852.

Weingartner, J. C. & B. T. Draine (2001c, June). Photoelectric Emission from Interstellar Dust: Grain Charging and Gas Heating. *ApJS 134*, 263–281.

Weiss, A. & J. W. Ferguson (2009, December). New asymptotic giant branch models for a range of metallicities. *A&A 508*, 1343–1358.

Weiss, A. & H. Schlattl (2008, August). GARSTEC. The Garching Stellar Evolution Code. The direct descendant of the legendary Kippenhahn code. *Ap&SS 316*, 99–106.

Werner, M. W., T. L. Roellig, F. J. Low, G. H. Rieke, M. Rieke, W. F. Hoffmann, E. Young, J. R. Houck, B. Brandl, G. G. Fazio, J. L. Hora, R. D. Gehrz, G. Helou, B. T. Soifer, J. Stauffer, J. Keene, P. Eisenhardt, D. Gallagher, T. N. Gautier, W. Irace, C. R. Lawrence, L. Simmons, J. E. Van Cleve, M. Jura, E. L. Wright, & D. P. Cruikshank (2004, September). The Spitzer Space Telescope Mission. *ApJS 154*, 1–9.

Whitford, A. E. & R. M. Rich (1983, November). Metal content of K giants in the nuclear bulge of the galaxy. *ApJ 274*, 723–732.

Whittet, D. C. B. (Ed.) (2003). *Dust in the galactic environment*.

Whittet, D. C. B. (2010, February). Oxygen Depletion in the Interstellar Medium: Implications for Grain Models and the Distribution of Elemental Oxygen. *ApJ 710*, 1009–1016.

Wilson, T. L. & W. Batrla (2005, February). An alternate estimate of the mass of dust in Cassiopeia A. *A&A 430*, 561–566.

Wise, M. W. & D. R. Silva (1996, April). The Effects of Dust on Broadband Color Gradients in Elliptical Galaxies. *ApJ 461*, 155.

Witt, A. N., H. A. Thronson, & J. M. Capuano (1992, July). Dust and the transfer of stellar radiation within galaxies. *ApJ 393*, 611–630.

Woosley, S. E. & T. A. Weaver (1995). *ApJS 101*, 181.

Wyse, R. F. G. & J. Silk (1989, April). Star formation rates and abundance gradients in disk galaxies. *ApJ 339*, 700–711.

Xia, L., X. Zhou, J. Ma, H. Wu, W.-H. Sun, Z. Jiang, S. Xue, J. Chen, & W. Chen (2002, December). Photometric Redshift Determination with the BATC Multicolor System. *PASP 114*, 1349–1358.

Yamasawa, D., A. Habe, T. Kozasa, T. Nozawa, H. Hirashita, H. Umeda, & K. Nomoto (2011, July). The Role of Dust in the Early Universe. I. Protogalaxy Evolution. *ApJ 735*, 44.

Yan, H., D. Burstein, X. Fan, Z. Zheng, J. Chen, Y.-I. Byun, R. Chen, W.-p. Chen, L. Deng, Z. Deng, L. Z. Fang, J. J. Hester, Z. Jiang, Y. Li, W. Lin, P. Lu, Z. Shang, H. Su, W.-h. Sun, W.-s. Tsay, R. A. Windhorst, H. Wu, X. Xia, W. Xu, S. Xue, Z. Zheng, J. Zhu, & Z. Zou (2000, May). Calibration of the BATC Survey: Methodology and Accuracy. *PASP 112*, 691–702.

Yin, J., J. L. Hou, N. Prantzos, S. Boissier, R. X. Chang, S. Y. Shen, & B. Zhang (2009, October). Milky Way versus Andromeda: a tale of two disks. *A&A 505*, 497–508.

Yong, D., B. W. Carney, & M. L. Teixera de Almeida (2005, August). Elemental Abundance Ratios in Stars of the Outer Galactic Disk. I. Open Clusters. *AJ 130*, 597–625.

Yong, D., B. W. Carney, M. L. Teixera de Almeida, & B. L. Pohl (2006, April). Elemental Abundance Ratios in Stars of the Outer Galactic Disk. III. Cepheids. *AJ 131*, 2256–2273.

Young, P. (2006, February). The Progenitor of Cas A. In *KITP Conference: Supernova and Gamma-Ray Burst Remnants*.

Zhukovska, S. & H.-P. Gail (2009, December). Modeling of Dust Evolution in the Interstellar Medium. In T. Henning, E. Grün, & J. Steinacker (Ed.), *Cosmic Dust - Near and Far*, Volume 414 of *Astronomical Society of the Pacific Conference Series*, pp. 199.

Zhukovska, S., H.-P. Gail, & M. Trieloff (2008, February). Evolution of interstellar dust and stardust in the solar neighbourhood. *A&A 479*, 453–480.

Zoccali, M., A. Renzini, S. Ortolani, L. Greggio, I. Saviane, S. Cassisi, M. Rejkuba, B. Barbuy, R. M. Rich, & E. Bica (2003, March). Age and metallicity distribution of the Galactic bulge from extensive optical and near-IR stellar photometry. *A&A 399*, 931–956.